

Characterizing accretion phenomena on planetary-mass objects

Dorian Demars

▶ **To cite this version:**

Dorian Demars. Characterizing accretion phenomena on planetary-mass objects. Astrophysics [astro-ph]. Université Grenoble Alpes [2020-..], 2024. English. ⟨NNT : 2024GRALY047⟩. ⟨tel-04972671⟩

HAL Id: tel-04972671

https://theses.hal.science/tel-04972671v1

Submitted on 1 Mar 2025

HAL is a multi-disciplinary open access archive for the deposit and dissemination of scientific research documents, whether they are published or not. The documents may come from teaching and research institutions in France or abroad, or from public or private research centers.

L'archive ouverte pluridisciplinaire **HAL**, est destinée au dépôt et à la diffusion de documents scientifiques de niveau recherche, publiés ou non, émanant des établissements d'enseignement et de recherche français ou étrangers, des laboratoires publics ou privés.



HAL Authorization

THÈSE

Pour obtenir le grade de

DOCTEUR DE L'UNIVERSITÉ GRENOBLE ALPES

École doctorale : PHYS - Physique
Spécialité : Astrophysique et Milieux Dilués
Unité de recherche : Institut de Planetologie et d'Astrophysique de Grenoble

Caractérisation des phénomènes d'accrétion sur les objets de masse planétaire

Characterizing accretion phenomena on planetary-mass objects

Présentée par :

Dorian DEMARS

Direction de thèse :

Catherine DOUGADOS DIRECTRICE DE RECHERCHE, CNRS DELEGATION ALPES	Directrice de thèse
Mickaël BONNEFOY CHARGE DE RECHERCHE, CNRS DELEGATION ALPES	Co-encadrant de thèse

Rapporteurs :

AMELIA BAYO
ASTRONOME ADJOINTE, ESO EUROPEAN SOUTHERN OBSERVATORY
CLEMENT BARUTEAU
CHARGE DE RECHERCHE HDR, CNRS DELEGATION OCCITANIE OUEST

Thèse soutenue publiquement le **9 octobre 2024**, devant le jury composé de :

JONATHAN FERREIRA, PROFESSEUR DES UNIVERSITES, UNIVERSITE GRENOBLE ALPES	Président
AMELIA BAYO, ASTRONOME ADJOINTE, ESO EUROPEAN SOUTHERN OBSERVATORY	Rapporteure
CLEMENT BARUTEAU, CHARGE DE RECHERCHE HDR, CNRS DELEGATION OCCITANIE OUEST	Rapporteur
ANTHONY BOCCALETTI, DIRECTEUR DE RECHERCHE, CNRS ILE-DE-FRANCE MEUDON	Examinateur
MAGALI DELEUIL, PROFESSEURE DES UNIVERSITES, AIX-MARSEILLE UNIVERSITE	Examinatrice

Acknowledgements

Ce manuscrit est l'aboutissement de trois années de thèse à Grenoble. Bien que j'en sois la seule plume, un grand nombre de personnes y ont contribué, que ce soit scientifiquement ou humainement. Je souhaite les remercier et leur faire honneur en ces lignes.

Je tiens à remercier mes deux directeurs et encadrants de thèse, Mickaël et Catherine, sans qui cette thèse n'aurait jamais vu le jour. Trop de doctorants sont délaissés par leurs encadrants, et j'ai eu la chance d'avoir deux encadrants aux antipodes de cette situation, qui ont su être impliqués comme tout doctorant l'aurait rêvé. Merci d'avoir su me conseiller et me guider, d'avoir pris le temps de m'écouter. Merci beaucoup d'avoir supporté mon caractère pendant ces trois années et de m'avoir tenu tête, tout comme je l'ai aussi souvent fait. Merci de m'avoir donné la chance de découvrir le monde de l'astronomie.

Bien que cette thèse ait débuté en octobre 2021, elle fait partie d'un parcours qui a débuté dès ma plus petite enfance. Elle est le fruit du soutien indéfectible de famille. Merci à mes parents, Maman et Papa, ma sœur, Laura, de m'avoir soutenu et épaulé, que ce soit durant mon enfance ou par la suite dans une autre ville. Merci de m'avoir permis d'arriver au bout ces longues années d'université. Merci de m'avoir toujours accueilli avec un plat de lasagnes, de poisson, et un digestif. Je tiens à remercier le dernier arrivé dans la famille, Raikou, mon fidèle compagnon de jeu quadrupède, toujours prêt à grogner sur un chat ou quémander une saucisse. Merci également à mes oncles et tantes, cousins et cousines, pour ces repas partagés à Noël, ces raviolis, et ces moments passés. Enfin, une pensée pour Mamie, partie alors que j'écrivais ces lignes.

Cette thèse m'a permis de faire des rencontres des personnes qui ont eu une grande importance pour son déroulement, aussi bien à l'IPAG qu'en mission. Je tiens à mentionner Gabriel Marleau, avec qui j'ai pu avoir de longs échanges scientifiques, et qui m'a également prodigué de nombreux conseils dans tout le processus d'écriture d'articles. I also want to thank Markus, Simon and Gayathri, for having me in Stockholm for a week. Merci également à Philippe Delorme, qui m'a permis de découvrir le contact avec le public et l'astronomie amateur, grâce à qui j'ai également pu m'essayer à l'astrophotographie. Je tiens aussi à remercier les membres de mon CSI, Gaël Chauvin et Geoffroy Lesur, qui ont su guider aussi bien la trajectoire de ma thèse, que mes encadrants. Enfin, je souhaite mentionner l'équipe administrative de l'IPAG, sans qui le laboratoire aurait bien du mal à fonctionner.

À l'IPAG, et pendant mes dernières années d'étude, j'ai pu côtoyer nombre de doctorants qui sont devenus des amis, certains très proches. Maxime G. et Thibault, qui m'ont accueilli en début de thèse, puis tout au long de ces trois années, que ce soit pour un repas, une session de jeux de société, un thé, un tour à vélo, ou bien tant d'autres. Julien et Maxime P., mes deux Bébouwus, qui m'ont traîné de force à l'escalade, jusqu'à ce que je les y traîne moi-même, qui m'ont permis d'avoir une superbe chaise de bureau, aussi déménageurs de matelas. Alice et Thomas B., Jean-Michel, Victor, pour tous ces moments passés au Batour, toujours synonyme de havre de paix pour tous les présents, ainsi que nos moments musicaux à la Bobine, ces bières et sessions de jeux. Lucie, ma conductrice attirée pour toutes ces sorties ski, Thomas J. et Antoine J., qui m'ont sorti du lit pour aller skier, et m'y ont fait découvrir les joies de la poudre. Célia, toujours le sourire

aux lèvres, boule de bonne humeur à l'IPAG. Léopold, Simon et Tituan, avec qui j'ai longuement pu discuter musique, compagnons de concerts. Vittoria, membro emerito del comitato organizzatore del Coffee Break, en collaboration avec Benjamin. Marc, pewpewteur et mineur de toute heure. Filip, also pewpewter but always ready for a beer. Valentin, qui a partagé mon bureau et m'a aidé à (presque) relancer le Frigotts. Et tous les doctorants qui m'ont accompagnés, que je ne saurais oublier.

À Grenoble ou Avignon, j'ai pu rencontrer des personnes qui me sont chères, qui ont pu écouter mes déboires de doctorant. Yoann, ami d'enfance et inépuisable compagnon de jeu. Fabian, malgré nos différents occasionnels. Pierre-Francois, dont je me plains autant que j'apprécie sa compagnie. Arthur, ami d'enfance. Daminou et Swann, partenaires de concerts. Anissa, et son goût pour le sucre au thé, maintenant grimpeuse hors pair. Georges, qui m'a fait découvrir la beauté d'un ciel sans pollution. Sandy, Théo, Audrey, Sylvain, Lucas, Joseph, Emrick, Kévin, Claire, Laura, Fil, et toute l'équipe du nouvel an, à ces superbes Murder Party. Margaux/Mickey, Loic/Shinji, Robinou, Vincent, Joris, Neca, Balbu, et toute l'équipe WhatZePhoque.

Enfin, une mention spéciale pour mes voisins, avec qui j'ai pu établir une relation de confiance saine, rythmée de nombreux échanges musicaux qui m'auront bercé tout au long de ces trois années.

Abstract

With over 5000 confirmed exoplanets, the details of their formation mechanisms are still a mystery. Exoplanets are thought to form within the protoplanetary-disk of stars, either through slow growth of rocky cores, or by gravitational collapse of clumps. Planets typically accrete part of their mass directly from the protoplanetary-disk, but the exact mechanisms are not constrained yet. The discovery of the accreting planets PDS 70b&c, orbiting within the protoplanetary-disk of their host stars, provide a unique opportunity to directly study the accretion processes. Recent discoveries of similar class objects, Planetary-Mass Companions, add onto the sample of known accreting planets.

In this thesis, I present the results of 2 monitoring surveys of the accretion lines of young Planetary-Mass Companions: with VLT/SINFONI in the Near-Infrared, targeting the Pa_β line of two companions (GQ Lup b and GSC 06214-00210 b), and with VLT/UVES in the Visible/UV, targeting the Balmer and Helium lines of three other companions (Delorme 1 (AB)b, SR 12 c and 2MASS J11151597). Both provide constraints on the variability amplitudes of their respective lines, which are reminiscent of that found on T Tauri stars. With VLT/UVES, the high spectral resolution ($R \sim 50\,000$) provides access to the detailed lines profiles, while VLT/SINFONI only provides partly resolved lines ($R \sim 2\,000$), against which emission lines models can be tested. Magnetospheric accretion models are preferred for GQ Lup b and part of the lines of GSC 06214-00210 b, while shock-emission models are preferred for GSC 06214-00210 b. Other targets are not fully constrained.

This study provides the first sample study of emission lines from accreting Planetary-Mass Companions. This opens up for future observations, enriching the current sample, and future instrumentation which will permit a detailed study of accretion lines on inner-separation companions.

Summary

Today, over 5000 exoplanets have been confirmed. However, the details of their formation mechanisms is still to be unveiled. Planets typically form in the protoplanetary-disk of their host star, either through core-accretion or gravitational instability. While the former consists in slow growth of a rocky core, the latter requires clumps of gas to collapse in the protoplanetary disk. Once planets are formed, they typically migrate inwards or outwards, or are ejected from the disk through gravitational interactions.

Planets typically accrete part of their mass directly from the surrounding protoplanetary-disk. The details of these accretion mechanisms will dictate part of the planet's evolution, depending on how much energy is radiated away from the accretion shock. However, the mechanisms are not yet fully constrained, in part because of the difficulty of studying forming or accreting planets. This changed with the discovery of PDS 70b&c, two planets-like objects, embedded in the protoplanetary-disk of their host star, and that are actively accreting. This class of more massive objects are called Planetary-Mass Companions (PMCs) and may serve as proxy for the study of their inner separations counterparts. This is the subject of my thesis: Characterizing accretion phenomena on planetary-mass objects.

Accretion processes are studied through the related emission lines. Accretion always comes with a shock that heats up material, triggering lines emission. However, a competing scenario proposes an alternative explanation for the emission lines: they may be emitted in magnetospherically induced funnels, alike what is happening on stars. These two scenarios are not mutually exclusive, as magnetospheric accretion also comes with a shock at the planetary surface, in which emission lines may also be emitted. As the field is still nascent, these two emission models have hardly been tested. In fact, known emission lines have never been characterized in detail either. Variability of the lines may be present, and even has been hinted. This may explain the low-yield of detections in surveys using these emission lines as detection tools. In this thesis, I will test the variability of accretion lines on PMCs, and test the two accretion scenarios against observations.

I first present the results of a monitoring campaign of the Pa_β line for GQ Lup b and GSC 06214-00210 b, with VLT/SINFONI. The Pa_β line is predicted to be the brightest of the Near-Infrared accretion lines, less prone to chromospheric activity. It lies in the J-Band, where powerful Adaptive Optics can be used: a strong asset for characterizing companions whose signal is often contaminated by the PSF of their host star. I find the lines of GQ Lup b to be consistent with the magnetospheric accretion scenario, while the lines of GSC 06214-00210 b are more in line with a shock-emission scenario. Their variability amplitude can explain the H_α surveys low-yield of detection, if and only if Pa_β variability translates to H_α variability.

I then present the results of a monitoring campaign of the Optical lines (H_α, H_β, Helium lines, ...) for Delorme 1 (AB)b, SR 12 c and 2MASS J11151597, with VLT/UVES. They are high-separation PMCs that can be characterized without the need for adaptive optic. For the first time, I present accretion lines profiles at high resolution ($R > 50\,000$), along with the variability behavior of these profiles. Delorme 1 (AB)b and 2MASS J11151597 have similar profiles, weakly variable over a night, while SR 12 c shows great variability within a few tens of minutes, up to a few days. On Delorme 1 (AB)b, the UV excess is detected and is variable.

The lines profiles can be decomposed into two static components that only vary by their relative scaling. This decomposition is able to reproduce all lines features of all epochs. One of these components has red-shifted absorptions, reminiscent of that found in T Tauri stars. They are well fitted with magnetospheric accretion models, which on top of its high correlation with the UV excess, strongly advocates for a magnetospheric accretion origin. The other component, however, is not correlated with the UV excess, but still provides a decent fit to magnetospheric accretion models. Still, this component may be due to chromospheric activity.

This work provides the first study of variability of accretion lines on PMCs, along with their modeling at high resolution. They build up to a small sample of PMCs, spanning most of their conditions and properties. This work opens up to future observations to build a significant sample, that will be enriched from future instrumentation, be it in space (JWST) or on the ground (ELT).

Contents

I Introduction . . . **13**
1 Planetary formation and evolution . . . 16
1.1 Formation pathways . . . 16
1.2 The missing ingredient: accretion physics . . . 18
2 Planets-analogs: Planetary-Mass Companion . . . 20
2.1 Planetary-Mass Companions: crushed between planets and brown-dwarfs . . . 20
2.2 The formation tension . . . 21
2.3 Known Planetary-Mass Companions . . . 22
2.4 The study of accretion in the planetary-mass regime . . . 26
3 Accretion in the stellar regime . . . 28
3.1 Magnetospheric Accretion: Development . . . 28
3.2 Simple/Qualitative picture . . . 30
3.3 Column/Funnel structure . . . 31
3.4 The accretion shock . . . 32
3.5 Lines diagnostics: details . . . 35
3.6 Variability . . . 36
4 Accretion in the Planetary-Mass regime . . . 39
4.1 Theoretical standpoint . . . 39
4.2 Tools for their characterization . . . 41
4.3 Open questions and objectives of this thesis . . . 43

II Accretion tracers in the Near-Infrared with VLT/SINFONI . . . **47**
1 Introduction . . . 49
1.1 GQ Lup b . . . 50
1.2 GSC 06214-00210 b . . . 50
2 SINFONI: go-to tool for ground-based NIR characterization . . . 51
2.1 Instrument description . . . 51
2.2 Observations and Data reduction . . . 54
3 Atmospheric modeling . . . 58
3.1 Main spectral features . . . 58
3.2 The atmosphere of GQ Lup b and GSC 06214-00210 b . . . 58
4 The Paschen Beta line . . . 62
4.1 Line profiles . . . 62
4.2 Line flux variability . . . 63
5 Emission lines models . . . 65

5.1 Models description . . . 65
5.2 Model fitting . . . 66
6 Conclusion . . . 68

III Accretion tracers in the Visible/UV with VLT/UVES . . . 93
1 Introduction . . . 96
2 The UVES campaign: targets description . . . 96
2.1 Delorme 1 (AB)b . . . 97
2.2 SR 12 c . . . 98
2.3 2MASS J11151597+1937266 . . . 98
3 The UVES spectrograph . . . 98
3.1 Instrument description . . . 99
3.2 Data acquisition and reduction . . . 101
4 Observations and data reduction . . . 104
4.1 Observations . . . 104
4.2 Delorme 1 (AB)b: Reduction . . . 104
5 Delorme 1 (AB)b . . . 117
5.1 General description of the spectra . . . 117
5.2 Lines morphology . . . 118
5.3 Lines correlations . . . 122
5.4 Decomposing the lines . . . 124
5.5 Line ratios . . . 134
5.6 Lines variability . . . 135
5.7 Periodicity . . . 137
5.8 Model fitting . . . 142
5.9 Discussion . . . 146
6 SR 12 c . . . 151
6.1 Observations . . . 151
6.2 Quick-look: Data reduction . . . 153
6.3 Highly variable lines . . . 153
6.4 Discussion . . . 154
7 2MASS J11151597 . . . 155
7.1 Observations . . . 155
7.2 Data reduction . . . 155
7.3 Results . . . 156
8 Summary . . . 157

IV Conclusion and Perspectives . . . 161
1 Summary . . . 162
1.1 Constraints on the line formation mechanisms . . . 162
1.2 Variability behaviors . . . 163
2 Global picture . . . 163
3 Perspectives . . . 164
3.1 Main PMC properties . . . 164
3.2 Building an observing program . . . 165
3.3 Future instrumentation . . . 165



V French Summary **169**
1 Introduction 171
1.1 Formation et évolution planétaire 171
1.2 Analogues aux planètes: Companions de Masse Planétaire 173
1.3 Accrétion dans le régime stellaire 176
1.4 Accrétion dans le régime de masse planétaire 180
2 Traceurs d'accrétion dans le proche Infrarouge: VLT/SINFONI 182
2.1 Introduction 182
2.2 VLT/SINFONI: un spectrographe intégral de champ depuis le sol 183
2.3 Observations et réduction de données 184
2.4 Modélisation de l'atmosphère 185
2.5 La raie d'accrétion Paschen Beta 186
2.6 Modélisation des raies d'émission 189
2.7 Conclusion 191
3 Traceurs d'accrétion dans le Visible/UV avec VLT/UVES 192
3.1 Introduction 192
3.2 Une campagne d'observation avec VLT/UVES 193
3.3 Le spectrographe UVES 193
3.4 Observations et réduction de données 194
3.5 Réduction de données 194
3.6 Résultats 196
3.7 Conclusions 200
4 Conclusion et perspectives 200
4.1 Résumé 200
4.2 Une vue globale 201
4.3 Perspectives 202

Appendices **205**

A SINFONI appendix **207**

B UVES appendix **229**





Chapter I.

Introduction

With more than 5000 known exoplanets to date, the details of their formation processes are still a mystery. They are thought to form within protoplanetary disks surrounding their host star. A first possible scenario states that they are thought to form by the slow growth of dust particles, and/or pebbles. These are known as pebble-accretion and planetesimal-accretion. Alternatively, they might also form through gravitational instability, a process where clumps of gas within the protoplanetary disk eventually collapse under their gravity.

Planets accrete their mass from the surrounding protoplanetary disk, but the details of these accretion mechanisms are still unknown. While planets are usually too close to their host star to study accretion processes, recent detections of "Planetary-Mass Companions" (PMC) may be proxy study candidates: while they are on the higher end of planets mass range (10–30 M_{Jup}), they lie at higher separations that can be reached with current instrumentation. Recently, the discovery of the PDS system changed the race for the understanding accretion: it is host to 2 PMCs, embedded within the protoplanetary disk, both still actively accreting. They provide a unique opportunity to study and test accretion models predictions.

Similarly to what is done on stars, the study of accretion is done with the emission lines related to accretion. Two competing (but not mutually exclusive) scenarios exist for these lines: one where lines are emitted in magnetospherically induced funnels like on stars, and one in which lines would rather be emitted by the accretion shock itself. These models have never been tested before on PMCs (or planets). Furthermore, emission lines have never been characterized in detail either. My work consists in the characterization of accretion processes on PMCs, through their emission lines and other accretion signatures.

Chapter's contents

1 Planetary formation and evolution 16
1.1 Formation pathways 16
1.1.1 Core-accretion: a differentiated process 16
1.1.2 Gravitational instability 17
1.2 The missing ingredient: accretion physics 18
2 Planets-analogs: Planetary-Mass Companion 20
2.1 Planetary-Mass Companions: crushed between planets and brown-dwarfs 20
2.1.1 From brown dwarfs to Planetary-Mass companions 20
2.1.2 From planets to Planetary-Mass companions 21
2.2 The formation tension 21
2.3 Known Planetary-Mass Companions 22
2.3.1 H_α surveys 22
2.3.2 The case of PDS 70 25
2.3.3 An (exhaustive?) list 25
2.4 The study of accretion in the planetary-mass regime 26
3 Accretion in the stellar regime 28
3.1 Magnetospheric Accretion: Development 28
3.1.1 The beginnings 28
3.1.2 Stellar accretion: evolution of the paradigm 28
3.2 Simple/Qualitative picture 30
3.3 Column/Funnel structure 31
3.3.1 Funnel morphology 31
3.3.2 Temperature structure 31
3.4 The accretion shock 32
3.4.1 Shock modeling 33
3.4.2 Hotspot structure 33
3.4.3 Accretion rates 34
3.5 Lines diagnostics: details 35
3.5.1 Lines morphologies 35
3.5.2 Chromospheric contribution 35
3.5.3 Correlations 36
3.5.4 Line ratios 36
3.6 Variability 36
3.6.1 Continuum variability 36
3.6.2 Lines variability 38
4 Accretion in the Planetary-Mass regime 39
4.1 Theoretical standpoint 39
4.1.1 Magnetospheric accretion 39
4.1.2 A new scenario: accretion fed by the circum-stellar disk 40
4.2 Tools for their characterization 41



4.3 Open questions and objectives of this thesis 43
4.3.1 Open questions 44
4.3.2 Objectives 44



1 Planetary formation and evolution

With more than 5000 known exoplanets to date, the details of their formation processes are still a mystery. Exoplanets range from a fraction of Earth masses, to several Jupiter masses, orbit their star from a fraction of an AU, all the way to thousands of AUs, and with quite varying intrinsic properties (temperature, clouds, composition, ...).

Planets form in protoplanetary disks surrounding their host star. However, the initial conditions for forming planets are still unconstrained. For a review of the various planet formation scenarios and limitations, see Drążkowska et al. (2023); Liu and Ji (2020); Johansen and Lambrechts (2017); Ormel (2017). Here, I focus on the planetary growth during and after the planetesimal seed formation, in cases applicable to giant gaseous planets, motivated by the discovery, in the past 10 years, of young ~ 10 M_{Jup} planets on wide orbits: the protagonists of my thesis.

1.1 Formation pathways

1.1.1 Core-accretion: a differentiated process

The core-accretion scenario dates back to the 1960s (e.g., Safronov, 1960, 1966; Safronov and Zvjagina, 1969; Safronov, 1972), with strong advancements in the 1980s and 1990s (e.g., Mizuno, 1980; Bodenheimer and Pollack, 1986; Pollack et al., 1996), whose development was aimed at explaining the observed properties of the Solar system. It still suffers from a few issues, for example the meter barrier, where due to aerodynamic drag, meter-sized objects fall onto the star faster than they are able to grow Weidenschilling (1977). However, it is still a candidate (if one of the only few) for planet formation. A representation of the process is shown in Fig. I.1 and follows three main phases:

- "Core-formation": The planet embryo only accretes solids through gravitational interaction and collisions. Technically, the planet does "accrete" gas, but its mass is not sufficient to retain a sufficient fraction to build on to gaseous planets. The core that is created during this phase has a high metallicity, at least compared to the typical interstellar medium value, because grains are by essence the storage medium for metals.
- "Slow gas-accretion": Once the embryo reaches up to 10 $M_\oplus$, its mass is sufficient to accrete gas. Gas accretion is possible and the embryo accretes both solids and gas.
- "Runaway gas-accretion": Once the total mass reaches a "critical" value (10-20 $M_\oplus$), the gas is accreted much faster than the solids. The accretion is therefore entirely dominated by gas accretion, permitting giant gaseous planets to form.

The details of the first phase follow either planetesimal or pebble growth. Planetesimal growth corresponds to bodies big enough ($\gtrsim$ 10 km) not to be affected by gas drag within the disk, thus only considering gravitational interactions between them (Wetherill and Stewart, 1989; Safronov, 1972; Lissauer and Stewart, 1993; Kokubo and Ida, 1996). Pebble growth, however, considers agglomeration from much smaller particles, where disk drag still plays a role (Ormel and Klahr, 2010; Lambrechts and Johansen, 2012; Visser and Ormel, 2016). Technically, planetesimal growth is only possible if said planetesimals are available, which likely required pebble formation (or another mechanism) for them to form.

In the core-accretion scenario, the build-up of a rocky core is always necessary in order to form a giant planet later on. Here are a few key points in giant formation. The final mass of a giant planet is set by both the balance between the growth timescale and the disk dispersal timescale, along with the quantity



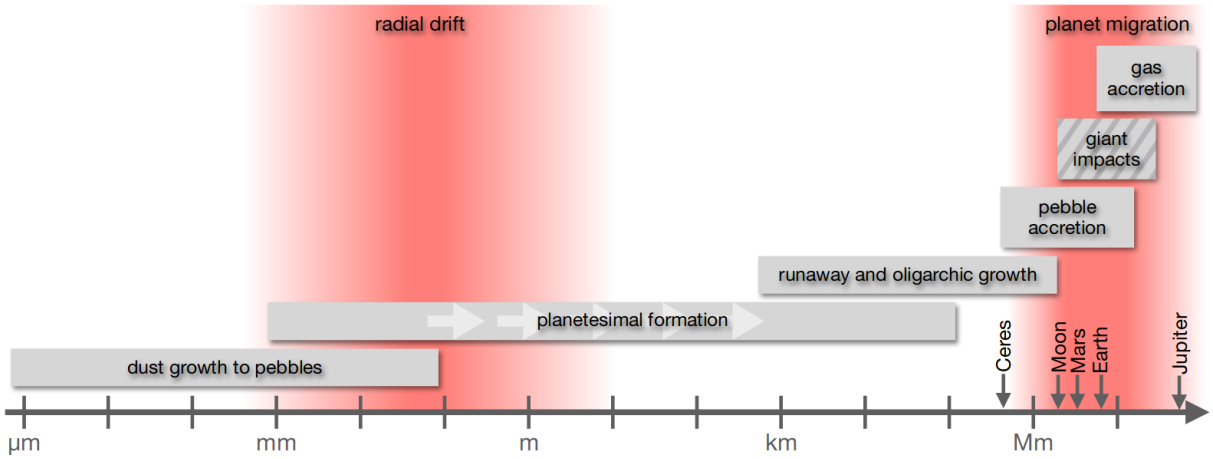


Figure I.1: From Drążkowska et al. (2023), their Fig. 3. Typical processes involved in planet formation, in the core-accretion scenario.

of available solids (Drążkowska et al., 2023). Either way, most giant planets should be formed in the inner protoplanetary-disk, typically $\lesssim 10 - 20$ AU, before inwards (or outwards) migration occurs, or they are scattered outside the system through dynamical perturbations.

1.1.2 Gravitational instability

Gravitational instability is another scenario for planet formation. In this context, protoplanetary disks have inhomogeneities that gravitationally collapse to form giant planets (Boss, 1997; Mayer et al., 2002). Unlike the core-accretion case, which is a bottom-up scenario, gravitational instability is a top-down mechanism.

Gravitational instability requires that the disk is cold and massive enough for clumps to overcome the gas pressure. Deng et al. (2017) found that that such clumps are generated in very-young, massive and cool protoplanetary disks. This typically only happens at wider separations ($\gtrsim 30$ AU, Toomre criterion Safronov, 1960; Toomre, 1964). However, it would only permit the formation of very massive gas giants, at least of a few M_{Jup}. The number of planets formed per disk is dependent on the radiative feedback between the planet and the disk: radiative feedback tends to stabilize the surrounding protoplanetary disk, hindering planet formation, therefore leading to less planets (Mercer and Stamatellos, 2017; Meru and Bate, 2010). In other words, heated disks are stable, while cold disks move towards fragmented and clumpy disks that permit planetary formation. One should note that at early stages, disks are likely heated by the accretion processes onto the star or planet.

While gravitational instability only forms clumps at large separations, a recent (re-)proposed scenario could link it to inner rocky planets: tidal downsizing. It was first proposed by Kuiper (1951), a scenario where clumps of gas form through gravitational instability. Due to interactions with the disk, these clumps migrate inwards, and are then divided by tidal forces from the star. Such clumps at inner separations, however, would migrate into the star too fast for rocky planets to form. Boley et al. (2010) found that such clumps can form at high separations, but migrate inwards on timescales sufficient for rocky cores to form. Gravitational instability could be the key for the presence of giant planets at high separations alike those



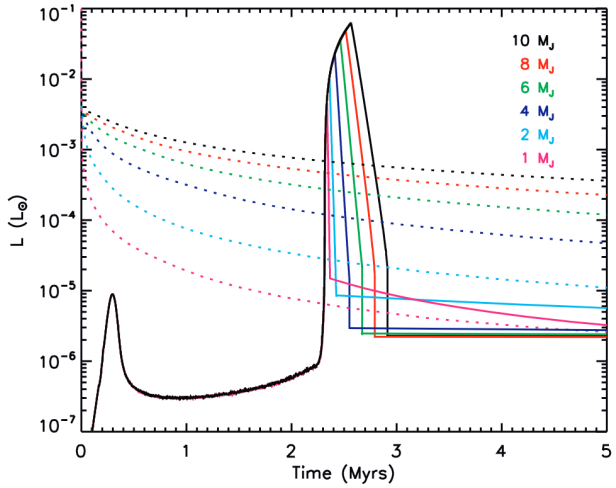


Figure I.2: Right: From Marley et al. (2007), their Fig. 3: luminosity of different Jupiter-like planets, as a function of time, for hot-starts (dotted lines) and cold-starts (solid lines).

found with direct imaging (Schlaufman, 2018), as well as rocky planets at small separations.

Many studies have focused on the dynamics and migration of such planets. While early studies predicted that clumps would migrate towards the star within 10 000–100 000 years, even without tidal-downsizing, recent studies (e.g., Schlaufman, 2018) found that planets may migrate inwards on timescales an order of magnitude slower than traditionally assumed, which is mostly important because they form on timescales too short to dig a gap in the proto-planetary disk that would slow down migration. However, Mercer and Stamatellos (2017) finds that all planets formed by gravitational instability are ultimately ejected from the system, thus a possible explanation to free-floating planets and brown-dwarfs. As a middle-ground, Stamatellos (2015) found that such planets initially migrate inwards before opening a gap, halting (at least severely limiting) both its growth and migration.

1.2 The missing ingredient: accretion physics

Up to the early 2000s, planetary evolution models would predict planets luminosities, radii, and other properties using quite simplistic models. They would start from an inflated ball of gas, and let it evolve over time. While this could, in principle, be somewhat representative of the gravitational instability scenario, this does not reflect the core-accretion physics. The first implementation of *physical* initial points belongs to Marley et al. (2007). They compare the usual (at the time) inflated-ball models (which they call *hot-start*) to the core-accretion results (later to be called *cold-start*). Put simply, the hot-start corresponds to the case where all initial entropy is kept within the planet, whereas cold-start corresponds to the case where all of its gravitational energy is radiated away.

The main results, shown in Fig. I.2 are that the planet luminosity inferred from cold-starts are much fainter (3–4 orders of magnitude) than that of hot-starts. They only catch up after some time: 1 Myr for 1 M_{Jup} planets, and up to 1 Gyr for ~ 10 M_{Jup} planets. This leads to uncertainties on the mass estimates of planets, depending on the model and luminosities inferred from observations. On top of that, cold-start planets even have a period of higher luminosity during their gas runaway accretion phase, due to the accretion



shock (see the peak around 2.5 Myr in Fig. I.2).

In fact these two extreme cases may only be outer bounds for evolutionary paths predictions. In the cold-start case, most of the energy is radiated away, which is an ad-hoc assumption for stars, but may not encapsulate the full picture for planets. Planets form within protoplanetary disks, where disk dynamics and gas flows towards the planet might be complicated. Also, because planets are thought to have a circum-planetary disk (at least partly), it is not so sure that the inflows are channeled directly to the planet, or if they are significantly processed through the disk. The exact physics of the accretion flow, and in turn of the accretion shock, may change how much energy is kept within the planet, and impact its luminosity during its early age.

While a few studies have attempted early modeling of the accretion shock (e.g., Marleau et al., 2017; Cumming et al., 2018), others authors have started focusing on emission lines (Betti et al., 2023). The topic of observational studies of accretion is still nascent where most of the work is still to be done. It was opened to constraints with the discovery of young and still accreting *planets* (or planets-looking siblings): Planetary-Mass Companions.



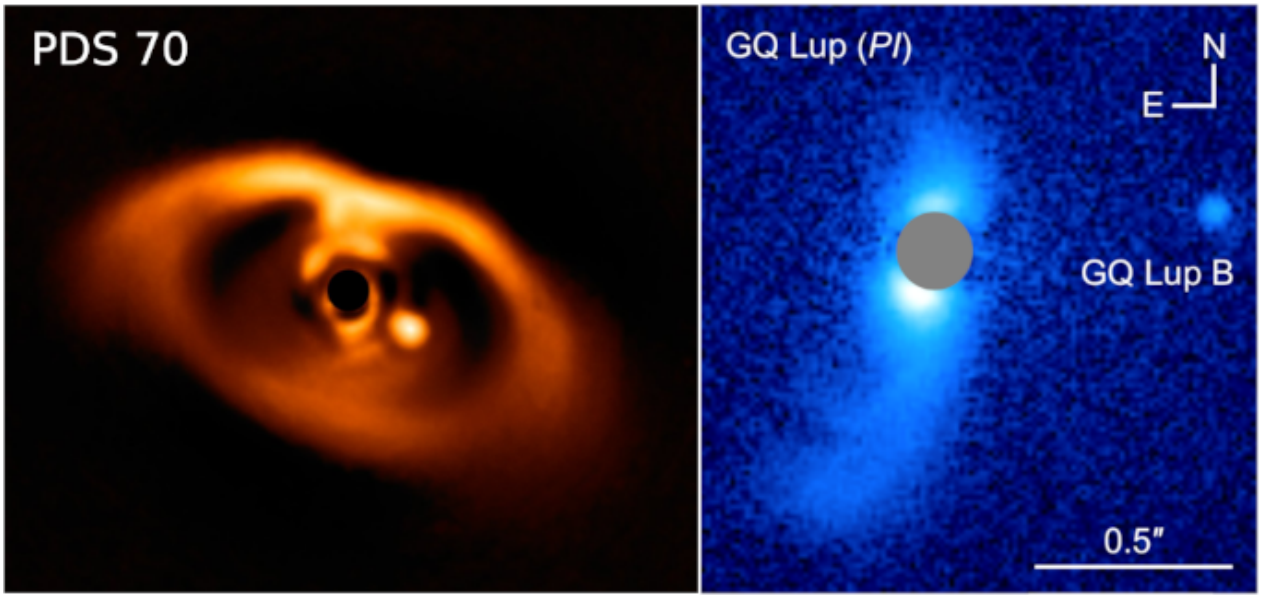


Figure I.3: A few examples of PMCs. Left: PDS 70 system (Müller et al., 2018). Right: GQ Lup b system (van Holstein et al., 2021).

2 Planets-analogs: Planetary-Mass Companion

Planetary-Mass Companions and Planetary-Mass Objects (hereafter PMCs and PMOs) are, by definition, objects with masses *similar to*, *on the order of*, planets. While PMCs are bound to a host star, PMOs are either isolated objects, or we do not know whether they are bound to their host or not. Due to observational constraints, known PMCs are typically on moderate to high separations (> 50 AU). Broadly speaking, "PMC" and "PMO" have been used to describe objects ranging from 1 M_{Jup} to $\sim$ 30 M_{Jup}, even though they are supposed to be categorized as brown dwarfs at $M > 13$ M_{Jup}.

PMCs lie just at the interface of planets and Brown Dwarfs (BDs), begging the question of their formation pathways and mechanisms: are they formed like planets, or brown dwarfs? If we must use them as proxies for close-in planets for the study of planetary-accretion, it would be wise to check whether they have a planetary formation pathway in the first place.

2.1 Planetary-Mass Companions: crushed between planets and brown-dwarfs

Here, I present the two main candidate scenarios for forming PMCs: planet formation and brown-dwarf formation.

2.1.1 From brown dwarfs to Planetary-Mass companions

Back in the late-1990s / early-2000s, the magnetospheric accretion model (circum-stellar disks are accreted onto the star through interactions between the disk and the star's magnetic field) found much success in explaining the shapes of the accretion lines of young T-Tauri stars, along with their IR/UV continuum



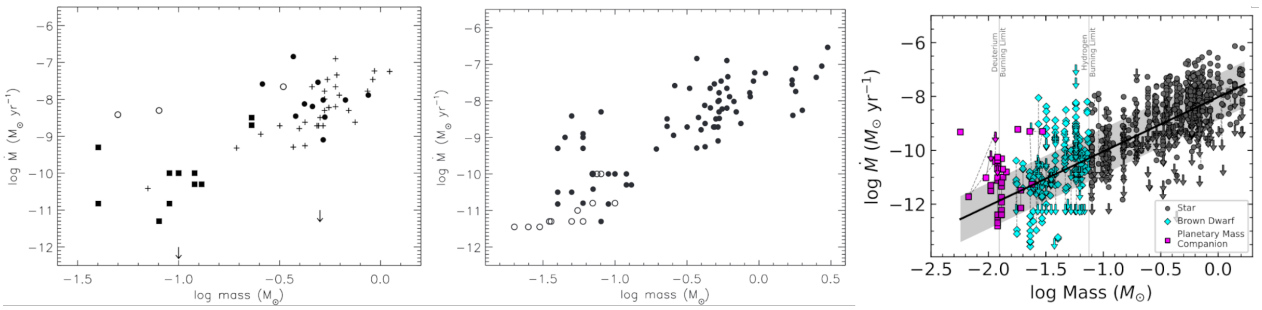


Figure I.4: Correlations between mass accretion rate and central object mass. Left: from Mohanty et al. (2005). Middle: from Muzerolle et al. (2005). Right: from Betti et al. (2023).

excess. However, this was limited to actual stellar objects, above the Hydrogen burning limit. As for objects below said limit, the origin of emission lines was still an open question. The number of known sub-stellar objects with accretion lines was still limited (~ 10), hindering henceforth put efforts amidst the community.

While a general trend between mass and mass accretion rate was known in the stellar regime, Muzerolle et al. (2003) first extended it to the stellar/sub-stellar limit, by adding measures from a few brown dwarfs / sub-stellar objects. Their results are shown in the left panel of Fig. I.4. These results were later extended by Muzerolle et al. (2005), adding more brown dwarfs to the sample, even some near the planetary-mass regime (Fig. I.4 middle panel). The general trend of decreasing accretion rate with decreasing mass was found to extend to the sub-stellar domain, and is now generally accepted. It appears even more obvious now that more data were added to the graph (e.g, Betti et al., 2023, Fig. I.4 right panel). This trend suggests that brown dwarfs share similar accretion mechanisms with stars. Whether this trend extends to the PMC domain is not so sure, because of the limited number of known PMCs/PMOs. Brown dwarfs may also follow the same formation mechanisms as stars: by fragmentation of a molecular cloud (Padoan and Nordlund, 2004). In this scenario, they are simply the result of the low-end mass of the IMF. It should be noted, however, that not all BDs may have formed in a stellar fashion, and some may also have formed as companions to heavier parents (Thies et al., 2015, e.g.,).

2.1.2 From planets to Planetary-Mass companions

Some of the low-mass brown-dwarfs, or high-mass planets, were found to be bound to another stellar/sub-stellar object, which made them not only companions (rather than lone objects), but high-separation ones, at a few hundred AUs. While they could have formed from fragmentation from a molecular cloud, their bound nature also makes them eligible to having been formed already bound to their host star, like a planet, either at their current location, or the inner circum-stellar disk, later to be ejected. This also begs the question of whether some isolated sub-stellar objects could be the results of ejections from early-bound systems or outwards migration. The origin of these objects, that we now call PMCs, is up to debate.

2.2 The formation tension

In-situ formation within Circumstellar-Disks (CSDs) at a few $\sim$ 100 AUs is rather unlikely. The growth of a rocky[1] core at such high separations, which is required to trigger gas accretion, occurs on timescales

[1] Rock and Stone!



much longer than the typical lifetime of the disk (Santamaría-Miranda et al., 2018). Alternatively, Brown-Dwarfs companions and PMCs may represent the low-mass end of the molecular cores fragmentation, this was hinted at by Thies et al. (2015) through IMF arguments. Still, core-accretion and gravitational instability may still form BD companions. However, they would still need to be ejected at higher separation (where they are observed today), a scenario that is predicted by both core-accretion and gravitational instability models (Pollack et al., 1996; Whitworth and Stamatellos, 2006; Stamatellos and Herczeg, 2015). However, Gravitational Instability does not seem so much of a viable scenario anymore, at least for BD companions: not only is it restricted to a very specific set of conditions (Meru and Bate, 2010; Kratter and Murray-Clay, 2011), it also leads to un-bound ejected companions when including radiation feedback (Mercer and Stamatellos, 2017), rather than high separation ones. This seems to leave both core-accretion and molecular cloud fragmentation as plausible scenarios.

Similarly to how the accretion processes on BDs were partly constrained using correlations between mass and mass accretion rate (Muzerolle et al., 2005), PMCs seem to follow the general trend (Fig. I.4, Betti et al., 2023). While objects at the stellar/sub-stellar interface were constrained not only through the $M - \dot{M}$ correlation, but also by highlighting their similarities with CTTS (e.g., Mohanty et al., 2005,; Alcalá et al., 2014), using a variety of accretion tracers (e.g., Ca/Na lines, forbidden lines, ...), accretion on PMCs is mostly not constrained at all. This might be the missing part for PMCs, and new instruments open the way for the subject (see Sect. 4.2). However, I first propose a compendium of the known properties of PMCs in the next section.

2.3 Known Planetary-Mass Companions

2.3.1 H_α surveys

With the discovery of H_α-emitting planets (HD 142527 b, LkCa 15 b,PDS 70b&c and more, Close et al., 2014; Sallum et al., 2015; Müller et al., 2018; Wagner et al., 2018; Haffert et al., 2019), surveys have changed their focus to the H_α line. Models started predicting planets to be located at such separations (Zhu, 2015; Szulágyi and Ercolano, 2020), with an H_α brightness that favors observations, as the contrast between the host star and the line is reduced. Zurlo et al. (2020) used SPHERE/ZIMPOL, surveyed 11 transitional disks, but did not detect any companion. Huélamo et al. (2022), also using SPHERE/ZIMPOL, surveyed 5 targets, and also did not detect any companion. Finally, Follette et al. (2023) presented the results of a 6-years survey (the GAPlanetS survey), and reached a detection rate of $\sim 36^{+26}_{-22}$ % among 14 transitional disks. However, most of the detections were previously known companions, and only 1 new detection was confirmed (CS Cha c).

Overall, the occurrence rate among surveys lied around ~ 1 % before H_α imaging surveys (Bowler and Nielsen, 2018), and surveys did not yield any new detection. In fact, most of the previous detections of the H_α line had been obtained as a by-product of non-dedicated surveys. The obvious explanations are: (i) planets simply are not where we're looking for them, (ii) planets do not have H_α-emission as strong as thought, (iii) emission lines are variable, so much that surveys are missing the detections. (iv) H_α-emitting targets are too embedded to be detected. The first explanation cannot really be constrained without a case study, unless a breakthrough in modeling provides a satisfactory explanation for the large gaps and spiral-structures in circum-stellar disks that are thought to be shaped by planets. However, H_α-brightness and variability can be constrained, and might even be linked. Brittain et al. (2020) proposed that giant planets at such separations could have formed mostly through the cold-start scenario, making them intrinsically too faint to be detected, in line with the core-accretion scenario. Observed planets would be those that formed through the hot-start scenario, intrinsically brighter (β Pic, HR 8799). However, this only holds for old planets, because young accreting planets should be visible at least through their accretion lines. Lines variability could then be the



Table I.1: Compilation of accreting Planetary-Mass-Companions and isolated objects. They are sorted by increasing mass. References for each parameter are available on the corresponding GSheet[2].

Name	isComp?	Sep (")	d (pc)	M (M_{Jup})	Age (Myr)	SpT	H_α	Pa_β	Pa_γ	Br_γ
TWA 27 B			64.67 ± 0.49	5.0 ± 2.0	10.0 ± 2.0	L0 $\pm$ 0.5		Y	Y	
KPNO Tau 12			140.00 ± 15.00	7.0 ± 1.0	1.5 ± 0.5	M9.25 $\pm$ 0.5	Y			
Lk Ca 15b	Y	0.09	157.19 ± 0.65	7.5 ± 2.5	2.0 ± 1.0		Y			
PDS 70 c	Y	0.22	112.39 ± 0.24	$7.8^{+5.0}_{-4.7}$	5.4 ± 1.0	M8	Y			
PDS 70 b	Y	0.19	112.39 ± 0.24	$7.9^{+4.9}_{-4.7}$	5.4 ± 1.0	M8	Y			
1RXS J1609-2105 b	Y	2.22	138.04 ± 0.34	$8.0^{+4.0}_{-2.0}$	5.0	L4 $\pm$ 1.0				
2M0441+2301 Bb	Y	0.10	122.22 ± 4.55	9.8 ± 1.8	2.0 ± 1.0	L1 $\pm$ 1.0		N		N
FW Tau b	Y	2.29	145.00	10.0 ± 4.0	$2.0^{+1.0}_{-0.5}$	pec				
ROXs 42B b	Y	1.14	146.45 ± 0.66	10.0 ± 4.0	$7.0^{+3.0}_{-2.0}$	L1 $\pm$ 1.0				
HD 106906 b	Y	7.10	102.38 ± 0.19	11.0 ± 2.0	13.0 ± 2.0	L2.5 $\pm$ 1.0				
2MASSJ0249–0557 c	Y	40.00	$48.90^{+4.40}_{-5.40}$	$11.6^{+1.3}_{-1.0}$	22.0 ± 6.0	L2.5				
DH Tau b	Y	2.31	133.45 ± 0.45	$12.0^{+10.0}_{-4.0}$	$1.5^{+1.0}_{-0.5}$	M9.25 $\pm$ 0.25	Y	Y		
Delorme 1 (AB)b	Y	1.77	47.20 ± 3.10	13.0 ± 1.0	37.5 ± 7.5	L0	Y	Y	Y	Y
CHXR 73 b	Y	1.30	191.37 ± 2.94	$13.0^{+8.0}_{-6.0}$	2.0	>M9.5				
2MASS J2126–8140	Y	217.00	34.66 ± 0.99	13.3 ± 1.7	80.0 ± 70.0	L3				
SR12 c	Y	8.70	125.00 ± 25.00	13.5 ± 1.5	2.0	L0 $\pm$ 1.0	Y	Y		
AB Pic b	Y	5.50	50.14 ± 0.03	13.5 ± 0.5	30.0	L0 $\pm$ 1.0				
Oph 1622-2405 B	Y	1.90	125.00 ± 25.00	$14.0^{+6.0}_{-5.0}$	11.0 ± 2.0	M9.5 $\pm$ 0.5				
UScoCTIO 108 b	Y	4.60	146.02 ± 2.82	$14.0^{+2.0}_{-8.0}$	4.5 ± 3.5	M9.5	Y			
USco1556 B	Y	24.78	141.00 ± 2.00	14.5 ± 2.5	7.5 ± 2.5	M9.5 $\pm$ 1.5	N			
GSC 6214-210 b	Y	2.20	108.80 ± 0.30	14.5 ± 2.0	$16.9^{+2.9}_{-1.9}$	M9.5 $\pm$ 1.0	Y	Y		Y
USCo 1606-2335			$141.00^{+77.00}_{-37.00}$	16.0 ± 4.0	7.5 ± 2.5	M9 $\pm$ 0.5	Y			
USco1621 b	Y	20.78	138.00 ± 1.00	16.0 ± 2.0	7.5 ± 2.5	M9 $\pm$ 1.0	N			
Oph 1622-2405 A	Y	1.90	125.00 ± 25.00	$17.0^{+4.0}_{-5.0}$	11.0 ± 2.0	M9 $\pm$ 0.5				
CT Cha b	Y	2.67	165.00 ± 30.00	18.0 ± 4.0	2.0 ± 1.0	M9 $\pm$ 1.0		Y		
USco 1610-1913B	Y	5.80	145.00 ± 2.00	$19.0^{+7.0}_{-4.0}$	7.5 ± 2.5	M9 $\pm$ 0.8	Y			
2M0441+2301 Ba	Y	0.10	122.22 ± 4.55	19.0 ± 3.0	2.0 ± 1.0	M7 $\pm$ 1.0		N		N
HIP 77900 b	Y	21.80	148.96 ± 1.25	$19.0^{+7.0}_{-4.0}$	7.5 ± 2.5					
TWA 27 A			64.67 ± 0.49	19.9 ± 5.0	10.0 ± 2.0	M9		N	N	
TWA 28			59.24 ± 0.46	20.9 ± 6.0	10.0 ± 2.0	M9	Y			
GQ Lup b	Y	0.71	154.10 ± 0.69	$22.0^{+2.0}_{-3.0}$	3.5 ± 1.5	M9	Y	Y		
USco 1612-1800B	Y	3.00	145.00 ± 2.00	$23.0^{+12.0}_{-6.0}$	7.5 ± 2.5					
USCO J1608-2315			$169.59^{+29.74}_{-22.02}$	24.0 ± 8.0	7.5 ± 2.5	M8.5 $\pm$ 1.0	Y			
USco 1610-2239			123.81 ± 9.02	24.0 ± 7.0	7.5 ± 2.5	M9	Y			
USco J160723.82-221102.0			125.14 ± 10.19	24.0 ± 8.0	7.5 ± 2.5	M8.5 $\pm$ 1.0	Y			
KPNO Tau 7			127.84 ± 5.23	24.0 ± 5.0	1.6 ± 0.2	M8.25 $\pm$ 0.5	Y			
USco 1610-1913B	Y	5.84	140.16 ± 5.17	24.1 ± 3.1	7.5 ± 2.5	M9 $\pm$ 0.5	Y			
KPNO Tau 6			$122.72^{+5.77}_{-5.77}$	24.1 ± 2.1	1.6 ± 0.2	M8.5	Y			
HIP 77900B		21.80	$156.05^{+10.23}_{-10.25}$	24.1 ± 3.1	10.0 ± 3.0	M9 $\pm$ 0.5	Y			
ISO-Oph GY10			138.00	24.1 ± 4.2	2.0 ± 1.2	M8.5 $\pm$ 0.5		Y		Y

Thesis' Table of Contents
Chapter's Table of Contents

KPNO Tau 4			$133.43^{+21.08}_{-16.01}$	25.0 ± 5.0	1.5 ± 0.5	L0 $\pm$ 0.5	Y			
Usco J160603.75-221930.0			$98.39^{+30.58}_{-18.86}$	26.2 ± 2.1	7.5 ± 2.5	M8.75	Y			
Cha Ha 7			188.25 ± 5.89	28.3 ± 2.1	1.5 ± 0.5	M8 $\pm$ 0.25	Y			
CHSM 17173			191.81 ± 4.14	28.3 ± 2.1	1.5 ± 0.5	M8	Y			
ISO-Oph 170			138.00	28.3 ± 2.1	2.0 ± 1.2	M8		Y		
ISO-Oph 070			140.00	28.3 ± 2.1	2.0 ± 1.2	M8				Y
GY92 11			138.00	28.3 ± 16.8	$0.3^{+2.7}_{-0.2}$	M6.5 $\pm$ 0.5	Y			
2MASS J16085953-3856275			155.85 ± 5.08	30.0 ± 10.0	1.0 ± 0.5	M8.5 $\pm$ 0.5	Y	Y	Y	Y
2M0441+2301 Ab	Y	0.23	122.22 ± 4.55	35.0 ± 5.0	2.0 ± 1.0	M7 $\pm$ 1.0		Y		N

[2]GSheet: https://docs.google.com/spreadsheets/d/1thVPq1NruUkmpemM01gRGfL3xN7qZoQsqUXaacpuMls/edit?usp=sharing

key if planets accrete through short high accretion-rate bursts. Surveys would therefore have likely missed those detections. Finally, it may also be possible that H_α-emitting planets are too embedded to be detected: either within the circumstellar disk of their host star, or within their own circumplanetary disk. The known H_α-emitting targets would therefore only be outliers.

2.3.2 The case of PDS 70

Perhaps the pinnacle of direct imaging: the confirmation of PDS 70 b&c. Through their H_α emission lines, they opened many doors. It would not be possible to write about PMCs without a dedicated section to the PDS 70 system. PDS 70 b was first detected by Keppler et al. (2018), within the gap of the transitional disk around PDS 70 (5.4 ± 1.0 Myr, ~ 22 AU at 113.43 ± 0.52 pc, Gaia Collaboration et al., 2018). Müller et al. (2018) provided the first characterization of the planet: at ~ 22 AU of the star, it is a 1.4–3.7 R_{Jup} companion with a mass poorly constrained: 2–17 M_{Jup}. Wagner et al. (2018) provides the first characterization of its H_α emission, and a tentative detection of another planet. This detection is confirmed with MUSE observations (Haffert et al., 2019). Benisty et al. (2021) provides ALMA detection of the circum-stellar disk, as well as the circum-planetary disk. Fast-forward a few years, Christiaens et al. (2024) shows JWST data of the system, possibly highlighting a third planet, along with some details on the interactions between the circum-stellar disk and the planets.

PDS 70 b&c are the only currently known planets to be both within a circum-stellar disk, and actively accreting. They are the ideal laboratory for PMC characterization: because they are still accreting, constraining accretion models is possible, and since they are embedded in the circum-stellar disk, it is possible to constrain disk-planet interactions. However, the short angular separation of the companions (~ 0.2") and the circum-stellar disk emission limit the study of these planets. The planetary signal is contaminated by the disk, and the foreground extinction from the disk itself limits the possibilities.

2.3.3 An (exhaustive?) list

Betti et al. (2023) presented the accretion rate trends towards the sub-stellar regime (purple and cyan points in Fig. I.4). But what about studying PMCs independently? The main question is whether the M–$\dot{M}$ correlation extends down the PMC regime, though the correlation seems to flatten-out at lower masses. Betti et al. (2023) argues that this could be explained by an evolution different from that of higher mass BDs, leading to no correlation between mass and accretion rate (Stamatellos and Herczeg, 2015). However, this trend could also be due to an observing bias, where lower accretion rates are not detectable.

I focus the study on PMCs, and PMOs, where PMOs are considered proxy of their similar PMCs, i.e., they may have formed similarly to PMCs, hence their relevance to the study. I used the CASPAR[3] database (Betti et al., 2023), which aims at cataloging known BDs, PMCs and PMOs, and derive their properties in a consistent manner. By defining an upper limit of 30 M_{Jup}, I identified 31 PMC/PMOs in CASPAR. According to Betti et al. (2023), their mass were obtained from evolutionary models (Baraffe et al., 2015) with age and temperature as input parameters. However, I added 18 PMC/PMOs that I did not find in the list, for a total of 49 objects. The list of known PMC/PMOs below 30 M_{Jup} and young ($\lesssim 50$ Myr) is given in Table I.1. The age, mass and separation parameters space is shown in Fig. I.5, for PMCs (left and middle panels) and all PMOs (right panel). The different colors represent whether they are accreting (red) or have and H_α line. The accreting status was determined by whether the targets have Pa_β, Pa_γ or Br_γ emission lines, which are thought not to be produced by activity (Natta et al., 2014). The H_α line can, in principle, be produced by chromospheric activity, in particular around the M9–L0 spectral types where PMCs reside

[3]**CASPAR**: https://zenodo.org/records/8393054



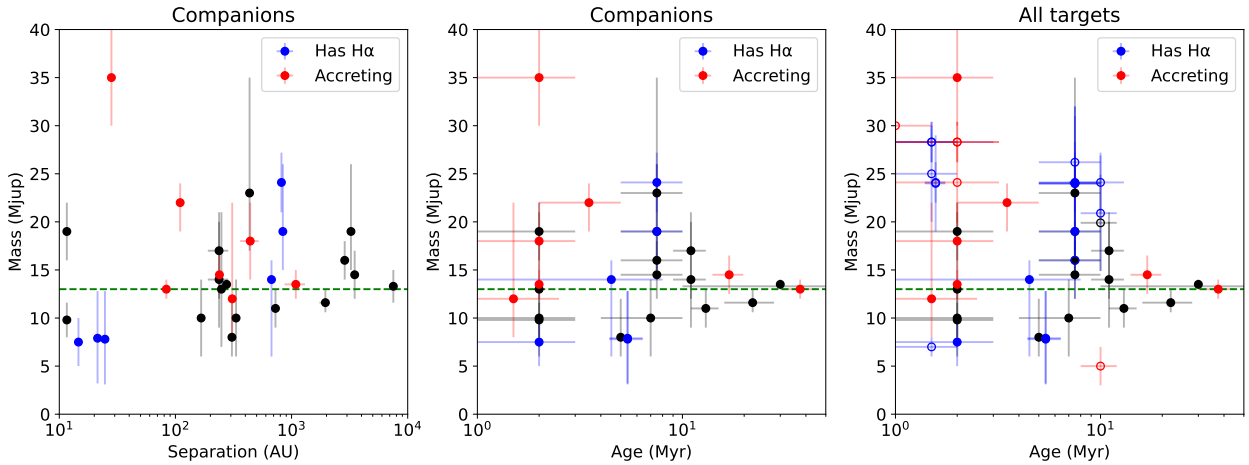


Figure I.5: Statistics of Planetary Mass Objects, as given in Table I.1. Filled circles are companions (PMCs), open circles are lone objects. Red points are confirmed accretors, determined by whether they have a confirmed Pa_β, Pa_γ or Br_γ line in emission: the assumption is that these lines cannot be formed in the chromosphere. Blue points are objects with confirmed H_α emission: H_α does not necessarily translates to accretion as it can be due to activity. Black points are objects for which the H_α or Accreting status is unknown from the list. This does not necessarily means that they are not accreting, it might simply be due to missing data in the Table.

(Stelzer et al., 2013; Frasca et al., 2017; Manara et al., 2017; Venuti et al., 2019). However, H_α is predicted to be the brightest line produced by accretion and its study definitely should not be excluded (see UVES chapter). Some PMOs have confirmed non-detections of some lines and are marked as such in the Table.

Among the 49 PMOs, there is a total of 29 PMCs. Most targets below 4 Myr are labeled accretors, while there are only 3 above 4 Myr, which follows the trend that disk dispersal occurs on timescales of a few Myr. However, the older accreting systems, like GSC 06214-00210 b and Delorme 1 (AB)b (known to bear disks), are quite puzzling, as they question whether PMCs also should stop accreting after similar timescales as stars, or if they formed much later than estimated from the age of their host star. This could be solved if H_α emitting targets could also be confirmed accretors. There seems to be a gap of known PMOs around 3–4 Myr, but it is likely due to the star-forming regions that were surveyed: Upper Scorpius ($\sim$ 11 Myr) and Taurus ($\sim$ 1 Myr). Any statistics is therefore biased by the number of systems surveyed in each regions. I did not try to correct for that bias, but this may be material for a future study.

2.4 The study of accretion in the planetary-mass regime

Planets are though to form within circum-stellar disks. However, planets are also thought to also have Circum-Planetary Disks (CPD) around them (Miki, 1982). The physics of CPDs is a fairly new field, especially given that only a handful of them were detected (see next sections). On top of that, some planets can be embedded in the CSD of their host star, while others were found as isolated objects. The interactions between the planet, CPD and CSD may affect its accretion properties and evolution. These CPDs, however, are poorly constrained. They have been detected with ALMA (Wu and Sheehan, 2017; Benisty et al., 2021, e.g.,



FW Tau c, PDS 70 b,), polarized light with SPHERE (e.g., DH Tau b, GSC 06214-00210 b, van Holstein et al., 2021), IR excess (e.g., GSC 06214-00210 b Bowler et al., 2011) and even JWST recently (GQ Lup b, PDS 70 b Cugno et al., 2024; Christiaens et al., 2024).

Some young PMCs are found to be currently accreting and provide the perfect opportunity to directly study the accretion processes, similarly to what was done on stars. Accretion processes drive the energy budget of the planet, setting how much energy is kept within their atmospheres. The two extreme cases are the cold and hot starts models, where the accreted energy is either entirely radiated away, or fully kept within the planet (Marley et al., 2007). Accretion processes may also set the angular momentum of the planet. If young planets do have strong magnetic fields (Reiners and Christensen, 2010), they may be able to accrete their CPD through magnetospheric accretion, which could also lead to jets and outflow (Gressel et al., 2013), thus limiting the rotational speeds of said planets. Accretion may play a role in regulating the angular momentum of PMCs and PMOs. Finally, feedback of accretion to the circum-stellar disk may also regulate migration. Understanding the accretion processes is therefore required, as they will drive the whole life-span of the planets.

The efforts towards the understanding of accretion in the planetary-mass regime has been driven by the knowledge of accretion processes on stars. In Sect. 3, I review the accretion processes and signatures in the stellar-regime. In Sect. 4, I then expand on the accretion in the planetary-mass regime.



3 Accretion in the stellar regime

In this section, I focus on the late stages of accretion, where most of the mass has already been accreted on the star. This is therefore not applicable to early stages where the infalling envelope dominates accretion.

This section is highly inspired by the review of Hartmann et al. (2016). However, I do not expand much on the angular momentum questions in the context of Magnetospheric accretion. For a review, refer to Bouvier et al. (2014).

3.1 Magnetospheric Accretion: Development

The study of accretion in the planetary-mass regime has unsurprisingly been mostly driven by the knowledge of accretion processes in the stellar regime. This section will focus on these processes, and the next section will expand them to the planetary-mass regime.

3.1.1 The beginnings

Stars form through the collapse of interstellar clouds, where after a few thousands years, they *ignite* their deuterium fusion if their mass if sufficient (M>13 M_{Jup}). They divide into two main categories: (i) brown dwarfs are stars below 75 M_{Jup}, which are not massive enough to fuse regular hydrogen, and will cool down (and dim) once their deuterium is depleted, (ii) stars above 75 M_{Jup} are able to fuse hydrogen and will live a star life.

At early stages (<100 kyr) stars are usually deeply embedded within the dense and opaque residual infalling gas envelope (Class 0), making their study only possible at IR wavelengths. They are usually identified through their strong IR excess, directly linked to the large scale envelope ($T = 10 - 100$ K). The star accretes most of its mass during this stage. As time goes on (few 100 kyr), the envelope becomes fainter and the protostar itself becomes visible (Class I). The lesser IR excess is linked to a lesser accretion rate from the envelope, and in turn a lesser accretion rate from the disk onto the star. At ∼1 Myr, the envelope is mostly gone, and accretion is entirely driven by star-disks interactions (Class II).

Star formation, and the segregation into classes has historically been driven by their infrared excesses. However, the understanding of accretion processes from the disk onto the star is fairly recent and has mostly focused on Class II objects, where the disk itself is clearly visible,. The study of accretion tracers can easily be distinguished from any effects due to the strong and variable extinction from the surrounding matter around the enshrouded central object. T-Tauri stars ($\sim M_\odot$), around few Myr old, were the primary focus. Earlier (more massive) types will be left aside in this section (for a review, see Section 3 in Hartmann et al., 2016). Similarly to planets, emission lines (hydrogen, helium, sodium, ...) were the key to understanding the accretion mechanisms.

3.1.2 Stellar accretion: evolution of the paradigm

In a time where large telescopes and observatories such as the VLT, ALMA, Keck or CHARA did not exist, nor did adaptive optics; a time where spectra were directly etched into spectral plates; Joy (1945) presented a sample of 11 stars, all of which had spectral similarities with the brightest one: T Tauri. They all showed light-curve variability, similar spectral types (F to G) with emission lines comparable with the Sun's chromosphere (Hydrogen, Helium, Potassium, Calcium, ...), relatively low luminosity, and an association with either dark or bright *nebulosity*. Hence began decades of research into the T-Tauri star type.

The first decade, up until the early 60s, would build the foundation of spectral features along with attempts to understand them. T Tauri stars were known to be variable, be it from their light curves (Joy,



1942, 1945) or colors variations (Varsavsky, 1960). Still, this variability was observed mostly fortuitously by comparing spectrometric plates of different epochs. Emission and absorption lines were also known. They were in fact among the key points for the determination of the T Tauri class. They were also shown to be variable (Weston and Aller, 1955), but this would raise more questions as to why. It was also shown that absorption lines, on top of emission lines, were shifted by ∼100 km/s, which pointed towards mass ejection. This was linked to an expanding and envelope around the sources (e.g., Herbig, 1961). This envelope would be fed by the star in some process. Evidence of absorption lines can be directly seen in, for example, Kuhi (1964). Finally, continuum features were either really sharp and clear, or completely *washed-out* (Joy, 1949; Herbig, 1962) (later to be named *veiling*). On top of that, UV excess had already been evidenced (Varsavsky, 1960), further adding the particular properties of T Tauri stars.

From 1960 to 1980, not many explanations were successful at explaining the picture, most of observations only adding to characteristics of T Tauri stars. Kuhi (1966, 1974) showed that there was a correlation between the intensity of H_α and the level of UV continuum, hinting that the two processes were likely linked, and that UV emission found its origin into Balmer lines. It was proposed that an optically thick region, coupled with poor spectral resolution, could result in a blending of high-order Balmer lines, resulting in an apparent UV excess. On top of the UV excess, the presence of IR excess was also evidenced in multiple T Tauri stars (Mendoza V., 1966, 1968). Rydgren et al. (1976) would successfully propose a new picture: T Tauri stars would be best described by a hot (20 000 K) gaseous envelope, capable of explaining infrared excess, the presence of emission lines, as well as veiling. Because of the high projected rotational velocity found in T Tauri star compared to much older stars, they proposed that the star's magnetic field, coupled with its rotation, would be responsible for mass-loss, an *out-flow*. However, this did not encapsulate any wind and/or jet geometry at the time. Further observations (e.g., Kuan, 1976) would show that the envelope picture is also consistent with UV excess variations. Note that a similar picture had already been proposed by Herbig (1970): deep-lying chromosphere responsible for both emission lines and UV excess, although this was not accounting for the IR excess.

In the 80s, numerical simulations started to predict the presence of disks around young stars (Terebey et al., 1984; Boss, 1987). During the same epoch, Smith and Terrile (1984) presented the observations of the disk around β Pic, while earlier clues were mostly using indirect measurements (Bally et al., 1983; Gehrz et al., 1982). This is because at the time, observations could only reach ∼5" spatial resolution, comparable with the extent of disks they were observing. Disks were already suspected from the shape of the solar system (e.g., Lin and Papaloizou, 1985; Lin, 1986), and had already been theorized a decade earlier, by Lynden-Bell and Pringle (1974). They predict both an IR spectrum originating from the disk, and UV continuum originating from the boundary-layer at which the disk hits the stellar surface. This work was extended a decade later by Bertout et al. (1988), who found especially good agreement with observations of IR excess originating from the disk, and UV excess originating from the boundary layer. The model also was able to reproduce the extended wings of emission lines, which should be hidden by the optically-thick disk near the emitting region.

It took only a couple of years to highlight what the boundary-layer scenario was lacking, and for it to be put aside. Hartmann et al. (1994) presents the key points towards a change of paradigm: (i) most T Tauri stars had hot-spots rotating with the star (Bouvier et al., 1993), which boundary-layer accretion fails to explain; (ii) spin-rates of T Tauri stars should be associated with stellar winds as a mean to counteract the spin-up induced by boundary-layer accretion, but Bouvier et al. (1993) found that the presence of an accretion disk correlates with lower spin-rates than those without disks (incompatible with spin-down from a stellar wind); (iii) inverse P-Cygni profiles present in T-Tauri emission lines (e.g., Appenzeller and Wolf, 1977; Bertout et al., 1977) imply an infall of material over large distances, which is not encapsulated by the boundary-layer model. Although, Bertout et al. (1988) had already proposed that magnetic field could play



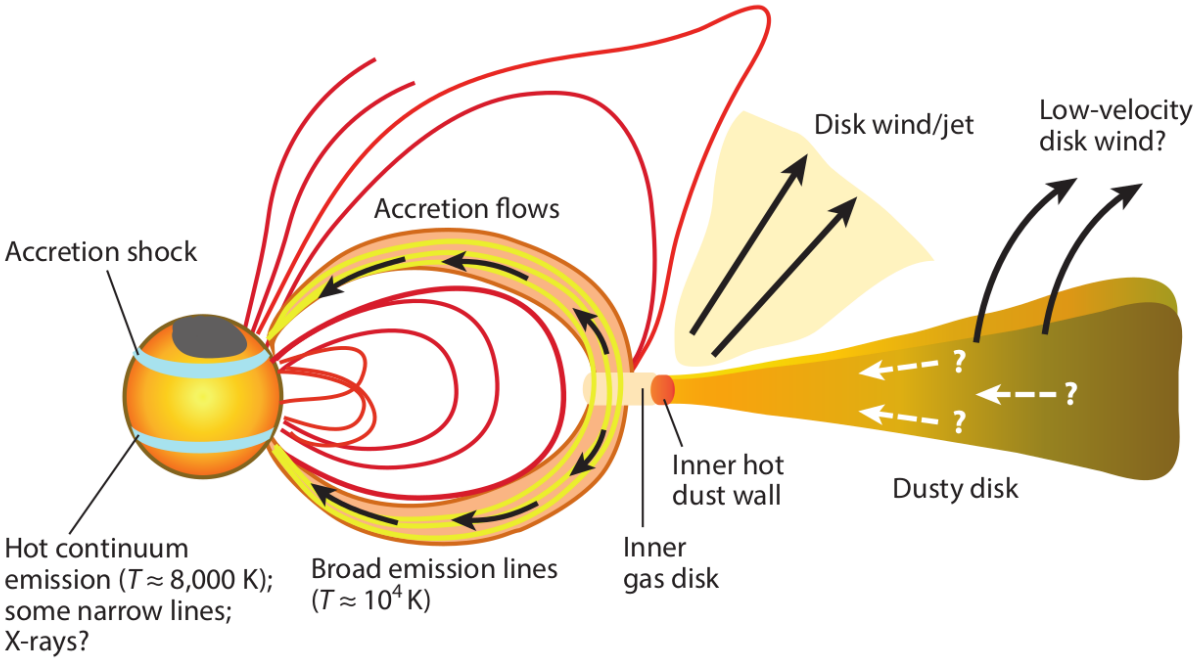


Figure I.6: From Hartmann et al. (2016). Schematic view of the magnetospheric accretion process on a young star.

a role, this led multiple authors to propose a new scenario: Magnetospheric Accretion.

3.2 Simple/Qualitative picture

A general, qualitative picture of magnetospheric accretion is shown in Fig. I.6. Following a right-to-left (outwards to inwards) description:

- Large-scale magnetic fields are thought to thread the disk, triggering low-velocity winds, and inwards disk migration.
- The dipolar magnetic field is sufficient to truncate the circumstellar disk (CSD), roughly at the co-rotation radius: where the Keplerian period is equal to the stellar period. Note that this co-rotation radius is usually free of dust, as it has been sublimated at higher radii ("Inner hot dust wall" in Fig. I.6).
- The magnetic field lines, coupled with the gas, act as a mean for angular momentum exchange between the disk and the star. Magnetic field lines extending outwards are responsible for winds and jets ("Disk wind/jet" on Fig. I.6), spinning down the star.
- Magnetic field lines that couple slightly below the co-rotation radius transfer angular momentum from the disk to the star: the star spins up while the gas falls onto the star. However, the magnetic field lines act as a barrier that prevent the gas from falling directly onto the star. Instead, it is guided by the magnetic field lines and fall via high latitude columns ("Accretion flows" on Fig. I.6).



- The columns crash down on the stellar surface, forming a bright "Accretion shock" that is responsible for the UV excess and X-Rays.
- Both the accretion shock and columns are responsible for emission lines. The columns are heated to $T \sim 10^4$ K, sufficient to trigger Hydrogen, Helium, and metal lines. While the emission from a single column will be red-shifted, it is possible to see multiple columns at once, symmetry may make emission lines symmetrical. However, self absorption from the columns leads to red-shifted absorption features in the lines, up to ~ 100 km/s, that tend to shift the apparent line centroid blue-wards. The accretion shock lines, however, are usually slightly red-shifted, as material is still slightly infalling into the photosphere.

It is important to note that this is only a schematic, idealized representation. In fact, it is likely that there are multiple columns at once, without a given symmetry. The columns themselves might not be perfectly cylindrical, hence the common name "funnels" that is more appropriate to the curtain-like structures that are seen in simulations.

3.3 Column/Funnel structure

The stellar magnetic field lines reconnect within the disk. When the magnetic field strength is sufficient to counteract the disks' gas pressure it acts as a shield, preventing inward radial transport of the disk material. Instead, the gas is channeled to higher latitudes, into columns.

3.3.1 Funnel morphology

The actual shape of the funnel is debated, and is likely highly dependent on the inclination of the stellar magnetic field with respect to the inclination of the disk. For an axis-symmetrical magnetic field, Romanova et al. (2003) predict an axis-symmetrical curtain all around the star (see Fig. I.7, Panel A), while any inclination leads to two opposite funnels (see Fig.I.7, Panels B/C). The same authors expanded their simulations to various accretion rate regimes (Romanova et al., 2008), showing branching between stable and unstable accretion regimes that lead to multiple funnels (see Fig. I.7, Panel E). Recent models (Tessore et al., 2023) use a simpler approach, similar to that of Romanova et al. (2003) and Esau et al. (2014) (see Fig. I.7, Panel D). Overall, the funnels have to be at least quite anti-symmetrical, which is in line with the magnetic field topology found on at least V2129 (Zeeman effect measurements, Donati et al., 2007).

3.3.2 Temperature structure

The temperature structure is also quite poorly constrained. Only few studies have attempted to predict temperature structures in a self-consistent manner (e.g., Martin, 1996): they find an increasing temperature along the funnel, mostly due to the gas compression by converging field lines, with temperatures up to $\sim 6\,500$ K. However, Muzerolle et al. (1998) found that this structure does not accommodate to observations. Instead, they use observations to *fit* a temperature profile (Muzerolle et al., 2001). The funnels have to be heated somewhere in the range $7\,000$ – $10\,000$ K. Lower temperatures would make the emission lines too faint, while higher temperatures would make the gas optically thick, turning emission lines into absorption lines. Still, they find the acceptable range of temperatures to be degenerated with the accretion rate. More recent studies have tried probing directly the temperature structure. Petrov et al. (2014) used metal line ratios in order to retrieve the emitting conditions. They find strong correlation of increasing temperature with increasing density, in line with a temperature increasing in the funnel closer to the star. They find a



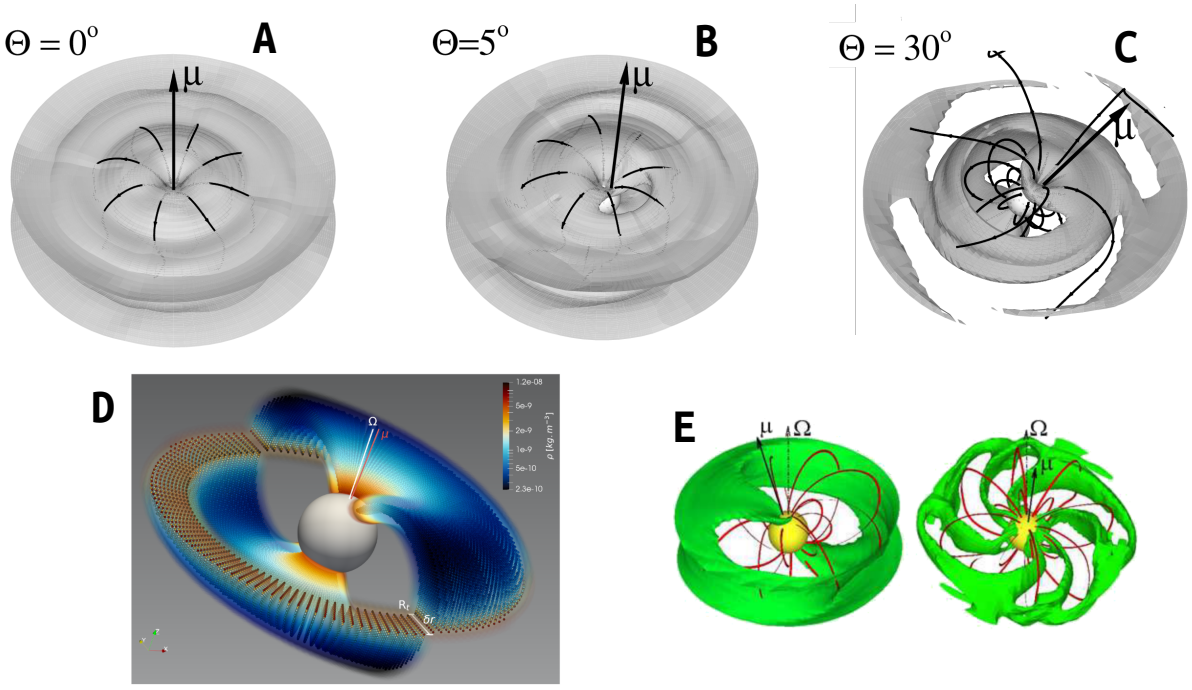


Figure I.7: Various accretion funnels geometries. Panels A/B/C: from Romanova et al. (2003), for different dipole inclination. Panel D: from Tessore et al. (2023). Panel E: from Romanova et al. (2008), stable and unstable regimes.

a temperature structure that is more in line with that of Martin (1996), although they warn that Martin's model have different parameters than that of their target. A more recent study (Marleau et al., 2022), albeit in the planetary-mass regime, found temperature structures also more in line with that of Martin (1996).

3.4 The accretion shock

An accretion shock is expected to happen when the accreted material hits the object photosphere at velocities above the local sound speed. The UV continuum excess found on CTTS (Fig. I.8 B) is usually attributed to the accretion shock that occurs when the accretion funnels end up crashing into the stellar surface (Fig. I.6). This excess is responsible for the veiling of the lines that historically *blurred* the lines in spectral plates, reducing the contrast between lines and continuum. Its most defining feature is the Balmer jump at 3647 Å, although the blending of Balmer series lines tends to shift the apparent jump location at $\sim$ 3700 Å. A few key parameters could be derived from simple physics principles (temperature, density, energy, Koenigl, 1991; Gullbring, 1994; Lamzin, 1995) before the first models gave actual predictions of the features and shape of the excess (Calvet and Gullbring, 1998).



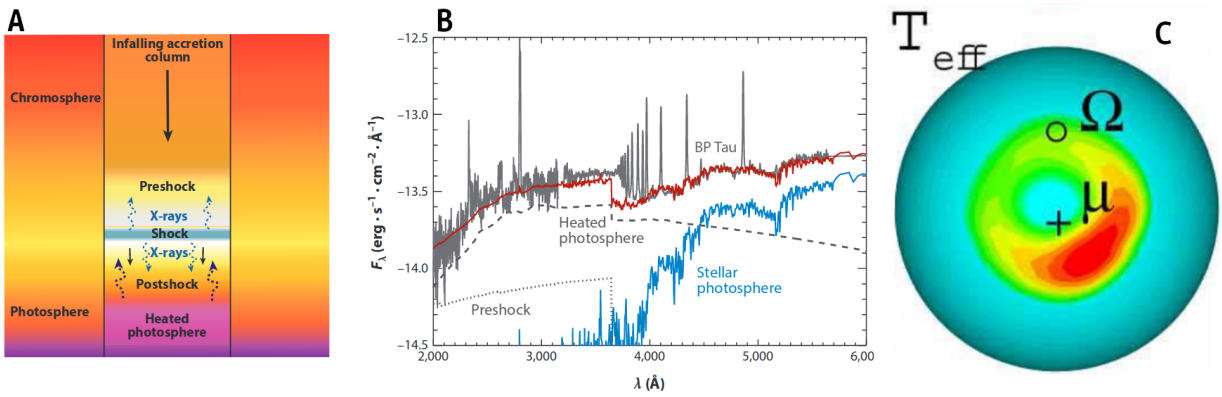


Figure I.8: From Hartmann et al. (2016). Panel A: idealized picture of the accretion shock. The shock itself emits X-Rays, that are partly reprocessed in UV wavelengths in the preshock region. Panel B: Contribution of the accretion shock to the spectrum of BP Tau. Panel C: example of the temperature structure of the accretion shock in the case of an inclined dipole (μ), with respect to the rotation axis (Ω) (Romanova et al., 2004).

3.4.1 Shock modeling

Shock models are usually 1D (see Fig. I.8A for a representation), which assumes a single set of parameters (temperature, density, ...) over the whole shock region. Such *simple* models were surprisingly quite successful at reproducing independently both UV and X-Ray spectral features (Günther et al., 2007), but never simultaneously. Günther et al. (2007) predicts accretion rates that are 2–3 orders magnitudes apart between UV/optical and X-Ray, which could be explained by the 1D assumption: if the column were to be stratified, with varying densities and/or temperatures, then this would translate in different regions of the shock emitting at different wavelengths, especially in the case of inclined dipoles where the accretion flow is not axis-symmetrical. The hotspot (induced by the shock) therefore spreads over different areas depending on the structure of the column and inner disk. Its size strongly depends on the density of the funnel, and the inclination of the dipole (Romanova et al., 2004). These simulations predict the hotspot to spread over ∼1–20 % of the stellar surface (filling factor) depending on the density and temperature of the column and/or disk. However, spectrum-modeling using the aforementioned 1D models tend to predict filling factors in the range 0.01–1 %, with some targets reaching ∼ 10 %. These are based on flux-scaling to reproduce the flux level of the continuum excess. Because the flux level is directly related to the emitting area, they are likely more reliable estimates of the filling factor. This filling factor can be used to constrain otherwise degenerated mechanisms.

3.4.2 Hotspot structure

Still, the simplistic 1D modeling approach does not account for the likely stratified column structure. Espaillat et al. (2021) found time lags between UV/Optical flux peaks, advocating for different emitting regions rotating around the star: a stratified hotspot. This can be modeled by assuming that the column is made of homogeneous layers. Espaillat et al. (2021) used this approach to fit the UV/Optical excess of GM Aurigae, its temporal evolution, and in turn model the rotation of the rotational modulation of the hotspot. They



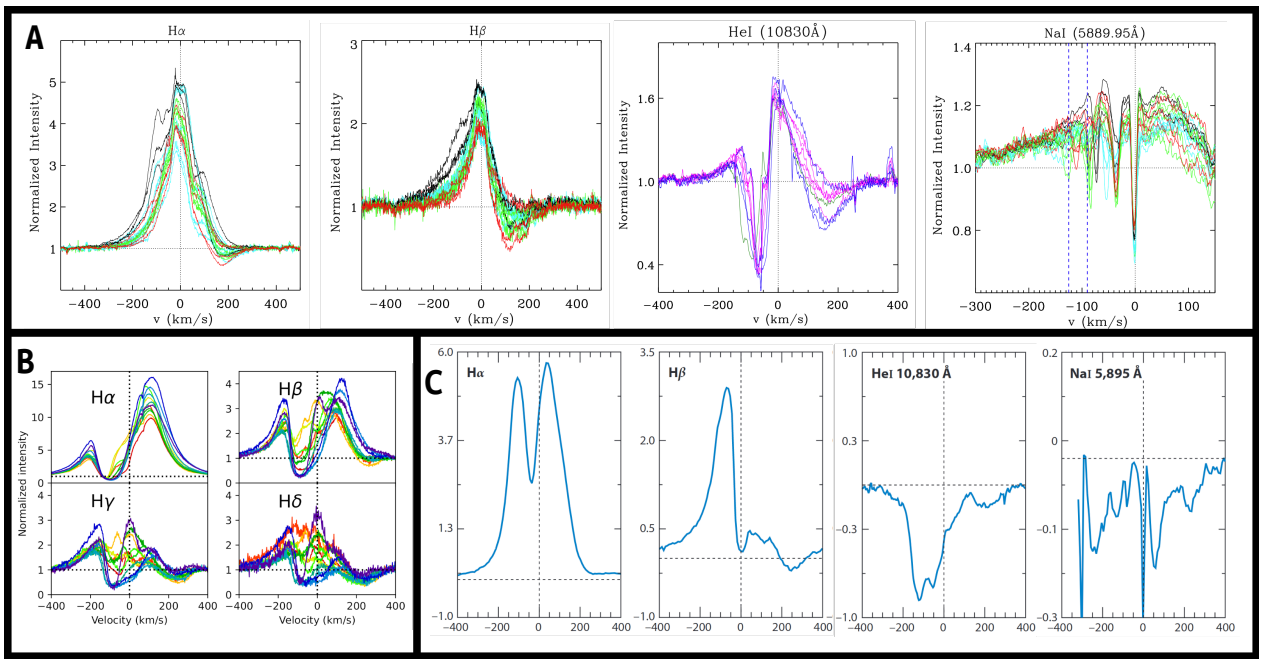


Figure I.9: Emission/Absorption lines of 3 T Tauri stars, showing how some CTTS have emission features that are absorption features on others. Panel A: lines of V2129 Ophiuchi (Sousa et al., 2021). Panel B: lines of S CrA N (Nowacki et al., 2023). Panel C: lines of DK Tau (Hartmann et al., 2016).

divide the hotspot into 3 density regions, where simulations predict that the highest densities have filling-factor of < 1 %, and lower densities 10–20 %, consistent with earlier simulations. These higher values are in line with the size of magnetic cells obtained from polarization studies (although on another target, V2129 Oph, Donati et al., 2007). A similar stratification had already been done by Ingleby et al. (2013), however they could not conclude on the spatial extension of each.

3.4.3 Accretion rates

Overall, the accretion shock luminosity is a good tracer of the spread of the columns (from the filling factor), and of the accretion rate itself. Because the energy at the shock is almost entirely emitted in the form of continuum excess, one can find the accretion rate by assuming that the whole kinetic energy is radiated away:

$$L_{\rm acc} = \frac{GM_*\dot{M}}{R_*}\left(1 - \frac{R_*}{R_{\rm in}}\right) \tag{I.1}$$

where $\dot{M}$ is the accretion rate, and $R_{\rm in}$ the truncation radius. The conversion from excess flux to accretion luminosity is commonly done using a *slab* model: a region of constant temperature, density and optical depth, to extend the observed excess to the full accretion luminosity (Valenti et al., 1993; Gullbring et al., 1998). Accretion rates are usually in the range 10^{-9} to 10^{-7} $M_\odot$/yr.

3.5 Lines diagnostics: details

Emission lines have been (one of) the primary mean of studying magnetospheric accretion. Not only were they used to define the T Tauri class as a whole, they also discriminate between the *classical* and *weak*-line T Tauri stars. These lines are usually transitions from Hydrogen, Helium, or metals (Na, Fe, ...)

3.5.1 Lines morphologies

Accretion lines, whether they are in emission or absorption, exist in a wide variety of shapes and intensities (see Fig. I.9). The gas flow and its dynamics are directly imprinted into the emission/absorption line profiles, and some emission line on a CTTS may actually be absorption lines on others. Within a line itself, some emission components may be absorption components for another star. Lines may have different origins, which translate into different components. High velocity components are directly tracing the inflow/outflow. Positive velocities trace the inflow of material within the accretion funnel (+150–200 km/s), whereas negative velocities tend to trace the winds and/or jets (-150–200 km/s). However, not all features may be present in all lines at all times. In the case of an accretion funnel, absorption features appear when the base (near the stellar surface) is cold in comparison to the accretion shock, and it intercepts the line of sight. Both stellar- and shock- continuum are absorbed by the infalling column, translating into absorption features that can extend below the continuum level (Fig. I.9A, H_α and HeI 10830Å) or suppress the emission component (Fig. I.9C, H_β). In the case of a jet/wind, spectral features appear when the line of sight intercepts the wind, translating into blue-shifted absorption.

Lines can often be found as the sum of multiple components. Broad emission components must find their origins in a wide velocity range area, such as the infalling column or winds. Narrow components, however, are mostly associated with the emission from the shock. In the case of Helium lines, for example, they are often made of a combination of broad and narrow components. Beristain et al. (2001) found that among their 31 CTTS sample of Helium lines, 28 of them bear narrow emission components, and 22 of them bear broad emission components. Narrow components have width varying depending on the transition, but relatively uniform over their sample. Broad components are a combination of the infalling magnetosphere, and hot low-velocity winds (-30 km/s). Wind emission tend to have a wider velocity spread and are responsible for higher observed velocity (-200 km/s). Some Helium lines may be more prone to absorption components, such as the HeI 10830Å (Kwan et al., 2007), whereas they are only rarely observed at H_α, despite it being the brightest accretion lines.

3.5.2 Chromospheric contribution

Part of the line emission can be produced by chromospheric activity, as shown by the line emission in WTTS spectra (non accreting). This component is likely to be present in CTTS as well, and has been accounted for in recent studies, whether for profile fitting (e.g., Thanathibodee et al., 2020) or determining line fluxes relationships (Manara et al., 2013). On a side note, the chromospheric contribution to Hydrogen emission lines increases strongly towards late-M objects. Activity-induced lines tend to have lower EW and narrower H_α lines. Criterions of Equivalent Widths $\mathrm{EW}(\mathsf{H}_\alpha) < 36$ Å and $\mathsf{H}_\alpha(10\%) < 270$ km/s have been used to discriminate accreting from non-accreting stars (White and Basri, 2003). Other authors have used a criterion of $L(\mathsf{H}_\alpha)/L_{\rm bol} = 10^{-3.3}$ (Barrado y Navascués and Martín, 2003).

For the sake of accretion, activity can be considered as a noise component on added to the accretion rates (Fig. 7 in Venuti et al., 2019). However, the effect is quite dependent on the mass, temperature and spectral type. The complete characterization of activity is still quite challenging and not fully within the scope of this



thesis. For starting points, see Stelzer et al. (2013); Frasca et al. (2017); Manara et al. (2017); Venuti et al. (2019).

3.5.3 Correlations

Most lines are usually easier accessed than a full broadband UV excess characterization, despite it being a better tracer of accretion luminosity. However, lines were shown to be strongly correlated with accretion luminosity (Rigliaco et al., 2012; Alcalá et al., 2014, 2017), providing linear relations between the two. Given that line-emission is directly linked to the accretion process, these relations are not surprising. However, they are likely biased by activity: Manara et al. (2013) provides estimates of $L_{acc,noise} \sim 10^{-3}$ $L_\odot$, and $\dot{M}_{acc,noise} \sim 10^{-11.6} - 10^{-9.2}$ $M_\odot$/yr. In turn, Alcalá et al. (2014) finds that the Pa_β and Br_γ lines are the least affected by chromospheric noise, unlike optical lines for which correlations have the widest spread. CaII lines however, are among the most affected by activity effects.

Links between stellar mass and accretion rates have been observed on a wide range of masses (Muzerolle et al., 2003; Mohanty et al., 2005; Alcalá et al., 2014, 2017), with an M_*–$\dot{M}$ relationship following roughly a power-law of order 2. This relationship is actually predicted by simulations, and linked to gravitational torques within disks ($\dot{M} \propto M_*^{1.7}$, Vorobyov and Basu, 2008).

3.5.4 Line ratios

Line ratios are able to give insights in the local emission state, in particular, the temperature distribution and gas density (Kwan and Fischer, 2011). Antoniucci et al. (2017) presents a compendium of Hydrogen line ratios for 36 T Tauri stars. They find that lines decrements are best described by 4 different types, only one of which (Type 3) is not reproduced by models, while others correspond to different physical scenarios and predictions from Kwan and Fischer (2011). There is not any clear link between stellar properties and decrement shape, which comforts the idea that it is modulated solely by accretion. They also find that stars that have the same type of decrement have usually similar lines shapes, further hinting at a common emitting mechanism and the importance of gas dynamics.

3.6 Variability

As observables are directly linked to the underlying emitting conditions, their variability give direct measurement of the physical parameters, and accretion processes variability. Thus, variability has always been at the core of CTTS studies. Variability, however, comes in different flavors: photometric and spectroscopic variability. Spectroscopy gives access to the lines variability, while photometric variability rather relates to the continuum variability. Both were a strong requirement for the development of the magnetospheric accretion scenario. A general picture of all known variable processes in young stars can be found in Fig. I.10A. . Here, I focus on variability related to (magnetospheric) accretion, in the case of *low*-mass stars ($\lesssim 1$ $M_\odot$), which mainly comes in two main flavors: continuum variability and line variability. For a more general review of stellar variability, see Fischer et al. (2023)

3.6.1 Continuum variability

Continuum variability refers to broad-band variations, as opposed to line (or narrow-filter) variability. The stellar continuum is made of both the intrinsic stellar spectrum (dependent on its spectral type), and an additional accretion-related component, mostly due to the accretion shock. In the IR, continuum variability may also be driven by the hot inner-wall of the circum-stellar disk.



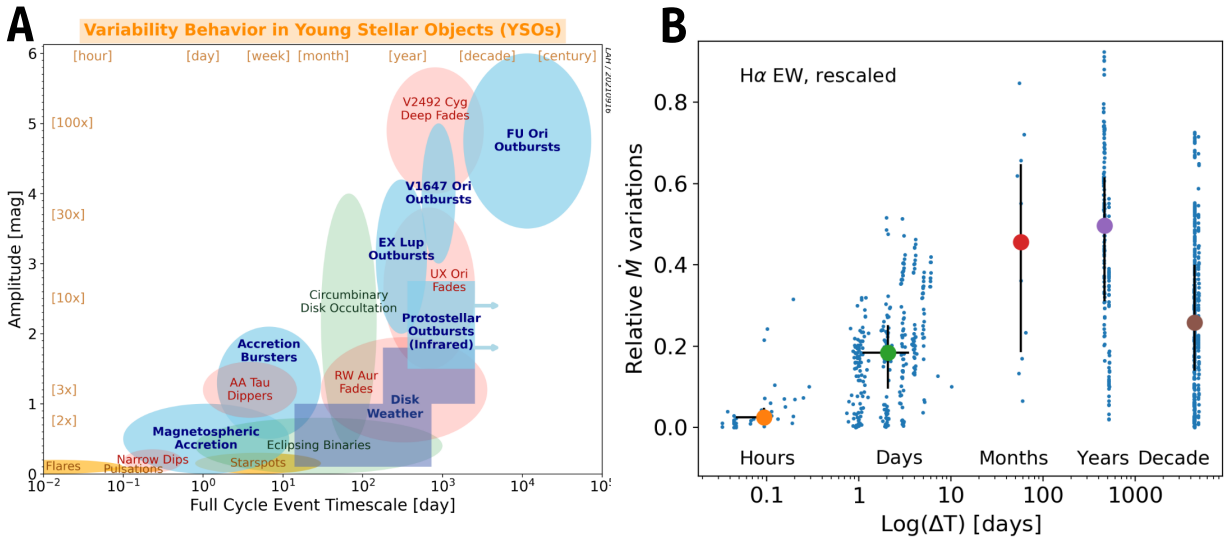


Figure I.10: Panel A: variability amplitude and timescales of various processes in the case of young stellar objects (from Fischer et al., 2023). Panel B: accretion rate variability as a function of the timescale, for CR Cha (from Zsidi et al., 2022).

The stellar spectrum is intrinsically stable on human timescales, however, cold/dark spots may affect its luminosity. This happens on timescales about the rotational period as they come and go out of the line of sight. Venuti et al. (2019) finds that low-mass stars have such variability that is compatible with spots induced from dipolar magnetic fields, while higher mass stars have quasi null variability, compatible with an homogeneous spread of spots over the stellar surface, due to higher-order magnetic fields. On a side note, such dark spots are an issue in the case of transit-spectroscopy and planets detection, as they can induce false positives (Meunier and Lagrange, 2019; Meunier et al., 2019, 2020; Meunier and Lagrange, 2020; Meunier et al., 2023).

In the case of hotspot from an accretion funnel, variability of the X-Ray/UV/Vis excess is bound to occur as the hotspot comes in and out of view as the star rotates. Such variations can be used to infer the star rotational period (e.g., AA Tau, Espaillat et al., 2021). Accretion rates changes may also directly impact the variability amplitude, but rather on timescales slightly larger than the rotational period. Accretion rates measurement and characterization of its variability found that it is mostly modulated by the disk-magnetosphere interactions, and that its effects appear at about the rotational period (Fig. I.10B, Zsidi et al., 2022).

Global modulations were given an explanation in the late 90s. Bouvier et al. (1999) used multi-wavelengths time series observations of AA Tau, and found that global modulations had periodicity of $\sim$ 8.5 days, compatible with the expected period of the star. They find that this is best explained by the magnetosphere interacting with the inner disk, warping the disk, thus allowing dust to occult the star (Bouvier et al., 2003). However, this is only valid for highly inclined systems, while for others, modulations from other origins can still be present.



3.6.2 Lines variability

Accretion processes introduce a wide range of variability behaviors, as already illustrated in Fig. I.9. Apart from the physical conditions variability, lines shapes are directly affected by the inclination of the system. As funnels come in and out of the line of sight, red-shifted absorption is bound to appear and disappear, imprinting rotationally modulated effects within the lines themselves. Multiple authors have used spectral-periodograms to infer the period(s) of the magnetosphere, although they find varying periods depending on the line and spectral channel (e.g., Zsidi et al., 2022; Sousa et al., 2021). The typical timescales and amplitude of variability are shown in Fig. I.10. In the case of non time-resolved observations, auto-correlations diagrams inform on the various lines regions (broad vs narrow components) and links between processes (e.g., Figs. 12&13 in Bouvier et al., 2003).

In short, lines profiles modulations permits the study of geometry variation (Alencar et al., 2012), along with an access to physical properties through modeling and established correlations (Alcalá et al., 2014, 2017; Venuti et al., 2019). However, they require access to high resolution spectrographs, which do not often come alongside powerful adaptive optics required for imaging planets. Testing such as scenario at the planetary-mass regime is not so straightforward.



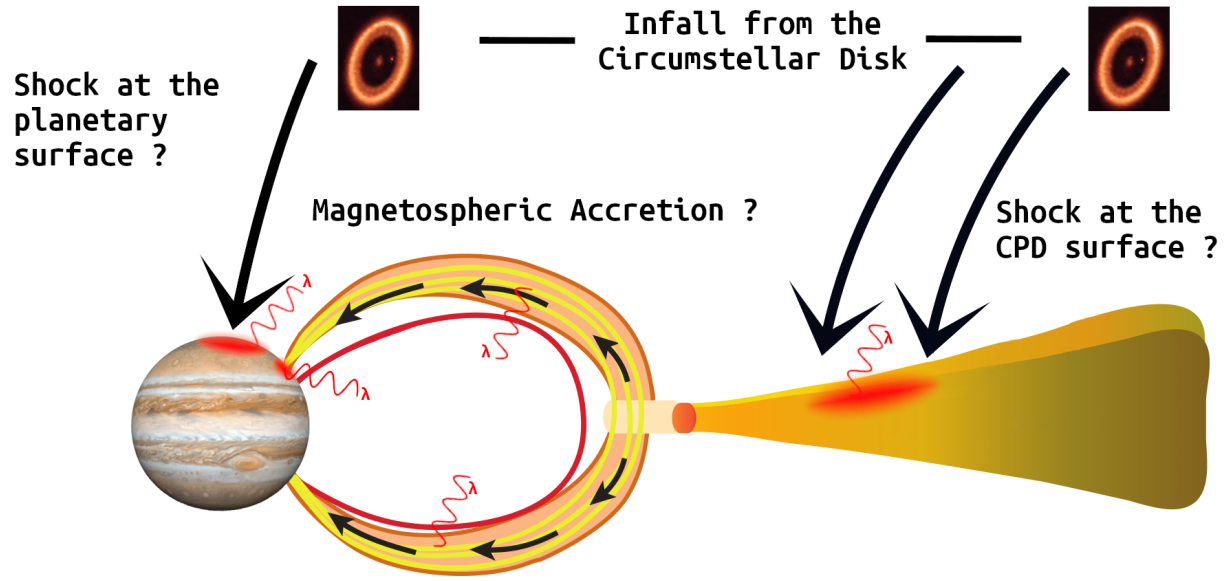


Figure I.11: Overview of the possible accretion processes onto a planet. Adapted from Hartmann et al. (2016). Red shaded areas are shocks, and λ-waves represent possible lines-emitting regions.

4 Accretion in the Planetary-Mass regime

4.1 Theoretical standpoint

While in the previous sections, the use of the term "accretion" was oblivious to the different scales involved, they should be distinguished. Due to clear uncertainties on the exact mechanisms, what happens at small scales, where the gas directly interacts with the planet, is usually treated independently from interactions between CSD and CPD. The assumption is that for gas to be accreted by the planet itself, it first has to enter the Hill sphere. Put simply, two kinds of models coexist: hydrodynamic models that study interactions with the CSD (and to some extent the flows into the Hill sphere), and line-emission models that explain observational features as well as interactions between the planet and its CPD. However they are not incompatible, as some hydrodynamic models also predict line-emission. Fig. I.11 shows a compilation of the three main accretion mechanisms, they will be developed in the following sections.

4.1.1 Magnetospheric accretion

As magnetospheric accretion is the paradigm for the stellar regime, and clues of its extension to the substellar regime were provided (Sect. 2.1.1), it was natural to try and extend it to the PMC regime. Moreover, accretion lines were used as a diagnostic of ongoing accretion, but this diagnostic has mostly been interpreted in the context of accreting stars, where magnetospheric accretion is the paradigm.



Thanathibodee et al. (2019) proposed an extension of the magnetospheric accretion scenario, in the planetary-mass range. The exact details of magnetospheric accretion are given in Sect. 3. They assume an axis-symmetrical magnetosphere, and only model the emission from the funnels. The model assumes coupling between the magnetosphere and the inner disk. The magnetic field lines truncate the inner CPD, and launch funnels by serving as guides for the infalling material. The heated column emits hydrogen lines, and parts where the line of sight intercepts the shock location induce absorption features. Typically, Thanathibodee et al. (2019) assumes a magnetic field around 0.5–1 kG. In Fig. I.11, this model corresponds to the emission from the column.

As for CTTS, the column temperature is a free parameter in the model. For a given planet mass and radius, the model is fully described by the inner launching radius, the width at the base of the column, the column temperature and the column accretion rates. Columns are shaped by the dipole field lines, they follow $r = r_m \sin^2(\theta)$, with r_m the launching radius: $r_m = \mathrm{R_{in}} + \frac{1}{2}\mathrm{Width}$.

This scenario assumes that planets do have a sufficient magnetic field. This has not been confirmed yet, but predicted by a few studies (Reiners and Christensen, 2010). However, the story could go the other way around: a confirmation of magnetospheric accretion would be a confirmation of magnetic field, and in turn place constraints on evolutionary models.

4.1.2 A new scenario: accretion fed by the circum-stellar disk

Both hydrodynamic and magneto-hydrodynamic simulations predict that planets open gaps in circum-stellar disks (Gressel et al., 2013), which could in principle set the final mass of the planet: as much as the gas available within the gap (assuming the planet does not migrate). Typically, planets grow up until 5–10 $\mathrm{M_{Jup}}$ (Kley, 1999; Lubow and D'Angelo, 2006). All simulations predict the formation of a Circum-Planetary Disk (CPD), through which the matter is then accreted to the planet. The shape of the CPD is mostly defined by the high latitudes flows (Szulágyi et al., 2014), as they dominate the accretion flow from the CSD to the CPD (Tanigawa et al., 2012). These flows shock either at the disk or planetary surface (see red shaded areas in Fig. I.11, Szulágyi and Ercolano, 2020; Takasao et al., 2021). The temperature of the disk also helps in determining the dynamics within the disk (Szulágyi, 2017).

However, in the absence of constraints from observations, simulations do not yield results always compatible with each other. For example, the new picture that gas is accreted from the CSD to the CPD mostly through high latitudes flows (Tanigawa et al., 2012; Gressel et al., 2013) was not always the main picture: Ayliffe and Bate (2009) instead predict that high latitude flows would hardly be significant to the total accretion rate onto the system. Most importantly, a main result of the high-latitude inflow is the prediction of outflows. Just beneath the shock on the CPD, gas moves inward, as the incoming material does not have sufficient angular momentum to sustain the keplerian rotation, thus triggering inwards migration within the CPD. However, gas flows outwards in the mid-plane, towards Lagrange points L1 and L2, and simulations also predict collimated jets, a direct by-product of the twisted magnetic field lines by the infalling material (Gressel et al., 2013).

With the discovery of PMCs embedded within the circum-stellar disk of their host star (e.g., PDS 70 b&c Haffert et al., 2019), came the opportunity to place constraints on hydrodynamic models. Accretion lines could be the tracers of the shocks induced by the accretion flows on the CPD and/or the planetary surface. The picture shifted from simulations driven studies, constrained only from observations of the surrounding CSD, to PMC observations driven studies, where lines luminosity modeling would constrain the endpoint of the flow itself.

Physics of an accretion shock, although on a stellar surface, had already been theorized by Calvet and Gullbring (1998). However, they assumed magnetic effects that would reduce shock heating, which might



not be reproduced at the surface of the CPD. Instead, Aoyama et al. (2018) developed a shock model with parameters typical of what is expected from numerical simulations. In principle, this could also be applied to the shock at the base of magnetospherically-induced funnel. They assume a plane parallel shock, and solve for radiative-hydrodynamics of the flow in the pre/post-shock regions, and were able to derive scaling relationships between the lines fluxes and the accretion rate (Aoyama et al., 2021), similar to that obtained for stars a few years earlier (Alcalá et al., 2014, 2017).

The main two parameters are the pre-shock velocity v_0 and Hydrogen number density n_0. They predict that H_α is the brightest of all lines, compatible with what was observed for LK Ca 15 b (Sallum et al., 2015). The details of the lines profiles, however, are quite simplistic, as they are intrinsic to the shock itself, and do not include absorption by foreground material, in particular the accretion flow itself. Because of the only two input parameters, the model can be applied, in principle, to any shock, anywhere. Thus, Marleau et al. (2022) used these models to predict line profiles in the case of a shock at the planetary surface, for multiple flow geometries: (i) magnetospheric accretion geometry, where the shock is located at the base of a conical funnel, (ii) polar inflow, where the shock is located in the poles of the planets, this correspond to high-latitudes inflows from the CSD, and (iii) spherical inflow, where the gas comes from all directions, which seems a simplistic view, but may correspond to large scales flows for planets with a relatively small Hill radius compared to the pressure scale of the CSD (typically, highly embedded planets). The general trend is that lines show spiky features at high accretion rates, which traces higher extinction on the line of sight. However, these are only true for a shock at the planetary surface, whereas a shock on the CPD would yield smooth lines, at similar accretion rates. This is because the shock would be spread over a wide area on the CPD, making the extinction per surface-element basically null. Nevertheless, simulations tend to focus either on the planetary shock, or the CPD shock.

Takasao et al. (2021) tried to bridge this gap, and performed simulations of an accretion flow, originating from the CSD, coming down to the CPD and planetary surface. They used shock physics from Aoyama et al. (2018). They find that the line originating from CPD shock are negligible compared ($\times$10–100)to that originating from the planetary shock. However, the accretion shock on the planetary surface is highly affected by the accretion shock on the CPD. This is because the CPD shock heats the accretion flow and changes the relative density at the CPD surface, on top of more retro-feedback effects. Overall, they find time-variable accretion rate on the planet, even with constant mass input in the system. They also find radial outflows, similar to that found by Tanigawa et al. (2012).

The theoretical standpoint of accretion in the case of PMCs is still quite unconstrained. Future observations will help disentangle competing models.

4.2 Tools for their characterization

PMCs and PMOs cannot always be observed with the same instruments, for the sole reason that observations of companions are intrinsically limited by the contrast to their host star. With the advent of adaptive optics in the last two decades, the limiting separation for detecting companions has been pushed further, now granting access to *close-in* companions. Furthermore, accretion processes have also opened up a new way to detect companions: through their accretion lines.

There are two main kinds of data when it comes to PMCs/PMOs: imagers and spectrographs. Imagers usually provide broad/narrow-band images that usually come with great spatial resolution, thanks to their adaptive optics. An example is SPHERE/VLT. Broad-band images mostly only provide photometry points, as they are unable to unveil the intrinsic properties of the planets. Narrow-band images, however, can be used to provide measurements of lines fluxes. Recent studies have also used narrow-band imaging to obtain UV excess measurements of some PMCs (Zhou et al., 2014, 2021). On the other hand, spectrographs provide



access to the intrinsic emission spectrum of the targets, as well as emission/absorption lines profiles when the spectral resolution is sufficient. The three most commonly found types of spectrographs are:

- Single-Fiber Spectrographs: they are the most simple ones, with single optical fiber directly feeding the spectrograph,thus providing access to the λ dimension. They are usually seeing-limited, but provide as high a resolution as desired ($R \gtrsim 100\,000$). They are best used for single objects, where there is no risk of contamination from a nearby star. However, the wings of the PSF are usually cut-out by the fiber itself, which means that in poor seeing conditions, a significant part of the flux will be missed out. While this is not necessarily an issue for bright stars, faint PMOs may lack a significant fraction of their flux, which may affect the final S/N, especially at such high resolutions. As an example: ESPRESSO is a single-fiber spectrograph, though it combines signals from multiple telescopes.

- Long-Slit Spectrographs: they provide access to (1+λ)D: 1 spatial and 1 spectral dimensions. They are made of a single long-slit opening, usually of adaptable width, that is dispersed through the (typically echelle) spectrograph. While the aperture width does provide a way to solve the wings-off problem from single-fiber spectrographs, their spectral resolution is usually linked with the width of the aperture. In order to reach high spectral resolutions ($R \gtrsim 50\,000$), wings will still be cut off. However, since they provide access to a spatial dimension, they can be used to disentangle signals from a host star and its companion, at least to some extent. While some long-slit spectrographs are seeing limited (e.g., UVES, althought UVES can also work as a fiber-entrance) and can therefore only be used for *wide* companions or single objects, others like CRIRES do have an adaptive optics system and can be used to observe close-in companions (e.g., GQ Lup b)

- Integral-Field Spectrographs: they provide access to (2+λ)D: both spatial dimensions, as well as the spectral dimension. They are usually quite complex systems, and are also limited to medium resolutions ($R \sim 5000$). However, they are often coupled with an adaptive optics, and prove to be capable of studying both close-in (PDS 70 b/c) and wide (GSC 06214-00210 b) planets. Examples are VLT/SINFONI (now VLT/ERIS), VLT/MUSE, or even JWST/MIRI in space.

Similarly to CTTS, accretion in the planetary-mass regime can be studied through their accretion lines, as their respective profile and flux are highly dependent on the geometry of the accretion flow. Figure I.12 shows the available instrumentation, in terms of the observed spectral range and the spectral resolution. There is clearly an instrument available for every spectral band, and most accretion lines, in all three aforementioned configurations. In the optical, the H_α line can be accessed through most instruments, depending on the separation. It is supposed to be the brightest of the accretion lines, and can be studied at both high resolution ($R \gtrsim 50\,000$, UVES) thanks to its flux, and medium-resolution (MUSE, $R \sim 5000$) for close-in planets. However, it is in the infrared that the most powerful adaptive optics are found, making the Pa_β line (the brightest in the infrared) a great candidate for the study of accretion processes. However, its study is hardly possible at resolutions similar to that of H_α: the IR sibling to UVES would be CRIRES, but its transmission is relatively poor, making only Delorme 1 (AB)b a good candidate for the study of Pa_β at such resolutions. Still, most PMCs and PMOs have fluxes sufficient to be studied at a moderate resolution ($R \sim 10\,000$), with ERIS or XSHOOTER. $R = 10\,000$ happens to be the resolution at which different accretion models can be differentiated (Marleau et al., 2022).

Both the atmosphere and CPD studies are closely linked together, as the CPD modeling is usually fitted to the IR excess to the theoretical spectra of the object. The atmosphere composition is derived from spectral absorption bands and lines, obtained from mid-resolution spectrographs (ERIS, XSHOOTER, MUSE, NIRPSEC), as well as photometry points (HST, SPHERE). Up until JWST was launched, CPD modeling



was only possible from photometry points, mostly in the L and M bands. Now, JWST/NIRSpec/MIRI also provides a spectrum at these wavelengths (e.g., Cugno et al., 2024). Alternatively, constraints on CPDs have also been placed with ALMA at mm-wavelengths (e.g., Wu and Sheehan, 2017). Last but not the least, near-infrared interferometry is now also providing new opportunities to study PMCs, for example with the GRAVITY interferometer at VLTI (Gravity Collaboration et al., 2023), allowing for accurate astrometry and characterization at inner separations (e.g., Wang et al., 2021) .

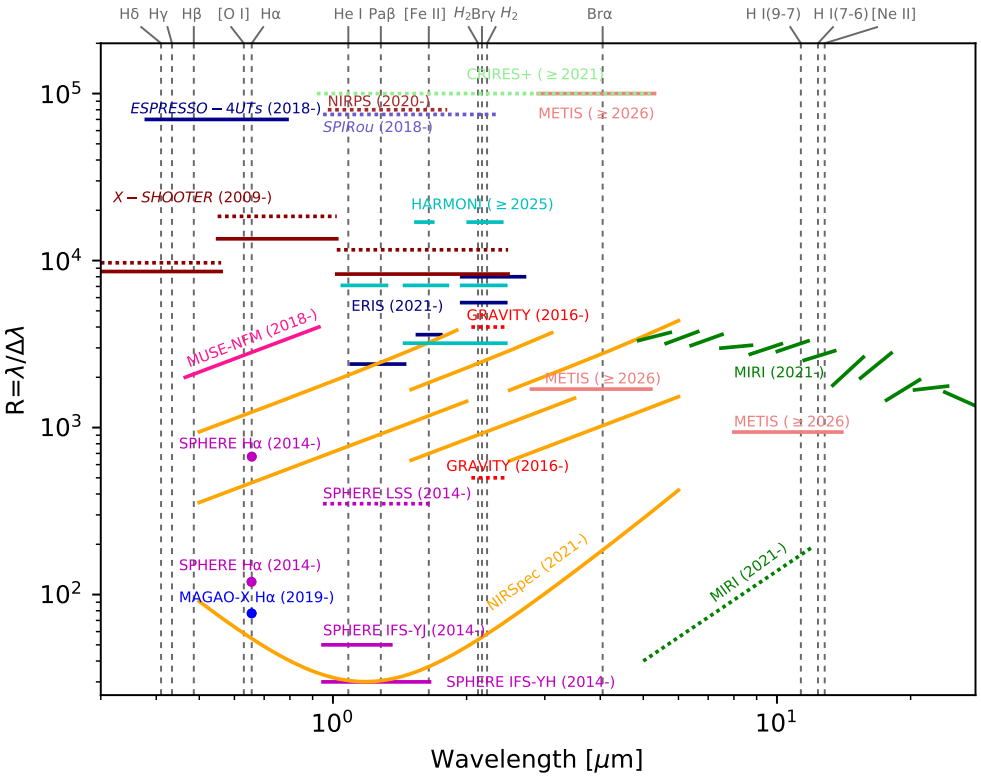


Figure I.12: Current instrumentation, as a function of the observed wavelength range and spectral resolution. Courtesy of M. Bonnefoy.

In summary, the main instruments for studying accretion lines are MUSE, UVES, ERIS and XSHOOTER. In the mid-IR, NIRSpec/MIRI also provides access to the Pfund Hydrogen series, although they are now mostly used for CPD characterization.

4.3 Open questions and objectives of this thesis

So far, most PMCs detections have been fortuitous. Dedicated campaigns had only barely started at the start of my PhD, but still have now only discovered a few PMCs.



4.3.1 Open questions

With theoretical emission models only now being available, accretion-focused papers had focused on three main signatures: lines, CPD, and shock components.

Most studies have focused on the detection of accretion lines, mostly following the detection of PDS 70 b&c in H_α (Haffert et al., 2019). The fluxes of these lines have been used to convert to accretion rates (Haffert et al., 2019; Eriksson et al., 2020; Betti et al., 2022,). However, the relationships they used for that purpose were derived from stellar studies, and Betti et al. (2023) recently showed that it may not extend to the PMC regime. Efforts have been made, in fact, to use the more recent planetary scaling relationships Aoyama et al. (2021).

In order for these conversions to be meaningful, there needs to be a gas reservoir. The question is: what is this gas reservoir? The natural candidates are circum-planetary disks, and studies have tried characterizing them, would they detect them in the first place. Most work has focused on photometry points (e.g., Bowler et al., 2011), as spectra at relevant wavelengths (LM bands) are hardly accessible with the current instrumentation. Others have used ALMA observations (Wu and Sheehan, 2017; Wu et al., 2017) , which only traces the dust. Only recently, JWST has opened new windows for CPD in-depth characterization (Cugno et al., 2024).

Combining accretion lines and CPD characterization proved difficult so far, given the limited spectral resolution at which each observation was obtained: ~ 2000 for lines, photometry points for CPDs. Instead, the UV excess is thought to be a more direct tracer of the accretion shock, and its study could help unravel the physical conditions ($\dot{\mathrm{M}}$, temperature, density, ...) where it is emitted. However, observations of the UV excess have so far used photometry points (Zhou et al., 2014, 2021), as spectrographs at these wavelengths are not common, which hinders most of the modeling and interpretation. A spectrum of the UV excess and surrounding continuum would instead provide a detailed picture of the relevant mechanism, alike what was performed by Espaillat et al. (2021).

Finally, it should be noted that accretion has long been considered steady. It has been shown that accretion on stars is variable (therefore not steady), and hints have shown that it is also variable for PMCs. This will be developed in the later sections, and in this manuscript. Overall, the reader should keep in mind that accretion is intrinsically a variable process.

4.3.2 Objectives

This naturally yields four axes of study. First, testing emission lines models (Aoyama et al., 2018; Thanathibodee et al., 2019) that were developed following the discovery of PDS 70 b&c. In fact, high-resolution ($R \gtrsim 50\,000$) observations of Hydrogen and Helium lines have been shown to be possible (Ringqvist et al., 2023), which was not even considered before. Second, lines have been hinted to be variable (Zhou et al., 2014; Eriksson et al., 2020), but this has never been characterized and may explain the H_α surveys non-detections, as well as constrain accretion timescales of PMCs. Finally, shock-modeling only ever was performed with photometry points, but it might be possible to obtain a spectrum of this UV excess, following the same methods that allow for the study of accretion lines at high-resolution.

I choose to focus my thesis on two of these points. The lines variability may be assessed with dedicated programs, both in terms of flux and lines profiles. For that matter, I will use instruments such as VLT/SINFONI, that permits combining a medium-resolution spectrographs with a powerful adaptive optics. This permits the study of the variability of the Pa_β line flux, as well as some profile variability to some extent. Then, I will focus on the line-modeling itself, with a dedicated high-resolution instrument (VLT/UVES), although for some older PMCs. Instead of the Pa_β line, this will be focused on optical Balmer and Helium



lines, as it was shown feasible by Ringqvist et al. (2023). I will also discuss the variability of these lines, as well as the UV excess of the studied targets. Overall, I will build a sample study of PMCs, with a wide range of physical conditions: young, old, *close* and *wide* separations (rather, *wide* and *wider*), thus allowing me to test the magnetospheric accretion and shock-emission scenarios in a variety of conditions, and infer the underlying physical parameters relevant to accretion mechanisms.

I first present the results of VLT/SINFONI monitoring program of the Pa_β line of 2 PMCs (Chapter II), then the high-resolution study of the optical lines of 3 other PMCs with VLT/UVES (Chapter III), and conclude on this thesis (Chapter IV).





Chapter II.

Accretion tracers in the Near-Infrared with VLT/SINFONI

The Pa_β line is the brightest of the near-infrared accretion lines. Furthermore, it is less contaminated by chromospheric emission than other optical lines. I use the power adaptive optics of VLT/SINFONI, in the J band, to observe GQ Lup b and GSC 06214-00210 b, two wide orbit Planetary-Mass Companions of $\sim$ 5 Myr and $\sim$ 17 Myr. The Pa_β is partly resolved ($R \sim 2000$). Each target is observed at 3–5 independent epochs over a year. Individual epochs provide access to the ∼hour timescales variability. I also add archival data to the sample to scan ∼decade timescales variability of the line.

The Pa_β line of both targets reaches a variability amplitude of < 50 % at ∼hours timescales, ~ 100 % at days to months, and up to ~ 1000 % on the decade timescale. The behavior is reminiscent of what is seen on T Tauri stars. I test magnetospheric accretion models and shock-emission models against the observations. The Pa_β line of GQ Lup b is only reproduced by the magnetospheric accretion model, while the shock model is preferred for GSC 06214-00210 b.

The observations are not sufficient to firmly disentangle the two (non-exclusive) mechanisms, but a monitoring at $R > 10\,000$ would be sufficient. However, this study places constraints on the variability amplitude and timescales on such PMCs, that may explain the low yield of detection of H_α imaging campaigns.

Chapter's contents

1 Introduction 49
1.1 GQ Lup b 50
1.2 GSC 06214-00210 b 50
2 SINFONI: go-to tool for ground-based NIR characterization 51
2.1 Instrument description 51
2.1.1 Adaptive Optics 52
2.1.2 SPIFFI: the Integral Field Unit 53
2.1.3 Performances and observing notes 53
2.2 Observations and Data reduction 54
2.2.1 Observations 54
2.2.2 Data reduction 54
3 Atmospheric modeling 58
3.1 Main spectral features 58
3.2 The atmosphere of GQ Lup b and GSC 06214-00210 b 58
3.2.1 Correlations 60
3.2.2 Resulting values and interpretation 60
4 The Paschen Beta line 62
4.1 Line profiles 62
4.2 Line flux variability 63
5 Emission lines models 65
5.1 Models description 65
5.2 Model fitting 66
6 Conclusion 68



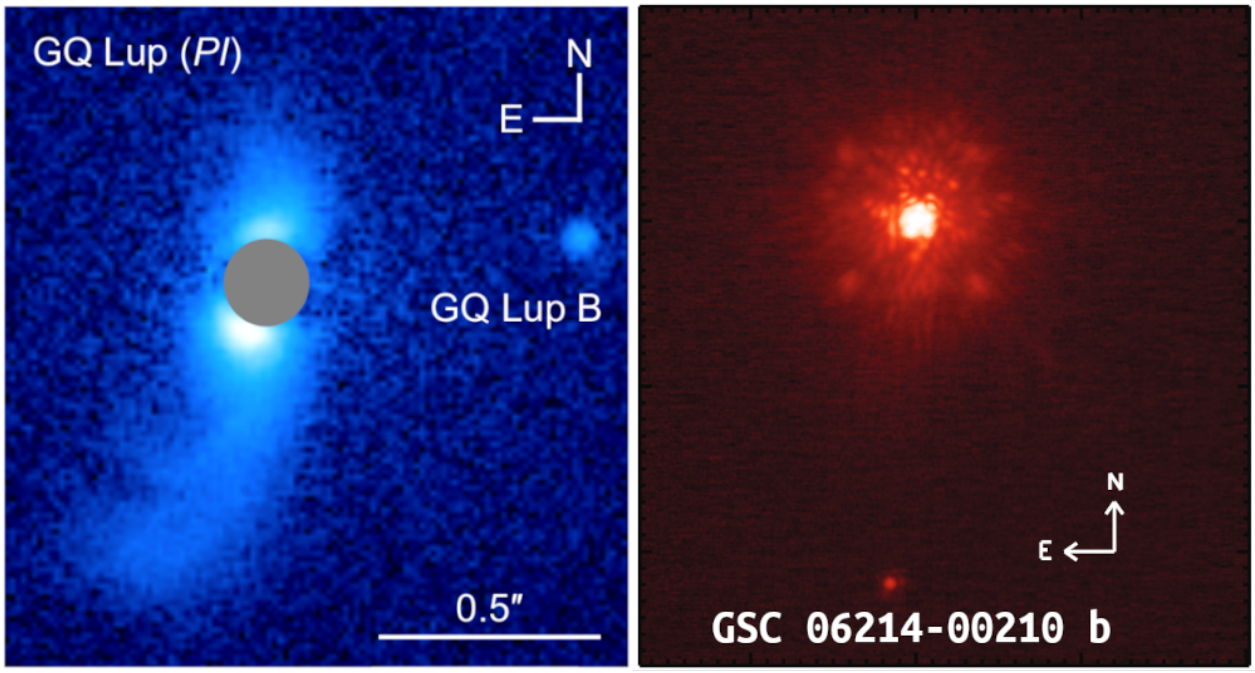


Figure II.1: Left: SPHERE/VLT polarization image of GQ Lup b (van Holstein et al., 2021). Right: NIRC2/KeckII image of GSC 06214-00210 b (Ireland et al., 2011).

1 Introduction

The most direct way to study accretion is through accretion lines. Historically, which line to study mostly depends on the available instrumentation, and since PMCs are usually close from their host star, the use of adaptive optics is required to disentangle the companion signal from that of the star. The best performing adaptive optics have historically been in in NIR wavelengths, where atmospheric variations are slower, and easier to correct for. A set of accretion lines are located at wavelengths where adaptive optics system perform best, in particular the K band, which hosts both the Br_γ and Pa_γ lines. However, only a handful of PMCs had seen a successful detection of these lines (e.g., Br_γ: Delorme 1 (AB)b, GSC 06214-00210 b; Pa_γ: Delorme 1 (AB)b, TWA 27 b, Betti et al., 2023; Lachapelle et al., 2015; Manjavacas et al., 2024). And at the time of the observations presented in this work, only GSC 06214-00210 b was known to bear a Br_γ line. With so little detections and limited line flux, any attempt at modeling would be restricted by the S/N of the line with respect to the continuum. Other lines may therefore be more appropriate. Moving to adjacent bands, the Pa_β (1.8 µm) line lies in the J band. This line is known to be the brightest of the NIR lines, and still within a reasonable performance range for adaptive optics systems, making it a great asset for characterizing accretion properties of Planetary-Mass Companions. Cherry on the cake, the Pa_β line is known not to be contaminated by chromospheric activity, at least on stars (Natta et al., 2014). This line had previously been detected on a few companions, among which GQ Lup b and GSC 06214-00210 b.

Understanding the emitting mechanism of accretion lines comes in many ways and flavors. The current sample of accreting companions is still quite sparse, making a general analysis hardly possible. Instead, I



focus on characterizing the specifics of two companions: GQ Lup b and GSC 06214-00210 b. I focus on the variability aspects of the lines both in terms of profiles and amplitude, as well as the link with their atmosphere properties. This chapter serves as a summary of the work, which was published in Demars et al. (2023).

In this Section, I present the two targets: GQ Lup b and GSC 06214-00210 b. In Sect. 2, I present the instrument: SINFONI, followed by the observations and data reduction. Then, I present the atmospheric features in (Sect. 3), followed by the Pa_β line analysis (Sect. 4) and modeling (Sect. 5). In Sect. 6, I sum up this work.

1.1 GQ Lup b

GQ Lup b was originally identified as a companion to the GQ Lup star by Neuhäuser et al. (2005). It is a 10–40 M_{Jup} companion, at ∼0.7" from its host star (∼ 108 AU at 154.10 ± 0.69 pc Gaia Collaboration et al., 2023). The host is a K7Ve star, on the higher end of the T Tauri stars mass spectrum ($M_* = 1.02 \pm 0.05$ $M_\odot$, MacGregor et al., 2017). While the companion itself is not located within the circum-stellar disk, the disk does show spiral structures (van Holstein et al., 2021) extending to 129 AU. GQ Lup b seems to be on a polar orbit with low eccentricity (Stolker et al., 2021), which has been proposed to explain replenishment of the gas reservoir of GQ Lup b as it crosses the circum-stellar disk. Another companion to the system (GQ Lup c) was recently found, albeit at much higher mass and separation ($M \sim 0.15$ $M_\odot$, ∼ 2400 AU, Alcalá et al., 2020; Lazzoni et al., 2020).

Near-Infrared spectra photosphere modeling (Stolker et al., 2021) yields $T_{\rm eff} = 2700$ K, consistent with M9 spectral type. They infer extinction in the line of sight of $A_v = 2.3$ mag, with an IR excess above 2.5 µm, sign of a Circum-Planetary Disk and/or gas reservoir around the companion. However, ALMA observations did not detect this reservoir (MacGregor et al., 2017; Wu and Sheehan, 2017), nor did SPHERE polarized-light observations (van Holstein et al., 2021). This analysis used JHK SINFONI spectra from the pilot observations (Seifahrt et al., 2007), which proved to be contaminated with stellar light (McElwain et al., 2007; Lavigne et al., 2009). While they could have biased the IR excess determination, recent JWST/MIRI observations confirmed the IR excess and the presence of a disk (Cugno et al., 2024) with no silicate features, consistent with important grain growth and thin and compact disk. This is also consistent with the non-detection from ALMA observations, which had proposed a compact disk as an explanation for the non detections: they would only emit in sub-mm regime. CRIRES observations have yielded a projected rotational velocity of $5.3^{+0.9}_{-1.0}$ km/s (Schwarz et al., 2016). They argue that the slow spin may be due to its youth: the companion may not have had time (yet) to accrete angular momentum.

The companion displays a bright H_α line, that has been consistently detected on four occasions from its detection (April 10, 1999, Marois et al., 2007) to recently (April 19, 2019 Stolker et al., 2021). Line variability has been proposed (Wu et al., 2017), but not yet evidenced. The Pa_β line has first been observed on September 18, 2006 (Seifahrt et al., 2007), but no Br_γ line has ever been found in K band spectra (Neuhäuser et al., 2005; McElwain et al., 2007; Seifahrt et al., 2007; Lavigne et al., 2009).

1.2 GSC 06214-00210 b

GSC 06214-00210 b was first evidenced as a companion to the K5 T Tauri star GSC 06214-00210 ($M_* = 0.80 \pm 0.11$ $M_\odot$, Kraus et al., 2008; Ireland et al., 2011; Bowler et al., 2014; Pearce et al., 2019), part of the Scorpios-Centaurus association (Preibisch et al., 1998). However, Gagné et al. (2018) provides an alternative membership to the Upper-Scorpus Centaurus sub-group. Previous studies had yielded mass-luminosity-age estimates that were biased by the estimated distance. The updated distance (108.8 ± 0.3 pc, Gaia



Collaboration et al., 2023) provides better constraints. For the companion, Pearce et al. (2019) provides an age of $16^{+1.9}_{-2.9}$ Myr, $L \sim 10^{-3.35\pm0.02} L_{\odot}$. Its mass is 14.5 ± 2 M_{Jup}, at 2.2" from its host (240 AU at 108.8 ± 0.3 pc, Gaia Collaboration et al., 2023), and it is classified with an M9-M9.5 spectral type (Lavigne et al., 2009; Bowler et al., 2014).

The companion is already known to bear the Pa_{β} line, along with an infrared excess evidenced through K–L' bands photometry (Ireland et al., 2011; Bowler et al., 2011). Its host star, however, does not have any clear reported excess, with the only clue being 2σ excess in the WISE W1–W4 photometry at ~ 22 µm (Bowler et al., 2011). Similarly to GQ Lup b the companion disk has not been detected with ALMA Bowler et al. (2015); Wu et al. (2017), also a sign of a compact disk. van Holstein et al. (2021) did however detect an intrinsic polarization signal with VLT/SPHERE, yielding a possible inclination of ~ 48 °, that constrain its rotational period to 22–77 h using its projected rotational velocity ($6.1^{+4.9}_{-3.8}$ km/s, Bryan et al., 2018). Unlike GQ Lup b, this companion does have a Br_{γ} line (Lachapelle et al., 2015).

2 SINFONI: go-to tool for ground-based NIR characterization

This section provides an overview of the instrument and data reduction procedures. For detailed informations, refer to SINFONI User Manual[1] and SINFONI Pipeline Manual[2].

2.1 Instrument description

The Spectrograph for INtegral Field Observations in the Near Infrared (SINFONI) was an instrument mounted at the Cassegrain focus of the 4rd Unit Telescope, at VLT/Paranal (note that it was transfered to UT3 a few months before its decommissioning in August 2019). It operated from 2005 to 2019. It has now been replaced with ERIS, mounted at UT4, whose design is heavily inspired and similar to that of SINFONI, and even re-uses some of the optical parts of SINFONI.

SINFONI is an Integral Field Spectrograph (IFS), which means it is able to provide a spectrum for every point of the image within its Field of View. This is particularly useful for characterizing exoplanets and companions that often have their signal contaminated by the extended PSF of their host star, as the spatial dimensions information can be used to disentangle the two signals. This comes in contrast to single-fiber spectrograph, which only provide access to a single spectrum at a single spatial location.

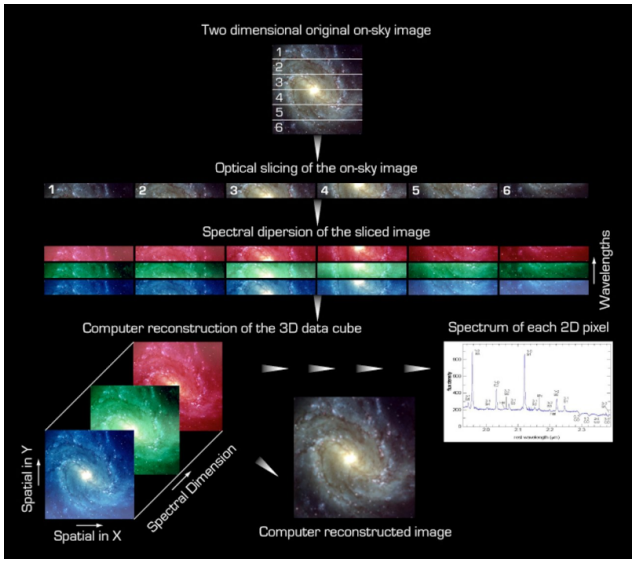


Figure II.2: Summary of the field slicer and dispersal by SINFONI. Credits: ESO.

[1] **SINFONI User Manual**:
https://www.eso.org/sci/facilities/paranal/decommissioned/sinfoni/doc/VLT-MAN-ESO-14700-3517-P103.1.pdf
[2] **SINFONI Pipeline Manual**:
https://ftp.eso.org/pub/dfs/pipelines/instruments/sinfoni/sinfo-pipeline-manual-3.3.4.pdf

However, this is often limited by the observing conditions: at Paranal, the atmospheric turbulence implies a seeing that averages to $\sim 1''$ at 2.2 µm, SINFONI's optimal operating wavelength. On its own, this means that SINFONI should intrinsically be limited to the study of companions at higher separation, but it is equipped with an Adaptive Optics system, which improves the limitations to the diffraction limit (0.057" at 2.2 µm) to Strehl Ratios between 0.2–0.6 (at seeing 1.0–0.6" respectively) depending on the observing condition and reference star for the AO system (SINFONI User Manual[3], Fig. 17).

Another advantage of the IFS design is its capabilities to disentangle the target's spectrum from the sky emission spectrum. The sky emission (OH lines, black-body) and absorption features (intrinsic absorption) are highly and rapidly variable in the near-infrared, as they are highly dependent on the observing conditions (e.g., water vapor pressure). An IFS provides access to the target's spectrum, and the surrounding sky emission spectrum that appears as baseline over the field, which can easily be estimated and subtracted. However, absorption features still require a calibration standard, typically a Telluric Standard Star.

SINFONI is made of two main sub-modules. The light beam is splitted between the Adaptive Optics (AO) system and the SPIFFI IFS system. The visible wavelength range (450–950 nm) is sent to the AO system, and the NIR range (1.05–2.45 µm) to the SPIFFI system. The Adaptive Optics module, and the integral field spectrograph SPIFFI, are detailed in the following sub-sections.

2.1.1 Adaptive Optics

The Adaptive Optics (AO) system corrects the aberrations induced by the atmosphere, thus providing a PSF that is nearly diffraction-limited. It consists in a closed-loop system, that both measures wavefront curvature aberration, and corrects for it with a dedicated Deformable Mirror (DM, not to be confused with Dungeon Master).

Deformable Mirror (DM) The DM is placed in the light path just before the beam-splitter. Its role is to provide the wavefront/AO correction. The wavefront aberrations come from two factors: the atmosphere aberration, and the telescope aberrations. The DM itself only corrects for atmospheric aberrations, but is mounted on a Tip/Tilt Mount that is designed to correct for lower order aberrations. The DM is made of an aluminum mirror placed above a grid of 60 electrodes that induce curvature deformations to the DM when they are applied a voltage. The electrodes are arranged in a 5 concentric rings, of which only the inner 4 provide the field AO correction, with the 5-th ring providing edge-effects corrections. The grid of electrodes are placed in the same grid as the wavefront curve measurement grid, so as to provide an accurate correction where it was measured.

The wavefront sensor The wavefront sensor of SINFONI is made of a series of optics that collimate the beam to the Lenslet Array and through a membrane mirror. The Lenslet Array is subdivided into 60 sub-apertures with the same configuration as the electrodes beneath the DM. Each of them divides the beam to 60 fibers that drive the beam to the Avalanche Photo Diodes, that yield counts. The membrane mirror vibrates as a set rate (2.1 kHz), projecting the light beam alternatively on both sides of the Lenslet Array. This means that the counts alternatively correspond to inner-pupil and outer-pupil counts, whose difference is proportional to the local field curvature. This provides the curvature correction that is sent to the DM.

[3]**SINFONI User Manual**:
https://www.eso.org/sci/facilities/paranal/decommissioned/sinfoni/doc/VLT-MAN-ESO-14700-3517-P103.1.pdf



Band	250 mas	100 mas	25 mas
J	1870	**1800**	**2360**
H	2920	2730	5500
K	4490	5090	5950
H+K	1640	2050	2710

Table II.1: SINFONI Spectral resolution depending on the band and plate-scale. See instrument manual. Bold settings were used in this study.

Band	250 mas	100 mas	25 mas
J	4.47	**4.64**	**3.53**
H	2.83	3.02	1.50
K	1.96	1.73	1.48
H+K	2.37	1.90	1.44

Table II.2: SINFONI sampling resolution (in px) for 1 FWHM of a spectral resolution element. See instrument manual. Bold settings were used in this study.

Overall, the AO performance is highly dependent on the observing conditions, mainly the seeing and coherence time of the atmosphere. The performance also varies depending on the distance to the reference star, although this is not so much of an issue in the context of direct imaging of planetary-mass companions, as they are usually close enough to their host star, which is used as the reference star.

2.1.2 SPIFFI: the Integral Field Unit

The integral Field Unit SPIFFI is the core module of the instrument: the *science* module. It is responsible for slicing the field into sub-slitlets, and diffract all of them to build a spectral cube of the field. It is made of 3 main parts: the pre-optics, the image slicer, and the grating wheel, before imaging on the detector itself.

Pre-optics The pre-optics are responsible for collimation and magnification of the light beam, providing access to different plate-scales on the detector. The three offered modes are 25mas/px, 100mas/px and 250mas/px.

Image slicer The image slicer is responsible for slicing the field into multiple *sub-images*: so called "slitlets" or "pseudo-slits". It is made of a arrangement of 32 mirrors, each responsible for one slitlet.

Grating wheel SINFONI operates in the NIR, with its grating wheel providing access to the J, H, H+K and K bands, one at a time.

Detector The detector is a Rockwell Hawaii 2RD detector, of size 2k × 2k pixels. Its saturating limit is at 45,000 ADU, but it was shown that persistence effects appear as low as 10 000 ADU.

2.1.3 Performances and observing notes

SINFONI provides access to the spectral dimension over the whole field of view. However, the field itself is not sliced equally in both axes. The image slicer divides the vertical axis into 30 independent slitlets, but each of them is then sampled by 64 pixels on the detector along the horizontal axis. This makes elongated spaxels in one of the spatial dimension, with the plate-scale name referring to the larger dimension (100 mas/px = 50 × 100 px). Furthermore, the spectral sampling is not constant over the whole band, nor is constant depending on the plate-scale and observing band (see Fig. 27–30 in SINFONI User manual[4]). Both the

[4]**SINFONI User manual**:
https://www.eso.org/sci/facilities/paranal/decommissioned/sinfoni/doc/VLT-MAN-ESO-14700-3517-P103.1.pdf



spectral resolution of SINFONI and the line-sampling are given in Tables. II.1 and II.2 respectively, as a function of the observing band and platescale. The spectral resolution varies significantly between the J and K band (as low as 1870, up to 5950). This study used both the J bands 25 mas and 100 mas platescales for GQ Lup b and GSC 06214-00210 b respectively, for spectral resolutions of 2360 and 1800 respectively. In terms of sampling of the lines, it can be as low as 1.44px/FWHM for the 25 mas setup of the H+K and K band, which is not Nyquist sampled. In fact, the whole K band, no matter what the plate-scale is, is not Nyquist sampled. This is not an issue for the study here (3.53px/FWHM and 4.64px/FWHM for GQ Lup b and GSC 06214-00210 b), but should be accounted for when dealing with K band data.

2.2 Observations and Data reduction

2.2.1 Observations

GQ Lup b was observed on the nights ending on 2017-04-25, 2017-04-30 and 2017-06-01. GSC 06214-00210 b was observed on the nights ending on 2017-04-25, 2071-05-04, 2017-06-01 and 2017-08-19. Both were part of program 099.C-0760(D)[5] (PI: Bonnefoy). Both were observed in the J band, targeting the Pa_β line (1.28 µm), with the 25 mas/px plate-scale for GQ Lup b, and the 100 mas/px plate-scale for GSC 06214-00210 b, yielding spectral resolutions of 2360 and 1800 respectively. The primary stars were placed out of the field of view to avoid detector saturation. The 25 mas/px plate-scale was used for GQ Lup b because it is relatively close to its host star (0.7"), therefore providing a fine sampling of the primary's PSF wings around the companion. In the case of GSC 06214-00210 b, the separation is much more favorable (2.2"), so a larger plate-scale was chosen to mitigate the detector noise effects.

We also added archival data to the sample. GQ Lup b had already been observed in the same setup on 2006-09-18, as part of program 077.C-0264(A)[6] (PI: Neuhäuser). Others nights of the programs had too poor observing conditions to be useful. These data had already been published by Seifahrt et al. (2007), although the extraction of the companion spectrum showed sign of residual contamination from the primary (McElwain et al., 2007; Lavigne et al., 2009), so we re-reduced the data-cubes. We also used the low resolution spectrum obtained by Lavigne et al. (2009) with NIFS/GEMINI (2007-05-30, $R = 5000$ but the spectra had previously been smoothed to match SINFONI resolution). As for GSC 06214-00210 b, we used the public spectrum from Bowler et al. (2011), obtained with the Keck/OSIRIS spectrograph (2010-07-09, R $\sim$ 3800).

In both GQ Lup b and GSC06214b cases the datacubes showed a dark area in the lower half of the detector. Its origin is still unknown, but proved a flattening/calibration issue in this region. All datacubes for which the companion was placed in this region were excluded from the analysis ($\sim$ 25 % for GQ Lup b, $\sim$ 50 % for GSC06214b).

2.2.2 Data reduction

The data reduction was performed in multiple steps: static noise correction, cubes reconstruction, wavelength calibration, spectra extraction and telluric correction.

Static noise SINFONI had previously been found to bear static noise elements (Bonnefoy et al., 2014) in the raw data, that were not accounted for by the pipeline. These were corrected with dedicated routines available in TExTRIS (Petrus et al., 2021, Bonnefoy et al, in prep.).

[5] **099.C-0760(D)**: https://archive.eso.org/wdb/wdb/eso/sched_rep_arc/query?progid=099.C-0760(D)
[6] **077.C-0264(A)**: https://archive.eso.org/wdb/wdb/eso/sched_rep_arc/query?progid=077.C-0264(A)



Cube reconstruction The raw frames were turned into the (2+1)D data-cubes using the regular SINFONI pipeline (Abuter et al., 2006). The position of the 30 slitlets is identified on calibration frames to make a 2D association map, which is then used to reconstruct data-cubes from science frames. Sky emission lines are also subtracted from the data-cubes with dedicated tools within the pipeline. Still there were lots of residual lines that were removed at a later stage. Each exposure was processed independently, thus providing access to small time-variations of the Pa_β line.

Wavelength calibration While SINFONI pipeline provides a wavelength solution, it has been shown to be biased depending on the data-set (Petrus et al., 2021). A new wavelength solution was therefore computed by cross-correlating (TExTRIS) a template sky spectrum (computed with SkyCalc[7], Noll et al., 2012; Jones et al., 2013) with the spectrum at every spatial position of the cube. This process is applied to Tel. Std. observations that have an intrinsic higher S/N. The solution was chosen to be equal to that of the Tel. Std. of said sequence, computed on spaxels with S/N > 10. The exact solution was chosen as the median value across the FoV at each spectral bin. The typical uncertainty on the calibration is ~ 0.2 Å, which converts to ~ 4.7 km/s at Pa_β, which is about 1/30-th of the spectral resolution FWHM.

Spectra extraction In both GQ Lup b and GSC06214b cases, the primary's PSF wings extend to the companion location, therefore contaminating the signal of the companion, and imprinting the primary's spectrum into the companion spectrum. The targeted spectral feature is the Pa_β line, which is the line the host stars of both GQ Lup b and GSC06214b also bear (in emission for GQ Lup b, in absorption for GSC06214b). Would they have a relatively flat continuum around and within Pa_β, the contamination could be subtracted directly from the spectra, by interpolating the primary continuum on either side of the line. Instead, it is required to perform a proper subtraction of the primary's wings contamination, directly on the data-cubes. The primary's wings are approximated directly from the reconstructed cube, as a 3rd-order 2D polynomial gradient. It is fitted for each spectral bin, and subtracted from the data. The companion PSF is then fitted with a reference PSF: that of the Telluric Standard star of the sequence. However, this simple procedure will intrinsically be biased. The fit of the primary's wings, are themselves contaminated by the companion's wings. The fitting process is therefore performed iteratively, where at the beginning of each iteration, the previously fitted companion PSF is subtracted from the data. Over time, the process stabilizes and converges. We found that a total of 4 iterations is enough for the process to reach a relatively stabilized level (see Fig. II.4). In fact, most of the bias that was presented in the 1-st iteration is almost completely

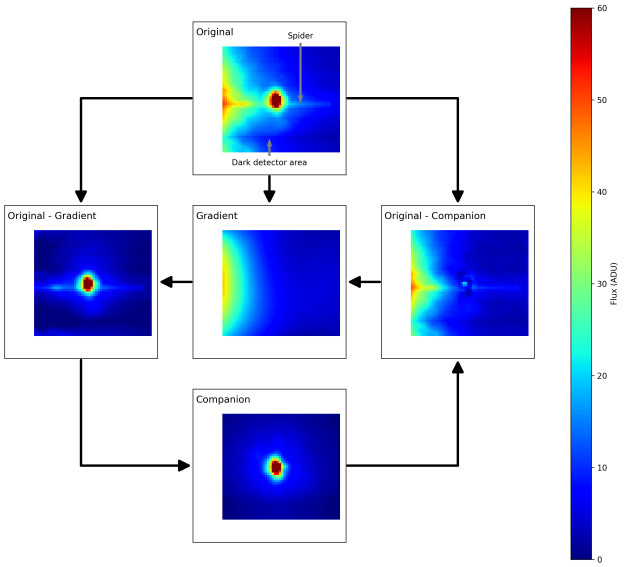


Figure II.3: Illustration of the primary's PSF wings subtraction, in the case of GQ Lup b, for the first exposure of the 2017-04-30 epoch (median along the wavelength axis).

[7] **SkyCalc**: https://www.eso.org/observing/etc/bin/gen/form?INS.MODE=swspectr+INS.NAME=SKYCALC

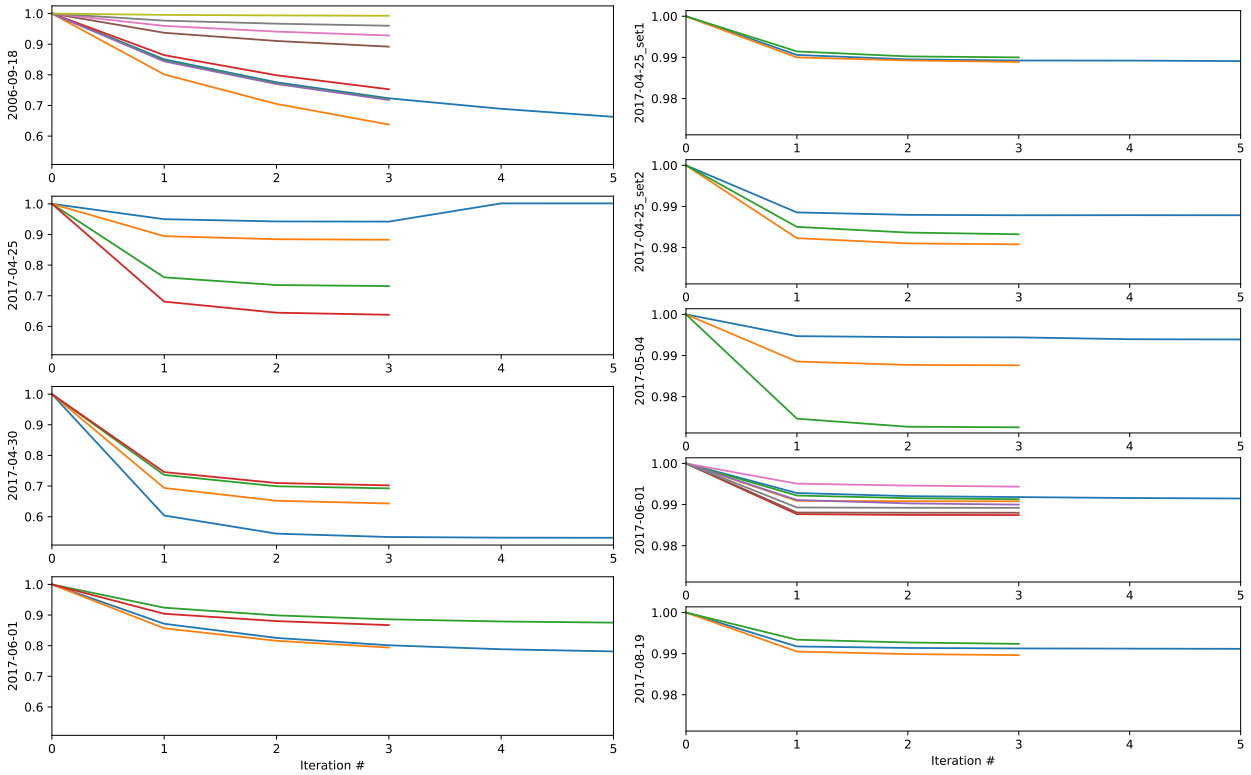


Figure II.4: Evolution of the χ^2_r along extraction iterations. The χ^2_r are normalized to 1 at the value for the first iteration (#0).

gone during the 2-nd iteration. Subsequent iterations mostly serve as a fine-tuning aspect. In general, worse observing conditions require a higher number of iterations to reach a stable level. Note that residual sky lines are subtracted here: they correspond to the 0-th order parameter of the 2D gradient in each spectral frame. While independent spectral bins are fitted independently, I believe today that a better S/N would have been achieved by smoothing the parameters along the wavelengths, as I did for Delorme 1 (AB)b (see next Chapter). The procedure is equivalent to a CLEAN-like reduction (Högbom, 1974), adapted to a 2D case. A general working sketch of the procedure is shown in Fig. II.3. Finally, the spectra are obtained by integrating over a circular aperture in the gradient-subtracted cubes. The aperture radius was chosen as the one maximizing the S/N in the spectrum (3–5px).

Telluric correction and flux calibration The data-cubes were flux calibrated using the Telluric Standard (Tel. Std.) data-cubes. For GQ Lup b, their spectral type was B3V, B2V, B9V, B9V, B9V, G3V, B4V, B5V, B3III, B9V, B9V, B9V for HIP 104320, HIP 095147, HIP 095105, HIP 087140, HIP 087125, HIP 084435, HIP 082670, HIP 082652, HIP 081208, HIP 079599, HIP 079410. For GSC 06214-00210 b, their spectral type was B9V, B3V, B3III, B5V, B4V, G3V, B2V, B3V, for HIP 079599, HIP 081214, HIP 082652, HIP 082670, HIP 084435, HIP 087125, HIP 095105, HIP 095147, HIP 104320. The expected signal and spectrum of the



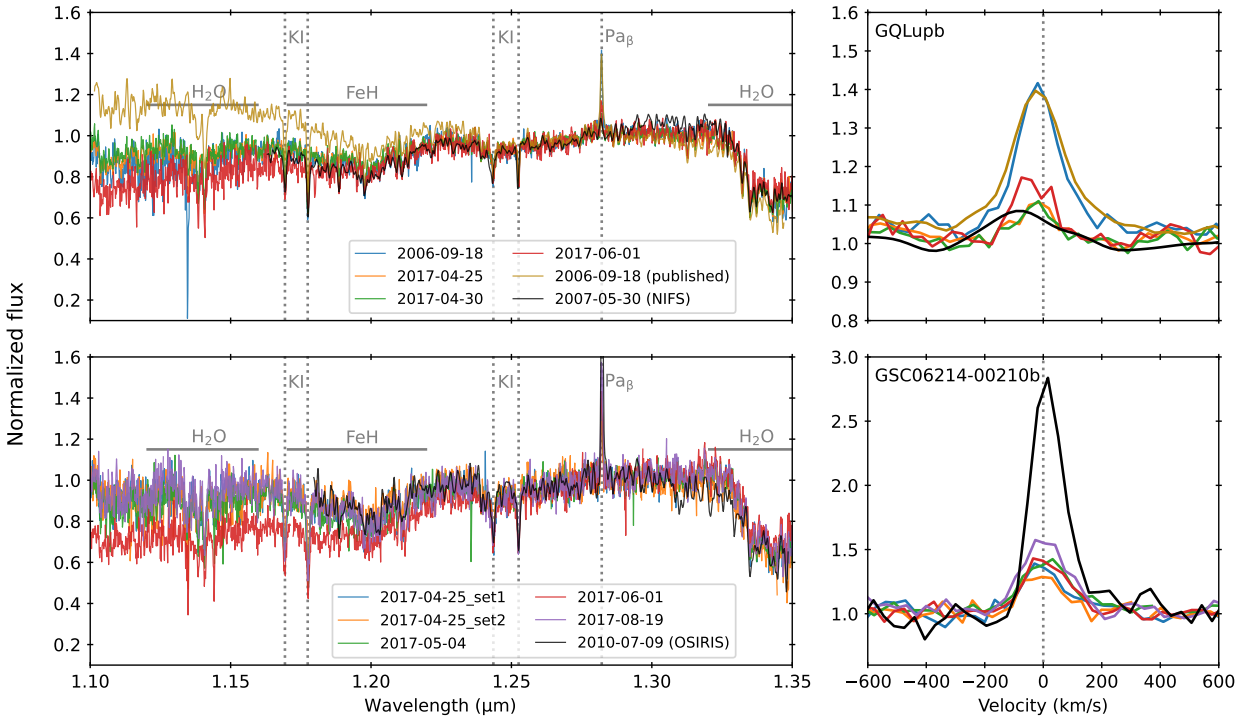


Figure II.5: Left: full J-band spectra of GQ Lup b and GSC 06214-00210 b. Right: Pa_β line. For GQ Lup b, the original spectrum extracted by Seifahrt et al. (2007) is shown in yellow, and the NIFS spectrum in black (Lavigne et al., 2009). For GSC 06214-00210 b, the OSIRIS spectrum is shown in black (Bowler et al., 2011), convolved to SINFONI resolution (R = 1800).

Tel. Std. are known, so they are used as calibrators for both the instrument and atmosphere transmission. The Tel. Std. have spectra that are mostly black bodies, except for some absorption lines: in particular Pa_β. The spectra of the Tel. Std. are corrected from atmosphere transmission using a template obtained with the SkyCalc[8] tool (Noll et al., 2012; Jones et al., 2013). With this correction, the Pa_β absorption line of the Tel. Std. has a Voigt-like shape, which is subtracted by replacing it with a straight line (see Fig. A.2). The atmosphere transmission spectrum is then applied back to this corrected spectrum. This obtained spectrum corresponds to the Tel. Std. spectrum, without the Pa_β absorption line, but with atmosphere+instrument transmission effects imprinted in the spectrum. A template flux calibrated spectrum of the Tel. Std. is obtained using the VOSA[9] tool (it fits a synthethic spectrum to the published photometry of the target), and used to derive a correction factor to apply to the observations: $\alpha(\lambda) = \mathrm{Template}(\lambda)/\mathrm{Std.}_{\not\mathrm{Pa}_\beta}(\lambda)$. The correction factor is derived with the Tel. Std. of each observing sequence.

[8]**SkyCalc**: https://www.eso.org/observing/etc/bin/gen/form?INS.MODE=swspectr+INS.NAME=SKYCALC
[9]**VOSA**: http://svo2.cab.inta-csic.es/theory/vosa/



Teff (K)	log(g) (dex)	[M/H]	C/O	γ
[800–3000]/50	[2.5–5.5]/0.5	[-0.6–0.6]/0.3	[0.3–0.7]/0.25	[1.01–1.05]/0.02

Table II.3: ATMO models parameters range and sampling (Tremblin et al., 2015, 2016). The values are given as [lower_limit – upper_limit]/step. γ is the adiabatic index.

3 Atmospheric modeling

3.1 Main spectral features

Both GQ Lup b and GSC06214b have really similar extracted spectra, typical of M9 dwarfs. They display K I absorption lines, H2O and FeH bands, as well as the Pa_β line. All spectral features are marked in Fig. II.5. The spectral slope of GQ Lup b is much more in agreement with that of Lavigne et al. (2009) than was Seifahrt et al. (2007), even for the common data-cube (2006-09-18), further building the argument on residual contamination from the primary in the published spectrum. However, even this extraction is not perfect and there are residual spectral slope differences, which dispersion provides an idea of the typical error induced by the extraction method. This dispersion will serve as the typical uncertainty for atmospheric parameters in the section below.

The J-2MASS magnitude for both companions is computed as the average of all epochs. For GQ Lup b, the 2006-09-18 is excluded from this analysis as the observing conditions were fairly poor. The final spectra have magnitudes of $J = 14.38^{+0.13}_{-0.12}$ and $J = 16.21^{+0.26}_{-0.21}$ for GQ Lup b and GSC06214b respectively. The individual magnitude for each exposure are shown in Fig. A.1, which shows the discrepancy of the 2006-09-18 epoch of GQ Lup b, even with the sequence itself. The value for GSC06214b is in good agreement with the published ones ($J = 16.25 \pm 0.04$ and $J = 16.19 \pm 0.04$, Bowler et al., 2011; Lachapelle et al., 2015). However, the value for GQ Lup b is brighter than that found in literature ($J = 15.13 \pm 0.44$ and $J = 14.90 \pm 0.11$ Lavigne et al., 2009; McElwain et al., 2007). It should be noted that their values were obtained from the contrast to the primary, which is known to be variable ($\Delta J = 0.87$ Batalha et al., 2001; Broeg et al., 2007). The discrepancy lies well within the variability range of the primary. This extraction was not dependent on the primary and likely provides a more accurate estimate of the magnitude of the companion.

3.2 The atmosphere of GQ Lup b and GSC 06214-00210 b

All absorption features of the spectra, along with their slope, are direct tracers of the composition of the atmosphere of GQ Lup b and GSC06214b. Fine molecular absorptions are prodicted to form at the location of Pa_β and over the whole spectrum for young late-M/early-L companions. We therefore modeled the photospheric features using `ForMoSA` (Petrus et al., 2020, 2021, 2023). `ForMoSA` is a forward-modeling tool that compares grids of atmospheric models with observations through the Nested Sampling Bayesian inference algorithm (Skilling, 2004). Its advantages over traditional MCMC tools is to cover a much more homogeneous parameter space, thus avoiding local minima. The input atmospheric models were the ATMO models (Tremblin et al., 2015, 2016). They are cloudless models that explore the range of parameters expected for these two companions. The parameters range and sampling are given in Table. II.3. To these parameters are also added the Radius, extinction (A_V), Radial Velocity (RV) and rotational broadening ($v \sin i$). The Radius is used as a flux-scaling parameters, the A_V allows for spectral slope variations, the RV is used as a final fine-tuning parameter for the wavelength calibration, and the $v \sin i$ is used to broaden absorption lines accordingly. The grid is only sparsely sampled in some parameters (e.g., γ), but `ForMoSA` is able to



Table II.4: Atmospheric parameters retrieved with `ForMoSA`.

	Date YYYY-MM-DD	Teff (K)	log(g)	[M/H]	γ	C/O	Radius (R_{Jup})	A_v	RV (km/s)
GQ Lup b	2006-09-18	2587	4.16	[1] > 0.59	[1] > 1.05	0.57	4.45	2.38	3.03
	2017-04-25	2671	4.16	0.30	[1] > 1.05	0.42	4.08	2.13	5.59
	2017-04-30	2655	4.22	0.17	[1] > 1.05	0.33	4.07	1.91	13.59
	[2]2017-06-01	2711	3.92	0.30	[1] > 1.05	0.55	[1] > 5.00	4.32	13.11
	adopted	2638^{+33}_{-51}	$4.18^{+0.04}_{-0.02}$	$0.23^{+0.06}_{-0.06}$	> 1.05	$0.44^{+0.13}_{-0.11}$	$4.20^{+0.25}_{-0.13}$	$2.14^{+0.24}_{-0.23}$	-
GSC06214b	2017-04-25_set1	2274	4.30	−0.13	1.03	0.50	1.45	0.45	−18.06
	2017-04-25_set2	2230	4.10	−0.33	1.03	[1] < 0.30	1.47	[1] < 0.00	−8.78
	2017-05-04	2317	4.30	−0.15	1.03	0.42	1.56	1.50	−12.73
	[2]2017-06-01	2269	4.33	−0.18	1.02	0.39	2.45	[1] > 4.99	−19.58
	2017-08-19	2189	4.36	0.00	1.01	0.64	1.58	[1] < 0.00	−6.51
	2010-07-09	2232	4.17	−0.21	1.04	0.36	1.37	[1] < 0.00	−11.90
	adopted	2248^{+69}_{-59}	$4.24^{+0.11}_{-0.15}$	$-0.16^{+0.17}_{-0.17}$	$1.03^{+0.01}_{-0.02}$	$0.48^{+0.16}_{-0.12}$	$1.49^{+0.10}_{-0.12}$	$0.97^{+0.53}_{-0.53}$	-

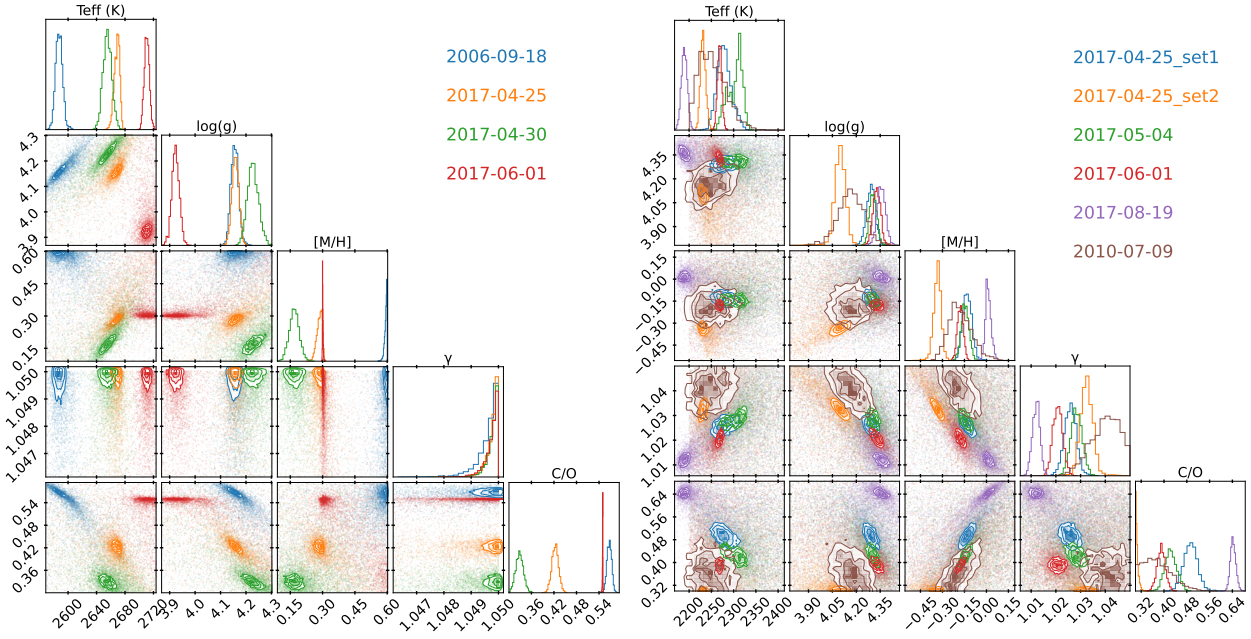


Figure II.6: `ForMoSA` resulting photosphere parameters. Left: GQ Lup b results. Right: GSC06214b results. The Radius, Av, radial velocity (RV), and limb-darkening coefficients are omitted from these plots for the sake of clarity.

[1]Unconstrained parameter, fit converged at the edge of the parameter range.
[2]Epoch ignored when computing the adopted value

create super-sampled grid by linear-interpolation within the -dimensional space of the grid of models. This is obviously not as good as having a properly generated grid, but this makes the models generation a lot faster.

The resulting parameters on the mean spectrum of each epoch are shown in Table. II.4. The parameter space is shown as corner plots in Fig. II.6. The adopted values are computed as the average of all epochs, excluding the 2017-06-01 epoch, as it converged in some local minima for both objects. Some parameters sometimes converge at the edge of the grid (mainly γ).

3.2.1 Correlations

Overall, the temperature and log(g) are quite consistent between epochs, while the C/O and [M/H] are the most spread. There are quite a lot (anti-)correlations between parameters:

Teff – log(g) The parameters are correlated with each other for GQ Lup b only, and only within single-epochs. The behavior is the same on all epochs, and similar to that of HIP 78530b, also analyzed with `ForMoSA`, coupled with BT-SETTL models (Petrus et al., 2020). The correlation is possibly caused by the increased strength of K I and FeH absorptions with decreasing Teff and increasing log(g) at the M-L transition (Rice et al., 2010; Bonnefoy et al., 2014).

Teff–[M/H] and log(g)–[M/H] For GQ Lup b only, on epochs 2017-04-25 and 2017-04-30, there are correlations between parameters. Although slightly less important than for Teff–log(g), the correlation to [M/H] are likely artifacts due to the Teff–log(g) correlation itself.

γ–log(g) and γ–[M/H] While it was said in the paper (Demars et al., 2023), that there were no clear correlations involving γ, I realize now that the different epochs of GSC06214b have clear anti-correlations of log(g) and [M/H] with γ.

C/O–Teff and C/O–log(g) For GQ Lup b, within single epochs, C/O has a slight anti-correlation with both Teff and log(g). As for the [M/H] correlations, this is likely due to the correlation of Teff-log(g) itself.

[M/H]–C/O Within single epochs, GSC06214b shows positive correlations between [M/H] and C/O. However, this positive correlation also appears when comparing different epochs, for both GQ Lup b and GSC06214b. The reason is unknown.

3.2.2 Resulting values and interpretation

Previous studies had already provided some atmospheric values for GQ Lup b and GSC06214b. For GQ Lup b, Stolker et al. (2021) found Teff within the 2500–2700 K range, and log(g) = 4.0. We find Teff = 2638^{+33}_{-51} and log(g) = $4.18^{+0.04}_{-0.02}$, which is well in agreement with their values given their grid sampling. For GSC06214b, Lachapelle et al. (2015) found Teff = 2300 ± 200 K, and log(g) = 3.0 − 4.0. We find Teff = 2248^{+69}_{-59} and log(g) = $4.24^{+0.11}_{-0.15}$. While our log(g) is slightly higher than that of Lachapelle et al. (2015), the parameters are broadly similar, given the error bars.

However, this study presents the first estimate of both C/O and [M/H] for GQ Lup b and GSC06214b. Both have C/O values compatible with solar value ($C/O_\odot = 0.55$) at 1σ. However, their metallicity is quite different. GSC06214b has an overall solar metallicity (GSC06214b: [M/H] = -0.16 ± 0.17), while GQ Lup b is slighlty super-solar (GQ Lup b: [M/H] = 0.23 ± 0.06), even at 3σ. However, a recent study has



published quite different values of both C/O and [M/H] for both these targest (Xuan et al., 2024). They find C/O = $0.70^{+0.01}_{-0.02}$ and C/O = $0.70^{+0.07}_{-0.06}$ for GQ Lup b and GSC06214b respectively, and [M/H] = $0.40^{+0.20}_{-0.22}$ and [M/H] = $0.14^{+0.33}_{-0.29}$ for GQ Lup b and GSC06214b respectively. While the metallicity values are consistent with our own at 1σ, the C/O values are much higher than that we find. Even though they do estimate the systematics of their models, this is done by approximating the standard deviation of the measurements from different datasets as the systematic error. While this is somewhat equivalent to the way we obtained the error-bars in this study, we also mentioned that such a procedure does not encapsulate the systematic of the models themselves. In fact, a proper way to estimate them should be to compare estimate with a known target. Overall, I doubt that their error-bars really encapsulate the actual systematics of the model (although ours do not either). They imply a ~ 2 % accuracy on the C/O measurement, which seems overwhelmingly accurate given the complexity of exoplanets atmospheres. I do not know a study that explores different models systematics between petitRadTrans and ATMO models.

Both the GQ Lup and GSC06214 systems are located in regions expected to have broadly solar C/O and [M/H] (Bubar et al., 2011; Biazzo et al., 2017; Murphy et al., 2021; Suárez-Andrés et al., 2018; Tautvaišienė et al., 2022). However, Swastik et al. (2021) found that the host stars have metallicities that are below-solar for both targets: [M/H] = -0.35 ± 0.01 and [M/H] = $-0.06 \pm 0..01$ for GQ Lup A and GSC06214A respectively. The value is surprisingly low for GQ Lup A, and it should be noted that its H_α line is the brightest of their sample. Even though they chose the region where veiling is less affecting the measure, it is still possible that residual veiling could be present for GQ Lup A, biasing the value for that star. While this value would make GQ Lup b significantly metal-rich compared to its host star, it would still be enriched in metals even if the primary had a solar value. As for GSC06214b, the value is comparable to that of the primary at 1σ. Overall, the metallicity values are compatible with prediction of both core-accretion frameworks (Fig. 9 of Petrus et al., 2021) and formation within a circumstellar disk (Boley et al., 2011). The predictions currently do not permit to distinguish between the two.

Resulting parameters from the fits (in particular Teff, log(g) and radii) can be directly used as inputs for evolutionary tracks, in order to obtain a better understanding of the characteristics of these objects. In other words, the previous work inferred parameters through spectra modeling, whereas this work derives parameters from evolutionary tracks predictions. For consistency, we use the same ATMO evolutionary tracks. They predict that GQ Lup b has a mass of 22^{+2}_{-3} M_{Jup}, radius within 2.65–3.3 R_{Jup}, and log(g) $\sim 3.8 - 3.9$. The radius and log(g) values are not compatible with that obtained with `ForMoSA`. However, the values obtained for GSC06214b (15.5 ± 0.5 M_{Jup}, radius within 1.8–2.0 R_{Jup}, and log(g) = $4.04 - -4.07$ depending on the membership) do agree with the ones from `ForMoSA`, except for the radius which is slightly larger. The GQ Lup b discrepancy could be explained by the degeneracy between extinction and radii, which would make our results in better agreement with that of Stolker et al. (2021) (3.55–4.13 R_{Jup}, A_V=2.3–2.7 mag). Another explanation (which might be simpler given the young age and topic of this manuscript) could be an additional flux component of the continuum, namely: veiling. However, we would expect the intrinsic emission of the companion to be dominant over the veiling component. Petrus et al. (2020) had proposed (however, for another companion) binarity as an explanation. This would make the apparent companion intrinsically brighter than expected from evolutionary tracks, while maintaining the apparent Teff, C/O and [M/H] values. Assuming two components adding up to the $R = 3^{+0.2}_{0.1}$ obtained with `ForMoSA`, the Teff would match with the predictions from evolutionary tracks. However, this would need confirmation from other sources.



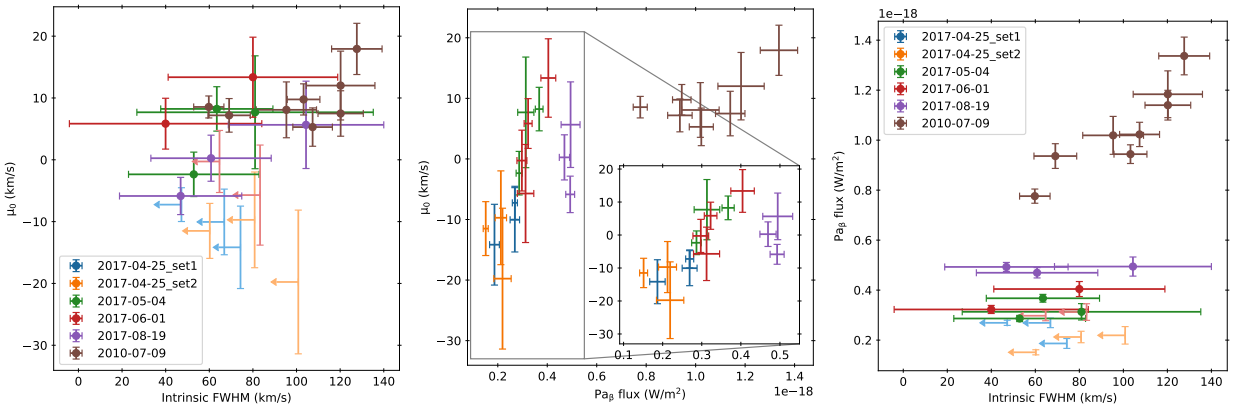


Figure II.7: Gaussian-fitted parameters for the Pa_β line of GSC06214b. Left: intrinsic FWHM vs line centroid. Middle: line flux vs peak location (line centroid). The intrinsic FWHM is computed as the square root of the quadratic difference between the measured line FWHM and the LSF FWHM. Right: intrinsic FWHM vs line flux.

4 The Paschen Beta line

Right panels of Fig. II.5 show the mean Pa_β line of each epoch for both GQ Lup b and GSC06214b. However, the line of individual exposures within a sequence are also available (see Fig. 3 in the paper). These allow to scan variability amplitudes at timescales varying from 5 minutes (DIT), to months (spread of observations within the program) and years/decade (including archival data).

4.1 Line profiles

At first glance, both GQ Lup b and GSC06214b have similar Pa_β line profiles, that look symmetrical with respect to the location of their peak. However, all lines of GQ Lup b seem slightly blue-shifted. The lines were fitted with Gaussian profiles to infer their parameters (line flux, centroid, width) and we find that GQ Lup b's lines are blue-shifted at mostly constant shift across all epochs. GQ Lup b lines are mostly unresolved, i.e., their width is consistent with that of the LSF (R=2360), except for the 2006-09-18 epoch where the lines width are about 1–1.5 times the LSF width (at 1–3σ confidence). GSC06214b's lines are unresolved (R=1800) in all 2017 epochs. However, OSIRIS data (2010-07-09 epoch) have twice the resolution (R=3800), and the lines are resolved at 1.2–1.9 the LSF width (4–8σ confidence). For all lines, the intrinsic FWHM is computed as the square root of the quadratic difference between the measured line FWHM and the LSF FWHM ($\mathrm{FWHM}^2_{\mathrm{in}} = \mathrm{FWHM}^2_{\mathrm{obs}} - \mathrm{FWHM}^2_{\mathrm{LSF}}$).

There is no clear trend nor correlation in GQ Lup b's lines parameters. However, GSC06214b's lines show great trends between the line centroid, flux and width. Results are shown in Fig. II.7. The left panel shows the correlations between the intrinsic FWHM of the line, and the line centroid, with arrows representing upper limits on the intrinsic FWHM. The middle panel shows the correlations between the Pa_β line flux and the Pa_β centroid location, with respect to the rest frame. The right panel shows the correlations between the Pa_β line flux and its intrinsic FWHM, and was not included in the paper (Demars et al., 2023) as I missed it at the time of writing it. There is a trend between the intrinsic FWHM and the line centroid (left



panel): the line is wider as it becomes red-shifted / not-blue-shifted. There is also a trend between the line centroid and the line flux (middle panel), in particular within the 2017 epoch: as the line gets brighter, it moves from blue-shifted to red-shifted, up until a shift-saturation-limit, as shown by the 2010-07-09 points location. However, within that saturated shift, there is a correlation between the intrinsic FWHM and the line flux (right panel). This can only be explained by adding flux ∼equally to the blue and red side of the line, but not in the core of the line, in order to widen the profile. This can only be explained if the wings and the core of the lines are somewhat un-correlated, at least within that epoch. However, the exact shape of such wings–core components are impossible to de-convolve from the current profiles given the S/N of the data. It will be seen in the next chapter that the decomposition of the lines of Delorme 1 (AB)b provide a perfect candidate from this behavior.

Without going for higher spectral resolution (just yet!) it is still possible to explain some of the correlations. The μ_0–$\mathrm{FWHM_{in}}$ correlation can be explained by variation within the red wing only: as the red wing gets brighter, the apparent width of the line increases and the line center moves to the red. This can be explained if a red-shifted absorption features overlays on the line profile, as commonly seen in the context of CTTS. The absorption could be variable in depth (depending on the accretion rate) for example), and not be fully correlated with the line intensity, thus changing its apparent width. This would also explain the Flux–μ_0 correlation (right panel of Fig. II.7): as the red-shifted absorption increases, the red wing contribution decreases and the line moves to the blue.

If Magnetospheric Accretion holds, it is still possible that part of the lines profiles variations could be attributed to two different components: a shock component and a funnel component. Shock models are expected to provide slightly red-shifted emission lines (Aoyama et al., 2018). While I previously mentioned red-shifted absorption as a possible explanation to the red-wing variation, a red-shifted emission component could also explain the FWHM–μ_0 correlation: as the red-shifted shock component brightens, the line apparent centroid moves to the red, and the line widens as the flux is added un-uniformly with respect to the line center. However, even if this would match the variations in the 2017 epochs, this would not be able to explain the 2010-07-09 variations where the, line centroid is mostly constant, while both the line flux and FWHM increase. It is possible that GSC06214b has two different accretion/emission regimes that were apparent in the 2017 observing run and the 2010-07-09 sequence.

4.2 Line flux variability

Each pair of line can be given as their relative flux variation$((F_1 - F_2)/F_1)$, and their timescales difference $(t_1 - t_2)$. These are plotted in Fig. II.8, for all possible pairs of lines of both GQ Lup b and GSC06214b. The markers colors correspond to how significant the measurement is, i.e., the distance to 0 given as the number of σ (error-bars). In other words, it is equivalent to the error-bar of the measurement, without making the plot too dense with error-bars themselves. Colored points mean that the measurement is significant (red: $3 - 5\sigma$, purple: $> 5\sigma$), while gray points mean that the measurement is compatible with no flux variation ($< 3\sigma$). The black crosses represent the spread of the variability over a timescale bin. The procedure is similar to that of Zsidi et al. (2022), with the addition of colors for error-bars which are not required for the bright lines of CTTS.

GQ Lup b shows a variability pattern where the variability amplitude is quite low at the hour timescale ($\sim 20 - 30\%$) and higher at months to years timescales ($\sim 200 - 300\%$). Note however, that the sampling is fairly low, with only 3 epochs in 2017 and 2 epochs in 2006-2007 (including the spectrum from Lavigne et al., 2009)). The pattern is similar to that seen in CTTS Zsidi et al. (2022). GSC06214b, however, provides a much better sampling, with a different pattern. While the overall trend also shows that their is a greater amplitude of variability at greater timescales, the amplitudes themselves are quite different. The variability at hours



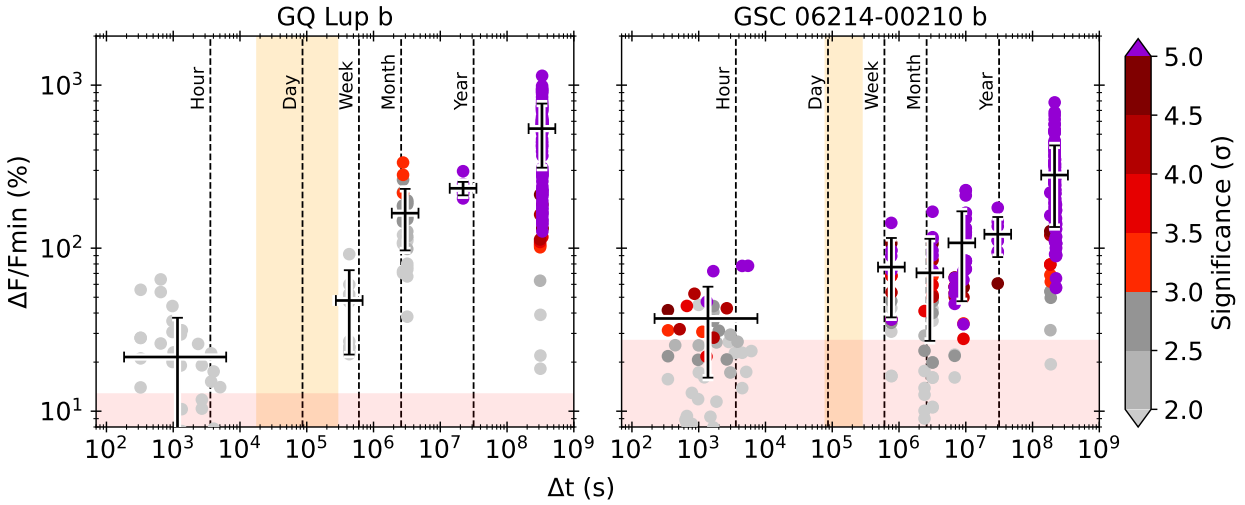


Figure II.8: Relative variability diagrams for the Pa_β line of GQ Lup b and GSC 06214-00210 b. The color of the points correspond to the significance of the measurement, given as the number of σ (i.e., gray points are compatible with 0 amplitude variability). Black crosses are **not** error-bars: they represent the spread of variability for various timescale bins. The yellow shaded region represents the expected rotational period of each object. The red shaded region represents the observed continuum variability of the spectra.

timescales is greater (factor 2) than that of GQ Lup b, while also being actually observed (colored points). The variability at months timescales only reaches up to $\sim 80-100\%$ relative variability, while maintaining a plateau. This plateau is also observed on CTTS: the relative variation reaches a constant value of ~ 300 % on all timescales longer than the rotation period fo the star. This is interpreted as the rotational modulation of the magnetosphere being the main source of variability for line emission (Costigan et al., 2014). The expected rotational periods of both GQ Lup b and GSC06214b are given as the yellow shaded regions, which for GSC06214b lies just before the observed plateau of variability. This advocates for magnetospheric accretion to be occurring on GSC06214b. However, the blue-shifted lines of GQ Lup b also advocate for magnetospheric accretion, despite the poor time-sampling of the data.

It is possible that these two objects are the signatures of the same mechanism, observed in different regimes. Aoyama et al. (2021) (see their Fig.2) provides a comparison of the $\dot{M}$–L(H_α) relation for two main emitting mechanisms: a shock

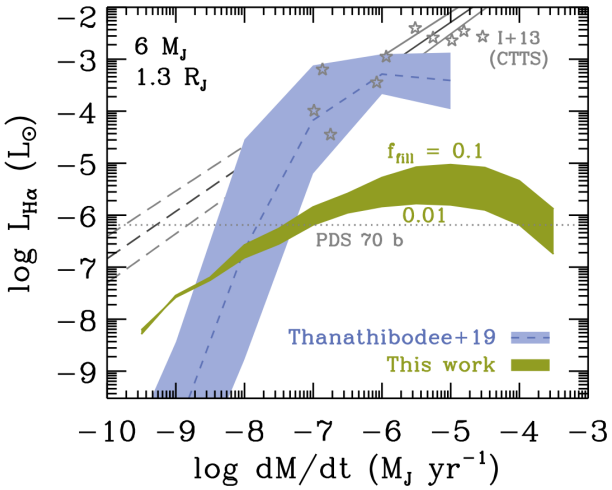


Figure II.9: H_α contribution of the shock and column emission, in the magnetospheric accretion scenario (Aoyama et al., 2021).

(green) and a funnel (blue) model, that were already mentioned. They show that at high accretion rates ($\dot{M} > 10^{-7}$ M_{Jup}/yr), the funnel emission dominates over that of the shock, while at low accretion rates ($\dot{M} < 10^{-9}$ M_{Jup}/yr), the shock emission becomes dominant. GQ Lup b and GSC06214b could be the two extremes of these two scenarios. The only way to be sure is to try and fit these models to the lines to see whether they match or not: hence the next section.

Both GQ Lup b and GSC06214b have lines that are clearly variable from an epoch to another, and even within the sequences themselves, both in terms of flux and shape (as shown in the previous section). With the many imaging campaigns using accretion lines to push the detection limits of the instruments, line flux variability comes as the big question for Planetary-Mass Companions. However, these campaigns are usually focused on the H_α line for its brightness (Haffert et al., 2019; Follette et al., 2023; Adams Redai et al., 2023), and only a few authors have used therePa_β line for exoplanets imaging Uyama et al. (2017); Biddle et al. (2024). H_α imaging surveys have mostly yielded poor success rates, despite its brightness. The Pa_β variability amplitude observed, if it translates to H_α (spoiler from the next chapter: it does not), could be sufficient to send most planets below the detection thresholds of MUSE, for example. Given that GQ Lup b and GSC06214b show some Pa_β burst behaviors in their respective archival epochs, it is not unlikely that surveys may have missed these burst epochs that would have otherwise made some companions detectable. The set of currently known planetary-mass companions might just be outliers that have bright enough baseline flux levels to be detectable.

5 Emission lines models

The preliminary and empirical analysis of the Pa_β line already gives clue towards Magnetospheric Accretion for both GQ Lup b and GSC06214b although for different reasons. Still, it is not excluded that part of the line emission may be triggered at a shock, rather than within a funnel. I propose to use emission line models (Magnetospheric Accretion and Shock models) to try and disentangle to two (non-exclusive) mechanisms.

5.1 Models description

Thanathibodee et al. (2019) proposed Magnetospheric Accretion models, adapted for the case of Planetary-Mass Companions. They are the same models proposed by Hartmann et al. (1994), although for a lower mass of central object. The magnetosphere is assumed to be axis-symmetrical, the dipole aligned with the rotation axis of the planet. The magnetic field truncates the inner Circum-Planetary Disk at a radius called R_{in}, over an area of a given Width (in particular, the base the funnel extends from R_{in} to R_{in} + Width). The accretion rate ($\dot{M}$) and column temperature (T_{col}) set the emitting conditions. The inclination of the system is responsible for some asymmetries of the lines profiles (e.g., red-shifted absorption if the line of sight crosses both the funnel and the shock region and/or the photosphere). The Mass and Radius of the planet set the dynamics of the accretion flow. Finally, the temperature of the planet sets the baseline for continuum emission. The models are the results of numerical simulations performing radiative transfer coupled with ray tracing of intrinsic emission and absorption depth along the line of sight. They are able to produce line profiles for most of the Hydrogen lines. Here, the models focus on the Pa_β line. As a side note, only the line emission originating from the funnel is accounted for in the model. It does not include line emission from the shock or emission/absorption from any outflow. The range of parameters for the Magnetospheric Accretion models are given in Table. II.5.

Aoyama et al. (2018) proposed a different scenario for accretion lines emission. Because the intrinsic conditions of these objects are quite different from stars (e.g., they can be embedded in the circum-stellar



disk of their host star), material could flow down from high latitudes in the circum-stellar disk, down to either the planet itself, or the surrounding circum-planetary disk. These flows, would they be faster than the local sound speed, would therefore induce a shock at the circum-planetary disk and/or planetary surface. This shock would sufficiently heat the material to trigger line emission. The model itself only has 2 inputs parameters: the velocity of the flow (v_0), and the pre-shock density (n_0). I added an additional parameter, $S_{\rm eff}$, that accounts for the effective shock surface (i.e., the emitting area, $4\pi R_p^2 f_{\rm fill}$ if it takes place at the planetary surface, with $f_{\rm fill}$ the filling factor). While this model was motivated by embedded protoplanets, it can be, in principle, applied to any kind of shock. Therefore, would it fit the lines, the resulting parameters could also be interpreted as a shock at the base of a magnetospherically induced funnel. The range of parameters for the Shock models are given in Table. II.6.

5.2 Model fitting

The fits are performed on the photosphere-subtracted data (obtained with the `ForMoSA` fit), and scaling each model to the respective distances of GQ Lup b and GSC06214b. Each model is therefore also subtracted from its continuum level (linear-fit on both sides of the line). The models are convolved to the respective spectral resolution of the data (R=2360 for GQ Lup b, R=1800 for the 2017 epochs of GSC06214b, and R=3800 for the 2010-07-09 epoch of GSC06214b). The grid of models is relatively small, making it possible to brute-force the χ^2_r values over the whole grids. The best-fit models are shown in Fig. II.10 for the mean line of each epoch. The shaded regions represent the range of models that match the line at a $\chi^2_{r,\rm min}+1$ level, both for the Magnetospheric Accretion (red) and Shock models (blue). Figure II.11 shows typical correlations for parameters of Magnetospheric Accretion (left) and Shock (right) models. The χ^2_r grids for GQ Lup b, Magnetospheric Accretion models, are given in Figs. A.3 to A.6. The χ^2_r grids for GQ Lup b, Shock models, are given in Figs. A.7 to A.10. The χ^2_r grids for GSC06214b, Magnetospheric Accretion models, are given in Figs. A.11 to A.16. The χ^2_r grids for GSC06214b, Shock models, are given in Figs. A.17 to A.22.

For GQ Lup b, only the Magnetospheric Accretion models are able to reproduce the blue-shifted lines. The best-fit shock models always appear too red-shifted, which is consistent with the intrinsic nature of their red-shifted lines, due to the infalling emitting material. The Magnetospheric Accretion models seem to reproduce red-shifted absorption features below the continuum level, however we caution that these deviations are purely noise in the data that is not obvious when zooming in on the Pa_β line. For GSC06214b, both the Magnetospheric Accretion and Shock models are able to reproduce the lines of all 2017 epochs. However, the 2010-07-09, which has a higher spectral resolution, is only reproduced by the Shock models, whereas the Magnetospheric Accretion models produce lines that are too narrow.

The Magnetospheric Accretion Model produces strong anti-correlations between the column temperature and the accretion rate (Fig. II.11, left panel). This was already seen in the context of CTTS (Muzerolle et al., 2001), and relates to the line flux being broadly proportional to both the temperature and density. However, this provides a lower-limit on the accretion rate: $\dot{M} > 10^{-11}$ $\rm M_\odot$/yr for GQ Lup b and $\dot{M} > 10^{-12}$ $\rm M_\odot$/yr for GSC06214b. They are consistent with the values inferred by Zhou et al. (2014) from UV excess fitting ($10^{-10.8}$ $\rm M_\odot$/yr and $10^{-9.3}$ $\rm M_\odot$/yr) respectively.

From the blue-shifted lines of GQ Lup b, Magnetospheric Accretion seems to be the obvious scenario. For GSC06214b, however, the Shock scenario seems to be preferred (at least for the brighter epoch), but the origin of the shock it still to be constrained. The best-fit parameters are mostly degenerated with the shock surface for the 2017 epoch (Figs. A.17 to A.22). However, the 2010-07-09 epoch provides constraints (Fig. II.11, right panel) on both the infall velocity and the pre-shock density: $v_0 > 150$ km/s, $n_0 \sim 10^{20}$ $\rm m^3$. Assuming that material is coming from infinity, the infall velocity is consistent with a shock located at $R < 2.4$ $\rm R_{Jup}$, which is consistent with the planetary radius inferred from `ForMoSA` (1.8–2.0 $\rm R_{Jup}$). The best fit parameters



Table II.5: Parameters range for the magnetospheric accretion models (Thanathibodee et al., 2019).

R_{in} (R_p)	Width (R_p)	$\dot{M}$ ($M_\odot$/yr)	Tcol (K)	i (°)	M_p (M_{Jup})	R_p (R_{Jup})	T_{eff} (K)
1.5 – 6.0	0.5–2.5	$9.5 \times (10^{-13} - 10^{-10})$	6 000 – 10 000	15 – 75	11–13–15	1.4-1.5-1.6	1800

Table II.6: Parameters range for the Shocks models (Aoyama et al., 2018).

S_{eff} $4\pi R_{jup}^2$	v_0 km/s	n_0 m^{-3}
$10^{-3} - 10^{3}$	$30 - 200$	$10^{15} - 10^{20}$

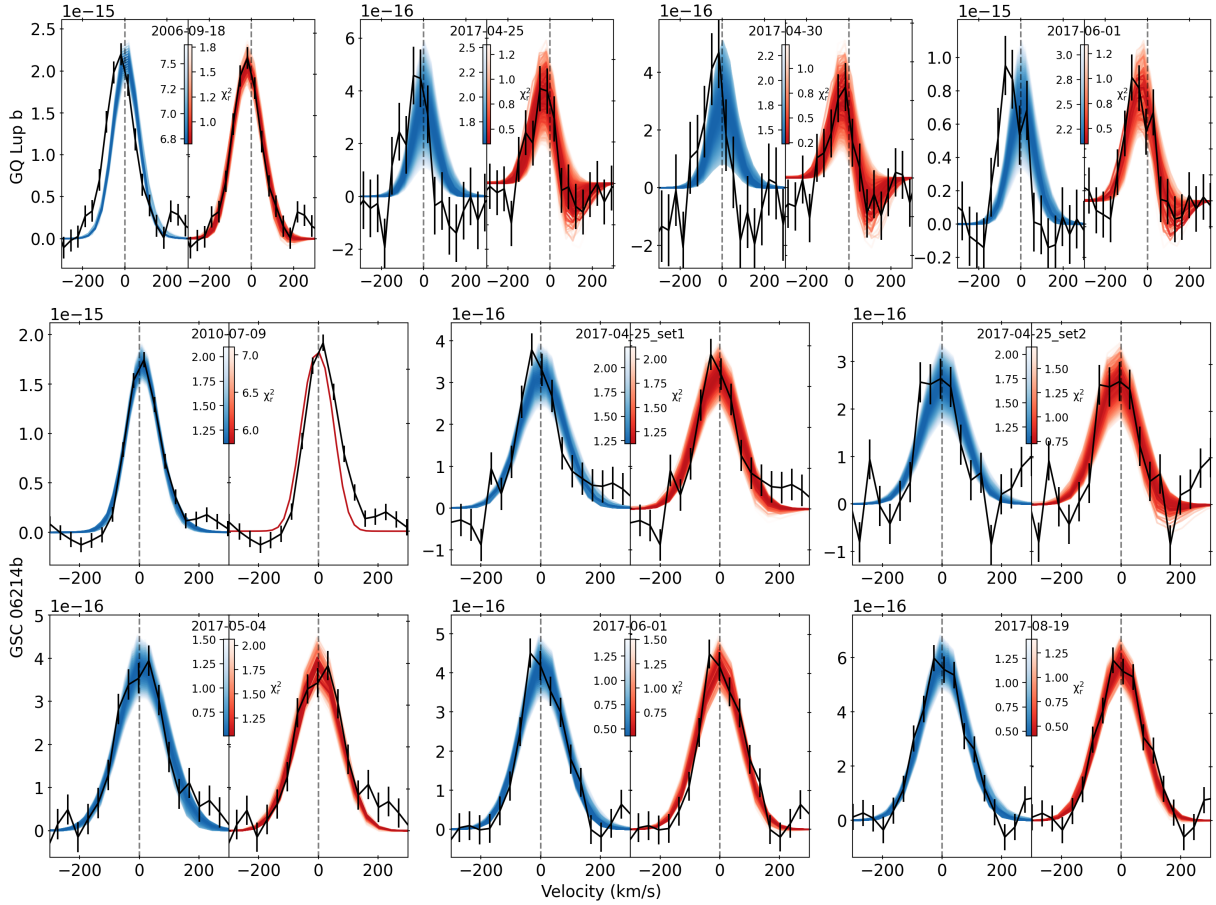


Figure II.10: Best fits models for Magnetospheric Accretion models (red, Thanathibodee et al., 2019) and Shock models (blue, Aoyama et al., 2018). First row: GQ Lup b, second and third rows: GSC06214b. Colored shaded regions are the best fit models, where the color corresponds to the χ^2_r given in the colorbar.

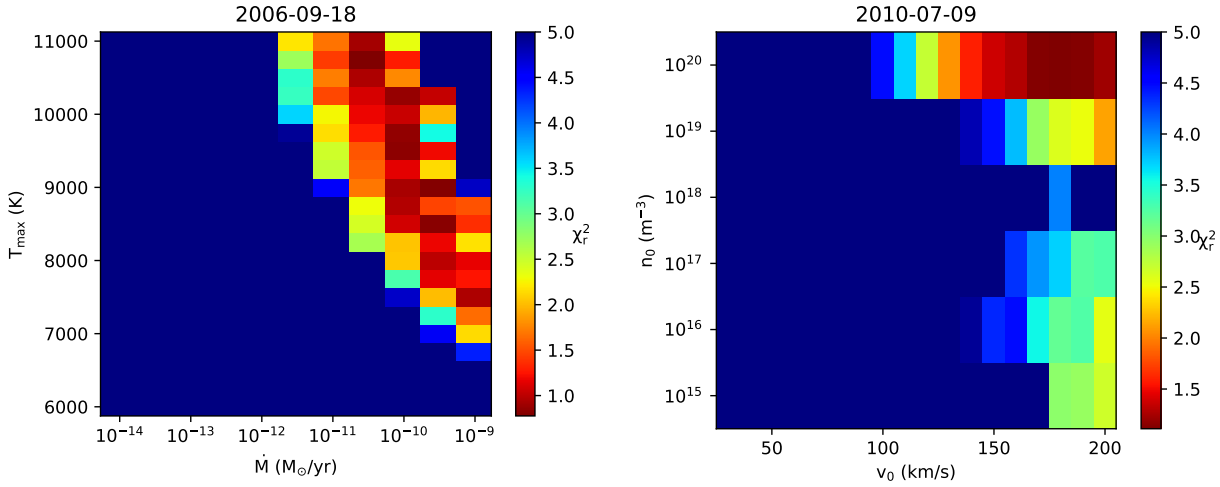


Figure II.11: Left: anti-correlation between the accretion rate and the column temperature, as observed when fitting with Magnetospheric Accretion models (2006-09-18 epoch, Thanathibodee et al., 2019). Right: best-fit parameters values when fitting with Shock models (2010-07-09 epoch, Aoyama et al., 2018).

($S_{\rm eff} = 1.5{\times}10^{-2}$ $S_{\rm jup}$, $v0 = 180$ km/s, $n_0 = 10^{20}$ m^{-3}) provide a direct estimate of the accretion rate (Aoyama et al., 2018, 2021): $\dot{M} \sim 10^{-9}$ $M_\odot$/yr. The effective surface corresponds to a filling factor of 0.38–0.47 %. This is about the same order of magnitude as Ringqvist et al. (2023) found for Delorme 1 (AB)b, another (albeit older) Planetary-Mass Companion of a similar mass. It is still possible that GSC 06214-00210 b also has Magnetospheric Accretion going on, but in a different regime, as was mentioned in the previous section. Magnetospheric Accretion models are still able to reproduce the lines in the 2017 epochs, and while only the Shock models reproduce the 2010-07-09 epoch, it could only be the case because of the too simplistic nature of an axis-symmetrical model, as is the case for Thanathibodee et al. (2019). The Shock parameters also match with what is expected from a Magnetospheric Accretion scenario. To disentangle to the two (non-exclusive) scenarios, higher resolution observations would be required, as their main differences can be resolved at R > 10 000. I have proposed several proposals to disentangle the scenarios on two companions. One with ERIS (GSC 06214-00210 b), which was rejected, and one with CRIRES (Delorme 1 (AB)b), which was granted. The proposal itself is given in appendix of the next chapter.

6 Conclusion

This chapter presented the results of a monitoring campaign of the Pa_β line of GQ Lup b and GSC 06214-00210 b with SINFONI/VLT. The analysis was published in Demars et al. (2023) and yielded a few key points for the understanding of accretion in the context of Planetary-Mass Companions.

GQ Lup b and GSC 06214-00210 b are young and hot planetary-mass companions, with C/O values compatible with solar values. Their metallicities, however, are either solar (GSC 06214-00210 b) or slightly super-solar (GQ Lup b). A more recent study (Xuan et al., 2024) provided super-solar C/O values for both targets, although their error-bars might be underestimated.

The Pa_β line of both objects is found to be variable at least in intensity, and also in shape for GSC 06214-



00210 b. The lines seem to be intrinsically different for both objects, at least given the blue-shifted line of GQ Lup b. Their amplitude of variability has a similar pattern, where greater amplitudes of variability are found at greater timescales, although with a smaller relative amplitude for GSC 06214-00210 b. Both objects show burst epochs (archival data) that may be, along with their variability amplitude (even at short timescales), the reason for the lack of H_α surveys detections. However, the next chapter will show that short timescales variability ($\sim$ hour) cannot actually explain this lack of detection, although on different objects.

GSC 06214-00210 b lines, in particular in the burst epoch, have shape variations where the intrinsic FWHM is correlated with the line flux. This can only happen if flux is added to the wing, so as to reduce the contrast between the core and the wings of the lines. The origin of this flux, is unknown, but a proposition will be made in the next chapter.

Both objects have lines that are reproduced by Magnetospheric Accretion models, and only GSC 06214-00210 b is also reproduced by Shock models. This favors Magnetospheric Accretion for GQ Lup b (in particular with its blue-shifted line), while GSC 06214-00210 b seems to be a more exotic target: its brightest epoch (and highest spectral resolution) is only reproduced by Shock models which parameters are consistent with a shock at the planetary surface. However, the constraints are not sufficient to determine the origin of the material. It is possible that the different epochs of GSC 06214-00210 b represent different accretion regimes of the same mechanism.

Overall, there are still lots of uncertainties in the understanding of GQ Lup b and GSC 06214-00210 b, and Planetary-Mass Companions in general. Higher spectral resolution observations (R $>$ 10 000) are required to (at least) disentangle Magnetospheric Accretion from Shock models, or determine whether they both play a role in line emission. I have submitted several proposals in that sense: two VLT/ERIS proposals targeting the Pa_β line of GSC 06214-00210 b and Delorme 1 (AB)b, at R $>$ 10,000. For GSC 06214-00210 b, the goal was to observe the target during successive nights to check for fine-variations of the Pa_β lines along these timescales. For Delorme 1 (AB)b (which was submitted as Science Verification material for ERIS) the goal was to refine the Shock parameters models obtained by Betti et al. (2022,) for Delorme 1 (AB)b. both proposals were ranked 2nd quartile but rejected. I have also developed a CRIRES proposal, also targetting the Pa_β line. More informations on this one in the next chapter.

While higher spectral resolution observations are not (yet) available for GQ Lup b or GSC 06214-00210 b, the next chapter will focus on R $\sim$ 50 000 observations of another target: Delorme 1 (AB)b. While older than GQ Lup b or GSC 06214-00210 b, it is about the same mass as GSC 06214-00210 b.



A&A, 676, A123 (2023)
https://doi.org/10.1051/0004-6361/202346221
© The Authors 2023

Astronomy & Astrophysics

Emission line variability of young 10–30 $M_{\rm Jup}$ companions

I. The case of GQ Lup b and GSC 06214-00210 b[⋆,⋆⋆]

D. Demars[1], M. Bonnefoy[1], C. Dougados[1], Y. Aoyama[2,3,4], T. Thanathibodee[5,6], G.-D. Marleau[7,8,9,10], P. Tremblin[11], P. Delorme[1], P. Palma-Bifani[12], S. Petrus[13,14], B. P. Bowler[15], G. Chauvin[12,1], and A.-M. Lagrange[16,1]

(Affiliations can be found after the references)

Received 22 February 2023 / Accepted 26 April 2023

ABSTRACT

Context. Emission lines that are indicative of active accretion have been observed for a number of low-mass companions (M < 30 $M_{\rm Jup}$) to stars. Line variability is ubiquitous on stellar accretors, but it has never been characterized in detail for low-mass companions. Such characterizations can offer insights into the accretion mechanism at play.

Aims. We aim to characterize the short-to-long-term H I Paschen β emission line variability of two 10 to 30 $M_{\rm Jup}$ companions on wide orbits: GQ Lup b and GSC 06214-00210 b. We also aim to clarify their accretion mechanisms.

Methods. We used J-band observations at R = 1800–2360, obtained with VLT/SINFONI in 2017, to record time-series investigations of the hours-to-weeks variability of the H I Paschen β emission line (1.282 μm). Contrary to H_α, it should be less affected by chromospheric activity contamination. The photospheric emission was analyzed at each epoch and removed with the `FORMOSA` forward-modeling tool, using new grids of ATMO models exploring different C/O and [M/H] values. The time series of line profiles and intensities were compared to those of more massive accretors and to predictions from the latest magnetospheric accretion and shock models. To complement these results, we also re-investigated archival spectroscopic observations at near-infrared wavelengths of each target to increase the time frame up to a decade and to build a more comprehensive understanding of the variability processes at play.

Results. For GQ Lup b, we find line variability on timescales of several months to decades, whereas it is within the acceptable noise levels on shorter timescales. For GSC 06214-00210 b, we find line variability on timescales of tens of minutes all the way up to a decade. The line profiles of GSC 06214-00210 b are partially resolved in at least one epoch. Both objects show H I Paschen β flux variability that is moderate (<50%), on timescales that are below their rotation period, and that is more significant on longer timescales (up to ∼1000% on decade-long timescales). This behavior resembles that of classical T Tauri stars. The line profiles of GQ Lup b are blue-shifted and can only be reproduced by magnetospheric accretion models, while those of GSC 06214-00210 b are fairly well reproduced by both magnetospheric accretion and shock models, except for one epoch for which the shock model is highly favored. The companions have C/O values broadly consistent with solar values.

Conclusions. While magnetospheric accretion is favored for GQ Lup b, higher resolution (R > 10 000) observations are required to disentangle the two (non-exclusive) emitting mechanisms. The similar variability behavior observed in these low mass companions and in classical T Tauri stars may support similar accretion mechanisms. The high amplitude of variability on timescales of over a month and longer that is found for both objects could be key to explaining the low yield of H_α imaging campaigns.

Key words. planets and satellites: formation – planets and satellites: individual: GQ Lup b – planets and satellites: individual: GSC 06214-00210 b – accretion, accretion disks

1. Introduction

Gas accretion on giant planets and brown-dwarf companions undergoing formation processes is a critical step in determining their early physical evolution and internal structure (e.g., Marley et al. 2007; Baraffe et al. 2009; Cumming et al. 2018), as well as the dissipation of their angular momentum (e.g., Bryan et al. 2018; Batygin 2018). It may also drive disk-planet migration (e.g., Pierens & Raymond 2016) as well as the formation and water content of exo-moons (e.g., Heller & Pudritz 2015), which can potentially harbor life.

The theoretical understanding of the accretion processes is still in its infancy. Companions are expected to accrete part of their mass from circumplanetary disks (hereafter CPDs, Miki 1982) that form around them. A boundary-layer accretion is assumed to develop if the CPD hits the planet surface (e.g., Dong et al. 2021; Fu et al. 2023, and ref. therein), producing a shock within a thin boundary at the disk-planet interface. The most recent radiative-hydrodynamic (RHD) simulations of planets embedded in CPDs predict that part of the mass should fall onto the planet embryo from the circumstellar disk via high-altitude flows and producing an accretion shock at the CPD surface or directly on the planet surface (e.g., Szulágyi et al. 2014, or Fig. 1 in Szulágyi & Ercolano 2020 for a representation).

⋆ Individual spectra are only available at the CDS via anonymous ftp to `cdsarc.cds.unistra.fr` (`130.79.128.5`) or via `https://cdsarc.cds.unistra.fr/viz-bin/cat/J/A+A/676/A123`

⋆⋆ Based on observations collected at the European Organisation for Astronomical Research in the Southern Hemisphere under ESO program 099.C-0760.

Open Access article, published by EDP Sciences, under the terms of the Creative Commons Attribution License (https://creativecommons.org/licenses/by/4.0), which permits unrestricted use, distribution, and reproduction in any medium, provided the original work is properly cited.
This article is published in open access under the Subscribe to Open model. Subscribe to A&A to support open access publication.

The picture of accretion may not, in fact, be fully captured by the RHD approach. The strength of the dipole component of Jupiter's current magnetic field is only about 4 G (Smith et al. 1974), but the interiors of young exoplanets and low-mass brown dwarfs are predicted to be strongly convective and ionized, and so, they should be able to fuel ∼kG magnetic fields (Reiners & Christensen 2010) that are sufficient to affect the gas flow (Cridland 2018) and truncate the CPD (Fendt 2003). It thus remains to be seen to what extent the magnetospheric accretion framework applies in the planetary-mass regime.

The heated gas, either at the accretion shock or within the funnels, produces a set of emission lines from the UV to the NIR whose intensity and spectral profiles can start to be predicted by accretion models (e.g., Thanathibodee et al. 2019; Szulágyi & Ercolano 2020; Aoyama et al. 2020; Marleau & Aoyama 2022). These lines have now been found on a handful of young directly-imaged young companions with mass below ∼30 $M_{\rm Jup}$ (TWA 5 B, GQ Lup B, CT Cha B, USco CTIO 108 B, DH Tau B, GSC 06214-00210 B, SR 12 C, PDS 70 b and c, 2M0249c, Delorme 1(AB)b, HIP 77900B, HIP 78530B, USco 161031.9-16191305B, and YSES 1b; Neuhäuser et al. 2000; Seifahrt et al. 2007; Schmidt et al. 2008; Béjar et al. 2008; Bonnefoy et al. 2014; Bowler et al. 2011; Santamaría-Miranda et al. 2018, 2019; Wagner et al. 2018; Zhou et al. 2014; Haffert et al. 2019; Chinchilla et al. 2021; Petrus et al. 2020; Zhang et al. 2021) and are estimated to be frequent (∼50% frequency, Bowler et al. 2017) below 15 Myr. These companions are found in systems spanning a wide range of ages (1–40 Myr) and with diverse architectures – within the cavity of circumstellar disks, in hierarchical systems, or orbiting single or binary stars of various masses.

All the line detections have also been fortuitous and follow up-studies are starting to improve the understanding of their origin and to constrain the accretion models. Zhou et al. (2014) and Zhou et al. (2021) recorded measurements of the shock emission of four companions in the UV (GQ Lup b, GSC 06214-00210 b, DH Tau b and PDS 70 b, all within 10–30 $M_{\rm Jup}$ and <15 Myr). They were able to measure accretion rates in the range 10^{-9}–10^{-11} $M_\odot$ yr^{-1}. They also argued that a significant fraction of the energy released at the accretion shock is reprocessed at H_α. Line ratio measurements on Delorme 1 (AB)b (∼14 $M_{\rm Jup}$, ∼40 Myr, Delorme et al. 2013) at near-infrared wavelengths (Betti et al. 2022b,a) were found to be compatible with non-LTE accretion-shock models for planets (Aoyama et al. 2018). High-resolution observations of the Balmer lines of Delorme 1 (AB)b in the UV show line profiles suggestive of magnetospheric accretion operating on that 40 Myr old companion (Ringqvist et al. 2023). Constraints on the $\mathsf{H}_\alpha/\mathsf{H}_\beta$ line-ratio of PDS 70 b indicate significant extinction in the line-of-sight due to surrounding dust or a CPD (Hashimoto et al. 2020).

Variability among the emission lines is observed across a wide stellar mass spectrum (for a review, see Fischer et al. 2022) and it traces episodic variability in the accretion and ejection over the course of the stars evolution. Non-steady accretion is predicted to occur on low-mass companions and has a significant impact on their early physical evolution (Baraffe et al. 2009; Cumming et al. 2018) as well as our ability to detect them (Brittain et al. 2020). Global hydrodynamic and magneto-hydrodynamic simulations of protoplanets embedded in a circumstellar disk indicate modulations on decades-long timescales (see Gressel et al. 2013; Szulágyi & Ercolano 2020). Instabilities or dead zones developing through the CPD (Lubow & Martin 2012; Zhu et al. 2016) are expected to modulate the accretion flow on Keplerian timescales (from months to years). If magnetospheric accretion is in operation, then hot spots and funnel flows should produce variability of the emission lines along the object rotation period as it does for to stars (e.g., Sicilia-Aguilar et al. 2015). A variable extinction in the line of sight should modulate the line emission further (Szulágyi & Ercolano 2020; Marleau et al. 2022).

The study of the emission line variability timescales and amplitude thus offers an opportunity to probe both the accretion mechanism and the effect of the local environment of young companions. Line variability has been detected on a timescale of about 1 yr on GQ Lup b and GSC 06214-00210 b (see below). Wolff et al. (2017) found the Pa_β line of DH Tau b (a ∼1Myr old ∼15 $M_{\rm Jup}$ companion, Itoh et al. 2005) to disappear within ∼5 weeks. Eriksson et al. (2020) found the H_α line of Delorme 1(AB)b (a 30–40 Myr old, ∼14 $M_{\rm Jup}$ companion Delorme et al. 2013) to vary over a few hours. Zhou et al. (2021) reported several measurements of the H_α line of PDS 70 b over timescales of days to months, and an upper limit of 30% for the variability.

In this paper, we focus on the spectroscopic monitoring of the Pa_β emission line of two low-mass companions, GQ Lup b and GSC 06214-00210 b, with previously reported line variability over the course of a semester (Lavigne et al. 2009). We combine these observations with archival data to probe line variability for timescales ranging from several minutes to decades. The Pa_β line is well adapted to a monitoring with standard adaptive-optics fed instruments from the ground and is more intense above the continuum than the Br_γ line in young accreting late-type objects (Natta et al. 2004; Betti et al. 2022b). Moreover, it is known to be less affected by chromospheric activity than H_α in the stellar and sub-stellar mass regimes (Natta et al. 2004; Antoniucci et al. 2011; Rigliaco et al. 2012; Manara et al. 2013).

We present a compendium of the presently known properties of the two objects in Sect. 2. The observations of GQ Lup b and GSC 06214-00210 b are detailed in Sect. 3, followed by the data extraction strategy in Sect. 4. The photospheric parameters, and emission line variability (timescale, intensity, profiles) are presented in Sect. 5 and compared to models. We analyze how the Pa_β line behavior relates to other accretors, contextualize possible line profile variations, and discuss the implication of line variability for the detectability of protoplanets in Sect. 6. Our results are summarized in Sect. 7.

2. Information on targets

2.1. GQ Lup system

GQ Lup b is a 10–40 $M_{\rm Jup}$ companion resolved by Neuhäuser et al. (2005) at ∼0.7″ (∼108 au at 154.10 ± 0.69 pc; Gaia Collaboration 2022) from a 2–5 Myr old K7Ve-type T Tauri star ($M_\star$ = 1.02 ± 0.05 $M_\odot$; MacGregor et al. 2017; Gaia Collaboration 2022) that is a member of the Lupus I cloud (Herbig 1977). The star is surrounded by a circumstellar disk inclined at 60° showing spiral structures (e.g., van Holstein et al. 2021) in scattered light up to 0.84" (129 au), while the disk shows smaller extension at millimeter and sub-millimeter wavelengths both in the continuum and ^{12}CO (20–46 au; MacGregor et al. 2017; Wu et al. 2017b; Long et al. 2020). Long et al. (2020) report a gap at 10 au in the dust component of the disk at millimeter wavelengths, which might be carved by a planet at this separation. It is unclear whether this possible planet could explain the significant radial-velocity variation of GQ Lup A noticed by Donati et al. (2012) over a 2-yr time span. The star has a reported spin axis inclination of ∼30° misaligned with the disk and is

experiencing dominantly pole-ward magnetospheric accretion that produces a set of emission lines, including Pa_β (Broeg et al. 2007; Donati et al. 2012; Frasca et al. 2017; Seifahrt et al. 2007).

GQ Lup b is also known to display a bright H_α emission line found at four epochs spanning two decades: 1) on April 10, 1999 HST/WFPC2 wide-field imaging data (F606W filter; λ_{cen} = 605.4, $FWHM$ = 220.5 nm; Marois et al. 2007); 2) in HST/WFC3-UVIS2 data (Zhou et al. 2014) acquired on February 25, 2012 with a narrower filter (F656N, λ_{cen} = 656.2 nm, $FWHM$ = 187.1 nm); 3) on ground-based *Magellan*/MagAO imaging (Wu et al. 2017b) with a custom H_α filter on April 16, 2015 (λ_{cen} = 656.0 nm, $FWHM$ = 6.3 nm); and 4) with VLT/MUSE medium-resolution (R = 2516) optical spectroscopy on April 19, 2019 (Stolker et al. 2021). Wu et al. (2017b) has argued that the line could be showing variability, but the different instrumental setup stands in the way of a robust homogeneous comparison of the reported H_α fluxes. The MUSE spectrum shows the Ca II triplet in emission (λ8498, 8542, 8662 Å), but no H_β line.

The companion displays a Pa_β emission line first seen on September 18, 2006 (EW = −3.83 ± 0.12 Å) from data acquired with VLT/SINFONI (Seifahrt et al. 2007) at R = 2360. The line is also detected in Gemini/NIFS data (R ∼ 5000) collected on May 30, 2017, but at a significantly weaker flux level (EW = −0.46 ± 0.08 Å), supporting the observed variability at H_α. The No Br_γ emission line is reported in K-band spectra obtained at four epochs (Neuhäuser et al. 2005; McElwain et al. 2007; Seifahrt et al. 2007; Lavigne et al. 2009).

The set of available near-infrared spectra revealed an inconsistency in the spectral slope of the SINFONI spectrum of Seifahrt et al. (2007), which we re-investigate in Sect. 4. The compendium of 0.6–5 μm spectro-photometry on the companion allowed Stolker et al. (2021) to derive $T_{\rm eff}$ of 2700 K consistent with the optical spectral type of M9 (e.g., Luhman et al. 2003) and the luminosity-based "hot-start" mass of 30 $M_{\rm Jup}$. The analysis also confirms a significant in-line extinction (Av = 2.3 mag) and an excess emission long-wards of 2.5 μm that could be caused by infalling material from the circumplanetary disk or a CPD. ALMA observations have failed to detect this CPD thus far (MacGregor et al. 2017; Wu et al. 2017b) and no intrinsic linear polarization is detected at the location of the companion (van Holstein et al. 2021). High-resolution spectroscopy (VLT/CRIRES, R ∼ 100 000) of GQ Lup b centered on the ^{12}CO overtone at K-band allowed for the measurement of a projected rotational velocity ($5.3^{+0.9}_{-1.0}$ km s^{-1}; Schwarz et al. 2016), which is in the lower range of values measured on young 10–50 $M_{\rm Jup}$ objects (Kurosawa et al. 2006; Bryan et al. 2018, 2020), setting an upper limit on the rotation period of 82 h.

GQ Lup b's orbital motion has been monitored since its original discovery (Ginski et al. 2014; Schwarz et al. 2016) and now it covers ∼1% of its estimated orbit. Tentative constraints on the mutual inclination with the circumstellar disk indicate the companion might be on a polar orbit (Stolker et al. 2021) with a semi-major axis of a = 117^{+24}_{-23} au and low eccentricity possibly crossing the circumstellar disk.

A second accreting low-mass stellar companion (2MASS 15491331-3539118; projected separation ∼2400 au; M ∼ 0.15 $M_\odot$, GQ Lup C) was recently found to be bound to the star. GQ Lup c bears its own detached disk that is roughly aligned with the one of the primary star and with the large-scale dust filament of Lupus I containing GQ Lup (Alcalá et al. 2020; Lazzoni et al. 2020).

In summary, this system shows companions of different masses and offers a unique means to better understand the early formation and dynamical evolution of planetary systems.

2.2. GSC 06214-00210 system

GSC 06214-00210 b (hereafter, GSC06214b) is a 14.5 ± 2 $M_{\rm Jup}$ co-moving companion (Kraus et al. 2008; Ireland et al. 2011; Pearce et al. 2019) resolved on a wide orbit (2.2″ separation, corresponding to a projected physical separation of 240 au at 108.8 ± 0.3 pc; Gaia Collaboration 2022) from the weak-line T Tauri star GSC 06214-00210 (K5 ± 1; $M_\star$ = 0.80 ± 0.11 $M_\odot$; Bowler et al. 2014; Pearce et al. 2019).

The star is reported to be a member of the Upper Scorpius sub-group of the Scorpius-Centaurus (Sco-Cen) OB association (Preibisch et al. 1998), with a median age of ∼10 Myr (Pecaut et al. 2012; Feiden 2016). We notice that the kinematic analysis tool BANYAN Σ (Gagné et al. 2018b) now suggests a possible alternative membership (58.8% probability) to the older Upper-Scorpius Centaurus (UCL) sub-group of Sco-Cen (16 Myr; Pecaut et al. 2012) based on the *Gaia*-DR3 astrometry. This possible membership to UCL is better consistent with the revised isochronal age of 24^{+7}_{-5} Myr reported in Pearce et al. (2019) and based on the Baraffe et al. (2015) evolutionary tracks and their $16.9^{+2.9}_{-1.9}$ Myr age inferred using the magnetized evolutionary models of Feiden (2016) and a prior on the age of Sco-Cen. We adopted this latter value in our study.

The star is known to have no reported excess emission, a weak H_α emission line, and no Pa_β emission (Preibisch et al. 1998; Bowler et al. 2011). Conversely, medium-resolution 1.17–1.83 μm spectroscopy (R = 3800) of the system with OSIRIS at Keck in 2010 (Bowler et al. 2011) revealed a bright Pa_β emission line (EW= −11.4 ± 0.3 Å) on GSC06214b. The HST/WFC3 photometry also reveals the companion to emit at H_α (Zhou et al. 2014). The companion has a continuum excess emission noticeable at K- and L'- bands (1.8–4.2 μm; Bowler et al. 2011; van Holstein et al. 2021), which indicates it is likely to bear a CPD. The CPD has remained elusive at sub-millimeter wavelengths (Bowler et al. 2015; Wu et al. 2017a) indicative of a compact detached disk. However, a likely intrinsic polarization signal (van Holstein et al. 2021) was detected with VLT/SPHERE. van Holstein et al. (2021) argued that the CPD must have an inclination of ∼48° to explain the measured degree of polarization. They used the possible constraints on the CPD inclination and the measured rotational velocity of $6.1^{+4.9}_{-3.8}$ km s^{-1} of GSC06214b (Bryan et al. 2018) to narrow down the companion rotation period to 22–77 h.

An additional 0.9–2.5 μm spectrum of GSC06214b was obtained with GNIRS on June 23, 2011 by Lachapelle et al. (2015), with a resolution that is lower than that of OSIRIS (R ∼ 1000). It shows a weaker Pa_β emission (EW = −4.4 ± 0.5 Å) than in Bowler et al. (2011) and a Br_γ emission line (EW = −0.24 ± 0.05 Å), making GSC06214b the third companion with mass below 20 $M_{\rm Jup}$ to display this line (Zhang et al. 2021; Betti et al. 2022b). K-band (1.965–2.381 μm) OSIRIS spectra obtained on June 26, 2012 at R = 3800 do not show the reported Br_γ line. Bryan et al. (2018) do not mention the detection of this line in their R = 25 000 Keck/NIRSPEC spectrum (2.03–2.38 μm) of the target obtained on June 3, 2015 either. But this line was detected again in archival VLT/SINFONI spectra (R ∼ 5000) obtained on May 28, 2014 and July 07, 2014 (Palma-Bifani et al., in prep.), further hinting

at a significant year-to-year variability for the accretion lines on that companion. All sets of near-infrared spectra allow for this companion to be classified as an M9-M9.5 low-gravity object (Lavigne et al. 2009; Bowler et al. 2014). GSC06214b offers the opportunity to probe the accretion processes at the Deuterium-burning boundary in a more evolved system, thus complementing the analysis of GQ Lup b.

3. Observations and data reduction

3.1. Monitoring sequences with VLT/SINFONI

We monitored GQ Lup b and GSC06214b with the Integral Field Spectrograph (IFS) SINFONI. SINFONI is a now decommissioned instrument previously installed at VLT/UT4 Cassegrain focus and composed of a custom adaptive optics module (MACAO) feeding an IFS (SPIFFI). SPIFFI splits the field-of-view into 32 horizontal slices (slitlets) and re-arranges them to form a pseudo-slit that is dispersed by a grating on a 2k × 2k HAWAII-2RG detector (Eisenhauer et al. 2003; Bonnet et al. 2004). The instrument was operated with pre-optics and gratings in the J-band (1.1–1.35 µm). For GQ Lup b, the setup provided a 0.8" square field of view (FoV) composed of 12.5×25 mas spaxels, with a resolving power of $R_\lambda = \frac{\lambda}{\Delta\lambda} = 2360$. For GSC06214b, the setup provided a 3.2" square field of view (FoV) composed of 50×100 mas spaxels, with a resolving power of $R_\lambda = \frac{\lambda}{\Delta\lambda} = 1800$. They translate into line spread function (LSF) widths of 127 and 167 km s^{-1} for GQ Lup b and GSC06214b, respectively.

MACAO used the host stars for wavefront sensing. The derotator at the Cassegrain focus was used to align the star and companions horizontally in the FoV at acquisition. A telescope offset was then applied to place the host stars PSF cores outside of the FoV and allow for deeper exposures. Small additional dithering were applied along the vertical direction of the FoV in-between each exposure to ensure that the companion signal did not fall all the time on bad pixels. A blank-sky exposure (with identical DIT) was performed at the end of the dithering sequence to ensure a proper removal of the OH- emission lines and thermal background. We then moved the star back in the FoV and recorded an additional short-exposure to record a PSF, to be used for calibration purposes.

GSC06214b was observed on April 25, May 4, June 1, and August 18, 2017 as part of our program (099.C-0760). GQ Lup b was observed on April 25, 30, 2017 and June 1, 2017 as part of the same program (UT dates). We also decided to re-process SINFONI data of GQ Lup b obtained on 2006-09-18 (program 077.C-0264) and presented in Seifahrt et al. (2007) for consistency and given that the published SINFONI spectrum has been shown to be discrepant with respect to other studies (McElwain et al. 2007; Lavigne et al. 2009). These observations used the same setup and followed an identical data-extraction strategy as for the 2017 observations. The log of observations is detailed in Table 1.

3.2. SINFONI cube reconstruction and calibration

SINFONI records bi-dimensional raw frames of the 32 dispersed slitlets. We used the Toolkit for Exoplanet deTection and chaRacterization with IfS (hereafter `TExTRIS`; Petrus et al. 2021, Bonnefoy et al., in prep.) to correct them for any static noise caused by the detector electronics (Bonnefoy et al. 2014).

The SINFONI data handling pipeline v3.0.0 (Abuter et al. 2006) was then used to reconstruct calibrated data cubes encoding the spatial and spectral dimensions (X, Y, λ) from these raw data. The pipeline uses calibration frames obtained at day time to apply basic cosmetic steps on the raw frames and correct them from the distortion introduced by optical elements and the detector. It identifies the position of slitlets on the raw frames and builds a reference 2D map associating the pixels to given wavelengths. The sky emission was evaluated and removed through the field subtracting cubes of reconstructed exposures on sky. Sky OH- emission lines residuals were then evaluated and subtracted using the method of Davies (2007). Because residuals hot/cosmics pixels were found in the cubes, they were corrected for by using the LACOSMIC Python package on each individual wavelength frame (van Dokkum 2001).

The wavelength solution relies on day-time calibration frames obtained with an Argon lamp and that has proven to be inaccurate on other datasets (Petrus et al. 2021; Zhang et al. 2021). We therefore improved the pipeline wavelength calibration with routines from `TExTRIS`, comparing the many telluric absorption lines contained in each spaxel to a model generated for the observing conditions using the ESO Skycalc tool (Noll et al. 2012; Jones et al. 2013). The method is applicable whenever the spaxels contain enough stellar light to infer the telluric absorptions. We evaluated the shifts in the wavelength interval 1.1–1.3 µm using cross-correlations of spaxels with a signal-to-noise ratio (S/N) above 10 at Pa_β. A master median-combined map of wavelength shift was then created and each individual cube was corrected from the median of the shifts of individual spaxels meeting the S/N criterion. The corrected wavelength shifts at each epochs are reported in Table 1, for an average wavelength calibration uncertainty of ∼0.2 Å and ∼0.3 Å for GQ Lup b and GSC06214b, respectively. Because of the relatively low S/N in the science target cubes, we used the wavelength solution found with the telluric standard stars (relying on the same original calibration as the science target) as the solution for the whole sequence.

3.3. New investigation of Keck/OSIRIS data

In the analysis, we also included the individual spectra of GSC06214b obtained on July 9, 2010 with the OH-Suppressing Infrared Imaging Spectrograph (OSIRIS; Larkin et al. 2006) mounted on Keck II. OSIRIS is a lenslet-based IFS operated with the Keck adaptive optics system. The instrument produced data cubes sampling a rectangular FoV ($0.8 \times 3.2''$) with $0.05 \times 0.05''$ spaxels. The Jbb band grating provided 1.18–1.416 µm spectra at $R \sim 3800$. Eight 5-min long exposures were recorded. The stacked data cubes are presented in Bowler et al. (2011) and the companion is sufficiently separated from the star to directly extract its spectrum within a circular aperture. The data analysis is described in more detail in Bowler et al. (2011). Here, we re-analyzed the individual data cubes in an attempt to detect the Pa_β variability from one exposure to the next.

4. Spectral extraction

4.1. Halo removal

Both GQ Lup b and GSC06214b spectra are contaminated by the PSF wings of the primary stars located outside of the FoV. The data cubes obtained at the end of each sequence of observations with the host stars in the FoV do not probe the extended wings of the PSF and therefore do not allow for a direct subtraction of the contamination. Therefore, we had to develop a specific procedure (described below) that was applied to each individual SINFONI data cube on both targets.

Table 1. Log of SINFONI observations.

Target	Date	UT start (h:m:s)	UT end (h:m:s)	Setup mas px^{-1}	DIT × NDIT (s)	Seeing (")	Airmass	τ_0 (ms)	J-mag	$\Delta\lambda$ Å
GQ Lup b	2017-04-25	05:21:16	05:26:16	25	300 × 1	0.62	1.04	–	14.59	1.32 ± 0.21
GQ Lup b	2017-04-25	05:26:40	05:31:40	25	300 × 1	0.56	1.04	–	14.43	1.32 ± 0.21
GQ Lup b	2017-04-25	05:37:30	05:42:30	25	300 × 1	0.56	1.03	–	14.35	1.32 ± 0.21
GQ Lup b	2017-04-25	05:42:55	05:47:55	25	300 × 1	0.43	1.03	–	14.10	1.32 ± 0.21
GQ Lup A	2017-04-25	05:54:10	05:54:25	25	15 × 1	0.64	1.02	–	–	1.32 ± 0.21
Hip081208	2017-04-25	06:05:03	06:05:06	25	3 × 1	0.65	1.04	–	–	1.32 ± 0.21
GQ Lup b	2017-04-30	05:34:35	05:39:35	25	300 × 1	0.45	1.02	–	13.95	0.95 ± 0.21
GQ Lup b	2017-04-30	05:56:16	06:01:16	25	300 × 1	0.44	1.02	–	14.24	0.95 ± 0.21
GQ Lup b	2017-04-30	05:50:51	05:55:51	25	300 × 1	0.43	1.02	–	14.27	0.95 ± 0.21
GQ Lup b	2017-04-30	05:40:00	05:45:00	25	300 × 1	0.40	1.02	–	13.96	0.95 ± 0.21
GQ Lup A	2017-04-30	06:07:36	06:07:51	25	15 × 1	0.58	1.02	–	–	0.95 ± 0.21
Hip079410	2017-04-30	06:17:30	06:17:34	25	4 × 1	0.53	1.00	–	–	0.95 ± 0.21
GQ Lup b	2017-06-01	06:29:29	06:34:29	25	300 × 1	0.60	1.24	15.51	14.14	1.34 ± 0.18
GQ Lup b	2017-06-01	06:34:55	06:39:55	25	300 × 1	0.57	1.25	13.92	14.26	1.34 ± 0.18
GQ Lup b	2017-06-01	06:45:44	06:50:44	25	300 × 1	0.69	1.29	9.70	14.53	1.34 ± 0.18
GQ Lup b	2017-06-01	06:51:09	06:56:09	25	300 × 1	0.70	1.31	10.15	14.50	1.34 ± 0.18
GQ Lup A	2017-06-01	07:02:25	07:02:40	25	15 × 1	0.67	1.35	9.85	–	1.34 ± 0.18
Hip082670	2017-06-01	07:12:57	07:13:17	25	20 × 1	0.56	1.26	11.90	–	1.34 ± 0.18
GQ Lup b	2006-09-18	23:22:53	23:27:53	25	300 × 1	0.87	1.24	1.96	13.01	1.30 ± 0.16
GQ Lup b	2006-09-18	23:39:49	23:44:49	25	300 × 1	0.93	1.30	1.74	12.79	1.30 ± 0.16
GQ Lup b	2006-09-18	23:45:21	23:50:21	25	300 × 1	0.86	1.32	1.95	13.06	1.30 ± 0.16
GQ Lup b	2006-09-18	00:02:15	00:07:15	25	300 × 1	0.84	1.40	1.96	13.12	1.30 ± 0.16
GQ Lup b	2006-09-18	00:07:41	00:12:41	25	300 × 1	0.90	1.42	1.92	13.01	1.30 ± 0.16
GQ Lup b	2006-09-18	00:24:36	00:29:36	25	300 × 1	0.73	1.52	2.23	13.67	1.30 ± 0.16
GQ Lup b	2006-09-18	00:30:08	00:35:08	25	300 × 1	0.75	1.55	2.18	13.76	1.30 ± 0.16
GQ Lup b	2006-09-18	00:47:01	00:52:01	25	300 × 1	0.95	1.67	1.76	14.44	1.30 ± 0.16
GQ Lup b	2006-09-18	00:52:33	00:57:33	25	300 × 1	1.17	1.72	1.43	14.81	1.30 ± 0.16
Hip078754	2006-09-18	01:34:42	01:36:42	25	120 × 1	1.08	1.95	1.59	–	1.30 ± 0.16
Hip087140	2006-09-18	01:17:36	01:19:36	25	120 × 1	1.17	1.22	1.30	–	1.30 ± 0.16
GSC06214b	2017-04-25	06:21:07	06:26:07	100	300 × 1	0.54	1.01	–	16.44	1.46 ± 0.30
GSC06214b	2017-04-25	06:32:12	06:37:12	100	300 × 1	0.52	1.00	–	16.15	1.46 ± 0.30
GSC06214b	2017-04-25	06:48:51	06:53:51	100	300 × 1	0.60	1.00	–	16.35	1.46 ± 0.30
GSC06214A	2017-04-25	07:05:42	07:05:57	100	15 × 1	0.46	1.00	–	–	1.46 ± 0.30
Hip079599	2017-04-25	07:17:56	07:17:57	100	1 × 1	0.52	1.01	–	–	1.46 ± 0.30
GSC06214b	2017-04-25	07:35:50	07:40:50	100	300 × 1	0.60	1.02	–	16.30	1.46 ± 0.30
GSC06214b	2017-04-25	07:46:53	07:51:53	100	300 × 1	0.63	1.03	–	16.46	1.46 ± 0.30
GSC06214b	2017-04-25	08:03:31	08:08:31	100	300 × 1	0.66	1.05	–	16.50	1.46 ± 0.30
Hip095105	2017-04-25	08:32:45	08:32:48	100	3 × 1	0.57	1.05	–	–	1.46 ± 0.30
GSC06214b	2017-05-04	04:29:49	04:34:49	100	300 × 1	0.48	1.10	–	16.18	1.62 ± 0.33
GSC06214b	2017-05-04	04:40:54	04:45:54	100	300 × 1	0.56	1.07	–	16.06	1.62 ± 0.33
GSC06214b	2017-05-04	04:57:38	05:02:38	100	300 × 1	0.46	1.05	–	16.00	1.62 ± 0.33
GSC06214A	2017-05-04	05:14:44	05:14:59	100	15 × 1	0.62	1.03	–	–	1.62 ± 0.33
Hip081214	2017-05-04	05:27:03	05:27:05	100	2 × 1	0.86	1.08	–	–	1.62 ± 0.33
GSC06214b	2017-06-01	01:54:27	01:59:27	100	300 × 1	0.86	1.21	7.73	16.09	1.28 ± 0.33
GSC06214b	2017-06-01	02:16:29	02:21:29	100	300 × 1	0.74	1.15	11.25	15.88	1.28 ± 0.33
GSC06214b	2017-06-01	02:27:32	02:32:32	100	300 × 1	0.66	1.12	10.24	15.98	1.28 ± 0.33
GSC06214b	2017-06-01	02:44:12	02:49:12	100	300 × 1	0.72	1.09	10.56	15.91	1.28 ± 0.33
GSC06214A	2017-06-01	03:01:00	03:01:15	100	15 × 1	0.85	1.06	14.31	–	1.28 ± 0.33
Hip084435	2017-06-01	03:16:58	03:17:04	100	6 × 1	0.60	1.13	13.61	–	1.28 ± 0.33
Hip084435	2017-06-01	06:11:06	06:11:14	100	8 × 1	0.65	1.03	16.46	–	1.28 ± 0.33
GSC06214b	2017-08-19	01:28:50	01:33:50	100	300 × 1	0.64	1.18	4.58	16.34	1.80 ± 0.35
GSC06214b	2017-08-19	01:39:28	01:44:28	100	300 × 1	0.66	1.21	4.67	16.39	1.80 ± 0.35
GSC06214b	2017-08-19	01:55:28	02:00:28	100	300 × 1	0.70	1.27	4.90	16.84	1.80 ± 0.35
GSC06214A	2017-08-19	02:11:40	02:11:55	100	15 × 1	0.71	1.32	6.09	–	1.80 ± 0.35
Hip082670	2017-08-19	01:20:24	01:20:26	100	2 × 1	0.57	1.18	5.48	–	1.80 ± 0.35

Notes. Dates are given in the YYYY-MM-DD format. DIT and NDIT and correspond to the Detector Integration Time per frame, the number of individual frames per exposure. Here, τ_0 corresponds to the coherence time. Both seeing and coherence time were gathered from the ESO/ASM tool at corresponding UT times, while the airmass was computed as the mean value between the starting and ending values in the files headers. The J-mag is our computed J-2MASS magnitude. $\Delta\lambda$ corresponds to the applied wavelength calibration, as described in Sect. 3.2, i.e., the value found for the telluric standard of that sequence.

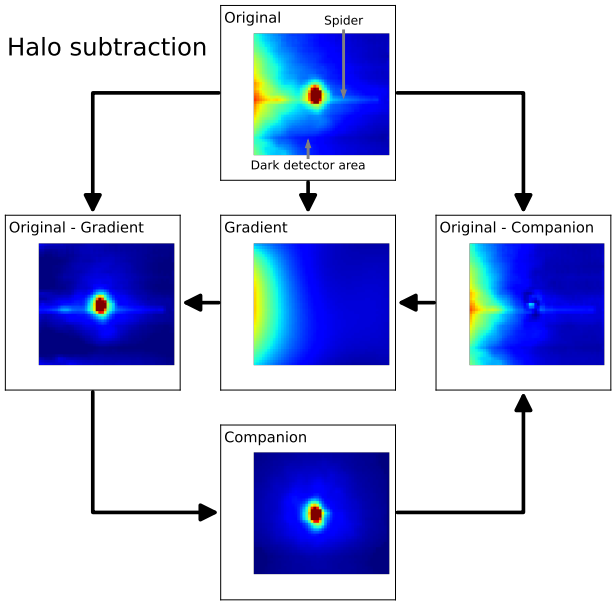


Fig. 1. Illustration of the halo subtraction, for the first data cube of the GQ Lup b 2017-04-30 epoch (median along the wavelength axis). We also report the location of the diffraction pattern of the telescope spiders, along with the identified area with improperly calibrated instrument transmission that affects the lower half of the images.

Prior to the halo removal, the cube rectangular spaxels were linearly interpolated to produce a regular spatial sampling of 12.5 mas in the horizontal and vertical directions. The contamination was then evaluated and corrected in each individual frame of the data cubes, with a CLEAN-like algorithm (Högbom 1974). The algorithm fits a two-component flux model made up of: (i) a third-order bi-dimensional gradient, approximating the primary star PSF wings and (ii) a PSF model placed at the companion location and scaled to the companion's flux. The latter step requires the definition of a PSF model. We used the primary star data cubes (normalized to 1) for that purpose in the 2017 data. Data cubes of the primary star were not available in the 2006 data and we chose to use those corresponding to the telluric standard star instead. The two flux components were successively fitted and subtracted from the original frames, for a total of four iterations, which is a trade-off between χ^2_r and S/N optimization. See Fig. 1 for a visual representation and Fig. A.1 for residuals.

The host star gradient subtraction allows us to subtract the large-scale structures but cannot remove more complex features such as the diffraction pattern caused by the telescope spiders. This component is most important on GQ Lup b and was then approximated as a 1-day Gaussian profile in the direction perpendicular to the spider axis and subtracted in the gradient-subtracted cubes.

SINFONI shows a static dark horizontal area in the lower half part of all data cubes (see Fig. 1) likely caused by some persistence appearing in the lamp flat-fields taken in the day time. This was discovered during data reduction and affected the spectra profiles when the companion was located in this region. We decided to exclude the corresponding cubes and spectra from the analysis.

4.2. Extraction and flux calibration

The PSF model estimated from the primary (or telluric standard) star was not a good enough match to the companion PSF to extract spectra from profile fitting. Therefore, the companions spectra were extracted within a circular aperture on the contamination-corrected data cubes of constant radius with wavelengths. The size of the aperture was chosen to conserve the spectral slope and to avoid integrating noise due to the imperfect removal of the stellar halo in the background-limited area. This procedure is similar as the one adopted in Bonnefoy et al. (2014) and proven to provide a robust extraction of the spectral features and slope on J-band SINFONI data. The adopted radii were ranging from 50 to 75 mas. We retrieve spectra of various S/N depending on the observing conditions. For GQ Lup b, the S/N ranges from 20 to 30 in the 2006-09-18 and 2017-06-01 epochs, while it ranges from 35 to 50 in the 2017-04-25 and 2017-04-30 epochs. For GSC06214b, the S/N is relatively stable, within the 15–30 range for all epochs.

The atmospheric transmission was evaluated computing the ratio between the extracted spectra of telluric standard stars and their synthetic spectra: black-bodies scaled to the 2MASS JHK, and WISE W1 and W2 photometry of the objects (Cutri et al. 2003; Cutri & et al. 2012) collected with the VOSA[1] tool (Bayo et al. 2008). The Pa_β absorption line of the standards were evaluated and removed beforehand as follows. The telluric standard star spectrum was corrected from telluric absorptions by a model created with the SkyCalc tool (Noll et al. 2012; Jones et al. 2013). The line profile was then fitted in the by a Voigt profile function, then subtracted from the spectrum. The spectrum was then applied the same telluric absorption model. This ensures that the line shape evaluation is not impacted by weak telluric features in the line wings and that it does not bias the companion emissions at these wavelengths.

We performed an absolute flux calibration of the individual spectra using the telluric standard star as a spectro-photometric reference (2MASS J-band photometry). The use of the telluric standard stars was favored over the use of the host stars because of their potential photometric variability. This is the case for GQ Lup A which is a known high-amplitude variable star ($\Delta J = 0.87$, Batalha et al. 2001; Broeg et al. 2007). The remaining J-band magnitudes inferred from the individual epochs were averaged to remove part of the uncertainty on the photometric calibration due to variation in observing conditions and AO performance between the telluric standard stars and the companion observations. We decided to exclude the 2006 epoch on GQ Lup b from this process because the companion and the telluric standard were observed under poor and variable adaptive-optics conditions.

We find a magnitude of $J = 16.21^{+0.26}_{-0.21}$ on GSC06214b. The value is well consistent with the one measured by Lachapelle et al. (2015) and Bowler et al. (2011) ($J = 16.19 \pm 0.04$ and $J = 16.25 \pm 0.04$, respectively) derived from the contrast between the primary and the companion and the tabulated 2MASS J-band magnitude of the system. We decided to use the latter value.

We find $J = 14.38^{+0.13}_{-0.12}$ for GQ Lup b. Lavigne et al. (2009) found $J = 15.13 \pm 0.44$ but the measurement accuracy was limited by the partial saturation of the host star in their data and the photometry relies on the 2MASS magnitude of the host star, which is known to be variable (as previously mentioned). McElwain et al. (2007) found $J = 14.90 \pm 0.11$ using a similar procedure as ours and this photometry was used in all contemporaneous studies on the system (e.g., Stolker et al. 2021). However, this measurement was performed on OSIRIS data at a high airmass with a narrower wavelength range and at a lower signal-to-noise ratio. Given the amplitude of variability of the primary

[1] http://svo2.cab.inta-csic.es/theory/vosa/

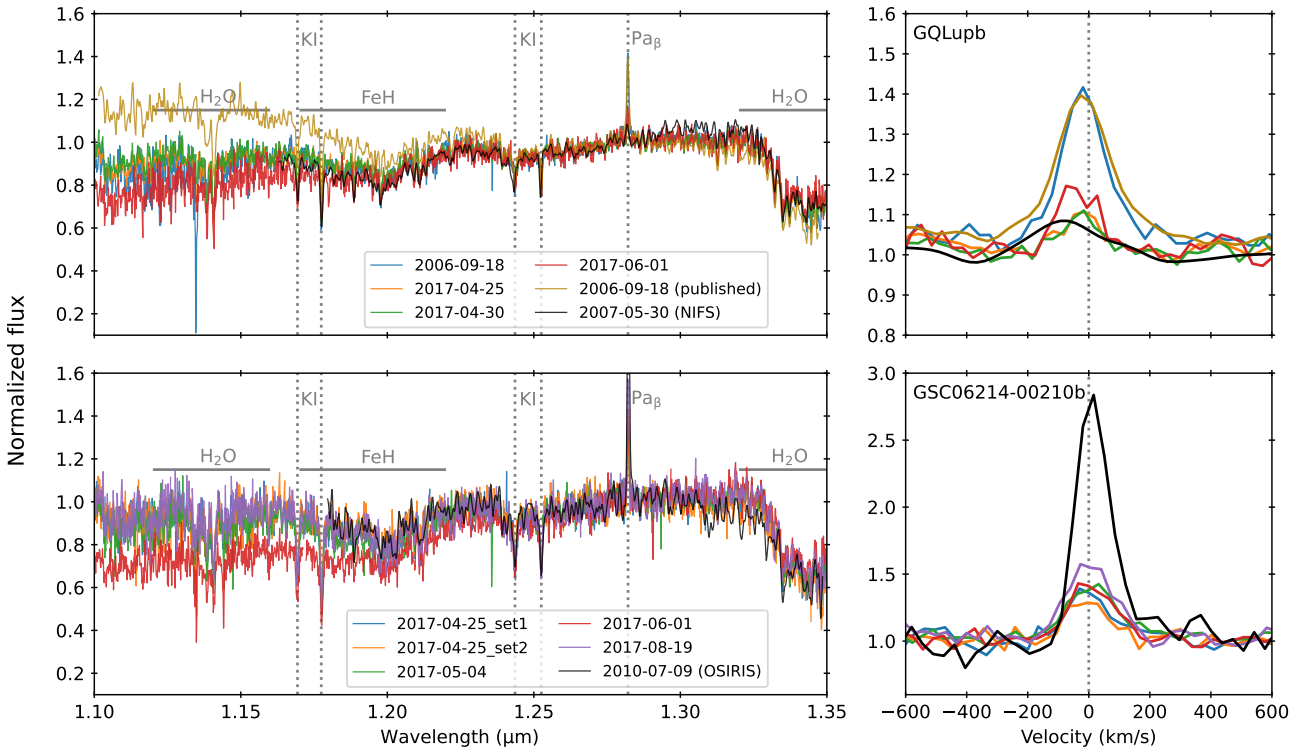


Fig. 2. Companion spectra. Top row: GQ Lup b spectra. Bottom row: GSC 06214-00210 b spectra. Left column: full spectra. Right column: Zoom on the Pa$_\beta$ line. In both cases, the spectra continuum are normalized to 1 as the mean value on the 1.27–1.28 μm and 1.29–1.30 μm ranges. The 2010-07-09 (OSIRIS) epoch of GSC06214b was degraded to SINFONI resolution (R = 1800) in the left column, but is shown at full resolution (R = 3800) in the right column. The spectral slopes differences are the results of different Strehl Ratios between epochs, despite the AO correction. Our re-extraction of GQ Lup b spectrum initially presented in Seifahrt et al. (2007) produces a pseudo-continuum short-wards of 1.24 μm that is in better agreement with the more recent SINFONI epochs and observations produced by NIFS.

star (ΔJ = 0.87, Broeg et al. 2007), the discrepancy between published values and ours is not surprising. The SINFONI photometry makes the J-K color of GQ Lup b (1.0 ± 0.2 mag, assuming the K-band magnitude of GQ Lup bre-evaluated by Neuhäuser et al. 2008) in better agreement with that of other companions of the same luminosity, spectral type, and age range (e.g., Fig. 4 of Gagné et al. 2018a). Furthermore, our value is also consistent with the magnitude correction (0.30–0.66 mag) found by Stolker et al. (2021) to use a single atmospheric model to adjust the J-band scaled to the McElwain et al. (2007) photometry with the rest of the companion spectral energy distribution. We therefore chose to adopt the J-band magnitude inferred from the SINFONI data later on (see Sect. 6.3 for a discussion on possible photometric variations).

The spectra were also corrected for the Barycentric Earth Radial Velocity (BERV), the primary radial velocities, and the companion keplerian motions. The BERV is computed following Piskunov & Valenti (2002) for each individual data cube. The GQ Lup b radial velocity is -0.8 ± 0.4 km s^{-1} (Schwarz et al. 2016). The GSC06214b radial velocity is -3.98 ± 0.88 km s^{-1}, computed from a combination of its orbital velocity (0.61 ± 0.09 km s^{-1}, Pearce et al. 2019) and the radial velocity of the primary star (-4.59 ± 0.88 km s^{-1}, *Gaia* DR2). Radial velocities are given in the heliocentric system.

For the remainder of this analysis, error bars were computed from the dispersion around Pa$_\beta$, on the residual photosphere-subtracted and baseline-corrected (polynomial approximation of residual baselines, see Sect. 5.3) spectra. For velocity conversion (e.g., right panels of Fig. 2), we used the Pa$_\beta$ rest-frame wavelength gathered on NIST (Kramida et al. 2022), λ_0 = 1.2821578 μm (vacuum, Chang & Deming 1996).

4.3. Photospheric contribution

Both GQ Lup b and GSC06214b exhibit a rich spectrum of molecular absorption lines and shallow KI doublets at 1.169/1.177 μm and 1.243/1.253 μm that are characteristic of young M-L transition objects (e.g., Bonnefoy et al. 2014). Molecular absorption lines overlap with the Pa$_\beta$ line, affecting the emission line profiles. The spectra were therefore corrected for the photospheric features using our forward modeling tool `ForMoSA` (Petrus et al. 2020, 2023).

This tool compares pre-computed grids of atmospheric models with observations using the Nested Sampling Bayesian inference algorithm (Skilling 2004). As input, we used the ATMO models (Tremblin et al. 2015, 2016), which explore effective temperature and surface gravity in the expected range of values for the late-M companions. The grids, described in more details in Table C.1 of Petrus et al. (2023), allowed us to explore non-solar C/O and [M/H] values, as well as the adiabatic index γ. `ForMoSA` also allows for fitting of the radial velocity (RV), rotational broadening (vsin(i)), limb-darkening coefficient (ϵ), and interstellar extinction (Av). We did not fit the photospheric contribution on each individual spectrum, but rather on the averaged spectrum at each epoch and we used the RV shift to compensate for residual wavelength shifts from one epoch

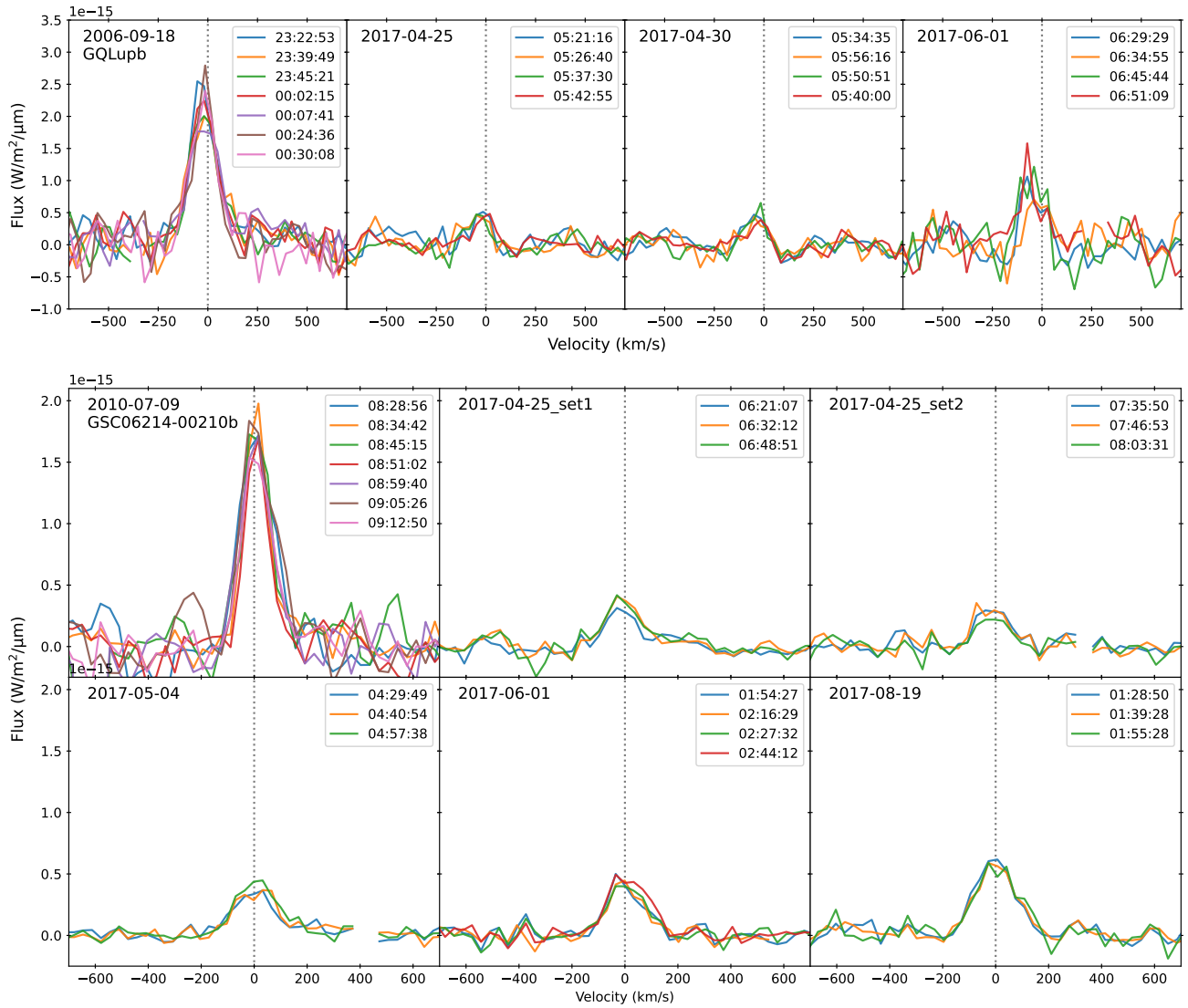


Fig. 3. Pa_β profiles, corrected from the atmospheric contribution and baseline subtracted (see Sects. 5.2 and 5.3). Each spectrum is labeled with the corresponding UT time at the start of the integration. First row: GQ Lup b lines for each epoch. Second and third rows: Same but for GSC06214b, with the addition of the individual OSIRIS lines from Bowler et al. (2011) (2010-07-09 epoch).

to another, which may have arised from imperfect wavelength re-calibrations.

The resulting parameter corner plots are presented in Sect. 5.2. The 1D histograms were used to find the resulting best values for each parameter's bi-modal Gaussian fitting (different σ for the upper and lower halves). The free parameters are the peak location μ_0 and the two sigmas, σ_1 and σ_2. The retained value is μ_0 with the corresponding error bars. The dispersion of values between epochs makes it clear that the Bayesian process on individual epochs provides posterior distributions whose extents are not representative of the true error bars on the values. We therefore estimated the adopted value as the mean of all epochs and the error bars from the dispersion of the ensemble of posteriors of the different epochs. Values at the edge of the grid (upper or lower limits) were ignored when computing the adopted value. The results are presented in Table 2 and discussed in the following section.

5. Results

In this section, we present the resulting spectra and atmospheric parameters, along with their line properties (profiles and variability) and modeling.

5.1. Companion J-band spectra

The mean spectra for each epoch are presented in Fig. 2, along with a zoom on the Pa_β lines. Pa_β lines of individual data cubes are presented in Fig. 3. The spectra all have a relatively similar spectral slope, with a discrepancy for the 2017-06-01 epoch for both objects. We argue that this is due to the lower Strehl ratios for that night, with the AO performance being significantly worse than for other epochs, affecting mostly the blue part of the spectrum, leading to larger flux loss at smaller wavelengths. Overall, our spectral slope is in agreement with the already

Table 2. Atmospheric parameters retrieved with `ForMoSA`.

	Date YYYY-MM-DD	$T_{\rm eff}$ (K)	log(g)	[M/H]	γ	C/O	Radius ($R_{\rm Jup}$)	A_v	RV (km s^{-1})
GQ Lup b	2006-09-18	2587	4.16	[1] >0.59	[1] >1.05	0.57	4.45	2.38	3.03
	2017-04-25	2671	4.16	0.30	[1] >1.05	0.42	4.08	2.13	5.59
	2017-04-30	2655	4.22	0.17	[1] >1.05	0.33	4.07	1.91	13.59
	[2] 2017-06-01	2711	3.92	0.30	[1] >1.05	0.55	[1] >5.00	4.32	13.11
	Adopted	2638^{+33}_{-51}	$4.18^{+0.04}_{-0.02}$	$0.23^{+0.06}_{-0.06}$	>1.05	$0.44^{+0.13}_{-0.11}$	$4.20^{+0.25}_{-0.13}$	$2.14^{+0.24}_{-0.23}$	–
GSC06214b	2017-04-25_set1	2274	4.30	−0.13	1.03	0.50	1.45	0.45	−18.06
	2017-04-25_set2	2230	4.10	−0.33	1.03	[1] <0.30	1.47	[1] <0.00	−8.78
	2017-05-04	2317	4.30	−0.15	1.03	0.42	1.56	1.50	−12.73
	[2] 2017-06-01	2269	4.33	−0.18	1.02	0.39	2.45	[1] >4.99	−19.58
	2017-08-19	2189	4.36	0.00	1.01	0.64	1.58	[1] <0.00	−6.51
	2010-07-09	2232	4.17	−0.21	1.04	0.36	1.37	[1] <0.00	−11.90
	Adopted	2248^{+69}_{-59}	$4.24^{+0.11}_{-0.15}$	$-0.16^{+0.17}_{-0.17}$	$1.03^{+0.01}_{-0.02}$	$0.48^{+0.16}_{-0.12}$	$1.49^{+0.10}_{-0.12}$	$0.97^{+0.53}_{-0.53}$	–

Notes. Adopted values are obtained as described in Sect. 4.3. [1]Unconstrained parameter, fit converged at the edge of the parameter range. [2]Epoch ignored when computing the adopted value.

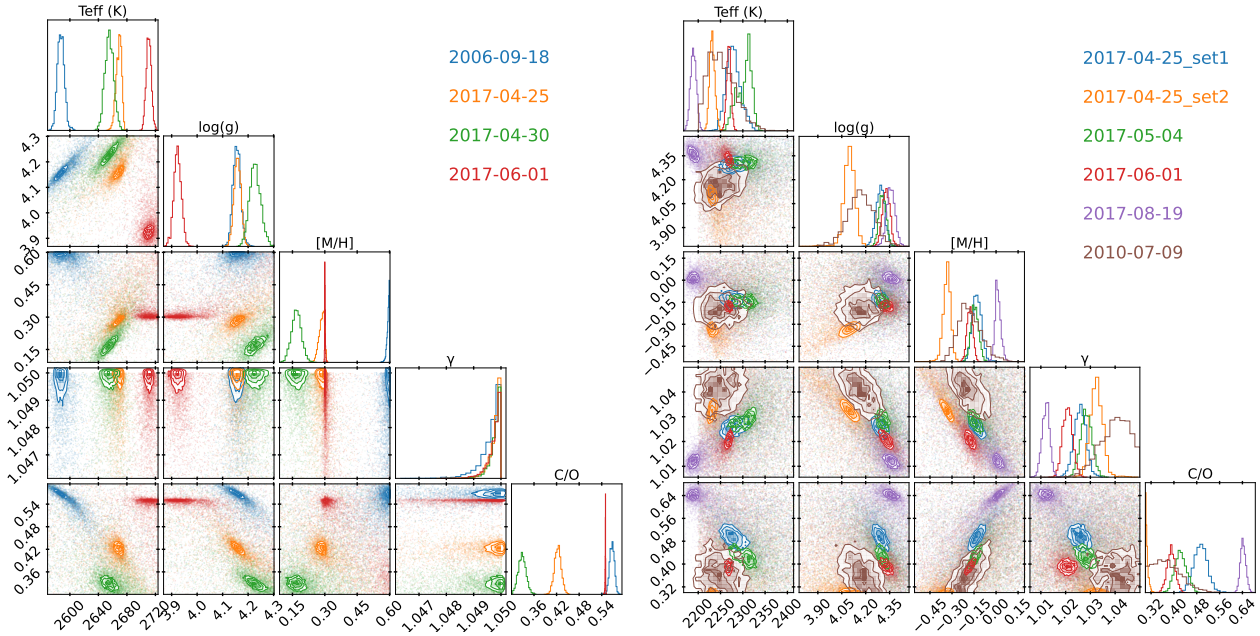


Fig. 4. `ForMoSA` resulting photosphere parameters. Left: GQ Lup b results. Right: GSC06214b results. The Radius, Av, radial velocity (RV), and limb-darkening coefficients are omitted from these plots for the sake of clarity.

published spectra (Lavigne et al. 2009; Bowler et al. 2011), but the GQ Lup b spectra differ from the Seifahrt et al. (2007), which has already been pointed out by Lavigne et al. (2009). This may be explained by residual primary flux in their spectrum, which is in line with the wider Pa_β line profile (see Fig. 2, top-right panel). We observed spectroscopic features typical of late-M/early-L dwarfs for both objects at all epochs: the two KI doublets (1.17 and 1.25 µm), the FeH absorption band (1.17–1.22 µm), and the numerous H_2O absorption lines (1.13–1.16 µm and >1.32 µm, see Fig. 2). The spectra are also composed of numerous less prominent molecular features all over the band, which are best described by photosphere models (see Sect. 5.2).

5.2. Atmospheric and physical parameters

Here, we present the results from atmospheric modeling of the J-Band spectra with `ForMoSA` (Sect. 4.3). The best fits for both sources can be found in Table 2. A comparison of the various atmospheric parameters can be found in Fig. 4, as corner plots. A visual comparison of data and fitted spectra can be found in Fig. 5. Some parameters have converged at the edge of the parameter range, such as the adiabatic index γ, either consistently or occasionally. The spectral slopes of both companions on June 1, 2017 are discrepant with regard to the other epochs and the retrieved atmospheric parameters (at the very least $T_{\rm eff}$ and Av) are likely to be non-representative.

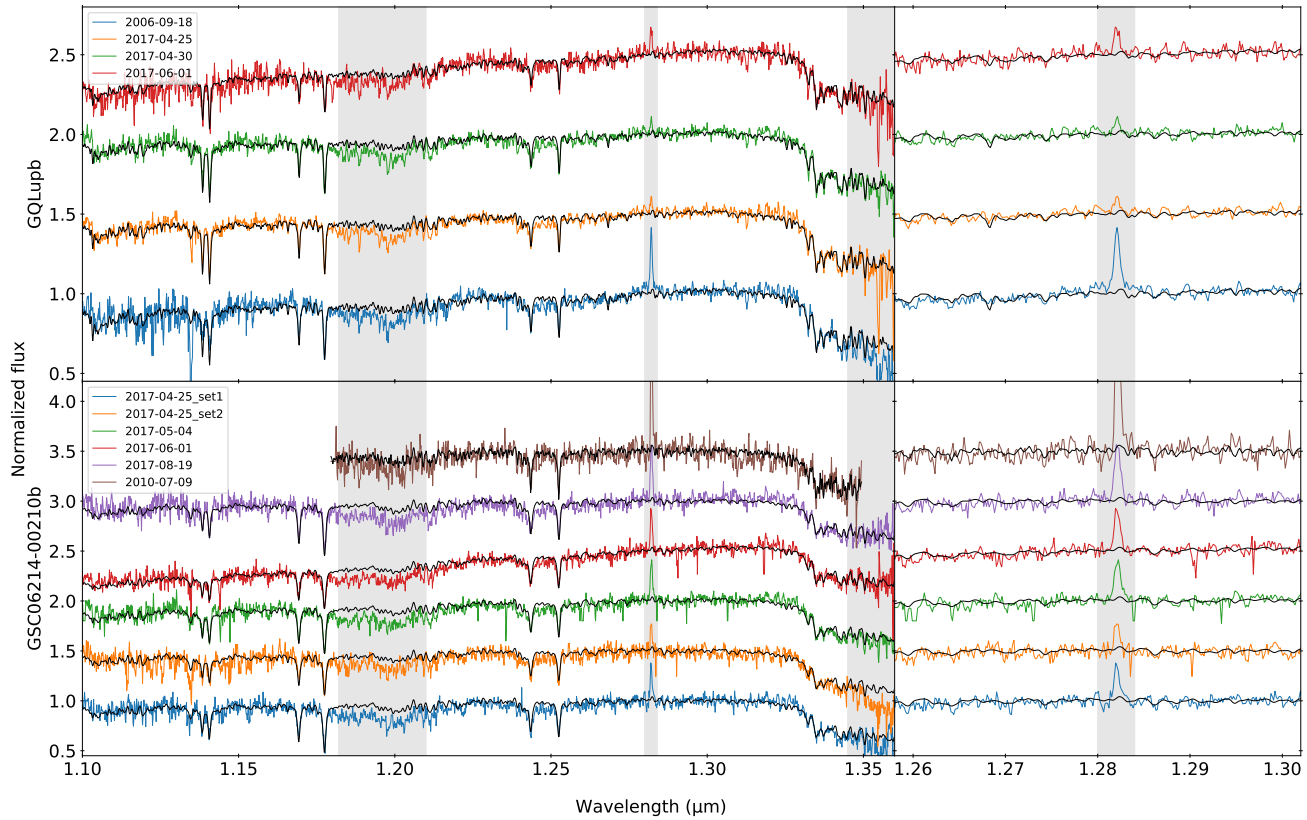


Fig. 5. Visual comparison of the photosphere fitting with `ForMoSA`, for each epoch of both objects, with a zoom on Pa_β in the right column. Grayed-out wavelength ranges were excluded from fitting as the model either did not include corresponding species (FeH absorption band, Pa_β) or the data were too noisy (>1.34 μm).

5.2.1. Inferred values and correlations

Correlations have been observed between $T_{\rm eff}$ and $\log g$. The behavior is similar to that observed on the spectral analysis of the young late-M companion HIP 78530B with `ForMoSA` in Petrus et al. (2020) (although these authors used BT-SETTL atmospheric models). The correlation might be caused by the increase in strength of the K I and FeH absorptions with both decreasing $T_{\rm eff}$ and increasing surface gravities at the M-L transition (Rice et al. 2010; Bonnefoy et al. 2014).

On the other hand, the $\log g$ and C/O are anti-correlated. This is due to the sensitivity to these two parameters of the numerous FeH and H_2O absorptions at J-band. Finally, both sources show either no correlations between [M/H] and C/O, or a positive one. We do not notice strong degeneracies between γ and the others parameters, which suggests that the limited exploration of that parameter does not bias the estimate of the other parameters.

For GQ Lup b, atmospheric parameters are consistent for all epochs: $\log g \sim 4.2$, $T_{\rm eff} = 2638^{+33}_{-51}$ K (we caution that error bars do not include systematics of the model) and $\gamma > 1.05$. The $\log g$ and $T_{\rm eff}$ are both well consistent with the values found in Stolker et al. (2021) adjusting the VLT/MUSE optical spectrum of the companion with BT-SETTL models. We however find with `ForMoSA` a higher radius than the estimates of Stolker et al. (2021) (found by adjusting a synthetic spectra on the companion's spectro-photometry). This might be due to the increased J-band apparent flux that we measure in Sect. 4.2. Part of the difference could also be caused by the use of different atmospheric models (see more below).

For GSC06214b, we find $\log g \sim 4.24$, $T_{\rm eff} = 2248^{+69}_{-59}$ K and $\gamma = 1.03^{+0.01}_{-0.02}$. Lachapelle et al. (2015) found $T_{\rm eff} = 2300 \pm 200$ K and $\log g = 3.0$–4.0 using different models (BT-SETTL and DRIFT-PHOENIX, Allard et al. 2011; Helling et al. 2008; Witte et al. 2009, 2011) and spectra, but which remain broadly consistent with our values.

We present the first estimates of C/O and [M/H] for both companions. Both objects have C/O values that are compatible with solar value ($C/O_\odot = 0.55$) within 1σ. However, they exhibit different kinds of behavior in terms of metallicity: GSC06214b has a solar metallicity (within 1σ), while that of GQ Lup b appears slightly super-solar (>3σ). We interpret these abundances in Sect. 6.1.

The extinction of GQ Lup b is consistent with the value found by (Av ∼ 2.3 mag, Stolker et al. 2021). It is above the values reported on GQ Lup A and C (Av ∼ 1.0 mag, McElwain et al. 2007; Alcalá et al. 2020). The extinction of GSC06214b is within the range of values measured on the primary star (Av = 0.7 ± 0.5 mag, Barenfeld et al. 2016; Anders et al. 2022).

5.2.2. Use of evolutionary tracks

Using our estimated $T_{\rm eff}$ from `ForMoSA`, recent "hot-start" evolution models (Phillips et al. 2020) predict a mass of

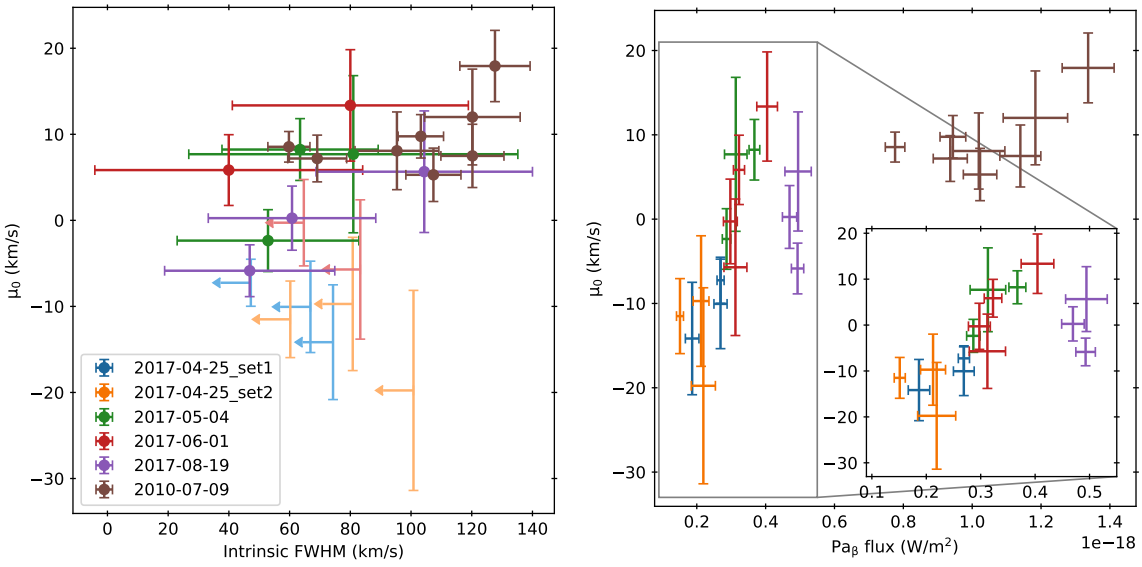


Fig. 6. Gaussian-fitting resulting parameters for the Pa_β line of GSC06214b. Left: correlations between intrinsic FWHM and the line peak location μ_0, arrows represent an upper limit on the intrinsic FWHM. Right: correlations between the Pa_β line flux and the line peak location μ_0. The intrinsic FWHM is computed as the square root of the quadratic difference between the measured line FWHM and the LSF FWHM. The μ_0 parameter is relative to the line expected wavelength in vacuum (1.2821578 μm).

15.5 ± 0.5 $M_{\rm Jup}$ at the age of the system (Sect. 2.2) for GSC06214b, which is consistent with previous estimates based on the bollometric luminosity. Our estimated surface gravity is also broadly consistent with expectations at the age of UCL ($\log g$ = 4.07 ± 0.01) and Upper Scorpius ($\log g$ = 4.04 ± 0.02) and does not allow for discrimination between the two possible system memberships. Predicted radii range from 1.8 to 2.0 $R_{\rm Jup}$, e.g. ∼20% larger than the value found with atmospheric models alone. The mismatch amplitude is consistent with the predictions of the same atmospheric models for VHS1256b, a cooler ($T_{\rm eff}$ ∼ 1400 K) companion of the same mass range as GSC06214b and might point to a systematic overestimation of the absolute near-infrared fluxes by the ATMO models across a broad $T_{\rm eff}$ range (Petrus et al. 2023). This is not, however, an issue with respect to removing the photospheric contribution, since the radii are only used to scale the synthetic spectrum to the companion's continuum emission level.

The use of GQ Lup b's $T_{\rm eff}$ from `ForMoSA` as input for the ATMO evolutionary tracks predict a mass of 22^{+2}_{-3} $M_{\rm Jup}$, a radius in the range of 2.65 –= 3.3 $R_{\rm Jup}$ and with $\log g$ ∼ 3.8–3.9 dex at the system age (Sect. 2.1). Both the predicted radius and $\log g$ are inconsistent with those inferred from `ForMoSA` and the deviation is at odds with that observed for GSC06214b. The use of the older AMES-DUSTY tracks (Chabrier et al. 2000) do not change the conclusions. This could arise from uncertainties in the evolutionary tracks not capturing the physics of the interior of this more massive companion (e.g., deuterium burning). However, the radius is degenerate with the extinction in our fit and higher extinction than estimated would naturally lead to a better agreement between `ForMoSA` and evolutionary model predictions. Stolker et al. (2021) found radii of 3.55–4.13 $R_{\rm Jup}$ and a higher extinction (2.3–2.7 mag), which remain slightly inconsistent with the Phillips et al. (2020) evolutionary models. The large radii and inconsistent $\log g$ derived from atmospheric models could also be produced because of additional flux contribution such as veiling increasing the flux and requiring a larger dilution factor (Sect. 6.3). A similar mismatch has also been observed on other companions of the same $T_{\rm eff}$ range in Upper Scorpius (Petrus et al. 2020) and an unresolved binarity has been proposed as an explanation. If GQ Lup b were to be an equal-luminosity equal-$T_{\rm eff}$ binary, the apparent J-band flux would be deviant, namely, overestimated by a factor two with respect to a single object. In such a case, the corresponding radius of individual components found with `ForMoSA` ($3^{+0.2}_{-0.1}$ $R_{\rm Jup}$) would match the evolutionary model predictions for the fitted $T_{\rm eff}$ well.

5.3. Analysis of Pa_β time series

Pa_β emission line profiles for individual data cubes are presented in Fig. 3. We performed a Gaussian fitting of the lines to infer their width, position, and flux (see Table A.2).

We find the Pa_β line profiles to be partly resolved in the 2006 epoch of GQ Lup b (1–1.5 times the LSF width, 1–3 σ) and mostly unresolved in the 2017 epochs of GSC06214b (1–1.2 times the LSF width, 1–2 σ). However, we do find the line to be partly resolved in the 2010-07-09 epoch (OSIRIS) (1.2–1.9 the LSF width, 4–8 σ). We refer to Table A.2 for details. We also find the peak of the Pa_β emission lines in GQ Lup b to be slightly blue-shifted. For GSC06214b, they are mostly centered at zero velocity and show no significant asymmetries (with respect to the line center), except for the 2017-06-01 epoch of GSC06214b, for which the line has a wider red-wing in comparison to the blue wing. This is reminiscent of emission lines formed in magnetospheric accretion columns in T Tauri stars, which show prominent blue-red asymmetry (Edwards et al. 1994). Shock-induced accretion lines also produce lines with a red-shifted peak, hence a wider red wing. These will be explored in more detail in Sect. 6.2.

We studied the variability for both the line profiles and fluxes. We note that studying integrated fluxes is equivalent to studying EWs, as they were all computed on a similar continuum baseline. Integrated fluxes were computed by Gaussian fitting of the line profiles after local baseline correction (polynomial, n = 2), for which the main results are reported in Table A.2 and shown in Fig. 6.

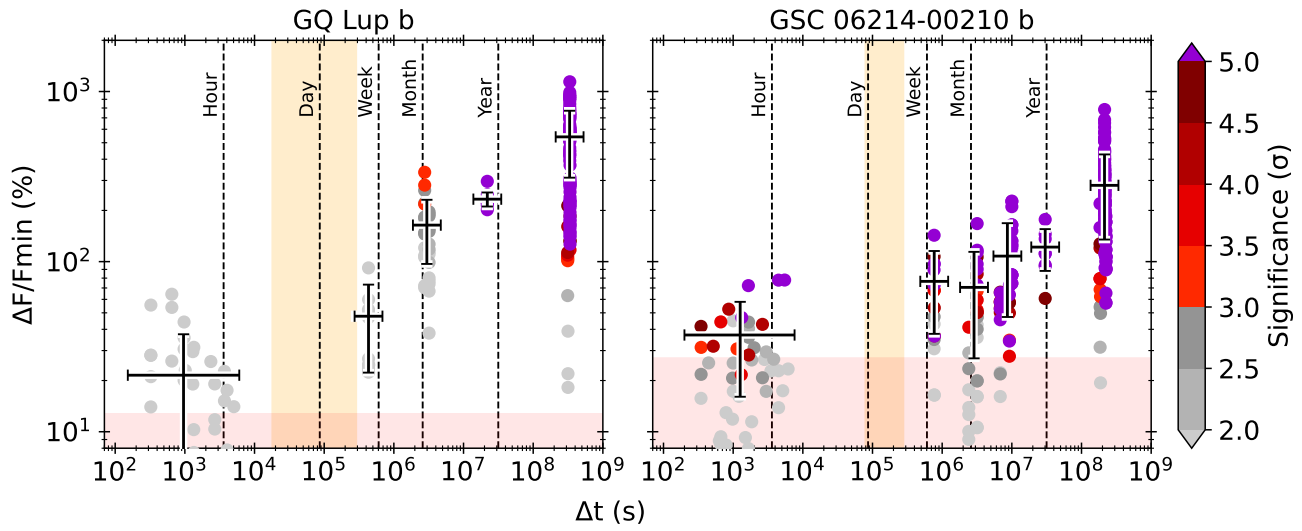


Fig. 7. Pa_β flux variability for both sources, as a function of the timescale, with respect to the lowest-flux point of the pair. For GQ Lup b, are included data points from this study as well as the spectrum from Lavigne et al. (2009). For GSC06214b, are included data points from this study as well as those from the individual Bowler data cubes (Bowler et al. 2011) and the mean spectrum from Lachapelle et al. (2015). The color of the points represents the significance of the measurement, i.e., the σ-distance between the two lines used to compute this value. The horizontal and vertical bars correspond respectively to the bin size, and the spread (weighted by significance) within that bin. The red-shaded regions mark the average observed continuum variability among the SINFONI sequences (see Table 1). The orange shaded regions represent the expected rotational period of the objects (see Sect. 2).

As illustrated in Fig. 6, we find, for GSC06214b, possible correlations between the line intrinsic width and its peak velocity ($FWHM_{in}$–μ_0, left panel) and between the line flux and its peak velocity ($F(Pa_\beta)$–μ_0, right panel). We computed Pearson's correlations coefficients and p-values using an MCMC approach almost equal to the `pymccorrelation` tool (Curran 2015; Privon et al. 2020), with the added constraint that the intrinsic FWHM distributions cannot be negative. For the first correlation, ignoring upper limits we find $r = 0.39^{+0.19}_{-0.22}$ and $\log p = -0.88^{+0.59}_{-0.87}$. We note that while they were excluded, upper limits still appear in the correct region for the trend. For the second correlation (excluding the 2010-07-09 epoch), we find $r = 0.52^{+0.10}_{-0.12}$ and $\log p = -1.43^{+0.52}_{-0.61}$. The $FWHM_{in}$–μ_0 correlation, if true, could be the sign of either (i) red-shifted absorption within the line (as absorption increases, the line centroid will be moved to the blue) or (ii) increasing red-wing contribution as the line flux increases. The $F(Pa_\beta)$–μ_0 correlation, if true could be explained in the same way as the second explanation for the peak-velocity-and-FWHM correlation. The possible implications are discussed in Sect. 6.2.

From Fig. 3, we see unambiguous EW variability from an epoch to another for both sources. There is no clear sign of line profile variability within the SINFONI sequences – with the exception of a possible red-wing variability on the GSC06214b 2017-06-01 epoch. However, we do see line flux variability within multiple sequences of GSC06214b, in particular the 2010-07-09 one.

Figure 7 shows the relative Pa_β flux variation, computed as (Fmax-Fmin)/Fmin for each individual pair of lines, as a function of their time difference. The marker's color reports the significance of the measurement, namely, the σ-distance between the two lines used to compute this value. While a small and noisy denominator may artificially increase the relative variation, the measurement will appear gray as the two values would not be statistically far apart. In other words, gray measurements are compatible with no relative flux variation (given our uncertainties), while colored points highlight an actual variation (given the σ level). GQ Lup b shows overall close to no flux variability (3σ confidence level, <50%) on timescales of an hour or more. However, we do see significant variability (>100%) on timescales of about a month and longer. We note that the ~year timescale corresponds to the variation between the 2006-09-18 and the Lavigne et al. (2009) (2007-05-30) epochs. GSC06214b, on the other hand, shows definitive flux variability around the 30-min and ~hour timescales (>5σ significance). We also do see clear (>5σ) line variability on timescales of weeks, months, and years. The line flux variability at the ~hour timescale appears within multiple datasets: the OSIRIS epoch (2010-07-09), the 2017-05-04 epoch and between the two sets of the 2017-04-25 epochs. In both objects, the amplitude of variability stays below 50–60% for timescales that are shorter than their estimated rotation periods, while stronger variability amplitude (up to a factor 10) is observed on longer timescales. We discuss these findings in the more general context of variable young stars in Sect. 6.2.

5.4. Comparison to protoplanet accretion models

Pa_β emission in the spectra of low-mass free-floating brown dwarfs of the same mass, age, and spectral-type range as the two companions studied here have been investigated by Natta et al. (2004) and Manara et al. (2013). The Pa_β line intensity is shown to be strongly correlated with the accretion luminosity, while the chromospheric activity does not contribute significantly to the line intensity for accretion rates above 10^{-11} – 10^{-12} $M_\odot\,yr^{-1}$ at ages 3–10 Myr. Furthermore, none of the non-accreting sources display Pa_β emission lines. We therefore assume that most, if not all, of the Pa_β emission is produced by accretion. In this section, we explore two accretion models in the planetary mass regime predicting Pa_β line flux and profiles, and compare their predictions to our time-series observations, in order to infer the corresponding physical parameters.

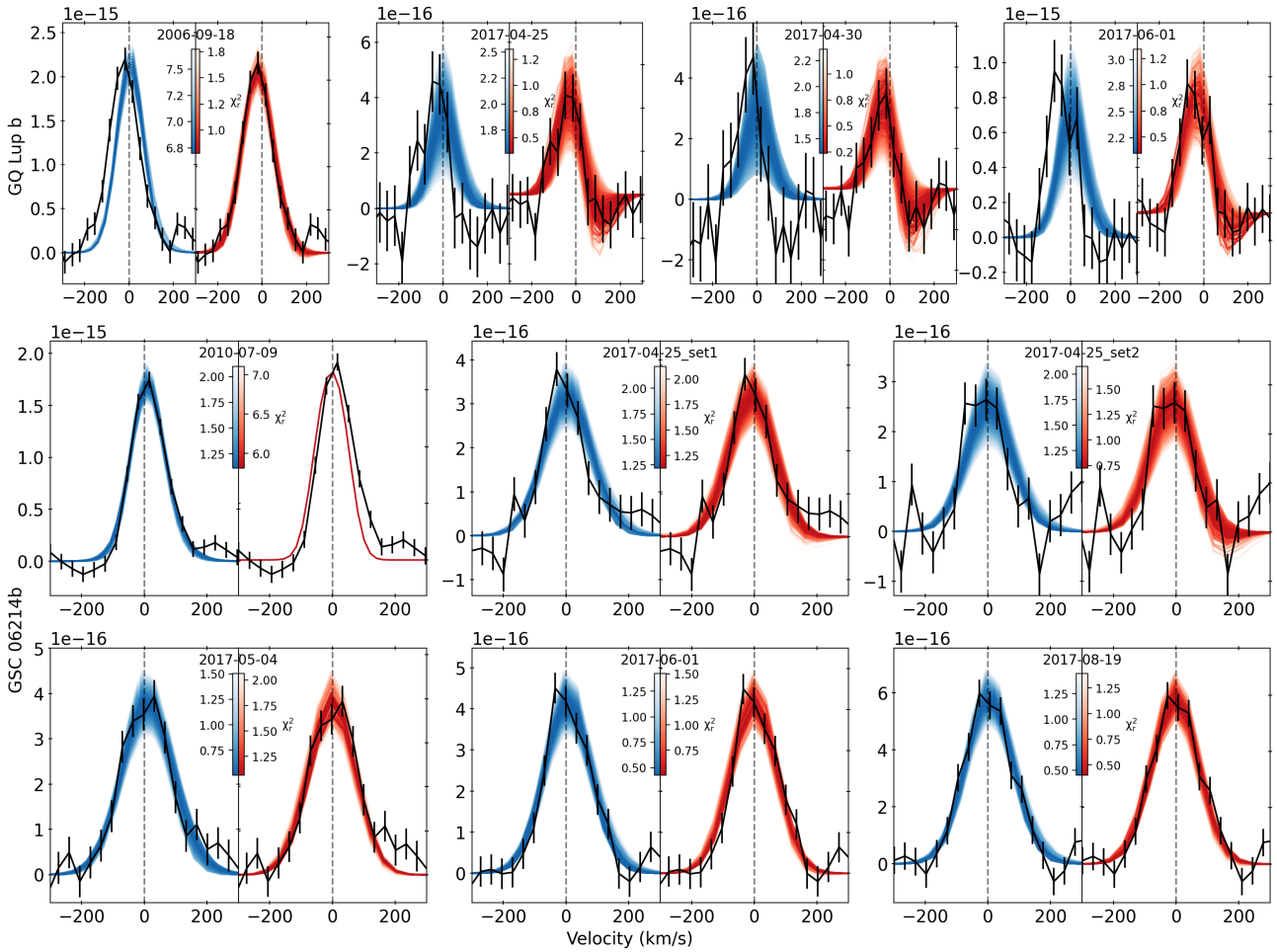


Fig. 8. Comparison of the best-fit models for both GQ Lup b (first row) and GSC06214b (2nd and 3rd rows). Colorbars represent the reduced χ^2 (χ^2_r) of the Shock (blue) and MagAcc (red) models. For each epoch, all best models (within the χ^2_r range given in the colorbar) are over-plotted with a color scaling with the reduced χ^2 color. The fitting limits and number of parameters of each model yield a number of degrees of freedom equal to 14 for the Shock model and 9 for the MagAcc model.

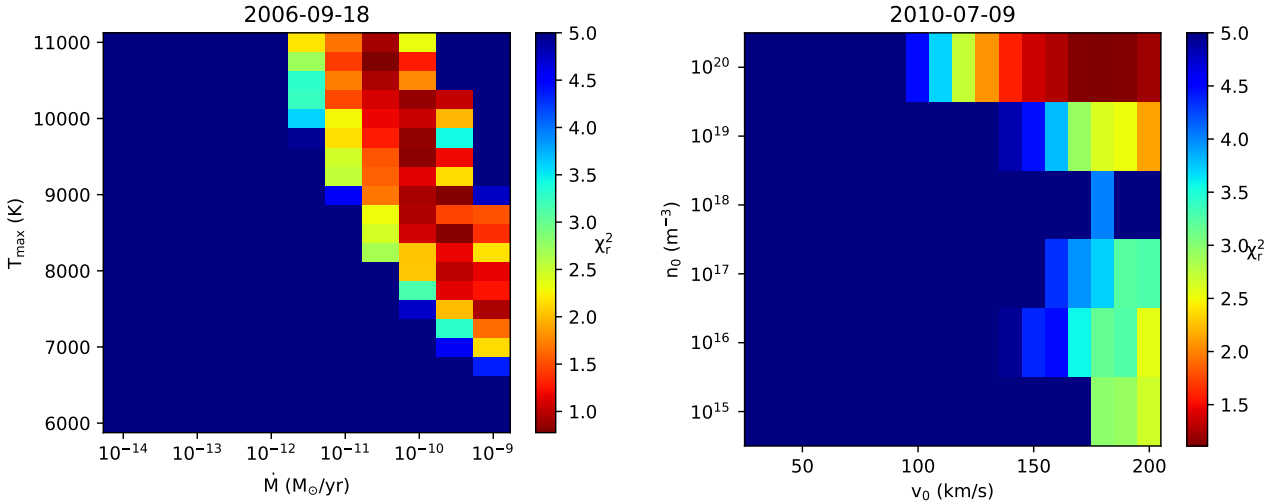


Fig. 9. χ^2_r maps illustrating the accretion models degeneracies when fitting the Pa_β lines. Left panel: T_{max} vs $\dot{M}$ degeneracy for the MagAcc model (GQ Lup b, epoch: 2006-09-18). Right panel: n_0 vs v_0 degeneracy for the Shock model (GSC06214b, epoch: 2010-07-09 – OSIRIS).

5.4.1. Description of accretion models

Thanathibodee et al. (2019) proposed a version of the magnetospheric accretion models developed for Classical T Tauri Stars (CTTS, see the review of Hartmann et al. 2016, and ref. therein) extended to the planetary mass range. It assumes that the central object's dipolar magnetic field is intense enough at young ages to truncate the inner CPD, lift material from the CPD, and channel it towards the central object. Material then falls down to the planetary surface at free fall velocity along accretion funnels. In these funnels, the material is heated to temperatures high enough ($\sim 10^4$ K) to trigger atomic Hydrogen line emission (H_α, Pa_β, Br_γ, ...). The free-falling material then creates a shock at the base of the funnel flows when it hits the planetary surface, which triggers hot continuum emission that can be absorbed by the infalling gas, leading to red-shifted absorption features within the emission line profiles. Red-shifted absorption also occurs when the accretion flow absorbs the photosphere emission itself. Blue-shifted absorption may also be present due to jets or outflows, but these are not accounted for by these models. The magnetospheric accretion model from Thanathibodee et al. (2019) is described by: the accretion column launching radius $R_{\rm in}$, its width, its maximum temperature $T_{\rm max}$, the accretion rate $\dot{M}$, the inclination, the planet mass M, the planet radius $R_{\rm p}$, and the planet effective temperature $T_{\rm eff}$. The model is axis-symmetric and assumes that the large scale dipolar magnetic field is aligned with the central object rotation axis. The model neglects line emission contribution from the shock at the base of the accretion funnels. This model will be referred to as the MagAcc model hereafter.

Conversely, Aoyama et al. (2018) proposed that accretion lines, rather than being triggered within accretion funnels, would be triggered within an accretion shock either at the planet or the CPD surface. In such a scenario, material flows from the circumstellar disk down to the planetary or CPD surface. This may happen for planet embedded within the circumstellar disk of their host star, through polar-inflow (Marleau et al. 2022) or, as was proposed for GQ Lup b, if material from the circumstellar disk channels up to the planet immediate environment (Stolker et al. 2021). Alternatively, this model could also describe line emission formed in the shock at the base of magnetospheric accretion columns. This model considers two parameters: the infall velocity v_0 and the pre-shock density n_0. We add an additional flux scaling parameter, $S_{\rm eff}$, the effective shock surface (i.e., $4\pi R_{\rm p}^2 f_{\rm fill}$ if it takes place at the planetary surface). We provide more details in the next section. We note that this model is referred to as the Shock model, hereafter.

5.4.2. Model fitting

We used both aforementioned models (MagAcc and Shock, Thanathibodee et al. 2019; Aoyama et al. 2018) to try to retrieve the physical parameters of the accretion mechanisms by fitting the Pa_β line of both GQ Lup b and GSC06214b.

Both models were scaled to the distance of the objects (Sect. 2). For the MagAcc model, this was performed by applying a factor $(R_{\rm p}/{\rm D})^2$, with D the distance and $R_{\rm p}$ the planet radius. For the Shock model, we applied a factor $S_{\rm eff}/(4\pi {\rm D}^2)$. The fits were performed on photosphere-subtracted and baseline-corrected Pa_β emission line profiles, with continuum-subtracted models. This allows accretion models fitting not to be biased by continuum discrepancies, and allows us to focus solely on the line profile. The models are then convolved to the instruments resolution (R = 2360 and R = 1800 for GQ Lup b and GSC06214b SINFONI data respectively, R = 3800 for OSIRIS).

The fits were performed on the mean emission line of each epoch, computing the χ^2_r on the whole grid of models. Fiducial results are presented in Fig. 8. The GQ Lup b lines are only reproduced by the MagAcc models: this is because the Shock models cannot reproduce a blue shifted emission line peak, as is clearly apparent from the first row of Fig. 8. Note that the red-shifted absorption in the 2017 epochs of GQ Lup b and fitted by the models is mostly likely caused by noise in the data. However, GSC06214b lines are well reproduced by both models. Maps of the best χ^2_r are shown in Fig. 9. We only represent the $T_{\rm eff}$–$\dot{M}$ axis in the figure for the MagAcc model, because others parameters are mostly unconstrained.

In the case of the MagAcc scenario, there is a clear degeneracy between the accretion column temperature and the accretion rate. This behavior was already seen in the context of magnetospheric accretion on T Tauri stars (Muzerolle et al. 2001) and the degeneracy could be lifted with very high resolution observations and/or fitting multiple accretion lines simultaneously. This shows that in the magnetospheric accretion framework, we cannot derive an accurate measurement of the accretion rate, but only a lower limit. For GQ Lup b, this leads to $\dot{M} \gtrsim 10^{-11}\ M_\odot\,{\rm yr}^{-1}$ for the (bright) 2006-09-18 epoch and $\dot{M} \gtrsim 10^{-11.5} M_\odot\,{\rm yr}^{-1}$ for the other epochs. For GSC06214b, this leads to a lower limit of $\dot{M} \gtrsim 10^{-12} M_\odot\,{\rm yr}^{-1}$ for all epochs. Zhou et al. (2014) derived values of $10^{-10.8}\ M_\odot\,{\rm yr}^{-1}$ and $10^{-9.3}\ M_\odot\,{\rm yr}^{-1}$ from fitting the UV-optical excess emission for GSC06214b and GQ Lup b, respectively, which are consistent with our lower limits.

GSC06214b lines are also well reproduced with the Shock model. In this scenario, fits are mostly degenerated over the parameter space, except for the 2010-07-09 (OSIRIS) epoch, for which high velocity models are strongly favored, as shown in Fig. 9. The high shock velocity models correspond to infall velocities $v_{\rm ff} > 150$ km s^{-1}, which imply a shock location at $R < 2.4\ R_{\rm Jup}$, consistent with the estimated radius of the object (Sect. 5.2). These solutions would indicate that the shock is located at the planetary surface. However, lower infall velocities in the range of 30–170 km s^{-1} cannot be fully excluded. They are consistent with a shock located anywhere within 60 $R_{\rm Jup}$, so either at the protoplanet surface or on the CPD at larger scales. In the 2010-07-09 (OSIRIS) epoch, our best-fit values of $S_{\rm eff}$, v_0, and n_0 ($1.5 \times 10^{-2}\ S_{\rm jup}$, 180 km s^{-1} and 10^{20} m^{-3}) yield a mass accretion rate of $\dot{M} \sim 10^{-9}\ M_\odot\,{\rm yr}^{-1}$. Assuming a shock at the planetary surface, the accretion rate can be given as $\dot{M} = S\mu n_0 v_0$, with μ the mean molecular weight (3.84×10^{-27} kg as per Aoyama et al. 2018). Inverting the equation, we find the shock surface given as a fraction of the planetary surface (with an estimated radius of 1.8–2.0 $R_{\rm Jup}$), this corresponds to a filling factor of 0.38–0.47%. This is of the same order (0.3%) as reported for the older analogue companion Delorme 1 (AB)b and using similar models on Balmer lines (Ringqvist et al. 2023).

6. Discussion

In this section, we first interpret the derived atmospheric abundances of both objects. We then discuss the implications brought by our results for the origin of the H I line emission in planetary-mass objects and the possible impact of variable veiling. Finally, we extrapolate how emission line variability, as seen here, could impact protoplanet detection surveys.

6.1. Atmospheric abundances as formation tracers

The star forming regions Sco-Cen and Lupus I are expected to have nearly solar metallicity (e.g., Bubar et al. 2011; Biazzo et al. 2017; Murphy et al. 2021, and ref. therein) and it has been shown that nearby solar-type stars with [M/H] = 0 have C/O distributed around the solar value (Suárez-Andrés et al. 2018; Tautvaišienė et al. 2022). We note, however, that there is a spectroscopic determination of [M/H] = −0.06 ± 0.01 and −0.35 ± 0.01 dex for GSC06214A and GQ Lup A, respectively (Swastik et al. 2021). The value found for GQ Lup A is at odd with expectations and implies that GQ Lup b is significantly enriched in metals (Δ[M/H] = $0.61^{+0.05}_{-0.10}$) with respect to its host star, while GSC06214b metallicity remains compatible within 1σ with that of GSC06214A. Swastik et al. (2021) accounted for veiling affecting the depth of stellar absorption lines of GQ Lup A in their inversion of the high-resolution optical spectra of the source. They chose, in particular, the less-contaminated and emission-free region of 5900–5965 Å for the analysis. However, the H_α line of GQ Lup A appears as the most intense of their sample and remaining effects of veiling at considered wavelengths might lead to an underestimation of the [M/H] value for that particular star.

The metallicity of GSC06214b and GQ Lup b are both compatible with the envelope of values predicted for planet population synthesis models based on the core-accretion framework assuming a pristine solar-composition (see Fig. 9 of Petrus et al. 2021). Disk-instability models predict a wide range of metallicity values, including solar (Boley et al. 2011). If the companions formed inside the circumstellar disks surrounding their host stars, the nearly-solar C/O implies they should have accreted a substantial fraction of solids. In summary, the derived abundances based on our J-band data do not permit us to firmly conclude on the formation scenario of either objects, but an in-situ formation via turbulent fragmentation remains plausible (i.e., fragmentation of the solar nebula into the primary and its companion, Padoan & Nordlund 1999, 2004).

6.2. Constraints on accretion processes in planetary mass objects

We show in Sect. 5.4.2 that the GQ Lup b lines are only reproduced by the MagAcc model, while the GSC06214b lines are well reproduced by both MagAcc and Shock models.

6.2.1. MagAcc and Shock models' relative contributions

Although we studied the MagAcc and the Shock scenarios independently, they are not mutually exclusive. The magnetospheric accretion scenario also involves a shock at the base of the accretion columns on the planetary surface, while the Shock model makes no assumptions as to where the accretion shock takes place. Therefore, the Shock model could very well explain the line emission at the base of a magnetospherically induced funnel.

The relative contributions of the accretion funnels and the accretion shock to the Pa_β emission line may vary over time. The MagAcc induced lines are usually asymmetric with a larger blue wing, whereas Shock-induced lines tend to be more symmetric with a slightly stronger red wing. A time modulation of the MagAcc-Shock contributions could then be the key to explaining the correlations observed between the line centroid, as well as its width and flux (Fig. 6).

Figure 2 of Aoyama et al. (2021) shows the relative contributions of the funnel flows and the planetary shock H_α emission, assuming a filling factor of 1–10% and planet mass of 6 $M_{\rm Jup}$ (corresponding to PDS 70 b) depending on the accretion rate. Our higher mass range and different line may quantitatively change the accretion rate threshold at which both emissions become comparable, but this will hardly change the qualitative picture. For the mass accretion rate of GSC06214b ($10^{-10.8}$ $M_\odot\,{\rm yr}^{-1}$, Zhou et al. 2014), both MagAcc and Shock contributions are about the same order of magnitude. For the mass accretion rate of GQ Lup b ($10^{-9.3}$ $M_\odot\,{\rm yr}^{-1}$, Zhou et al. 2014), the contribution from the accretion funnels largely dominates, which could explain why it is only the MagAcc model that is able to reproduce the blue-shifted lines of GQ Lup b.

6.2.2. Others explanations for line variability

While we focused the MagAcc and Shock scenarios, other physical mechanisms have been proposed to modulate the accretion lines properties. Marleau et al. (2022) studied the effects of gas and dust extinction on the H_α line intensity profile. According to their Fig. 5, for the gas extinction to alter significantly the H_α flux ($A_R > 1$) for an object of ∼15 $M_{\rm Jup}$, the accretion rate must be at least 10^{-5} $M_{\rm Jup}$ /yr, which is far above the accretion rates of GQ Lup b or GSC06214b. Figures 6, 7, and 8 in Marleau et al. (2022) show intrinsic H_α line profiles for the same Shock model, as in this work, both with and without gas extinction, for various accretion flow geometries, planet masses, and accretion rates. Some of these H_α lines show significant asymmetries (in their intrinsic profile), including an absorption of the red-wing of the line. If the behavior in the Pa_β line is similar, the correlations observed in Fig. 6 could be explained by such gas self-absorption effects. As for dust extinction, they find that it should be negligible for masses above a few $M_{\rm Jup}$.

Szulágyi & Ercolano (2020) performed 3D simulations of an accreting protoplanet embedded in a circumstellar disk and studied the lines variation due to the variable shock-front (as the planet orbits around the star) and density variations in the protoplanet vicinity. They find the Pa_β line amplitude variability to be about ∼8–41% (depending on the modeling hypothesis) for a 10 $M_{\rm Jup}$ planet, on Keplerian timescales. The different environments of GSC06214b and GQ Lup b (non-embedded) make this scenario implausible for these two objects and the proposed timescales do not match our observations.

6.2.3. Line variability on similar objects

Variability of PMCs has already been seen on various timescales. In the Pa_β study of DH Tau b by Wolff et al. (2017), the authors reported four epochs separated by a number of days and weeks. According to their Table 1, they find the Pa_β line to disappear within ∼5 weeks (3.8σ) and a tentative variability within a week (80 ± 50%, 1.7σ). Eriksson et al. (2020) conducted a multi-epoch H_α study of Delorme 1 (AB)b. Applying the same methods as in Fig. 7 to their Table B.1 data, we find H_α EW variability spanning ∼30 ± 20% along the ∼2 h sequence, with no difference between the <1 h and >1 h timescales. In comparison, we find the variability amplitude to be ∼7 ± 7% and ∼20 ± 17% for GQ Lup b and GSC06214b, respectively, for timescales of <2 h (noting that error bars represent the spread of the variability, and not an uncertainty), compatible with Delorme 1 (AB)b.

6.2.4. Similarities with CTTS

Both GQ Lup b and GSC06214b show maximum variability for timescales above their estimated rotation periods (see Fig. 7).

This behavior is also seen in CTTS (Costigan et al. 2014; Zsidi et al. 2022). The Pa_β line profiles of both companions also show strong similarities with the centrally peaked line profiles observed in solar mass accreting young stars (CTTS, see Folha & Emerson 2001). The line profile of GSC06214b on May 04, 2017 and August 19, 2017 matches that of DG Tau surprisingly well, which was observed at October 10, 1994 and December 15, 1995 by Folha & Emerson (2001). The blue-shifted Pa_β line of GQ Lup b is also well reproduced by their observations of DD Tau. Both objects are sub-solar-mass CTTS. Magnetospheric accretion models have been very successful at reproducing these line profiles (Muzerolle et al. 2001). These similarities suggest that the mechanisms proposed for the formation of the H I emission lines in CTTS (i.e., magnetospheric accretion) are at play down to the planetary mass regime. The estimates of mass accretion rates for GSC06214b and GQ Lup b are also in line with the global decrease of mass accretion rates with object mass, which extends down to isolated ∼15 $M_{\rm Jup}$ objects (e.g., Muzerolle et al. 2005; Joergens et al. 2013).

Ringqvist et al. (2023) reported recent high-resolution UV spectra (2 epochs taken within 1h) of the 13 ± 5 $M_{\rm Jup}$ companion Delorme 1 (AB)b where they find line blue-shifted profiles indicative of magnetospheric accretion. While the profiles of these lines cannot be directly compared to those of Pa_β, this further suggests this mechanism could be universal for young 10–30 $M_{\rm Jup}$ companions with ages from 3 to 40 Myr. Both Delorme 1 (AB)b and GSC06214b have estimated filling factors of the accretion shock of the order ∼1%. These values are consistent with those found in CTTS (e.g., Alencar & Batalha 2002; Batalha et al. 2002; Pittman et al. 2022), although the methodologies used to derive these factors on stars can be different.

Magnetospheric accretion holds only if the objects interior can generate powerful magnetic fields. Following Eq. (1) from Hartmann et al. (2016) with the values found from evolutionary tracks (Sect. 5.2, GQ Lup b: M = 22 $M_{\rm Jup}$, R = 3 $R_{\rm Jup}$, $\dot{M} = 10^{-9.3}$ $M_\odot\,{\rm yr}^{-1}$; GSC06214b: M = 15 $M_{\rm Jup}$, R = 2 $R_{\rm Jup}$, $\dot{M} = 10^{-10.8}$ $M_\odot\,{\rm yr}^{-1}$), the lower limits on their rotational period (5h for GQ Lup b, 20h for GSC06214b) and ξ = 0.7, they would require a minimum dipolar magnetic field of ∼70 G and ∼150 G, respectively. These increase to ∼750 G and 1.7 kG for the rotational period upper limits (80h). Magnetic field strengths on young companions are just starting to be investigated (Katarzyński et al. 2016; Cendes et al. 2022) but no measurement exists yet. Recent radio and H_α observations of low-mass brown dwarfs and planetary-mass objects in the same mass range as our companions suggest that the magnetic field strength could reach several k-Gauss at early ages (Kao et al. 2018). Time-series of line profiles at higher resolutions (R > 10 000) should further help to place constraints on the MagAcc and Shock models (Marleau et al. 2022). More direct measurements of the magnetic fields strength on accreting free-floating planets or companions on wider-orbits with spectropolarimeters (e.g., SPIRou) might be possible and would also help to confirm the MagAcc scenario.

6.3. Evidence for continuum variability?

In our analysis of the Pa_β line variability, we have assumed that the continuum emission remained constant. Photospheric emission of young dwarfs at the M-L transition is not expected to show high-amplitude modulation due to non-homogeneous cloud coverage (e.g., Artigau 2018; Vos et al. 2022). It remains possible that variable veiling or extinction due to accretion and the circum-"planetary" environment or magnetic spots affect the J-band and could change the contrast between the lines and their surrounding continua, thus producing at least a portion the observed variability. Carpenter et al. (2002) find a 0.15mag variability at J-band of the faintest members of Chameleon whose colors (J–K ∼ 0.8–1.0) are close to the one of GQ Lup b and correspond to spectral type in the mid- to late-M range (Cao et al. 2022).

Zhou et al. (2014) measured the shock contribution from 1D slab models (continuum excess produced by the accretion shock) and the H_α luminosity of both companions using HST data. Their model indicate a negligible contribution of the slab for GSC06214b beyond 1 µm and a contamination at the percent level for GQ Lup b at J-band. However, the shock contribution is expected to be linked to the line intensity, this could work as a variable continuum component at J band that could explain observed Pa_β equivalent width variations. Photometric variability of GQ Lup b is known to be negligible at K-band (σ_K = 0.073 mag, Neuhäuser et al. 2008), but no monitoring has been conducted at the J-band where the effect of veiling could be more important.

Veiling would both decrease the prominent K I doublets and the Pa_β emission lines. Figure 10 shows the EW of Pa_β and the KI absorption lines (corresponding values are given in Table A.1). A variation along a line with slope -1 is expected if the observed EW variability is only due to a variation in the continuum level. GQ Lup b lines show no clear correlations in 2017, although there might be a slight trend in 2006. Because the 2006 epoch and the 2017 epochs are not following the same slope, their EW difference cannot be explained only by continuum variability. To explain the EW variation observed within the 2006 epoch, a variation of the continuum level of ∼30–50% within 2 h would be required, corresponding to changes of J-band magnitudes of 0.3–0.4 mag, compatible with the dispersion of values reported in Table 1.

For GSC06214b, the trend appears between all epochs except 2017-08-19 and 2010-07-09. The Pa_β EW variability between those might therefore be explained by continuum variability. Although, in a similar fashion as for GQ Lup b, the Pa_β EW variation between the 2017-08-19/2010-07-09 and other 2017 epochs cannot be explained only based on continuum variability.

Given the current constraints, we assume that both objects have EW variability that is driven by intrinsic line flux variability. Accurate photometric monitoring of both companions at J-band simultaneous to Pa_β emission line variability campaign would be required to fully confirm this hypothesis.

6.4. Implications for protoplanet detection

Several surveys have been conducted to detect accreting planets nested in circumstellar disks using narrow-band imaging at H_α (Mendigutía et al. 2018; Wagner et al. 2018; Cugno et al. 2019; Uyama et al. 2020; Zurlo et al. 2020; Huélamo et al. 2022; Follette et al. 2023), or integral field spectroscopy targeting H_α (Haffert et al. 2019; Xie et al. 2020) and Pa_β emissions (Uyama et al. 2017, 2021). Thus far, H_α point source detections have been claimed in four systems (LkCa15, AB Aur, PDS70, CS Cha; Sallum et al. 2015; Huélamo et al. 2018; Currie et al. 2022; Zhou et al. 2021; Follette et al. 2023). The nature of the detection remains unclear in two of these systems (LkCa15, AB Aur; Whelan et al. 2015; Follette et al. 2023; Zhou et al. 2022). With the exception of Delorme 1 (AB)b, which does not seem to be in a protoplanetary-disk, no detection has ever been achieved at Pa_β.

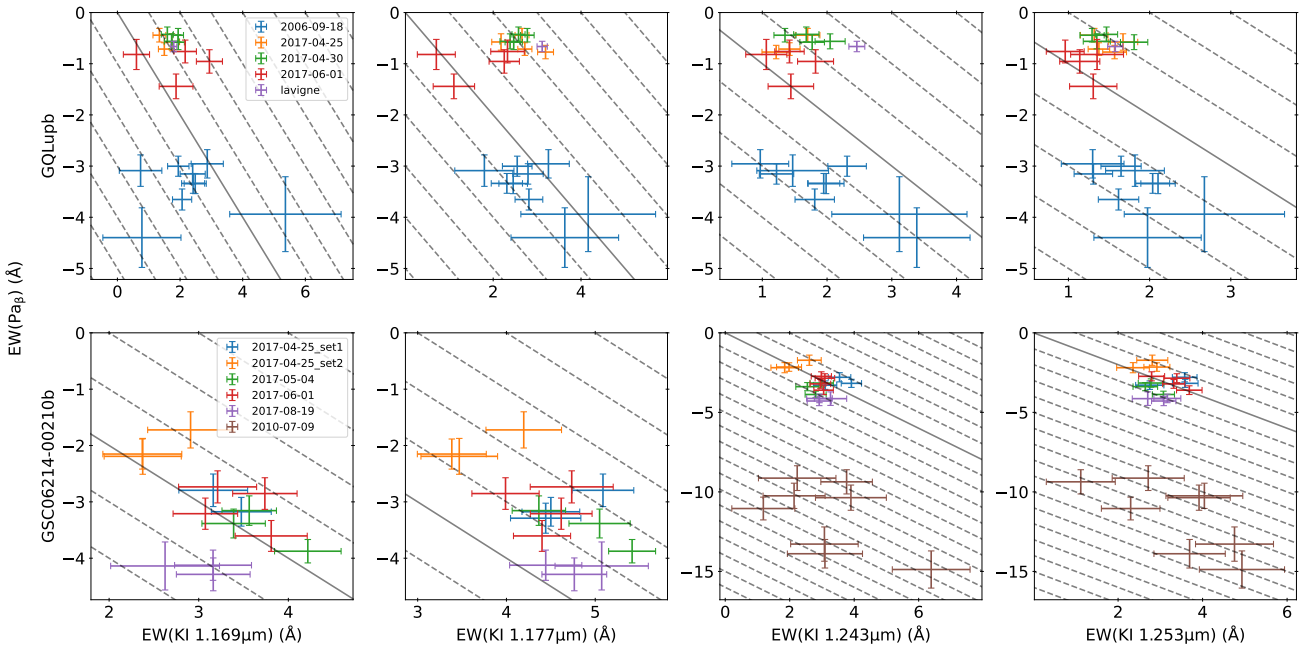


Fig. 10. Correlations between equivalent widths (EW) of both potassium absorption doublets and the Pa_β line. The equivalent width is positive for absorption lines and negative for emission lines. Gray lines correspond to a slope equal to -1, where the EW variability can be explained by sole continuum variability.

PDS 70 b and c are known to be affected by significant inline extinction (Hashimoto et al. 2020; Wang et al. 2021) caused by surrounding material, while they are otherwise found within a large cavity. Extinction is therefore a good candidate to explain the poor yield of H_α and Pa_β deep imaging searches, especially in disks with significant amount of gas and dust. However, most are single-epoch observations and emission line variability might also provide an additional explanation for the low yield of these observations.

Xie et al. (2020) report in their Fig. 11, the H_α detection limit achieved for 30min of effective VLT/MUSE observations of PDS 70. Their observations of PDS 70 are the deepest presented in the paper and probe deeper apparent line fluxes than all the narrow-band observations presented in Cugno et al. (2019) and Huélamo et al. (2022). They also report the measured apparent H_α emission line flux of the two accreting planets.

Both PDS 70 b & c, unlike GQ Lup b and GSC06214b, are embedded and interacting with the circumstellar disk. It is therefore reasonable to assume that the majority of variability happens on Keplerian timescales. Given the variety of ages and environments of known accreting objects, our Pa_β variability analysis might only serve as a first order approximation of the general H_α variability. Should our observed Pa_β variations still be representative of H_α variability of others companions, the 100 to 400% variability amplitude at year to decades-long timescales measured for GSC06214b and GQ Lup b would imply that at other epochs, both PDS 70 planets might have been emitting below the VLT/MUSE detection threshold. The various H_α flux measurements of PDS70 b shown in Zhou et al. (2021) tend to indicate that such amplitude of variability is plausible for the companion on a timescale of years. Our findings clearly advocate new visits of these young systems to maximize the detection probability. Similarly, variability might have also helped in detection surveys.

7. Conclusions

We present the results of a J-band spectroscopic monitoring campaign of GQ Lup b and GSC06214b at a medium resolving power (R = 1800–2360) with VLT/SINFONI. We also re-detect the Pa_β emission line at each epoch. We report our main conclusions below:

- We confirm that GQ Lup b is a ~2640 K, 22^{+2}_{-3} $M_{\rm Jup}$ companion, and GSC06214b is a ~2250 K, 15.5 ± 0.5 $M_{\rm Jup}$ companion, given photosphere fitting and evolutionary tracks. We note that error bars may not be representative of systematic uncertainties of the models;
- We measure C/O values on both objects compatible with solar value (GQ Lup b: C/O = $0.44^{+0.13}_{-0.11}$, GSC06214b: C/O = $0.48^{+0.16}_{-0.12}$, $C/O_\odot$ = 0.55). We find GSC06214b's [M/H] to be compatible with solar value (-0.16 ± 0.17), while GQ Lup b's is slightly super-solar (0.23 ± 0.06). The uncertainties on the atmospheric parameters are driven by small systematic errors in the data revealed by our multi-epoch observations, while Bayesian inference at single epoch provides overly optimistic estimates of the error bars;
- For both objects, the Pa_β intensity variability is found to be moderate (<50%) on timescales below their rotation period, and more important on longer timescales (up to ~1000% for a decade), a behavior similar to that of CTTS. We studied whether variable veiling could change the contrast of the line above the continuum. We find that such flux component does not explain the long-term variability of either object, but we cannot exclude it might explain the shorter term evolution of the lines;
- Both companions had their maximum recorded line brightness at first (historical) epochs. Their variability amplitude can be up to ~1000% on a decades-long timescale. Should that amplitude extend to H_α, this might explain the low yield

of H_α and Pa_β (spectro)-imaging campaigns for protoplanet detection.
- The blue-shifted Pa_β lines of GQ Lup b are reproduced only by the protoplanet magnetospheric accretion models. Those of GSC06214b are well reproduced by both magnetospheric accretion and shock models at quiescence, while the shock model is favored when the line is more intense (2010 epoch). We find filling factors of the accretion shock below 1% at that epoch and compatible with the value found on the older companion Delorme 1 (AB)b;
- We identify a tentative correlation between GSC06214b's emission line center and its width, which could be explained either by asymmetries in magnetospheric accretion-induced lines or by gas extinction in shock-induced lines.

Our study presents the first monitoring of emission lines of young accreting companions at the edge of the deuterium-burning boundary. It illustrates how variability timescales could be used to investigate whether the phenomena at play are a downsizing of those happening on protostars or more specific ones. Our results advocate multiple visits of young systems on a year-span at least to maximize the detection probability of young protoplanets. Observations at higher resolution ($R > 10\,000$, e.g., ERIS) would now be required to better constrain the line profiles and emitting mechanism.

Acknowledgements. We thank the ESO staff for the help during the preparation of the observations and their execution. We are grateful to B. Tessore and J. Bouvier for useful discussions on their magnetospheric accretion models. We acknowledge support in France from the French National Research Agency (ANR) through project grant ANR-20-CE31-0012 and the Programmes Nationaux de Planetologie et de Physique Stellaire (PNP and PNPS). This project has received funding from the European Research Council (ERC) under the European Union's Horizon 2020 research and innovation programme (COBREX; grant agreement 885 593). G.-D.M. acknowledges the support of the DFG priority program SPP 1992 "Exploring the Diversity of Extrasolar Planets" (MA 9185/1), and from the Swiss National Science Foundation under grant 200021_204847 "PlanetsInTime". Parts of this work have been carried out within the framework of the NCCR PlanetS supported by the Swiss National Science Foundation. This publication makes use of VOSA, developed under the Spanish Virtual Observatory (https://svo.cab.inta-csic.es) project funded by MCIN/AEI/10.13039/501100011033/ through grant PID2020-112949GB-I00. VOSA has been partially updated by using funding from the European Union's Horizon 2020 Research and Innovation Programme, under Grant Agreement nr. 776403 (EXOPLANETS-A).

References

Abuter, R., Schreiber, J., Eisenhauer, F., et al. 2006, New A Rev., 50, 398
Alcalá, J. M., Majidi, F. Z., Desidera, S., et al. 2020, A&A, 635, A1
Alencar, S. H. P., & Batalha, C. 2002, ApJ, 571, 378
Allard, F., Homeier, D., & Freytag, B. 2011, in Astronomical Society of the Pacific Conference Series, 448, 16th Cambridge Workshop on Cool Stars, Stellar Systems, and the Sun, eds. C. Johns-Krull, M. K. Browning, & A. A. West, 91
Anders, F., Khalatyan, A., Queiroz, A. B. A., et al. 2022, A&A, 658, A91
Antoniucci, S., García López, R., Nisini, B., et al. 2011, A&A, 534, A32
Aoyama, Y., Ikoma, M., & Tanigawa, T. 2018, ApJ, 866, 84
Aoyama, Y., Marleau, G.-D., Mordasini, C., & Ikoma, M. 2020, arXiv e-prints, [arXiv:2011.06608]
Aoyama, Y., Marleau, G.-D., Ikoma, M., & Mordasini, C. 2021, ApJ, 917, L30
Artigau, É. 2018, in Handbook of Exoplanets, eds. H. J. Deeg, & J. A. Belmonte, 94
Baraffe, I., Chabrier, G., & Gallardo, J. 2009, ApJ, 702, L27
Baraffe, I., Homeier, D., Allard, F., & Chabrier, G. 2015, A&A, 577, A42
Barenfeld, S. A., Carpenter, J. M., Ricci, L., & Isella, A. 2016, ApJ, 827, 142
Batalha, C., Lopes, D. F., & Batalha, N. M. 2001, ApJ, 548, 377
Batalha, C., Batalha, N. M., Alencar, S. H. P., Lopes, D. F., & Duarte, E. S. 2002, ApJ, 580, 343
Batygin, K. 2018, AJ, 155, 178
Bayo, A., Rodrigo, C., Barrado Y Navascués, D., et al. 2008, A&A, 492, 277
Béjar, V. J. S., Zapatero Osorio, M. R., Pérez-Garrido, A., et al. 2008, ApJ, 673, L185
Betti, S. K., Follette, K. B., Ward-Duong, K., et al. 2022a, ApJ, 941, L20
Betti, S. K., Follette, K. B., Ward-Duong, K., et al. 2022b, ApJ, 935, L18
Biazzo, K., Frasca, A., Alcalá, J. M., et al. 2017, A&A, 605, A66
Boley, A. C., Helled, R., & Payne, M. J. 2011, ApJ, 735, 30
Bonnefoy, M., Chauvin, G., Lagrange, A. M., et al. 2014, A&A, 562, A127
Bonnet, H., Conzelmann, R., Delabre, B., et al. 2004, SPIE Conf. Ser., 5490, 130
Bowler, B. P., Liu, M. C., Kraus, A. L., Mann, A. W., & Ireland, M. J. 2011, ApJ, 743, 148
Bowler, B. P., Liu, M. C., Kraus, A. L., & Mann, A. W. 2014, ApJ, 784, 65
Bowler, B. P., Andrews, S. M., Kraus, A. L., et al. 2015, ApJ, 805, L17
Bowler, B. P., Kraus, A. L., Bryan, M. L., et al. 2017, AJ, 154, 165
Brittain, S. D., Najita, J. R., Dong, R., & Zhu, Z. 2020, ApJ, 895, 48
Broeg, C., Schmidt, T. O. B., Guenther, E., et al. 2007, A&A, 468, 1039
Bryan, M. L., Benneke, B., Knutson, H. A., Batygin, K., & Bowler, B. P. 2018, Nat. Astron., 2, 138
Bryan, M. L., Ginzburg, S., Chiang, E., et al. 2020, ApJ, 905, 37
Bubar, E. J., Schaeuble, M., King, J. R., Mamajek, E. E., & Stauffer, J. R. 2011, AJ, 142, 180
Cao, L., Pinsonneault, M. H., Hillenbrand, L. A., & Kuhn, M. A. 2022, ApJ, 924, 84
Carpenter, J. M., Hillenbrand, L. A., Skrutskie, M. F., & Meyer, M. R. 2002, AJ, 124, 1001
Cendes, Y., Williams, P. K. G., & Berger, E. 2022, AJ, 163, 15
Chabrier, G., Baraffe, I., Allard, F., & Hauschildt, P. 2000, ApJ, 542, 464
Chang, E. S., & Deming, D. 1996, Sol. Phys., 165, 257
Chinchilla, P., Béjar, V. J. S., Lodieu, N., Zapatero Osorio, M. R., & Gauza, B. 2021, A&A, 645, A17
Costigan, G., Vink, J. S., Scholz, A., Ray, T., & Testi, L. 2014, MNRAS, 440, 3444
Cridland, A. J. 2018, A&A, 619, A165
Cugno, G., Quanz, S. P., Hunziker, S., et al. 2019, A&A, 622, A156
Cumming, A., Helled, R., & Venturini, J. 2018, MNRAS, 477, 4817
Curran, P. A. 2015, Astrophysics Source Code Library, [record ascl:1504.008]
Currie, T., Lawson, K., Schneider, G., et al. 2022, Nat. Astron., 6, 751
Cushing, M. C., Rayner, J. T., & Vacca, W. D. 2005, ApJ, 623, 1115
Cutri, R. M., et al. 2012, VizieR Online Data Catalog: II/311
Cutri, R. M., Skrutskie, M. F., van Dyk, S., et al. 2003, VizieR Online Data Catalog: II/246
Davies, R. I. 2007, MNRAS, 375, 1099
Delorme, P., Gagné, J., Girard, J. H., et al. 2013, A&A, 553, A5
Donati, J. F., Gregory, S. G., Alencar, S. H. P., et al. 2012, MNRAS, 425, 2948
Dong, J., Jiang, Y.-F., & Armitage, P. J. 2021, ApJ, 921, 54
Edwards, S., Hartigan, P., Ghandour, L., & Andrulis, C. 1994, AJ, 108, 1056
Eisenhauer, F., Abuter, R., Bickert, K., et al. 2003, Instrument Design and Performance for Optical/Infrared Ground-based Telescopes, 4841, 1548
Eriksson, S. C., Asensio Torres, R., Janson, M., et al. 2020, A&A, 638, A6
Feiden, G. A. 2016, A&A, 593, A99
Fendt, C. 2003, A&A, 411, 623
Fischer, W. J., Hillenbrand, L. A., Herczeg, G. J., et al. 2022, arXiv e-prints, [arXiv:2203.11257]
Folha, D. F. M., & Emerson, J. P. 2001, A&A, 365, 90
Follette, K. B., Close, L. M., Males, J. R., et al. 2023, AJ, 165, 225
Frasca, A., Biazzo, K., Alcalá, J. M., et al. 2017, A&A, 602, A33
Fu, Z., Huang, S., & Yu, C. 2023, ApJ, 945, 165
Gagné, J., Allers, K. N., Theissen, C. A., et al. 2018a, ApJ, 854, L27
Gagné, J., Mamajek, E. E., Malo, L., et al. 2018b, ApJ, 856, 23
Gaia Collaboration 2022, VizieR Online Data Catalog: I/355
Ginski, C., Schmidt, T. O. B., Mugrauer, M., et al. 2014, MNRAS, 444, 2280
Gressel, O., Nelson, R. P., Turner, N. J., & Ziegler, U. 2013, ApJ, 779, 59
Haffert, S. Y., Bohn, A. J., de Boer, J., et al. 2019, Nat. Astron., 3, 749
Hartmann, L., Herczeg, G., & Calvet, N. 2016, ARA&A, 54, 135
Hashimoto, J., Aoyama, Y., Konishi, M., et al. 2020, AJ, 159, 222
Heller, R., & Pudritz, R. 2015, ApJ, 806, 181
Helling, C., Ackerman, A., Allard, F., et al. 2008, MNRAS, 391, 1854
Herbig, G. H. 1977, ApJ, 214, 747
Högbom, J. A. 1974, A&AS, 15, 417
Huélamo, N., Chauvin, G., Schmid, H. M., et al. 2018, A&A, 613, A5
Huélamo, N., Chauvin, G., Mendigutía, I., et al. 2022, A&A, 668, A138
Ireland, M. J., Kraus, A., Martinache, F., Law, N., & Hillenbrand, L. A. 2011, ApJ, 726, 113
Itoh, Y., Hayashi, M., Tamura, M., et al. 2005, ApJ, 620, 984
Joergens, V., Bonnefoy, M., Liu, Y., et al. 2013, A&A, 558, A7
Jones, A., Noll, S., Kausch, W., Szyszka, C., & Kimeswenger, S. 2013, A&A, 560, A91

Kao, M. M., Hallinan, G., Pineda, J. S., Stevenson, D., & Burgasser, A. 2018, ApJS, 237, 25
Katarzyński, K., Gawroński, M., & Goździewski, K. 2016, MNRAS, 461, 929
Kramida, A., Yu. Ralchenko, Reader, J., & NIST ASD Team 2022, NIST Atomic Spectra Database (ver. 5.10), [Online]. Available: https://physics.nist.gov/asd (Gaithersburg, MD: National Institute of Standards and Technology)
Kraus, A. L., Ireland, M. J., Martinache, F., & Lloyd, J. P. 2008, ApJ, 679, 762
Kurosawa, R., Harries, T. J., & Littlefair, S. P. 2006, MNRAS, 372, 1879
Lachapelle, F.-R., Lafrenière, D., Gagné, J., et al. 2015, ApJ, 802, 61
Larkin, J., Barczys, M., Krabbe, A., et al. 2006, SPIE Conf. Ser., 6269, 62691A
Lavigne, J.-F., Doyon, R., Lafrenière, D., Marois, C., & Barman, T. 2009, ApJ, 704, 1098
Lazzoni, C., Gratton, R., Alcalá, J. M., et al. 2020, A&A, 635, A11
Long, D. E., Zhang, K., Teague, R., & Bergin, E. A. 2020, ApJ, 895, L46
Lubow, S. H., & Martin, R. G. 2012, ApJ, 749, L37
Luhman, K. L., Stauffer, J. R., Muench, A. A., et al. 2003, ApJ, 593, 1093
MacGregor, M. A., Wilner, D. J., Czekala, I., et al. 2017, ApJ, 835, 17
Manara, C. F., Testi, L., Rigliaco, E., et al. 2013, A&A, 551, A107
Marleau, G.-D., & Aoyama, Y. 2022, RNAAS, 6, 262
Marleau, G. D., Aoyama, Y., Kuiper, R., et al. 2022, A&A, 657, A38
Marley, M. S., Fortney, J. J., Hubickyj, O., Bodenheimer, P., & Lissauer, J. J. 2007, ApJ, 655, 541
Marois, C., Macintosh, B., & Barman, T. 2007, ApJ, 654, L151
McElwain, M. W., Metchev, S. A., Larkin, J. E., et al. 2007, ApJ, 656, 505
Mendigutía, I., Oudmaijer, R. D., Schneider, P. C., et al. 2018, A&A, 618, L9
Miki, S. 1982, Progr. Theor. Phys., 67, 1053
Murphy, S. J., Joyce, M., Bedding, T. R., White, T. R., & Kama, M. 2021, MNRAS, 502, 1633
Muzerolle, J., Calvet, N., & Hartmann, L. 2001, ApJ, 550, 944
Muzerolle, J., Luhman, K. L., Briceño, C., Hartmann, L., & Calvet, N. 2005, ApJ, 625, 906
Natta, A., Testi, L., Muzerolle, J., et al. 2004, A&A, 424, 603
Neuhäuser, R., Guenther, E. W., Petr, M. G., et al. 2000, A&A, 360, L39
Neuhäuser, R., Guenther, E. W., Wuchterl, G., et al. 2005, A&A, 435, L13
Neuhäuser, R., Mugrauer, M., Seifahrt, A., Schmidt, T. O. B., & Vogt, N. 2008, A&A, 484, 281
Noll, S., Kausch, W., Barden, M., et al. 2012, A&A, 543, A92
Padoan, P., & Nordlund, Å. 1999, ApJ, 526, 279
Padoan, P., & Nordlund, Å. 2004, ApJ, 617, 559
Pearce, L. A., Kraus, A. L., Dupuy, T. J., et al. 2019, AJ, 157, 71
Pecaut, M. J., Mamajek, E. E., & Bubar, E. J. 2012, ApJ, 746, 154
Petrus, S., Bonnefoy, M., Chauvin, G., et al. 2020, A&A, 633, A124
Petrus, S., Bonnefoy, M., Chauvin, G., et al. 2021, A&A, 648, A59
Petrus, S., Chauvin, G., Bonnefoy, M., et al. 2023, A&A, 670, L9
Phillips, M. W., Tremblin, P., Baraffe, I., et al. 2020, A&A, 637, A38
Pierens, A., & Raymond, S. N. 2016, MNRAS, 462, 4130
Piskunov, N. E., & Valenti, J. A. 2002, A&A, 385, 1095
Pittman, C. V., Espaillat, C. C., Robinson, C. E., et al. 2022, AJ, 164, 201
Preibisch, T., Guenther, E., Zinnecker, H., et al. 1998, A&A, 333, 619
Privon, G. C., Ricci, C., Aalto, S., et al. 2020, ApJ, 893, 149
Reiners, A., & Christensen, U. R. 2010, A&A, 522, A13
Rice, E. L., Barman, T., Mclean, I. S., Prato, L., & Kirkpatrick, J. D. 2010, ApJS, 186, 63
Rigliaco, E., Natta, A., Testi, L., et al. 2012, A&A, 548, A56
Ringqvist, S. C., Viswanath, G., Aoyama, Y., et al. 2023, A&A, 669, A12
Sallum, S., Follette, K. B., Eisner, J. A., et al. 2015, Nature, 527, 342
Santamaría-Miranda, A., Cáceres, C., Schreiber, M. R., et al. 2018, MNRAS, 475, 2994
Santamaría-Miranda, A., Cáceres, C., Schreiber, M. R., et al. 2019, MNRAS, 488, 5852
Schmidt, T. O. B., Neuhäuser, R., Seifahrt, A., et al. 2008, A&A, 491, 311
Schwarz, H., Ginski, C., de Kok, R. J., et al. 2016, A&A, 593, A74
Seifahrt, A., Neuhäuser, R., & Hauschildt, P. H. 2007, A&A, 463, 309
Sembach, K. R., & Savage, B. D. 1992, ApJS, 83, 147
Sicilia-Aguilar, A., Fang, M., Roccatagliata, V., et al. 2015, A&A, 580, A82
Skilling, J. 2004, in American Institute of Physics Conference Series, 735, Bayesian Inference and Maximum Entropy Methods in Science and Engineering: 24th International Workshop on Bayesian Inference and Maximum Entropy Methods in Science and Engineering, eds. R. Fischer, R. Preuss, & U. V. Toussaint, 395
Smith, E. J., Davis, L., J., Jones, D. E., et al. 1974, Science, 183, 305
Stolker, T., Haffert, S. Y., Kesseli, A. Y., et al. 2021, AJ, 162, 286
Suárez-Andrés, L., Israelian, G., González Hernández, J. I., et al. 2018, A&A, 614, A84
Swastik, C., Banyal, R. K., Narang, M., et al. 2021, AJ, 161, 114
Szulágyi, J., & Ercolano, B. 2020, ApJ, 902, 126
Szulágyi, J., Morbidelli, A., Crida, A., & Masset, F. 2014, ApJ, 782, 65
Tautvaišienė, G., Mikolaitis, Š., Drazdauskas, A., et al. 2022, ApJS, 259, 45
Thanathibodee, T., Calvet, N., Bae, J., Muzerolle, J., & Hernández, R. F. 2019, ApJ, 885, 94
Tremblin, P., Amundsen, D. S., Mourier, P., et al. 2015, ApJ, 804, L17
Tremblin, P., Amundsen, D. S., Chabrier, G., et al. 2016, ApJ, 817, L19
Uyama, T., Tanigawa, T., Hashimoto, J., et al. 2017, AJ, 154, 90
Uyama, T., Norris, B., Jovanovic, N., et al. 2020, J. Astron. Telescopes Instrum. Syst., 6, 045004
Uyama, T., Xie, C., Aoyama, Y., et al. 2021, AJ, 162, 214
van Dokkum, P. G. 2001, PASP, 113, 1420
van Holstein, R. G., Stolker, T., Jensen-Clem, R., et al. 2021, A&A, 647, A21
Vos, J. M., Faherty, J. K., Gagné, J., et al. 2022, ApJ, 924, 68
Wagner, K., Follete, K. B., Close, L. M., et al. 2018, ApJ, 863, L8
Wang, J. J., Vigan, A., Lacour, S., et al. 2021, AJ, 161, 148
Whelan, E. T., Huélamo, N., Alcalá, J. M., et al. 2015, A&A, 579, A48
Witte, S., Helling, C., & Hauschildt, P. H. 2009, A&A, 506, 1367
Witte, S., Helling, C., Barman, T., Heidrich, N., & Hauschildt, P. H. 2011, A&A, 529, A44
Wolff, S. G., Ménard, F., Caceres, C., et al. 2017, AJ, 154, 26
Wu, Y.-L., Close, L. M., Eisner, J. A., & Sheehan, P. D. 2017a, AJ, 154, 234
Wu, Y.-L., Sheehan, P. D., Males, J. R., et al. 2017b, ApJ, 836, 223
Xie, C., Haffert, S. Y., de Boer, J., et al. 2020, A&A, 644, A149
Zhang, Y., Snellen, I. A. G., Bohn, A. J., et al. 2021, Nature, 595, 370
Zhou, Y., Herczeg, G. J., Kraus, A. L., Metchev, S., & Cruz, K. L. 2014, ApJ, 783, L17
Zhou, Y., Bowler, B. P., Wagner, K. R., et al. 2021, AJ, 161, 244
Zhou, Y., Sanghi, A., Bowler, B. P., et al. 2022, ApJ, 934, L13
Zhu, Z., Ju, W., & Stone, J. M. 2016, ApJ, 832, 193
Zsidi, G., Manara, C. F., Kóspál, Á., et al. 2022, A&A, 660, A108
Zurlo, A., Cugno, G., Montesinos, M., et al. 2020, A&A, 633, A119

[1] Univ. Grenoble Alpes, CNRS, IPAG, 38000 Grenoble, France
e-mail: dorian.demars@univ-grenoble-alpes.fr
[2] Institute for Advanced Study, Tsinghua University, Beijing 100084, PR China
[3] Department of Astronomy, Tsinghua University, Beijing 100084, PR China
[4] Department of Earth and Planetary Science, The University of Tokyo, 7-3-1 Hongo, Bunkyo-ku, Tokyo 113-0033, Japan
[5] Department of Astronomy, University of Michigan, 1085 S. University Ave., Ann Arbor, MI 48109, USA
[6] Institute for Astrophysical Research and Department of Astronomy, Boston University, 725 Commonwealth Ave., Boston, MA 02215, USA
[7] Fakultät für Physik, Universität Duisburg-Essen, Lotharstraße 1, 47057 Duisburg, Germany
[8] Institut für Astronomie und Astrophysik, Universität Tübingen, Auf der Morgenstelle 10, 72076 Tübingen, Germany
[9] Physikalisches Institut, Universität Bern, Gesellschaftsstr. 6, 3012 Bern, Switzerland
[10] Max-Planck-Institut für Astronomie, Königstuhl 17, 69117 Heidelberg, Germany
[11] Maison de la Simulation, CEA, CNRS, Univ. Paris-Sud, UVSQ, Université Paris-Saclay, 91191 Gif-sur-Yvette, France
[12] Université Côte d'Azur, OCA, Lagrange CNRS, 06304 Nice, France
[13] Instituto de Física y Astronomía, Facultad de Ciencias, Universidad de Valparaíso, Av. Gran Bretaña 1111, Valparaíso, Chile
[14] Núcleo Milenio Formación Planetaria – NPF, Universidad de Valparaíso, Av. Gran Bretaña 1111, Valparaíso, Chile
[15] Department of Astronomy, The University of Texas at Austin, 2515 Speedway, Stop C1400, Austin, TX 78712, USA
[16] LESIA, Observatoire de Paris, PSL Research University, CNRS, Sorbonne Universités, UPMC Univ. Paris 06, Univ. Paris Diderot, Sorbonne Paris Cité, 5 place Jules Janssen, 92195 Meudon, France

Appendix A: Supplementary material

Figure A.1 contains a visual representation of the extraction process for both objects, along with residuals. Table A.1 contains the measured equivalent widths of the two KI doublets and the Pa_β line of each individual cube. Table A.2 contains the resulting fitted Gaussian parameters of the Pa_β line. The Pa_β integrated fluxes used for Fig. 7 were computed from these parameters as $I_{\rm tot} = \sigma I_0 \sqrt{2\pi}$. The error bar on the integrated flux accounts for correlations between parameters:

$$\left(\frac{\mathrm{err}(I_{\rm tot})}{I_{\rm tot}}\right)^2 = \left(\frac{\mathrm{err}(\sigma)}{\sigma}\right)^2 + \left(\frac{\mathrm{err}(I_0)}{I_0}\right)^2 + \frac{2\,\mathrm{cov}(\sigma, I_0)}{\sigma I_0}. \quad \text{(A.1)}$$

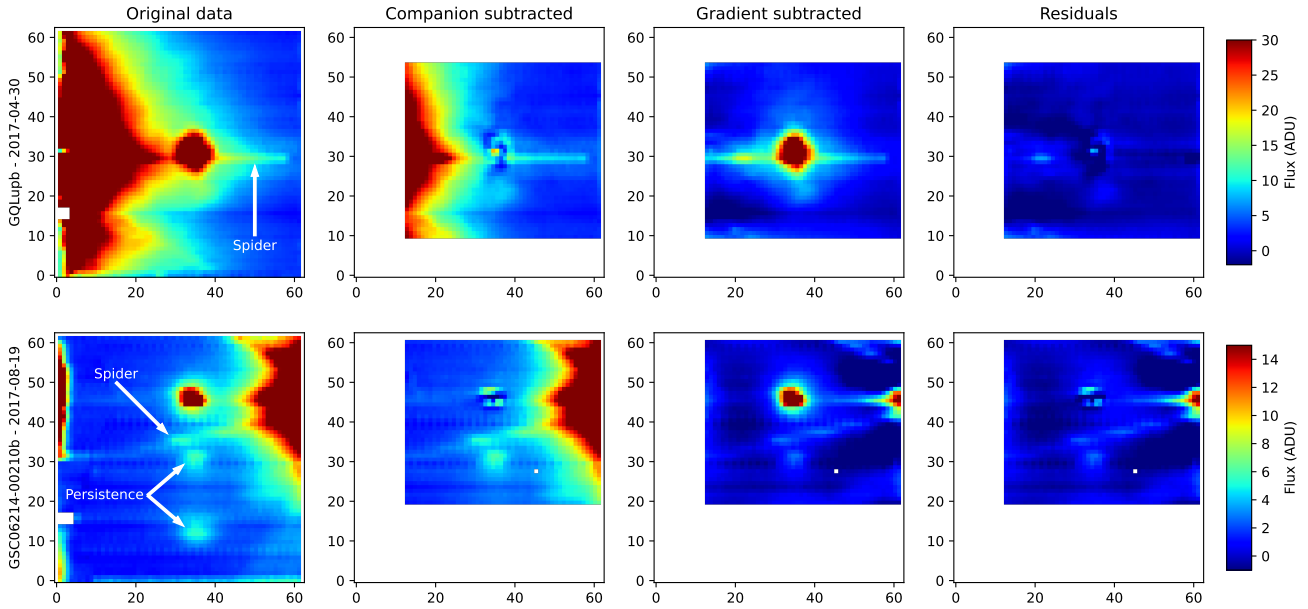


Fig. A.1. Visual representation of the last iteration of the extraction for both GQ Lup b and GSC06214b, on epochs 2017-04-30 and 2017-08-19 respectively. As mentioned in Sect. 4, the horizontal spider is subtracted for GQ Lup b, but not for GSC06214b as it does not extend below the companion. Are also marked the spiders locations for both targets and some persistence effects in the GSC06214b data.

Table A.1. Equivalent widths

Source	Date	KI 1.169 µm Å	KI 1.177 µm Å	KI 1.243 µm Å	KI 1.253 µm Å	Pa_β Å
GQ Lup b	2006-09-17 – 23:22:53	2.07 ± 0.31	2.81 ± 0.32	1.81 ± 0.30	1.62 ± 0.25	−3.65 ± 0.21
GQ Lup b	2006-09-17 – 23:39:49	2.42 ± 0.37	2.31 ± 0.36	1.95 ± 0.25	2.04 ± 0.21	−3.34 ± 0.19
GQ Lup b	2006-09-17 – 23:45:21	2.40 ± 0.40	2.79 ± 0.35	1.22 ± 0.27	1.31 ± 0.24	−3.15 ± 0.20
GQ Lup b	2006-09-18 – 00:02:15	2.48 ± 0.35	2.46 ± 0.33	1.99 ± 0.28	2.10 ± 0.21	−3.34 ± 0.20
GQ Lup b	2006-09-18 – 00:07:41	1.94 ± 0.34	2.55 ± 0.34	2.31 ± 0.30	1.65 ± 0.25	−3.00 ± 0.20
GQ Lup b	2006-09-18 – 00:24:36	2.87 ± 0.51	3.26 ± 0.47	0.97 ± 0.44	1.30 ± 0.39	−2.96 ± 0.28
GQ Lup b	2006-09-18 – 00:30:08	0.74 ± 0.68	1.80 ± 0.67	1.47 ± 0.55	1.82 ± 0.36	−3.09 ± 0.31
GQ Lup b	2006-09-18 – 00:47:01	0.78 ± 1.25	3.63 ± 1.22	3.39 ± 0.82	1.97 ± 0.66	−4.40 ± 0.58
GQ Lup b	2006-09-18 – 00:52:33	5.36 ± 1.78	4.16 ± 1.53	3.12 ± 1.04	2.67 ± 0.99	−3.94 ± 0.73
GQ Lup b	2017-04-25 – 05:21:16	1.74 ± 0.24	2.18 ± 0.21	cosmic	1.67 ± 0.18	−0.58 ± 0.16
GQ Lup b	2017-04-25 – 05:26:40	cosmic	3.19 ± 0.18	1.21 ± 0.22	1.57 ± 0.15	−0.77 ± 0.13
GQ Lup b	2017-04-25 – 05:37:30	1.34 ± 0.20	2.66 ± 0.16	1.70 ± 0.19	1.32 ± 0.17	−0.44 ± 0.13
GQ Lup b	2017-04-25 – 05:42:55	1.50 ± 0.19	2.72 ± 0.16	1.42 ± 0.16	1.38 ± 0.13	−0.71 ± 0.12
GQ Lup b	2017-04-30 – 05:34:35	1.94 ± 0.17	2.78 ± 0.15	1.35 ± 0.17	1.29 ± 0.15	−0.44 ± 0.13
GQ Lup b	2017-04-30 – 05:56:16	1.94 ± 0.20	2.47 ± 0.20	1.77 ± 0.19	1.81 ± 0.17	−0.58 ± 0.15
GQ Lup b	2017-04-30 – 05:50:51	1.73 ± 0.23	2.39 ± 0.23	2.05 ± 0.23	1.35 ± 0.17	−0.56 ± 0.15
GQ Lup b	2017-04-30 – 05:40:00	1.59 ± 0.19	2.58 ± 0.15	1.68 ± 0.20	1.47 ± 0.14	−0.43 ± 0.14
GQ Lup b	2017-06-01 – 06:29:29	2.16 ± 0.36	2.33 ± 0.38	1.42 ± 0.23	0.96 ± 0.23	−0.76 ± 0.22
GQ Lup b	2017-06-01 – 06:34:55	2.94 ± 0.42	2.25 ± 0.35	1.82 ± 0.28	1.14 ± 0.25	−0.96 ± 0.23
GQ Lup b	2017-06-01 – 06:45:44	0.61 ± 0.42	0.71 ± 0.43	1.06 ± 0.32	1.35 ± 0.33	−0.82 ± 0.29
GQ Lup b	2017-06-01 – 06:51:09	1.87 ± 0.54	1.11 ± 0.47	1.44 ± 0.35	1.31 ± 0.29	−1.44 ± 0.24
GSC06214b	2017-04-25 – 06:21:07	3.16 ± 0.38	5.09 ± 0.35	3.55 ± 0.35	3.58 ± 0.29	−2.79 ± 0.29
GSC06214b	2017-04-25 – 06:32:12	3.48 ± 0.33	4.50 ± 0.33	3.91 ± 0.31	3.59 ± 0.30	−3.18 ± 0.26
GSC06214b	2017-04-25 – 06:48:51	cosmic	4.44 ± 0.40	3.10 ± 0.36	2.75 ± 0.33	−3.29 ± 0.27
GSC06214b	2017-04-25 – 07:35:50	2.37 ± 0.44	3.38 ± 0.39	1.98 ± 0.39	2.92 ± 0.31	−2.15 ± 0.27
GSC06214b	2017-04-25 – 07:46:53	2.37 ± 0.43	3.47 ± 0.43	1.84 ± 0.43	2.35 ± 0.39	−2.19 ± 0.32
GSC06214b	2017-04-25 – 08:03:31	2.91 ± 0.48	4.19 ± 0.43	2.61 ± 0.37	2.81 ± 0.37	−1.72 ± 0.32
GSC06214b	2017-05-04 – 04:29:49	3.39 ± 0.35	5.05 ± 0.34	2.55 ± 0.36	2.64 ± 0.29	−3.38 ± 0.26
GSC06214b	2017-05-04 – 04:40:54	3.56 ± 0.30	4.37 ± 0.30	2.99 ± 0.36	2.78 ± 0.30	−3.16 ± 0.26
GSC06214b	2017-05-04 – 04:57:38	4.22 ± 0.37	5.42 ± 0.26	2.80 ± 0.33	3.07 ± 0.26	−3.88 ± 0.21
GSC06214b	2017-06-01 – 01:54:27	3.21 ± 0.44	4.74 ± 0.47	2.98 ± 0.31	2.79 ± 0.31	−2.73 ± 0.28
GSC06214b	2017-06-01 – 02:16:29	3.07 ± 0.36	4.62 ± 0.35	2.95 ± 0.32	3.32 ± 0.26	−3.21 ± 0.28
GSC06214b	2017-06-01 – 02:27:32	3.74 ± 0.36	3.99 ± 0.38	3.09 ± 0.30	3.39 ± 0.31	−2.85 ± 0.28
GSC06214b	2017-06-01 – 02:44:12	3.81 ± 0.40	4.40 ± 0.32	3.05 ± 0.30	3.69 ± 0.30	−3.60 ± 0.27
GSC06214b	2017-08-19 – 01:28:50	3.16 ± 0.41	4.76 ± 0.36	2.92 ± 0.37	3.08 ± 0.29	−4.29 ± 0.29
GSC06214b	2017-08-19 – 01:39:28	3.16 ± 0.43	4.44 ± 0.41	2.92 ± 0.40	3.17 ± 0.32	−4.12 ± 0.27
GSC06214b	2017-08-19 – 01:55:28	2.62 ± 0.61	5.07 ± 0.53	3.27 ± 0.50	2.70 ± 0.37	−4.14 ± 0.43
GSC06214b	2010-07-09 – 08:28:56	-	-	3.08 ± 1.05	4.76 ± 0.92	−13.28 ± 1.08
GSC06214b	2010-07-09 – 08:34:42	-	-	1.18 ± 0.98	2.30 ± 0.69	−11.05 ± 0.72
GSC06214b	2010-07-09 – 08:45:15	-	-	3.90 ± 1.10	3.92 ± 0.74	−10.36 ± 0.79
GSC06214b	2010-07-09 – 08:51:02	-	-	2.23 ± 1.20	2.71 ± 0.85	−9.13 ± 0.78
GSC06214b	2010-07-09 – 08:59:40	-	-	2.14 ± 0.96	4.04 ± 0.91	−10.25 ± 0.79
GSC06214b	2010-07-09 – 09:05:26	-	-	3.09 ± 1.17	3.69 ± 0.84	−13.89 ± 0.90
GSC06214b	2010-07-09 – 09:12:50	-	-	3.77 ± 0.80	1.12 ± 0.82	−9.37 ± 0.76
GSC06214b	2010-07-09 – 09:18:36	-	-	6.39 ± 1.21	4.93 ± 1.01	−14.88 ± 1.17

Notes. Measured equivalent widths of the various K I and Pa_β lines, following the method described in Sembach & Savage (1992) and Cushing et al. (2005). Date is given in YYYY-MM-DD – hh:mm:ss format. Possible correlations between the lines are shown in Fig. 10.

Table A.2. Gaussian fitting results

Source	Date	I_0	σ	μ_0	Int. Flux	Intrinsic FWHM
	YYYY-MM-DD – hh:mm:ss	10^{-16} W/m^2/μm	km/s	km/s	10^{-19} W/m^2	km/s
GQ Lup b	2006-09-17 – 23:22:53	25.0 ± 1.3	63.5 ± 3.7	−27.8 ± 3.7	17.0 ± 0.9	79.1 ± 16.5
GQ Lup b	2006-09-17 – 23:39:49	19.4 ± 1.2	79.5 ± 6.0	−19.0 ± 5.9	16.5 ± 1.1	137.5 ± 19.4
GQ Lup b	2006-09-17 – 23:45:21	20.5 ± 1.3	72.1 ± 5.3	−20.4 ± 5.3	15.8 ± 1.0	112.6 ± 18.9
GQ Lup b	2006-09-18 – 00:02:15	22.4 ± 0.5	67.9 ± 1.8	−22.5 ± 1.8	16.3 ± 0.4	97.0 ± 7.1
GQ Lup b	2006-09-18 – 00:07:41	19.0 ± 0.9	75.9 ± 4.1	−16.8 ± 4.0	15.4 ± 0.7	125.6 ± 13.7
GQ Lup b	2006-09-18 – 00:24:36	25.3 ± 2.2	54.5 ± 5.4	−17.1 ± 5.4	14.8 ± 1.3	18.8 ± 87.2
GQ Lup b	2006-09-18 – 00:30:08	22.5 ± 1.5	65.4 ± 4.9	−21.2 ± 4.9	15.8 ± 1.0	87.2 ± 20.5
GQ Lup b	2006-09-18 – 00:47:01	29.5 ± 3.3	61.5 ± 7.9	−1.3 ± 7.9	19.4 ± 2.2	69.3 ± 39.0
GQ Lup b	2006-09-18 – 00:52:33	45.5 ± 6.9	30.9 ± 5.5	−25.6 ± 5.4	15.1 ± 2.3	0.0 ± 58.6
GQ Lup b	2017-04-25 – 05:21:16	5.7 ± 1.3	38.3 ± 9.9	−19.2 ± 9.9	2.3 ± 0.5	0.0 ± 80.3
GQ Lup b	2017-04-25 – 05:26:40	4.4 ± 0.9	63.8 ± 15.0	−53.8 ± 14.8	3.0 ± 0.6	80.4 ± 66.3
GQ Lup b	2017-04-25 – 05:37:30	4.7 ± 1.3	46.9 ± 15.1	−41.4 ± 15.1	2.4 ± 0.7	0.0 ± 101.4
GQ Lup b	2017-04-25 – 05:42:55	4.9 ± 0.8	43.5 ± 7.9	−2.6 ± 7.9	2.3 ± 0.4	0.0 ± 71.1
GQ Lup b	2017-04-30 – 05:34:35	4.8 ± 1.3	47.0 ± 14.2	−49.0 ± 14.2	2.4 ± 0.6	0.0 ± 98.2
GQ Lup b	2017-04-30 – 05:56:16	3.9 ± 1.1	45.0 ± 14.3	−34.3 ± 14.3	1.9 ± 0.5	0.0 ± 98.6
GQ Lup b	2017-04-30 – 05:50:51	5.5 ± 1.5	40.4 ± 12.6	−37.1 ± 12.6	2.4 ± 0.6	0.0 ± 91.7
GQ Lup b	2017-04-30 – 05:40:00	4.1 ± 1.4	35.7 ± 13.9	−22.4 ± 13.9	1.6 ± 0.5	0.0 ± 96.8
GQ Lup b	2017-06-01 – 06:29:29	9.5 ± 2.4	49.3 ± 14.5	−55.9 ± 14.5	5.0 ± 1.3	0.0 ± 99.1
GQ Lup b	2017-06-01 – 06:34:55	7.4 ± 1.9	52.2 ± 15.7	−14.2 ± 15.7	4.1 ± 1.1	0.0 ± 103.6
GQ Lup b	2017-06-01 – 06:45:44	11.2 ± 2.6	56.6 ± 15.1	−54.0 ± 15.0	6.8 ± 1.6	40.1 ± 118.4
GQ Lup b	2017-06-01 – 06:51:09	11.6 ± 2.3	48.2 ± 11.0	−69.2 ± 10.9	6.0 ± 1.2	0.0 ± 85.1
GSC06214b	2017-04-25 – 06:21:07	3.2 ± 0.3	54.7 ± 6.7	−14.2 ± 6.7	1.9 ± 0.2	0.0 ± 74.3
GSC06214b	2017-04-25 – 06:32:12	4.0 ± 0.2	62.4 ± 2.8	−7.3 ± 2.7	2.7 ± 0.1	0.0 ± 47.2
GSC06214b	2017-04-25 – 06:48:51	3.8 ± 0.3	65.6 ± 5.5	−10.1 ± 5.3	2.7 ± 0.2	0.0 ± 66.9
GSC06214b	2017-04-25 – 07:35:50	3.2 ± 0.3	62.5 ± 7.9	−9.7 ± 7.7	2.1 ± 0.2	0.0 ± 80.8
GSC06214b	2017-04-25 – 07:46:53	3.2 ± 0.5	63.7 ± 11.9	−19.8 ± 11.6	2.2 ± 0.3	0.0 ± 100.8
GSC06214b	2017-04-25 – 08:03:31	2.5 ± 0.2	57.5 ± 4.5	−11.5 ± 4.4	1.5 ± 0.1	0.0 ± 60.2
GSC06214b	2017-05-04 – 04:29:49	3.6 ± 0.2	74.2 ± 3.8	−2.4 ± 3.6	2.9 ± 0.1	52.9 ± 29.9
GSC06214b	2017-05-04 – 04:40:54	3.7 ± 0.4	78.6 ± 10.1	7.7 ± 9.1	3.1 ± 0.3	81.0 ± 54.2
GSC06214b	2017-05-04 – 04:57:38	4.5 ± 0.2	75.7 ± 3.9	8.2 ± 3.6	3.7 ± 0.2	63.5 ± 25.7
GSC06214b	2017-06-01 – 01:54:27	4.4 ± 0.5	66.4 ± 8.3	−5.7 ± 8.1	3.1 ± 0.3	0.0 ± 83.3
GSC06214b	2017-06-01 – 02:16:29	4.3 ± 0.3	64.9 ± 5.1	−0.3 ± 5.0	3.0 ± 0.2	0.0 ± 64.7
GSC06214b	2017-06-01 – 02:27:32	4.1 ± 0.2	72.7 ± 4.4	5.8 ± 4.1	3.2 ± 0.2	40.0 ± 44.1
GSC06214b	2017-06-01 – 02:44:12	4.8 ± 0.3	78.5 ± 7.1	13.4 ± 6.5	4.0 ± 0.3	80.0 ± 38.9
GSC06214b	2017-08-19 – 01:28:50	6.3 ± 0.2	73.5 ± 3.2	−5.9 ± 3.0	4.9 ± 0.2	46.9 ± 28.0
GSC06214b	2017-08-19 – 01:39:28	5.8 ± 0.2	75.3 ± 4.0	0.3 ± 3.7	4.7 ± 0.2	60.8 ± 27.6
GSC06214b	2017-08-19 – 01:55:28	5.5 ± 0.4	83.5 ± 8.0	5.7 ± 7.1	4.9 ± 0.4	104.4 ± 35.6
GSC06214b	2010-07-09 – 08:28:56	17.4 ± 0.9	61.1 ± 3.7	7.5 ± 3.7	11.4 ± 0.6	120.2 ± 10.4
GSC06214b	2010-07-09 – 08:34:42	19.6 ± 1.0	44.5 ± 2.7	7.2 ± 2.7	9.4 ± 0.5	69.1 ± 9.7
GSC06214b	2010-07-09 – 08:45:15	18.1 ± 1.3	52.6 ± 4.5	8.1 ± 4.5	10.2 ± 0.8	95.4 ± 13.8
GSC06214b	2010-07-09 – 08:51:02	17.2 ± 0.6	42.0 ± 1.8	8.5 ± 1.8	7.8 ± 0.3	59.8 ± 6.9
GSC06214b	2010-07-09 – 08:59:40	16.9 ± 0.8	56.6 ± 3.1	5.3 ± 3.1	10.2 ± 0.5	107.4 ± 9.1
GSC06214b	2010-07-09 – 09:05:26	18.1 ± 1.4	61.1 ± 5.6	12.0 ± 5.6	11.8 ± 0.9	120.2 ± 15.7
GSC06214b	2010-07-09 – 09:12:50	16.0 ± 0.6	55.2 ± 2.5	9.8 ± 2.5	9.4 ± 0.4	103.2 ± 7.5
GSC06214b	2010-07-09 – 09:18:36	19.6 ± 1.1	63.7 ± 4.2	17.9 ± 4.1	13.4 ± 0.8	127.7 ± 11.6

Notes. Gaussian fitting results of the Pa_β lines. Date is given in YYYY-MM-DD – hh:mm:ss format. I_0 is the scaling parameter of the gaussian.



Thesis' Table of Contents
Chapter's Table of Contents

Chapter III.

Accretion tracers in the Visible/UV with VLT/UVES

The constraints placed on accretion models are limited by the spectral resolution of observations. However, it was shown recently that it is feasible to observe PMCs at resolutions sufficient ($R \sim (10\,000 - 50\,000)$) to highlight the specifics of the models. I therefore use VLT/UVES to observe Delorme 1 (AB)b in the Visible/UV, where the Balmer series lies, among which H_α, which is predicted to be the brightest of accretion lines.

The lines profiles are fully resolved and are reminiscent of some accreting low-mass brown dwarfs observed in the early 2000s. The lines profiles, along with their flux are variable. The H_α flux variability is lesser than that found for Pa_β, $\lesssim 10$ % at ∼hours timescales, and reaches ~ 50 % at months timescales. The profile variability is utilized to decompose it into two static components, that only vary by their relative flux from an epoch to another. This decomposition is able to explain most features in the lines profiles. The UV excess is also detected at low resolution, and is highly correlated with only one of the two components, while the other one may be linked to chromospheric activity.

Magnetospheric accretion models are able to reproduce the main features of both components, including the absorption features in the one correlated with the UV excess, which highly suggests that magnetospheric accretion is the mechanism for that component. For the other component, the Shock-emission is not excluded, although its low correlation with the UV excess likely discards that explanation. Overall, the amplitude of variability observed in H_α is not sufficient to explain the low yield of detection of H_α surveys.

Chapter's contents

1 Introduction . . . 96
2 The UVES campaign: targets description . . . 96
2.1 Delorme 1 (AB)b . . . 97
2.2 SR 12 c . . . 98
2.3 2MASS J11151597+1937266 . . . 98
3 The UVES spectrograph . . . 98
3.1 Instrument description . . . 99
3.1.1 The preslits . . . 100
3.1.2 The two spectrograph arms . . . 101
3.1.3 The scientific CCDs . . . 101
3.2 Data acquisition and reduction . . . 101
3.2.1 Observations setup . . . 101
3.2.2 General reduction – ESO pipeline . . . 103
4 Observations and data reduction . . . 104
4.1 Observations . . . 104
4.1.1 Delorme 1 (AB)b . . . 104
4.2 Delorme 1 (AB)b: Reduction . . . 104
4.2.1 ESO automated reduction . . . 104
4.2.2 Cosmics rejection . . . 106
4.2.3 Hynes method and spectra exctraction . . . 106
4.2.4 Contamination correction . . . 113
4.2.5 Instrument response and atmospheric extinction . . . 116
4.2.6 Flux calibration . . . 117
5 Delorme 1 (AB)b . . . 117
5.1 General description of the spectra . . . 117
5.2 Lines morphology . . . 118
5.2.1 Resolved profiles . . . 118
5.2.2 H_α and H_β plateau-slope . . . 119
5.2.3 Low resolution impact . . . 119
5.3 Lines correlations . . . 122
5.3.1 Auto-Correlations . . . 123
5.3.2 Cross-correlations . . . 124
5.4 Decomposing the lines . . . 124
5.4.1 Helium–Hydrogen correlations . . . 124
5.4.2 Two-components fitting . . . 127
5.4.3 An alternative decomposition . . . 132
5.4.4 Lines components and other correlations . . . 134
5.5 Line ratios . . . 134
5.6 Lines variability . . . 135
5.6.1 Lines behaviors . . . 135



5.6.2 Short-term variability . . . 135
5.7 Periodicity . . . 137
5.7.1 2D periodograms . . . 137
5.7.2 Sub-components periodograms . . . 140
5.8 Model fitting . . . 142
5.8.1 Models description . . . 142
5.8.2 Sub-components fitting . . . 143
5.9 Discussion . . . 146
5.9.1 Lines variability . . . 146
5.9.2 Lines origin: clues from Helium . . . 147
5.9.3 The Magnetospheric Accretion scenario . . . 147
5.9.4 Shock contribution . . . 148
5.9.5 Chromospheric contribution to the lines? . . . 148
5.9.6 Spectral type and apparent continuum . . . 149
5.9.7 Is Delorme 1 (AB)b an outlier? . . . 151
6 SR 12 c . . . 151
6.1 Observations . . . 151
6.2 Quick-look: Data reduction . . . 153
6.3 Highly variable lines . . . 153
6.4 Discussion . . . 154
7 2MASS J11151597 . . . 155
7.1 Observations . . . 155
7.2 Data reduction . . . 155
7.3 Results . . . 156
8 Summary . . . 157



1 Introduction

The previous chapter showed that the lines modeling and analysis are severely limited by the relatively low resolution of SINFONI ($R \sim 2000$). However, working with a higher resolution instrument is not so straightforward, and most instrumentation is a balance between angular and spectral resolution. In other words, increasing the spectral resolution often comes at the cost of reducing the spatial resolution. On top of that, increased spectral resolution does narrow the LSF width, but accretion lines are predicted to be intrinsically large (and is confirmed by the slight resolved lines of GSC 06214-00210 b), therefore increased spectral resolution spreads the flux over more pixels, thus reducing S/N for a given spectral element. In order to provide stronger constraints on the models, simulations showed that they could be distinguished at resolutions above 10 000.

Most of the *high* spectral resolution instruments (XSHOOTER, UVES) are seeing-limited, which is obviously an issue for PMCs that can be fairly close from their host star. However, some are found to be located at angular separations just reachable with such instruments. GSC 06214-00210 b is one of them, at 2.2" from its host star, but its lines are quite faint, which raise questions on the feasibility. The use of CRIRES ETC, even with its AO, hardly allows for IR observation of that target, mostly because of the *low* throughput of the instrument. ERIS, however, could likely be used for the Pa_β and Br_γ lines (see perspectives for a discussion on high-R characterization of IR lines).

Instead, Balmer lines (in the optical), are predicted to be a lot brighter than IR lines (Marleau and Aoyama, 2022). Delorme 1 (AB)b, one of the closest PMC, was even shown to have really bright H_α and H_β lines (Eriksson et al., 2020). On top of that, pilot observations had actually shown the feasibility of observing that target with UVES (Ringqvist et al., 2023). XSHOOTER would provide a broader wavelength coverage and observations of SR 12 c had already been shown to be possible, with a double-lobed profile for its H_α line (Santamaría-Miranda et al., 2018). However, UVES provides the resolution that was lacking in resolving SR 12 c's H_α profile, and the ETC showed that the H_α line of SR 12 c could be probed with UVES. Finally, complex structures can arise from the accretion flow at scales of $\sim$ 10 km/s, as shown by Marleau et al. (2022). Therefore, UVES naturally came as the perfect instrument for characterizing *wide* (> 1.5") separation PMCs.

For Delorme 1 (AB)b, we aimed at characterizing long term variability behaviors (across several months), while for SR 12 c, we aimed at characterizing its short term variability, hopefully highlighting rotational modulation effects across consecutive nights. Additionally, the previous chapter showed that the line variability is significant, at least in Pa_β. Whether this translates to H_α is not verified. Therefore, this chapter will also try to infer variability properties of optical lines. I first present the three targets that were studied (Sect. 2), introduce the UVES echelle spectrograph (Sect. 3), present the observations and data reduction procedures for Delorme 1 (AB)b (Sect. 4), the results and associated discussion (Sect. 5), similar procedures on SR 12 c (Sect. 6) and 2MASS J11151597 (Sect. 7), then conclude on these first-of-a-kind observations (Sect. 8). A paper on these results is in preparation.

2 The UVES campaign: targets description

Targets were chosen over two consecutive years. First, Delorme 1 (AB)b was selected, for reasons mentioned above. Delorme was observed during an odd semester. The following (even) semester, we switched to targets observable at reasonable airmass during several consecutive days and therefore picked up SR 12 c as our prime target. We also performed snapshot observations of additional targets at twilight with the instrument to confirm their H_α emissions and start an in-depth characterization of their properties. Unlike



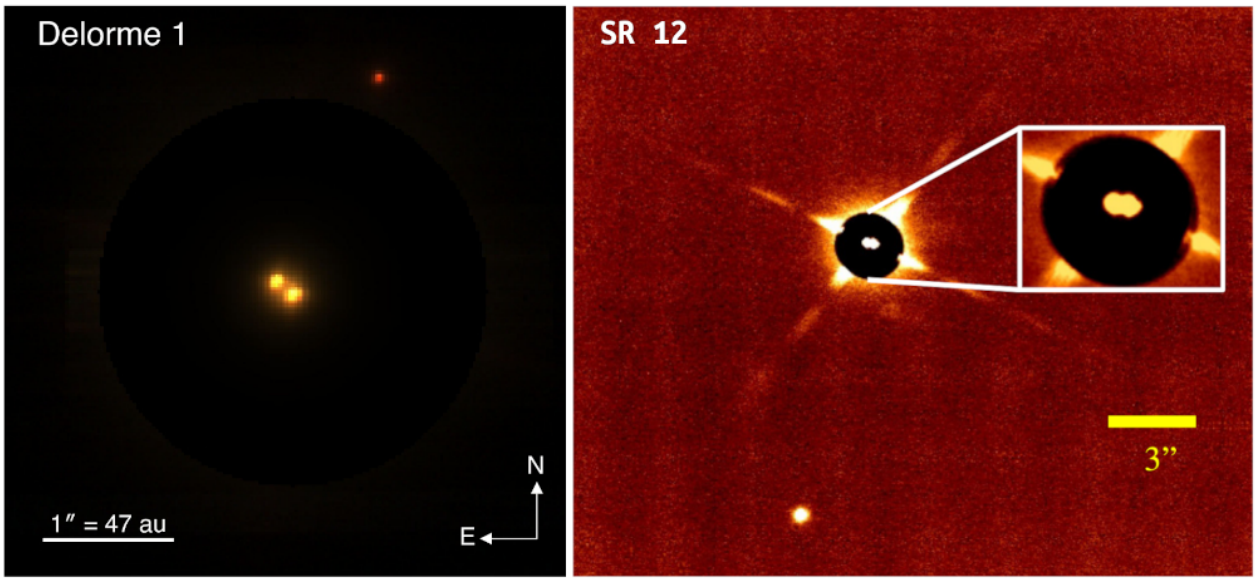


Figure III.1: Left: image of the Delorme 1 AB system, with the binary in the middle and the companion Delorme 1 (AB)b in the upper right (Eriksson et al., 2020). Right: Image of the SR 12 system, with the binary in the middle and the companion SR 12 c at the bottom Kuzuhara et al. (2011).

for Delorme 1 (AB)b, where the variability would be sampled from randomly spaced observations, SR 12 c was observed over 4 consecutive nights, for 4 hours each night, thus sampling the short term variability. For data reduction and and results of SR 12 c and 2MASS J11151597, see the dedicated sections (Sects. 6 and 7). In this section, I present the three targets.

2.1 Delorme 1 (AB)b

Delorme 1 (AB)b is a relatively *wide* separation $\sim$ 13 M_{Jup} companion ($\sim$ 1.77" – 84 AU Delorme et al., 2013), orbiting a tight binary ($\sim$ 0.25" – 12 AU) of M5.5 stars. It is the nearest of the known accreting PMCs, located at 47.2 ± 3.1 pc (Riedel et al., 2014). While relatively young, it is much older than commonly studied young PMCs: it is associated to the Tucana-Horologium association (Gagné et al., 2018), which makes it $\sim 30 - -45$ Myr old. This companion was classified as an $\sim$ L0 spectral type (Eriksson et al., 2020).

If we assume that accretion scales down to the PMC regime, its age should make it an unfavorable target for the study of accretion. It is not not embedded in a disk, and should have had its disk dispersed already. However, still in the context of accreting stars, some low-mass stars have been shown to bear disks even at advanced ages (Luhman, 2022). It is also possible that accretion follows a different trend in the PMC regime, and that older system with a disk are not that uncommon. Nevertheless, JWST observations are showing that it bears an infrared excess, sign of a CPD (Kim Ward-Duong, priv. com.).

Only a few authors have studied Delorme 1 (AB)b and its accreting properties. The first detection of an accretion line on that target was done by Eriksson et al. (2020). They detected strong H_α and H_β emission, Helium and CaII lines, with the Helium line being the most defining features of accretion, as they require temperatures that can only be attained in an accretion shock. Using stellar relations (Alencar et al., 2012;



Alcalá et al., 2017), they derived accretion rates of $\log \dot{M} \sim (-9.37 - 9.79) \pm 0.5$ M_{Jup}/yr[1], depending on the line. Pa_β, Pa_γ and Br_γ lines were also identified on that target (Betti et al., 2022,), yielding accretion rates of $\log \dot{M} \sim (-8.25 - 8.82) \pm 0.75$ M_{Jup}/yr using the same scalings, and $\log \dot{M} \sim -7.30 \pm 0.30$ M_{Jup}/yr using planetary scalings Aoyama et al. (2018). The higher end of the Balmer series (H_γ, H_δ, H_ϵ, ...) also was detected by Ringqvist et al. (2023), although with UVES and resolutions never reached before in the context of PMC ($R \sim 50\,000$), from which was derived an accretion rate of $\log \dot{M} \sim -7.70$ M_{Jup}/yr using planetary scaling, compatible with the value derived by Betti et al. (2022) from NIR lines. This makes Delorme 1 (AB)b the perfect candidate for study of PMC accretion, with bright lines, and a reasonable angular separation that can be achieved under good seeing conditions with VLT-like telescopes..

2.2 SR 12 c

SR 12 c is a 13.5 ± 1.5 M_{Jup} PMC (Kuzuhara et al., 2011). Its age is estimated that that of its formation region (ρ Oph): $2.1^{+7.9}_{-1.8}$ Myr. Similarly to Delorme 1 (AB)b, SR 12 c is orbiting a tight binary (~ 0.21" – ~ 26 AU) of K4 and M2.5 stars (respectively 1.05 $M_\odot$ and 0.5 $M_\odot$). However, it is located at a much higher separation than Delorme 1 (AB)b: ~ 8.7" – 975 AU at 112.3 ± 5.4 pc (Gaia Collaboration et al., 2018). Bowler et al. (2014) classified it as a M9 $\pm$ 1 spectral type, with $T_{\rm eff} = 2400^{+155}_{-100}$ K.

Santamaría-Miranda et al. (2018) presented XSHOOTER observations of SR 12 c. They retrieved the whole Balmer series, the Pa_β line, as well as OI8446 and CaII8542 lines, clearly advocating for ongoing accretion. The gas reservoir of that system was unknown until recently, as no evidence of an IR excess was found. However, given its young age and the many different tracers of accretion, it is likely that SR 12 c bears a disk. This was confirmed recently when ALMA observations detected mm-emission from the target (Wu et al., 2022).

2.3 2MASS J11151597+1937266

2MASS J11151597 was identified as young object (5–45 Myr) with low surface gravity and L2 spectral type (Theissen et al., 2017). Its mass is still unconstrained, within the 7–21 M_{Jup} range (Theissen et al., 2018). It is located at 45.21 ± 2.20 pc, and is not part of any clear moving group: a true lonely PMO. However, Theissen et al. (2018) also identified a potential companion: 2MASS J11131089+2110086, though recently published GAIA distance (57.67 ± 0.84 pc) now raises questions on the co-evolution of these two objects (see Sect. 7).

In the context of accretion, 2MASS J11151597 has Hydrogen and Helium lines (Theissen et al., 2018) that were also retrieved from archival spectra (SDSS, York et al., 2000). They are the clear sign of ongoing accretion, confirmed by the presence of a disk from MIR excess (Theissen et al., 2018).

3 The UVES spectrograph

The UV-Visual Echelle Spectrograph (UVES, Dekker et al., 2000) is a seeing-limited echelle spectrograph located at the Nasmyth focus of UT2 at the Very Large Telescope (VLT, Chile/Paranal). Its first light was in September 27, 1999[2]. It is designed to have a *high*-throughput (1%) and a high spectral resolution in the near UV and Visible range (300–1100nm), using a long-slit of adaptable width. It provides access to (1+1λ)D dimensions image (so-called trace): 1 spatial dimension and 1 spectral dimension, and was originally

[1]The error bar is the mean of error bars of the different lines
[2]**September 27, 1999**: https://www.eso.org/public/news/eso9944/



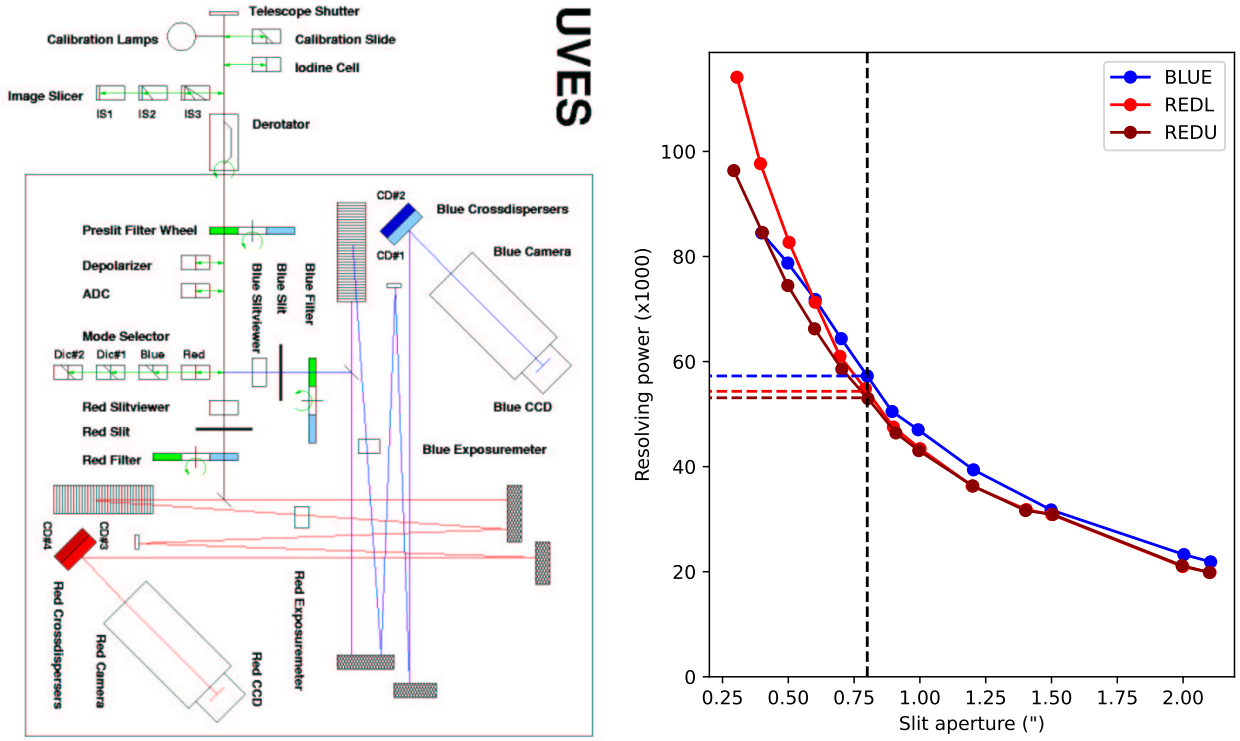


Figure III.2: Left: schematic of the UVES light path. Obtained from UVES manual. Right: resolving power depending on the detector, as a function of the slit aperture, for a 1×1 binning setup. The points were digitialized from UVES manual using WebPlotDigitizer[4]. The black dashed and corresponding colored dashed lines represent the slit aperture used for this study, and the corresponding resolving powers.

designed for high mechanical, transmission, and wavelength calibration stability. Another mode allows for multi-objects spectroscopy, coupled with FLAMES (on the otherside of the Nasymth platform), but was not used in this work.

3.1 Instrument description

As per UVES manual[3], it is made of 4 sub-systems: the preslits, two spectrograph arms, the Slit-Viewer (SV) CCDs and the scientific CCDs, all described below. It is able to cover a broad wavelength range (3000–11000 AA) in a single observation, with the use of its two BLUE and RED arms. This whole section is *highly* inspired by the instrument description from the manual. A schematic view of the optical path is shown in Fig. III.2.

[3]**UVES manual**: https://www.eso.org/sci/facilities/paranal/instruments/uves/doc.html



3.1.1 The preslits

The *preslits* refer to all systems that take place, in the optical path, before the slit that causes the main diffraction. These can be pictured as pre-processing functions for the light beam. For simplicity, green elements were used in this study, red elements were not used in this study. The relevant elements for this chapter are:

- The calibration unit contains the arc lamps (Thorium-Argon and Deuterium) that are used for day-time calibrations and provide the wavelength solution.
- The iodine cell, which is used to add a template transmission component within the observed spectrum, later to be used a wavelength calibration reference. It is only useful if the target is bright enough to be able to see transmission effects, which is not the case for neither SR 12 c nor 2MASS J11151597. The iodine cell was never used in our observations, although the binary host star in the Delorme system would have been bright enough for its use. However, we chose to keep the default wavelength calibration plan.
- The image slicer allows to reach high resolutions (R∼50 000–100 000) without enduring slit-losses due to the limited slit opening. However, this also eliminates the spatial dimension of the instrument. The spatial dimension was key to disentangle host star and companion for Delorme 1 (AB)b, therefore the image slicer was not used. In the case of SR 12 c and 2MASS J11151597 however, the targets are isolated and slit-loss effects may be important in cases of bad seeing. According to Fig. 2.3 of the manual, the image slicer #3 has slightly better througput than a straight 0.7" slit aperture, and could have been relevant for these targets.
- The virtual image slicer is only relevant in the case of bright stars that would otherwise saturate the detectors, even at the lower DITs. This is irrelevant to the case of planetary-mass companions, and therefore was not used.
- The derotator allows for field derotation of the field that is induced by earth rotation. Two modes are available: SKY mode which rotates the field to a constant orientation, ELEV mode which rotates the field so that the slit is always aligned with the atmospheric dispersion axis. Because in the case of Delorme 1 (AB)b we wanted the slit to be always placed in the host–companion axis, we chose the SKY mode, and corrected for atmospheric dispersion using the ADC.
- The Atmospheric Dispersion Corrector (ADC) allows for correction of the atmospheric dispersion, which is best suited for the derotator SKY mode. It is made of two counter-rotating prisms.
- The arm selector consists in a set of mirrors that can reflect lights to either of the RED/BLUE arms, or both at once using the dichroic plates. The single-arm mirrors, however, have better efficiencies than the dichroic plates. We used the dichroic plates as the goal was to target the whole Balmer series, of which lines are located in both arms.
- The slit-viewer images the field of view of the telescope, with slit-field overlapped. It is used for the acquisition and permits to track where the telescope is pointing at any time, along with what is actually within the slit aperture. However, in the case of isolated companions/targets, it is likely that no stars would be visible in the field. With most of the light from the target being within the slit aperture, only wings of the PSF would be apparent in the slit-viewer, but likely too faint to be visible.

[4] **WebPlotDigitizer:** https://apps.automeris.io/wpd/



Table III.1: Instrument setup

Target	DIT	Derotator–ADC	Guiding	Mode	Cross Disp.	Filter	Read-out
Delorme 1 (AB)b	1482s	SKY–AUTO	BLUE	DIC1	CD#2	HER_5	225 kHz, 1 × 2, low
					CD#3	SHP700	225 kHz, 1 × 2, low
SR 12 c	1482s	SKY–AUTO	RED	DIC1	CD#2	HER_5	225 kHz, 1 × 2, low
					CD#3	SHP700	225 kHz, 1 × 2, low
2MASS J11151597	740s	SKY–AUTO	RED	DIC1	CD#2	HER_5	225 kHz, 1 × 2, low
					CD#3	SHP700	225 kHz, 1 × 2, low

3.1.2 The two spectrograph arms

UVES is divided into two spectrographic arms, that can be used simultaneously (or not) depending on the mirrors or dichroic plates. The main elements of each arm are: (i) the slit itself, (ii) the below-slit filter and (iii) the echelle grating. The adjustable slit can be opened to widths between 0.15 and 20". Maximum resolutions are achieved for an opening of $\sim$ 0.3". Its technical maximum length is 30", but it is limited by the echelle grating: typically 8–10" in the BLUE arm, and 10–12" in the RED arm (see Table. 3.1 in UVES manual). The slit opening is the only way to affect the spectral resolution: a higher slit opening leads to lesser slit-losses, but lower spectral resolution (see Fig. III.2b). The below-slit filter serve the purpose of stray-light rejection and orders sorting. They are used in combination with the BLUE/RED mirrors or dichroic plates. The echelle gratings provide the final resolving tools.

3.1.3 The scientific CCDs

The BLUE arm detector consists in a single CCD (2048×3000 px, 15 µm/px), while the RED arm is made of a mosaic of two CCDs (2×2048×4096 px, 15 µm/px). The two RED-arm CCDs have a small gap between them, which translates in a sectral gap 50–100 Å gap in the final spectrum. Both detectors can be read in *low*-gain and *fast* read-out, or *high*-gain and *slow* read-out modes. Pixels binning is also possible for faster read-out in the following configurations: (1 × 1), (1 × 2), (2 × 2), (2 × 3), (spatial_dimension × spectral_dimension). The spectral binning does affect the effective spectral resolution through sampling criterion, but the effect is marginal. In this study, we used the low-gain, fast read-out (225 kHz), 1 × 2 binning mode. he choice was giving the best signal-to-noise per resolution element for our exposure times according to the exposure time calculator of the instrument (ETC[5]).

3.2 Data acquisition and reduction

3.2.1 Observations setup

The instrument setup was almost the same for all three targets (Delorme 1 (AB)b, SR 12 c, 2MASS J11151597). We only changed the guiding camera, which was the BLUE one for Delorme 1 (AB)b, and the RED one for SR 12 c and 2MASS J11151597. The reason is that Delorme 1 (AB)b observations followed the pilot study (Ringqvist et al., 2023), that used the BLUE arm as the guiding arm. We chose to keep the exact same instrumental setup for the Delorme 1 (AB)b series. For SR 12 c and 2MASS J11151597, however, we chose to perform the acquisition in the RED arm because of their context: SR 12 c is quite *far* from its host star, while 2MASS J11151597 is a lonely target. We performed Even though the acquisition was performed on a

[5]**ETC**: https://www.eso.org/observing/etc/bin/gen/form?INS.NAME=UVES+INS.MODE=spectro



nearby bright star (the host star for SR 12 c), followed by a *blind-offset* to the target, both objects are intrinsically brighter in the RED arm than in the BLUE arm, and were easier to detect in the RED slit-viewer, especially given the fact that only the PSF wings are visible in the slit-viewer. All-in-all, using the RED arm allowed us to be more confident on the target-centering without having to wait for the full exposure to be complete to check for the H_α line in the detector. Both SR 12 c and 2MASS J11151597 observations were performed in (designated/remote) Visitor Mode, in which I was involved. This gave me the opportunity to gain experience in the preparation and execution of observations at VLT. We did manage to see the PSF wings in the slit-viewer after $\sim$ 10mins of integration.

All observations were performed with the setup shown in Table III.1. Slit lengths are 8" for the BLUE arm and 12" for the RED arm. The first Dichroic plate (390–580nm), along with cross-dispersers CD#2 and CD#3 give wavelength ranges of 3260–4540 and 4760–6840 Å respectively. This provides access to the whole Balmer series (H_α, H_β, H_γ, ...) along with some Helium (HeI6680, HeI5877) and metal lines (NaII4836 doublet, FeI6233).

Delorme 1 (AB)b Delorme 1 (AB)b observations were performed by aligning the slit with the binary-companion axis (slit PA=335°), so as to see both the primary and the companion. Because of their relatively close separation ($\sim$ 1.8"), the primary's PSF will contaminate the companion signal, and we will be able to disentangle the primary's from he companion's signal using PSF fitting.

SR 12 c SR 12 c observations were performed by aligning the slit perpendicular to the primary-companion axis. The separation between the two is relatively large (8.7"), so contamination is quite unlikely. However, the primary is a CTTS, which is likely to show some variability. We cannot really predict the state of the star (quiescence/active phase) at the time of observations, so we chose to put it out of the field of view to avoid saturating the detectors. Even if we tried, the limited slit length in the BLUE arm (8") would not allow us to have access to both the companion and the star anyway. Looking back at these observations, it might still have been interesting to align the slit with the star-companion axis, at least to image the wings of the star's PSF, to check whether there is really, in fact, no contamination from the star. This probably does not matter too much as the PSF wings should be almost flat over the whole slit in the current setup, and a simple baseline subtraction should be sufficient to subtract any contamination. Another improvement could have been to use the ELEV mode for the derotator: the slit orientation does not matter so much for SR 12 c, so using the derotator to directly correct for atmospheric dispersion would have given the observations slightly more S/N compared to using the ADC. However, this would have made the primary enter the field at specific orientations, which would have required dedicated post-processing.

2MASS J11151597 2MASS J11151597 observations were performed with the derotator set to SKY (same as other targets), with PA set to 0°. Similarly to SR 12 c, using the ELEV mode would have provided a slightly better S/N, at the cost of observing a Tel. Std. in that specific setup as well.

Standard stars During the SR 12 c run, in which we also observed 2MASS J11151597, we performed observations of two Telluric Standard stars: HD 123426 and LTT 6248. Because the run was done in Visitor Mode, ESO does not provide automatic calibration observations, and it was our duty to perform them. For Delorme 1 (AB)b, however, observations were performed in Service Mode, so standard stars were observed during the observing nights as part of the ESO Calibration Plan. The standard stars are crucial for determining the instrument response curve, as will be detailed in the following section.



Thesis' Table of Contents
Chapter's Table of Contents

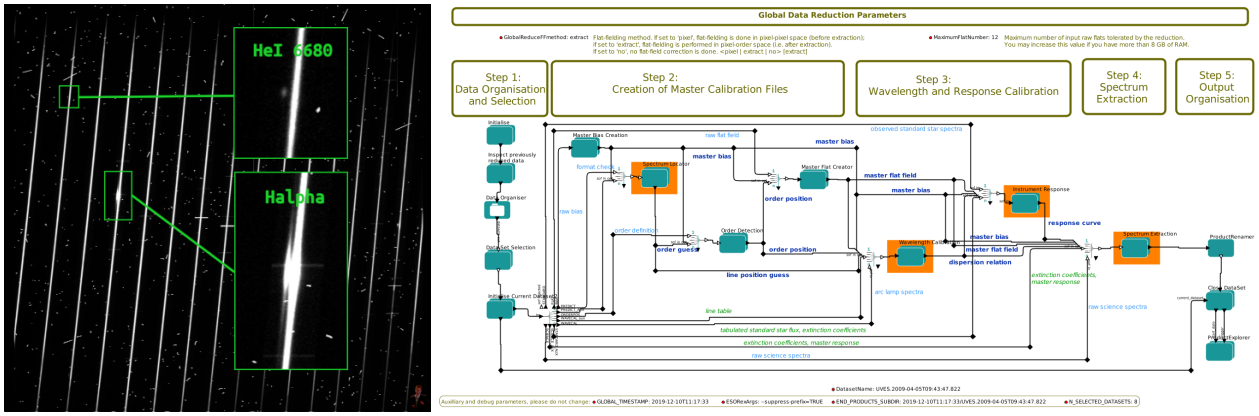


Figure III.3: Left: Raw image of the REDU detector of one of Delorme 1 (AB)b observations. Tilted lines correspond to different diffraction orders (wavelengths) of the primary star. Green boxes show the location of the H_α and HeI6680 lines, where the companion is clearly distinguishable from the primary star. Right: schematic view of the pipeline reduction chain: screenshot from EsoReflex (Freudling et al., 2013).

3.2.2 General reduction – ESO pipeline

ESO provides an automated pipeline for data reduction of observations from ESO telescopes. It is accessible as the EsoReflex[6] software. Esoreflex is designed as a all-in-one software, that corrects raw data from all instrumental (and atmospherical effects), with outputs being straight science products (1D spectra) or (un)calibrated ancillary files (2D spectra).

As per Sect. 9.3 of the pipeline manual[7], the data reduction cascade is as follows:

- Creates the master BIAS from day-time calibration files.
- Creates the master DARK frame from day-time calibration files.
- Finds the location/orientation of each diffraction order on the detector, using continuum-lamps exposures.
- Creates the master flat from day-time calibration files.
- Creates the wavelength solution using exposures with an internal calibration source producing multiple well-calibrated emission lines: so-called arc lamps.
- Computes the instrument response curve, using Standard Star exposures, master bias, master dark, master flat, orders positions, wavelength solution, atmospheric extinction curve (static calibrations within the pipeline) and a reference flux ($f(\lambda)$) for the standard star.
- Runs the main reduction routine (uves_obs_redchain), that generates either the 1D (not-)calibrated spectrum or the 2D (not-)calibrated 2D spectrum.

[6] **EsoReflex**: https://www.eso.org/sci/software/esoreflex/
[7] **pipeline manual**: https://www.eso.org/sci/software/esoreflex/



An example of a raw frame is shown in Fig. III.2, left panel, for one of Delorme 1 (AB)b observations. A schematic view of the reduction chain is shown in Fig. III.2, right panel. The exact details of data reduction for each target (Delorme 1 (AB)b, SR 12 c, 2MASS J11151597) will be given in the corresponding sections, as the process was slightly different between targets, in particular for Delorme 1 (AB)b which did not really require us to re-run the ESO pipeline.

4 Observations and data reduction

4.1 Observations

The description of observations is given below, for each target. The instrument setup for each target is provided in Table. III.1. The observation log for each target is provided in Tables. III.2, III.4 and III.5.

4.1.1 Delorme 1 (AB)b

Delorme 1 (AB)b was observed with VLT/UVES in Service Mode (SM), as the main (and only) target of the program 110.23VU.001[8] (PI: Bonnefoy). The observations were performed randomly during the Fall-Winter of 2022-2023. We aligned the slit on the primary–companion axis (PA=334.9° in ESO/P2[9]), so as to observe both of them at once, thus using the primary as a reference for flux calibration. The observations make use of the DIC#1 mode, providing access to both the BLUE and RED arm simultaneously, with the 225 kHz, 1x2, low-gain readout mode. The slit was opened at 0.8", for an effective spectral resolution of $\sim 50\,000$. For each observation sequence, dithering was performed in an ABBA pattern to mitigate bad-pixels effects. Each OB consists in 2 exposures of DIT=1482s each. The derotator was set to SKY mode, therefore following the field rotation and keeping the slit aligned on the primary–companion axis. The ADC was set to AUTO, therefore correcting for atmospheric dispersion. The guiding was performed in the BLUE arm. This study also uses observations performed in the same setup, on 2021-10-25 (Program 108.21ZE.001[10], PI: Janson). The observation log is provided in Table. III.2.

4.2 Delorme 1 (AB)b: Reduction

Delorme 1 (AB)b observations were reduced following the steps presented in this section: PSF profile fitting, contamination correction, instrumental effects, flux calibration. All work was performed using the 2D reconstructed slit, described in the next section.

4.2.1 ESO automated reduction

In the case of UVES, ESO provides an automated data reduction of all UVES observations, performed every couple months[11]. This reduction is performed by running the UVES pipeline in its default settings.

Available data files include: calibration files, raw exposures, fully processed 1D spectra and ancillary files. The fully processed 1D-spectra are corrected for both instrumental effects (if possible) and atmospheric extinction. According to the manual, instrument transmission can only be computed if a Standard Star observation is available. While no Tel. Std. was observed as part of our observations, Tel. Std.s are included

[8] **110.23VU.001**: https://archive.eso.org/wdb/wdb/eso/sched_rep_arc/query?progid=110.23VU.001
[9] **ESO/P2**: https://www.eso.org/sci/observing/phase2/p2intro.html
[10] **108.21ZE.001**: https://archive.eso.org/wdb/wdb/eso/sched_rep_arc/query?progid=108.21ZE.001
[11] https://www.eso.org/rm/api/v1/public/releaseDescriptions/163



Target	Date (HH-MM-DD)	UT start (hh:mm:ss)	UT end (hh:mm:ss)	DIT (s)	seeing (")	airmass	τ_0 (ms)
Delorme 1 (AB)b	2021-10-25	05:42:33	06:07:15	1482	0.53	1.31	10.50
Delorme 1 (AB)b	2021-10-25	06:07:57	06:32:39	1482	0.49	1.38	11.30
Delorme 1 (AB)b	2022-10-13	02:52:03	03:16:45	1482	1.06	1.20	1.90
Delorme 1 (AB)b	2022-10-13	03:17:23	03:42:05	1482	1.25	1.18	2.20
Delorme 1 (AB)b	2022-10-14	06:52:50	07:17:32	1482	0.45	1.38	7.70
Delorme 1 (AB)b	2022-10-14	07:18:09	07:42:51	1482	0.52	1.46	8.10
Delorme 1 (AB)b	2022-10-15	04:40:38	05:05:20	1482	0.62	1.17	7.40
Delorme 1 (AB)b	2022-10-15	05:05:57	05:30:39	1482	0.56	1.19	10.20
Delorme 1 (AB)b	2022-10-15	06:30:49	06:55:31	1482	0.54	1.33	4.50
Delorme 1 (AB)b	2022-10-15	06:56:07	07:20:49	1482	0.53	1.40	6.90
Delorme 1 (AB)b	2022-10-17	03:02:29	03:27:11	1482	0.91	1.18	4.70
Delorme 1 (AB)b	2022-10-17	03:27:48	03:52:30	1482	0.81	1.17	4.50
Delorme 1 (AB)b	2022-11-01	01:21:16	01:45:58	1482	0.78	1.22	2.20
Delorme 1 (AB)b	2022-11-01	01:46:35	02:11:17	1482	0.69	1.19	3.80
Delorme 1 (AB)b	2022-11-04	00:49:41	01:14:23	1482	0.68	1.25	6.40
Delorme 1 (AB)b	2022-11-04	01:15:00	01:39:42	1482	0.59	1.21	7.40
Delorme 1 (AB)b	2022-11-04	01:42:04	02:06:46	1482	0.54	1.19	5.10
Delorme 1 (AB)b	2022-11-04	02:07:24	02:32:06	1482	0.50	1.17	7.30
Delorme 1 (AB)b	2022-11-05	00:57:06	01:21:48	1482	0.90	1.23	6.10
Delorme 1 (AB)b	2022-11-05	01:22:25	01:47:07	1482	0.69	1.20	5.50
Delorme 1 (AB)b	2022-11-05	01:48:25	02:13:07	1482	0.68	1.18	4.40
Delorme 1 (AB)b	2022-11-05	02:13:44	02:38:26	1482	0.66	1.17	4.40
Delorme 1 (AB)b	2022-11-05	02:40:34	03:05:16	1482	0.68	1.16	6.10
Delorme 1 (AB)b	2022-11-05	03:05:51	03:30:33	1482	0.64	1.17	7.10
Delorme 1 (AB)b	2022-11-05	03:36:05	04:00:47	1482	0.73	1.19	5.80
Delorme 1 (AB)b	2022-11-05	04:01:24	04:26:06	1482	0.84	1.21	5.30
Delorme 1 (AB)b	2022-12-04	00:46:22	01:11:04	1482	0.64	1.16	8.40
Delorme 1 (AB)b	2022-12-04	01:11:41	01:36:23	1482	0.64	1.17	9.20
Delorme 1 (AB)b	2022-12-04	01:41:03	02:05:45	1482	0.63	1.19	6.60
Delorme 1 (AB)b	2022-12-04	02:06:22	02:31:04	1482	0.74	1.21	5.60
Delorme 1 (AB)b	2022-12-31	01:05:53	01:30:35	1482	0.61	1.28	4.60
Delorme 1 (AB)b	2022-12-31	01:31:12	01:55:54	1482	0.56	1.34	5.10
Delorme 1 (AB)b	2023-01-02	01:13:31	01:38:13	1482	0.45	1.32	7.00
Delorme 1 (AB)b	2023-01-02	01:38:50	02:03:32	1482	0.53	1.38	6.50

Table III.2: Delorme 1 (AB)b's observation log.



as part of ESO calibration plan (Stds. are observed within the same night with common instrumental setups), thus making instrument transmission correction possible. Ancillary files include both the 1D and 2D spectra. The automated reduction plan's manual mentions that 2D spectra are corrected for both instrument transmission and atmospheric transmission. However, we found that they were not: the manually extracted spectrum from a 2D file is equal to that of an 1D un-calibrated spectrum. We corrected for these effects as per Sect. 4.2.5.

The point of this chapter is to study accretion properties of the Delorme 1 (AB)b companion, which is hidden within the wings of the primary's PSF. This whole section therefore uses 2D ancillary files (which include 1 spatial dimension) to try and retrieve its spectrum. These files are the starting point of the following data-reduction. All the work was performed on individual frames. There was no prior combination of the jittered frames.

4.2.2 Cosmics rejection

Cosmics identification is a crucial step, as they may lead to fitting problems or other un-physical results. For example, they can mimic the presence of an emission line. In the context of Delorme 1 (AB)b, they were identified in the data using a custom version of the *modified-z-score* approach, as described here[12]. The default method consists in evaluating the standard variations (i.e., standard deviation of the first order derivative) in the data, and thresholding to a certain level. This works surprisingly well for identifying cosmics on a small wavelength range of a spectrum, where the continuum level is flat on average. This method was applied to the 2D reconstructed trace, for each spatial position, over successive small wavelength ranges. This avoids recognizing true variations of the spectrum (in particular in the primary's continuum), while also removing cosmics form the noise-level data. Cosmics were identified successively on 4 Å windows, with a threshold of 7σ on the standard variation. The process was performed iteratively, as existing cosmics may overestimate the *typical variation* estimate, letting fainter cosmics filter through the identification. This method iterates until no cosmic is found in the data. Typically, this takes about 50–200 iterations to complete.

4.2.3 Hynes method and spectra exctraction

In the trace, the wings of the primary's PSF extend to the companion location and contaminate its signal, in particular within its bright emission lines. I therefore developed a dedicated method, adapted from that of Hynes (2002), to correct for this effect.

Spectra were extracted from the reconstructed slitlet (ANCILLARY.2DSPECTRUM files from ESO archive), by PSF modeling and spatial integration over the model at each wavelength bin. The challenge is to find an appropriate PSF model. For UVES, the slit length is 12"/64px in the RED arm, and 8"/32px in the BLUE arm, which means the sampling is not the same. In fact, because the RED arm is divided into two detectors, the sampling even varies within the RED arm itself, this will be addressed later.

It is important to note that this PSF-fitting step is not as crucial for the extraction as it may sound. In fact, the crucial step is the computation of the residual contamination from the spectra. The PSF-fitting presented here only serves the purpose of obtaining a PSF that is better than a naive Gaussian, because the PSF has wings extending further than a Gaussian. If the PSF model were to be not satisfactory, the effects that this would introduce in the companion spectrum would be post-processed in the contamination subtraction step (see Sect. 4.2.4).

[12]**here**: https://towardsdatascience.com/removing-spikes-from-raman-spectra-8a9fdda0ac22



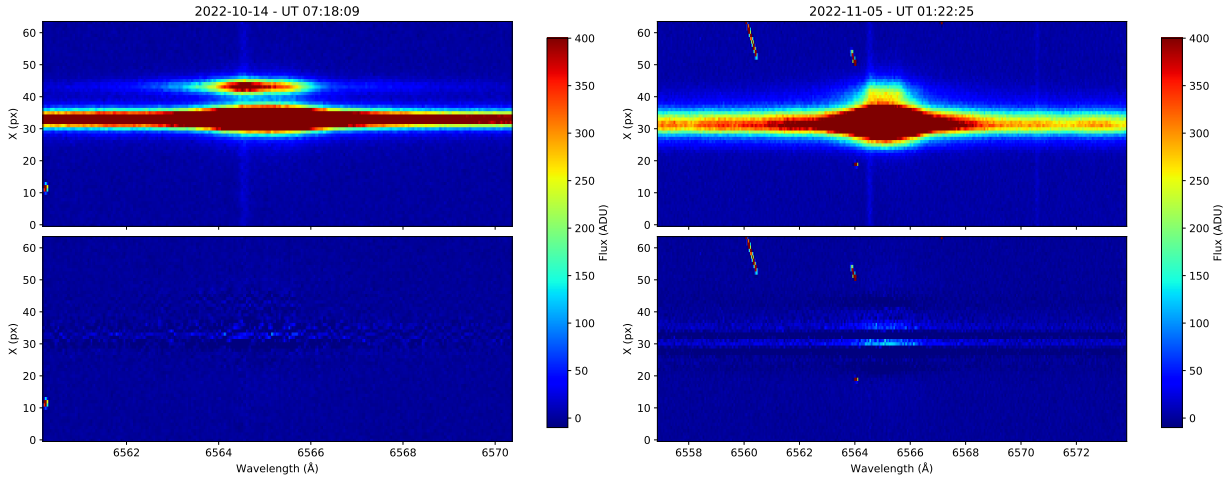


Figure III.4: 2D reconstructed slitlet (top) and the corresponding residuals (bottom) after PSF modeling for typical extraction results: good (left) and bad (right) observing conditions.

PSF model choice The companion is not visible in the raw data anywhere else than within its lines (see Fig. III.4), and even the primary's wings at the location of the companion are fairly noisy. Because the PSF shape is not expected to vary significantly over a small wavelength range, I decided to work on binned data, so as to increase the S/N at the companion expected location. The binning factor was 41, yielding an effective resolution of ∼1200. Even then, the companion is still not clearly visible outside of its emission lines. In fact, it only becomes visible for binning factors > 100, but this tends to reduce the number of data points too much for the PSF fitting method to be meaningful, especially in the BLUE arm, which wavelength's range is shorter than the RED arm. As for the PSF model, the choice was made with lots of trial-and-errors. UVES PSF is known to be intrinsically non-symmetrical. Therefore, my first idea was to choose a model that is made of multiple Gaussians, of varying width, intensity and position. However, the fitting procedure was quite unstable, slow, and hardly possible to generalize to all epochs as it required a lot of adhoc fine-tuning depending on the epoch. A much simpler and stable approach was to assume (at least at first) that the PSF *is* symmetrical, hence requiring all the Gaussians to be centered on the same value. This is the solution that was chosen: in the RED arm, the PSF is made of 3 overlapping Gaussians, of varying width and relative intensity, and only 2 Gaussians for the BLUE arm. The BLUE/RED arm discrepancy was motivated by their different sampling: the BLUE arm does not have enough data points to allow for a 3 Gaussians model. However, even if the companion signal's is intrinsically fainter in the BLUE arm than in the RED arm, so is the primary's signal. What really matters is the contrast between the two, which is actually much more favorable in the BLUE arm than in the RED arm, thus making contamination less of an issue (see Sec. 4.2.4).

PSF fitting – short story The PSF-modeling was performed following the procedure described in Hynes (2002). In short: the PSF is fitted at each wavelength bin, then all parameters are smoothed through polynomial regularization, which polynomial expression will give the value of each parameter. That method was specifically developed for de-blending targets in slit-spectroscopy observations. However, the method was proposed for de-blending two **bright**-ish targets, whose PSF's are somewhat clearly visible. This is not the case here, and I therefore propose an adapted version of that method, developed for the case of



Delorme 1 (AB)b, but which could be (in principle at least) extended to any 2D-slit based observations. Put simply, the PSF is assumed to be the sum of 3 Gaussians in the RED arm, and 2 in the BLUE arm. Their parameters are regularized in the wavelength dimension to reduce the fitting noise at a given spectral bin.

PSF fitting – long story The PSF fitting is performed in an iterative fashion, by fitting only the Primary's PSF and successively setting every single parameter. The companion will be dealt with in the next step. Each of the 3 (or 2 for the BLUE arm) Gaussians are described relative to the previous one, to keep the ordering. In practice, both the normalization factor and width of a Gaussian are given as ratios of the previous one. Only the first Gaussian parameters are given *as is*. All Gaussians have the same centroid. An additional parameter, a baseline (flat/uniform), is included to account for sky emission. Fits are performed at each wavelength bin, they are plotted as black crosses in the first column of Figs. III.5 & III.6 for the RED arm, and Figs.III.7 & III.8 for the BLUE arm, each representing cases of a narrow and wide PSF. There is quite a wide spread of some parameters (especially *constrast1* and *contrast2*), that cannot be fitted with a polynomial straight away: here is the difference with Hynes (2002) method. Instead, regularization is performed in an iterative fashion. In this first iteration, the width of the brightest Gaussian (*sigma0*) is regularized with a 5th-order polynomial (1st-order for the BLUE arm), as represented by the red line in the same figures. From now on, that parameter will be set to its polynomial expression. The fit is performed once again (2nd column), an another parameter is set to its polynomial expression. This repeats until all Gaussians width and contrasts have been set to a polynomial expression. The centroid (position), main normalization factor ($\sim$ primary spectrum), and baseline (flat/uniform sky component), are never set to a polynomial expression, and instead are always set as free parameters. The order in which parameters are successively regularized is also always the same. It was set by order of importance of each Gaussian: main Gaussian, secondary Gaussian, third Gaussian. In terms of parameters: width of the main Gaussian, relative width of the secondary Gaussian to the main Gaussian, contrast between the secondary and main Gaussian, relative width of the third Gaussian to the secondary Gaussian. Same thing happens in the BLUE arm, without the third Gaussian.

Companion fitting The final PSF model (with regularized parameters) is now used to fit simultaneously the primary and the companion PSF (see Fig. III.9). This requires two additional parameters: a normalization factor for the companion, and the position of the companion. The relative position of the companion to the primary (*dx)* is supposed to be constant, and should be properly set. I found that leaving the position as a free parameter led to bi-modal distribution of the continuum noise: the algorithm would fit noise rather than the faint signal of the companion. This would hinder any attempts at retrieving the continuum signal of the companion at a later stag. The algorithm does not use physical positions of pixels, therefore *dx* may vary depending on the optical path, either due to magnification or pixel sizes variations. This is especially true for the BLUE arm, for which the slit-length to pixel-number ratio is very different from that of the RED arm. In fact, I even find differences between the two detectors of the RED arm (REDL and REDU). *dx* for each detector is estimated a-posteriori, after having performed the full reduction process once with *dx* free. This is necessary, as *dx* is computed as the mean of all epochs. This step is thus only relevant for the second extraction. Only *dx* values within accretion lines (BLUE: H_γ to H_η; REDL: H_β; REDU: H_α, HeI6680, HeI5877) are used, because they are those where contamination from the primary's wings are only marginal. *dx*s are analyzed on a lines-per-line basis to find any wavelength-dependent effect other than that of the detector. I find that all lines of a single detector have *dx* consistent with each other, and they end up being merged for the final solution. Each distribution (Fig. B.1) is fitted with a 3-Gaussian mixture, of which the one with the smallest width is chosen as the value for dx. The associated errorbar is used as a



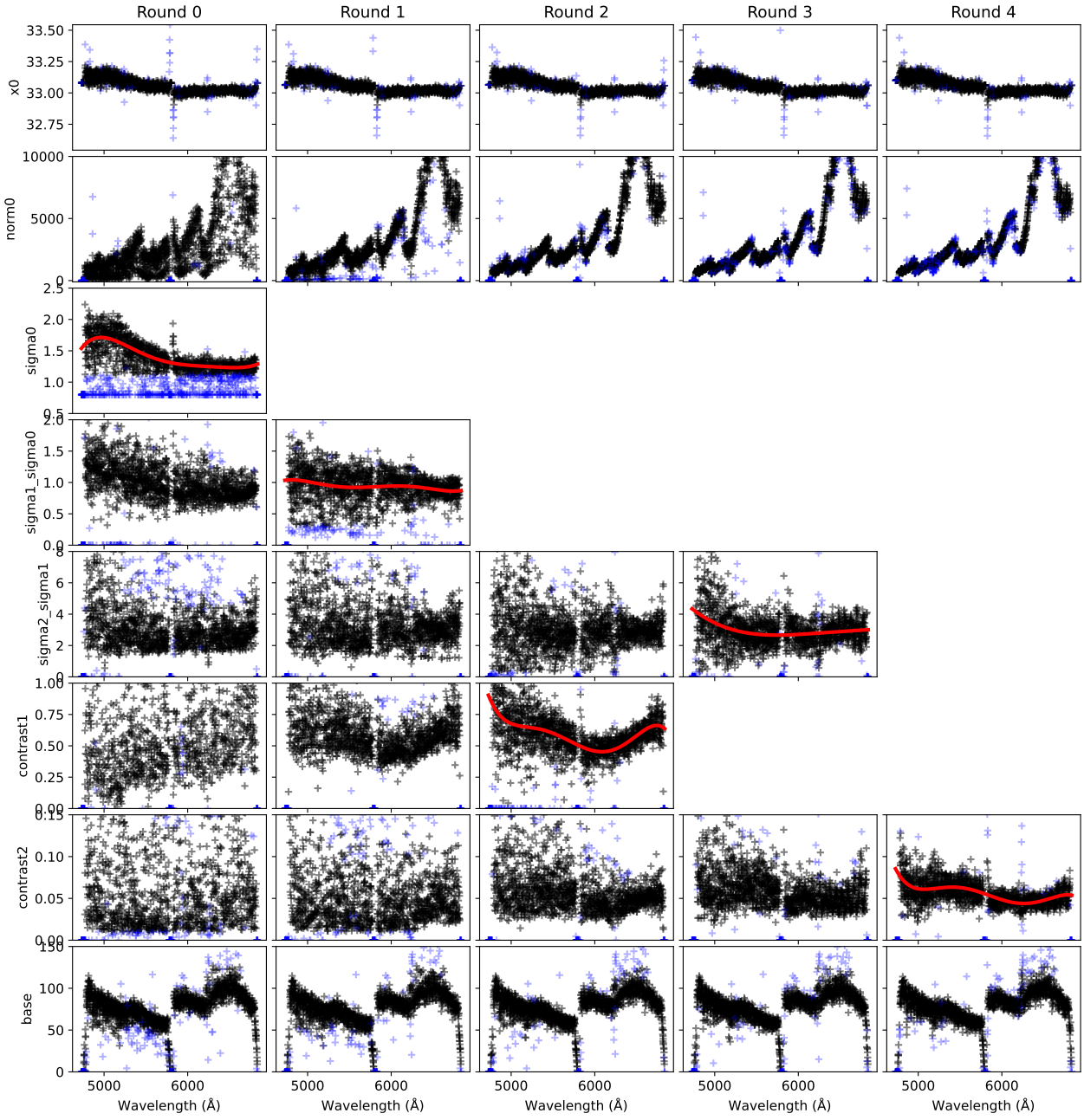


Figure III.5: Parameters regularization for epoch 2022-10-14 UT 07:18:09, last iteration, in the RED arm. Typical of an epoch with a narrow PSF. The red line is the 5th order polynomial by which the corresponding parameter was fitted for the given fitting round. After fitting, this parameter is set to its polynomial expression. Blue points were excluded from the polynomial fitting.

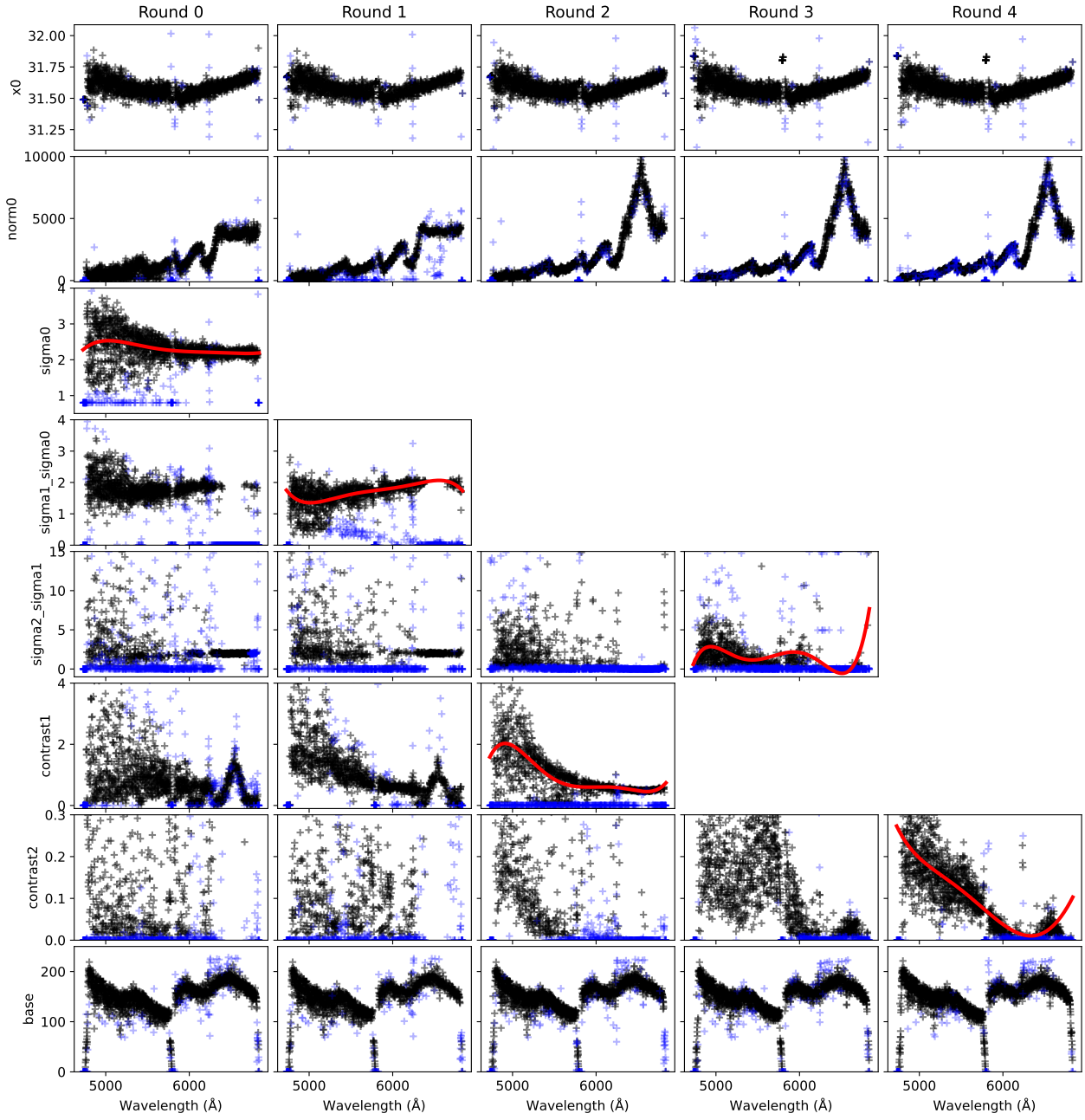


Figure III.6: Parameters regularization for epoch 2022-11-05 UT 01:22:25, last iteration, in the RED arm. Typical of an epoch with a wide PSF. The red line is the 5th order polynomial by which the corresponding parameter was fitted for the given fitting round. The blue points were excluded from the fit. After fitting, this parameter is set to its polynomial expression. Blue points were excluded from the polynomial fitting.

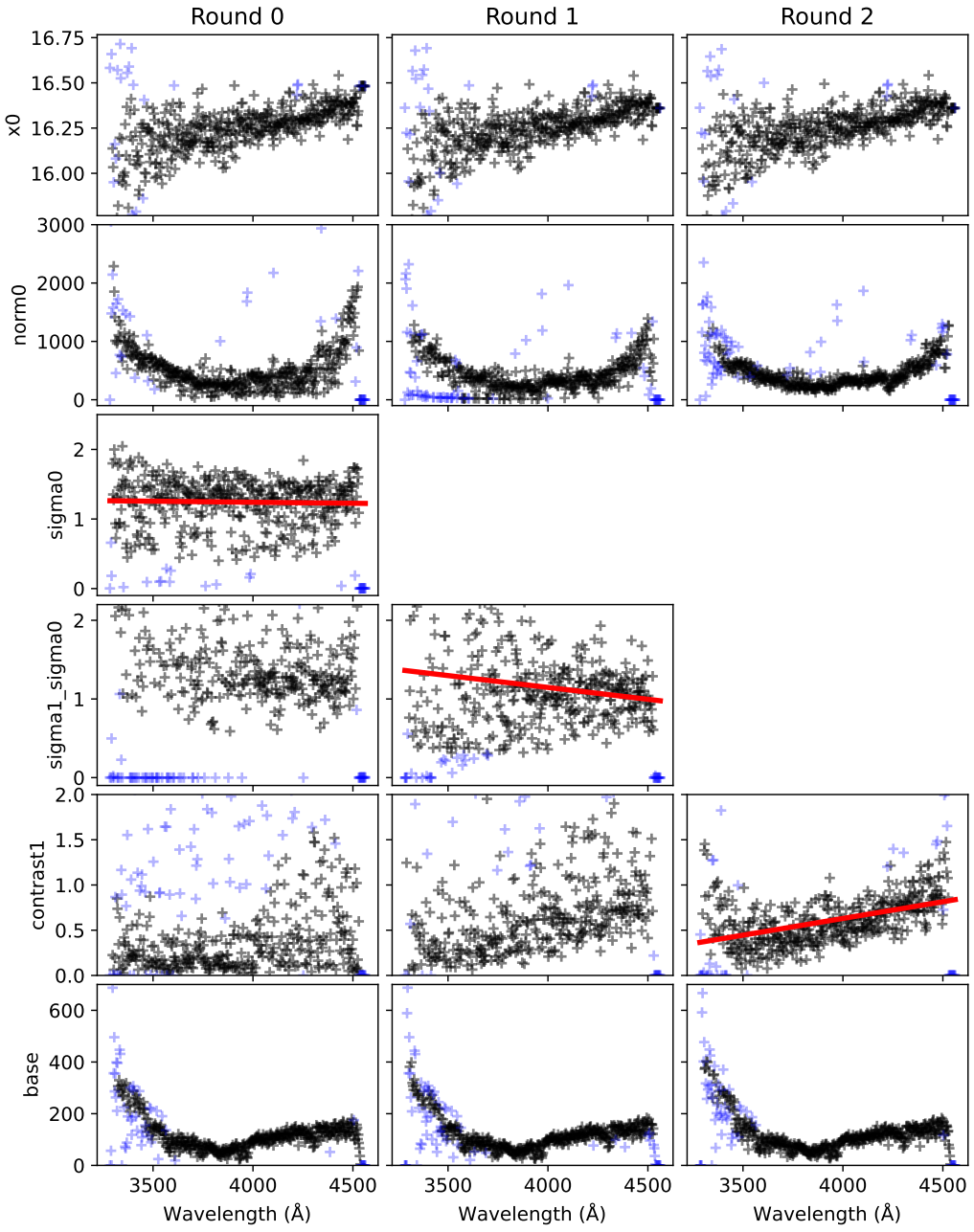


Figure III.7: Parameters regularization for epoch 2022-10-14 UT 07:18:09, last iteration, in the BLUE arm. Typical of an epoch with a narrow PSF. The red line is the 1st order polynomial by which the corresponding parameter was fitted for the given fitting round. After fitting, this parameter is set to its polynomial expression. Blue points were excluded from the polynomial fitting.

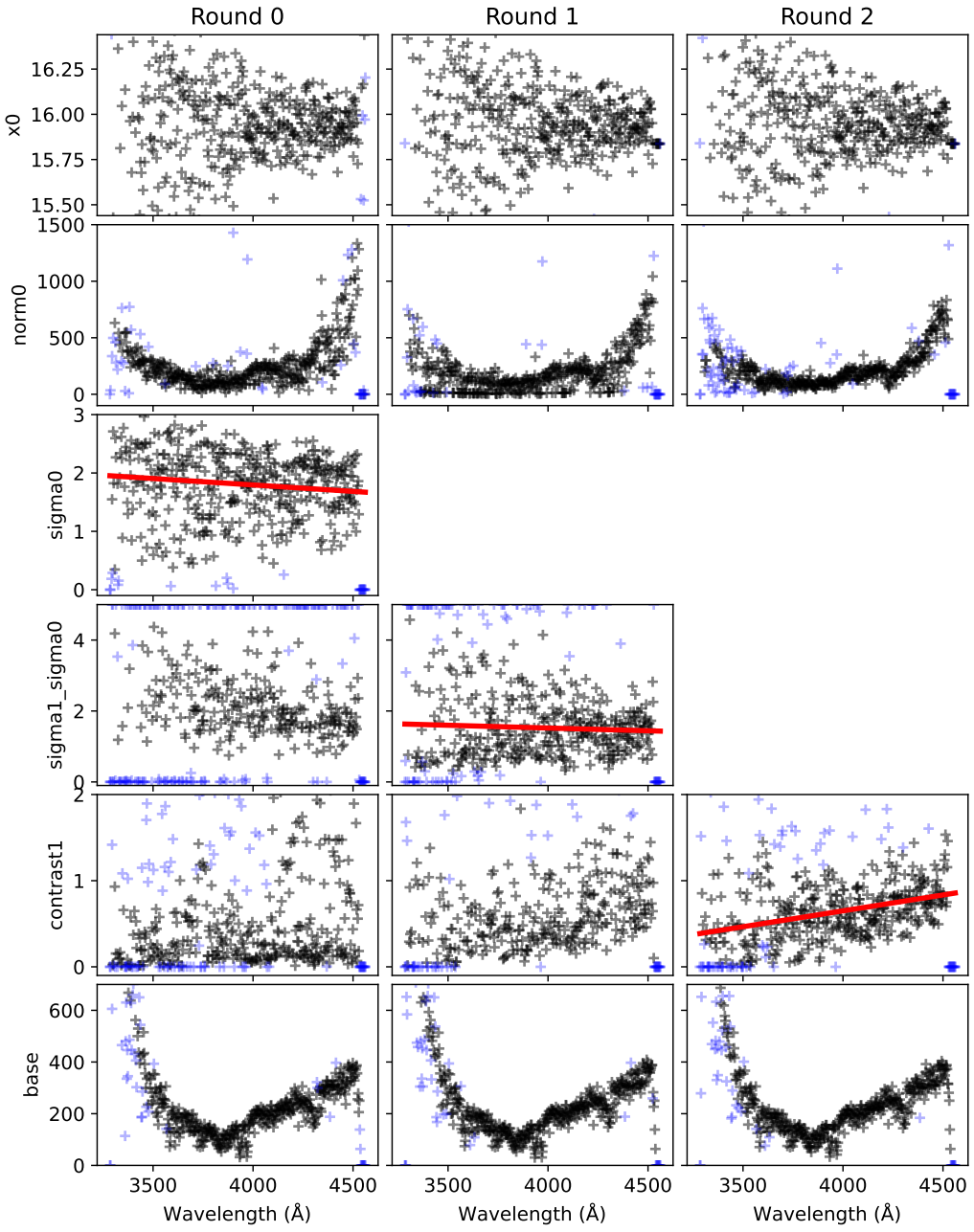


Figure III.8: Parameters regularization for epoch 2022-11-05 UT 01:22:25, last iteration, in the BLUE arm. Typical of an epoch with a wide PSF. The red line is the 1st order polynomial by which the corresponding parameter was fitted for the given fitting round. The blue points were excluded from the fit. After fitting, this parameter is set to its polynomial expression. Blue points were excluded from the polynomial fitting.

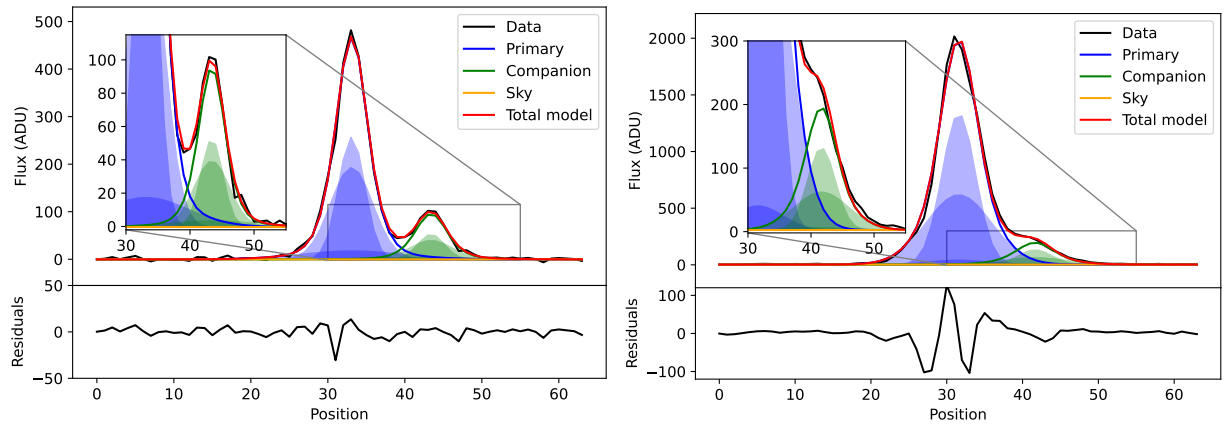


Figure III.9: Model fitting of both the primary (blue) and companion (green) within H_α on the reconstructed 2D slit. Left: epoch 2022-10-14, UT 07:18:09, which is typical of good observing conditions, with a narrow PSF. Right: epoch 2022-11-05, UT 01:22:25, which is typical of bad observing conditions with a wide PSF.

small window for *dx* variation for that second fitting, and is shown as the shaded regions in Fig. B.1. Once the *dx* parameter is set, both the primary's and companion's PSFs are fitted simultaneously. On a final note, setting the *dx* avoids fitting noise: the noise level is higher than that of the companion continuum level (at each wavelength bin), so letting *dx* free would make the algorithm fit noise, without being able to average it over multiple bins.

Iterations on the PSF fitting Once the fit on both the primary and companion PSF is complete, the companion model is subtracted from the initial data. Then, the whole process is repeated, fitting the primary's PSF, regularizing parameters one by one, then fitting the companion and primary PSF simultaneously. This repeats for a total of 4 iterations (see next paragraph). On the final iteration, both the primary's and companion's spectra are obtained by integration over their respective PSF model. This iterative process is able to mitigate the companion contribution to the PSF. This is especially important in epochs with *bad* observing conditions, where the companion is hardly distinguished from the primary, even within its bright lines (Fig. III.9, right panel).

On the convergence of the method The method involves a total of 4 iterations. The corresponding χ^2_r are shown in Fig. B.2. While the value decreases and converges for most epochs, others have their value increase with iterations. However, it should be noted that these χ^2_r values all stay within 5% of the value at the first iteration. This means that the PSF model does not change much along iterations. Once again, I stress that this PSF-fitting step mostly serves as a way of obtaining a PSF that fits the data better than a simple Gaussian. The next section will deal with all residual contamination in the spectra.

4.2.4 Contamination correction

The main assumption that allowed for PSF fitting is that the PSF is symmetrical. However, UVES' PSF is known to be intrinsically asymmetrical (see manual). I did not see any particular correlation with the seeing.



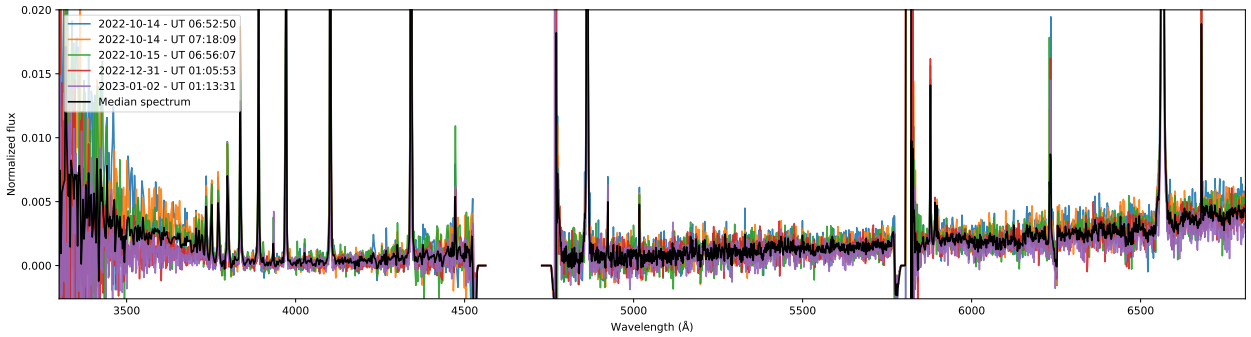


Figure III.10: Master spectrum used for the contamination correction.

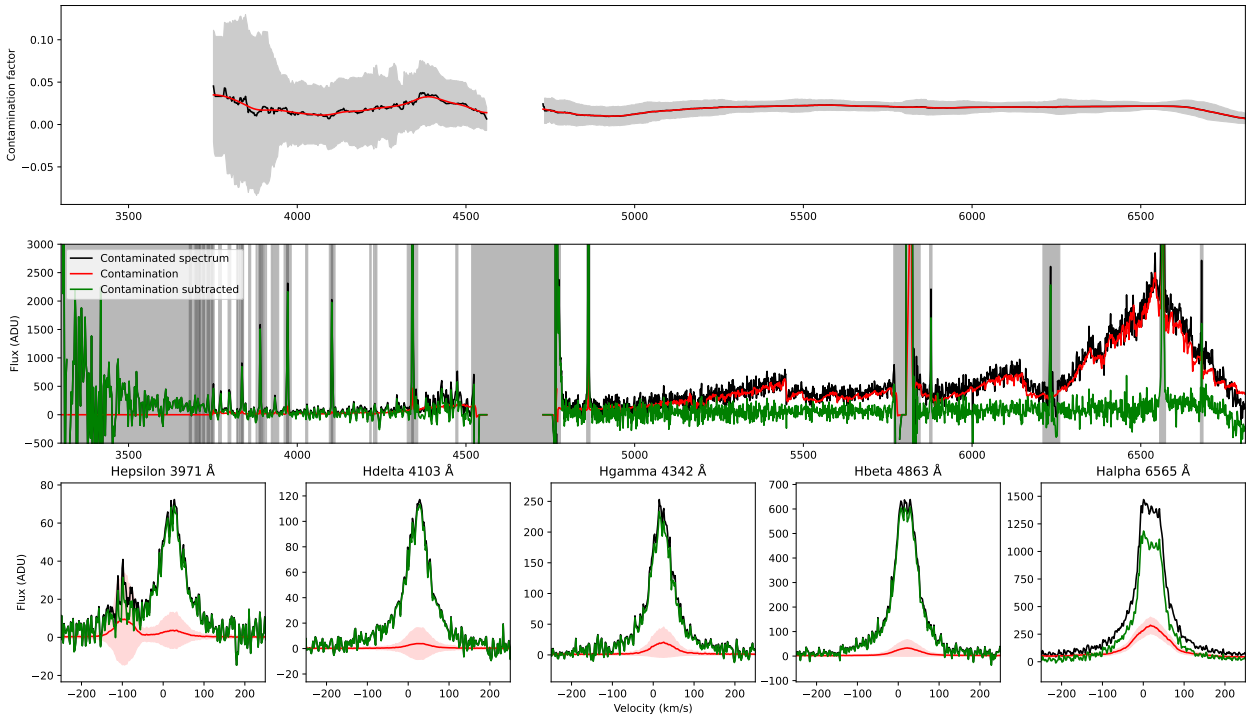


Figure III.11: Contamination correction for the worst epoch : 2022-11-05 UT 01:22:25. First row: the contamination factor (black). The contamination itself is computed as the product of this factor and the primary spectrum of the same epoch. Second row: contamination correction over the whole spectrum, with the original spectrum as extracted in the previous step (black), contamination (red) and corrected spectrum (green). The black shaded regions were excluded from the fitting process, they correspond to the expected lines of the companion, bad detector regions and the UV excess. Spectra are shown at low resolution for clarity. Third row: individual lines corrected from contamination.



This leads to an intrinsic contamination from the primary to the companion spectrum, no matter how good the PSF fit is. It is, however, worsen in the case of a *bad* PSF fit.

All-in-all, contamination does clearly appear in some epochs, either positive or negative, translating in the primary's spectrum features imprinting on the companion spectrum (see for example epoch 2022-11-05, first exposure, Fig. III.11, 2nd row, black line). The residual contamination is either:

- positive (positive imprint of the primary spectrum): when the primary's signal was underestimated at the location of the companion. The companion compensates for the lack of flux.
- negative (negative imprint of the primary spectrum): when the primary's signal was overestimated at the location of the companion. The companion compensates for the lack of flux.

The companion spectrum can be written $F(\lambda) = C(\lambda) + \alpha(\lambda) \cdot P(\lambda)$, where $C(\lambda)$ is the true signal of the companion, $P(\lambda)$ is the signal of the primary and $\alpha(\lambda)$ is the contamination factor. The goal, here, is to find the value of $\alpha(\lambda)$, by proceeding as follows:

- A master-spectrum for the companion ($C(\lambda)$) is produced by averaging epochs that are least affected (by eye) by contamination (i.e., no obvious spectral features of the primary in its continuum). These epochs, and the master-spectrum, are shown in Fig. III.10.
- The companion spectrum is fitted as $F(\lambda) = k(\lambda) \cdot C(\lambda) + \alpha(\lambda) \cdot P(\lambda)$, where $k(\lambda)$ and $\alpha(\lambda)$ are the fitted parameters where $k(\lambda)$ accounts for instrumental effects and transmission, and $\alpha(\lambda)$ the aforementioned contamination. Given the S/N of each spectrum, the parameters $k(\lambda)$ and $\alpha(\lambda)$ are indeed anti-correlated. This is done by excluding the companion emission lines regions (Hydrogen, Helium, Sodium, ...) that would bias the fit as they are also present in the primary's spectrum. The fit was performed for each wavelength bin, on a (-5000,+5000) km/s window centered in the given wavelength bin.
- Wavelength-dependent effects are already imprinted in both the companion and primary's spectrum, so $k(\lambda)$ really only should be a constant (per epoch) over the whole wavelength range. The fit is therefore refined by removing the λ-dependence of $k(\lambda)$. The underlying assumption is that the companion's continuum only has a flux-scaling variability from an epoch to another and no shape variability.
- The final contamination removal was therefore performed by fitting the whole companion as $F(\lambda) = k \cdot C(\lambda) + \alpha(\lambda) \cdot P(\lambda)$, with k and $\alpha(\lambda)$ as free parameters. Again, the fitted data was, for each wavelength bin, a (-5000,+5000) km/s window centered in the given wavelength bin. Unlike the first fit, this one was performed on k and all $\alpha(\lambda)$ parameters simultaneously, because the k parameter affects all wavelength bins. The error bars to the contamination were computed as the $\chi^2_r + 1$ contours on the $C(\lambda)$ parameters' χ^2_r maps for the given k.
- The parameter $\alpha(\lambda)$ were finally smoothed with a 10px-wide Gaussian kernel to remove all the jagged local minima of the fits (Fig. III.11, first row). This smoothing keeps $\alpha(\lambda)$ well within its error bars. Finally, the contamination $\alpha(\lambda) \cdot P(\lambda)$ was subtracted from the companion spectrum (Fig. III.11, 2nd and third row). Contamination was also added back to the primary spectrum for consistency, although this barely changes the primary spectrum as most of its flux is located within the core of its PSF.

Due to the UV excess (of both the companion and the primary) below $\sim$ 3700 Å, the assumption that the companion spectrum does not change in shape is not necessarily valid in that region. Therefore, no contamination correction was performed below 3750 Å. This is only moderately an issue because the contrast



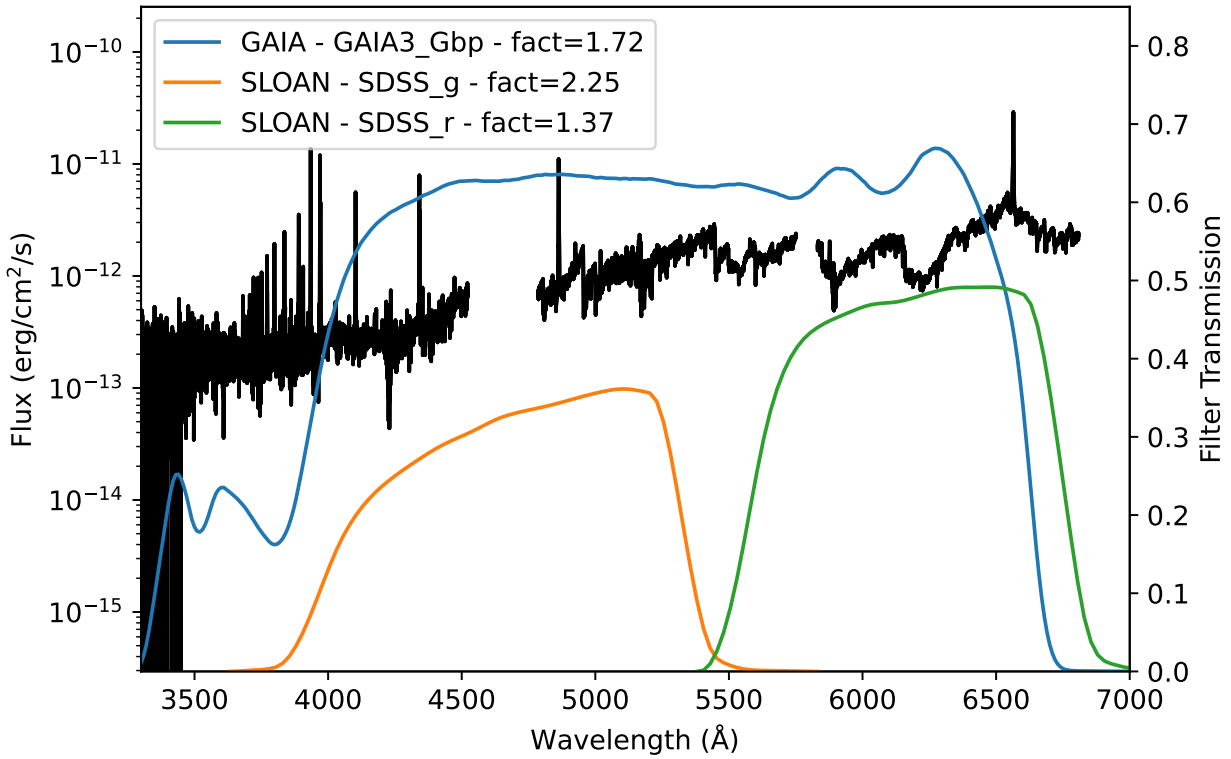


Figure III.12: Mean primary spectrum (black). Over-plotted in colors are different filters for which the primary has a published magnitude. The "fact" in the legend corresponds to the normalization factor required to calibrate the spectrum to the given filter's magnitude. The transmission curves were obtained from the SVO filter profile service (Rodrigo et al., 2024, 2012; Rodrigo and Solano, 2020).

between the primary and the companion is much more favorable at these wavelengths (contrast $\sim 5-10$), leading to a much lesser contamination.

The "goodness" of the reduction can be broadly assessed from the final line profiles of the companion and the primary. The companion lines have a plateau-like shape (at least for H_α and H_β). The primary, however, has very symmetrical and Gaussian-like lines (see Fig. B.6). These lines of the primary were already seen in the contamination correction, see red lines in Fig. III.11 lower panels.

4.2.5 Instrument response and atmospheric extinction

As mentioned in Sect. 4.2.1, the 2D spectra (ANCILLARY.2DSPECTRUM) used for disentangling the companion from the primary signal happened not to be corrected for instrument transmission nor atmospheric correction. However, the 1D science spectra (SCIENCE.SPECTRUM) from ESO archive are corrected for both these effects, while the 1D ancillary files (ANCILLARY.SPECTRUM) are the corresponding uncorrected spectra. It should be noted that these science spectra are the (corrected) sum of the two exposures within a single OB. Still, the instrument transmission itself is extremely stable as highlighted by how stable



the primary spectra are from an epoch to another. Only the airmass changes between two exposures, but as they were so close in time (20mins), I assume that the airmass and corresponding atmospheric extinction is stable across a single OB. This allows to correct all spectra for both instrument transmission and atmospheric transmission, by applying factor SCIENCE.SPECTRUM/ANCILLARY.SPECTRUM.

4.2.6 Flux calibration

The limited slit width of UVES (0.8") is not wide enough to provide an absolute flux calibration on its own, especially given the fact that small offsets in the acquisition can have some effects on the amount of slit-losses. Since the Tel. Std.s were acquired with a wide-slit, it is unknown the extent to which the centering of the slit actually affects the flux level. However, the binary is known to display very little flux variability, both in the NIR (∼3%, Bowler et al., 2023, their Fig. 20) and the visible (GAIA DR3, ∼1%, Gaia Collaboration et al., 2016, 2023). Therefore, all spectra of the primary-binary were normalized to the same flux level around H_α to make a mean spectrum of the binary, which was then scaled to the mean flux level of MUSE observations in the same region (Eriksson et al., 2020). Spectra were then calibrated to their published magnitude, which is not directly compatible with Eriksson et al. (2020) flux level, as shown by the value of the normalization factors in Fig. III.12. The various filters that were considered for calibration are shown in Fig. III.12. The resulting flux level is not fully compatible with the published magnitudes of the binary (as shown in Fig. III.12) and was thus re-scaled accordingly. The Bp filter is only slightly larger by ∼50 Å on the lower wavelength, making it best suited for calibration. It should be noted that different filters yield different scaling factors, possibly hinting at residual flux level differences between detectors, general spectral slope error, or chromatic losses. At this point, this is not corrected for, and there might be a general factor ∼ 2 error on the flux level at any wavelength. However, given that UVES was not built for photometric calibration, and even less for the case of faint companions, I guess that's not too bad.

5 Delorme 1 (AB)b

5.1 General description of the spectra

The full spectrum of Delorme 1 (AB)b is shown in Fig. III.13, with all epochs overlapped in black, and the mean spectrum (R=5000) in red. We find that the mean spectrum of Delorme 1 (AB)b is broadly consistent with that of SR 12 c, a young (∼2 Myr) companion of spectral type L0 (XSHOOTER, Santamaría-Miranda et al., 2018). We find a GAIA Bp magnitude of Bp $= 20.6 \pm 0.2$ for Delorme 1 (AB)b.

The spectrum is mostly flat with no clear molecular absorption features. The flux depletion at ∼6250 Å is likely due to an error in the data-reduction of that specific order. Even though there is possibly a FeI emission line in there, I do not study nor consider that wavelength range. Multiple Helium lines are found over the whole spectrum, some single peaked, some with a broad and narrow component. Helium lines are usually a clear sign of ongoing accretion, and thought to be formed at the shock Beristain et al. (2001). The sodium doublet at 4925–5021 Åis also present, with both lines single-peaked and mostly with a single narrow component. I do not expand much on these lines, and rather focus this chapter on the Hydrogen Balmer lines (H_α, H_β, ...).

A UV excess is clearly seen in the spectrum of Delorme 1 (AB)b below ∼3600 Å (Fig. III.13), as well as the Balmer Jump. The presence of a UV excess is usually associated with ongoing accretion (Valenti et al., 1993; Gullbring et al., 1998; Herczeg and Hillenbrand, 2008; Ingleby et al., 2013) and has only been evidenced on a handful of PMCs (Zhou et al., 2014, 2021). While previous studies mostly used photometric points at the UV excess location, this work provides the first *high*-resolution spectrum of an UV excess on a PMC.



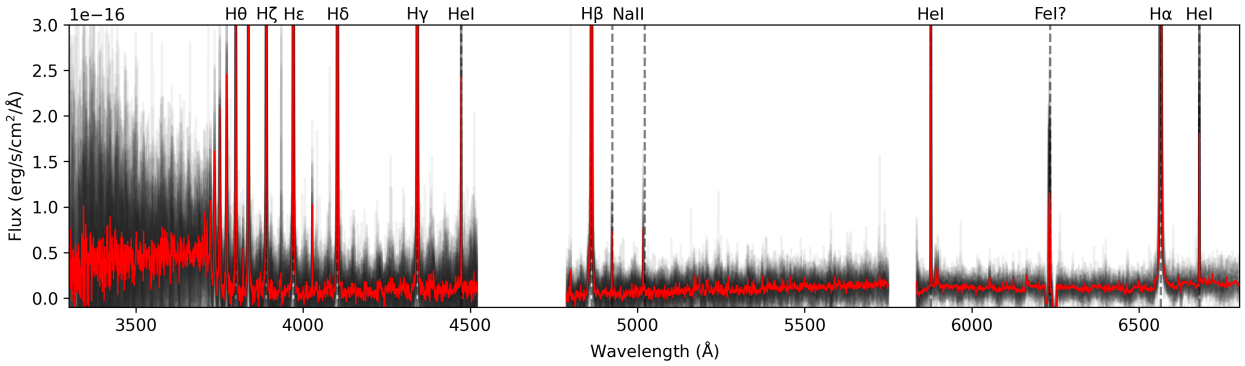


Figure III.13: All Delorme 1 (AB)b spectra from individual epochs, overlapped (black), with the mean spectrum on top (red). All spectra were convolved to R=5000 for clarity. The UV excess of Delorme 1 (AB)b is clearly visible below ∼3700 Å.

However, I do not expand much on it, as its study would require modeling of the accretion shock, which I did not have to conduct during my PhD. This is, however, matter for future work.

5.2 Lines morphology

The mean hydrogen lines for each epoch are shown in Fig. III.14. Individual lines are shown in Figs. III.15, III.16, III.17 and III.18, for H_α, H_β, H_γ and H_δ respectively.

5.2.1 Resolved profiles

The H_α and H_β lines have asymmetrical profiles with wide extended wings (up to ±500 km/s) with a tilted-plateau core. Higher order lines, however, have mostly symmetrical and centered profiles. H_ϵ has a narrow emission component around −120 km/s, likely a CaII or FeIII line, though CaII's rest wavelength is a better match (NIST[13] database, Kramida, 2010). H_ζ has a double-peaked profile, which is likely also a superposition with another weak line: possibly HeI or FeI.

High order lines (> H8) have a well defined profile, similar to that of H_ϵ/H7, but with flux levels compatible with primary contamination. However, the contamination component to the errorbar was computed in quite a conservative fashion ($\min(\chi^2_r) + 1$), making high-order lines likely to actually be present in the spectrum.

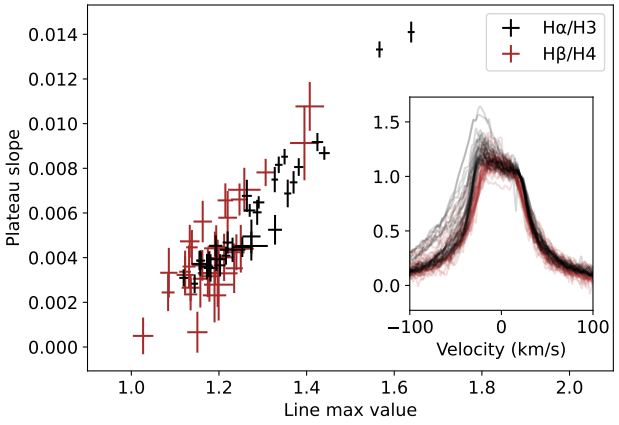


Figure III.19: For both H_α and H_β, the correlation between the plateau slope (fitted as $ax + b$) and the line maximum value when normalized to 1 at the "right shoulder", as shown in the inset.

[13]**NIST**: https://physics.nist.gov/PhysRefData/ASD/lines_form.html

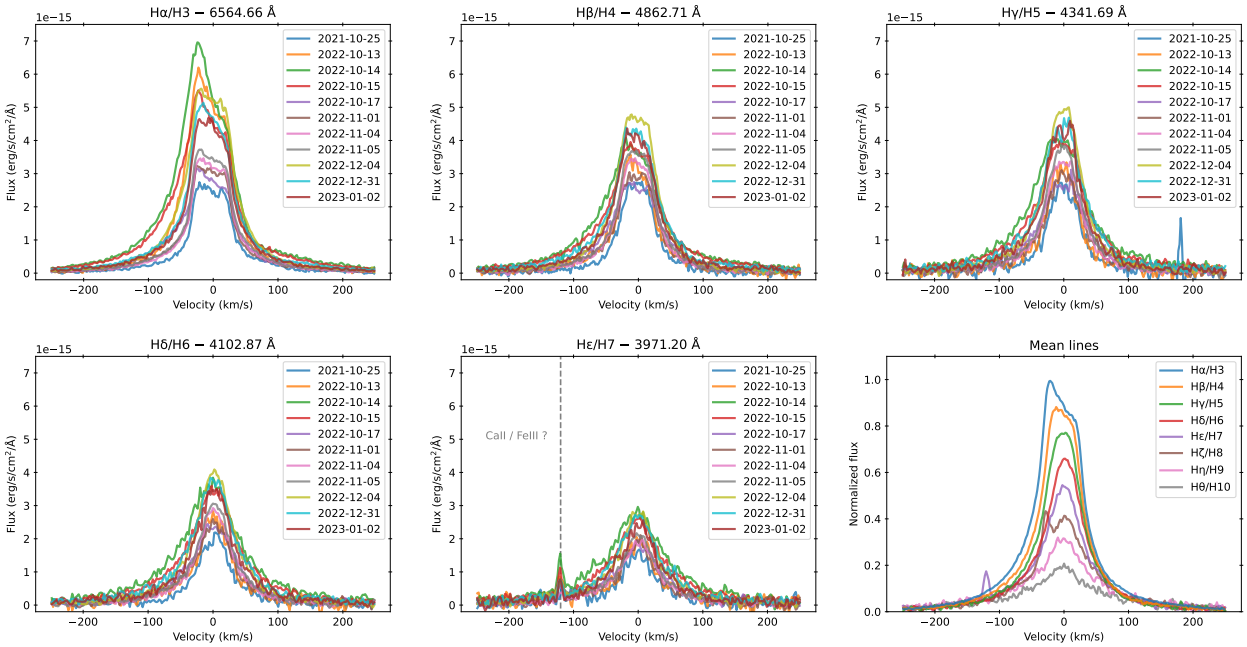


Figure III.14: Balmer lines of Delorme 1 (AB)b. Each panel shows the mean line of each observing epoch, from H_α to H_ϵ. The last panel shows the mean line (over all epochs) for each transition order, all the way up to H_θ/H10. Higher order lines are detected but compatible with contamination from the host binary in single epochs. Note that in this last panel, the line ratios are not truthful: the lines were successively scaled between 0.1 and 1.0 so that higher orders are actually visible. All lines are plotted after subtracting the local continuum baseline, averaged between $(-750; -400)$ and $(+400; +700)$ km/s.

5.2.2 H_α and H_β plateau-slope

Both H_α and H_β have a plateau-like core. The slope of this plateau is strongly correlated with the intensity of the line, as illustrated in Fig. III.19. The trend, however, is not seen in higher order lines, and the plateau is most tilted on successive epochs 2022-10-13/14/15 that coincides with an extended blue wing on epochs 2022-10-14/15. This might be hinting at an additional component within the profiles. Alternatively, this could be linked to variable red-shifted absorption component, linked to some extent with the line intensity to retrieve an overall ∼constant flux level. These variations really only call for a decomposition of the lines, which is done in Sect. 5.4.

5.2.3 Low resolution impact

Unlike the observations presented here, most studies of PMC have used *low-* to *medium-* resolution spectrograph, usually in the range R = 2000–3000. When the line is barely resolved, it is common practice to deconvolve its apparent width from the instrument broadening function (Line Spread Function – LSF), following $\mathrm{FWHM}^2_{\mathrm{in}} = \mathrm{FWHM}^2_{\mathrm{obs}} - \mathrm{FWHM}^2_{\mathrm{LSF}}$ (Demars et al., 2023; Marleau et al., 2024), where $\mathrm{FWHM}^2_{\mathrm{in}}$ is the intrinsic FWHM of the line. However, this intrinsically assumes that FWHMs sum quadratically, which



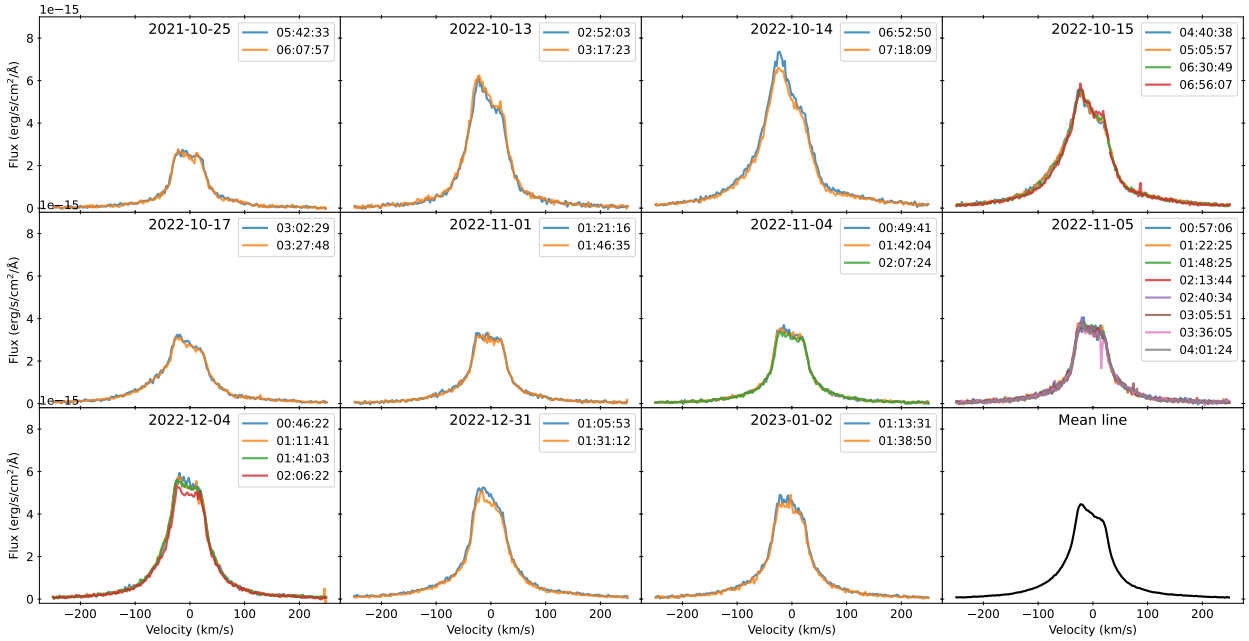


Figure III.15: H_α line for all individual epochs. $\lambda_0 = 6564.66464$ Å(vacuum).

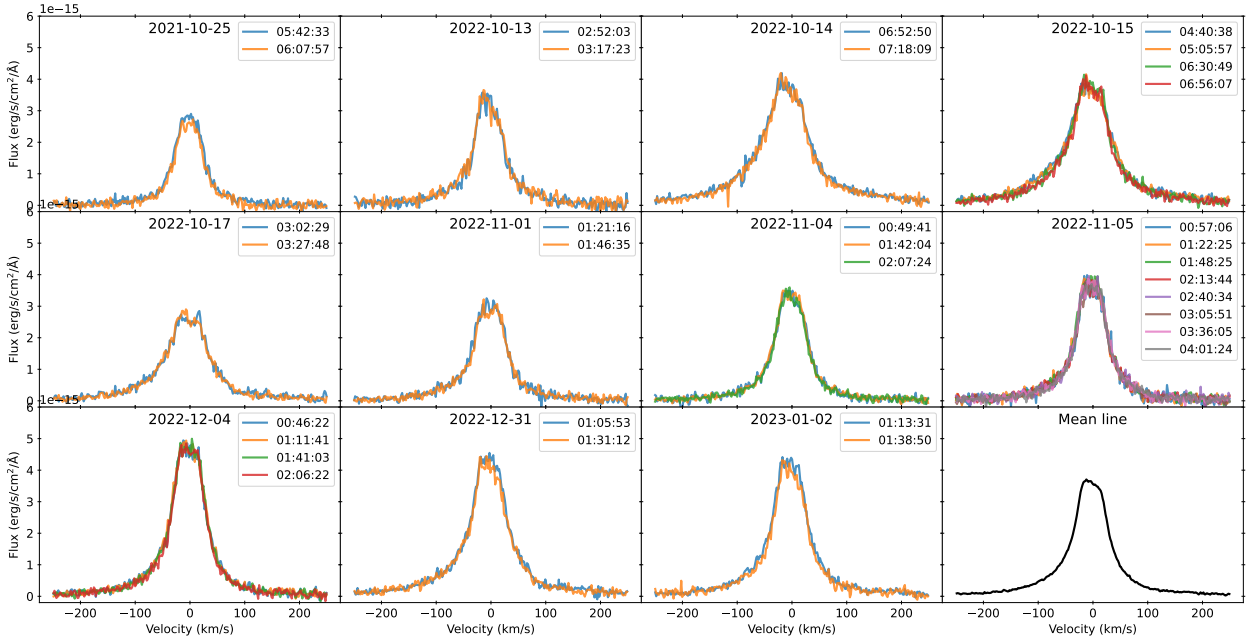


Figure III.16: H_β line for all individual epochs. $\lambda_0 = 4862.71$ Å(vacuum).

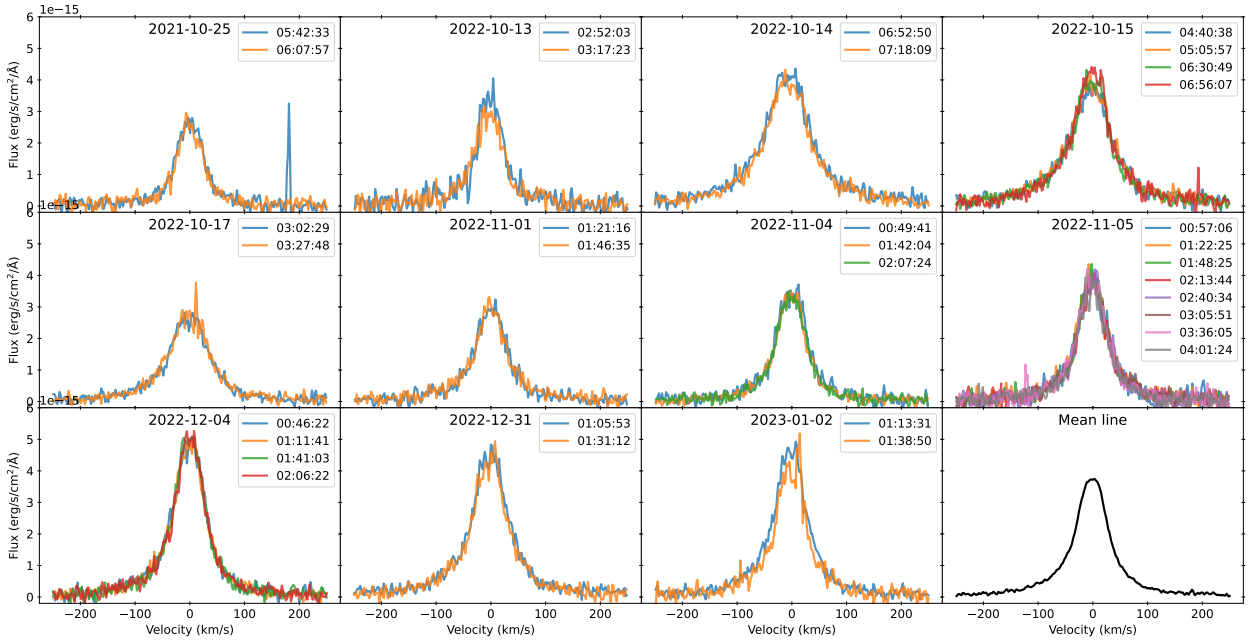


Figure III.17: H_γ line for all individual epochs. $\lambda_0 = 4341.692$ Å(vacuum).

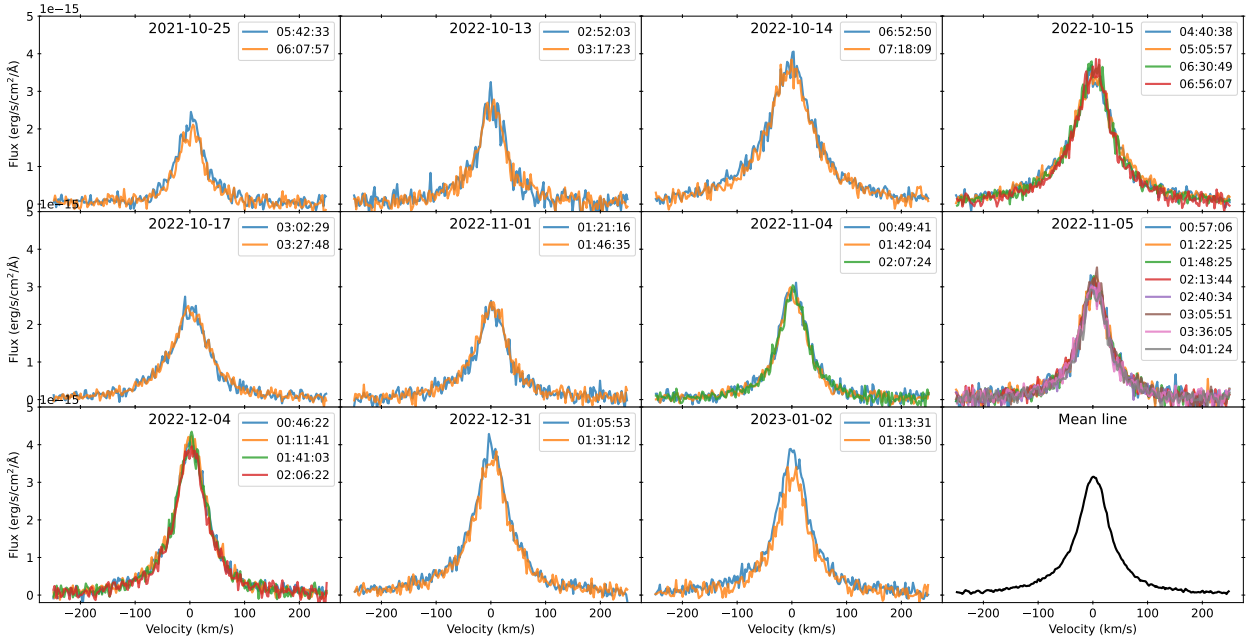


Figure III.18: H_δ line for all individual epochs. $\lambda_0 = 4102.86503488$ Å(vacuum).

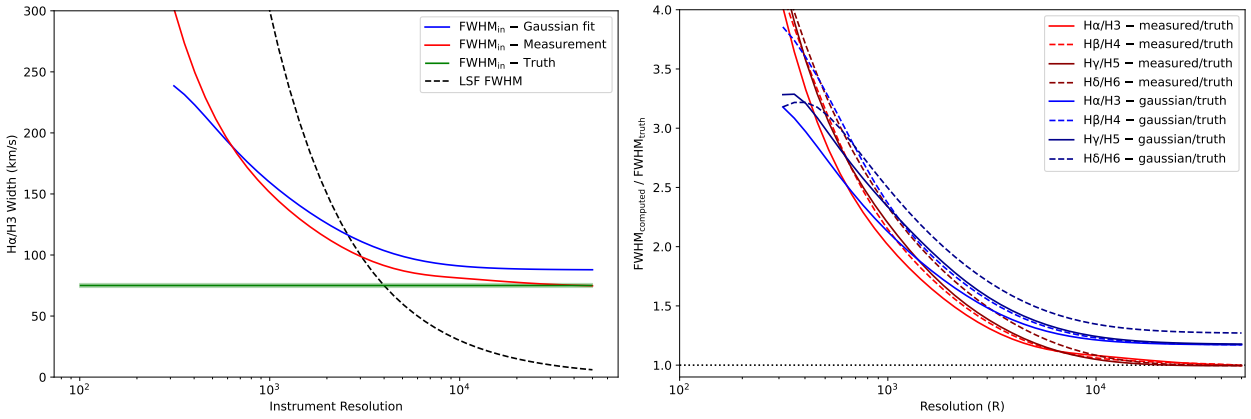


Figure III.20: Left: H_α width as a function of the observed resolution. Other lines are shown in Fig. B.3. Green line is the true intrinsic FWHM, measures on the line at full resolution. Blue line is the intrinsic FWHM, inferred from Gaussian fitting. Red line is the intrinsic FWHM, inferred from direct measurement on the low-resolution line. Black dashed-line is the LSF FWHM at a given resolution. Intrinsic FWHMs are computed as $FWHM^2_{in} = FWHM^2_{obs} - FWHM^2_{LSF}$. Right: ratio between the obtained intrinsic FWHM (for a given method) and the true intrinsic FWHM. Different colors and linestyles represent different measurement methods (Gaussian fit or direct measurement) and lines (H_α, H_β, H_γ and H_δ).

is only true for Gaussian-like profiles. In the case of Delorme 1 (AB)b, this is clearly not the case, at least for the first few Balmer lines. Thanks to the great S/N of the data, I can directly measure the FWHM of each line and compare that to what a lower-resolution data would predict through different methods. The left panel of Fig. III.20 shows the actual width of H_α (green line), and the inferred $FWHM^2_{in}$ of the line when observed at various resolution. Blue line is the inferred $FWHM^2_{in}$ through Gaussian fitting of the line, while red line corresponds to a direct measurement of the observed FWHM of the line, converted to its $FWHM^2_{in}$. The black dashed line is the LSF width at a given resolution (Gaussian kernel used for degradation). Other lines are shown in Fig. B.3. The right panel, however, is the ratio between either of these methods and the true FWHM of the line, for H_α, H_β, H_γ and H_δ. Depending the line and the method, the ratio ranges between 1.5 and 2.0. This means that studies using that deconvolution method have likely overestimated the intrinsic FWHM by a factor 1.5–2.0. However, I have performed this work in an extremely favorable case, where error-bars are negligible. Most PMC do not have lines as bright as Delorme 1 (AB)b, and are usually coming with a much worse S/N, even at lower resolutions (R∼2000–3000).

Overall, this parenthesis off of the main topic serves as a warning for future studies. Due to the intrinsic non-Gaussian aspect of the lines of Delorme 1 (AB)b, and if this applies to other PMCs, the traditional deconvolution the lines FWHM from the instrumental broadening may not be an accurate determination of the intrinsic width of the lines.

5.3 Lines correlations

In this section, I focus on the information obtained from the variability of the lines, and in particular the inferred correlations.



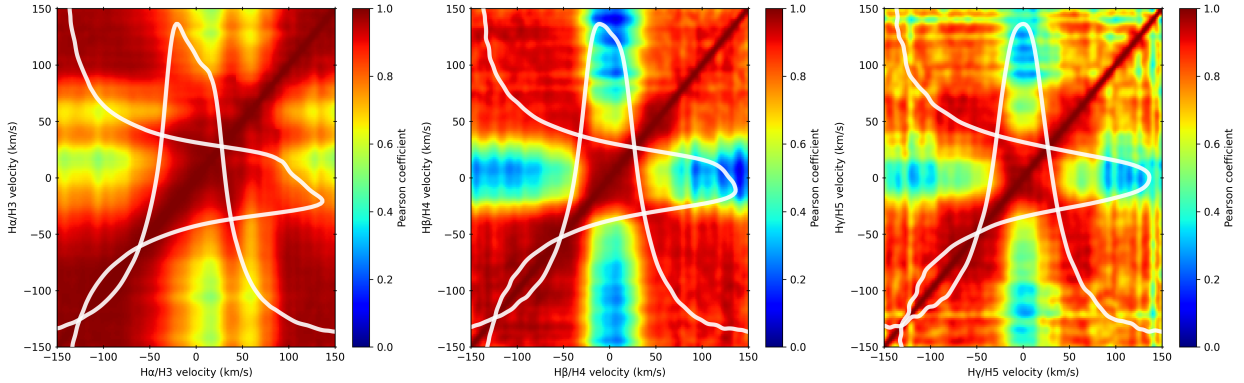


Figure III.21: Lines correlations with themselves for H_α, H_β and H_γ, with the mean lines overlayed in white. The lines were smoothed to R∼40,000 to remove some of the noisy features. The correlation diagrams for higher order lines have the same overall shape as H_β and H_γ.

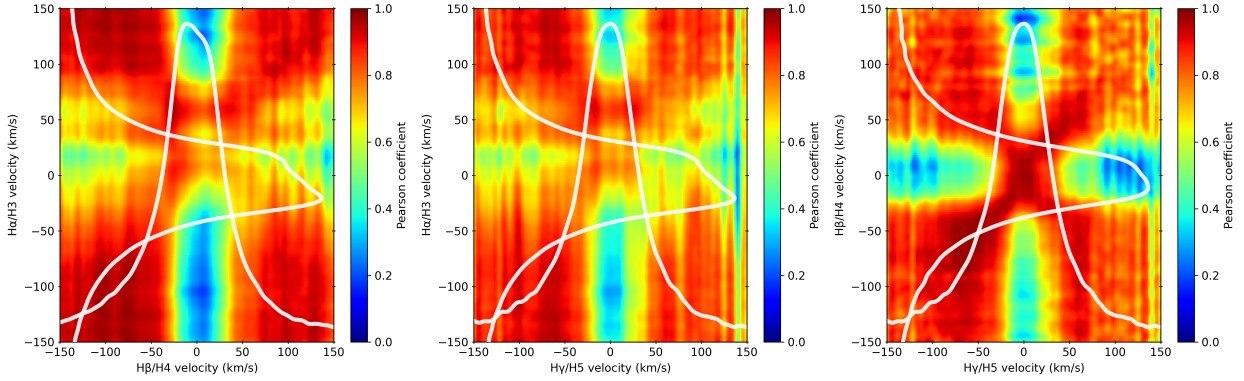


Figure III.22: Lines correlations with each others, with the mean lines overlayed in white.

5.3.1 Auto-Correlations

With the good amount of individual epochs, it is possible to derive the various correlation factors between different parts of the lines. This corresponds to which part of the line evolves with what other part of the line. This had already been done for T Tauri stars (e.g., Alencar et al., 2012).

Figure III.21 shows the Pearson correlation coefficient between different parts of a given line (H_α, H_β and H_γ). While the error-bars were included in the computation of the Pearson coefficient, these plots do not represent their extent for single points. However, since the goal is to compare the variations of the coefficient between different regions of the lines, and the error-bars are mostly constant over different regions, the absolute values of the error-bars is mitigated by the relative variation of the Pearson coefficient. Both H_β and H_γ have wings that are uncorrelated with the core. H_α has its profile correlated with itself over the full velocity range, with the minimum correlation factor of ~ 0.6. Similarly to H_β and H_γ, its core is slightly less correlated with the wings. For all three lines, the core decorrelation region is about ∼50 km/s wide. However, H_α shows an additional uncorrelated region around ∼60 km/s. It seems that H_α might be



made of 2 components: a wide core, and a broad one with a peak at$\sim$ 40 km/s. It could also be made of 3 components: the wings, the core, and the $\sim$ 60 km/s one.

In the case of H_β and H_γ, the correlation coefficient between the core and the wing reaches $\sim$0, which means both components are completely independent. However, for H_α, the correlation coefficient between the core and the wings only goes as low as 0.5. This means that if the core and wings components were to be completely independent (as for H_β and H_γ), the contrast between the core and wings has to be lower than for H_β or H_γ. In other words: for H_β and H_γ, the core component would be bright compared to the broad component, whereas for H_α, the core component would be somewhat of the same brightness as the broad component.

5.3.2 Cross-correlations

Figure III.22 shows the Pearson correlation coefficient between parts of different lines: H_α, H_β and H_γ. The last panel shows correlations between the H_β and H_γ lines. Both core components are strongly correlated and same goes for the wings components. However, the core component of each line is uncorrelated with the wings of the other lines. This indicates that the wings and core components of H_β and H_γ likely have the same emitting mechanisms.

The first and second panel of Fig. III.22 show the correlations between the H_α and H_β/H_γ lines respectively. The two diagrams have the same overall shapes, which makes sense given that the H_β/H_γ one showed that they have similar behaviors. Still, the H_α/H_β diagram has more contrast, likely due to the better S/N in the H_β line. The H_α uncorrelated component at $\sim$60 km/s that appeared in the H_α/H_α component also appears in the H_α/H_β: it is uncorrelated with most of the H_β line, at the exception of the -40 km/s part of the H_β line.

5.4 Decomposing the lines

The line shapes, in particular the H_α line, are quite uncommon. The plateau-like feature is not something that is often seen on CTTS (although there are a few examples, Mohanty et al., 2005; Muzerolle et al., 2005), and still, the question is whether or not, or to what to degree, these lines are due to accretion. The auto- and cross-correlations of the lines indicate at least 2 independent components. In this section, I attempt to decompose the H_α line into multiple (accretion?) components. While most of the results are interpreted in the context of accretion, the first step (Helium–Hydrogen correlation) is only a way to give the upcoming algorithm a meaningful starting point. Similar conclusions could (in principle) be reached by letting the algorithm run free, without a proper initial guess.

5.4.1 Helium–Hydrogen correlations

Helium lines are usually strongly linked to accretion, emitted within an accretion shock. This shock translates into a continuum component that is most apparent with the Balmer jump, at $\sim$ 3700 AA. However, it can extend quite far into the visible, with a contribution that can be greater at $\sim$ 6500 Å than at the base of the Balmer jump (see Fig. 7 in Zhou et al., 2021). Therefore, we might expect at least some of the Balmer lines emission to be correlated with both their surrounding continuum level, and the Helium lines.

Figures III.23 and III.24 show the correlation between each of the Balmer lines and their local continuum (Fig. III.23) or the HeI6680 line flux (III.24), respectively. Each of the line is well correlated with the HeI6680 flux. However, the correlation with the local continuum is lesser with increasing line order, except for the last two lines, H_η and H_θ. Assuming that the data is properly flux calibrated, multiple things stand out:



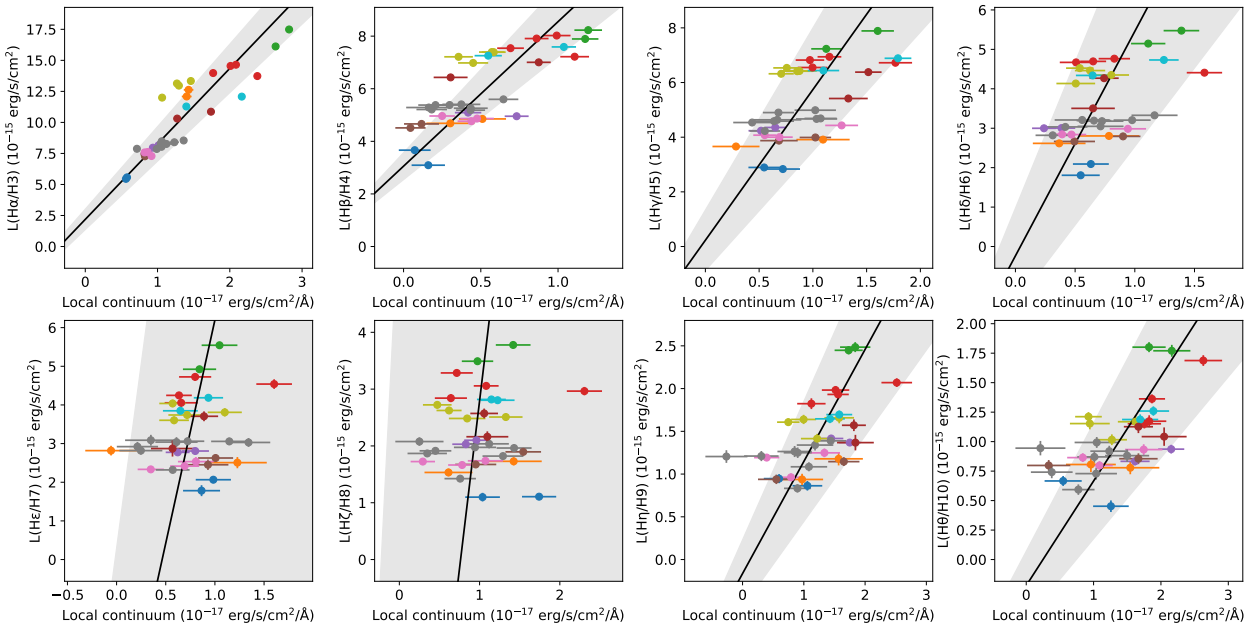


Figure III.23: For Balmer lines, correlations between the line integrated flux and the mean local continuum. Colored points correspond to a single epoch (same colors as in Fig. III.14. The black line is the best linear fit to the correlation.

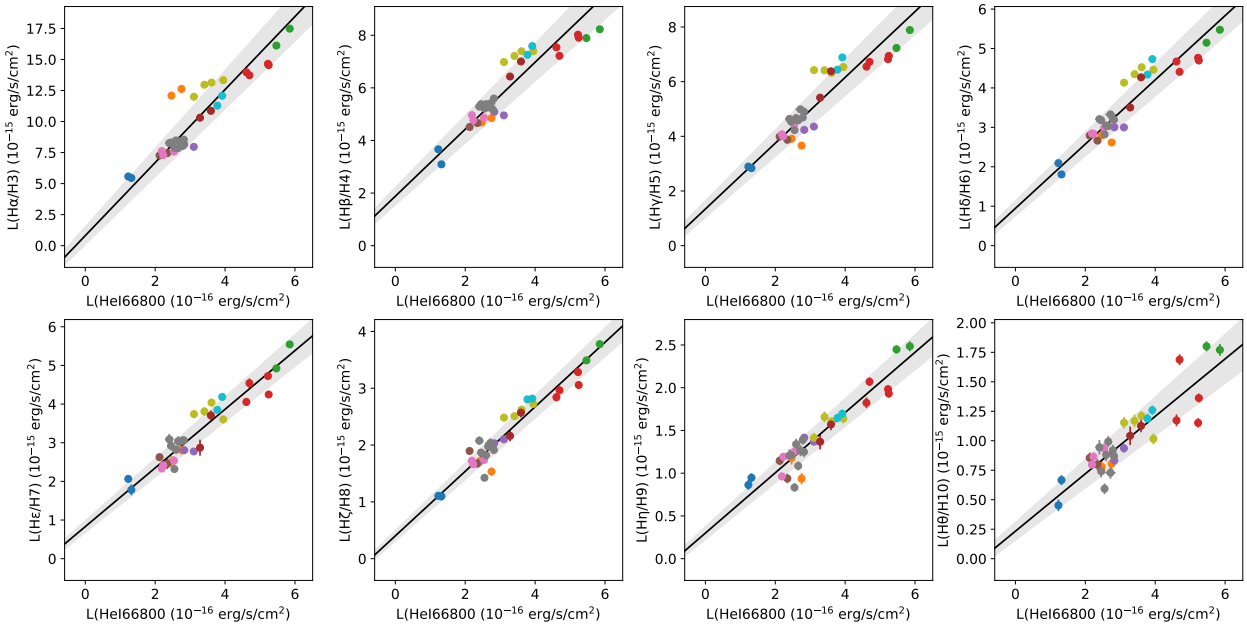


Figure III.24: Same as Fig. III.23, but correlations with the HeI6680 integrated flux.

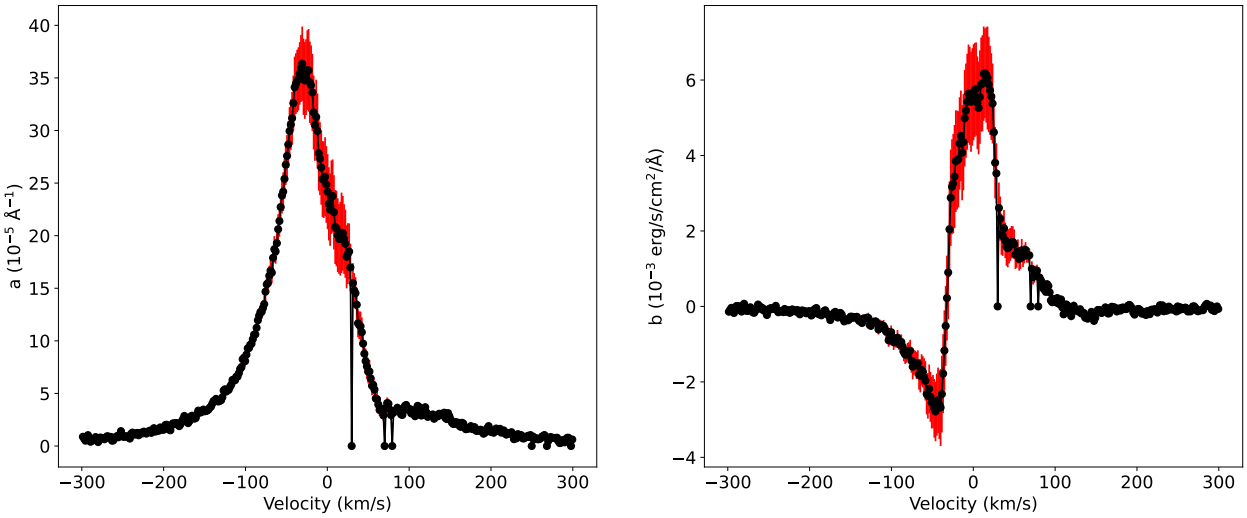


Figure III.25: Correlation parameters (y=ax+b) between the flux of the H_α line at a given velocity bin, and the HeI6680 integrated flux. This is the same plot as Fig. III.24, performed at each velocity bin, and represented only by the a and b parameter of the black line. The red lines are the error-bars.

- The continuum is variable, and this will be addressed in depth later,
- The high degree of correlation between the HeI6680 line and all Balmer lines suggest that they are indeed linked to accretion (or at least that much of their flux is),
- Balmer lines and Helium lines correlation decreases as the order of the Balmer lines increase. This is also anti-correalted with the reference wavelength of the Balmer line. This is consistent (in the picture of the accretion component from (Zhou et al., 2021, Fig. 7) with the decreasing level of the shock continuum component. The correlation appearing again at the higher orders (H_η, H_θ) may be due to blending of the Balmer Jump at these wavelengths, artificially increasing the apparent local continuum.

Continuum variability The continuum is variable between roughly 0.5–3 erg/s/cm^2/Å at H_α, and mostly constant at 0.5–1 erg/s/cm^2/Å at H_ϵ and H_ζ. When the continuum is brighter at H_α (red and green points), it is around 2–3 times as bright as the continuum at H_ϵ/H_ζ, which is roughly compatible with the amplitude of the shock component found by Zhou et al. (2021). Keep in mind, however, that they performed their shock-component fitting for PDS 70 b, which has not of the same mass or age.

H_α – HeI6680 correlation The constant high degree of correlation between Balmer and Helium lines does bring strong clues towards the accretion origin of the lines. While these correlations were obtained using the full line flux, it's possible to obtain correlations between a single wavelength bin and either the Helium or local-continuum flux. However, this requires a good S/N for every wavelength-bin, and is therefore only possible for the H_α line. Figure III.25 shows the correlation parameters (a and b) for the H_α line, as a function of the velocity. In this framework, the a parameter corresponds to the part of the line that is proportional to the HeI6680 line, and b corresponds to the H_α flux when the HeI6680 is not detected.



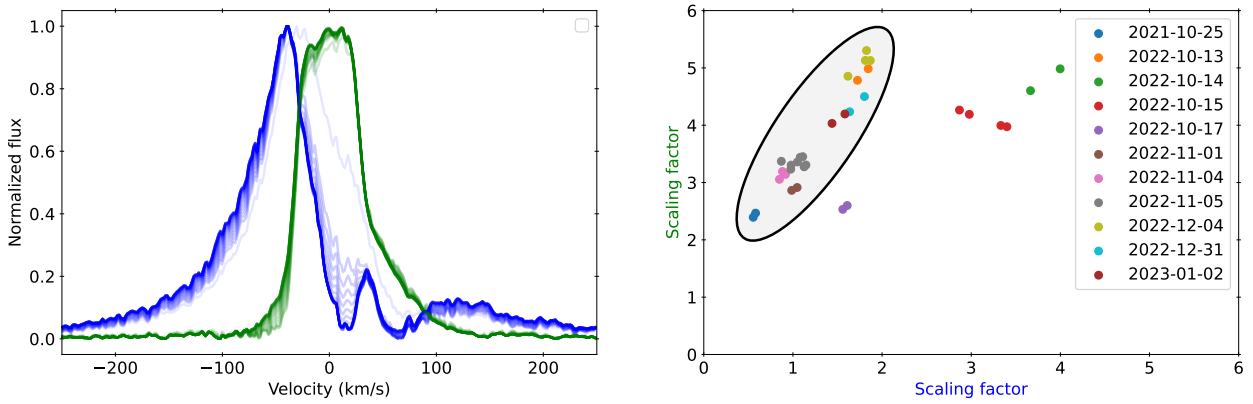


Figure III.26: Left: Shape of the individual components (blue and green), along iterations (transparent lines). Right: correlation between the blue and green components scaling factors, at the last iteration, for each epoch. The black ellipse highlights a main correlation between the two parameters.

The *a* parameter The a parameter shape (i.e., the slope), multiplied with the HeI6680 total flux at a given epoch, gives the shape of the H_α component that it's proportional to. In the hypothesis that the Helium line is emitted by the material at the shock, this means that the shape of a corresponds to the part of H_α that is proportional to the accretion shock. However, this does **not** mean that this corresponds to the shock component of H_α, as feedback from the shock to the base of the funnel will also make part of the funnel have H_α emission. a is therefore the overall mean of multiple components that are somewhat related to the shock contribution.

The *b* parameter The b parameter corresponds to the base H_α flux when the HeI6680 line is non-detected. In the context of accretion, this would correspond to a base H_α component the shock component is not sufficient to emit HeI6680. This lines up with either of two things: (i) a chromospheric component, independent of accretion, or (ii) an accretion component that is not linked to HeI6680 emission, meaning an accretion level that is not sufficient to emit HeI6680.

5.4.2 Two-components fitting

Because of the strong correlation between H_α and HeI6680, both a and b seem to be able to describe the H_α lines of all epochs. However, the spread in the correlation translates the fact that they are not a perfect decomposition in which to describe the lines: what was done in the previous section is reminiscent of Principle Components Analysis (PCA). I propose here a method to refine the decomposition. The previously derived correlation between H_α and HeI6680 will serve as an initial guess, but the same results were achieved with a random prior.

Brute-forcing the components The lines are described as their flux as a function of the velocity. Because there are multiple independent epochs (33), I propose to disentangle the various components profiles using the epochs diversity. The method goes as follows.



- I choose to describe the lines as the sum of two components, that only change in relative scaling from one epoch to another. The shape of the components will be the same at all epochs.
- Each component is described by a series of (X, Y) points, that define the shape at all velocities. The Xs are fixed and correspond exactly to the sampling of the data, while Ys are all free.
- Each component is given a scaling parameter for each epoch.
- Both components are fitted simultaneously on the whole dataset (33 epochs), in the range $(-250, +250)$ km/s, centered on H_α (322 bins, 1.55 km/s per bin).
- Because of the high number of free parameters, the fit is performed in an iterative fashion, by only fitting the shape of one component at a time, by letting both scalings free.

Therefore, the number of parameters at first and second iterations are:

$$\begin{aligned} N_{\text{it1}} &= N_{\text{comp1}} + N_{\text{comp2}} && \text{(III.1)} \\ &= N_{\text{epochs}} + (N_{\text{bins}} + N_{\text{epochs}}) && \text{(III.2)} \\ N_{\text{it2}} &= N_{\text{comp1}} + N_{\text{comp2}} && \text{(III.3)} \\ &= (N_{\text{bins}} + N_{\text{epochs}}) + N_{\text{epochs}} && \text{(III.4)} \end{aligned}$$

The total number of parameters, after all iterations are complete is:

$$N_{\text{params}} = N_{\text{components}} \, (N_{\text{bins}} + N_{\text{epochs}}) \quad \text{(III.5)}$$

The shape of both components at each iteration is shown in Fig. III.26, in transparent lines (blue and green). The right panel shows the correlation between the two scaling parameters for each component, at the last iteration, for all epochs. The black ellipse corresponds to the main correlation between the two parameters. This correlation is not as clear for H_β and H_γ (see Fig. B.8). The fit for all epochs at the last iteration is shown in Fig. III.27, with $\chi^2_r = 3.44$. The same fit for the H_β and H_γ lines are shown in Figs. III.28 and III.29.

Straight from the first iteration, the blue component diverges from its initial guess, while the green component broadly resembles the shape of the b parameter in Fig. III.25. The scaling parameters of each components are quite strongly correlated (black ellipse), except in the 2022-10-14/15/17 epochs, where the blue component is most prominent and correspond to the extended blue-wing epochs. From the residuals in Fig. III.27, it is clear that some of details are not fully reproduced by a two-components model. For H_β and H_γ (Figs. III.28 and III.29), however, the residuals are mostly within noise level, with some hints at similar residuals shapes as H_α. There is also a slight correlation between their respective components amplitudes.

The two components were actually already hinted at by the shape of H_α auto-correlations (Fig. III.30). The green component correlates almost perfectly with the core component from the auto-correlation, as-well as the reduced correlation between 50-100 km/s. The correlated wings are explained by the sole blue component, as well as their correlation with the $\sim$ 40 km/s peak, also seen in the blue component. The reduced correlation between -50–0 km/s corresponds to the blending of the blue peak with the green wing.

The overall shape of the blue component, overplotted into the auto-correlation profile of H_α, also matches the correlation between H_α and $\mathsf{H}_\beta/\mathsf{H}_\gamma$ (Fig. III.22), clearly highlighted by the $\sim$ 40 km/s component in both these cross-correlations. This means that the blue component likely has some signatures in higher orders lines. However, the $\mathsf{H}_\beta/\mathsf{H}_\gamma$ correlation does not have any significant $\sim$ 40 km/s feature, meaning that the



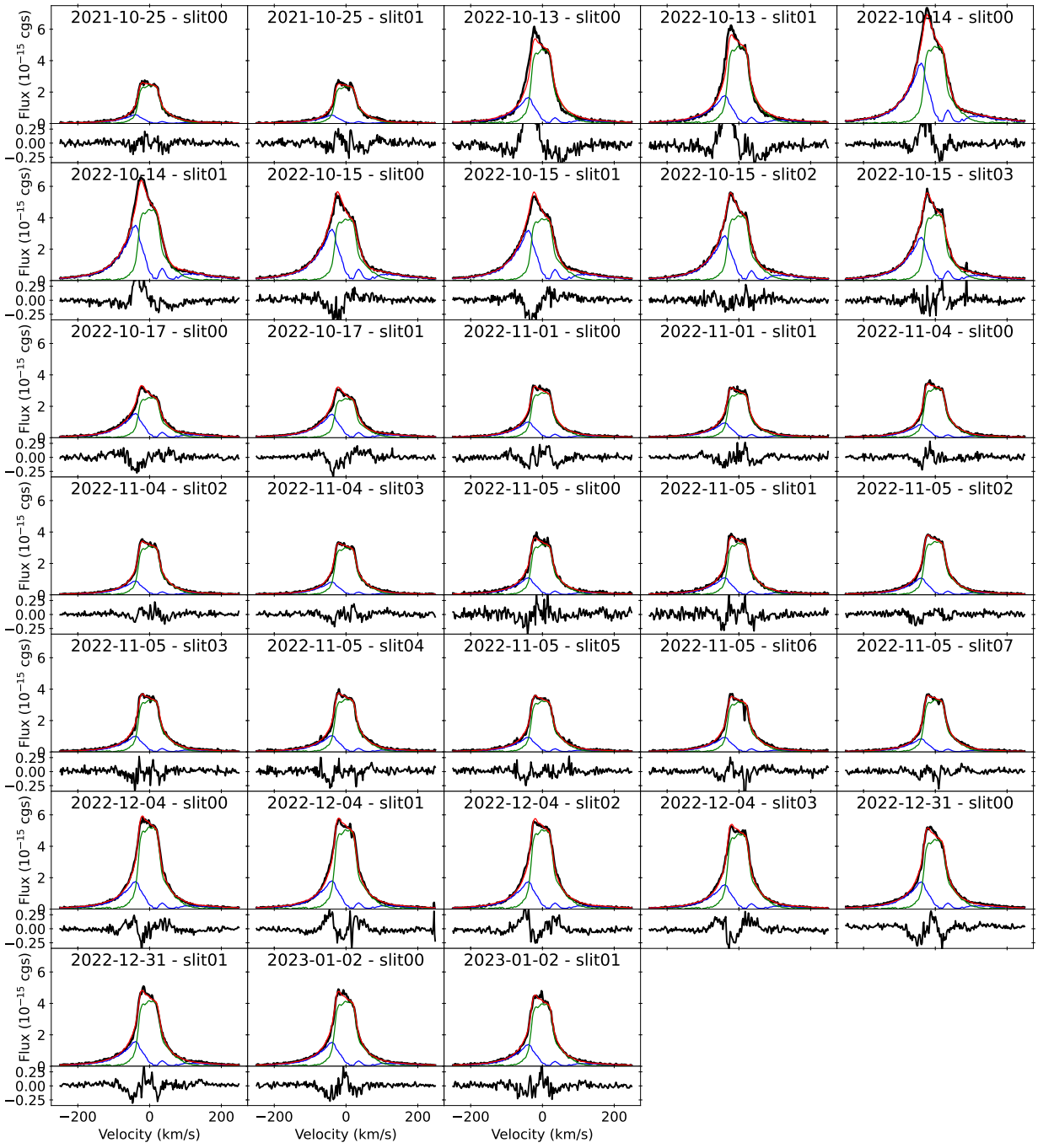


Figure III.27: Two-components fits of H_α, for all epochs, at the last iteration. Each sub-panel is divided in the fit and the corresponding residuals.

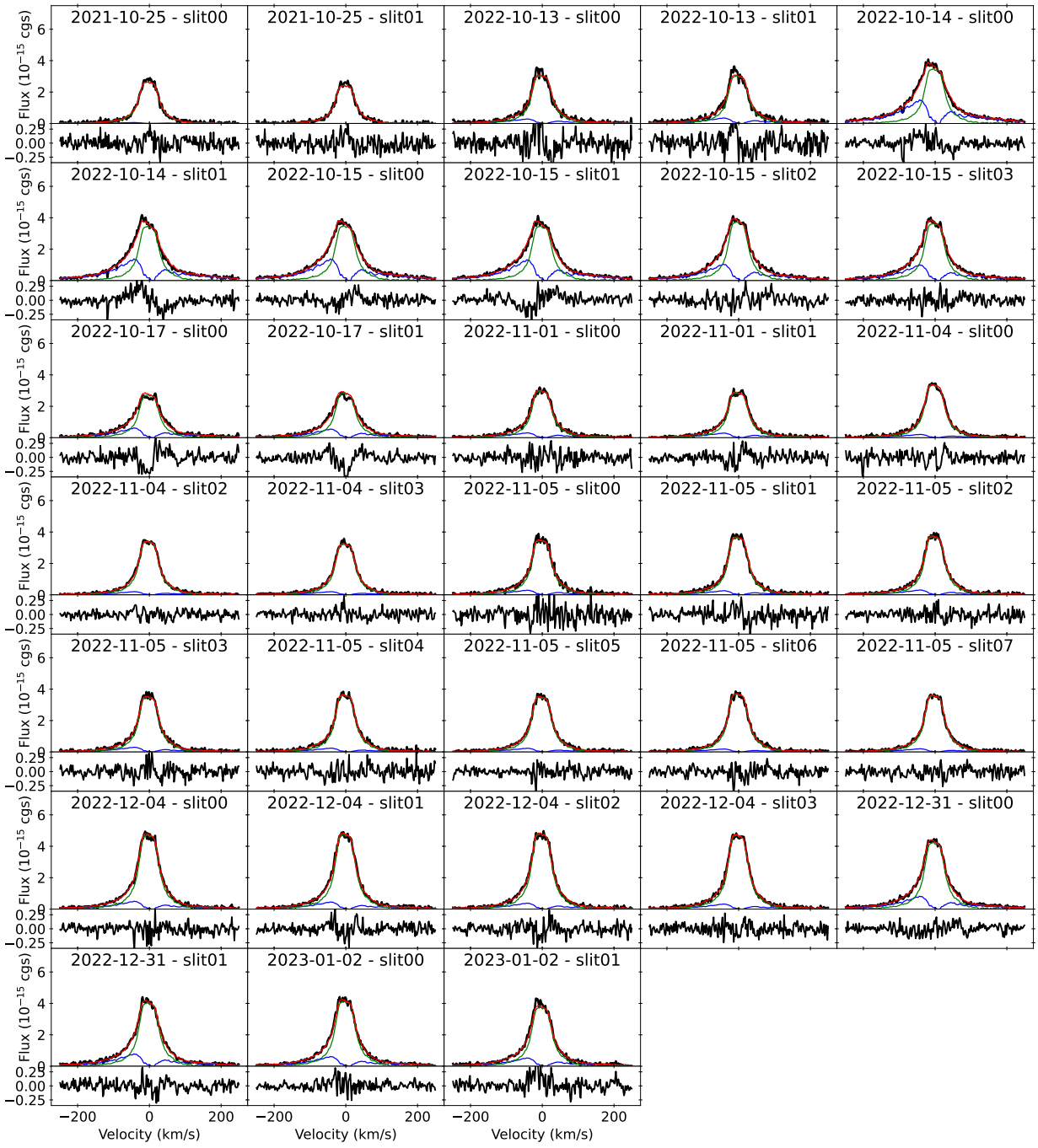


Figure III.28: Two-components fits of H_β, for all epochs, at the last iteration. Each sub-panel is divided in the fit and the corresponding residuals.

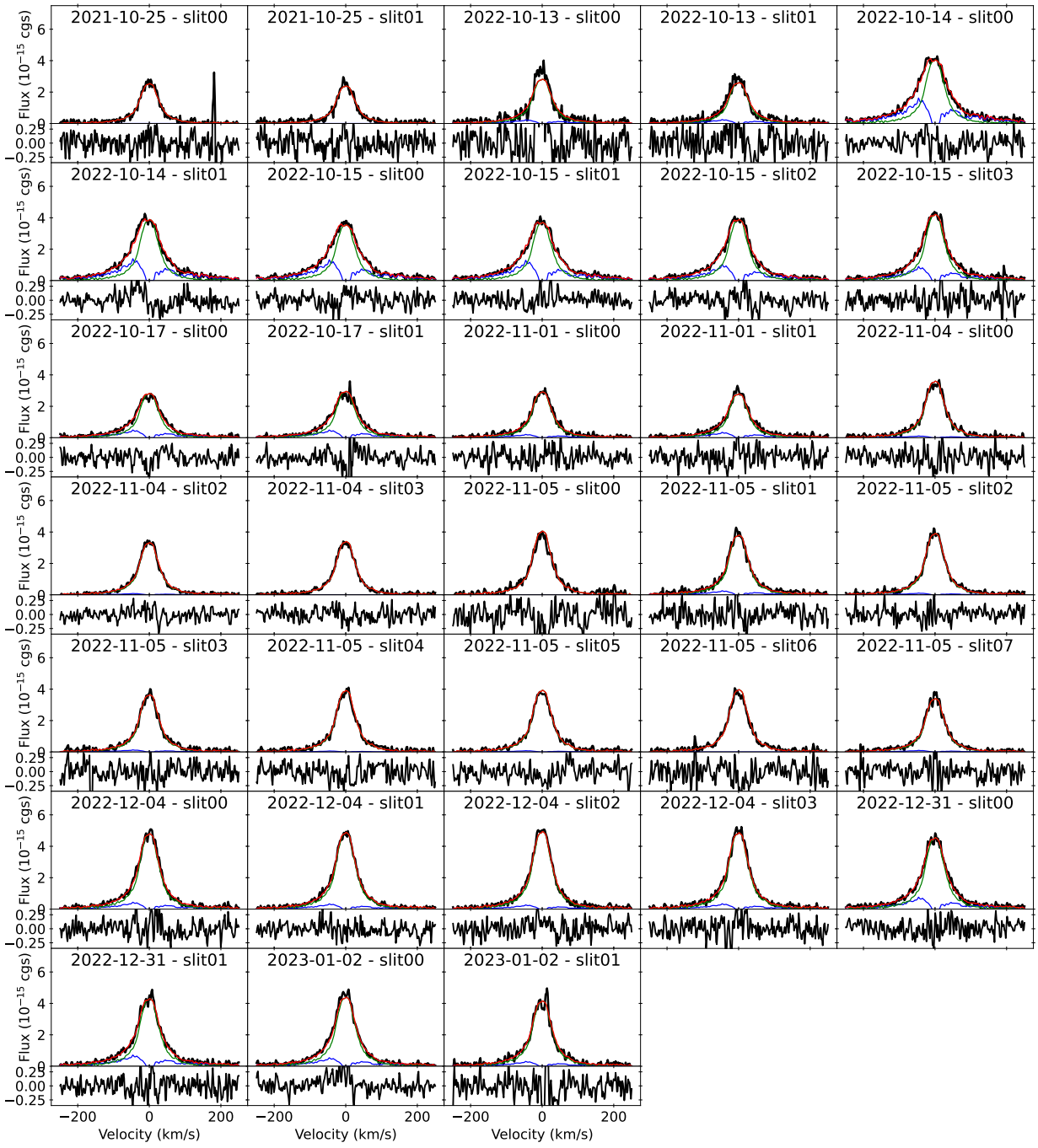


Figure III.29: Two-components fits of H_γ, for all epochs, at the last iteration. Each sub-panel is divided in the fit and the corresponding residuals.

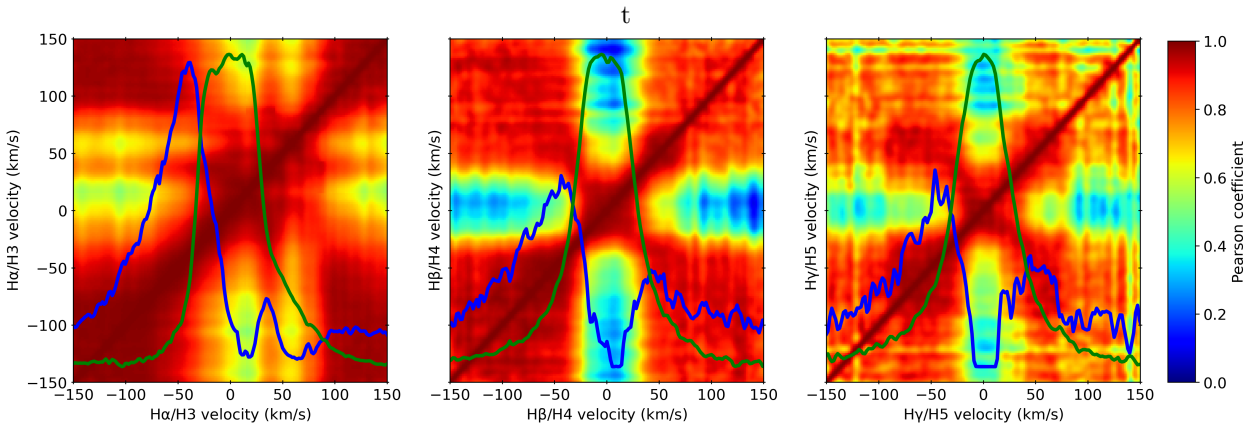


Figure III.30: Same as Fig. III.21, with the blue and green components overplotted.

blue component in H_α likely does not have the same shape in the H_β and H_γ lines. This is confirmed by the decomposition of the H_β and H_γ lines, where their blue component does not have any significant secondary absorption at ~ 60 km/s.

Both H_β and H_γ auto-correlation shapes are perfectly explained by their two-components decomposition. Similarly to H_α, the uncorrelated core and wings are explained by the two independent components. Their blue wing have a stronger auto-correlation than their red wing, which is explained by the shape of the blue component: its blue wing is brighter than its red wing, inducing a better blue-to-green contrast, making the blue wing more auto-correlated.

It is quite surprising that only two components provide quite a good fit to the whole dataset, especially given their fixed shapes. The fact that both components can fit the profiles from all the epochs at once and explain all of the features of the H_α auto-correlation provides a strong argument for its validity. This type of decomposition is usually made with Gaussians. To my knowledge, this is the first time this kind of decomposition is attempted, in particular in the planetary-mass domain.

In the case of magnetospheric accretion on stars, lines usually have variable components that vary not only in amplitude, but also in velocity. For such a two-components decomposition to be valid in the case of magnetospheric accretion, it seems Delorme 1 (AB)b would need to be almost pole-on, to mitigate the effects of rotational modulation. Despite this, the shape of the blue component suggests red-shifted absorption, which is usually seen at high inclinations, nothing alike a pole-on view. However, if Delorme 1 (AB)b has an axis-symmetrical magnetosphere, then it would not be so surprising that the lines are constant, as the accretion flow would also be axis-symmetrical. Still, there is some structure in the residuals, which means there might be a non-stationary component, either a chromospheric emission component, or projection effect if the magnetosphere is only slighlty inclined. What these components correspond to, if physical, is quite puzzling.

5.4.3 An alternative decomposition

As an alternative decomposition, I included an additional absorption component, following the same procedure as for the two-components one, iteratively fitting the two emission components shapes. The idea was that the absorption component could refine some of the residuals.



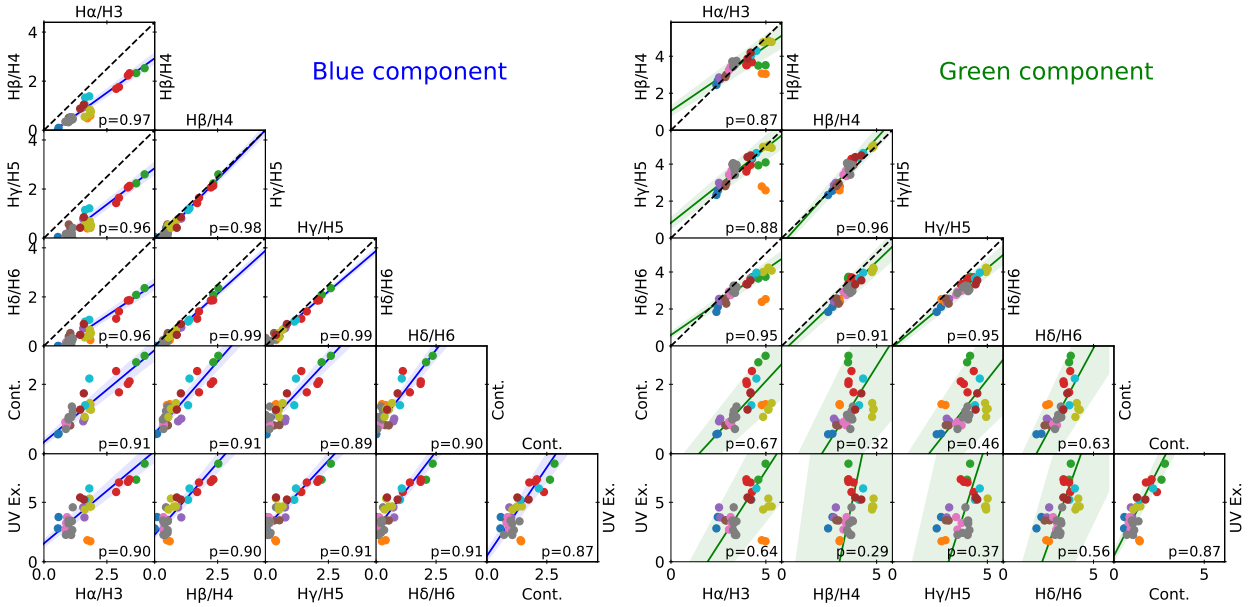


Figure III.31: Correlations between the blue/green components over multiple lines (H_α to H_δ), as well as the mean continuum level around H_α (in 10^{-17} erg/s/cm^2/Å), and the mean level of the UV excess (in 10^{-17} erg/s/cm^2/Å). The Pearson correlation coefficient is given as text in each panel. The black dashed line is the y=x line. The blue/green lines and shaded regions are the best affine fit. The color coding of the data points are the same as in Fig. III.14. The x/y units are normalized scaling factors of each component. The 2022-10-13 epoch (orange) was excluded from the analysis as it is so far off the correlation in the green H_α component.

The results are shown in Fig. B.9. The overall χ^2_r is $\chi^2_r = 2.39$, better than the previous decomposition (3.44). The overall shape of the blue and green components are quite similar. The residuals are better for some epochs, but the overall trend is quite similar. The change in χ^2_r seems to be mostly affected by the 2022-10-13, which had strong residuals in the previous decomposition. Residuals are still quite strong here, but a little bit better.

The absorption appears double-lobed, which could be interpreted as both red-shifted absorption from an inflow, and blue-shifted absorption from an outflow/wind, but its shape is strongly anti-correlated with the shape of the blue component. Another clue towards its bias is that the absorption component is not apparent in the 2022-10-13 epoch, which was the most problematic epoch in the previous decomposition. It appears that the algorithm uses this absorption as a way to *cherry-pick* the shape of the blue/green components to fit the 2022-10-13 epoch, using the absorption to put them back to their original shape.

Absorption might not be present, but I still think it was interesting to see how that fitting method behaves with a higher number of components. All-in-all, the previous two-components decomposition is likely sufficient for the sake of this manuscript.



5.4.4 Lines components and other correlations

Figure III.31 shows the correlation of each component (blue or green) from a line to another, with the Pearson correlation coefficient as text in each panel. The blue/green shaded regions correspond to the best affine fit to the correlation, and the black dashed line to the y=x line. Both components are well correlated from a line to another. This was already hinted by the fact that the scaling factors deviation in Fig. III.26 is actually seen in all lines (Fig. B.8). The continuum level around H_α is strongly correlated with the UV excess. This hints that the apparent continuum may actually only be the extension of the UV excess component. The blue components are strongly correlated with both the continuum level (around H_α) and the UV excess level ($p = 0.90$ in all panels). The green components, however, are only slightly correlated with the continuum and UV excess ($p \sim 0.4$), except for the H_α line ($p \sim 0.65$).

Given the similarity of the shapes of the blue and green components from a line to another, the correlations are not necessarily surprising. However, since the H_α behavior is so different from that of other lines (e.g., 2D periodograms, Sect. 5.7.1), it is surprising to see that its sub-components (both blue and green) are so strongly correlated from one line to another.

A key point of these correlations is how they relate to each other. The correlations do not cross the (0,0) point, which means some can be emitted while others are not. The blue components correlations show that H_α can be emitted while H_β, H_γ, or H_δ are not (the lines cross $y = 0$ at $x > 0$). All three H_β, H_γ and H_δ are emitted broadly at similar levels (the lines cross $y = 0$ at $x \simeq 0$). The relation to the continuum and UV excess, however, are the opposite: all lines are emitted after the UV excess has reached a certain threshold. In other words, it is possible to see the UV excess without seeing the blue component, which can be interpreted as UV excess threshold for the blue components to be observed

The green component correlations are almost symmetrical to that of the blue component: the ordering is reversed. This means that there *can be* H_β, H_γ or H_δ emission without H_α emission (the lines cross $x = 0$ at $y > 0$). Similarly as the blue component, the H_β, H_γ and H_δ lines are all emitted at similar levels (the lines cross $y = 0$ at $x \simeq 0$) However, the UV excess to lines correlations are more puzzling: there can be H_α, H_β, H_γ or H_δ emission without UV excess (the lines cross $y = 0$ at $x > 0$). This means that if the green component and the UV excess emission processes are linked (which is debatable because of the small correlation factor), then there would be a threshold of line emission that would be required for the UV excess to be visible.

5.5 Line ratios

Figure III.32 shows the line ratios (with respect to H_β) of our data (in black) compared to the typical ones found in T Tauri stars (Antoniucci et al., 2017). Their study focuses on line decrements in the Lupus region ($\sim 3-4$ Myr), for a sample of 36 stars with masses in the range 30 M_{Jup} – 1.5 $M_\odot$, with only 4 objects below 100 M_{Jup}.

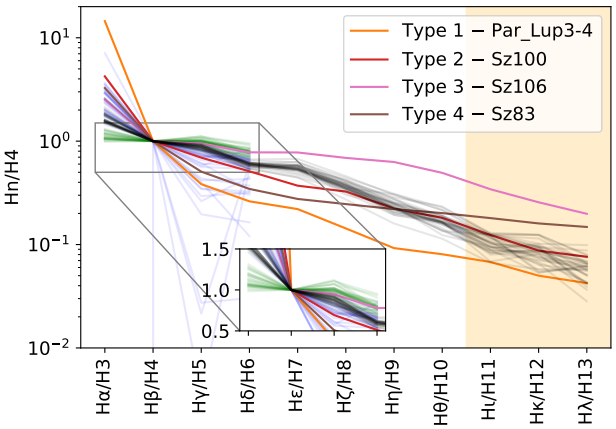


Figure III.32: Line ratios decrements. For each line, the line ratio to H_β/H4. In black, the line ratios of all epochs in this study. In blue and green, the line ratios of the blue/green components identified in this study. Colored lines are the four decrement types identified in Antoniucci et al. (2017) (see their Fig. 3). The yellow shaded region marks lines compatible with contamination from the host binary.

The overall line ratios of Delorme 1 (AB)b (black lines) are consistent with the general trend of Antoniucci et al. (2017) decrements. However, the curve does not perfectly match any of their Types. It mostly resembles their Type 2 decrement at higher orders (low accretion rate, lines emitted in optically thin region), but the earlier ratios are consistently above that curve. Surprisingly, The H_α/H_β ratio is consistently below all of the Types, ranging on 1–3. We also note that our H_α/H_β ratios are inconsistent with the one obtained from MUSE/VLT on 2018-09-18 ($H_\alpha/H_\beta = 9.8$ Eriksson et al., 2020).

The blue component line ratios have a really messy shape, likely due to its low emission level in H_γ/H_δ, that is degenerated with the noise in the data: it is hard to conclude anything about this component. The green component, however, has a curve compatible with the Type 3 sources from Antoniucci et al. (2017), except for the H_α/H_β ratio that is far below all of these types. Citing Antoniucci et al. (2017): "Type 3 [and type C] shapes cannot be well reproduced by current models and remain the most difficult to interpret".

5.6 Lines variability

All lines show great profile and amplitude variability over different epochs and minimal variability within each night. Figure III.33 presents the variability of the integrated flux of both H_α and H_β as a function of the timescales: all possible lines-pairs were associated with their relative flux ratio (with respect to the fainter of the pair) and the time-difference between the observations. This was performed using the same methodology as in Demars et al. (2023), and is similar to that of Costigan et al. (2014) and Zsidi et al. (2022). Beware that in our case, the ∼year timescale is driven by a single data point: the 2021-10-25 epoch (Ringqvist et al., 2023). Figure III.34 shows the variability amplitudes at ∼hour timescale, i.e., the lower timescales in Fig. III.33 and with the same color-coding. We can already note that the blue component has a greater relative variability than the green one.

5.6.1 Lines behaviors

Both H_α and H_β have variability amplitudes that is low at ∼hour timescales (∼8 %), and reaches a plateau at days to months timescales. Higher order lines have variability diagrams that are really similar to that of H_β (not shown) at >days timescales, whereas H_α displays a few top-ups in amplitude at days and months timescales. These are likely driven by the blue-shifted outburst/flare in epochs 2022-10-14 and 2022-10-15 (see Fig. III.14).

The blue and green points in Fig. III.33 correspond to the blue and green components described earlier (Sect. 5.4). The green component has a variability amplitude that is mostly in line with the overall profile, except for the month timescale where its amplitude is lesser. It makes sense given that this timescale is driven by the burst epoch, which is a translation of the increased importance of the blue component. The importance of the blue component clearly appears at the month timescale. However, and most importantly, the blue component has variability amplitude greater than both the green component and the overall profile, at all timescales, and so is the case for all lines. It is clearly apparent from the respective blue/green/crosses that represent the average variability amplitude in a given bin.

5.6.2 Short-term variability

The variability amplitude at ∼hour timescales seems to be increasing with the order of the transition (see Fig. III.34). The correlation is not seen at days to months timescales. This is consistent with the much higher variability amplitudes observed in Pa_β for GQ Lup b and GSC 06214-00210 b at the same timescales (∼50 %). The origin of that trend is still unknown, but may be intrinsic to the emitting mechanism.



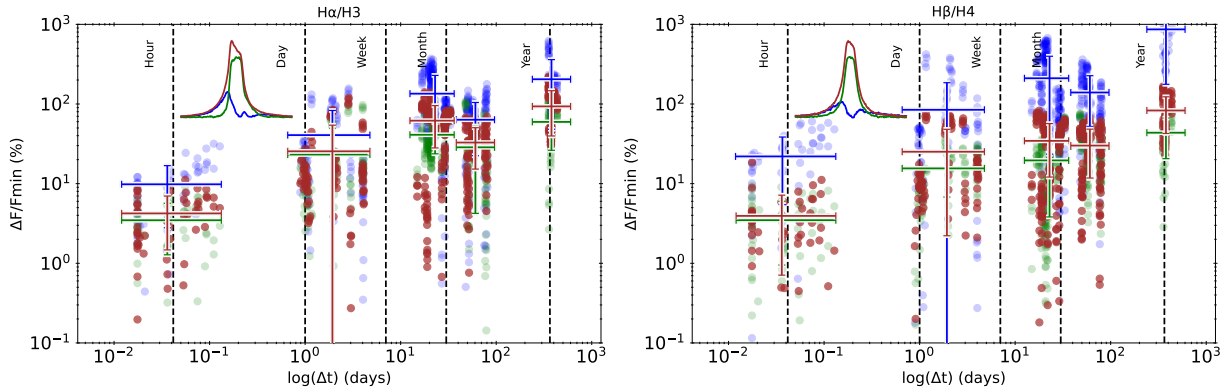


Figure III.33: Variability diagrams of the H_α (left) and H_β (right) relative flux variability for all flux pairs, as a function of the timescale. For H_α, blue and green points represent the variability amplitude of the respective components. The "error bars" represent the spread of the variability within a given timescales bin, weighted by the significance of the measurement: the σ-distance between the two lines corresponding to the measurement. The figure is highly inspired from Fig. 7 in Demars et al. (2023), but without the coloring for the significance as both H_α and H_β have really high S/N. Higher order lines have variability diagrams similar to that of H_β, with slightly increased variability amplitude at ∼hour timescales (see Fig. III.34).

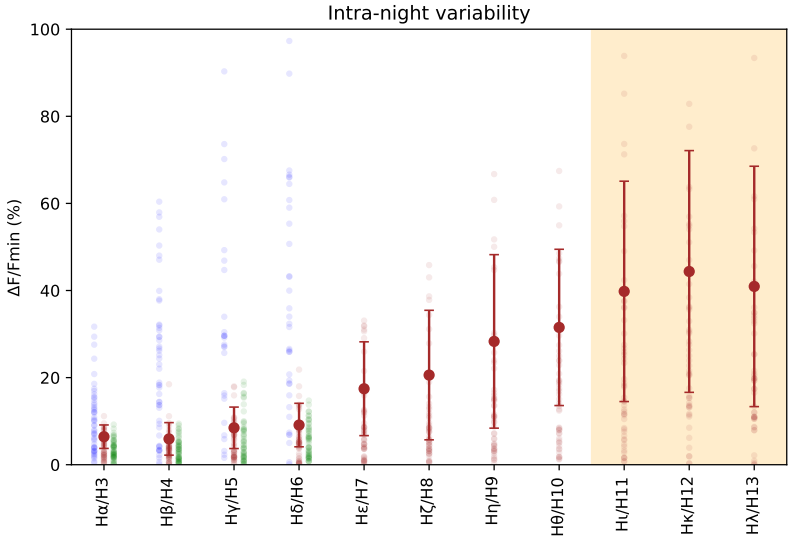


Figure III.34: Intra-night variability of the Balmer lines. Brown dots represent the variability between two data points within a single night, i.e., the ∼hour timescales points in Fig. III.33. "Error-bars" represent the spread of the variability (weighted by significance), i.e., the brown crosses in Fig. III.33. The yellow shaded region corresponds to lines where the detection is compatible with contamination from the host binary.

The blue component has a much stronger variability amplitude at short timescales than both the green component, and total line. More specifically, the blue component has variability amplitude that can reach above ~ 1000 % (cut-out by the plot limits), even at the hour timescale, in particular in H_γ and H_δ. This is mostly an artifact because some epochs have a blue component so faint that this is basically equivalent to dividing by zero.

5.7 Periodicity

Young exoplanets often have variable photometry and spectral bands that are usually associated with an inhomogeneous cloud deck in their atmosphere, that translate to rotational modulations and periodic evolution of the light curve. In the case of our objects, the hotter atmosphere yields clouds that will not impact photometry as much. Therefore, any periodic evolution of their light curves (or lines) is likely to be driven by accretion. What is the meaning of that period, however, is not so straightforward: continuum and Helium lines periodicity may be associated with a hotspot rotating around the planet, while Hydrogen lines can display multiple periods, not necessarily compatible with the rotational period (e.g., Sousa et al., 2021). In this section, I attempt to identify periodicity in the line profiles in spite of the temporal sampling of our observations which has not been designed to look for rotational modulations. The number of independent epochs is limited (11 epochs) and are unevenly spaced among 4 months, while a continuous monitoring is usually preferred for such analysis. Furthermore, each of the epoch includes a variable number of individual exposures, which induces what is known as red-noise in the frequency space. In sum, the results of this section should be interpreted with caution. For all periodograms, the 2021-10-25 epoch was excluded from the analysis, to avoid adding aliasing as it was observed a full year apart from the rest of the program. On a side note, the primary has a rotational period of 0.1664 ± 0.0008 days (Bowler et al., 2023), thus would any such period arise from the periodograms, this would likely be do to residual contamination from the primary.

5.7.1 2D periodograms

Unlike in the case of low-resolution spectroscopy, echelle spectrographs provide access to the resolved line-profile. This means that the periodogram analysis can be done independently for each spectral bin, which permits to check for different periods in different parts of the line. This produces a "2D" periodogram, with 1 spectral and 1 frequency dimension. The periodogram itself can be computed in a number of ways. The most common one is the Lomb-Scargle periodogram (Lomb, 1976; Scargle, 1982) which was developed specifically to detect periodic signals in unevenly spaced data. However, astronomical data are rarely completely randomly spaced, due to scheduling constraints at the telescopes. This biases the method by introducing periodicity in the time-sampling, that translates in multiple peaks that are only due to the sampling itself: this is known as *aliasing*. This can be overcome using the CLEAN deconvolution method, as proposed by Roberts et al. (1987): the CLEAN algorithm suppresses peak that are due to the sampling windows.

Figures III.35, III.36, III.37 and III.38 show both the 2D Lomb-Scargle and 2D CLEAN periodograms of the H_α, H_β, H_γ and H_δ lines respectively. These 2D periodograms were obtained by concatenating the 1D periodograms of each spectral bin. The Lomb-Scargle periodograms have a lot of aliasing, and are pretty much unusable, even when thresholding the peaks using the False Alarm Probability (FAP). It is still possible to see the differences between the core and wings of the lines: there appears to be shifts in the periods between the core and wings. The CLEAN periodograms, however, are a lot CLEANer. Whether these peaks are significant, however, is not so straightforward. By phase-folding the various measurements of the lines at a given location (λ, F_λ) to a given period, it is possible to highlight that some of the peaks in the periodogram do not correspond to any periodic signal. The phase-folded data for the main peaks of each line is shown in



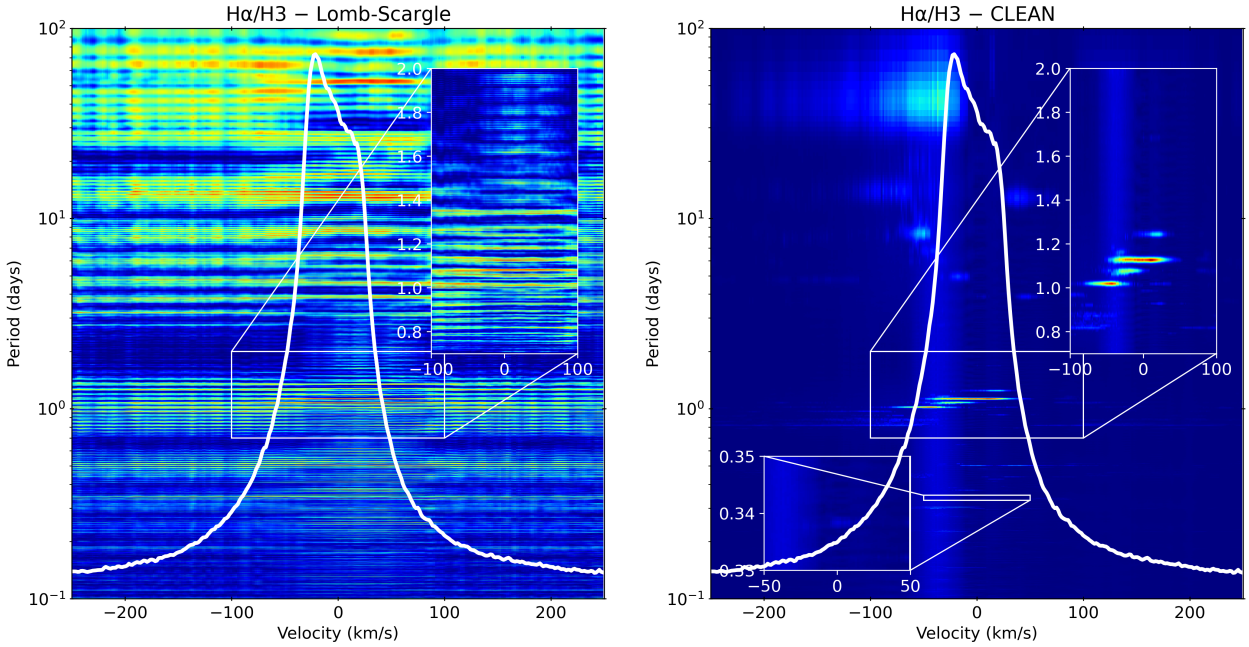


Figure III.35: H_α periodograms. Left: Lomb-Scargle periodogram. Right: CLEAN periodogram. Overplotted in white is the mean line shape.

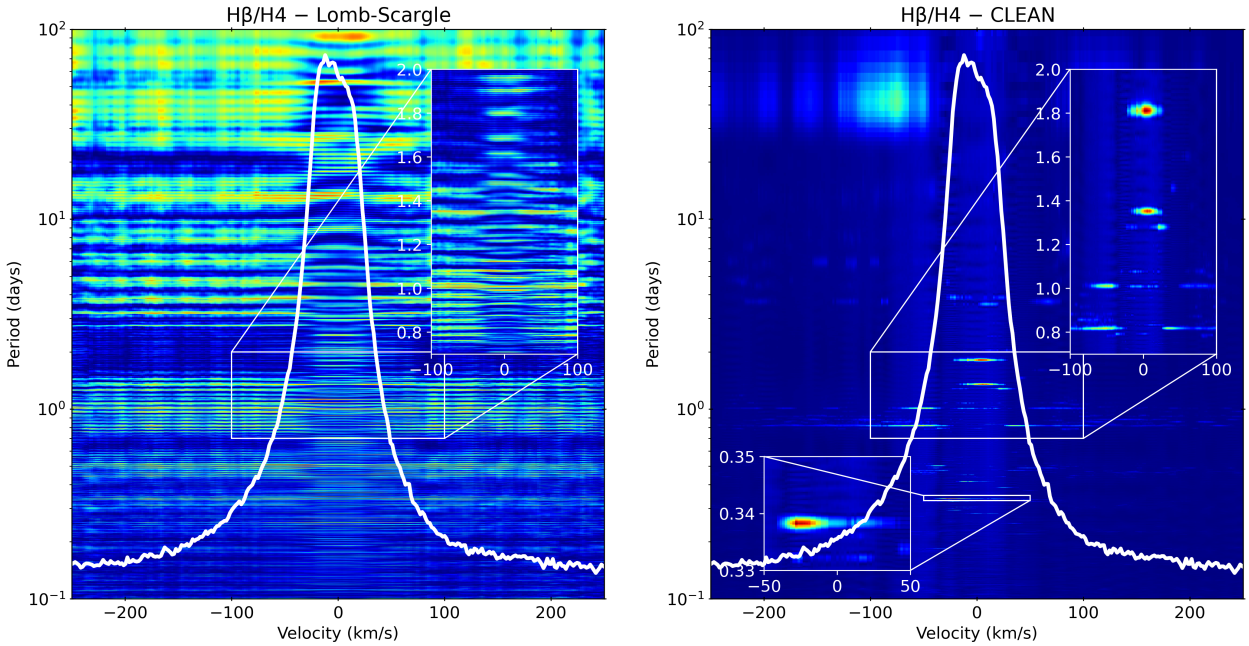


Figure III.36: H_β periodograms, same as Fig. III.35.

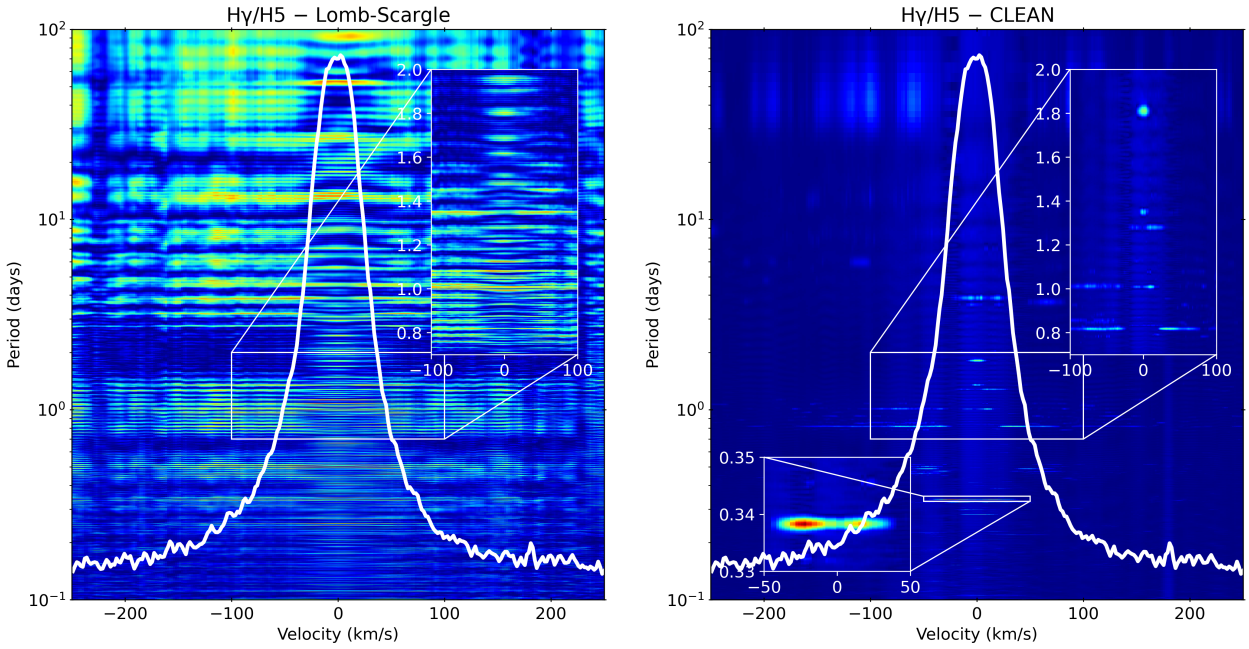


Figure III.37: H_γ periodograms, same as Fig. III.35.

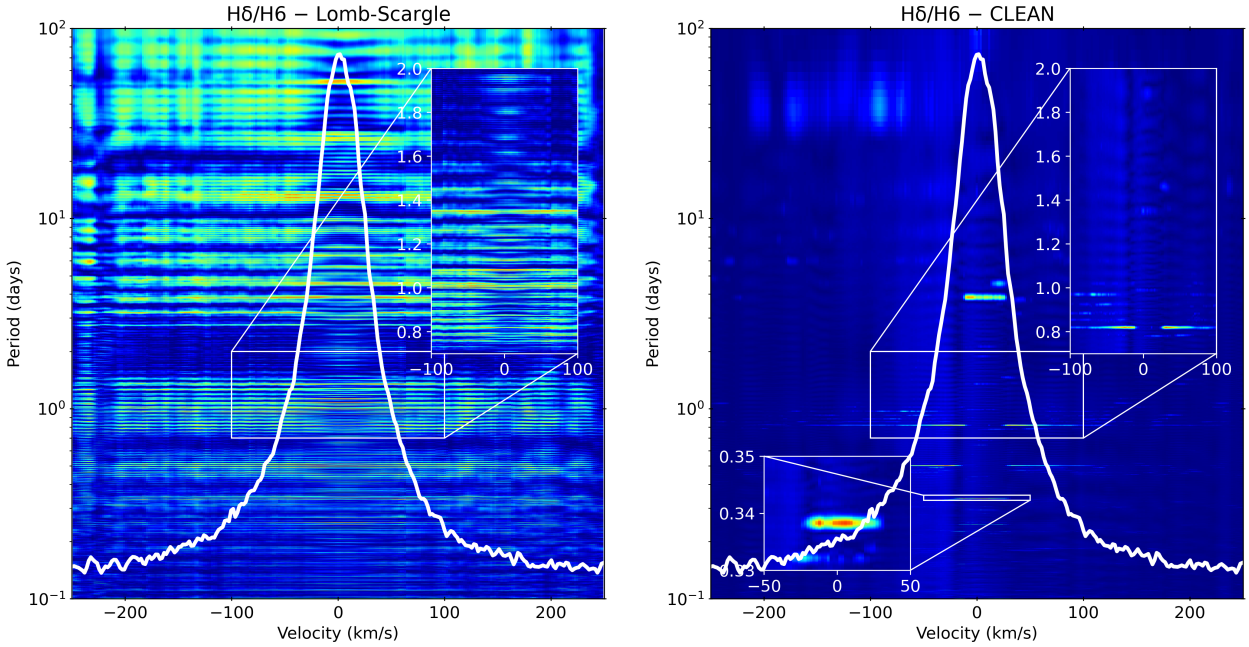


Figure III.38: H_δ periodograms, same as Fig. III.35.

Fig. B.11. It is clear that the 1.8 days peaks for both H_β and H_γ do not correspond to a real periodic (at least sinusoidal) signal. The 0.338 days peak for H_β, H_γ and H_δ, however, do provide a decent sinusoidal modulation, but is surprisingly absent from H_α. H_α has a peak at 1.126 days that is absent from other lines. While this peak does not provide any sinusoidal modulation, it is still not as obviously wrong as were the 1.8 peaks at H_β and H_γ. It could translate a non-sinusoidal periodic pattern. It should be noted that the 0.338 days peak is found at the velocity bin ~ -25 km/s in H_β and H_γ. It does not correspond to any of the two components that make up any of lines, that have peaks at ~ -50 km/s. Instead, it corresponds to the transition between the blue and green components.

5.7.2 Sub-components periodograms

A periodogram for the scaling factor of of the sub-components of each line was derived, following the same methodology: the CLEAN method to clean up the Lomb-Scargle periodogram. The resulting periodograms are shown in Fig. III.39 (blue and green lines respectively), with the addition of the integrated flux periodogram (black line). The location of the brightest peak is given in text in the top right corner of each periodogram. For each of these peaks, the wrapped phases are shown in Fig. B.12. Similarly to the 2D periodograms, thresholding the Lomb-Scargle periodograms with False Alarm Probability does not help so much to disentangle aliased peaks from real peaks.

The integrated flux periodograms show Lomb-Scargle peaks at ~ 3.83 days in all lines. However, they disappear in the CLEAN periodogram. This is not so surprising as even if the phase-folded curves (Fig. B.12, left column, black points) provide a reasonable sinusoidal shape, there are a lots of gaps. It is more likely that, if real, this corresponds to the harmonic of a higher frequency component. The CLEANed version provides an almost uniform solution, with a ~ 0.5 days peak, except for H_α. Instead, H_α has its brightest peak at ~ 1.014 days. This peak was already shown in the 2D periodogram (Fig. III.35), but was not the brightest: the ~ 1.12 days peak is the brightest one. This is not so surprising, as the 2D periodogram already showed that the ~ 1.12 days peak only spanned the width of the green component, therefore the integrated flux periodogram is rather the average sum of the variation of both the blue and green components. The study of both the blue and green components independently is bound to provide more consistent results.

The blue component's flux periodogram shows Lomb-Scargle peaks at ~ 0.501 days for all lines. However, their corresponding wrapped phases (Fig. B.12, left column, blue points) do not provide a reasonable shape to be really significant. Furthermore, the 0.501 days period being so close to a half-day is likely the sign of some sampling effects. The CLEAN periodograms, however, show bright peaks at ~ 38 days for all lines. They are the highest for both H_α and H_β, but not for H_γ and H_δ that have stronger ~ 0.853 days peaks. Still, both peaks are present in all lines. However, similarly to the Lomb-Scargle phases, these wrapped phases (Fig. B.12, right column, blue points) do not provide any reasonable periodic shape, with multiple epochs not having overlapping values, despite being at the same phase. Even if they are the brightest peak, it does not necessarily mean they are significant nonetheless. It appears especially obvious when looking at the *continuum* of the CLEAN periodogram for that blue component: there are lots of wave residual peaks and bands. All-in-all, it seems that the blue component has no significant periodicity.

The green component's flux periodogram shows Lomb-Scargle peaks that vary depending on the line. The H_α line shows the ~ 1.126 days peak that was seen in the 2D periodogram, while the H_β and H_γ lines have peaks at ~ 0.99 days, and the H_δ at ~ 1.01 days. When looking at the corresponding wrapped phases (Fig. B.12, left column, green points), all of them seem reasonable, despite H_β, H_γ and H_δ having wide gaps in the phase. The CLEAN version keeps the ~ 1.126 days peak in H_α and ~ 0.990 days peak in H_β, but suppresses all ~ 1 days peaks in H_γ and H_δ, instead giving rise to the ~ 0.338 days peak. It should be noted that in H_β, the ~ 0.338 days peak is the 3rd brightest peak, and is absent from H_α. The presence of that



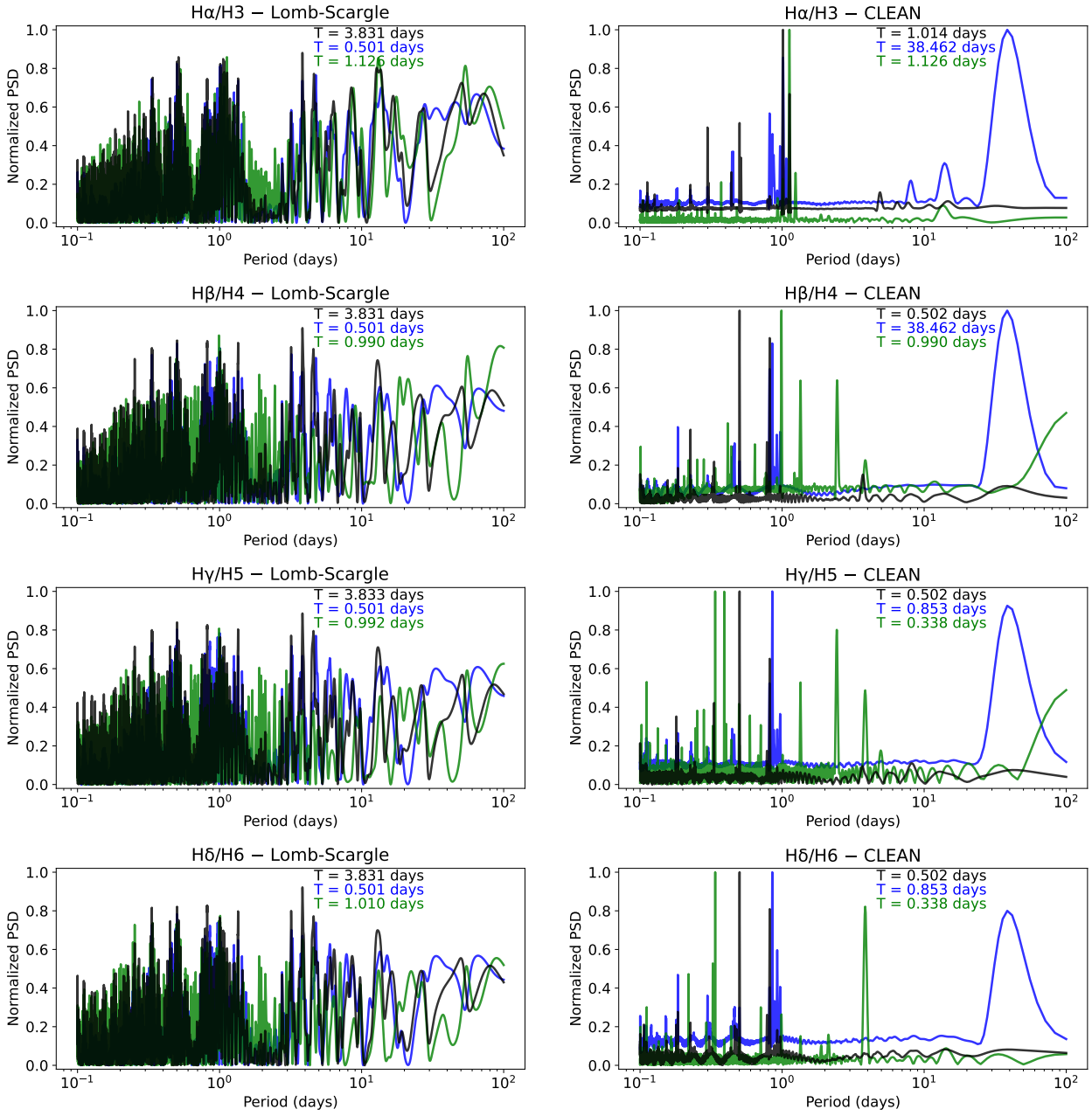


Figure III.39: Wrapped data for the main peaks highlighted in Figs. III.35, III.36, III.37 & III.38, with the CLEAN method. The color coding is the same as in Fig. III.14. The periods and velocity bins used for plotting are given in the top left corner of each panel.



peak in mostly H_γ and H_δ is in line with the location of that peak in the 2D periodograms, where it slowly moves to ~ 0 km/s at higher order lines. All of the wrapped phases seem reasonable (Fig. B.12), and match those found for 2D periodograms (Fig. B.11).

In summary, the ~ 1.12 days peak that was found in H_α is best explained by the green centered component, but the ~ 0.338 days peaks found for H_β, H_γ and H_δ are surprisingly well explained by the green component as well. One would have expected it to be a composition of both the blue and green components because of its location at transition between both components, but the blue component itself does not have any significant peak. These results are obviously to be interpreted with caution due to the low and random sampling occurrence: the observing program was not designed for such an analysis, but rather in Service Mode to profit from the best seeing possible. A visitor program would provide a much finer sampling (see for example, SR 12 c Sect. 6).

5.8 Model fitting

Accretion lines had never been observed at such resolution for PMCs. They provide the opportunity to constrain the accretion flow, and models predicting emission lines. In this section, I compare the lines to predictions of magnetospheric accretion models from Thanathibodee et al. (2019). The same study will be done for shock models (Aoyama et al., 2018), although not in this manuscript.

5.8.1 Models description

The models are the Magnetospheric Accretion models from Thanathibodee et al. (2019): the same ones as those used for modeling the Pa_β line of GQ Lup b and GSC 06214-00210 b. The Shock models from Aoyama et al. (2018) (at least those we have access to) do not have the sufficient spectral resolution to perform a similar analysis. The magnetospheric accretion models exist for both H_α and H_β. They assume an axis-symmetrical dipolar magnetic field. This means that the accretion flow should also be axis-symmetrical, and can therefore be described in a 2D (r,z) plane. At the time of writing, the parameters range in the model is given in Table. III.3. Respectively, they correspond to the inner truncation radius (R_{in}), width of the column (Width), accretion rate ($\dot{M}$), column temperature (Tcol), inclination of the system (i), planet mass (M_p), radius (R_p) and effective temperature (T_{eff}).

Table III.3: Parameters range for the magnetospheric accretion models (Thanathibodee et al., 2019).

R_{in} (R_p)	Width (R_p)	$\dot{M}$ ($M_\odot$/yr)	Tcol (K)	i (°)	M_p (M_{Jup})	R_p (R_{Jup})	T_{eff} (K)
1.5 – 6.0	0.5–2.5	$9.5 \times \left(10^{-13} - 10^{-10}\right)$	6 000 – 10 000	15 – 75	11–13–15	1.4-1.5-1.6	1800

The fits are performed by computing the χ^2_r over the whole grid. However, the models output are the sum of both the accretion line and the photosphere continuum. While this makes sense in the context of CTTS, the continuum is barely visible in the case of Delorme 1 (AB)b. In our case, the line is so bright compared to the continuum that the continuum itself lies within the noise level. The photospheric continuum was fitted as a linear function, and subtracted from the models. This procedure leaves some models with negative values in some places (where the absorption components were deeper than the continuum) but this is the best that can be done with the current models. I therefore only fit the line profile, after subtraction of the continuum, and normalization of the lines to 1 around ~ 0 km/s.



5.8.2 Sub-components fitting

I test both the blue and green components with these magnetospheric accretion models. The resulting χ^2_r parameters spaces for the blue and green components of both H_α and H_β are shown in Figs. B.15 to B.22. Fig. III.40 shows a sketch of the best fit of the core of each line, for both blue and green components, along with the fit itself as insets. Fig. III.41 shows the same thing, when fitting on the full width of the line.

H_α's blue component fitting is able to broadly reproduce the main absorption features of the line, both in the core and full-range fitting. However, the best-fit model appears to yield a much narrower magnetosphere in the full-range fitting than in the core-fitting. This is explained by the degeneracy between the accretion rate and the column width seen in the full-range fit (Fig. B.17): a higher accretion rate with a wider column broadly yields a similar column density, with similar shaped absorption features. Therefore, the core and full-range fitting of H_α's blue component are compatible, with respect to that $\dot{\mathrm{M}}$–Width degeneracy. Both fits broadly yield a low accretion rate, and high column temperature, that is degenerated with the opposite: high accretion rate and low column temperature (Figs. B.15 and B.17). Both core and full-range fitting yield high inclination, in the $60 - 75°$ range.

H_α's green component fitting also is able to reproduce the main features of the line, but differently in the core and full-range fitting cases. In the core-fitting, the line's wobbles at the peak are reproduced by the models, although this might just be over-fitting of the noise within the data. The blue wing is nicely reproduced, but extended red wing is still higher than the model. In the full-range fitting, the line width at the top is narrower than the data, but the red extended wing is nicely reproduced. The blue wing, however, largely differs between the model and data, with the model being mostly symmetrical. Both the core and full-range fitting yield magnetosphere that are relatively thin. However, the truncation radius is large in the core-fitting case, and low in the full-range fitting case. This difference might be explained by the fact that the core-fitting displays two minima in the χ^2_r grid (Fig. B.16), at truncation radii of 1.5 $\mathrm{R_{Jup}}$ and 3.0 $\mathrm{R_{Jup}}$. The column temperature and accretion rates of the two, however are not compatible: the core-fitting yields a low accretion rate and high column temperature (Fig. B.16, similar to the core fitting of the blue component), while the full-range fitting yields a high accretion rate and low column temperature (Fig. B.18, similar to the full-range fitting of the blue component). Note however, that the core and full-range fitting yield different inclinations: $\sim 30°$ for the core-fitting, and $\sim 75°$ for the full-range fitting.

H_β's blue component has a different behavior. The main absorption in the center of the line is only reproduced in the core-fitting, which does not reproduce the wings of the component. However, the full-range fitting is able to reproduce the wings, without the central absorption. Both best-fits yield magnetosphere that have similar extents, that mostly differ by their respective $\dot{\mathrm{M}}$ and temperature. However, the χ^2_r grids show that there are huge (but different) degeneracies in both cases. In the core-fitting case, the magnetosphere shape is hardly constrained, all geometries (Rin, Width) are possible, as long as the inclination is higher than 30°, with a preference for small Rin and high Width. The accretion rate and column temperatures also are highly degenerated. In the case full-range case, the geometry also prefers a small Rin and high Width, but with all inclinations possible. However, the model highly prefers a high accretion rate, as well as a high column temperature, likely explaining how it is able to reproduce the wings. Still, the general shape of the magnetosphere is compatible with that seen on H_α's blue component, in both core and full-range fitting cases.

H_β's green component has a similar behavior to that of H_α, both in the core and full-range fitting cases. In the core-fitting case, the width of the line is well reproduced, as well as the red-wing, but not the blue wing. The slope at the top of line, however, does not match that of the data. In the full-range fitting case, both wings are fairly well reproduced, along with the width of the line. The magnetosphere extent is similar in both cases, and in agreement with that of H_α's: a thin an close-in funnel. It is, however, slightly degenerated



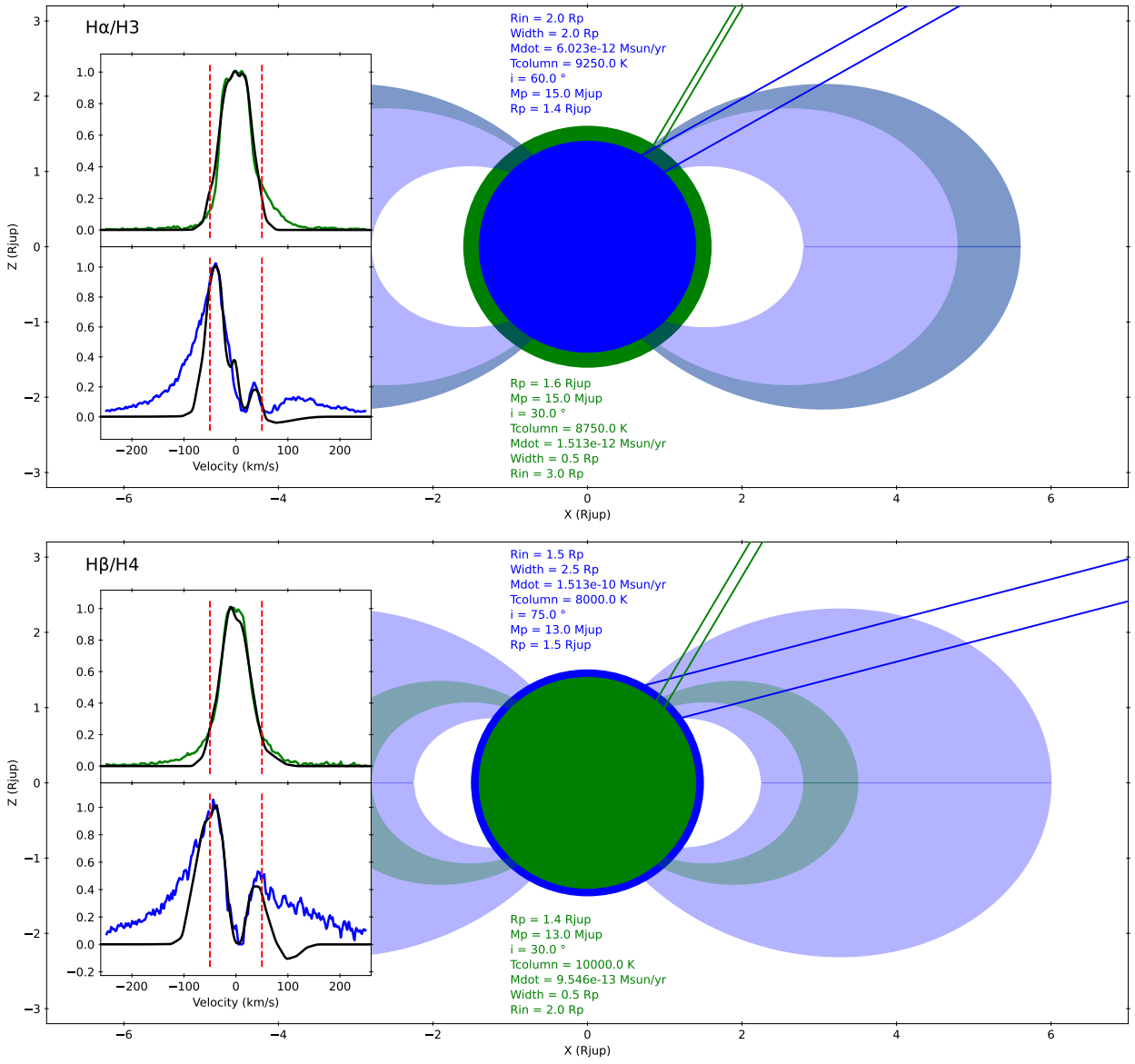


Figure III.40: Sketch of the best fit model for the core of both the blue and green components of H_α (top) and H_β (bottom). The blue/green line in the top right of the image corresponds to the line of sight intercepting the shock. The insets on the left show the fitted data (blue/green) and the best fit (black line), along with the fitting limits (red dashed lines).

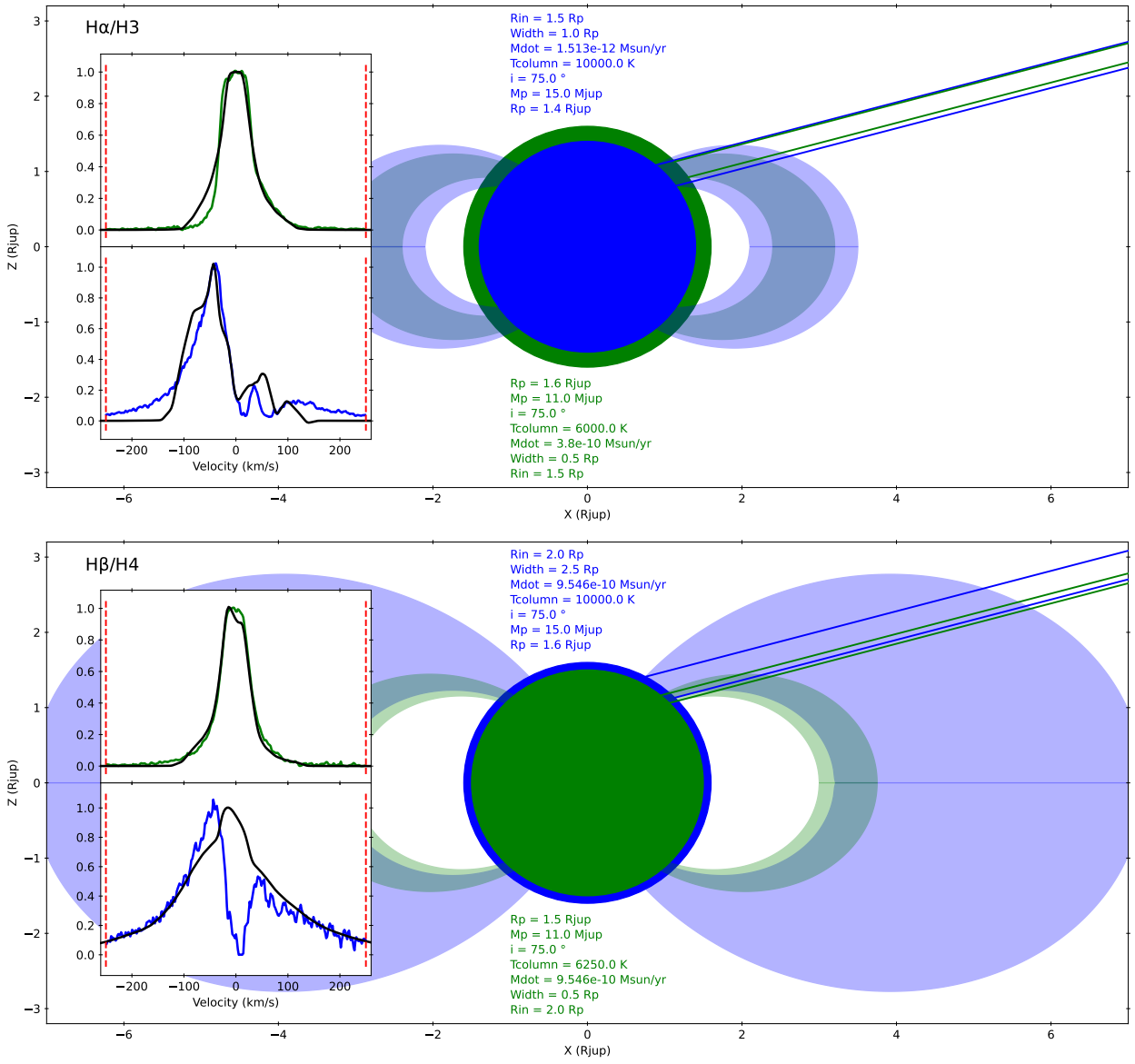


Figure III.41: Same as Fig. III.40, for the full fitting range. Sketch of the best fit model for the full range of both the blue and green components of H_α (top) and H_β (bottom). The blue/green line in the top right of the image corresponds to the line of sight intercepting the shock. The insets on the left show the fitted data (blue/green) and the best fit (black line), along with the fitting limits (red dashed lines).



with a wider and extended magnetosphere. Its inclination slightly differs between the core and full-range fitting cases: the full-range prefers a highly inclinated system, while the core-fitting has two minimas, at low ($< 30°$) and high ($75°$) inclinations. The degeneracy is lifted by the fitting of the wings in the full-range fitting. The temperature and accretion rates, in both cases, are degenerated between low-$\dot{M}$/high-Tcol and high-$\dot{M}$/low-Tcol, similarly as H_α's green component.

In general, the radii and masses of the planet in all fitting cases slightly differ. However, all geometrical parameters are given in terms of planetary radius. The planet radius therefore serves a scaling parameter for the truncation radius and column width, and the fitted solutions should not be interpreted as a robust determination of that parameter. The best-fit value varies from a fit to another, but may also only serve as a scaling parameter for the location and intensity of various absorption features. This would be especially be true for a low sampling rate of geometrical parameters, in particular the inclination, which only increments in 15° bins. Overall, the Mass variation are relatively two small over the grid to be studied in details (11–15 M_{Jup}), especially given the qualitative aspect and the non reproducibility of some of the profiles by the models.

5.9 Discussion

5.9.1 Lines variability

Eriksson et al. (2020) had already given a glimpse into the lines variability of Delorme 1 (AB)b, and this work provides a detailed picture of its variability behavior, both in terms of shape and luminosity. The variability diagrams (Fig. III.33) show that, similarly to GQ Lup b and GSC 06214-00210 b, the variability at ∼hour timescale is a lot lesser than that at longer timescale. However, while GQ Lup b and GSC 06214-00210 b had non-negligible variability at the ∼hour timescale, Delorme 1 (AB)b lines only vary by a few %, up until H_δ (Fig. III.34). Higher order lines do reach 10–40% variability, similar to that of the Pa_β line of GQ Lup b and GSC 06214-00210 b. However, the line-flux variability is mostly driven by its green component, whereas the blue component does reach several ∼ 10 % variability right from H_α and up. The blue-component variability mostly affects the shape of the line profile, with the blue-wings excess in the outburst epochs. The amplitude of variability for each timescales, however, is similar to that of GSC 06214-00210 b, which may hint at a common emitting mechanism.

Previous studies had proposed line variability as an explanation for the low yield of detection of H_α imaging campaigns (Demars et al., 2023; Follette et al., 2023), as most surveys do not consider multiple visits of a given target. However, if Delorme 1 (AB)b properties are typical of most PMCs, then its overall low variability range (< 10 %) at the ∼ hour timescale cannot explain the yields. Even longer timescales (∼months) only reach about ∼50 % variability, which seems too low as well for having missed so many companions. The variability at the year timescale does reach factors of 2–3, but it is only driven by the pilot epoch (Ringqvist et al., 2023), and might not represent the full variability at this timescale. However, Delorme 1 (AB)b does show some tentative signs of rotational modulation of the lines, as highlighted by the periodograms. The sampling is currently too scarse to be really conclusive, but dedicated campaigns with a finer sampling should be able to provide stronger constraints on the lines variability and periodicity, at a reasonable observing cost. Because the lines have been shown to only vary by a few % at the ∼hour timescale, a dedicated campaign should focus on the day-to-day variability, only adding to ∼ 1 hour per night. The length of the campaign should be of at least 2 periods, which could be anywhere between 0.3 and 5 days.



5.9.2 Lines origin: clues from Helium

Delorme 1 (AB)b shows a lot of differently shaped lines: the Balmer lines (H_α, H_β, ...), but also the Helium lines. While they were not presented earlier, a first order analysis of HeI6680 and HeI5877 are shown in Fig. B.13 and Fig. B.14 respectively. They show the results of Gaussian fitting of these two lines, along with the correlation between the Helium lines scaling and the UV excess and the blue/green components of H_α. The Helium lines have a slight correlation between their width and their amplitude, and a clear correlation between their amplitude and the UV excess. The UV excess, when seen in CTTS, is linked to the accretion shock when the funnel hits the star. While boundary-layer accretion can also generate an UV excess, its generation at the base of a funnel is strongly supported by the only slight red-shift of the Helium lines: it is consistent with emission in the post-shock region, where material has converted its kinetic energy into heat/radiation, sufficient to trigger Helium emission. The lack of variability in the Helium lines peak velocity does show that the emission is likely axis-symmetrical, or could result from a low $v \sin i$ of the planet (although, if seen edge-on, the 3 km/s spread of the HeI lines peak would result in a rotational period of ~ 60 h).

The Helium lines are also strongly correlated with the Blue component of H_α, which was to be expected given that H_α's blue component is also strongly correlated with the UV excess, and so are all blue components of all Balmer lines. It does not mean, however, that the Helium lines, the blue components, and the UV excess, are all emitted in the same region. It would even be quite unlikely given that the blue components have widely extended wings, up to 250 km/s on either side, while the HeI lines are really narrow, even when blended with other lines (e.g., HeI5877 line doublet). The Helium lines are only slightly correlated with the Green component of H_α, which is also consistent with the lesser correlation between the green component and the UV excess. This strongly suggests that Helium lines and Hydrogen blue components are linked to the same process, like in CTTS. Helium lines and the UV excess would be formed in the shock, and H_α's blue component would be formed at the base of the funnel, just above the shock.

5.9.3 The Magnetospheric Accretion scenario

Magnetospheric Accretion models show that both blue and green components can be reproduced (to some extent) by an infalling funnel. The main absorption features in the core of the blue component can be reproduced, but not simultaneously with the extended wings. As for the green component, the general narrow emission feature is consistent with a thin accretion funnel. The fact that axis-symmetrical models are able to reproduce the main lines features, along with the constant velocity shifts of the Helium lines, the sole static shapes decomposition (blue/green) of Balmer lines, and the overall stable shape of the full lines, supports an axis-symmetrical system, likely accreting through Magnetospheric Accretion. In that scenario, the rotation of the magnetosphere would not have any effect on the accretion flow, and the whole observed variability would not be due to the rotation of the magnetosphere, but rather to changes in the accretion rate and column temperature. Still, this could also mean that the planet is viewed from the pole, but would go against the models that are able to reproduce the line at high inclinations.

However, the sole fact that Magnetospheric Accretion models are capable of fitting both the blue and green components, is surprising. This naively implies that two magnetospheres, or two sets of funnels, are at play. This could mean that Delorme 1 (AB)b is actually an unresolved binary, which would accrete from their surrounding circum-binary disk. This is consistent with the correlation between H_α's blue and green component (Fig. III.26), where the 2022-10-14/15/17 outburst would trace epochs where the gas would have preferentially accreted on one of the planets. However, the correlation should then be observed for all lines, which is not the case: the blue/green components correlation diminishes with higher order lines (Fig. B.8).



Should the two sets of funnels be induced by a single magnetosphere, this naively would match with an axis-symmetric magnetosphere, as it expects the accretion pattern to be axis-symmetrical as well. This would hold if the magnetic field is not sufficient to entirely truncate the inner disk, letting some gas go past a first launching radius, to a second launching radius, and therefore a second funnel. This should be apparent in the physical parameters of the best models. The blue component always fits with high inclination models, while only full-range fitting of the green component yields a high-inclination. However, the full-range fitting of the green component, whether it is for H_α or H_β, provides a way better fit of the wings. H_β's blue component wings are reproduced with an extended magnetosphere, where the funnel is fairly hot (10 000 K), while the secondary (inner) funnel that would be responsible for the green component would be much cooler (6 250 k, Fig. III.40), with similar accretion rates. Overall, the current degeneracies in the model are too complex to paint a clear picture of the scenario. It is also possible the physics involved in the Magnetospheric Accretion models are too simplistic to fully reproduce the underlying scenario. Alternatively, one component may arise from a different mechanism: likely the green one which is not correlated with the UV excess (see Sect. 5.9.5).

5.9.4 Shock contribution

The correlations between blue components and UV excess (Fig. III.31) show that the blue component is only emitted past a *threshold* of UV excess: the correlation does not extend to (0,0), but crosses the X axis. As for the green component, the correlation could be interpreted as a threshold of green component emission for UV excess to appear. However, the poor correlation likely means that if green component and UV excess emission are linked, this is only to a moderate degree. Still, the width of the green component is broadly compatible with what is expected from Shock models (Aoyama et al., 2018), which would suggest that it is emitted there, but then a strong correlation with the excess and the Helium lines would be expected, as they would trace more-or-less the same region. Radiative transfer, optical depths and opacities effects could be the explanation. While the blue component would be emitted in a broadly optically thin medium (the part of the accretion column close to the planet), the post-shock region emission could be saturated, explaining the plateau-like shape at the peak of the green component. This plateau diminishes with higher order lines (H_β, H_γ, H_δ), and increases the correlation with the UV excess, as is the case from Fig. III.31. However, this would not encapsulate that trend fails when including H_α's green component, which is more correlated with the UV excess than H_β's, H_γ's and H_δ's. A complete modelisation of Balmer lines emission from Shock models is required, and is currently in progress.

5.9.5 Chromospheric contribution to the lines?

A possible explanation to the emission lines is chromospheric activity, where the lines would not be emitted through accretion processes, but rather in the chromosphere of the object. Chromospheric activity is known to play an important role in the emission lines of M dwarfs, and has been considered as a noise in the context of accretion. Manara et al. (2013, 2017) proposed that the lines brightness could be seen as two regimes: one where the line intensity is below a threshold where it is compatible with chromospheric activity, and one where it is above that threshold and most of the line flux comes from accretion. In the case of Delorme 1 (AB)b, Eriksson et al. (2020) found that using common line-luminosity–$\dot{M}$ relations (although obtained from CTTS observations), Delorme 1 (AB)b mass accretion rate is far above the threshold for the lines to be originating from chromospheric activity. However, they used VLT/MUSE observations, in which the lines profiles were unresolved. The work presented here shows that Balmer lines profiles have plateau-like shapes for H_α and H_β, and symmetrical profiles for higher order lines. This plateau-like shape is surprisingly similar to that found for active M dwarfs (M4–M5, Fuhrmeister et al., 2018; Muheki et al., 2020), although these do not



have extended wings such as Delorme 1 (AB)b. The green-component obtained from line decomposition, however, does not display these wings, and serves as a good match to the profiles of active M-dwarfs. If the green component is in fact a sign of chromospheric activity, it would still go against the chromospheric noise limit, which is supposed to go down with later spectral types, making its apparent brightness even more of an issue. This is verified in Fig. B.25, which shows that the green components converted accretion luminosity is not compatible with the threshold for chromospheric contamination from Manara et al. (2017). It even seems that the blue component does have fluxes compatible with chromospheric emission, although this is quite unlikely given the highly different profiles to that of Fuhrmeister et al. (2018) and Muheki et al. (2020).

Overall, the chromospheric explanation to the green component may still hold. The number of samples at such low masses from Manara et al. (2017) is quite low, and the chromospheric noise limit may simply be underestimated. Furthermore, Venuti et al. (2019) results seem to show a greater chromospheric contribution for objects alike Delorme 1 (AB)b. If the green component is in fact emitted from chromospheric processes, then the responsible magnetic field would not correlate with accretion rate changes. They would be produced by small magnetic field loops at the surface of the planet, decorrelated from the large scale dipolar magnetic field.

However, chromospheric activity could be the key to the low correlation factor of the green component with the UV excess. If magnetic field variations are responsible for changes in the chromospheric component (green component), they are also likely to induce changes in the accretion rate at the column launching radius. However, these accretion rate changes would not immediately reflect in the accretion-components, as they would only be affected once the material reaches the emitting regions. In this scenario, the green components changes variations should on average be correlated with UV excess changes, but the correlation would be blurred in our data because of the time-delay between each other's variation. This scenario can only be marginally constrained with the data at hand. Fig. B.23 shows the velocity profile along an accretion funnel, and the time it takes to reach the shock, depending on the launching radius. It takes $\sim$ 0.5 h for a funnel launching at $\sim$ 1.5 Rp, up to $\sim$ 3 h for a funnel launching at $\sim$ 5 Rp. Each epoch only covers $\sim$ 1 h of observations, in two exposures of 25 mins. Fig. B.24 shows the H_α's green component correlation with the UV excess, for varying time delays between the two. Only the time-delay of $\sim$ 25 mins (the typical timescale between two exposures) can be checked, while others have too low data-points to be meaningful. Testing this scenario would be quite expensive in terms of observing time, as it would require several runs of $\sim$ 3 hours to check for all possible time-delays. However, would that scenario be evidenced by other means, such observations could serve as a way to infer the actual size of the magnetosphere.

5.9.6 Spectral type and apparent continuum

As shown by the correlation between the UV-excess and the continuum at longer wavelengths, such as around H_α, it is likely that the observed continuum is actually only tracing the accretion shock, at least where H_α lies. However, as shown in the right panel of Fig. III.42, the UV excess flux does not correlate so well with the observed magnitude of the companion (GAIA GBp). This means that the aforementioned UV–continuum relation likely only exists at longer wavelengths. Zhou et al. (2021), their Fig. 7, shows the fitted UV excess of PDS 70 b. It shows that the UV excess flux can be more important at H_α wavelengths than red-wards of the Balmer jump, which could explain the lack of correlation shown in Fig. III.42, right panel.

Figure III.42, left panel, shows the evolutionary tracks relations for cloudless brown dwarfs (ATMO2020 models, Phillips et al., 2020; Tremblin et al., 2015, 2016), in particular the Mass–GAIA_Gbp relations, for ages between 1 Myr and 45 Myr. On this image, observed magnitudes are corrected from the distance modulus, therefore the values plotted are the intrinsic magnitudes. It is clear that apart from two exposures of epochs 2022-11-04 and 2022-11-05, which are likely non-representative given the poor Strehl ratios of these



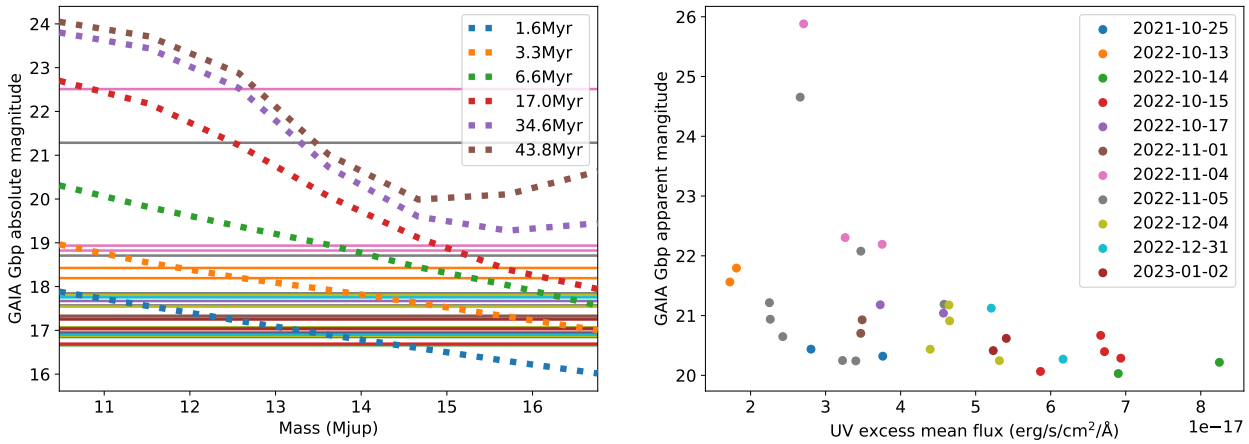


Figure III.42: Left: Mass–GAIA_Gbp absolute magnitudes relationships for ATMO evolutionary models (Phillips et al., 2020; Tremblin et al., 2015, 2016). The horizontal lines are the measured GAIA GBp magnitudes from the observations in this study. If the evolutionary models hold, the crossing point between the horizontal lines and the dotted lines provide an estimate of the planet mass at a given age. Right: GAIA_Gbp apparent magnitude relation to the UV excess mean flux level.

nights, neither the 34.6 Myr nor the 43.8 Myr isochrones match the observed magnitudes. Only isochrones for ages within 1–7 Myr are able to catch these values, incompatible with the estimated age of the system (45 Myr). However, if the GAIA GBp magnitude is in fact dominated by the UV excess, a shift (of unknown value) to greater magnitudes should be applied.

Still, Delorme 1 (AB)b has been identified as an M9-L0, $\sim$ 13 M_{Jup} companion on several occasions (Delorme et al., 2013; Betti et al., 2022,; Eriksson et al., 2020), and it is likely the data presented in this work have some bias in their continuum given that it is so close to the noise limit. However, if the continuum values are correct, this could have multiple implications:

- The isochrones could simply be unable to reproduce the flux values due to intrinsic biases in the models,
- The companion could be a lot younger than is currently thought from membership arguments. This could imply that it has formed a lot later than the rest of its siblings, or that it formed in the circumstellar disk of the host binary at a later stage. However, this is unlikely as the disk would have long been gone by the time the companion would have formed. Alternatively, it could have formed independently from Delorme 1 (AB), and simply captured during its early stages (late stages of the central binary).
- The whole system could be a lot younger than estimated. Its age was derived from its membership to the Tucana-Horologium group with the BANYAN tool (Gagné et al., 2018). However, the binarity of the central star might have biased the GAIA astrometric solution. No study has yet provided an estimate of this possible bias.
- The companion continuum could be dominated by the accretion shock to a much greater level than is possible to assess through UV-Gbp correlations, while the correlation would not be a straight cause-



and-effect from one to another. This is supported by the fact that there are slope variations of the UV excess itself (Fig. B.4).

The answer to that question lies in a full-spectrum modeling of the accretion shock (and photosphere), to not only assess its parameters, but also its effects on the continuum of the companion itself. Unfortunately, this has not been done during my PhD, but this is planned for the months to come, in collaboration with E. Rigliaco.

5.9.7 Is Delorme 1 (AB)b an outlier?

Delorme 1 (AB)b is the best-case scenario in terms of ease of study. It is close to us ($\sim$ 47.2 pc), making it appear at a relatively high separation from its host stars ($\sim$ 1.8") while still being physically relatively close to them ($\sim$ 85 AU). Given its really old estimated age (45 Myr) compared to other usually young companion, this yields the question of whether there are other similar companions, and even whether it shares any similarity with any other PMC. Delorme 1 (AB)b is definitely not alone: Boucher et al. (2016) had presented 2M0226, which is also an old companion, with a disk and Pa_β emission. Even if Delorme 1 (AB)b lines are not alike those of SR 12 c (younger PMC, see Sect. 6) they are really similar to that of 2MASS J11151597, with the same plateau-like shape (see Sect. 7). GSC 06214-00210 b lines are also probably similar to that of Delorme 1 (AB)b. Fig. II.7 showed the correlation between different Gaussian-fitted parameters for the Pa_β line of GSC 06214-00210 b. The third panel showed the correlation between the line intensity and the line width, which were correlated. This means that the wings of the lines are likely independently scaling from the core of the line, to permit the width variation. This can be explained is the same blue/green component applies to the Pa_β line of GSC 06214-00210 b, where the blue component would permit adding flux in the wings, without modifying the core, hence increasing the apparent width of the line. Still, GSC 06214-00210 b is not that much of an extremely young companion either, as its estimated age is 16.9 Myr (Pearce et al., 2019), which is still above the typical timescales for disk dispersal ($<$ 10 Myr). 2MASS J11151597 has quite an unconstrained age (5–45 Myr, Theissen et al., 2017). Delorme 1 (AB)b definitely has some similar PMCs, however, it is still unsure whether they are similar to much younger targets.

6 SR 12 c

6.1 Observations

SR 12 c was observed with VLT/UVES in designated Visitor Mode (dVM), as the main target of the program 111.24P3.001[14] (PI: Bonnefoy). The observations were performed on four consecutive half-nights, in the first half of nights ending on 2023-06-11/12/13/14. The observing setup was the same as the one used for Delorme 1 (AB)b, at the exception of the guiding arm which was the RED arm for this observing sequence. Companions are intrinsically brighter in the RED arm than in the BLUE arm, making it best suited for the guiding. The slit was aligned on the axis perpendicular to that of the primary–companion axis. The primary is a young CTTS, which is prone to sudden brightness variations. Even if the large separation (8.7") ensures that there is no contamination at the companion location, it was estimated at the time that there was a chance of saturating the detector if the slit was aligned on the primary–companion detector, especially with the high DIT values used in this run (1482s) and in case of excellent seeing and sky transparency.

The observing conditions varied a lot during the nights, with sudden spikes in seeing, in particular in the second round of observations. Most importantly, we noticed drifting of the field along the night. It

[14] **111.24P3.001**: https://archive.eso.org/wdb/wdb/eso/sched_rep_arc/query?progid=111.24P3.001



Target	Date (HH-MM-DD)	UT start (hh:mm:ss)	UT end (hh:mm:ss)	DIT (s)	seeing (")	airmass	τ_0 (ms)
SR 12 c	2023-06-11	23:46:53	00:11:35	1482	1.00	1.66	3.62
SR 12 c	2023-06-11	00:12:12	00:36:54	1482	0.98	1.48	3.51
SR 12 c	2023-06-11	00:38:02	01:02:44	1482	0.95	1.34	3.46
SR 12 c	2023-06-11	01:03:24	01:28:06	1482	0.91	1.23	3.93
SR 12 c	2023-06-11	01:29:16	01:53:58	1482	0.63	1.16	5.16
SR 12 c	2023-06-11	01:54:35	02:19:17	1482	0.66	1.10	5.08
SR 12 c	2023-06-11	02:20:25	02:45:07	1482	0.63	1.06	5.96
SR 12 c	2023-06-11	02:45:46	03:10:28	1482	0.50	1.03	6.76
SR 12 c	2023-06-11	03:11:36	03:36:18	1482	0.56	1.01	6.94
SR 12 c	2023-06-12	23:45:20	00:10:02	1482	1.66	1.64	2.19
SR 12 c	2023-06-12	00:10:38	00:35:20	1482	2.02	1.46	1.76
SR 12 c	2023-06-12	00:36:28	01:01:10	1482	1.41	1.33	2.35
SR 12 c	2023-06-12	01:01:51	01:26:33	1482	1.49	1.23	2.36
SR 12 c	2023-06-12	01:27:41	01:52:23	1482	1.70	1.15	2.32
SR 12 c	2023-06-12	01:53:03	02:17:45	1482	1.36	1.09	2.17
SR 12 c	2023-06-12	02:18:54	02:43:36	1482	1.28	1.05	1.97
SR 12 c	2023-06-12	02:45:45	03:10:27	1482	1.18	1.02	2.05
SR 12 c	2023-06-12	03:11:35	03:33:58	1343	0.83	1.01	2.54
SR 12 c	2023-06-13	23:21:21	23:46:03	1482	1.13	1.83	1.82
SR 12 c	2023-06-13	23:46:45	00:11:27	1482	1.01	1.60	2.00
SR 12 c	2023-06-13	00:12:36	00:37:18	1482	1.16	1.43	1.98
SR 12 c	2023-06-13	00:37:56	01:02:38	1482	0.90	1.30	1.86
SR 12 c	2023-06-13	01:03:47	01:28:29	1482	0.82	1.21	2.00
SR 12 c	2023-06-13	01:29:08	01:53:50	1482	0.97	1.14	1.85
SR 12 c	2023-06-13	01:54:58	02:19:40	1482	1.10	1.08	1.74
SR 12 c	2023-06-13	02:20:21	02:45:03	1482	0.97	1.04	1.96
SR 12 c	2023-06-13	02:46:11	03:10:53	1482	0.87	1.02	2.35
SR 12 c	2023-06-13	03:11:33	03:29:52	1099	0.82	1.01	2.50
SR 12 c	2023-06-14	23:37:11	00:01:53	1482	0.70	1.65	4.22
SR 12 c	2023-06-14	00:02:30	00:27:12	1482	0.84	1.46	3.90
SR 12 c	2023-06-14	00:28:21	00:43:04	883	0.94	1.35	3.20
SR 12 c	2023-06-14	01:02:14	01:26:56	1482	1.00	1.20	3.32
SR 12 c	2023-06-14	01:27:33	01:52:15	1482	0.94	1.13	3.06
SR 12 c	2023-06-14	01:54:36	01:55:47	71	0.90	1.10	2.89
SR 12 c	2023-06-14	01:58:46	02:23:28	1482	0.91	1.07	2.60
SR 12 c	2023-06-14	02:24:09	02:48:51	1482	0.92	1.04	2.59
SR 12 c	2023-06-14	02:56:48	03:21:30	1482	1.04	1.01	2.60
SR 12 c	2023-06-14	03:22:06	03:28:06	360	0.96	1.00	2.91

Table III.4: SR 12 c's observation log.



first appeared to us as we were live-reducing data: the H_α line became continuously fainter, to the point it reached noise-level of the detector after $\sim$ 2 hours. A quick look into the Slit-viewer confirmed that the target was drifting out of the slit, however it required integration of 10–15 mins on the SV to actually see the companion's wings behind the slits. We realized the existence of that effect on the second or third night, and decided to re-perform the acquisition every $\sim$ 1–2 hours to mitigate. We still do not know what was the cause of that drifting, and any flux calibration will likely be challenging because of it. The observation log is provided in Table. III.4.

6.2 Quick-look: Data reduction

With its high separation from its host binary, SR 12 c appears alone in the field of view of UVES, making the extraction trivial. However, I present here a simplified version of the extraction, performed straight from the raw detector, during the observing run. Future work should perform a proper extraction and calibration.

H_α lines for each exposures were extracted from the raw, uncalibrated, detector. Cosmics were identified using routines presented in Sect. 4. The order in which the H_α line lies was isolated, then each spectral bin was fitted with a single Gaussian (for the PSF of the companion) and a baseline (Sky emission, and detector defects). The wavelength solution is the one found for Delorme 1 (AB)b, with the added correction of the radial velocity of the system ($\sim$ 7 km/s, Santamaría-Miranda et al., 2018, 2019). While UVES was built for stability of the instrument, it is likely that the wavelength solution is off by a few km/s. This quick reduction should only provide a quick look of the lines profiles.

With the drift of the target outside of the FoV (mentioned in the previous section), the flux calibration is not possible. Therefore, all lines were normalized to 1 around $\sim$ 0 km/s. The H_α lines are shown in Fig. III.43. The H_β line is only visible in the raw data when stacking exposures, so are higher order lines. However, there are no obvious Helium lines, but a proper reduction may highlight their presence.

6.3 Highly variable lines

The H_α line of SR 12 c clearly is variable in shape, and likely also in flux. While the first and last nights have double-lobed profiles, the other two nights have more single-peaked profiles. On top of the night-to-night variability, there is some variability within the nights, as quick as on 20 mins timescales.

In Night #1, the line peak seems to slightly shift to the blue between the 23:45/00:10 and 00:36 exposure. This is seen by the shift of the blue wing, between the blue/orange lines and others: the wing seems to shift blue-wards by a few km/s.

In the Night #2, part of the line suddenly shifted to the blue, between the 00:37 and 01:03 exposures. While a smooth change in the line shape accross the run duration could be explained by a physical component moving around the target (say, an accretion column), this sudden change instead suggests a component coming in or out of the line of sight, which could correspond to the shock contribution at the base of the funnel, coming in the line of sight.. The change is similar to that of Night #1, with the peak moving blue-wards by 5–10 km/s, although it is much more evident here on Night #2.

In Night #3, the red wing flux lowers along the night, while the line peak slightly shifts to the red. This can mostly be seen between the 23:37/00:02 and later exposures. However, the change is not as abrupt as for the two previous nights. This analysis will be presented in a future paper.



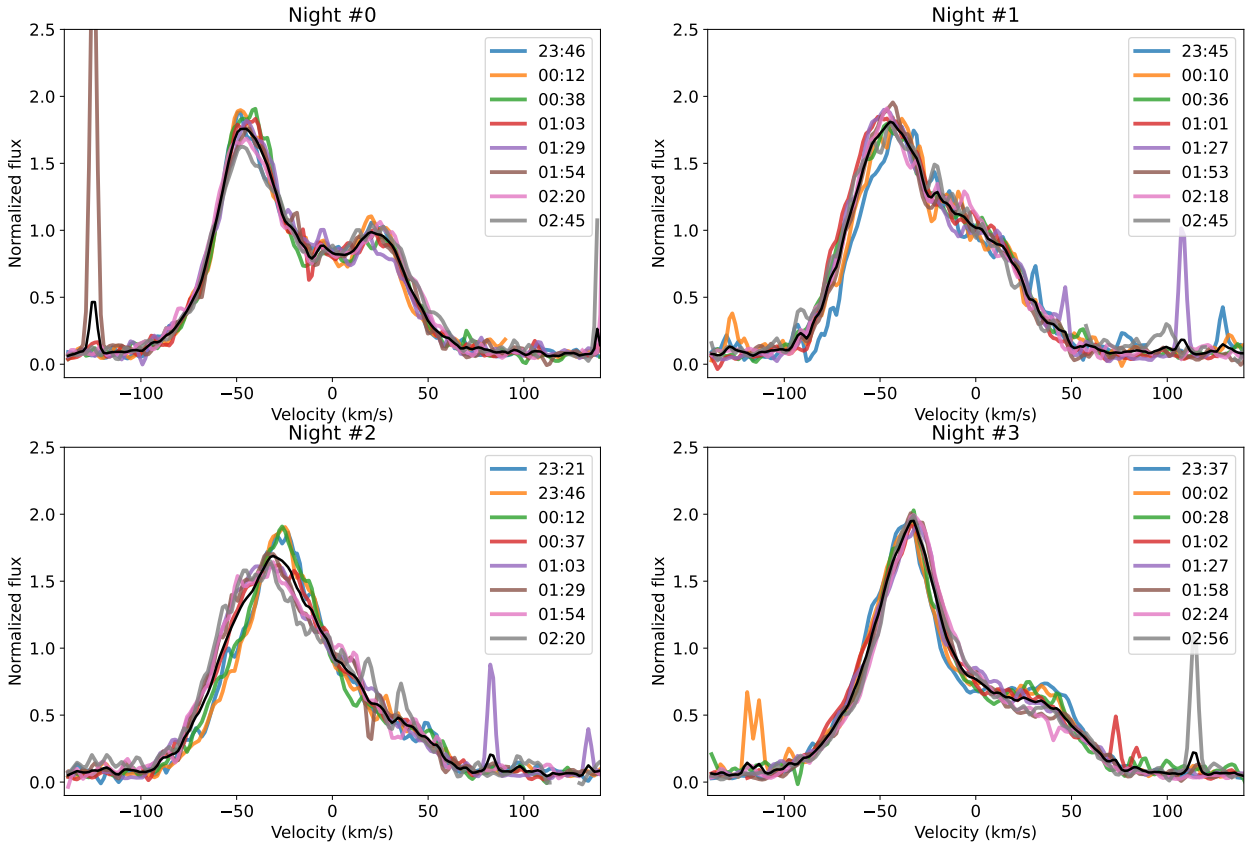


Figure III.43: SR 12 c H_α lines along the 4 consecutive nights. Lines are scaled to 1 around 0 km/s. Exposures with too low S/N are not shown. The black line corresponds to the mean of the night. For clarity, lines have been convolved by a Gaussian of width $\sigma = 1$ px $= 1.55$ km/s. This corresponds to an effective resolution of $R = 42\,000$, instead of $50\,000$.

6.4 Discussion

This analysis is really preliminary, and there is not much to say about SR 12 c's lines yet. Further analysis is required to be really conclusive on the details. However, a few things can be still be highlighted. With the short variability timescales observed here ($\sim$ 20 mins), it is likely it is driven by something occurring close to the planetary surface, otherwise one would expect variations on keplerian timescales.

Whether this variability is the sign of activity or accretion processes is less clear, as both are expected to have features rotating with the planet. However, the absence of Helium lines seems to put aside the presence of a shock, or at least not strong enough for the lines to be visible in the raw data. This would favor activity over accretion, but the variable shape of the lines, and blue asymmetry still are reminiscent of that observed in T Tauri stars, in which magnetospheric accretion is occurring.

The impossibility to flux-calibrate the data also means that it is not possible to obtain accurate lines fluxes. One could still assume that the first exposure was properly centered and calibrate everything with



Target	Date (HH-MM-DD)	UT start (hh:mm:ss)	UT end (hh:mm:ss)	DIT (s)	seeing (")	airmass	τ_0 (ms)
2MASS J11151597	2023-06-11	23:13:47	23:26:07	740	1.56	1.42	4.53
2MASS J11151597	2023-06-11	23:26:49	23:39:09	740	1.53	1.43	4.09
2MASS J11151597	2023-06-12	23:10:27	23:22:47	740	1.59	1.42	3.03
2MASS J11151597	2023-06-12	23:23:24	23:35:44	740	1.31	1.44	3.44

Table III.5: 2MASS J11151597's observation log.

that first exposure, but the error-bars would still be large. An other method could consist in binning the data of each exposure: when stacking all exposures, the continuum seems to be slightly visible, at $\sim 0.5\sigma$ (per pixel, broadly estimated by eye). Similarly to Delorme 1 (AB)b, the continuum may be visible when degrading individual exposures, which could then be used as a calibration baseline. The same method could be used to check whether a UV excess is present or not, and therefore whether it could extend below H_α, thus providing a check of the correct assumption of no continuum variability. That is, of course, unless the continuum is dominated by the extension of the UV excess.

7 2MASS J11151597

The observations of 2MASS J11151597 led to a paper that was submitted to A&A, and was just accepted at the time of writing these lines. While I did not submit the paper as first author, I did contribute to the work. In this section, I present a summary of the analysis, and highlight my contribution. The submitted version of the paper is given in appendix B.

7.1 Observations

2MASS J11151597 was observed with VLT/UVES in designated Visitor Mode (dVM, on which I was observing), as a bonus target of the program 111.24P3.001[15] (PI: Bonnefoy), making use of the twilight time. The observations were performed on two consecutive nights, the ones ending on 2023-06-11 and 2023-06-12. The observing setup was the same as the one used for Delorme 1 (AB)b, at the exception of the guiding arm which was the RED arm for this observing sequence. The observations are likely not too much affected by drifting as they were not obtained during prolonged sequences, which makes flux calibration with respect to the standard star possible. The observation log is provided in Table. III.4.

7.2 Data reduction

The UVES pipeline was developed to extract spectra when the continuum is visible. This is not the case for 2MASS J11151597. Spectra for 2MASS J11151597 were extracted using a custom method that follows the standard procedures flat-dark-bias processing, as well as orders extraction. However, the flux calibration was performed using a mix of ESO pipeline procedures, and publicly available calibration data. While not mentioned above, we observe a Tel. Std. star at the beginning of each run, which I used to reconstruct the instrument response curve. However, because we had found in Delorme 1 (AB)b's observations that the response curve was stable over consecutive days, I only used one of the two Tel. Std. : LTT 6248, which is the

[15] **111.24P3.001**: https://archive.eso.org/wdb/wdb/eso/scheobservedd_rep_arc/query?progid=111.24P3.001



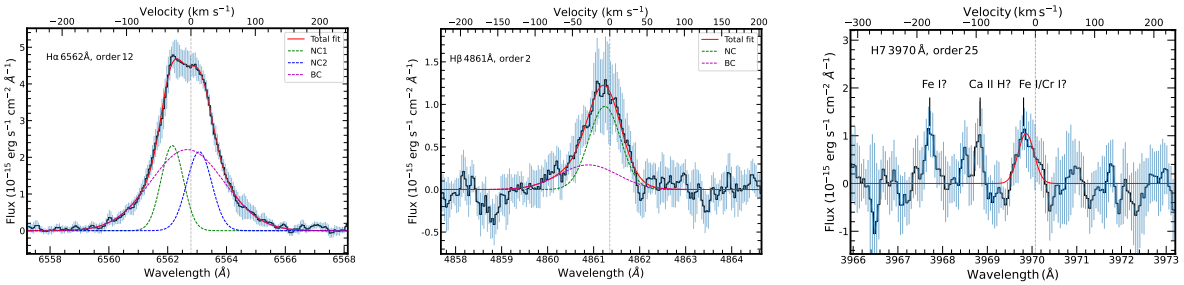


Figure III.44: From left to right: H_α, H_β and metal lines of 2MASS J11151597. Figures from Visnavath et al. (in prep.). Paper available in Appendix B. The blue, green and red dotted lines are the best Gaussian fits to the lines.

one for which a properly calibrated observational-template spectrum was available (SNIFS data, $R \sim 750$, Rubin et al., 2022).

I obtained the instrument response by dividing the observed, non-calibrated, LTT 6248 spectrum, with that from Rubin et al. (2022). I also corrected for airmass and DIT. The resulting curve corresponds to both the instrument response curve, and flux calibration factor. I then applied that curve to 2MASS J11151597 after correcting it for airmass and DIT.

7.3 Results

Figure III.44 shows the H_α, H_β and possible metal lines of 2MASS J11151597, along with the corresponding best Gaussian fits. The H_α shape is reminiscent of that of Delorme 1 (AB)b, although with less extended wings (Delorme 1 (AB)b's wings go as far as ±250 km/s). H_β is much more symmetrical, with a slightly more extended blue wing. H_α is nicely fitted with the sum of 3 Gaussians, 1 broad component (BC) and 2 narrow components (NC), while H_β only requires 1 BC and 1 NC, where the BC mostly allows the extended blue wing. Higher order lines are also detected, but their S/N prevents a fine study of the lines profiles. Some metal lines are possibly present (Fig. III.44), although they are within the noise level. Helium are tentatively detected.

Given the similarity of the line profiles with Delorme 1 (AB)b, it is possible that the same blue/green components decomposition would work for 2MASS J11151597. The H_α line could largely be dominated by the green component, given that it is much narrower than the line of Delorme 1 (AB)b. However, this would require a much more extensive monitoring. Still, in particular for H_β, the broad component is reminiscent of the blue component: the BC is used to reproduce the extended blue wing, which is mostly what the blue component of Delorme 1 (AB)b is for. As for the narrow component, this would reproduce the green component.

Assuming the lines are emitted at a shock, the planetary scaling relations (Aoyama et al., 2021) provide accretion rates of $\log \dot{M} \sim -(7.45 - 8.08) \pm 0.50$ $M_\odot$/yr, depending on the lines. Stellar relations (Alcalá et al., 2017) provide accretion rates of $\log \dot{M} \sim -(8.19 - 8.93) \pm 0.68$ $M_\odot$/yr.

Additionally the possibility of 2MASS J11151597 being bound to 2MASS J1113+2110 is revised. New GAIA distances (Gaia Collaboration et al., 2023) provide an estimate of the physical separation of 1.28 pc, given their 1.62° angular separation. The BANYAN tool (Gagné et al., 2018) provides 99% probability that 2MASS J11151597 is a field object.



While the variability of the lines of 2MASS J11151597 is unknown from this study alone, archival epochs from SDSS provide part of the answer. 2MASS J11151597 had been observed twice with SDSS, once in DR9, once in DR12. The H_α line had varied by ~ 7 % between the two archival epochs, and by ~ 70 % up to the UVES epoch. The number of points is way to small to conduct a detail study of variability, but the spread is at least consistent with what is observed on Delorme 1 (AB)b. However, higher order lines do not have the same behavior. Between DR9 and DR12, H_β, H_γ and H_δ varied by 200–300 %, and by 100-200 % up to the UVES epoch. This spread is not compatible with that of Delorme 1 (AB)b, and it is surprising to observe such different behaviors given the similarity of the line profile, and the high correlation between lines on Delorme 1 (AB)b. It is even more puzzling that H_ϵ had variability much more compatible with Delorme 1 (AB)b (~ 15 %). This target would definitely profit from a campaign similar to that of Delorme 1 (AB)b, to assess its variability amplitude.

8 Summary

This chapter presented the pilot programs of the UVES ExoplaNet accRetion mOnitoring sPectroscopic surveY (ENTROPY, a unicorn in nowadays customs of name-to-acronym robustness). With early results of lines variability (previous chapter, Demars et al., 2023) and the demonstration of the feasibility at achieving high spectral resolution of young PMCs (Ringqvist et al., 2023), the need to combine both came as the natural outcome. I presented high resolution observations of Delorme 1 (AB)b, SR 12 c and 2MASS J11151597, all with different probes of their respective variability behavior. Delorme 1 (AB)b was probed at random timescales, which led to its variability behavior across successive months, while SR 12 c was probed along successive nights, with the hope of highlighting any rotational modulation of the lines.

Delorme 1 (AB)b lines have a limited profile variability, but a high variability amplitude range. However, all of its profile variability can be described with two unique components, whose shape are reminiscent of magnetospheric accretion induced lines, as well as chromospheric and/or shock induced lines. That same decomposition is able to explain the cross-correlation profiles of the lines. Among these two blue/green components, the blue component is the one that resembles most the magnetospheric accretion profiles, with clear absorption features that are slightly red-shifted. These features are reproduced by axi-symmetrical magnetospheric accretion models, but they fail at reproducing simultaneously the core and the extended wings of the lines. This interpretation is supported by the high correlation of the blue component and the UV excess intensity. The variability, however, has no obvious periodic signal, but there are still some tentative signals at 0.338 days in H_β, H_γ and H_δ, and at 1.126 days for H_α.

This study presents, for the first time, the UV excess spectra of a PMC at high-resolution. Its intensity is highly correlated with both the Helium lines, and the continuum level below H_α, which suggests that most of the continuum level is due to the accretion shock. While no modeling of the accretion shock was done, this is matter for future work with collaborators from Padova.

SR 12 c, however, has lines whose shape is much more variable (although the outburst of Delorme 1 (AB)b has some variable lines profiles as well). The analysis is currently limited, and preliminary results do not hint at a periodicity in the lines, although this may still be the case once a proper reduction has been performed. The appearance (or disappearance) of lines features in a matters of minutes is quite puzzling.

While magnetospheric accretion seems the favored scenario for both Delorme 1 (AB)b and SR 12 c, it is still debated. In this optic, I have written several proposals to try and detect red-shifted absorption features, which would be one of the decisive criterion towards magnetospheric accretion. In particular, I have submitted an ERIS proposal, targetting the Pa_β line of GSC 06214-00210 b, with the same idea as for SR 12 c: monitoring the line during successive nights. While this proposal was rejected, I have also submitted



a CRIRES proposal targetting the Pa_β line of Delorme 1 (AB)b. Delorme 1 (AB)b has the brightest known Pa_β line, and is the only PMC for which CRIRES observations are possible (mostly because of the low throughput of the instrument). Both the Pa_β line and the continuum level are expected to be visible (see the proposal in Appendix B). The proposal has been approved and I am currently awaiting for the observations, they should be performed during July-August-September.

The unconstrained variability behaviors of both Delorme 1 (AB)b and SR 12 c advocate for more visits. The broadly long-term variability behavior of Delorme 1 (AB)b has been probed in this study. However, it is still lacking the fine monitoring which would have made periodograms much more accurate. A similar monitoring to that of SR 12 c is advised, and will be performed in the upcoming Large Program (3h per night, 6 consecutive nights). For SR 12 c, next visits should focus on its long term monitoring. However, another short-term monitoring would only be useful if one can find a way to properly calibrate the data. This means that future observations should perform acquisition of couple exposures, to avoid the drift issue that occurred on SR 12 c, and acquire a standard star exposure ever so often.

In the context of high-resolution spectroscopy of young PMCs, I advise that efforts focus on line-modeling. I believe only through this method would the true nature of the underlying mechanisms be unveiled. If magnetic field strength on Delorme 1 (AB)b were to be measured, an in depth study of the target, similar to that of Alencar et al. (2012) and Espaillat et al. (2021), would provide a strong understanding of one of the perfect PMC laboratory.







Thesis' Table of Contents
Chapter's Table of Contents

Chapter IV.

Conclusion and Perspectives

One may draw realistic objects by tracing lines, converging to one, or two points in the distance: the so-called vanishing point. This process is called perspective drawing.

This work presented the results of PMCs accretion lines monitoring campaigns, with Near-Infrared and Visible/UV instruments: VLT/SINFONI and VLT/UVES. This work showcased in particular the typical case study of accretion lines of several PMCs at high resolution with VLT/UVES. Studied PMCs have lines profiles different from each others, but with similarity in their variability behaviors. While this work only provides the first hints towards the underlying accretion mechanisms, there are hints of magnetospheric accretion on at least two of them, while others may be accreting in a different regime. This work has opened up to a large program study of accretion lines, which will build a sample of the typical behaviors of PMCs. Future work and instrumentation will provide rich insights into the mechanisms at play.

Chapter's contents

1 Summary 162
1.1 Constraints on the line formation mechanisms 162
1.2 Variability behaviors 163
2 Global picture 163
3 Perspectives 164
3.1 Main PMC properties 164
3.2 Building an observing program 165
3.2.1 An (un?)realistic program 165
3.2.2 A realistic program 165
3.3 Future instrumentation 165

1 Summary

The characterization of accretion process on planetary-mass companions and their free-floating siblings remains a nascent field of investigation. It has had a renewed interested following the discovery of the archetypal protoplanets PDS 70 b&c. During my PhD, started three years following this landmark discovery, I have built on the expertise gathered in the field of high-contrast imaging of exoplanets and star formation to investigate the accretion on key companions, focusing on the variability of the emission lines which had only be very marginally studied at this time.

1.1 Constraints on the line formation mechanisms

Models of emission lines profiles had been published a few years before the start of my PhD, but had not yet been extensively tested with observations. The first comparison dates to Aoyama and Ikoma (2019) with PDS 70 b MUSE observations, but they were largely limited by the spectral resolution of the instrument $r \sim 2500$. In fact, the first observations that provided a partly resolved line profile were those from the Pa_β line of GSC 06214-00210 b ($R \sim 3800$, OSIRIS, Bowler et al., 2011), presented in the second chapter of this thesis and Demars et al. (2023). However, UVES observations (presented in the previous chapter) are the first ones to provide fully resolved lines profiles of a PMC. The decomposition of the line profiles even provides insights in possibly multiple mechanisms for the lines profiles. At first order, magnetospheric accretion model Thanathibodee et al. (2019) provides a satisfactory fit to both the blue and green components, although the blue component core and wings are not reproduced simultaneously. Future work may include a detailed phase-resolved modeling of the accretion lines, as was done for T Tauri stars (Alencar et al., 2012).

The study is currently missing a comparison to the shock models, which were not computed at a sufficient spectral resolution. This has now been done and is work-in progress, and preliminary results show a tentative agreement between the shock models and the green component. A detailed study of the line ratios predictions of both scenarios should be considered. Future efforts should also focus on the infalling gas, as was shown to be a strong source of extinction (Marleau et al., 2022). In fact, some of their profiles also resemble the blue component of H_α. Finally, Helium lines do not have any predictions yet. Should they be provided, they would give strong constraints on the physics of the accretion shock itself, as they are not expected to form anywhere else. I should also mention the local contribution of the SPIDI team and project, led by J. Bouvier,



with the contribution of B. Tessore and J. Pantolmos, who have been working on phase-resolved line profiles for non axis-asymmetrical accretion flows.

1.2 Variability behaviors

Before this thesis, lines variability had only been hinted. At the time, if it were to be confirmed, it was thought to be linked to either variations in the accretion flow, or variations of the planets themselves, would lines be linked to chromospheric activity. This work provided the first estimate of the amplitude of variability of accretion lines for a few PMCs. I would argue GQ Lup b could gain from another dedicated variability study, in particular at the ∼months timescales where the number of points was too scarce (2 epochs separated by a week, and a single epoch a month later). However, the variability behavior for GQ Lup b, GSC 06214-00210 b and Delorme 1 (AB)b is similar to that seen on T Tauri stars: faint variability at the hours timescales, and reaches a greater plateau at weeks to months timescales. Still, the sample is beginning to include quite a few PMCs, albeit their variability was studied at different timescales.

This work definitely showed profiles variability for Delorme 1 (AB)b and SR 12 c. The two have greatly different lines profiles, which raises the question of whether they even share a common emitting mechanism. Yet, they both are similar in terms of environment (host binary, wide companion), and only differ by their age: SR 12 c is really young, while Delorme 1 (AB)b is much older. In principle, the difference could be due to a different viewing angle, if Delorme 1 (AB)b were to be seen pole-on and SR 12 c were to be seen edge-on, although this explanation likely would only work in the context of magnetospheric accretion lines. Still, this would be quite surprising, because magnetospheric accretion models for Delorme 1 (AB)b predict a highly inclined system. Alternatively, the parallel study of both these objects may give insights and upper/lower limits on the age at which the magnetic field becomes sufficient to truncate the CPD, and the shift of boundary-layer to magnetospheric accretion regimes.

Overall, this work highlighted the specifics of lines variability, but fails at providing a Satisfactory explanation. There is still currently *beta* in-progress work that is being done, in particular on the green component modeling, which might be tracing the shock component. Although this would be surprising given the poor correlation to the UV excess variability. Future work could also focus on the variability of the Helium lines and UV excess, which directly trace the accretion Shock.

2 Global picture

The main question addressed in this thesis is: How do planets accrete mass, and how do these processes affect their evolution? While current instrumentation does not permit the study of close-in planets, PMCs could serve as proxies for the study of possible processes that could develop on similar mass objects at closer separations, although not including interactions with the circum-stellar disk. The idea was to characterize the accretion process of young PMCs that are still accreting. Indeed, answering this question is a little ambitious, but this work still has contributed with some clues.

The variability properties of PMCs, as mentioned in the previous section, are one of them. Line variability had been proposed as an explanation for non detections of H_α surveys, and it seems that it could be the reason. However, I found that H_α variability (for Delorme 1 (AB)b, at least) only becomes important on timescales of months to years. Short term (hours) variability only reaches a few %, which cannot explain non-detections. Longer timescales variability, however, could be the key: they reach 50–100 % at years timescales, which could have sent some planets below the detection threshold. Still, a factor 2 likely does not



explain all the non-detections and it is also possible that planets are too embedded in the circum-stellar disk as some authors have proposed (Szulágyi et al., 2018).

These results still advocate for new visits of surveyed systems, but only every couple of months to year. However, line-profile study requires monitoring on short timescales, in particular for SR 12 c. Unfortunately, these aims do not align in terms of observational needs. This work also showed that the UV excess, which was previously observed with photometric points, can in fact be accessed with medium-resolution spectroscopy.

3 Perspectives

3.1 Main PMC properties

This work focused on characterizing the accretion properties of *specific* PMCs, although the sample now covers most of the typical ages and masses of known PMCs (5–15 M_{Jup}, 2–45 Myr). It is still lacking the case of embedded planets. Other authors have chosen a statistical approach (e.g., Betti et al., 2023) which are also currently limited by the size of the sample for constraining accretion properties of PMCs. Today, the picture of accreting PMCs is still a rich field to explore, where pieces of information are scattered all around. However, most authors have focused on a single piece of the puzzle at a time, which makes sense as any one piece is worth its own article. I strongly believe that future efforts should include all of the pieces at once, at least for the study of a single PMC.

I think the most important pieces of information are correlations between multiple parameters. While a correlation does not mean the two parameters are necessarily the cause of each other, models attempting to paint a picture of the scene should be able to reproduce said correlations. For example, the magnetic field nature of V2129 Ophiuchi was obtained by Donati et al. (2011), and later used to model its H_α profile at multiple phases (Alencar et al., 2012). The auto-correlations of that line (Alencar et al., 2012, their Fig. 19) are surprisingly similar to that of Delorme 1 (AB)b presented in this work (Fig. III.21), despite the different line profile. In this thesis, the idea of decomposing the lines solely came from the shape of these auto-correlation diagrams (although I had already developed the method as a way of disentangling the PSF of the primary and the companion). Other parameters for which to check correlations are:

- The UV excess, the continuum level, emission lines fluxes and shape. This was shown to be feasible with UVES. While the lines shape variability was explained for Delorme 1 (AB)b with the blue/green decomposition, it is much harder for SR 12 c. It does not appear that two components may easily explain the line variability (although it does provide reasonable results). Therefore, correlations between individual lines spectral bins, and other parameters such as, for example, UV excess, may be able to unveil the true nature of these lines. Additionally, the modeling of the UV emission should provide accurate physical parameters of the accretion shock. While this was done from photometric points (Zhou et al., 2014, 2021), it is still lacking the details of the Balmer Jump modeling. This will provide a much more accurate estimate of the accretion luminosity (Lacc) and accretion rate $\dot{M}$.

- Absorption lines depth and shape. This was shown to be feasible with SINFONI, and now ERIS. The EW of absorption lines may inform on the extent of continuum variability, as well as possibility lines filling from accretion. Preliminary results (not shown in this thesis) showed that some metal emission lines were present in Delorme 1 (AB)b data during the outburst epochs, and absent from others. It is possible that these lines would have been present in absorption otherwise, but not observable because of the low continuum level. Alternatively, should absorption features be detected within emission lines, they will provide direct indications of the accretion and ejection processes on the planet.



3.2 Building an observing program

3.2.1 An (un?)realistic program

Could all these tracers be concatenated in a single observing program? As a first step, let's assume that there is an unlimited amount of observing time dedicated for a single target. Obviously, we would like to have the highest spectral resolution, with the broadest wavelength range and the highest S/N in any given observation. However, such a program should include the variability aspect of the target's lines. If targeting SR 12 c, its variability has shown that lines vary on $\sim$ 20 mins timescales. If targeting Delorme 1 (AB)b, the lines are instead quite stable over the night. This means that a program for a Delorme 1 (AB)b-like target does not have to worry about short term variability, whereas it should for a SR 12 c-like target. The richest wavelength range is the UV and optical, with a broad forest of lines, as well as its UV excess. However, this is also where the continuum flux is fainter, making the study of absorption lines hardly achievable at resolutions such as that of UVES. However, Santamaría-Miranda et al. (2018) showed that this is possible with XSHOOTER for SR 12 c, which is intrinsically fainter than Delorme 1 (AB)b. XSHOOTER could therefore be used to probe both the UV excess and NIR absorption lines at the same time. However, it would lack the high-resolution capabilities of UVES. Also, their observations used a total DIT of 4000s, which is quite expensive for a single exposure, and far above the $\sim$ 20 mins variations for that target. Instead, Delorme 1 (AB)b could be the target for XSHOOTER observations, as it does not require $\sim$ 20 mins monitoring. Even more, simultaneously observing with UVES and XSHOOTER would provide both the high resolution spectroscopy of many (many!) accretion lines in the optical, and the medium-resolution spectroscopy of absorption lines in the NIR. Indeed, this would be quite time-expensive, and the primary stars may also saturate the detectors of XSHOOTER, as spectral pixels would be bigger. However, correlations between high-resolution emission lines and absorption lines could provide a definite answer to the accretion dynamics in this system.

3.2.2 A realistic program

The study that was done for Delorme 1 (AB)b has led to important results. It is now required to check for the universality of these findings. A way to solve the pending questions could be to perform the same study for other PMCs. Each target's sequence could be analyzed in the frame of each other, thus building not only towards that target understanding, but also to a more general picture of accretion properties of various PMCs. This is how the ExoplaNet accRetion mOnitoring sPectroscopic surveY (ENTROPY) large program was developed. It was accepted, and observations should start next January. It consists in observations of 8 PMCs and PMOs, for 6 consecutive nights (3h per night), as well as some snapshots of others companions if twilight time allows it. This will build the encyclopedia of high-resolution profiles of young PMCs/PMOs. Alternatively, observing NIR lines may provide a different picture: Helium lines at 10 830 Å are meta-stable, and bound to display absorption features that may directly inform on the accretion flow. Simon Ringqvist (Stockholm, Sweden) has submitted a CRIRES proposal for that matter, which was accepted along the one I submitted for Pa_β. The two should be executed this summer. On a side note, CRIRES could also be used to detect the magnetic field of PMCs, as is done for stars, although detailed modeling would be required to test the feasibility. Preliminary work with the ETC does seem to confirm that the throughput of the instrument is too low for any line other than Delorme 1 (AB)b's.

3.3 Future instrumentation

In this thesis, a few topics have not been addressed in sufficient depth. In particular, most known PMCs and PMOs are either far away from their host star, outside of its disk, or lonely. This means that for them to



be actively accreting, they need a gas reservoir: likely their own Circum-Planetary Disk. CPDs have been detected on a few objects, from excess photometry (e.g., GSC 06214-00210 b) or from ALMA detections (e.g., GQ Lup b). More recently, JWST observations even provided a spectrum of GQ Lup b's CPD, thus opening the way for their in depth characterization. However, while ALMA angular resolution is too low to do more than confirm dust origin, it may be possible for NIR interferometry (GRAVITY) to provide actual measurements of these CPDs. Future J-Band interferometer at VLTI: ASGARD/BIFROST (Kraus et al., 2022), may even provide a way to resolve the Pa_β emission regions, similar to what was done in Br_γ on CI Tau (Gravity Collaboration et al., 2023).

RISTRETTO is currently under development, as a power IFU (although limited number of pixels: 7) for VLT. It will be able to reach $R > 140\,000$, and angular resolution of a few tens of mas (Lovis et al., 2022). This may be the perfect instrument for the study of close-in accreting companions.

Similarly to MUSE, MAVIS (McDermid et al., 2020) will provide an optical IFU, assisted with a powerful AO that is supposed to send it to the VLT diffraction limit. It should be comissioned around the same time as the ELT, but should reach a much better angular resolution than the ELT in the optical, while still providing 4-digits spectral resolutions. MAVIS will certainly be a key instrument for the characterization of accreting PMCs.

Last but not the least, the ELT and its first light instruments should be available to the community in the upcoming years. For the sake of characterizing accreting PMCs, HARMONI will provide the ELT resolving power, combined with a $R \sim 25\,000$ IFU in part of the J band, and the full K band. This will basically be a better version of ERIS, with the light influx of the ELT. On the other hand, METIS will provide an IFU mode in the L and M bands, at 100 000 resolution, which will prove useful for the study of CPD, and some higher order hydrogen lines, like Br_α. If future observations with JWST confirm the presence of the Pfund lines on PMCs in these bands, METIS could provide access to their detailed line profile.







Chapter V.

French Summary

Avec plus de 5000 exoplanètes confirmées, les détails de leurs mécanismes de formation restent un mystère. On pense que les exoplanètes se forment dans le disque protoplanétaire des étoiles, soit par la croissance lente de noyaux rocheux, soit par l'effondrement gravitationnel d'amas. Les planètes accrètent généralement une partie de leur masse directement à partir du disque protoplanétaire, mais les mécanismes exacts ne sont pas encore connus. La découverte des planètes accrétantes PDS 70 b&c, orbitant dans le disque protoplanétaire de leur étoile hôte, offre une occasion unique d'étudier directement les processus d'accrétion. Les découvertes récentes d'objets de classe similaire, les compagnons de masse planétaire, s'ajoutent à l'échantillon des planètes accrétantes connues.

Dans cette thèse, je présente les résultats de deux études de surveillance des raies d'accrétion des jeunes compagnons de masse planétaire : avec le VLT/SINFONI dans le proche infrarouge, ciblant la raie Pa_β de deux compagnons (GQ Lup b et GSC 06214-00210 b), et avec le VLT/UVES dans le Visible/UV, ciblant les raies de Balmer et d'hélium de trois autres compagnons (Delorme 1 (AB)b, SR 12 c et 2MASS J11151597). Tous deux fournissent des contraintes sur les amplitudes de variabilité de leurs raies respectives, qui rappellent celles trouvées sur les étoiles T Tauri. Avec le VLT/UVES, la haute résolution spectrale ($R \sim 50,000$) permet d'accéder aux profils détaillés des raies, alors que le VLT/SINFONI ne fournit que des raies partiellement résolues ($R \sim 2000$), contre lesquelles les modèles de raies d'émission peuvent être testés. Les modèles d'accrétion magnétosphérique sont préférés pour GQ Lup b et une partie des raies de GSC 06214-00210 b, tandis que les modèles d'émission par choc sont préférés pour GSC 06214-00210 b. Les autres cibles ne sont pas entièrement contraintes.

Cette étude fournit le premier échantillon des raies d'émission des compagnons de masse planétaire en accrétion. Cela ouvre la voie à de futures observations, enrichissant l'échantillon actuel, et à de futurs instruments qui permettront une étude détaillée des raies d'accrétion sur les compagnons à séparation interne.

Table des matières

1 Introduction 171
1.1 Formation et évolution planétaire 171
1.1.1 Accrétion sur coeur 171
1.1.2 Instabilité gravitationelle 172
1.1.3 L'ingrédient manquant: la physique de l'accrétion 172
1.2 Analogues aux planètes: Companions de Masse Planétaire 173
1.2.1 Planètes, naines brunes et compagnons de masse planétaire 173
1.2.2 Qu'en est-il de leur formation ? 174
1.2.3 Les compagnons de masse planétaire connus aujourd'hui 175
1.3 Accrétion dans le régime stellaire 176
1.3.1 Description qualitative du processus 176
1.3.2 Structure des colonnes 177
1.3.3 Le choc d'accrétion 178
1.3.4 Raies d'émission 178
1.3.5 Variabilité 179
1.4 Accrétion dans le régime de masse planétaire 180
1.4.1 Théorie et modèles actuels 180
1.4.2 Questions et objectifs de cette thèse 181
1.4.3 Questions ouvertes 181
1.4.4 Objectifs 182
2 Traceurs d'accrétion dans le proche Infrarouge: VLT/SINFONI 182
2.1 Introduction 182
2.1.1 GQ Lup b 183
2.1.2 GSC 06214-00210 b 183
2.2 VLT/SINFONI: un spectrographe intégral de champ depuis le sol 183
2.3 Observations et réduction de données 184
2.3.1 Observations 184
2.3.2 Réduction de données 184
2.4 Modélisation de l'atmosphère 185
2.4.1 Modélisation 185
2.4.2 Interprétation 186
2.5 La raie d'accrétion Paschen Beta 186
2.5.1 Profils de raie 187
2.5.2 Variabilité 188
2.6 Modélisation des raies d'émission 189
2.6.1 Description des modèles 189
2.6.2 Ajustement des modèles 190
2.7 Conclusion 191
3 Traceurs d'accrétion dans le Visible/UV avec VLT/UVES 192
3.1 Introduction 192



3.2 Une campagne d'observation avec VLT/UVES . . . 193
3.3 Le spectrographe UVES . . . 193
3.4 Observations et réduction de données . . . 194
3.5 Réduction de données . . . 194
3.5.1 Ajustement de la PSF . . . 195
3.5.2 Contamination résiduelle . . . 195
3.6 Résultats . . . 196
3.6.1 Profils de raies résolus . . . 196
3.6.2 Décomposition des raies . . . 197
3.6.3 Modélisation des raies . . . 198
3.7 Conclusions . . . 200
4 Conclusion et perspectives . . . 200
4.1 Résumé . . . 200
4.2 Une vue globale . . . 201
4.3 Perspectives . . . 202
4.3.1 Charactéristiques principales des PMCs . . . 202
4.3.2 Instrumentation future . . . 203

1 Introduction

Avec plus de 5000 exoplanètes connues à ce jour, les détails de leur processus de formation restent un mystère. Les exoplanètes vont d'une fraction de masse terrestre à plusieurs masses de Jupiter, orbitent autour de leur étoile depuis une fraction d'unité astronomique jusqu'à des milliers d'unités astronomiques, et présentent des propriétés intrinsèques très variables (température, nuages, composition, ...).

Les planètes se forment dans des disques protoplanétaires entourant leur étoile hôte. Cependant, les conditions initiales de formation des planètes ne sont pas encore définies. Pour une revue des différents scénarios de formation de planètes et de leurs limitations, voir Drążkowska et al. (2023); Liu and Ji (2020); Johansen and Lambrechts (2017); Ormel (2017). Ici, je me concentre sur la croissance planétaire pendant et après la formation de la graine planétésimale, dans les cas applicables aux planètes gazeuses géantes, motivé par la découverte, au cours des 10 dernières années, de jeunes planètes ~ 10 M_{Jup} sur des orbites larges : les protagonistes de ma thèse.

1.1 Formation et évolution planétaire

1.1.1 Accrétion sur coeur

Le scénario de l'accrétion du noyau remonte aux années 1960 (par exemple, Safronov, 1960, 1966; Safronov and Zvjagina, 1969; Safronov, 1972), avec de fortes avancées dans les années 1980 et 1990 (par exemple, Mizuno, 1980; Bodenheimer and Pollack, 1986; Pollack et al., 1996), dont le développement visait à expliquer les propriétés observées du système solaire. Elle souffre encore de quelques problèmes, par exemple la barrière du mètre, où, en raison de la traînée aérodynamique, les objets de la taille d'un mètre tombent sur l'étoile plus vite qu'ils ne peuvent grandir Weidenschilling (1977). Le processus est représenté sur la Fig. I.1 et suit trois phases principales :



- "Formation du noyau" : L'embryon de planète n'accrète des solides que par l'interaction gravitationnelle et les collisions. Techniquement, la planète "accrète" du gaz, mais sa masse n'est pas suffisante pour en retenir une fraction suffisante pour construire des planètes gazeuses. Le noyau créé au cours de cette phase présente une métallicité élevée, du moins par rapport à la valeur typique du milieu interstellaire, car les grains sont par essence le moyen de stockage des métaux.
- "Accrétion lente de gaz" : Une fois que l'embryon atteint jusqu'à 10 $M_\oplus$, sa masse est suffisante pour accréter du gaz. L'accrétion de gaz est possible et l'embryon accrète à la fois des solides et du gaz.
- "Accrétion de gaz rapide" : Lorsque la masse totale atteint une valeur "critique" (10-20 $M_\oplus$), l'accrétion du gaz est beaucoup plus rapide que celle des solides. L'accrétion est donc entièrement dominée par l'accrétion de gaz, ce qui permet la formation de planètes gazeuses géantes.

1.1.2 Instabilité gravitationelle

L'instabilité gravitationnelle est un autre scénario de formation des planètes. Dans ce contexte, les disques protoplanétaires présentent des inhomogénéités qui s'effondrent gravitationnellement pour former des planètes géantes (Boss, 1997; Mayer et al., 2002). Contrairement au cas de l'accrétion du noyau, qui est un scénario ascendant, l'instabilité gravitationnelle est un mécanisme descendant.

L'instabilité gravitationnelle exige que le disque soit suffisamment froid et massif pour que les amas surmontent la pression du gaz. Deng et al. (2017) a découvert que de tels amas sont générés dans des disques protoplanétaires très jeunes, massifs et froids. Cela ne se produit généralement qu'à des séparations plus grandes ($\gtrsim$ 30 AU, critère de Toomre Safronov, 1960; Toomre, 1964). Cependant, il ne permettrait que la formation de géantes gazeuses très massives, au moins de quelques M_{Jup}. Le nombre de planètes formées par disque dépend de la rétroaction radiative entre la planète et le disque : la rétroaction radiative tend à stabiliser le disque protoplanétaire environnant, ce qui entrave la formation des planètes et conduit donc à une diminution du nombre de planètes (Mercer and Stamatellos, 2017; Meru and Bate, 2010). En d'autres termes, les disques chauffés sont stables, tandis que les disques froids évoluent vers des disques fragmentés et agglutinés qui permettent la formation de planètes. Il faut noter qu'aux premiers stades, les disques sont probablement chauffés par les processus d'accrétion de l'étoile ou de la planète.

1.1.3 L'ingrédient manquant: la physique de l'accrétion

Jusqu'au début des années 2000, les modèles d'évolution planétaire prédisaient la luminosité, le rayon et d'autres propriétés des planètes à l'aide de modèles assez simplistes. Ils partaient d'une boule de gaz gonflée et la laissaient évoluer au fil du temps. Bien que cela puisse, en principe, être quelque peu représentatif du scénario d'instabilité gravitationnelle, cela ne reflète pas la physique de l'accrétion du noyau. La première mise en œuvre des points initiaux *physique* appartient à Marley et al. (2007). Ils comparent les modèles habituels (à l'époque) de boules gonflées (qu'ils appellent *hot-start*) aux résultats de l'accrétion du noyau (qui seront plus tard appelés *cold-start*). En d'autres termes, le démarrage à chaud correspond au cas où toute l'entropie initiale est conservée à l'intérieur de la planète, tandis que le démarrage à froid correspond au cas où toute l'énergie gravitationnelle de la planète est rayonnée.

Les principaux résultats, présentés dans la Fig. I.2 sont que la luminosité des planètes déduite des démarrages à froid est beaucoup plus faible (3–4 ordres de grandeur) que celle des démarrages à chaud. Elles ne sont rattrapées qu'après un certain temps : 1 Myr pour les planètes de 1 M_{Jup}, et jusqu'à 1 Gyr pour les planètes de $\sim$ 10 M_{Jup}. Cela entraîne des incertitudes sur les estimations de la masse des planètes, en fonction du modèle et des luminosités déduites des observations. En outre, les planètes à démarrage à froid



ont même une période de luminosité plus élevée pendant leur phase d'accrétion par emballement du gaz, en raison du choc d'accrétion (voir le pic autour de 2,5 Myr dans la Fig. I.2).

En fait, ces deux cas extrêmes ne sont peut-être que des limites extérieures pour les prédictions des trajectoires d'évolution. Dans le cas d'un démarrage à froid, la majeure partie de l'énergie est rayonnée, ce qui est une hypothèse ad hoc pour les étoiles, mais qui peut ne pas refléter l'ensemble du tableau pour les planètes. Les planètes se forment dans des disques protoplanétaires, où la dynamique du disque et les flux de gaz vers la planète peuvent être compliqués. De plus, comme on pense que les planètes ont un disque circumplanétaire (au moins en partie), il n'est pas certain que les flux entrants soient canalisés directement vers la planète ou qu'ils soient traités de manière significative à travers le disque. La physique exacte du flux d'accrétion, et à son tour du choc d'accrétion, peut changer la quantité d'énergie conservée à l'intérieur de la planète, et avoir un impact sur sa luminosité au cours de son jeune âge.

Alors que quelques études ont tenté une modélisation précoce du choc d'accrétion (par exemple, Marleau et al., 2017; Cumming et al., 2018), d'autres auteurs ont commencé à se concentrer sur les raies d'émission (Betti et al., 2023). Le thème des études observationnelles de l'accrétion est encore naissant et la majeure partie du travail reste à faire. Il a été ouvert aux contraintes avec la découverte de *planètes* jeunes et encore en accrétion (ou de frères et soeurs ressemblant à des planètes) : les compagnons de masse planétaire (PMC).

1.2 Analogues aux planètes: Companions de Masse Planétaire

Les compagnons de masse planétaire et les objets de masse planétaire (ci-après PMC et PMO) sont, par définition, des objets dont la masse est *similaire à*, *de l'ordre de*, des planètes. Alors que les PMC sont liés à une étoile hôte, les PMO sont soit des objets isolés, soit des objets dont on ne sait pas s'ils sont liés ou non à leur hôte. En raison des contraintes observationnelles, les PMCs connus sont typiquement à des séparations modérées ou élevées (> 50 AU). D'une manière générale, les termes "PMC" et "PMO" ont été utilisés pour décrire des objets allant de 1 M_{Jup} à $\sim 30 M_{Jup}$, même s'ils sont censés être classés comme naines brunes à $M > 13 M_{Jup}$.

Les PMC se situent juste à l'interface entre les planètes et les naines brunes (BD), ce qui soulève la question de leurs voies et mécanismes de formation : sont-elles formées comme des planètes ou comme des naines brunes ? Si nous devons les utiliser comme substituts de planètes proches pour l'étude de la création de planètes, il serait judicieux de vérifier si elles ont une voie de formation planétaire en premier lieu.

1.2.1 Planètes, naines brunes et compagnons de masse planétaire

À la fin des années 1990 et au début des années 2000, le modèle d'accrétion magnétosphérique (les disques circumstellaires sont accrétés sur l'étoile grâce aux interactions entre le disque et le champ magnétique de l'étoile) a permis d'expliquer avec succès la forme des lignes d'accrétion des jeunes étoiles T-Tauri, ainsi que leur excès de continuum IR/UV. Cependant, ces résultats étaient limités aux objets stellaires réels, au-dessus de la limite de combustion de l'hydrogène. Pour les objets situés en dessous de cette limite, l'origine des lignes d'émission restait une question ouverte. Le nombre d'objets sub-stellaires connus présentant des lignes d'accrétion était encore limité (~ 10), ce qui entravait désormais les efforts de la communauté.

Alors qu'une tendance générale entre la masse et le taux d'accrétion était connue dans le régime stellaire, Muzerolle et al. (2003) l'a d'abord étendue à la limite stellaire/sous-stellaire, en ajoutant des mesures provenant de quelques naines brunes/objets sub-stellaires. Leurs résultats sont présentés dans le panneau gauche de la Fig. I.4. Ces résultats ont ensuite été étendus par Muzerolle et al. (2005), en ajoutant plus de naines brunes à l'échantillon, même certaines proches du régime de masse planétaire (Fig. I.4 panneau du milieu). La tendance générale à la diminution du taux d'accrétion en fonction de la masse s'est étendue au



domaine sub-stellaire et est aujourd'hui généralement acceptée. Elle semble encore plus évidente maintenant que d'autres données ont été ajoutées au graphique (par exemple, Betti et al., 2023, Fig. I.4 panneau de droite). Cette tendance suggère que les naines brunes partagent des mécanismes d'accrétion similaires à ceux des étoiles. Il n'est pas certain que cette tendance s'étende au domaine des PMC, en raison du nombre limité de PMC/PMO connus. Les naines brunes peuvent également suivre les mêmes mécanismes de formation que les étoiles : par fragmentation d'un nuage moléculaire (Padoan and Nordlund, 2004). Dans ce scénario, elles sont simplement le résultat de la masse basse de l'IMF. Il convient toutefois de noter que tous les BD ne se sont pas formés de manière stellaire, et que certains ont pu se former en tant que compagnons de parents plus lourds (par example, Thies et al., 2015).

Certaines naines brunes de faible masse ou planètes de masse élevée sont liées à un autre objet stellaire ou sub-stellaire, ce qui en fait non seulement des compagnons (plutôt que des objets isolés), mais aussi des objets à forte séparation, à quelques centaines d'unités astronomiques. S'ils ont pu se former à partir de la fragmentation d'un nuage moléculaire, leur nature liée les rend également éligibles pour avoir été formés déjà liés à leur étoile hôte, comme une planète, soit à leur emplacement actuel, soit dans le disque circumstellaire interne, pour être éjectés plus tard. Cela soulève également la question de savoir si certains objets sub-stellaires isolés pourraient être le résultat d'éjections de systèmes liés précocement ou d'une migration vers l'extérieur. L'origine de ces objets, que nous appelons aujourd'hui PMCs, reste à débattre.

1.2.2 Qu'en est-il de leur formation ?

La formation in situ dans les disques circumstellaires (CSD) à quelques $\sim$ 100 AUs est plutôt improbable. La croissance d'un noyau rocheux à de telles séparations, nécessaire pour déclencher l'accrétion de gaz, se produit sur des échelles de temps beaucoup plus longues que la durée de vie typique du disque (Santamaría-Miranda et al., 2018). Alternativement, les compagnons des naines brunes et les PMC peuvent représenter l'extrémité de faible masse de la fragmentation des noyaux moléculaires, ce qui a été suggéré par Thies et al. (2015) à travers des arguments de FMI. Cependant, l'accrétion du noyau et l'instabilité gravitationnelle peuvent encore former des compagnons BD. Cependant, ils devraient toujours être éjectés à une plus grande séparation (là où ils sont observés aujourd'hui), un scénario qui est prédit par les modèles d'accrétion du noyau et d'instabilité gravitationnelle (Pollack et al., 1996; Whitworth and Stamatellos, 2006; Stamatellos and Herczeg, 2015). Cependant, l'instabilité gravitationnelle ne semble plus être un scénario viable, du moins pour les compagnons BD : non seulement elle est limitée à un ensemble de conditions très spécifiques (Meru and Bate, 2010; Kratter and Murray-Clay, 2011), mais elle conduit également à des compagnons éjectés non liés lorsqu'on inclut le retour de rayonnement (Mercer and Stamatellos, 2017), plutôt qu'à des compagnons à forte séparation. Cela semble laisser à la fois l'accrétion du noyau et la fragmentation du nuage moléculaire comme des scénarios plausibles.

De la même manière que les processus d'accrétion sur les BD ont été partiellement contraints en utilisant les corrélations entre la masse et le taux d'accrétion de masse (Muzerolle et al., 2005), les PMC semblent suivre la tendance générale (Fig. I.4, Betti et al., 2023). Alors que les objets à l'interface stellaire/sous-stellaire ont été contraints non seulement par la corrélation $M - \dot{M}$, mais aussi par la mise en évidence de leurs similitudes avec CTTS (par exemple, Mohanty et al., 2005,; Alcalá et al., 2014), en utilisant une variété de traceurs d'accrétion (par exemple, les raies Ca/Na, les raies interdites, ...), l'accrétion sur les PMCs n'est généralement pas contrainte du tout. C'est peut-être la partie manquante pour les PMCs, et de nouveaux instruments ouvrent la voie à ce sujet (voir Sect. 4.2). Cependant, je propose d'abord un recueil des propriétés connues des PMC dans la section suivante.



1.2.3 Les compagnons de masse planétaire connus aujourd'hui

Relevés H_α Avec la découverte de planètes émettant des rayons H_α (HD 142527 b, LkCa 15 b,PDS 70b&c et d'autres, Close et al., 2014; Sallum et al., 2015; Müller et al., 2018; Wagner et al., 2018; Haffert et al., 2019), les études ont changé leur objectif pour la ligne H_α. Les modèles ont commencé à prédire la présence de planètes à de telles séparations (Zhu, 2015; Szulágyi and Ercolano, 2020), avec une luminosité H_α qui favorise les observations, car le contraste entre l'étoile hôte et la raie est réduit. Zurlo et al. (2020) a utilisé SPHERE/ZIMPOL, a étudié 11 disques de transition, mais n'a pas détecté de compagnon. Huélamo et al. (2022), utilisant également SPHERE/ZIMPOL, a étudié 5 cibles, et n'a pas non plus détecté de compagnon. Enfin, Follette et al. (2023) a présenté les résultats d'une étude de 6 ans (l'étude GAPlanetS), et a atteint un taux de détection de $\sim 36^{+26}_{-22}$ % parmi 14 disques transitionnels. Cependant, la plupart des détections étaient des compagnons déjà connus, et seule une nouvelle détection a été confirmée (CS Cha c).

Le cas PDS 70 Peut-être l'apogée de l'imagerie directe : la confirmation de PDS 70 b&c. Grâce à leurs raies d'émission H_α, ils ont ouvert de nombreuses portes. Il ne serait pas possible d'écrire sur les PMC sans consacrer une section au système PDS 70. PDS 70 b a été détecté pour la première fois par Keppler et al. (2018), dans l'espace du disque transitionnel autour de PDS 70 (5.4±1.0 Myr, $\sim$ 22 AU à 113.43±0.52 pc, Gaia Collaboration et al., 2018). Müller et al. (2018) a fourni la première caractérisation de la planète : à $\sim$ 22 AU de l'étoile, c'est un compagnon de 1,4–3,7 R_{Jup} avec une masse mal contrainte : 2–17 M_{Jup}. Wagner et al. (2018) fournit la première caractérisation de son émission H_α et une détection provisoire d'une autre planète. Cette détection est confirmée par les observations de MUSE (Haffert et al., 2019). Benisty et al. (2021) fournit une détection ALMA du disque circum-stellaire, ainsi que du disque circum-planétaire. Quelques années plus tard, Christiaens et al. (2024) présente les données JWST du système, mettant éventuellement en évidence une troisième planète, ainsi que des détails sur les interactions entre le disque circum-stellaire et les planètes. PDS 70 b&c sont les seules planètes actuellement connues à être à la fois à l'intérieur d'un disque circum-stellaire et en accrétion active. Elles constituent le laboratoire idéal pour la caractérisation des PMC : parce qu'elles sont encore en accrétion, il est possible de contraindre les modèles d'accrétion, et parce qu'elles sont intégrées dans le disque circum-stellaire, il est possible de contraindre les interactions entre le disque et les planètes. Cependant, la faible séparation angulaire des compagnons ($\sim$ 0.2") et l'émission du disque circum-stellaire limitent l'étude de ces planètes. Le signal planétaire est contaminé par le disque, et l'extinction d'avant-plan du disque lui-même limite les possibilités d'étude.

PMCs: la liste Betti et al. (2023) a présenté les tendances du taux d'accrétion vers le régime substellaire (points violets et cyan dans la figure I.4). Mais qu'en est-il de l'étude indépendante des PMC ? La question principale est de savoir si la corrélation M–$\dot{M}$ s'étend jusqu'au régime des PMC, bien que la corrélation semble s'aplatir à des masses plus faibles. Betti et al. (2023) soutient que cela pourrait s'expliquer par une évolution différente de celle des BD de masse plus élevée, ce qui n'entraînerait aucune corrélation entre la masse et le taux d'accrétion (Stamatellos and Herczeg, 2015). Cependant, cette tendance pourrait également être due à un biais d'observation, où les faibles taux d'accrétion ne sont pas détectables. Je concentre l'étude sur les PMC et les PMO, ces derniers étant considérés comme des substituts de leurs PMC similaires, c'est-à-dire qu'ils peuvent s'être formés de manière similaire aux PMC, d'où leur pertinence pour l'étude. J'ai utilisé la base de données CASPAR[1] (Betti et al., 2023), qui vise à cataloguer les BD, PMC et PMO connus, et à en déduire leurs propriétés de manière cohérente. En définissant une limite supérieure de 30 M_{Jup}, j'ai identifié 31 PMC/PMO dans CASPAR. Selon Betti et al. (2023), leur masse a été obtenue à partir de modèles évolutifs

[1] **CASPAR**: https://zenodo.org/records/8393054



(Baraffe et al., 2015) avec l'âge et la température comme paramètres d'entrée. Cependant, j'ai ajouté 18 PMC/PMO que je n'ai pas trouvés dans la liste, pour un total de 49 objets. La liste des PMC/PMO connus de moins de 30 M_{Jup} et jeunes (de moins de 50 Myr) est donnée dans le tableau I.1. L'espace des paramètres d'âge, de masse et de séparation est représenté sur la figure I.5, pour les PMC (panneaux de gauche et du milieu) et tous les PMO (panneau de droite). Les différentes couleurs indiquent si elles sont en accrétion (rouge) ou si elles ont une raie H_α. Le statut d'accrétion a été déterminé en fonction de la présence ou non de raies d'émission Pa_β, Pa_γ ou Br_γ sur les cibles, qui ne seraient pas produites par l'activité (Natta et al., 2014). La raie H_α peut, en principe, être produite par l'activité chromosphérique, en particulier autour des types spectraux M9–L0 où résident les PMC (Stelzer et al., 2013; Frasca et al., 2017; Manara et al., 2017; Venuti et al., 2019). Cependant, on prévoit que la raie H_α sera la plus brillante des raies produites par accrétion et son étude ne doit absolument pas être exclue (voir le chapitre UVES). Certaines PMO ont confirmé la non-détection de certaines raies et sont marquées comme telles dans le tableau. Parmi les 49 PMO, on compte un total de 29 PMC. La plupart des cibles de moins de 4 Myr sont étiquetées comme étant en accrétion, alors qu'il n'y en a que 3 au-dessus de 4 Myr, ce qui suit la tendance selon laquelle la dispersion du disque se produit sur des échelles de temps de quelques Myr. Cependant, les systèmes d'accrétion plus anciens, comme GSC 06214-00210 b et Delorme 1 (AB)b (connus pour porter des disques), sont assez déroutants, car ils remettent en question le fait que les PMC devraient également cesser d'accréter après des périodes similaires à celles des étoiles, ou s'ils se sont formés beaucoup plus tard que ce qui est estimé à partir de l'âge de leur étoile hôte. Cela pourrait être résolu si les cibles émettant dans le domaine Halpha pouvaient également être confirmées comme étant des accrétions. Il semble y avoir un écart de PMO connues autour de 3-4 Myr, mais cela est probablement dû aux régions de formation d'étoiles qui ont été étudiées : le Scorpion supérieur (environ 11 Myr) et le Taureau (environ 1 Myr). Toute statistique est donc biaisée par le nombre de systèmes étudiés dans chaque région. Je n'ai pas essayé de corriger ce biais, mais cela pourrait faire l'objet d'une étude future.

1.3 Accrétion dans le régime stellaire

Dans cette section, je me concentre sur les derniers stades de l'accrétion, où la majeure partie de la masse a déjà été accrétée sur l'étoile. Cela ne s'applique donc pas aux premiers stades où l'enveloppe en chute domine l'accrétion.

Cette section s'inspire fortement de la revue de Hartmann et al. (2016). Cependant, je ne développe pas beaucoup les questions de moment cinétique dans le contexte de l'accrétion magnétosphérique. Pour une revue, reportez-vous à Bouvier et al. (2014).

1.3.1 Description qualitative du processus

Une description générale et qualitative de l'accrétion magnétosphérique est présentée dans la figure I.6. En suivant une description de droite à gauche (de l'extérieur vers l'intérieur) :

- On pense que des champs magnétiques à grande échelle traversent le disque, déclenchant des vents à faible vitesse et une migration vers l'intérieur du disque.

- Le champ magnétique dipolaire est suffisant pour tronquer le disque circumstellaire (CSD), à peu près au rayon de co-rotation : où la période keplerienne est égale à la période stellaire. Notez que ce rayon de co-rotation est généralement exempt de poussière, car il a été sublimé à des rayons plus élevés ("Mur de poussière chaude interne" dans la Fig. I.6).



- Les lignes de champ magnétique, couplées au gaz, agissent comme un moyen d'échange de moment angulaire entre le disque et l'étoile. Les lignes de champ magnétique s'étendant vers l'extérieur sont responsables des vents et des jets ("Vent/jet de disque" sur la Fig. I.6), ralentissant l'étoile.

- Les lignes de champ magnétique qui se couplent légèrement en dessous du rayon de co-rotation transfèrent le moment angulaire du disque vers l'étoile : l'étoile accélère alors que le gaz tombe sur l'étoile. Cependant, les lignes de champ magnétique agissent comme une barrière qui empêche le gaz de tomber directement sur l'étoile. Au lieu de cela, il est guidé par les lignes de champ magnétique et tombe via des colonnes de haute latitude ("Flux d'accrétion" sur la Fig. I.6).

- Les colonnes s'écrasent sur la surface stellaire, formant un "choc d'accrétion" lumineux qui est responsable de l'excès d'UV et des rayons X.

- Le choc d'accrétion et les colonnes sont tous deux responsables des raies d'émission. Les colonnes sont chauffées à $T \sim 10^4$ K, ce qui est suffisant pour déclencher les raies de l'hydrogène, de l'hélium et des métaux. Alors que l'émission d'une seule colonne sera décalée vers le rouge, il est possible de voir plusieurs colonnes à la fois, la symétrie pouvant rendre les raies d'émission symétriques. Cependant, l'auto-absorption des colonnes entraîne des caractéristiques d'absorption décalées vers le rouge dans les raies, jusqu'à $\sim$ 100 km/s, qui ont tendance à décaler le barycentre apparent de la raie vers le bleu. Les raies de choc d'accrétion, cependant, sont généralement légèrement décalées vers le rouge, car la matière continue de tomber légèrement dans la photosphère.

Il est important de noter qu'il ne s'agit que d'une représentation schématique et idéalisée. En fait, il est probable qu'il y ait plusieurs colonnes à la fois, sans symétrie donnée. Les colonnes elles-mêmes pourraient ne pas être parfaitement cylindriques, d'où le nom commun d'"entonnoirs" qui est plus approprié aux structures en forme de rideaux que l'on voit dans les simulations.

1.3.2 Structure des colonnes

Les lignes de force du champ magnétique stellaire se reconnectent à l'intérieur du disque. Lorsque l'intensité du champ magnétique est suffisante pour contrebalancer la pression du gaz du disque, il agit comme un bouclier, empêchant le transport radial vers l'intérieur de la matière du disque. Au lieu de cela, le gaz est canalisé vers des latitudes plus élevées, en colonnes.

La forme réelle de la colonne fait l'objet de débats et dépend probablement fortement de l'inclinaison du champ magnétique stellaire par rapport à l'inclinaison du disque. Pour un champ magnétique à symétrie axiale, Romanova et al. (2003) prédisent une colonne à symétrie axiale tout autour de l'étoile (voir Fig. I.7, panneau A), tandis que toute inclinaison conduit à deux colonnes opposées (voir Fig.I.7, panneaux B/C). Les mêmes auteurs ont étendu leurs simulations à différents régimes de taux d'accrétion (Romanova et al., 2008), montrant une ramification entre les régimes d'accrétion stables et instables qui conduisent à des colonnes multiples (voir Fig. I.7, panneau E). Les modèles récents (Tessore et al., 2023) utilisent une approche plus simple, similaire à celle de Romanova et al. (2003) et Esau et al. (2014) (voir Fig. I.7, Panneau D). Dans l'ensemble, les colonnes doivent être au moins assez antisymétriques, ce qui correspond à la topologie du champ magnétique trouvée au moins sur V2129 (Mesures de l'effet Zeeman, Donati et al., 2007).

La structure de température est également assez mal connue. Seules quelques études ont tenté de prédire les structures de température de manière autocohérente (par exemple, Martin, 1996) : elles trouvent une température croissante le long de la colonne, principalement due à la compression du gaz par les lignes de champ convergentes, avec des températures allant jusqu'à $\sim$ 6,500 K. Cependant, Muzerolle et al. (1998) a



constaté que cette structure ne correspond pas aux observations. Au lieu de cela, ils utilisent les observations pour *ajuster* un profil de température (Muzerolle et al., 2001). Les colonnes doivent être chauffées quelque part dans la plage de 7 000 à 10 000 K.

Des températures plus basses rendraient les raies d'émission trop faibles, tandis que des températures plus élevées rendraient le gaz optiquement épais, transformant les raies d'émission en raies d'absorption. Néanmoins, ils trouvent que la plage de températures acceptable est liée au taux d'accrétion. Des études plus récentes ont tenté de sonder directement la structure des températures. Petrov et al. (2014) a utilisé des rapports de raies métalliques afin de déterminer les conditions d'émission. Ils trouvent une forte corrélation entre l'augmentation de la température et l'augmentation de la densité, ce qui correspond à une augmentation de la température dans la colonne plus proche de l'étoile. Ils trouvent une structure de température qui correspond davantage à celle de Martin (1996), bien qu'ils avertissent que le modèle de Martin a des paramètres différents de celui de leur cible. Une étude plus récente (Marleau et al., 2022), bien que dans le régime de masse planétaire, a également trouvé des structures de température plus conformes à celle de Martin (1996).

1.3.3 Le choc d'accrétion

Un choc d'accrétion est censé se produire lorsque le matériau accrété heurte la photosphère de l'objet à des vitesses supérieures à la vitesse du son local. L'excès de continuum UV observé sur les CTTS (Fig. I.8 B) est généralement attribué au choc d'accrétion qui se produit lorsque les colonnes d'accrétion finissent par s'écraser sur la surface stellaire (Fig. I.6). Cet excès est responsable du voile des raies qui, historiquement, *brouillait* les raies dans les plaques spectrales, réduisant le contraste entre les raies et le continuum. Sa caractéristique la plus distinctive est le saut de Balmer à 3647 Å, bien que le mélange des raies de la série de Balmer ait tendance à déplacer l'emplacement apparent du saut à $\sim$ 3700 Å. Quelques paramètres clés ont pu être déduits de principes physiques simples (température, densité, énergie, Koenigl, 1991; Gullbring, 1994; Lamzin, 1995) avant que les premiers modèles ne donnent des prédictions réelles des caractéristiques et de la forme de l'excès (Calvet and Gullbring, 1998).

L'approche simpliste de la modélisation unidimensionnelle ne tient pas compte de la structure probable de la colonne stratifiée. Espaillat et al. (2021) a constaté des décalages temporels entre les pics de flux UV/optique, ce qui plaide en faveur de différentes régions émettrices tournant autour de l'étoile : un point chaud stratifié. Cela peut être modélisé en supposant que la colonne est constituée de couches homogènes. Espaillat et al. (2021) a utilisé cette approche pour ajuster l'excès UV/optique de GM Aurigae, son évolution temporelle, et à son tour modéliser la rotation de la modulation rotationnelle du point chaud. Ils divisent le point chaud en 3 régions de densité, où les simulations prédisent que les densités les plus élevées ont un facteur de remplissage de < 1 %, et les densités plus faibles de 10–20 %, ce qui est cohérent avec les simulations antérieures. Ces valeurs plus élevées sont en accord avec la taille des cellules magnétiques obtenues à partir d'études de polarisation (bien que sur une autre cible, V2129 Oph, Donati et al., 2007). Une stratification similaire avait déjà été réalisée par Ingleby et al. (2013), mais ils n'avaient pas pu conclure sur l'extension spatiale de chacune.

1.3.4 Raies d'émission

Les raies d'émission ont été (l'un des) principaux moyens d'étudier l'accrétion magnétosphérique. Non seulement elles ont été utilisées pour définir la classe des T Tauri dans son ensemble, mais elles permettent également de distinguer les étoiles T Tauri *classiques* des étoiles T Tauri *à raie faible*. Ces raies sont généralement des transitions de l'hydrogène, de l'hélium ou des métaux (Na, Fe, ...).



Les raies d'accrétion, qu'elles soient en émission ou en absorption, existent sous une grande variété de formes et d'intensités (voir Fig. I.9). Le flux de gaz et sa dynamique sont directement imprimés dans les profils des raies d'émission/absorption, et certaines raies d'émission sur un CTTS peuvent en fait être des raies d'absorption sur d'autres. Au sein d'une même raie, certaines composantes d'émission peuvent être des composantes d'absorption pour une autre étoile. Les raies peuvent avoir des origines différentes, ce qui se traduit par des composantes différentes. Les composantes à haute vitesse tracent directement l'écoulement entrant/sortant. Les vitesses positives tracent l'écoulement entrant de matière dans la colonne d'accrétion (+150–200 km/s), tandis que les vitesses négatives ont tendance à tracer les vents et/ou les jets (-150–200 km/s). Cependant, toutes les caractéristiques ne sont pas nécessairement présentes dans toutes les raies à tout moment. Dans le cas d'une colonne d'accrétion, des caractéristiques d'absorption apparaissent lorsque la base (près de la surface stellaire) est froide par rapport au choc d'accrétion, et qu'elle intercepte la ligne de visée. Le continuum stellaire et le continuum de choc sont tous deux absorbés par la colonne en chute, ce qui se traduit par des caractéristiques d'absorption qui peuvent s'étendre en dessous du niveau du continuum (Fig. I.9A, H_α et HeI,10830Å) ou supprimer la composante d'émission (Fig. I.9C, H_β). Dans le cas d'un jet/vent, des caractéristiques spectrales apparaissent lorsque la ligne de visée intercepte le vent, se traduisant par une absorption décalée vers le bleu.

Une partie de l'émission de raies peut être produite par l'activité chromosphérique, comme le montre l'émission de raies dans les spectres des WTTS (non en accrétion). Cette composante est également susceptible d'être présente dans les CTTS, et a été prise en compte dans des études récentes, que ce soit pour l'ajustement de profil (par exemple, Thanathibodee et al., 2020) ou la détermination des relations de flux de ligne (Manara et al., 2013). Par ailleurs, la contribution chromosphérique aux raies d'émission de l'hydrogène augmente fortement vers les objets de type M tardif. Les raies induites par l'activité ont tendance à avoir une largeur de raie plus faible et des raies H_α plus étroites. Les critères de largeur de raie équivalente $\mathrm{EW}(\mathsf{H}_\alpha) < 36$ Å et $\mathsf{H}_\alpha(10\%) < 270$ km/s ont été utilisés pour distinguer les étoiles en accrétion des étoiles non en accrétion (White and Basri, 2003). D'autres auteurs ont utilisé un critère de $L(\mathsf{H}_\alpha)/L_{\rm bol} = 10^{-3,3}$ (Barrado y Navascués and Martín, 2003).

1.3.5 Variabilité

Comme les observables sont directement liés aux conditions d'émission sous-jacentes, leur variabilité permet de mesurer directement les paramètres physiques et la variabilité des processus d'accrétion. Ainsi, la variabilité a toujours été au cœur des études des CTTS. Cependant, la variabilité se présente sous différentes formes : la variabilité photométrique et la variabilité spectroscopique. La spectroscopie donne accès à la variabilité des raies, tandis que la variabilité photométrique est plutôt liée à la variabilité du continuum. Ces deux variabilités ont été une exigence forte pour le développement du scénario d'accrétion magnétosphérique. Une image générale de tous les processus variables connus dans les jeunes étoiles se trouve dans la figure A. Ici, je me concentre sur la variabilité liée à l'accrétion (magnétosphérique), dans le cas des étoiles de faible masse ($\lesssim 1$ $M_\odot$), qui se présente principalement sous deux formes principales : la variabilité du continuum et la variabilité des raies. Pour une revue plus générale de la variabilité stellaire, voir Fischer et al. (2023)

Dans le cas d'un point chaud provenant d'une colonne d'accrétion, la variabilité de l'excès de rayons X/UV/Vis est inévitable lorsque le point chaud apparaît et disparaît de la vue à mesure que l'étoile tourne. De telles variations peuvent être utilisées pour déduire la période de rotation de l'étoile (par exemple, AA Tau, Espaillat et al., 2021). Les variations des taux d'accrétion peuvent également avoir un impact direct sur l'amplitude de la variabilité, mais plutôt sur des échelles de temps légèrement supérieures à la période de rotation. La mesure des taux d'accrétion et la caractérisation de leur variabilité ont permis de constater qu'ils sont principalement modulés par les interactions entre le disque et la magnétosphère, et que leurs effets



apparaissent à peu près à la période de rotation (Fig. I.10B, Zsidi et al., 2022).

Les processus d'accrétion introduisent un large éventail de comportements de variabilité, comme l'illustre déjà la figure I.9. Outre la variabilité des conditions physiques, les formes des raies sont directement affectées par l'inclinaison du système. Lorsque les colonnes entrent et sortent de la ligne de visée, l'absorption décalée vers le rouge est appelée à apparaître et à disparaître, imprimant des effets modulés par la rotation dans les raies elles-mêmes. De nombreux auteurs ont utilisé des spectrogrammes pour déduire la ou les périodes de la magnétosphère, bien qu'ils trouvent des périodes variables en fonction de la ligne et du canal spectral (par exemple Zsidi et al., 2022; Sousa et al., 2021). Les échelles de temps et l'amplitude de variabilité typiques sont indiquées dans la figure I.10.

En bref, les modulations des profils de raies permettent d'étudier la variation de la géométrie (Alencar et al., 2012), ainsi que d'accéder aux propriétés physiques par la modélisation et les corrélations établies (Alcalá et al., 2014, 2017; Venuti et al., 2019). Cependant, ils nécessitent l'accès à des spectrographes à haute résolution, qui ne sont pas souvent accompagnés d'une optique adaptative puissante nécessaire à l'imagerie des planètes. Les tests tels que le scénario au régime de masse planétaire ne sont pas si simples.

1.4 Accrétion dans le régime de masse planétaire

Alors que dans les sections précédentes, l'utilisation du terme "accrétion" ne tenait pas compte des différentes échelles impliquées, il convient de les distinguer. En raison d'incertitudes évidentes sur les mécanismes exacts, ce qui se passe à petite échelle, là où le gaz interagit directement avec la planète, est généralement traité indépendamment des interactions entre la CSD et la CPD. L'hypothèse est que pour que le gaz soit accrété par la planète elle-même, il doit d'abord entrer dans la sphère de Hill. En d'autres termes, deux types de modèles coexistent : les modèles hydrodynamiques qui étudient les interactions avec le CSD (et dans une certaine mesure les flux dans la sphère de Hill), et les modèles d'émission de ligne qui expliquent les caractéristiques observées ainsi que les interactions entre la planète et son CPD. Cependant, ils ne sont pas incompatibles, car certains modèles hydrodynamiques prédisent également l'émission de ligne. La figureI.11 montre une compilation des trois principaux mécanismes d'accrétion, qui seront développés dans les sections suivantes.

1.4.1 Théorie et modèles actuels

Accrétion magnétosphérique Thanathibodee et al. (2019) a proposé une extension du scénario d'accrétion magnétosphérique, dans la gamme des masses planétaires. Les détails exacts de l'accrétion magnétosphérique sont donnés dans la section 3. Ils supposent une magnétosphère axisymétrique et ne modélisent que l'émission des colonnes. Le modèle suppose un couplage entre la magnétosphère et le disque interne. Les lignes de champ magnétique tronquent le CPD interne et lancent des colonnes en servant de guides à la matière qui tombe. La colonne chauffée émet des raies d'hydrogène, et les parties où la ligne de visée intercepte l'emplacement du choc induisent des caractéristiques d'absorption. En général, Thanathibodee et al. (2019) suppose un champ magnétique d'environ 0.5 à 1 kG. Dans la Fig. I.11, ce modèle correspond à l'émission de la colonne.

Accrétion depuis le disque protoplanétaire Les simulations hydrodynamiques et magnétohydrodynamiques prédisent que les planètes ouvrent des espaces dans les disques circumstellaires (Gressel et al., 2013), ce qui pourrait en principe déterminer la masse finale de la planète : autant que le gaz disponible dans l'espace (en supposant que la planète ne migre pas). En général, les planètes grandissent jusqu'à 5–10 M_{Jup} (Kley, 1999; Lubow and D'Angelo, 2006). Toutes les simulations prédisent la formation d'un disque circumplanétaire (DCP), à travers lequel la matière est ensuite accrétée sur la planète. La forme du DCP



est principalement définie par les flux des hautes latitudes (Szulágyi et al., 2014), car ils dominent le flux d'accrétion du DSC vers le DCP (Tanigawa et al., 2012). Ces flux se heurtent soit au disque, soit à la surface planétaire (voir les zones ombrées en rouge dans la Fig. I.11, Szulágyi and Ercolano, 2020; Takasao et al., 2021). La température du disque contribue également à déterminer la dynamique à l'intérieur du disque (Szulágyi, 2017). La physique d'un choc d'accrétion, bien que sur une surface stellaire, avait déjà été théorisée par Calvet and Gullbring (1998). Cependant, ils ont supposé des effets magnétiques qui réduiraient l'échauffement par choc, ce qui pourrait ne pas se reproduire à la surface du CPD. Au lieu de cela, Aoyama et al. (2018) a développé un modèle de choc avec des paramètres typiques de ce que l'on attend des simulations numériques. En principe, cela pourrait également s'appliquer au choc à la base de la colonne induite par la magnétosphère. Ils supposent un choc plan parallèle, et résolvent l'hydrodynamique radiative de l'écoulement dans les régions pré/post-choc. Ils ont pu en déduire des relations d'échelle entre les flux de lignes et le taux d'accrétion (Aoyama et al., 2021), similaires à celle obtenue pour les étoiles quelques années plus tôt (Alcalá et al., 2014, 2017).

1.4.2 Questions et objectifs de cette thèse

Jusqu'à présent, la plupart des détections de PMC ont été fortuites. Les campagnes dédiées venaient à peine de commencer au début de mon doctorat, mais n'ont encore découvert que quelques PMC.

1.4.3 Questions ouvertes

Les modèles d'émission théoriques n'étant disponibles que depuis peu, les articles consacrés à l'accrétion se sont concentrés sur trois signatures principales : les raies, le CPD et les composantes de choc.

La plupart des études se sont concentrées sur la détection des raies d'accrétion, principalement à la suite de la détection de PDS 70 b&c dans le H_α (Haffert et al., 2019). Les flux de ces raies ont été utilisés pour convertir en taux d'accrétion (Haffert et al., 2019; Eriksson et al., 2020; Betti et al., 2022,). Cependant, les relations qu'ils ont utilisées à cette fin ont été dérivées d'études stellaires, et Betti et al. (2023) a récemment montré qu'elles pourraient ne pas s'étendre au régime PMC. Des efforts ont été faits, en effet, pour utiliser les relations d'échelle planétaires plus récentes Aoyama et al. (2021).

Pour que ces conversions aient un sens, il faut qu'il y ait un réservoir de gaz. La question est la suivante : quel est ce réservoir de gaz ? Les candidats naturels sont les disques circumplanétaires, et des études ont tenté de les caractériser, de les détecter en premier lieu. La plupart des travaux se sont concentrés sur les points de photométrie (par exemple, Bowler et al., 2011), car les spectres aux longueurs d'onde pertinentes (bandes LM) sont difficilement accessibles avec l'instrumentation actuelle. D'autres ont utilisé les observations de l'ALMA (Wu and Sheehan, 2017; Wu et al., 2017) , qui ne font que tracer la poussière. Ce n'est que récemment que le JWST a ouvert de nouvelles fenêtres pour la caractérisation en profondeur des CPD (Cugno et al., 2024).

La combinaison des raies d'accrétion et de la caractérisation des CPD s'est avérée difficile jusqu'à présent, étant donné la résolution spectrale limitée à laquelle chaque observation a été obtenue : ~ 2000 pour les raies, points de photométrie pour les CPD. Au lieu de cela, on pense que l'excès UV est un traceur plus direct du choc d'accrétion, et son étude pourrait aider à élucider les conditions physiques ($\dot{\mathrm{M}}$, température, densité, ...) dans lesquelles il est émis. Cependant, les observations de l'excès UV ont jusqu'à présent utilisé des points de photométrie (Zhou et al., 2014, 2021), car les spectrographes à ces longueurs d'onde ne sont pas courants, ce qui entrave la plupart des modélisations et interprétations. Un spectre de l'excès d'UV et du continuum environnant fournirait à la place une image détaillée du mécanisme pertinent, comme cela a été fait par Espaillat et al. (2021).



Enfin, il convient de noter que l'accrétion a longtemps été considérée comme stable. Il a été démontré que l'accrétion sur les étoiles est variable (donc non stable), et des indices ont montré qu'elle est également variable pour les PMC. Ce point sera développé dans les sections suivantes et dans le présent manuscrit. Dans l'ensemble, le lecteur doit garder à l'esprit que l'accrétion est intrinsèquement un processus variable.

1.4.4 Objectifs

Cela donne naturellement quatre axes d'étude. Premièrement, tester les modèles de lignes d'émission (Aoyama et al., 2018; Thanathibodee et al., 2019) qui ont été développés à la suite de la découverte de PDS 70 b&c. En effet, il a été démontré qu'il était possible d'observer les raies de l'hydrogène et de l'hélium à haute résolution ($R \gtrsim 50,000$) (Ringqvist et al., 2023), ce qui n'avait même pas été envisagé auparavant. Deuxièmement, il a été suggéré que les raies sont variables (Zhou et al., 2014; Eriksson et al., 2020), mais cela n'a jamais été caractérisé et pourrait expliquer la non-détection des sondages H_α ainsi que limiter les échelles de temps d'accrétion des PMC. Enfin, la modélisation des chocs n'a jamais été réalisée qu'avec des points de photométrie, mais il serait peut-être possible d'obtenir un spectre de cet excès d'UV, en suivant les mêmes méthodes que celles qui permettent d'étudier les raies d'accrétion à haute résolution.

J'ai choisi de concentrer ma thèse sur deux de ces points. La variabilité des raies peut être évaluée à l'aide de programmes dédiés, tant en termes de flux que de profils de raies. Pour cela, j'utiliserai des instruments tels que VLT/SINFONI, qui permet de combiner un spectrographe à résolution moyenne avec une optique adaptative puissante. Cela permet d'étudier la variabilité du flux de la raie Pa_β, ainsi que, dans une certaine mesure, une certaine variabilité de profil. Ensuite, je me concentrerai sur la modélisation des raies elle-même, avec un instrument dédié à haute résolution (VLT/UVES), bien que pour certains PMC plus anciens. Au lieu de la raie Pa_β, je me concentrerai sur les raies optiques de Balmer et de l'hélium, comme cela a été démontré possible par Ringqvist et al. (2023). Je discuterai également de la variabilité de ces raies, ainsi que de l'excès UV des cibles étudiées. Dans l'ensemble, je vais construire une étude d'échantillon de PMC, avec un large éventail de conditions physiques : jeunes, vieux, séparations *proches* et *larges*, me permettant ainsi de tester les scénarios d'accrétion magnétosphérique et d'émission de choc dans diverses conditions, et d'inférer les paramètres physiques sous-jacents pertinents pour les mécanismes d'accrétion.

2 Traceurs d'accrétion dans le proche Infrarouge: VLT/SINFONI

2.1 Introduction

La manière la plus directe d'étudier l'accrétion est d'utiliser les raies d'accrétion. Historiquement, le choix de la raie à étudier dépend principalement de l'instrumentation disponible, et comme les PMC sont généralement proches de leur étoile hôte, l'utilisation de l'optique adaptative est nécessaire pour séparer le signal du compagnon de celui de l'étoile. Historiquement, l'optique adaptative la plus performante a été utilisée dans les longueurs d'onde du proche infrarouge, où les variations atmosphériques sont plus lentes et plus faciles à corriger. Un ensemble de raies d'accrétion se situe à des longueurs d'onde où le système d'optique adaptative est le plus performant, en particulier la bande K, qui contient à la fois les raies Br_γ et Pa_γ. Cependant, seule une poignée de PMC avait réussi à détecter ces raies (par exemple, Br_γ: Delorme 1 (AB)b, GSC 06214-00210 b; Pa_γ: Delorme 1 (AB)b, TWA 27 b, Betti et al., 2023; Lachapelle et al., 2015; Manjavacas et al., 2024). Et au moment des observations présentées dans ce travail, seule la GSC 06214-00210 b était connue pour porter une raie Br_γ. Avec si peu de détections et un flux de raie limité, toute tentative de modélisation serait limitée par le rapport signal/bruit de la raie par rapport au continuum. D'autres raies peuvent donc être plus appropriées. En passant aux bandes adjacentes, la raie Pa_β (1,8 µm) se trouve dans la bande J. Cette



raie est connue pour être la plus brillante des raies NIR, et se situe toujours dans une plage de performance raisonnable pour les systèmes d'optique adaptative, ce qui en fait un atout majeur pour caractériser les propriétés d'accrétion des compagnons de masse planétaire. Cerise sur le gâteau, la raie Pa_β n'est pas connue pour être contaminée par l'activité chromosphérique, du moins sur les étoiles (Natta et al., 2014). Cette raie avait déjà été détectée sur quelques compagnons, dont GQ Lup b et GSC 06214-00210 b.

La compréhension du mécanisme d'émission des raies d'accrétion se présente sous de nombreuses formes et saveurs. L'échantillon actuel de compagnons en accrétion est encore assez clairsemé, ce qui rend une analyse générale difficilement possible. Je me concentre plutôt sur la caractérisation des spécificités de deux compagnons : GQ Lup b et GSC 06214-00210 b. Je me concentre sur les aspects de variabilité des raies, tant en termes de profils que d'amplitude, ainsi que sur le lien avec les propriétés de leur atmosphère. Ce chapitre sert de résumé du travail, qui a été publié dans Demars et al. (2023).

2.1.1 GQ Lup b

GQ Lup b was originally identified as a companion to the GQ Lup star by Neuhäuser et al. (2005). It is a 10–40 M_{Jup} companion, at ∼0.7" from its host star (∼ 108 AU at 154.10 ± 0.69 pc Gaia Collaboration et al., 2023). The host is a K7Ve star, on the higher end of the T Tauri stars mass spectrum ($M_* = 1.02 \pm 0.05$ $M_\odot$, MacGregor et al., 2017). While the companion itself is not located within the circum-stellar disk, the disk does show spiral structures (van Holstein et al., 2021) extending to 129 AU. GQ Lup b seems to be on a polar orbit with low eccentricity (Stolker et al., 2021), which has been proposed to explain replenishment of the gas reservoir of GQ Lup b as it crosses the circum-stellar disk. Another companion to the system (GQ Lup c) was recently found, albeit at much higher mass and separation ($M \sim 0.15$ $M_\odot$, ∼ 2400 AU, Alcalá et al., 2020; Lazzoni et al., 2020).

2.1.2 GSC 06214-00210 b

GSC 06214-00210 b a d'abord été mis en évidence comme compagnon de l'étoile K5 T Tauri GSC 06214-00210 ($M_* = 0,80 \pm 0,11$ $M_\odot$, Kraus et al., 2008; Ireland et al., 2011; Bowler et al., 2014; Pearce et al., 2019), qui fait partie de l'association Scorpios-Centaurus (Preibisch et al., 1998). Cependant, Gagné et al. (2018) fournit une autre appartenance au sous-groupe Upper-Scorpus Centaurus. Les études précédentes avaient donné des estimations de masse-luminosité-âge biaisées par la distance estimée. La distance mise à jour ($108,8 \pm 0,3$ pc, Gaia Collaboration et al., 2023) fournit de meilleures contraintes. Pour l'étoile compagnon, Pearce et al. (2019) donne un âge de $16_{-2,9}+1,9$ Myr, $L \sim 10^{-3,35 \pm 0,02} L_\odot$. Sa masse est de $14,5 \pm 2$ M_{Jup}, à 2,2" de son hôte (240 AU à $108,8 \pm 0,3$ pc, Gaia Collaboration et al., 2023), et il est classé avec un type spectral M9-M9. 5 type spectral (Lavigne et al., 2009; Bowler et al., 2014).

2.2 VLT/SINFONI: un spectrographe intégral de champ depuis le sol

Le spectrographe SINFONI (Spectrographe pour les Observations en Champ Intégral dans l'Infrarouge Proche) était un instrument monté au foyer Cassegrain du 4ème télescope de l'unité, au VLT/Paranal (à noter qu'il a été transféré à l'UT3 quelques mois avant sa mise hors service en août 2019). Il a fonctionné de 2005 à 2019. Il a maintenant été remplacé par ERIS, monté sur UT4, dont la conception est fortement inspirée et similaire à celle de SINFONI, et réutilise même certaines des parties optiques de SINFONI.

SINFONI est un spectrographe à champ intégral (IFS), ce qui signifie qu'il est capable de fournir un spectre pour chaque point de l'image dans son champ de vision. Cela est particulièrement utile pour caractériser les exoplanètes et les compagnons dont le signal est souvent contaminé par la PSF étendue de leur étoile



hôte, car les informations sur les dimensions spatiales peuvent être utilisées pour démêler les deux signaux. Cela contraste avec le spectrographe à fibre unique, qui ne fournit qu'un seul spectre à un seul emplacement spatial.

Le système d'optique adaptative (OA) corrige les aberrations induites par l'atmosphère, fournissant ainsi une PSF presque limitée par la diffraction. Il s'agit d'un système en boucle fermée qui mesure l'aberration de courbure du front d'onde et la corrige à l'aide d'un miroir déformable dédié.

2.3 Observations et réduction de données

2.3.1 Observations

GQ Lup b a été observé les nuits se terminant le 25/04/2017, le 30/04/2017 et le 01/06/2017. GSC 06214-00210 b a été observé les nuits se terminant le 25 avril 2017, le 4 mai 2017, le 1er juin 2017 et le 19 août 2017. Les deux faisaient partie du programme 099.C-0760(D)[2] (PI : Bonnefoy). Les deux ont été observées dans la bande J, en ciblant la raie Pa_β (1,28 µm), avec l'échelle de plaque de 25 mas/px pour GQ Lup b, et l'échelle de plaque de 100 mas/px pour GSC 06214-00210 b, ce qui donne des résolutions spectrales de 2360 et 1800 respectivement. Les étoiles primaires ont été placées hors du champ de vision pour éviter la saturation du détecteur. L'échelle de plaque de 25 mas/px a été utilisée pour GQ Lup b car elle est relativement proche de son étoile hôte (0,7"), fournissant ainsi un échantillonnage fin des ailes de la fonction de distribution de la lumière de l'étoile primaire autour de l'étoile compagnon. Dans le cas de GSC 06214-00210 b, la séparation est beaucoup plus favorable (2,2"), donc une échelle de plaque plus grande a été choisie pour atténuer les effets du bruit du détecteur.

Nous avons également ajouté des données d'archives à l'échantillon. GQ Lup b avait déjà été observé dans la même configuration le 18 septembre 2006, dans le cadre du programme 077.C-0264(A)[3] (PI : Neuhäuser). D'autres nuits des programmes ont eu des conditions d'observation trop mauvaises pour être utiles. Ces données avaient déjà été publiées par Seifahrt et al. (2007), bien que l'extraction du spectre compagnon ait montré des signes de contamination résiduelle du primaire (McElwain et al., 2007; Lavigne et al., 2009), nous avons donc re-réduit les cubes de données. Nous avons également utilisé le spectre à basse résolution obtenu par Lavigne et al. (2009) avec NIFS/GEMINI (2007-05-30, $R = 5000$ mais les spectres avaient été préalablement lissés pour correspondre à la résolution SINFONI). Pour GSC 06214-00210 b, nous avons utilisé le spectre public de Bowler et al. (2011), obtenu avec le spectrographe Keck/OSIRIS (2010-07-09, R $\sim$ 3800).

Dans les cas GQ Lup b et GSC06214b, les cubes de données montraient une zone sombre dans la moitié inférieure du détecteur. Son origine est encore inconnue, mais il s'est avéré qu'il s'agissait d'un problème d'aplatissement/calibrage dans cette région. Tous les cubes de données pour lesquels le compagnon a été placé dans cette région ont été exclus de l'analyse ($\sim$ 25 % pour GQ Lup b, $\sim$ 50 % pour GSC06214b).

2.3.2 Réduction de données

La réduction des données a été effectuée en plusieurs étapes : correction du bruit statique, reconstruction des cubes, calibration des longueurs d'onde, extraction des spectres et correction tellurique.

Il avait été précédemment constaté que SINFONI contenait des éléments de bruit statique (Bonnefoy et al., 2014) dans les données brutes, qui n'étaient pas pris en compte par le pipeline. Celles-ci ont été corrigées à l'aide de routines dédiées disponibles dans TExTRIS (Petrus et al., 2021, Bonnefoy et al, en préparation).

[2] **099.C-0760(D)**: https://archive.eso.org/wdb/wdb/eso/sched_rep_arc/query?progid=099.C-0760(D)
[3] **077.C-0264(A)**: https://archive.eso.org/wdb/wdb/eso/sched_rep_arc/query?progid=077.C-0264(A)



Les images brutes ont été transformées en cubes de données (2+1)D à l'aide du pipeline SINFONI standard (Abuter et al., 2006). La position des 30 petites fentes est identifiée sur les images de calibration pour créer une carte d'association 2D, qui est ensuite utilisée pour reconstruire les cubes de données à partir des images scientifiques. Les raies d'émission du ciel sont également soustraites des cubes de données à l'aide d'outils dédiés au sein du pipeline. Il restait cependant de nombreuses raies résiduelles qui ont été supprimées à un stade ultérieur. Chaque exposition a été traitée indépendamment, ce qui a permis d'accéder aux petites variations temporelles de la raie Pa_β.

Bien que le pipeline SINFONI fournisse une solution de longueur d'onde, il s'est avéré biaisé en fonction de l'ensemble de données (Petrus et al., 2021). Une nouvelle solution de longueur d'onde a donc été calculée en corrélant (TExTRIS) un spectre de ciel modèle (calculé avec SkyCalc[4], Noll et al., 2012; Jones et al., 2013) avec le spectre à chaque position spatiale du cube. Ce processus est appliqué aux observations Tel. Std. qui ont un rapport signal/bruit intrinsèquement plus élevé. La solution a été choisie pour être égale à celle du Tel. Std. de ladite séquence, calculée sur des spaxels avec un rapport signal sur bruit > 10. La solution exacte a été choisie comme valeur médiane sur l'ensemble du champ de vision à chaque intervalle spectral. L'incertitude typique sur l'étalonnage est de $\sim 0,2$ Å, ce qui correspond à $\sim 4,7$ km/s à Pa_β, soit environ 1/30e de la résolution spectrale FWHM.

Dans les cas GQ Lup b et GSC06214b, les ailes de la PSF de l'étoile primaire s'étendent jusqu'à l'emplacement de l'étoile compagnon, contaminant ainsi le signal de l'étoile compagnon et imprimant le spectre de l'étoile primaire dans le spectre de l'étoile compagnon. La caractéristique spectrale ciblée est la raie Pa_β, qui est également la raie des étoiles hôtes de GQ Lup b et de GSC06214b (en émission pour GQ Lup b, en absorption pour GSC06214b). Si elles avaient un continuum relativement plat autour et à l'intérieur de Pa_β, la contamination pourrait être soustraite directement des spectres, en interpolant le continuum primaire de part et d'autre de la raie. Au lieu de cela, il est nécessaire d'effectuer une soustraction correcte de la contamination des ailes du primaire, directement sur les cubes de données. Les ailes du primaire sont approximées directement à partir du cube reconstruit, sous la forme d'un gradient polynomial 2D du troisième ordre. Il est ajusté pour chaque bin spectral, et soustrait des données. La PSF compagnon est ensuite ajustée avec une PSF de référence : celle de l'étoile tellurique standard de la séquence. Les cubes de données ont été étalonnés en flux à l'aide des cubes de données de l'étoile de référence tellurique (Tell. Std.).

2.4 Modélisation de l'atmosphère

2.4.1 Modélisation

Les spectres extraits de GQ Lup b et de GSC06214b sont très similaires, typiques des naines M9. Ils présentent des raies d'absorption K I, des bandes H2O et FeH, ainsi que la raie Pa_β. Toutes les caractéristiques spectrales sont indiquées dans la figure II.5. La pente spectrale de GQ Lup b est beaucoup plus en accord avec celle de Lavigne et al. (2009) que ne l'était Seifahrt et al. (2007), même pour le cube de données commun (2006-09-18), renforçant ainsi l'argument de la contamination résiduelle du primaire dans le spectre publié. Cependant, même cette extraction n'est pas parfaite et il existe des différences résiduelles de pente spectrale, dont la dispersion donne une idée de l'erreur typique induite par la méthode d'extraction. Cette dispersion servira d'incertitude typique pour les paramètres atmosphériques dans la section ci-dessous.

Toutes les caractéristiques d'absorption des spectres, ainsi que leur pente, sont des traceurs directs de la composition de l'atmosphère de GQ Lup b et GSC06214b. De fines absorptions moléculaires devraient se former à l'emplacement de Pa_β et sur l'ensemble du spectre pour les jeunes compagnons de type M tardif/L précoce. Nous avons donc modélisé les caractéristiques photosphériques à l'aide de `ForMoSA` (Petrus

[4]**SkyCalc**: https://www.eso.org/observing/etc/bin/gen/form?INS.MODE=swspectr+INS.NAME=SKYCALC



et al., 2020, 2021, 2023). `ForMoSA` est un outil de modélisation directe qui compare des grilles de modèles atmosphériques avec des observations grâce à l'algorithme d'inférence bayésienne par échantillonnage emboîté (Skilling, 2004). Son avantage par rapport aux outils MCMC traditionnels est de couvrir un espace de paramètres beaucoup plus homogène, évitant ainsi les minima locaux. Les modèles atmosphériques d'entrée étaient les modèles ATMO (Tremblin et al., 2015, 2016). Les paramètres résultants sur le spectre moyen de chaque époque sont présentés dans le tableau. II.4. L'espace des paramètres est représenté sous forme de diagrammes en coin dans la Fig. II.6. Les valeurs adoptées sont calculées comme la moyenne de toutes les époques, à l'exclusion de l'époque 2017-06-01, car elle a convergé vers certains minima locaux pour les deux objets. Certains paramètres convergent parfois en bordure de la grille (principalement γ).

2.4.2 Interprétation

Des études antérieures avaient déjà fourni certaines valeurs atmosphériques pour GQ Lup b et GSC06214b. Pour GQ Lup b, Stolker et al. (2021) a trouvé Teff dans la plage 2500–2700 K, et log(g) = 4.0. Nous trouvons Teff = 2638^{+33}_{-51} et log(g) = $4,18^{+0,04}_{-0,02}$, ce qui est tout à fait conforme à leurs valeurs compte tenu de leur échantillonnage par grille. Pour GSC06214b, Lachapelle et al. (2015) a trouvé Teff = 2300 ± 200 K, et log(g) = $3,0 - 4,0$. Nous trouvons Teff = 2248^{+69}_{-59} et log(g) = $4,24^{+0,11}_{-0,15}$. Bien que notre log(g) soit légèrement supérieur à celui de Lachapelle et al. (2015), les paramètres sont globalement similaires, compte tenu des barres d'erreur.

Cependant, cette étude présente la première estimation du rapport C/O et de la métallicité [M/H] pour GQ Lup b et GSC06214b. Les deux ont des valeurs de C/O compatibles avec la valeur solaire ($C/O_{\odot} = 0,55$) à 1σ. Cependant, leur métallicité est assez différente. GSC06214b a une métallicité globalement solaire (GSC06214b: [M/H] = $-0,16 \pm 0,17$), tandis que GQ Lup b est légèrement supersolaire (GQ Lup b: [M/H] = $0,23 \pm 0,06$), même à 3σ. Cependant, une étude récente a publié des valeurs assez différentes de C/O et [M/H] pour ces deux cibles (Xuan et al., 2024). Ils trouvent C/O = $0,70^{0,01}_{-0,02}$ et C/O = $0,70^{0,07}_{-0,06}$ pour GQ Lup b et GSC06214b respectivement, et [M/H] = $0,40^{+0,20}_{-0,22}$ et [M/H] = $0,14^{+0,33}_{-0,29}$ pour GQ Lup b et GSC06214b respectivement.

Les systèmes GQ Lup et GSC06214 sont tous deux situés dans des régions dont on s'attend à ce qu'elles aient des C/O et [M/H] largement solaires (Bubar et al., 2011; Biazzo et al., 2017; Murphy et al., 2021; Suárez-Andrés et al., 2018; Tautvaišienė et al., 2022). Cependant, Swastik et al. (2021) a constaté que les étoiles hôtes ont des métallicités inférieures à la valeur solaire pour les deux cibles : [M/H] = $-0,35 \pm 0,01$ et [M/H] = $-0,06 \pm 0..01$ pour GQ Lup A et GSC06214A respectivement. La valeur est étonnamment faible pour GQ Lup A, et il convient de noter que sa raie H_{α} est la plus brillante de leur échantillon. Même s'ils ont choisi la région où le voile n'affecte pas trop la mesure, il est toujours possible qu'un voile résiduel soit présent pour GQ Lup A, ce qui fausserait la valeur de cette étoile. Bien que cette valeur rende GQ Lup b significativement riche en métaux par rapport à son étoile hôte, elle serait toujours enrichie en métaux même si la primaire avait une valeur solaire. Quant à GSC06214b, sa valeur est comparable à celle de la primaire à 1σ. Dans l'ensemble, les valeurs de la métallicité sont compatibles avec la prédiction des deux cadres d'accrétion de noyau (Fig. 9 of Petrus et al., 2021) et de la formation dans un disque circumstellaire (Boley et al., 2011). Les prédictions ne permettent actuellement pas de faire la distinction entre les deux.

2.5 La raie d'accrétion Paschen Beta

Les panneaux de droite de la figure II.5 montrent la ligne moyenne Pa_{β} de chaque époque pour GQ Lup b et GSC06214b. Cependant, la ligne des expositions individuelles au sein d'une séquence est également disponible (voir la figure 3 dans l'article). Celles-ci permettent de scanner les amplitudes de variabilité à des échelles



de temps variant de 5 minutes (DIT), à des mois (diffusion des observations au sein du programme) et des années/décennies (y compris les données d'archives).

2.5.1 Profils de raie

À première vue, les profils de raies Pa_β de GQ Lup b et de GSC06214b sont similaires et semblent symétriques par rapport à l'emplacement de leur pic. Cependant, toutes les raies de GQ Lup b semblent légèrement décalées vers le bleu. Les raies ont été ajustées avec des profils gaussiens pour en déduire leurs paramètres (flux de raie, centroïde, largeur) et nous constatons que les raies de GQ Lup bsont décalées vers le bleu avec un décalage globalement constant à toutes les époques. Les raies de GQ Lup bsont pour la plupart non résolues, c'est-à-dire que leur largeur est cohérente avec celle du LSF (R=2360), sauf pour l'époque du 18/09/2006 où la largeur des raies est environ 1 à 1,5 fois la largeur du LSF (avec un niveau de confiance de 1 à 3 σ). Les raies de GSC06214bne sont pas résolues (R=1800) dans toutes les époques de 2017. Cependant, les données OSIRIS (époque du 09/07/2010) ont une résolution deux fois plus élevée (R=3800), et les raies sont résolues à 1,2-1,9 fois la largeur du LSF (confiance de 4-8σ). Pour toutes les raies, la FWHM intrinsèque est calculée comme la racine carrée de la différence quadratique entre la FWHM de la raie mesurée et la FWHM de la LSF ($\mathrm{FWHM}^2_{\mathrm{in}} = \mathrm{FWHM}^2_{\mathrm{obs}} - \mathrm{FWHM}^2_{\mathrm{LSF}}$).

Il n'y a pas de tendance ni de corrélation claire dans les paramètres des raies de GQ Lup b. Cependant, les raies de GSC06214bmontrent de grandes tendances entre le centroïde de la raie, le flux et la largeur. Les résultats sont présentés dans la figure 1. Le panneau de gauche montre les corrélations entre le FWHM intrinsèque de la raie et le centroïde de la raie, les flèches représentant les limites supérieures du FWHM intrinsèque. Le panneau du milieu montre les corrélations entre le flux de la raie Pa_β et la position du centroïde de la raie Pa_β par rapport au référentiel du repos. Le panneau de droite montre les corrélations entre le flux de la raie Pa_β et sa FWHM intrinsèque, et n'a pas été inclus dans l'article (Demars et al., 2023) car je l'avais manqué au moment de sa rédaction. Il existe une tendance entre le FWHM intrinsèque et le centroïde de la raie (panneau de gauche) : la raie est plus large à mesure qu'elle devient décalée vers le rouge / non décalée vers le bleu. Il existe également une tendance entre le centroïde de la raie et le flux de la raie (panneau du milieu), en particulier dans l'époque 2017 : lorsque la raie devient plus brillante, elle passe d'un décalage vers le bleu à un décalage vers le rouge, jusqu'à une limite de décalage-saturation, comme le montre l'emplacement des points du 09/07/2010. Cependant, dans ce décalage saturé, il existe une corrélation entre la FWHM intrinsèque et le flux de la raie (panneau de droite). Cela ne peut s'expliquer qu'en ajoutant le flux de manière $\sim$ égale du côté bleu et du côté rouge de la raie, mais pas dans le cœur de la raie, afin d'élargir le profil. Cela ne peut s'expliquer que si les ailes et le noyau des lignes sont quelque peu non corrélés, du moins à cette époque. Cependant, la forme exacte de ces composantes ailes-noyau est impossible à déconvoluer des profils actuels étant donné le rapport signal/bruit des données. On verra dans le chapitre suivant que la décomposition des lignes de Delorme 1 (AB)b fournit un candidat parfait à partir de ce comportement.

Sans aller chercher une résolution spectrale plus élevée (pas encore !), il est encore possible d'expliquer certaines des corrélations. La corrélation μ_0–$\mathrm{FWHM}_{\mathrm{in}}$ peut s'expliquer par une variation dans la seule aile rouge : à mesure que l'aile rouge s'éclaircit, la largeur apparente de la raie augmente et le centre de la raie se déplace vers le rouge. Cela peut s'expliquer si une absorption décalée vers le rouge se superpose au profil de la raie, comme on le voit souvent dans le contexte des CTTS. L'absorption pourrait être variable en profondeur (en fonction du taux d'accrétion, par exemple) et ne pas être entièrement corrélée à l'intensité de la raie, ce qui modifierait sa largeur apparente. Cela expliquerait également la corrélation Flux–μ_0 (panneau de droite de la Fig. II.7): à mesure que l'absorption décalée vers le rouge augmente, la contribution de l'aile rouge diminue et la raie se déplace vers le bleu.

Si l'accrétion magnétosphérique est valable, il est toujours possible qu'une partie des variations des profils



des raies puisse être attribuée à deux composantes différentes : une composante de choc et une composante de colonne. Les modèles de choc devraient fournir des raies d'émission légèrement décalées vers le rouge (Aoyama et al., 2018). Bien que j'aie précédemment mentionné l'absorption décalée vers le rouge comme une explication possible de la variation de l'aile rouge, une composante d'émission décalée vers le rouge pourrait également expliquer la corrélation FWHM–μ_0 : lorsque la composante de choc décalée vers le rouge s'éclaircit, le centroïde apparent de la raie se déplace vers le rouge, et la raie s'élargit lorsque le flux est ajouté de manière non uniforme par rapport au centre de la raie. Cependant, même si cela correspondait aux variations des époques de 2017, cela ne pourrait pas expliquer les variations du 09/07/2010 où le centroïde de la raie est principalement constant, alors que le flux de la raie et la FWHM augmentent. Il est possible que GSC06214b ait deux régimes d'accrétion/émission différents qui étaient apparents dans la campagne d'observation de 2017 et dans la séquence du 09/07/2010.

2.5.2 Variabilité

Chaque paire de lignes peut être donnée par sa variation de flux relative $(F_1 - F_2)/F_1$) et sa différence d'échelle de temps $(t_1 - t_2)$. Celles-ci sont représentées sur la figure 1, pour toutes les paires de lignes possibles de GQ Lup bet GSC06214b. Les couleurs des marqueurs correspondent à l'importance de la mesure, c'est-à-dire à la distance à 0 donnée par le nombre de σ (barres d'erreur). En d'autres termes, cela équivaut à la barre d'erreur de la mesure, sans rendre le graphique trop dense avec les barres d'erreur elles-mêmes. Les points colorés signifient que la mesure est significative (rouge : $3 - 5\sigma$, violet : $> 5\sigma$), tandis que les points gris signifient que la mesure est compatible avec une absence de variation de flux ($< 3\sigma$). Les croix noires représentent la dispersion de la variabilité sur une tranche de temps. La procédure est similaire à celle de Zsidi et al. (2022), avec l'ajout de couleurs pour les barres d'erreur qui ne sont pas nécessaires pour les lignes brillantes des CTTS.

GQ Lup b montre un modèle de variabilité où l'amplitude de la variabilité est assez faible à l'échelle horaire ($\sim 20 - 30\%$) et plus élevée à l'échelle des mois et des années ($\sim 200 - 300\%$). Notez cependant que l'échantillonnage est assez faible, avec seulement 3 époques en 2017 et 2 époques en 2006-2007 (y compris le spectre de Lavigne et al., 2009)). Le modèle est similaire à celui observé dans les CTTS Zsidi et al. (2022). Cependant, GSC06214bfournit un échantillonnage bien meilleur, avec un motif différent. Bien que la tendance générale montre également qu'il existe une plus grande amplitude de variabilité à des échelles de temps plus grandes, les amplitudes elles-mêmes sont assez différentes. La variabilité à l'échelle des heures est plus grande (facteur 2) que celle de GQ Lup b, tout en étant également observée (points colorés). La variabilité à l'échelle des mois n'atteint qu'une variabilité relative de $\sim 80 - 100\%$, tout en maintenant un plateau. Ce plateau est également observé sur les CTTS : la variation relative atteint une valeur constante de ~ 300 % sur toutes les échelles de temps supérieures à la période de rotation de l'étoile. Cela est interprété comme la modulation rotationnelle de la magnétosphère étant la principale source de variabilité pour l'émission de raies (Costigan et al., 2014). Les périodes de rotation attendues de GQ Lup b et de GSC06214b sont indiquées par les zones ombrées en jaune, qui pour GSC06214b se situent juste avant le plateau de variabilité observé. Cela plaide en faveur d'une accrétion magnétosphérique sur GSC06214b. Cependant, les raies décalées vers le bleu de GQ Lup b plaident également en faveur d'une accrétion magnétosphérique, malgré le mauvais échantillonnage temporel des données.

Il est possible que ces deux objets soient les signatures du même mécanisme, observé dans des régimes différents. Aoyama et al. (2021) (voir leur Fig.2) fournit une comparaison de la relation $\dot{M}$–L(H_α) pour deux principaux mécanismes d'émission : un modèle de choc (vert) et un modèle de colonne (bleu), qui ont déjà été mentionnés. Ils montrent qu'à des taux d'accrétion élevés ($\dot{M} > 10^{-7}$ M_{Jup}/an), l'émission de la colonne domine celle du choc, tandis qu'à des taux d'accrétion faibles ($\dot{M} < 10^{-9}$ M_{Jup}/an), l'émission du choc



devient dominante. GQ Lup b et GSC06214b pourraient être les deux extrêmes de ces deux scénarios. La seule façon d'en être sûr est d'essayer d'ajuster ces modèles aux lignes pour voir s'ils correspondent ou non : d'où la section suivante.

2.6 Modélisation des raies d'émission

L'analyse préliminaire et empirique de la raie Pa_β donne déjà des indices sur l'accrétion magnétosphérique pour GQ Lup b et GSC06214b, bien que pour des raisons différentes. Néanmoins, il n'est pas exclu qu'une partie de l'émission de la raie puisse être déclenchée par un choc, plutôt que par une colonne. Je propose d'utiliser des modèles de raies d'émission (modèles d'accrétion magnétosphérique et de choc) pour tenter de démêler ces deux mécanismes (non exclusifs).

2.6.1 Description des modèles

Thanathibodee et al. (2019) a proposé des modèles d'accrétion magnétosphérique, adaptés au cas des compagnons de masse planétaire. Ce sont les mêmes modèles que ceux proposés par Hartmann et al. (1994), mais pour une masse d'objet central plus faible. La magnétosphère est supposée être axisymétrique, le dipôle étant aligné avec l'axe de rotation de la planète. Le champ magnétique tronque le disque circumplanétaire interne à un rayon appelé $R_{\rm in}$, sur une zone d'une largeur donnée (en particulier, la base de la colonne s'étend de $R_{\rm in}$ à $R_{\rm in} + \text{Largeur}$). Le taux d'accrétion ($\dot{\rm M}$) et la température de la colonne ($\rm T_{col}$) déterminent les conditions d'émission. L'inclinaison du système est responsable de certaines asymétries des profils de raies (par exemple, l'absorption décalée vers le rouge si la ligne de visée traverse à la fois la colonne et la région de choc et/ou la photosphère). La masse et le rayon de la planète déterminent la dynamique du flux d'accrétion. Enfin, la température de la planète définit la ligne de base de l'émission continue. Les modèles sont le résultat de simulations numériques de transfert radiatif couplées à un lancer de rayons de l'émission intrinsèque et de la profondeur d'absorption le long de la ligne de visée. Ils sont capables de produire des profils de raies pour la plupart des raies de l'hydrogène. Ici, les modèles se concentrent sur la raie Pa_β. À noter que seule l'émission de la ligne provenant de la colonne est prise en compte dans le modèle. Il n'inclut pas l'émission de la ligne provenant du choc ni l'émission/absorption provenant d'un quelconque écoulement. La plage de paramètres des modèles d'accrétion magnétosphérique est donnée dans le tableau.

Aoyama et al. (2018) a proposé un scénario différent pour l'émission de raies d'accrétion. Comme les conditions intrinsèques de ces objets sont très différentes de celles des étoiles (par exemple, ils peuvent être intégrés dans le disque circumstellaire de leur étoile hôte), la matière pourrait descendre des hautes latitudes du disque circumstellaire, soit vers la planète elle-même, soit vers le disque circumplanétaire environnant. Ces flux, s'ils étaient plus rapides que la vitesse du son locale, induiraient donc un choc au niveau du disque circumplanétaire et/ou de la surface planétaire. Ce choc chaufferait suffisamment le matériau pour déclencher une émission de raies. Le modèle lui-même ne comporte que deux paramètres d'entrée : la vitesse du flux (v_0) et la densité avant choc (n_0). J'ai ajouté un paramètre supplémentaire, $S_{\rm eff}$, qui représente la surface effective du choc (c'est-à-dire la zone d'émission, $4\pi R_p^2 f_{\rm fill}$ si elle se produit à la surface de la planète, avec $f_{\rm fill}$ le facteur de remplissage). Bien que ce modèle ait été motivé par les protoplanètes en formation, il peut, en principe, être appliqué à tout type de choc. Par conséquent, s'il correspondait aux lignes, les paramètres résultants pourraient également être interprétés comme un choc à la base d'une colonne induite par la magnétosphère. La plage de paramètres pour les modèles de choc est donnée dans le tableau. II.6.



2.6.2 Ajustement des modèles

Les ajustements sont effectués sur les données photosphériques soustraites (obtenues avec l'ajustement `ForMoSA`), et en mettant à l'échelle chaque modèle aux distances respectives de GQ Lup b et GSC06214b. Chaque modèle est donc également soustrait de son niveau continu (ajustement linéaire des deux côtés de la ligne). Les modèles sont convolués à la résolution spectrale respective des données (R=2360 pour GQ Lup b, R=1800 pour les époques 2017 de GSC06214b, et R=3800 pour l'époque 2010-07-09 de GSC06214b). La grille des modèles est relativement petite, ce qui permet de calculer par force brute les valeurs χ^2_r sur l'ensemble des grilles. Les modèles les mieux adaptés sont présentés à la figure II.10 pour la ligne moyenne de chaque époque. Les zones ombrées représentent la plage de modèles qui correspondent à la ligne à un niveau $\chi^2_{r,\min} + 1$, à la fois pour les modèles d'accrétion magnétosphérique (rouge) et de choc (bleu). La figure II.11 montre les corrélations typiques des paramètres des modèles d'accrétion magnétosphérique (à gauche) et de choc (à droite).

Pour GQ Lup b, seuls les modèles d'accrétion magnétosphérique sont capables de reproduire les raies décalées vers le bleu. Les modèles de chocs les mieux adaptés apparaissent toujours trop décalés vers le rouge, ce qui est cohérent avec la nature intrinsèque de leurs raies décalées vers le rouge, en raison de la matière émettrice en chute. Les modèles d'accrétion magnétosphérique semblent reproduire les caractéristiques d'absorption décalées vers le rouge en dessous du niveau continu, mais nous avertissons que ces écarts sont purement dus au bruit dans les données et ne sont pas évidents lorsque l'on zoome sur la raie Pa_β. Pour GSC06214b, les modèles d'accrétion magnétosphérique et de choc sont capables de reproduire les raies de toutes les époques de 2017. Cependant, la raie du 09/07/2010, qui a une résolution spectrale plus élevée, n'est reproduite que par les modèles de choc, tandis que les modèles d'accrétion magnétosphérique produisent des raies trop étroites.

Le modèle d'accrétion magnétosphérique produit de fortes anticorrélations entre la température de la colonne et le taux d'accrétion (Fig. II.11, panneau de gauche). Cela a déjà été observé dans le contexte des CTTS (Muzerolle et al., 2001), et est lié au fait que le flux de la raie est globalement proportionnel à la température et à la densité. Cependant, cela fournit une limite inférieure du taux d'accrétion : $\dot{M} > 10^{-11}$ $M_\odot$/an pour GQ Lup b et $\dot{M} > 10^{-12}$ $M_\odot$/an pour GSC06214b. Ils sont cohérents avec les valeurs déduites par Zhou et al. (2014) de l'ajustement de l'excès UV (respectivement $10^{-10,8}$ $M_\odot$/an et $10^{-9,3}$ $M_\odot$/an).

D'après les raies décalées vers le bleu de GQ Lup b, l'accrétion magnétosphérique semble être le scénario évident. Pour GSC06214b, cependant, le scénario de choc semble être préféré (au moins pour l'époque la plus brillante), mais l'origine du choc reste à déterminer. Les paramètres les mieux adaptés sont pour la plupart liés à la surface de choc pour l'époque 2017 (fig. A.17 à A.22). Cependant, l'époque 2010-07-09 fournit des contraintes (Fig. II.11, panneau de droite) à la fois sur la vitesse d'injection et la densité pré-choc : $v_0 > 150$ kms, $n_0 \sim 10^{20}$ m^3. En supposant que le matériau provient de l'infini, la vitesse d'impact est cohérente avec un choc situé à $R < 2,4$ R_{Jup}, ce qui est cohérent avec le rayon planétaire déduit de `ForMoSA` (1,8–2,0 R_{Jup}). Les paramètres les mieux ajustés ($S_{\text{eff}} = 1,5 \times 10^{-2}$ S_{jup}, $v0 = 180$ km/s, $n_0 = 10^{20}$ m^{-3}) fournissent une estimation directe du taux d'accrétion (Aoyama et al., 2018, 2021) : $\dot{M} \sim 10^{-9}$ $M_\odot$/an. La surface effective correspond à un facteur de remplissage de 0,38 à 0,47 %. C'est à peu près le même ordre de grandeur que celui trouvé par Ringqvist et al. (2023) pour Delorme 1 (AB)b, une autre planète de type compagnon de masse planétaire (quoique plus ancienne) de masse similaire. Il est toujours possible que GSC 06214-00210 b subisse également une accrétion magnétosphérique, mais dans un régime différent, comme mentionné dans la section précédente. Les modèles d'accrétion magnétosphérique sont toujours capables de reproduire les raies dans les époques de 2017, et bien que seuls les modèles de choc reproduisent l'époque du 09/07/2010, cela ne pourrait être dû qu'à la nature trop simpliste d'un modèle à symétrie axiale, comme c'est le cas pour Thanathibodee et al. (2019). Les paramètres de choc correspondent également à ce que



l'on attend d'un scénario d'accrétion magnétosphérique. Pour démêler les deux scénarios (non exclusifs), des observations à plus haute résolution seraient nécessaires, car leurs principales différences peuvent être résolues à R > 10,000. J'ai fait plusieurs propositions pour démêler les scénarios sur deux compagnons. L'une avec ERIS (GSC 06214-00210 b), qui a été rejetée, et l'autre avec CRIRES (Delorme 1 (AB)b), qui a été acceptée. La proposition elle-même est donnée en annexe du chapitre suivant.

2.7 Conclusion

Ce chapitre présente les résultats d'une campagne de suivi de la ligne Pa_β de GQ Lup b et GSC 06214-00210 b avec SINFONI/VLT. L'analyse a été publiée dans Demars et al. (2023) et a permis de dégager quelques points clés pour la compréhension de l'accrétion dans le contexte des compagnons de masse planétaire.

GQ Lup b et GSC 06214-00210 b sont des compagnons de masse planétaire jeunes et chauds, avec des valeurs C/O compatibles avec les valeurs solaires. Leurs métallicités, cependant, sont soit solaires (GSC 06214-00210 b), soit légèrement super-solaires (GQ Lup b). Une étude plus récente (Xuan et al., 2024) a fourni des valeurs C/O super-solaires pour les deux cibles, bien que leurs barres d'erreur puissent être sous-estimées.

La raie Pa_β des deux objets s'avère variable, au moins en intensité, et également en forme pour GSC 06214-00210 b. Les raies semblent être intrinsèquement différentes pour les deux objets, du moins compte tenu de la raie décalée vers le bleu de GQ Lup b. Leur amplitude de variabilité présente une tendance similaire, des amplitudes de variabilité plus importantes étant observées à des échelles de temps plus grandes, bien qu'avec une amplitude relative plus faible pour GSC 06214-00210 b. Les deux objets présentent des époques de sursaut (données d'archives) qui pourraient expliquer, avec leur amplitude de variabilité (même à des échelles de temps courtes), l'absence de détection par les relevés H_α. Cependant, le chapitre suivant montrera que la variabilité à des échelles de temps courtes ($\sim$ heure) ne peut pas réellement expliquer cette absence de détection, bien que sur des objets différents.

Les raies GSC 06214-00210 b, en particulier à l'époque de l'explosion, présentent des variations de forme où la FWHM intrinsèque est corrélée au flux de la raie. Cela ne peut se produire que si du flux est ajouté à l'aile, de manière à réduire le contraste entre le noyau et les ailes des raies. L'origine de ce flux est inconnue, mais une proposition sera faite dans le chapitre suivant.

Les deux objets ont des raies qui sont reproduites par les modèles d'accrétion magnétosphérique, et seul GSC 06214-00210 b est également reproduit par les modèles de choc. Cela favorise l'accrétion magnétosphérique pour GQ Lup b (en particulier avec sa raie décalée vers le bleu), tandis que GSC 06214-00210 b semble être une cible plus exotique : son époque la plus brillante (et sa résolution spectrale la plus élevée) n'est reproduite que par les modèles de choc dont les paramètres sont cohérents avec un choc à la surface planétaire. Cependant, les contraintes ne sont pas suffisantes pour déterminer l'origine de la matière. Il est possible que les différentes époques de GSC 06214-00210 b représentent différents régimes d'accrétion du même mécanisme.

Dans l'ensemble, il existe encore de nombreuses incertitudes dans la compréhension des GQ Lup b et des GSC 06214-00210 b, et des compagnons de masse planétaire en général. Des observations à plus haute résolution spectrale ($R > 10,000$) sont nécessaires pour (au moins) distinguer les modèles d'accrétion magnétosphérique des modèles de choc, ou déterminer si les deux jouent un rôle dans l'émission de raies. J'ai soumis plusieurs propositions dans ce sens : deux propositions VLT/ERIS ciblant la raie Pa_β de GSC 06214-00210 b et Delorme 1 (AB)b, à R > 10000. Pour GSC 06214-00210 b, l'objectif était d'observer la cible pendant des nuits successives afin de vérifier les variations fines des raies Pa_β sur ces échelles de temps. Pour Delorme 1 (AB)b (qui a été soumis comme matériel de vérification scientifique pour ERIS), l'objectif était d'affiner les modèles de paramètres de choc obtenus par Betti et al. (2022,) pour Delorme 1 (AB)b. Les



deux propositions ont été classées dans le deuxième quartile mais rejetées. J'ai également développé une proposition CRIRES, qui cible également la raie Pa_β. Plus d'informations à ce sujet dans le chapitre suivant.

Bien que des observations à plus haute résolution spectrale ne soient pas (encore) disponibles pour GQ Lup b ou GSC 06214-00210 b, le chapitre suivant se concentrera sur les observations à R $\sim 50,000$ d'une autre cible : Delorme 1 (AB)b. Bien que plus ancienne que GQ Lup b ou GSC 06214-00210 b, elle a à peu près la même masse que GSC 06214-00210 b.

3 Traceurs d'accrétion dans le Visible/UV avec VLT/UVES

3.1 Introduction

Le chapitre précédent a montré que les lignes de modélisation et d'analyse sont sévèrement limitées par la résolution relativement faible de SINFONI ($R \sim 2000$). Cependant, travailler avec un instrument à plus haute résolution n'est pas si simple, et la plupart des instruments sont un équilibre entre la résolution angulaire et spectrale. En d'autres termes, l'augmentation de la résolution spectrale se fait souvent au détriment de la résolution spatiale. De plus, une résolution spectrale accrue réduit la largeur de la LSF, mais les lignes d'accrétion sont intrinsèquement grandes (ce qui est confirmé par les légères lignes résolues de GSC 06214-00210 b), donc une résolution spectrale accrue répartit le flux sur plus de pixels, réduisant ainsi le rapport signal/bruit pour un élément spectral donné. Afin de fournir des contraintes plus fortes sur les modèles, les simulations ont montré qu'ils pouvaient être distingués à des résolutions supérieures à 10 000.

La plupart des instruments à haute résolution spectrale (XSHOOTER, UVES) sont limités par la qualité de l'image, ce qui pose évidemment problème pour les PMC qui peuvent être assez proches de leur étoile hôte. Cependant, on constate que certains sont situés à des distances angulaires tout juste accessibles avec de tels instruments. GSC 06214-00210 b est l'un d'entre eux, à 2,2" de son étoile hôte, mais ses raies sont assez faibles, ce qui soulève des questions sur la faisabilité. L'utilisation de CRIRES ETC, même avec son AO, permet difficilement l'observation IR de cette cible, principalement en raison du faible débit de l'instrument. ERIS, cependant, pourrait probablement être utilisé pour les raies PaBeta et BrGamma (voir perspectives pour une discussion sur la caractérisation haute résolution des raies IR).

Au lieu de cela, les raies de Balmer (dans l'optique) devraient être beaucoup plus brillantes que les raies IR (Marleau and Aoyama, 2022). Il a même été démontré que Delorme 1 (AB)b, l'un des PMC les plus proches, possède des raies H_α et H_β très brillantes (Eriksson et al., 2020). De plus, des observations pilotes avaient en fait montré la faisabilité de l'observation de cette cible avec UVES (Ringqvist et al., 2023). XSHOOTER offrirait une couverture de longueur d'onde plus large et il avait déjà été démontré que des observations de SR 12 c étaient possibles, avec un profil à double lobe pour sa raie H_α (Santamaría-Miranda et al., 2018). Cependant, UVES fournit la résolution qui manquait pour résoudre le profil H_α de SR 12 c, et l'ETC a montré que la ligne H_α de SR 12 c pouvait être sondée avec UVES. Enfin, des structures complexes peuvent émerger du flux d'accrétion à des échelles de $\sim$ 10 km/s, comme le montre Marleau et al. (2022). Par conséquent, UVES s'est naturellement imposé comme l'instrument idéal pour caractériser les PMC à séparation *large* ($> 1,5$").

Pour Delorme 1 (AB)b, nous avons cherché à caractériser les comportements de la variabilité à long terme (sur plusieurs mois), tandis que pour SR 12 c, nous avons cherché à caractériser sa variabilité à court terme, en espérant mettre en évidence les effets de modulation rotationnelle au cours de nuits consécutives. De plus, le chapitre précédent a montré que la variabilité des raies est significative, du moins en Pa_β. Il n'a pas été vérifié si cela se traduit en H_α. Par conséquent, ce chapitre tentera également de déduire les propriétés de variabilité des raies optiques.



3.2 Une campagne d'observation avec VLT/UVES

Des cibles ont été choisies sur deux années consécutives. Tout d'abord, Delorme 1 (AB)b a été sélectionnée, pour les raisons mentionnées ci-dessus. Delorme a été observée pendant un semestre impair. Le semestre suivant (pair), nous sommes passés à des cibles observables à une masse d'air raisonnable pendant plusieurs jours consécutifs et avons donc choisi SR 12 c comme cible principale. Nous avons également effectué des observations instantanées d'autres cibles au crépuscule avec l'instrument pour confirmer leurs émissions H_α et commencer une caractérisation approfondie de leurs propriétés. Contrairement à Delorme 1 (AB)b, où la variabilité serait échantillonnée à partir d'observations espacées au hasard, SR 12 c a été observé pendant 4 nuits consécutives, pendant 4 heures chaque nuit, échantillonnant ainsi la variabilité à court terme. Pour la réduction des données et les résultats de SR 12 c et 2MASS J11151597, voir les sections dédiées (Sects. 6 et 7). Dans cette section, je présente les trois cibles.

Delorme 1 (AB)b Delorme 1 (AB)b est une séparation relativement *large* $\sim 13\ \mathrm{M_{Jup}}$ compagnon ($\sim 1,77$" – 84 UA Delorme et al., 2013), en orbite autour d'une binaire serrée ($\sim 0,25$" – 12 UA) d'étoiles M5,5. C'est le plus proche des PMC accrétants connus, situé à 47,2 ± 3,1 pc (Riedel et al., 2014). Bien que relativement jeune, il est beaucoup plus âgé que les jeunes PMC couramment étudiés : il est associé à l'association Tucana-Horologium (Gagné et al., 2018), ce qui lui donne un âge de $\sim 30 - 45$ Myr. Ce compagnon a été classé comme étant de type spectral $\sim$ L0 (Eriksson et al., 2020).

SR 12 c SR 12 c est un système binaire à $13,5 \pm 1,5 \mathrm{M_{Jup}}$ PMC (Kuzuhara et al., 2011). Son âge est estimé à celui de sa région de formation (ρ Oph) : $2,1_{-1,8}$ Myr. Comme Delorme 1 (AB)b, SR 12 c orbite autour d'un système binaire serré ($\sim 0,21$" – ~ 26 UA) d'étoiles K4 et M2,5 (respectivement 1,05 $\mathrm{M_\odot}$ et 0,5 $\mathrm{M_\odot}$). Cependant, il est situé à une séparation beaucoup plus grande que Delorme 1 (AB)b: $\sim 8,7$" – 975 UA à $112,3 \pm 5,4$ pc (Gaia Collaboration et al., 2018). Bowler et al. (2014) l'a classé dans le type spectral M9 ± 1, avec $T_{\mathrm{eff}} = 2400^{+155}_{-100}$ K.

2MASS J11151597 2MASS J11151597 was identified as young object (5–45 Myr) with low surface gravity and L2 spectral type (Theissen et al., 2017). Its mass is still unconstrained, within the 7–21 $\mathrm{M_{Jup}}$ range (Theissen et al., 2018). It is located at 45.21±2.20 pc, and is not part of any clear moving group: a true lonely PMO. However, Theissen et al. (2018) also identified a potential companion: 2MASS J11131089+2110086, though recently published GAIA distance (57.67 ± 0.84 pc) now raises questions on the co-evolution of these two objects (see Sect. 7).

3.3 Le spectrographe UVES

Le spectrographe UV-Visual Echelle Spectrograph (UVES, Dekker et al., 2000) est un spectrographe échelle à visibilité limitée situé au foyer Nasmyth de l'UT2 du Very Large Telescope (VLT, Chili/Paranal). Il est conçu pour avoir une haute transmission (1 %) et une haute résolution spectrale dans le proche ultraviolet et le visible (300-1100 nm), en utilisant une fente longue de largeur adaptable. Il permet d'accéder à une image en dimensions (1+1λ)D (appelée trace) : 1 dimension spatiale et 1 dimension spectrale, et a été conçu à l'origine pour une grande stabilité mécanique, de transmission et d'étalonnage des longueurs d'onde. Selon le manuel de l'https://www.eso.org/sci/facilities/paranal/instruments/uves/doc.html, il est composé de quatre sous-systèmes : les pré-fentes, deux bras de spectrographe, les capteurs CCD du Slit-Viewer (SV) et les capteurs CCD scientifiques, tous décrits ci-dessous. Il est capable de couvrir une large gamme de longueurs d'onde (3000-11000 AA) en une seule observation, grâce à ses deux bras BLEU et ROUGE. Cette section



entière est *largement* inspirée de la description de l'instrument dans le manuel. Une vue schématique du chemin optique est présentée dans la Fig. III.2.

3.4 Observations et réduction de données

La configuration instrumentale était presque la même pour les trois cibles (Delorme 1 (AB)b, SR 12 c, 2MASS J11151597). Nous n'avons changé que la caméra de guidage, qui était la caméra BLEUE pour Delorme 1 (AB)b, et la caméra ROUGE pour SR 12 c et 2MASS J11151597. La raison en est que les observations de Delorme 1 (AB)b ont suivi l'étude pilote (Ringqvist et al., 2023), qui utilisait le bras BLEU comme bras de guidage. Nous avons choisi de conserver exactement la même configuration instrumentale pour la série Delorme 1 (AB)b. Pour SR 12 c et 2MASS J11151597, cependant, nous avons choisi d'effectuer l'acquisition dans le bras RED en raison de leur contexte : SR 12 c est assez éloignée de son étoile hôte, tandis que 2MASS J11151597 est une cible isolée. Nous avons effectué Même si l'acquisition a été réalisée sur une étoile brillante proche (l'étoile hôte de SR 12 c), suivie d'un *blind-offset* vers la cible, les deux objets sont intrinsèquement plus brillants dans le bras RED que dans le bras BLUE, et étaient plus faciles à détecter dans le slit-viewer RED, d'autant plus que seules les ailes de la PSF sont visibles dans le slit-viewer. Dans l'ensemble, l'utilisation du bras ROUGE nous a permis d'être plus confiants quant au centrage de la cible sans avoir à attendre la fin de l'exposition complète pour vérifier la présence de la raie Halpha dans le détecteur. Les observations SR 12 c et 2MASS J11151597 ont toutes deux été réalisées en mode visiteur (désigné/à distance), dans lequel j'étais impliqué. Cela m'a permis d'acquérir de l'expérience dans la préparation et l'exécution d'observations au VLT. Nous avons réussi à voir les ailes de la PSF dans le viseur à fente après $\sim$ 10 minutes d'intégration.

Toutes les observations ont été réalisées avec la configuration indiquée dans le tableau III.1. Les longueurs de fente sont de 8 pouces pour le bras BLEU et de 12 pouces pour le bras ROUGE. La première plaque dichroïque (390-580 nm), ainsi que les disperseurs croisés CD#2 et CD#3, donnent des plages de longueurs d'onde de 3260-4540 et 4760-6840 Å, respectivement. Cela permet d'accéder à l'ensemble de la série de Balmer (H_α, H_β, H_γ, ...) ainsi qu'à certaines raies de l'hélium (HeI6680, HeI5877) et des métaux (doublet NaII4836, FeI6233).

Les observations Delorme 1 (AB)b ont été réalisées en alignant la fente avec l'axe binaire-compagnon (fente PA=335°), de manière à voir à la fois la primaire et la compagne. En raison de leur séparation relativement proche ($\sim 1,8$"), la PSF de la primaire contaminera le signal de la compagne, et nous pourrons démêler le signal de la primaire de celui de la compagne en utilisant l'ajustement de la PSF.

3.5 Réduction de données

Les observations de Delorme 1 (AB)b ont été réduites en suivant les étapes présentées dans cette section : ajustement du profil PSF, correction de la contamination, effets instrumentaux, calibration du flux. Tous les travaux ont été réalisés en utilisant la fente reconstruite en 2D, décrite dans la section suivante. Dans le cas de UVES, l'ESO fournit une réduction automatisée des données de toutes les observations de UVES, effectuée tous les deux mois[5]. Cette réduction est effectuée en exécutant le pipeline de l'UVES dans ses paramètres par défaut. Les fichiers auxiliaires comprennent à la fois les spectres 1D et 2D. Le manuel du plan de réduction automatisé mentionne que les spectres 2D sont corrigés à la fois pour la transmission de l'instrument et la transmission atmosphérique.

[5] https://www.eso.org/rm/api/v1/public/releaseDescriptions/163



3.5.1 Ajustement de la PSF

La modélisation de la PSF a été réalisée selon la procédure décrite dans Hynes (2002). En bref : la PSF est ajustée à chaque intervalle de longueur d'onde, puis tous les paramètres sont lissés par régularisation polynomiale, dont l'expression polynomiale donnera la valeur de chaque paramètre. Cette méthode a été spécifiquement développée pour séparer les cibles dans les observations de spectroscopie à fente. Cependant, la méthode a été proposée pour séparer deux cibles **brillantes**, dont les PSF sont assez clairement visibles. Ce n'est pas le cas ici, et je propose donc une version adaptée de cette méthode, développée pour le cas de Delorme 1 (AB)b, mais qui pourrait être (en principe du moins) étendue à toute observation basée sur une fente 2D. En termes simples, la fonction de transfert de puissance (PSF) est supposée être la somme de trois gaussiennes dans le bras ROUGE et de deux dans le bras BLEU. Leurs paramètres sont régularisés dans la dimension de la longueur d'onde afin de réduire le bruit d'ajustement à un intervalle spectral donné.

3.5.2 Contamination résiduelle

L'hypothèse principale qui a permis l'ajustement de la PSF est que la PSF est symétrique. Cependant, la PSF de l'UVES est connue pour être intrinsèquement asymétrique (voir le manuel). Je n'ai pas vu de corrélation particulière avec le seeing. Cela conduit à une contamination intrinsèque du spectre primaire vers le spectre compagnon, quelle que soit la qualité de l'ajustement de la PSF. Elle est cependant aggravée dans le cas d'un mauvais ajustement de la PSF. Dans l'ensemble, la contamination apparaît clairement à certaines époques, qu'elle soit positive ou négative, se traduisant par l'empreinte des caractéristiques du spectre du primaire sur le spectre de l'étoile compagnon (voir par exemple l'époque 2022-11-05, première exposition, Fig. III.11, 2e ligne, ligne noire).

Le spectre compagnon peut être écrit $F(\lambda) = C(\lambda) + \alpha(\lambda) \cdot P(\lambda)$, où $C(\lambda)$ est le signal réel du compagnon, $P(\lambda)$ est le signal du primaire et $\alpha(\lambda)$ est le facteur de contamination. Le but, ici, est de trouver la valeur de $\alpha(\lambda)$, en procédant comme suit :

- Un spectre maître pour l'étoile compagnon ($C(\lambda)$) est produit en faisant la moyenne des époques les moins affectées (à l'œil nu) par la contamination (c'est-à-dire sans caractéristiques spectrales évidentes de l'étoile primaire dans son continuum). Ces époques, ainsi que le spectre maître, sont illustrés dans la Fig. III.10.

- Le spectre compagnon est ajusté comme $F(\lambda) = k(\lambda) \cdot C(\lambda) + \alpha(\lambda) \cdot P(\lambda)$, où $k(\lambda)$ et $\alpha(\lambda)$ sont les paramètres ajustés, où $k(\lambda)$ tient compte des effets instrumentaux et de la transmission, et $\alpha(\lambda)$ de la contamination susmentionnée. Étant donné le rapport signal/bruit de chaque spectre, les paramètres $k(\lambda)$ et $\alpha(\lambda)$ sont en effet anticorrélés. Cela est réalisé en excluant les régions des raies d'émission des compagnons (hydrogène, hélium, sodium, etc.) qui biaiseraient l'ajustement car elles sont également présentes dans le spectre du primaire. L'ajustement a été effectué pour chaque intervalle de longueur d'onde, sur une fenêtre (-5000, +5000) km/s centrée dans l'intervalle de longueur d'onde donné.

- Les effets dépendants de la longueur d'onde sont déjà imprimés dans le spectre de la compagne et du primaire, donc $k(\lambda)$ ne devrait vraiment être qu'une constante (par époque) sur toute la gamme de longueurs d'onde. L'ajustement est donc affiné en supprimant la dépendance λ de $k(\lambda)$. L'hypothèse sous-jacente est que le continuum de la compagne n'a qu'une variabilité d'échelle de flux d'une époque à l'autre et aucune variabilité de forme.

- La suppression finale de la contamination a donc été effectuée en ajustant l'ensemble du compagnon comme $F(\lambda) = k \cdot C(\lambda) + \alpha(\lambda) \cdot P(\lambda)$, avec k et $\alpha(\lambda)$ comme paramètres libres. Là encore, les données



ajustées étaient, pour chaque intervalle de longueur d'onde, une fenêtre (-5000,+5000) km/s centrée dans l'intervalle de longueur d'onde donné. Contrairement au premier ajustement, celui-ci a été effectué simultanément sur les paramètres k et $\alpha(\lambda)$, car le paramètre k affecte tous les intervalles de longueur d'onde. Les barres d'erreur de la contamination ont été calculées comme les contours $\chi^2_r + 1$ sur les cartes χ^2_r des paramètres $C(\lambda)$ pour le k donné.

- Le paramètre $\alpha(\lambda)$ a finalement été lissé avec un noyau gaussien de 10 px de large pour supprimer tous les minima locaux irréguliers des ajustements (Fig. III.11, première ligne). Ce lissage maintient $\alpha(\lambda)$ bien à l'intérieur de ses barres d'erreur. Enfin, la contamination $\alpha(\lambda) \cdot P(\lambda)$ a été soustraite du spectre compagnon (Fig. III.11, 2e et 3e lignes). La contamination a également été rajoutée au spectre primaire par souci de cohérence, bien que cela ne modifie guère le spectre primaire, car la majeure partie de son flux se situe au cœur de sa PSF.

3.6 Résultats

Le spectre complet de Delorme 1 (AB)b est représenté sur la figure III.13, avec toutes les époques superposées en noir et le spectre moyen (R=5000) en rouge. Nous constatons que le spectre moyen de Delorme 1 (AB)b est globalement cohérent avec celui de SR 12 c, une jeune (∼2 Myr) compagne de type spectral L0 (XSHOOTER, Santamaría-Miranda et al., 2018). Nous trouvons une magnitude GAIA Bp de Bp $= 20,6 \pm 0,2$ pour Delorme 1 (AB)b.

3.6.1 Profils de raies résolus

Les raies H_α et H_β ont des profils asymétriques avec de larges ailes étendues (jusqu'à ±500 km/s) avec un noyau de plateau incliné. Les raies d'ordre supérieur, cependant, ont des profils principalement symétriques et centrés. H_ϵ a une composante d'émission étroite autour de −120 km/s, probablement une raie de CaII ou FeIII, bien que la longueur d'onde de repos de CaII corresponde mieux (base de données NIST, Kramida, 2010). H_ζ a un profil à double pic, qui est probablement aussi une superposition avec une autre raie faible : peut-être HeI ou FeI.

Avec le bon nombre d'époques individuelles, il est possible de déduire les différents facteurs de corrélation entre les différentes parties des lignes. Cela correspond à la partie de la ligne qui évolue avec l'autre partie de la ligne. Cela avait déjà été fait pour les étoiles T Tauri (par exemple, Alencar et al., 2012). La figure III.21 montre le coefficient de corrélation de Pearson entre différentes parties d'une ligne donnée (H_α, H_β et H_γ). Bien que les barres d'erreur aient été incluses dans le calcul du coefficient de Pearson, ces graphiques ne représentent pas leur étendue pour les points individuels. Cependant, comme l'objectif est de comparer les variations du coefficient entre différentes régions des raies, et que les barres d'erreur sont pour la plupart constantes sur différentes régions, les valeurs absolues des barres d'erreur sont atténuées par la variation relative du coefficient de Pearson. Les raies H_β et H_γ ont toutes deux des ailes qui ne sont pas corrélées avec le noyau. Le profil de H_α est corrélé avec lui-même sur toute la plage de vitesse, avec un facteur de corrélation minimum de $\sim 0,6$. Comme pour H_β et H_γ, son noyau est légèrement moins corrélé avec les ailes. Pour les trois raies, la région de décorrélation du noyau est d'environ ∼50 km/s de large. Cependant, H_α présente une région supplémentaire non corrélée autour de ∼60 km/s. Il semble que H_α puisse être composé de 2 éléments : un noyau large et un autre large avec un pic à ~ 40 km/s. Il pourrait également être composé de 3 éléments : les ailes, le noyau et celui à ~ 60 km/s.



3.6.2 Décomposition des raies

Les lignes sont décrites comme leur flux en fonction de la vitesse. Comme il existe plusieurs époques indépendantes (33), je propose de démêler les différents profils de composantes en utilisant la diversité des époques. La méthode est la suivante.

- Je choisis de décrire les lignes comme la somme de deux composantes, qui ne changent que dans leur échelle relative d'une époque à l'autre. La forme des composantes sera la même à toutes les époques.
- Chaque composante est décrite par une série de points (X, Y) qui définissent la forme à toutes les vitesses. Les X sont fixes et correspondent exactement à l'échantillonnage des données, tandis que les Y sont tous libres.
- Chaque composante se voit attribuer un paramètre d'échelle pour chaque époque.
- Les deux composantes sont ajustées simultanément sur l'ensemble des données (33 époques), dans la plage $(-250, +250)$ km/s, centrées sur H_α (322 bins, 1,55 km/s par bin).
- En raison du nombre élevé de paramètres libres, l'ajustement est effectué de manière itérative, en ajustant uniquement la forme d'une composante à la fois, en laissant les deux mises à l'échelle libres.

Par conséquent, le nombre de paramètres aux première et deuxième itérations est le suivant :

$$N_{\text{it1}} = N_{\text{comp1}} + N_{\text{comp2}} \tag{V.1}$$
$$= N_{\text{epochs}} + (N_{\text{bins}} + N_{\text{epochs}}) \tag{V.2}$$
$$N_{\text{it2}} = N_{\text{comp1}} + N_{\text{comp2}} \tag{V.3}$$
$$= (N_{\text{bins}} + N_{\text{epochs}}) + N_{\text{epochs}} \tag{V.4}$$

Le nombre total de paramètres, une fois toutes les itérations terminées, est le suivant :

$$N_{\text{params}} = N_{\text{components}} \, (N_{\text{bins}} + N_{\text{epochs}}) \tag{V.5}$$

La forme des deux composantes à chaque itération est représentée sur la figure 1, en lignes transparentes (bleu et vert). Le panneau de droite montre la corrélation entre les deux paramètres de mise à l'échelle pour chaque composante, à la dernière itération, pour toutes les époques. L'ellipse noire correspond à la corrélation principale entre les deux paramètres. Cette corrélation n'est pas aussi claire pour H_β et H_γ (voir Fig. B.8). L'ajustement pour toutes les époques à la dernière itération est montré dans la Fig. III.27, avec $\chi^2_r = 3,44$. Le même ajustement pour les raies H_β et H_γ est présenté dans les figures III.28 et III.29.

Dès la première itération, la composante bleue s'écarte de son estimation initiale, tandis que la composante verte ressemble globalement à la forme du paramètre b dans la figure III.25. Les paramètres de mise à l'échelle de chaque composante sont fortement corrélés (ellipse noire), sauf aux époques 14/15/17 octobre 2022, où la composante bleue est la plus importante et correspond aux époques prolongées de l'aile bleue. D'après les résidus de la figure III.27, il est clair que certains détails ne sont pas entièrement reproduits par un modèle à deux composantes. Pour H_β et H_γ (Figs. III.28 et III.29), cependant, les résidus se situent pour la plupart dans le niveau de bruit, avec quelques indices de formes de résidus similaires à H_α. Il existe également une légère corrélation entre les amplitudes de leurs composantes respectives.

Les deux composantes étaient en fait déjà suggérées par la forme des auto-corrélations de H_α (Fig. III.30). La composante verte est en corrélation presque parfaite avec la composante centrale de l'autocorrélation, ainsi



qu'avec la corrélation réduite entre 50 et 100 km/s. Les ailes corrélées s'expliquent par la seule composante bleue, ainsi que par leur corrélation avec le pic à $\sim$ 40km/s, également visible dans la composante bleue. La corrélation réduite entre -50 et 0 km/s correspond au mélange du pic bleu avec l'aile verte.

La forme générale de la composante bleue, superposée au profil d'autocorrélation de H_α, correspond également à la corrélation entre H_α et $\mathsf{H}_\beta/\mathsf{H}_\gamma$ (Fig. III.22), clairement mise en évidence par la composante $\sim$ 40 km/s dans ces deux corrélations croisées. Cela signifie que la composante bleue présente probablement des signatures dans les raies d'ordres supérieurs. Cependant, la corrélation $\mathsf{H}_\beta/\mathsf{H}_\gamma$ ne présente aucune caractéristique significative $\sim$ 40 km/s, ce qui signifie que la composante bleue en H_α n'a probablement pas la même forme dans les raies H_β et H_γ. Ceci est confirmé par la décomposition des raies H_β et H_γ, où leur composante bleue ne présente aucune absorption secondaire significative à $\sim$ 60 km/s.

Les formes d'autocorrélation des raies H_β et H_γ s'expliquent parfaitement par leur décomposition en deux composantes. Comme pour la raie H_α, le noyau et les ailes non corrélés s'expliquent par les deux composantes indépendantes. Leur aile bleue présente une autocorrélation plus forte que leur aile rouge, ce qui s'explique par la forme de la composante bleue : son aile bleue est plus brillante que son aile rouge, ce qui induit un meilleur contraste bleu-vert, rendant l'aile bleue plus autocorrélée.

Il est assez surprenant que seulement deux composantes fournissent un ajustement assez bon à l'ensemble des données, surtout compte tenu de leurs formes fixes. Le fait que les deux composantes puissent s'adapter aux profils de toutes les époques à la fois et expliquer toutes les caractéristiques de l'autocorrélation H_α fournit un argument fort en faveur de sa validité. Ce type de décomposition est généralement réalisé avec des gaussiennes. À ma connaissance, c'est la première fois que ce type de décomposition est tenté, en particulier dans le domaine des masses planétaires.

Dans le cas de l'accrétion magnétosphérique sur les étoiles, les raies ont généralement des composantes variables qui varient non seulement en amplitude, mais aussi en vitesse. Pour qu'une telle décomposition à deux composantes soit valable dans le cas de l'accrétion magnétosphérique, il semble que Delorme 1 (AB)b devrait être presque face au pôle, afin d'atténuer les effets de la modulation rotationnelle. Malgré cela, la forme de la composante bleue suggère une absorption décalée vers le rouge, ce qui est généralement observé à des inclinaisons élevées, ce qui ne ressemble en rien à une vue polaire. Cependant, si Delorme 1 (AB)b possède une magnétosphère axisymétrique, il ne serait pas si surprenant que les lignes soient constantes, car le flux d'accrétion serait également axisymétrique. Il y a tout de même une certaine structure dans les résidus, ce qui signifie qu'il pourrait y avoir une composante non stationnaire, soit une composante d'émission chromosphérique, soit un effet de projection si la magnétosphère n'est que légèrement inclinée.

3.6.3 Modélisation des raies

Les lignes d'accrétion n'avaient jamais été observées à une telle résolution pour les PMC. Elles permettent de contraindre le flux d'accrétion et les modèles prédisant les lignes d'émission. Dans cette section, je compare les lignes aux prédictions des modèles d'accrétion magnétosphérique de Thanathibodee et al. (2019). La même étude sera réalisée pour les modèles de choc (Aoyama et al., 2018), mais pas dans ce manuscrit.

Les modèles sont les modèles d'accrétion magnétosphérique de Thanathibodee et al. (2019) : les mêmes que ceux utilisés pour modéliser la raie Pa_β de GQ Lup b et GSC 06214-00210 b. Les modèles de choc de Aoyama et al. (2018) (du moins ceux auxquels nous avons accès) n'ont pas la résolution spectrale suffisante pour effectuer une analyse similaire. Les modèles d'accrétion magnétosphérique existent à la fois pour les H_α et les H_β. Ils supposent un champ magnétique dipolaire à symétrie axiale. Cela signifie que le flux d'accrétion doit également être symétrique par rapport à l'axe et peut donc être décrit dans un plan 2D (r, z). Au moment de la rédaction, la plage des paramètres du modèle est donnée dans le tableau. III.3. Ils correspondent respectivement au rayon de troncature interne (R_{in}), à la largeur de la colonne (Width), au



taux d'accrétion ($\dot{M}$), à la température de la colonne (Tcol), à l'inclinaison du système (i), à la masse de la planète (M_p), au rayon (R_p) et à la température effective ($T_{\rm eff}$).

Les ajustements sont effectués en calculant le χ^2_r sur l'ensemble de la grille. Cependant, les résultats des modèles sont la somme de la ligne d'accrétion et du continuum de la photosphère. Bien que cela ait du sens dans le contexte des CTTS, le continuum est à peine visible dans le cas de Delorme 1 (AB)b. Dans notre cas, la ligne est si brillante par rapport au continuum que le continuum lui-même se situe dans le niveau de bruit. Le continuum photosphérique a été ajusté comme une fonction linéaire et soustrait des modèles. Cette procédure laisse certains modèles avec des valeurs négatives à certains endroits (où les composantes d'absorption étaient plus profondes que le continuum), mais c'est le mieux que l'on puisse faire avec les modèles actuels. Je n'ajuste donc que le profil de la ligne, après soustraction du continuum, et normalisation des lignes à 1 autour de ~ 0 km/s.

L'ajustement de la composante bleue de Halpha est capable de reproduire largement les principales caractéristiques d'absorption de la raie, à la fois dans l'ajustement du noyau et dans l'ajustement de la gamme complète. Cependant, le modèle le mieux adapté semble produire une magnétosphère beaucoup plus étroite dans l'ajustement sur toute la gamme que dans l'ajustement sur le noyau. Cela s'explique par la dégénérescence entre le taux d'accrétion et la largeur de la colonne observée dans l'ajustement sur toute la gamme (Fig. B.17): un taux d'accrétion plus élevé avec une colonne plus large donne généralement une densité de colonne similaire, avec des caractéristiques d'absorption de forme similaire. Par conséquent, l'ajustement du noyau et de la gamme complète de la composante bleue de H_α sont compatibles, en ce qui concerne cette dégénérescence $\dot{M}$–Largeur. Les deux ajustements donnent globalement un faible taux d'accrétion et une température de colonne élevée, ce qui est en contradiction avec le contraire : un taux d'accrétion élevé et une température de colonne faible (fig. B.15 et B.17). L'ajustement sur le noyau et sur toute la gamme donnent une forte inclinaison, de l'ordre de 60 à 75°.

La composante verte de H_β a un comportement similaire à celui de H_α, à la fois dans les cas d'ajustement sur le noyau et sur toute la gamme. Dans le cas de l'ajustement sur le noyau, la largeur de la ligne est bien reproduite, ainsi que l'aile rouge, mais pas l'aile bleue. La pente en haut de la ligne, cependant, ne correspond pas à celle des données. Dans le cas de l'ajustement sur toute la gamme, les deux ailes sont assez bien reproduites, ainsi que la largeur de la ligne. L'étendue de la magnétosphère est similaire dans les deux cas, et en accord avec celle de H_α: une colonne mince et proche. Elle est cependant légèrement dégénérée avec une magnétosphère plus large et étendue. Son inclinaison diffère légèrement entre les cas de l'ajustement complet et du noyau : l'ajustement complet préfère un système fortement incliné, tandis que l'ajustement du noyau a deux minima, à faible ($< 30°$) et forte (75°) inclinaisons. La dégénérescence est levée par l'ajustement des ailes dans l'ajustement à gamme complète. Les taux de température et d'accrétion, dans les deux cas, sont dégénérés entre low-$\dot{M}$/high-Tcol et high-$\dot{M}$/low-Tcol, de manière similaire à la composante verte de H_α.

En général, les rayons et les masses de la planète diffèrent légèrement dans tous les cas d'ajustement. Cependant, tous les paramètres géométriques sont donnés en termes de rayon planétaire. Le rayon de la planète sert donc de paramètre d'échelle pour le rayon de troncature et la largeur de la colonne, et les solutions ajustées ne doivent pas être interprétées comme une détermination robuste de ce paramètre. La valeur la mieux ajustée varie d'un ajustement à l'autre, mais peut aussi servir uniquement de paramètre d'échelle pour l'emplacement et l'intensité de diverses caractéristiques d'absorption. Cela serait particulièrement vrai pour un faible taux d'échantillonnage des paramètres géométriques, en particulier l'inclinaison, qui n'augmente que par incréments de 15°. Dans l'ensemble, les variations de masse sont relativement faibles sur la grille à étudier en détail (11–15 $M_{\rm Jup}$), surtout compte tenu de l'aspect qualitatif et de la non reproductibilité de certains des profils par les modèles.



3.7 Conclusions

Ce chapitre a présenté les programmes pilotes de l'étude spectroscopique de surveillance de l'accrétion UVES ExoplaNet (ENTROPY, une licorne dans les habitudes actuelles de robustesse des noms aux acronymes). Avec les premiers résultats de la variabilité des raies (chapitre précédent, Demars et al., 2023) et la démonstration de la faisabilité d'atteindre une haute résolution spectrale des jeunes PMC (Ringqvist et al., 2023), la nécessité de combiner les deux est apparue comme une évidence. J'ai présenté des observations à haute résolution de Delorme 1 (AB)b, SR 12 c et 2MASS J11151597, toutes avec des sondes différentes de leur comportement de variabilité respectif. Delorme 1 (AB)b a été sondé à des échelles de temps aléatoires, ce qui a permis de déterminer son comportement de variabilité au cours des mois successifs, tandis que SR 12 c a été sondé au cours de nuits successives, dans l'espoir de mettre en évidence toute modulation rotationnelle des lignes.

Les raies Delorme 1 (AB)b ont une variabilité de profil limitée, mais une amplitude de variabilité élevée. Cependant, toute leur variabilité de profil peut être décrite par deux composantes uniques, dont la forme rappelle les raies induites par l'accrétion magnétosphérique, ainsi que les raies induites par la chromosphère et/ou les chocs. Cette même décomposition permet d'expliquer les profils de corrélation croisée des raies. Parmi ces deux composantes bleu/vert, la composante bleue est celle qui ressemble le plus aux profils d'accrétion magnétosphérique, avec des caractéristiques d'absorption claires qui sont légèrement décalées vers le rouge. Ces caractéristiques sont reproduites par des modèles d'accrétion magnétosphérique axisymétriques, mais ils ne parviennent pas à reproduire simultanément le noyau et les ailes étendues des lignes. Cette interprétation est étayée par la forte corrélation entre la composante bleue et l'excès d'intensité dans l'UV.

Cette étude présente, pour la première fois, les spectres d'excès UV d'un PMC à haute résolution. Son intensité est fortement corrélée à la fois avec les raies de l'hélium et le niveau du continuum en dessous de H_α, ce qui suggère que la majeure partie du niveau du continuum est due au choc d'accrétion. Bien qu'aucune modélisation du choc d'accrétion n'ait été effectuée, il s'agit d'un sujet de travail futur avec des collaborateurs de Padoue.

Les comportements de variabilité non contraints de Delorme 1 (AB)b et de SR 12 c plaident en faveur de visites supplémentaires. Le comportement de variabilité à long terme de Delorme 1 (AB)b a été étudié dans cette étude. Cependant, il manque encore la surveillance fine qui aurait rendu les périodogrammes beaucoup plus précis. Une surveillance similaire à celle de SR 12 c est recommandée et sera effectuée dans le cadre du prochain grand programme (3 h par nuit, 6 nuits consécutives). Pour SR 12 c, les prochaines visites devraient se concentrer sur sa surveillance à long terme. Cependant, une autre surveillance à court terme ne serait utile que si l'on pouvait trouver un moyen de calibrer correctement les données. Cela signifie que les observations futures devraient effectuer l'acquisition de quelques expositions, pour éviter le problème de dérive qui s'est produit sur SR 12 c, et acquérir une exposition d'étoile standard de temps en temps.

Dans le contexte de la spectroscopie haute résolution des jeunes PMC, je conseille que les efforts se concentrent sur la modélisation des raies. Je pense que seule cette méthode permettra de révéler la véritable nature des mécanismes sous-jacents. Si l'intensité du champ magnétique sur Delorme 1 (AB)b était mesurée, une étude approfondie de la cible, similaire à celle de Alencar et al. (2012) et Espaillat et al. (2021), permettrait de mieux comprendre l'un des meilleurs laboratoires d'étude pour PMCs.

4 Conclusion et perspectives

4.1 Résumé

La caractérisation du processus d'accrétion sur les compagnons de masse planétaire et leurs frères et sœurs en orbite libre reste un domaine d'investigation naissant. Il a suscité un regain d'intérêt suite à la découverte



des protoplanètes archétypales PDS 70 b&c. Au cours de mon doctorat, qui a débuté trois ans après cette découverte historique, je me suis appuyé sur l'expertise acquise dans le domaine de l'imagerie à haut contraste des exoplanètes et de la formation des étoiles pour étudier l'accrétion sur les compagnons clés, en me concentrant sur la variabilité des raies d'émission qui n'avait été que très peu étudiée à l'époque.

Des modèles de profils de raies d'émission avaient été publiés quelques années avant le début de mon doctorat, mais n'avaient pas encore été largement testés par des observations. La première comparaison remonte à Aoyama and Ikoma (2019) avec les observations de PDS 70 b MUSE, mais elles étaient largement limitées par la résolution spectrale de l'instrument $r \sim 2500$. En fait, les premières observations qui ont fourni un profil de raie partiellement résolu étaient celles de la raie Pa_β de GSC 06214-00210 b ($R \sim 3800$, OSIRIS, Bowler et al., 2011), présentées dans le deuxième chapitre de cette thèse et Demars et al. (2023). Cependant, les observations de l'UVES (présentées dans le chapitre précédent) sont les premières à fournir des profils de raies entièrement résolus d'un PMC. La décomposition des profils de raies permet même de mieux comprendre les mécanismes éventuellement multiples des profils de raies. Au premier ordre, le modèle d'accrétion magnétosphérique Thanathibodee et al. (2019) fournit un ajustement satisfaisant aux composantes bleue et verte, bien que le noyau et les ailes de la composante bleue ne soient pas reproduits simultanément. Les travaux futurs pourraient inclure une modélisation détaillée des lignes d'accrétion en fonction de la phase, comme cela a été fait pour les étoiles T Tauri (Alencar et al., 2012).

Les efforts futurs devraient également se concentrer sur le gaz en chute, qui s'est avéré être une forte source d'extinction (Marleau et al., 2022). En fait, certains de leurs profils ressemblent également à la composante bleue de H_α. Enfin, les raies de l'hélium n'ont pas encore de prédictions. Si elles étaient fournies, elles imposeraient de fortes contraintes sur la physique du choc d'accrétion lui-même, car on ne s'attend pas à ce qu'elles se forment ailleurs. Je dois également mentionner la contribution locale de l'équipe et du projet SPIDI, dirigés par J. Bouvier, avec la contribution de B. Tessore et J. Pantolmos, qui ont travaillé sur les profils de raies résolus en phase pour les flux d'accrétion non asymétriques par rapport à l'axe.

Avant cette thèse, la variabilité des raies n'avait été qu'évoquée. À l'époque, si elle devait être confirmée, on pensait qu'elle était liée soit à des variations du flux d'accrétion, soit à des variations des planètes elles-mêmes, les raies seraient liées à l'activité chromosphérique. Ce travail a fourni la première estimation de l'amplitude de variabilité des raies d'accrétion pour quelques PMC. Je dirais que GQ Lup b pourrait tirer profit d'une autre étude dédiée à la variabilité, en particulier aux échelles de temps de quelques mois où le nombre de points était trop faible (2 époques séparées d'une semaine, et une seule époque un mois plus tard). Cependant, le comportement de variabilité pour GQ Lup b, GSC 06214-00210 b et Delorme 1 (AB)b est similaire à celui observé sur les étoiles T Tauri : une faible variabilité à l'échelle horaire, et un plateau plus important à l'échelle hebdomadaire ou mensuelle. Néanmoins, l'échantillon commence à inclure un certain nombre de PMC, bien que leur variabilité ait été étudiée à différentes échelles de temps.

Dans l'ensemble, ce travail a mis en évidence les spécificités de la variabilité des raies, mais ne parvient pas à fournir une explication satisfaisante. Des travaux sont actuellement en cours, notamment sur la modélisation de la composante verte, qui pourrait tracer la composante de choc. Bien que cela soit surprenant compte tenu de la faible corrélation avec la variabilité de l'excès UV. Les travaux futurs pourraient également se concentrer sur la variabilité des raies de l'hélium et de l'excès UV, qui tracent directement le choc d'accrétion.

4.2 Une vue globale

La principale question abordée dans cette thèse est la suivante : comment les planètes accumulent-elles de la masse et comment ces processus affectent-ils leur évolution ? Bien que l'instrumentation actuelle ne permette pas l'étude des planètes proches, les PMC pourraient servir de substituts pour l'étude des processus possibles qui pourraient se développer sur des objets de masse similaire à des distances plus proches, sans inclure les



interactions avec le disque circumstellaire. L'idée était de caractériser le processus d'accrétion des jeunes PMC qui sont encore en cours d'accrétion. En effet, répondre à cette question est un peu ambitieux, mais ce travail a tout de même apporté quelques indices.

Les propriétés de variabilité des PMC, comme mentionné dans la section précédente, en font partie. La variabilité des raies avait été proposée comme explication des non-détections des relevés H_α, et il semble que cela puisse en être la raison. Cependant, j'ai constaté que la variabilité H_α (pour Delorme 1 (AB)b, au moins) ne devient importante que sur des échelles de temps de plusieurs mois à plusieurs années. La variabilité à court terme (quelques heures) n'atteint que quelques %, ce qui ne peut pas expliquer les non-détections. Cependant, la variabilité à plus long terme pourrait être la clé : elle atteint 50 à 100

Ces résultats plaident toujours en faveur de nouvelles visites des systèmes étudiés, mais seulement tous les deux ou trois mois. Cependant, l'étude des profils de raies nécessite une surveillance à court terme, en particulier pour les SR 12 c. Malheureusement, ces objectifs ne concordent pas en termes de besoins d'observation. Ces travaux ont également montré que l'excès UV, qui était auparavant observé avec des points photométriques, peut en fait être accessible avec la spectroscopie à moyenne résolution.

4.3 Perspectives

4.3.1 Charactéristiques principales des PMCs

Ces travaux se sont concentrés sur la caractérisation des propriétés d'accrétion de PMC *spécifiques*, bien que l'échantillon couvre désormais la plupart des âges et masses typiques des PMC connus (5–15 M_{Jup}, 2–45 Myr). Il manque encore le cas des planètes en orbite. D'autres auteurs ont choisi une approche statistique (par exemple, Betti et al., 2023) qui sont également actuellement limités par la taille de l'échantillon pour contraindre les propriétés d'accrétion des PMC. Aujourd'hui, l'image des PMC en accrétion est encore un domaine riche à explorer, où les informations sont dispersées un peu partout. La variabilité est partiellement caractérisée, les excès d'UV sont connus mais largement non contraints, les modèles en sont encore à leurs balbutiements, les disques sont en cours de découverte et même maintenant caractérisés (JWST). Cependant, la plupart des auteurs se sont concentrés sur une seule pièce du puzzle à la fois, ce qui est logique car chaque pièce vaut son propre article. Je crois fermement que les efforts futurs devraient inclure toutes les pièces à la fois, au moins pour l'étude d'un seul PMC.

Je pense que les informations les plus importantes sont les corrélations entre plusieurs paramètres. Bien qu'une corrélation ne signifie pas que les deux paramètres sont nécessairement la cause l'un de l'autre, les modèles qui tentent de brosser un tableau de la scène devraient être capables de reproduire ces corrélations. Par exemple, la nature du champ magnétique de V2129 Ophiuchi a été obtenue par Donati et al. (2011), puis utilisée pour modéliser son profil H_α à plusieurs phases (Alencar et al., 2012). Les auto-corrélations de cette raie (Alencar et al., 2012, leur Fig. 19) sont étonnamment similaires à celles de Delorme 1 (AB)bprésentées dans ce travail (Fig. III.21), malgré le profil de raie différent. Dans cette thèse, l'idée de décomposer les raies est venue uniquement de la forme de ces diagrammes d'autocorrélation (bien que j'aie déjà développé la méthode comme moyen de démêler la fonction de distribution de probabilité (PSF) de l'étoile primaire et de l'étoile compagnon). Les autres paramètres pour lesquels il faut vérifier les corrélations sont :

– L'excès d'UV, le niveau du continuum, les flux et la forme des raies d'émission. Cela s'est avéré possible avec UVES. Alors que la variabilité de la forme des raies a été expliquée pour Delorme 1 (AB)b par la décomposition bleu/vert, c'est beaucoup plus difficile pour SR 12 c. Il ne semble pas que deux composantes puissent facilement expliquer la variabilité des raies (bien que cela donne des résultats raisonnables). Par conséquent, les corrélations entre les bins spectraux des raies individuelles et d'autres paramètres tels que, par exemple, l'excès d'UV, pourraient permettre de dévoiler la véritable nature



de ces raies. De plus, la modélisation de l'émission UV devrait fournir des paramètres physiques précis du choc d'accrétion. Bien que cela ait été fait à partir de points photométriques (Zhou et al., 2014, 2021), il manque encore les détails de la modélisation du saut de Balmer. Cela permettra d'obtenir une estimation beaucoup plus précise de la luminosité d'accrétion (Lacc) et du taux d'accrétion $\dot{M}$.

– Profondeur et forme des raies d'absorption. Cela s'est avéré possible avec SINFONI, et maintenant ERIS. L'EW des raies d'absorption peut renseigner sur l'étendue de la variabilité du continuum, ainsi que sur la possibilité de remplissage des raies par l'accrétion. Les résultats préliminaires (non présentés dans cette thèse) ont montré que certaines raies d'émission métalliques étaient présentes dans les données Delorme 1 (AB)b pendant les époques d'éruption, et absentes des autres. Il est possible que ces raies auraient été présentes dans l'absorption autrement, mais non observables en raison du faible niveau de continuum. Par ailleurs, si des caractéristiques d'absorption sont détectées dans les raies d'émission, elles fourniront des indications directes sur les processus d'accrétion et d'éjection sur la planète.

4.3.2 Instrumentation future

Dans cette thèse, quelques sujets n'ont pas été abordés de manière suffisamment approfondie. En particulier, la plupart des PMC et des PMO connus sont soit éloignés de leur étoile hôte, en dehors de son disque, soit isolés. Cela signifie que pour qu'ils puissent s'accréter activement, ils ont besoin d'un réservoir de gaz : probablement leur propre disque circumplanétaire. Les CPD ont été détectés sur quelques objets, à partir de la photométrie (par exemple, GSC 06214-00210 b) ou des détections ALMA (par exemple, GQ Lup b). Plus récemment, les observations du JWST ont même fourni un spectre du CPD de GQ Lup b, ouvrant ainsi la voie à leur caractérisation approfondie. Cependant, alors que la résolution angulaire de l'ALMA est trop faible pour faire plus que confirmer l'origine de la poussière, il est possible que l'interférométrie NIR (GRAVITY) fournisse des mesures réelles de ces CPD. Le futur interféromètre en bande J du VLTI : ASGARD/BIFROST (Kraus et al., 2022), pourrait même permettre de résoudre les régions d'émission Pa_β, comme cela a été fait pour Br_γ sur CI Tau (Gravity Collaboration et al., 2023).

RISTRETTO est actuellement en cours de développement, en tant que IFU de puissance (bien que le nombre de pixels soit limité : 7) pour le VLT. Il pourra atteindre $R > 140,000$, et une résolution angulaire de quelques dizaines de mas (Lovis et al., 2022). Cela pourrait être l'instrument parfait pour l'étude des compagnons en accrétion rapprochée.

Tout comme MUSE, MAVIS (McDermid et al., 2020) fournira une IFU optique, assistée d'une puissante AO qui est censée l'envoyer à la limite de diffraction du VLT. Il devrait être mis en service à peu près en même temps que l'ELT, mais devrait atteindre une résolution angulaire bien meilleure que l'ELT dans l'optique, tout en offrant des résolutions spectrales à 4 chiffres. MAVIS sera certainement un instrument clé pour la caractérisation des PMC en accrétion.

Enfin, l'ELT et ses instruments de première lumière devraient être mis à la disposition de la communauté dans les années à venir. Pour caractériser les PMC en accrétion, HARMONI fournira le pouvoir de résolution de l'ELT, combiné à un IFU de $R \sim 25,000$ dans une partie de la bande J, et la totalité de la bande K. Il s'agira essentiellement d'une meilleure version d'ERIS, avec l'apport de lumière de l'ELT. D'autre part, METIS fournira un mode IFU dans les bandes L et M, avec une résolution de 100 000, qui s'avérera utile pour l'étude des CPD et de certaines raies d'hydrogène d'ordre supérieur, comme le Br_α. Si les futures observations avec le JWST confirment la présence des raies Pfund sur les PMC dans ces bandes, METIS pourrait permettre d'accéder à leur profil de raie détaillé.





Appendices

Chapter A.

SINFONI appendix

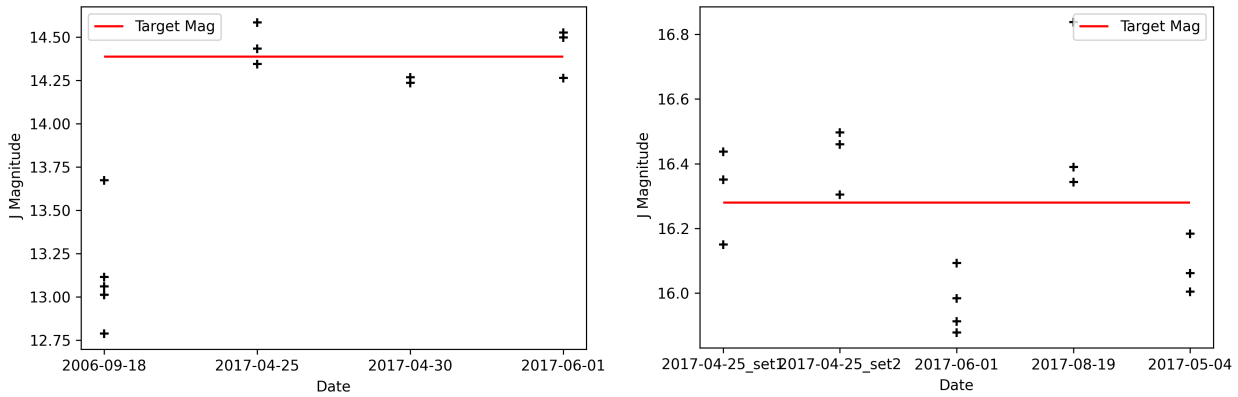


Figure A.1: Flux normalization for GQ Lup b (left) and GSC 06214-00210 b (right). The individual crosses are the computed magnitude for each exposure. The red line is the mean magnitude of all sequence. The 2006-09-18 epoch was excluded from the computation for GQ Lup b because the discrepancy is likely due to the observing conditions.

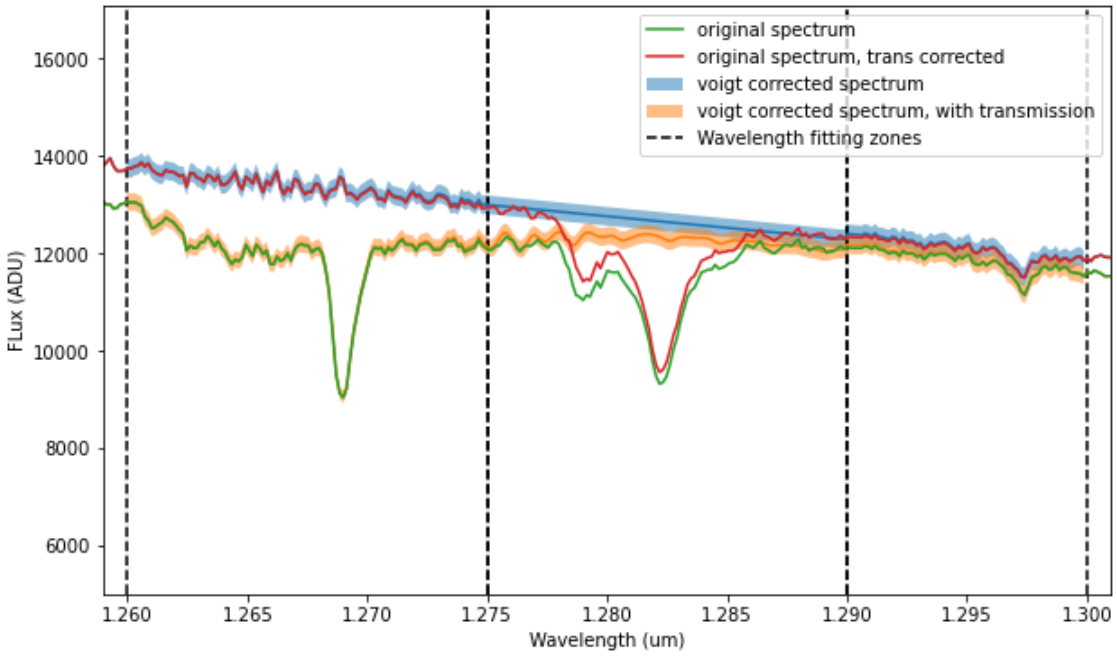


Figure A.2: Procedure for the correction from the Pa_{β} absorption features of the Telluric Standard, both for GQ Lup b and GSC 06214-00210 b. The original spectrum (green) is corrected from transmission, showing the voift-like shape of the Pa_{β} absorption line (red). It is replaced with a straight line between the inner two black dashed lines (blue), then re-applied the same atmospheric transmission spectrum (orange).

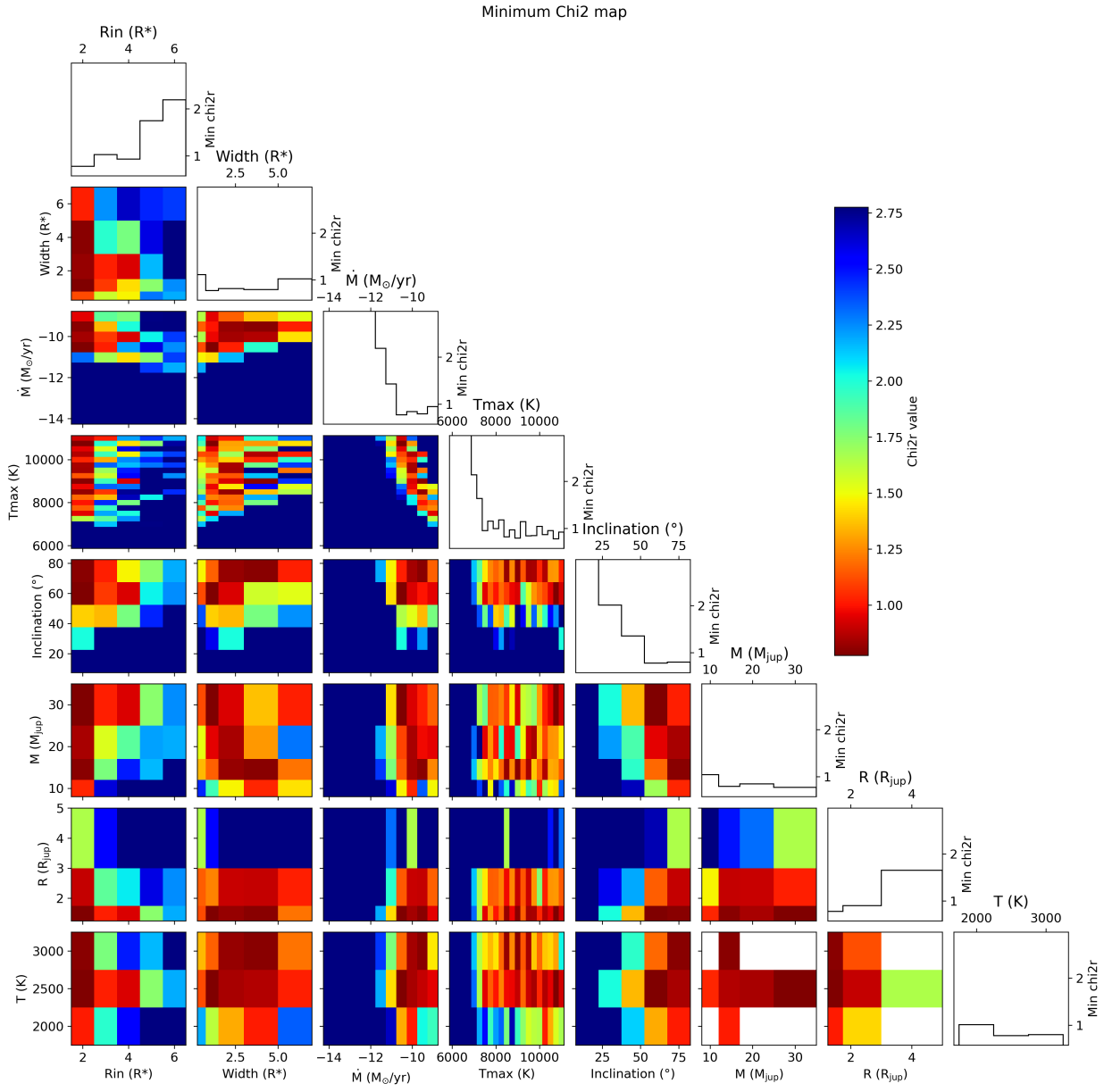


Figure A.3: GQ Lup b – 2006-09-18. Magnetospheric Accretion models for GQ Lup b, epoch 2006-09-18. χ^2_r slices represent the lowest value along the given axis.

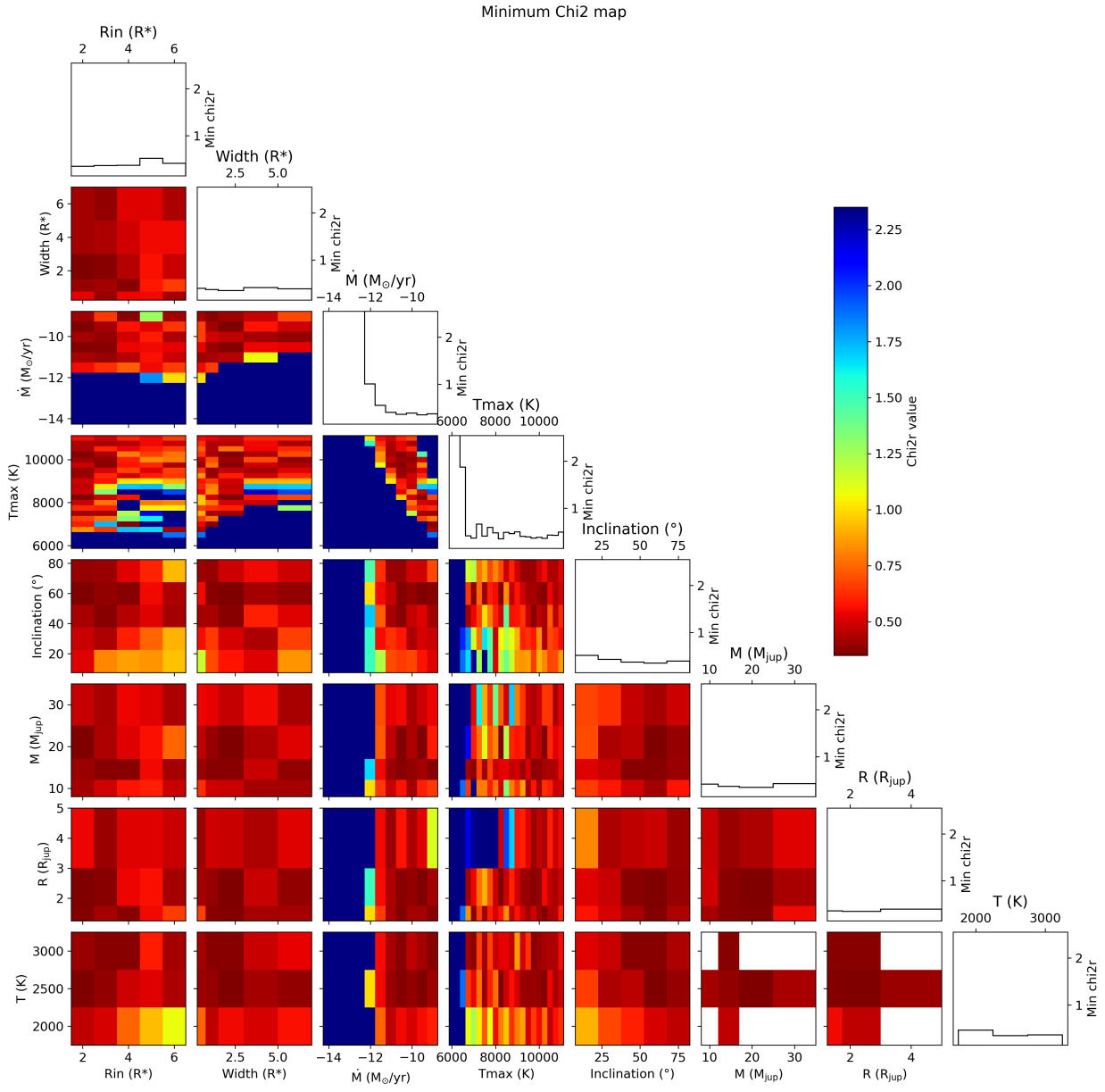


Figure A.4: GQ Lup b – 2017-04-25. Magnetospheric Accretion models for GQ Lup b, epoch 2017-04-25. χ^2_r slices represent the lowest value along the given axis.

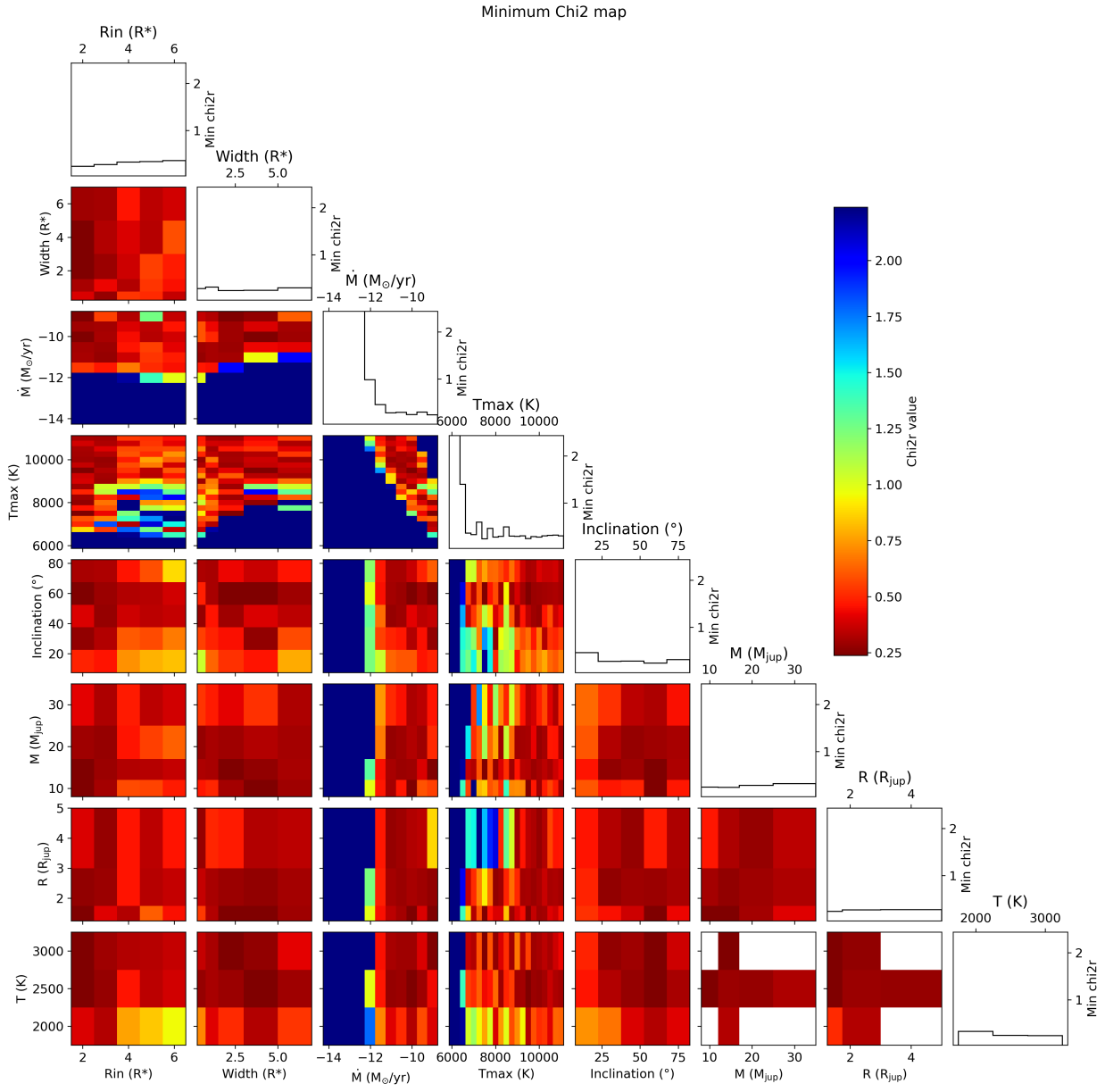


Figure A.5: GQ Lup b – 2017-04-30. Magnetospheric Accretion models for GQ Lup b, epoch 2017-04-30. χ^2_r slices represent the lowest value along the given axis.

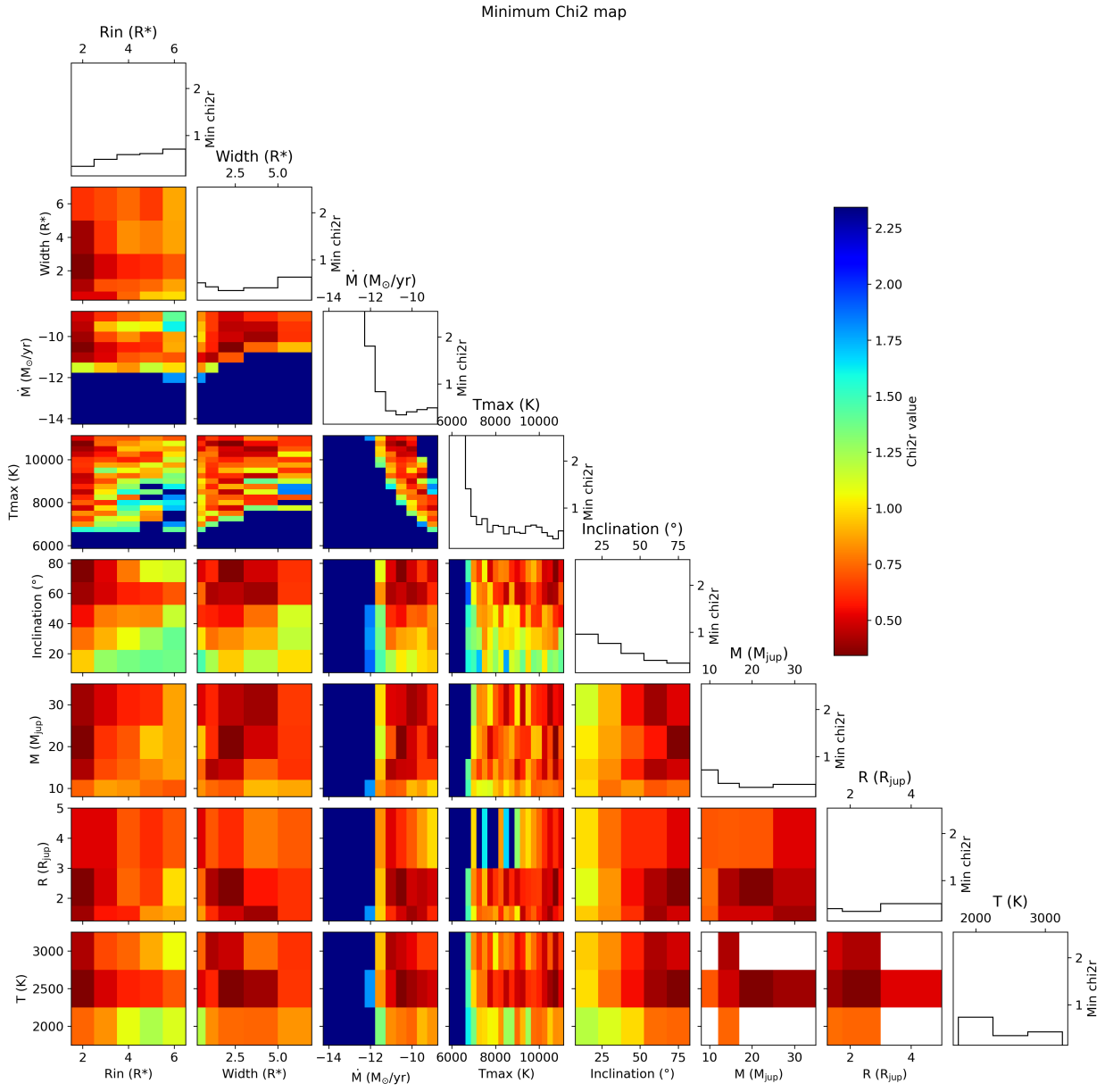


Figure A.6: GQ Lup b – 2017-06-01. Magnetospheric Accretion models for GQ Lup b, epoch 2017-06-01. χ^2_r slices represent the lowest value along the given axis.

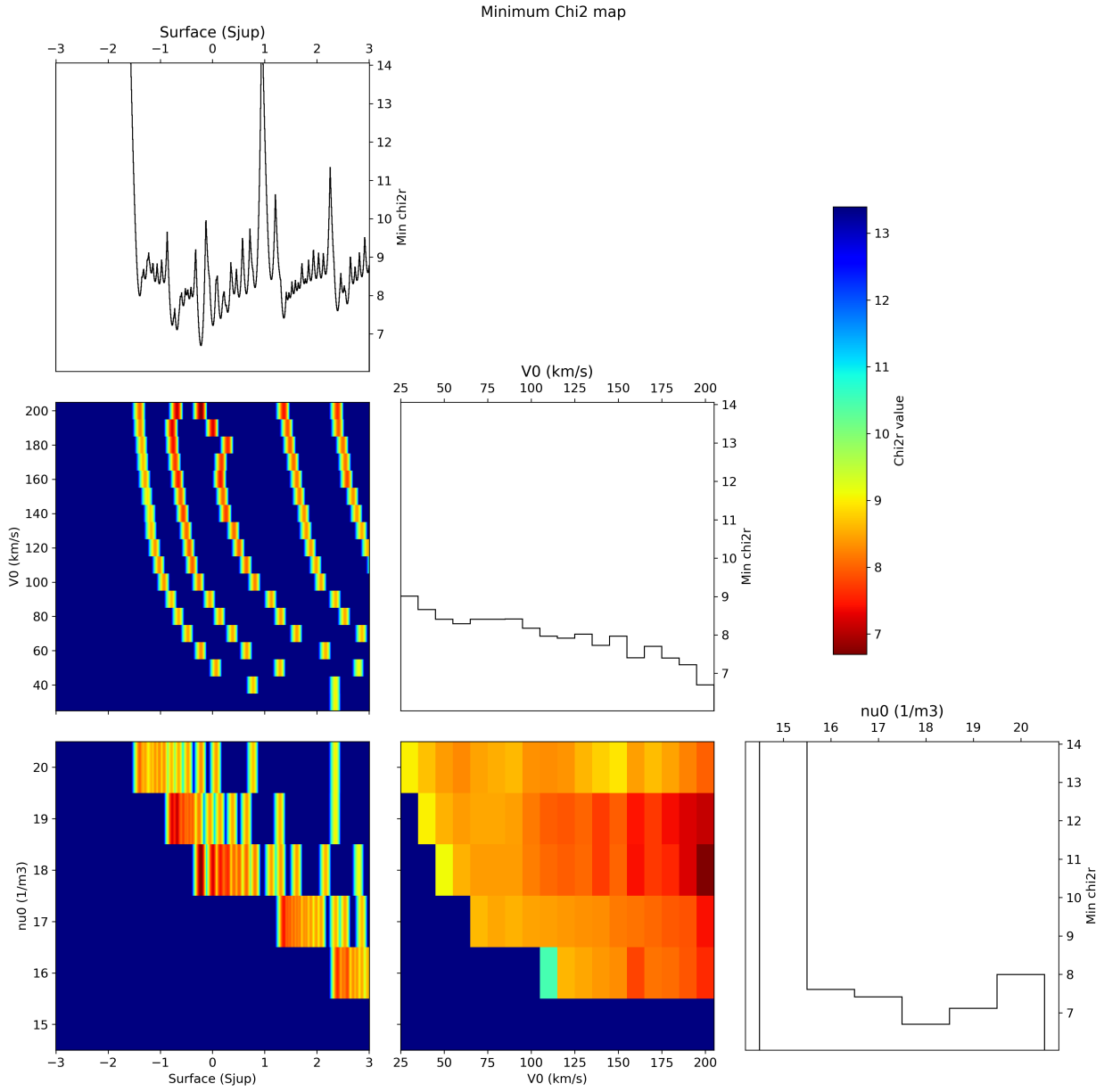


Figure A.7: GQ Lup b – 2006-09-18. Shock models for GQ Lup b, epoch 2006-09-18. χ^2_r slices represent the lowest value along the given axis.



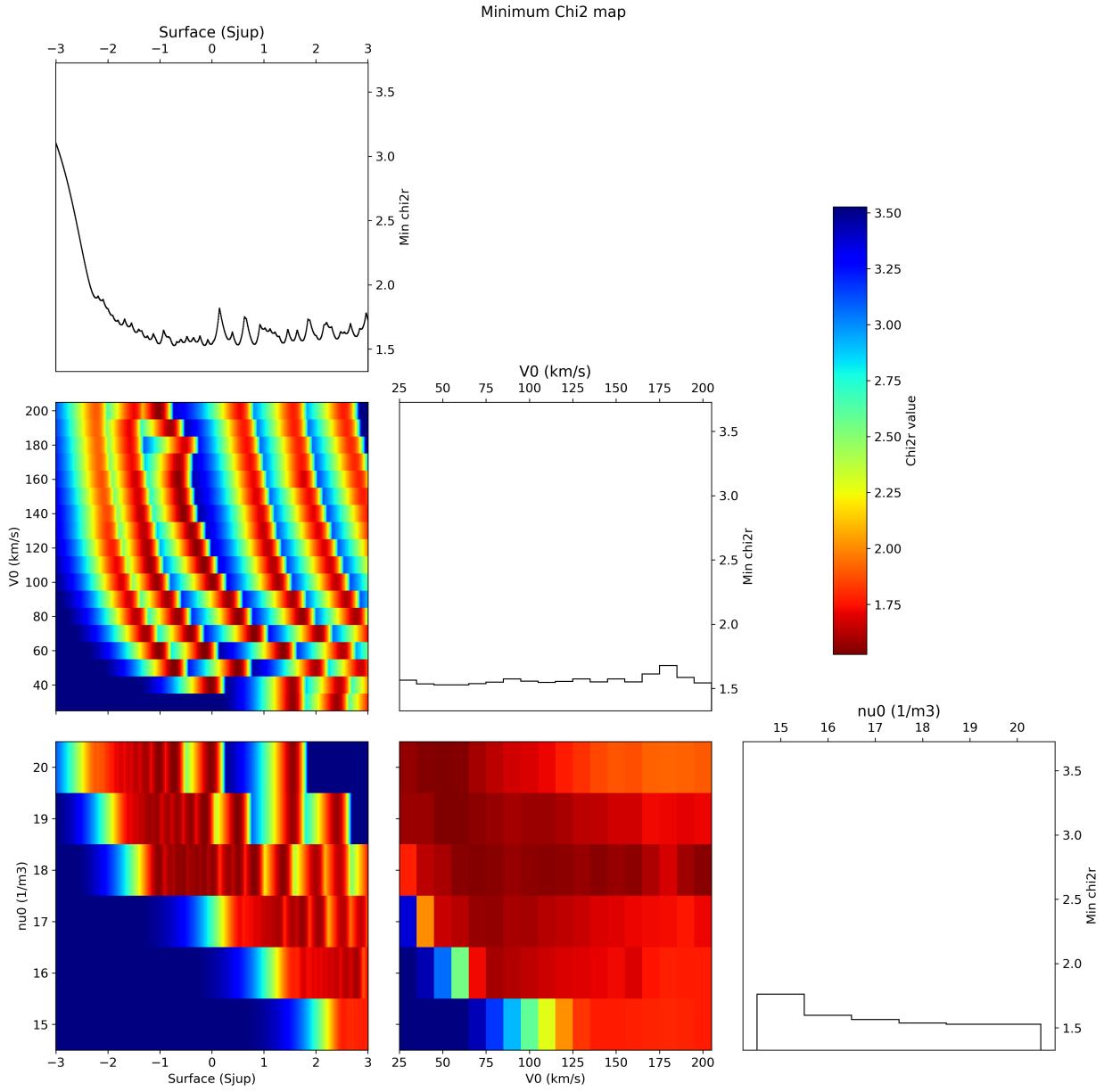


Figure A.8: GQ Lup b – 2017-04-25. Shock models for GQ Lup b, epoch 2017-04-25. χ^2_r slices represent the lowest value along the given axis.

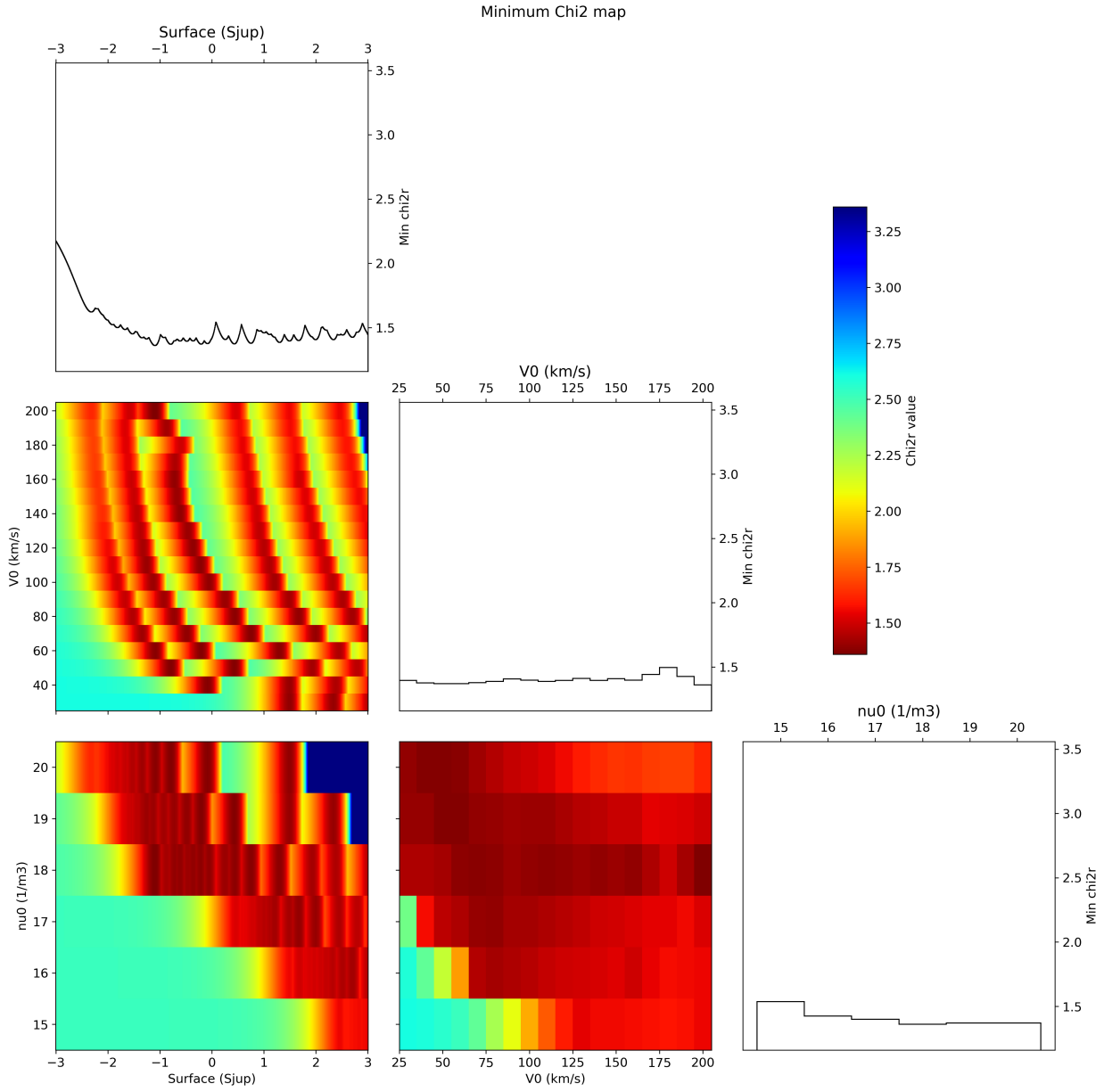


Figure A.9: GQ Lup b – 2017-04-30. Shock models for GQ Lup b, epoch 2017-04-30. χ^2_r slices represent the lowest value along the given axis.



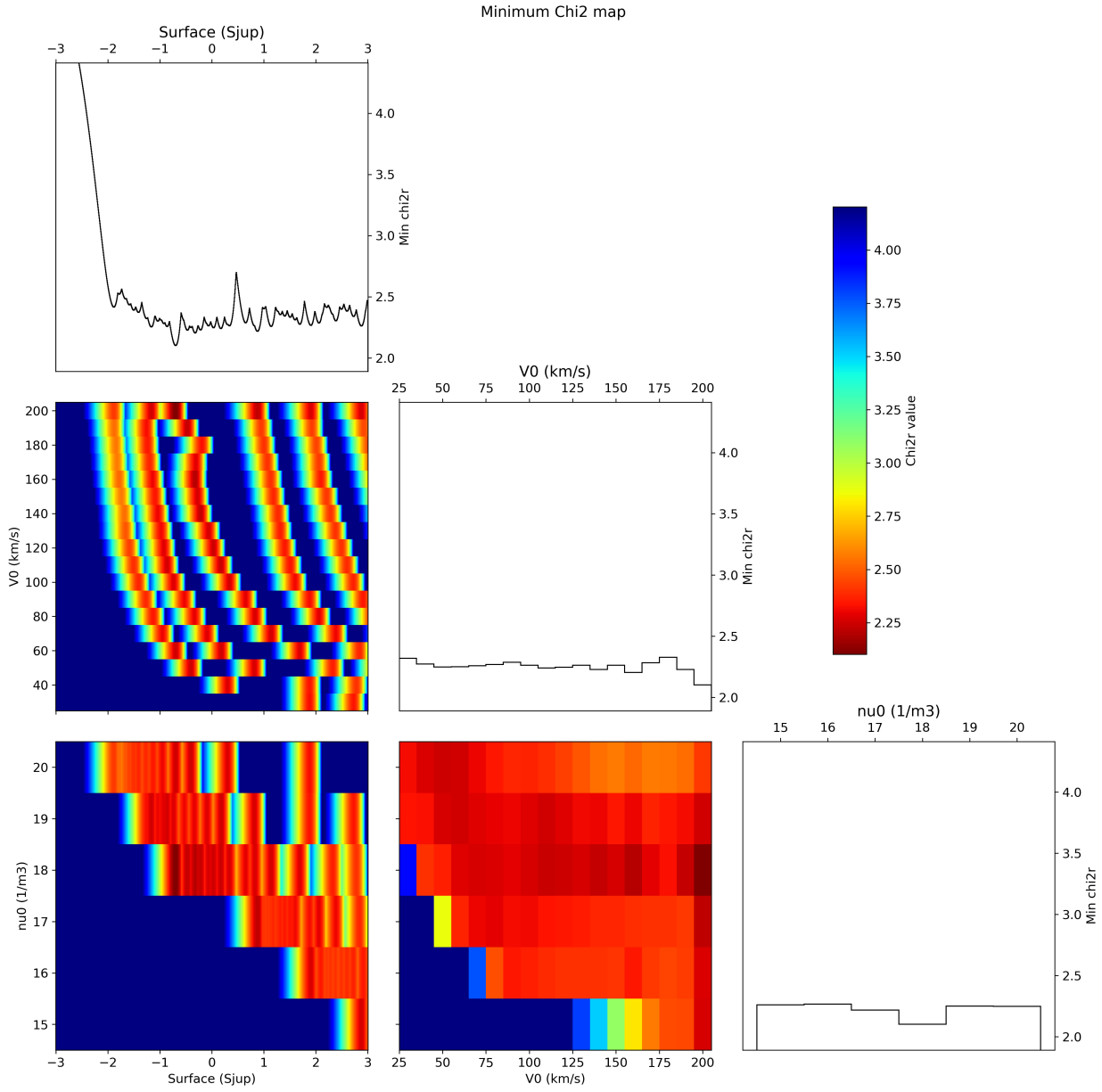


Figure A.10: GQ Lup b – 2017-06-01. Shock models for GQ Lup b, epoch 2017-06-01. χ^2_r slices represent the lowest value along the given axis.

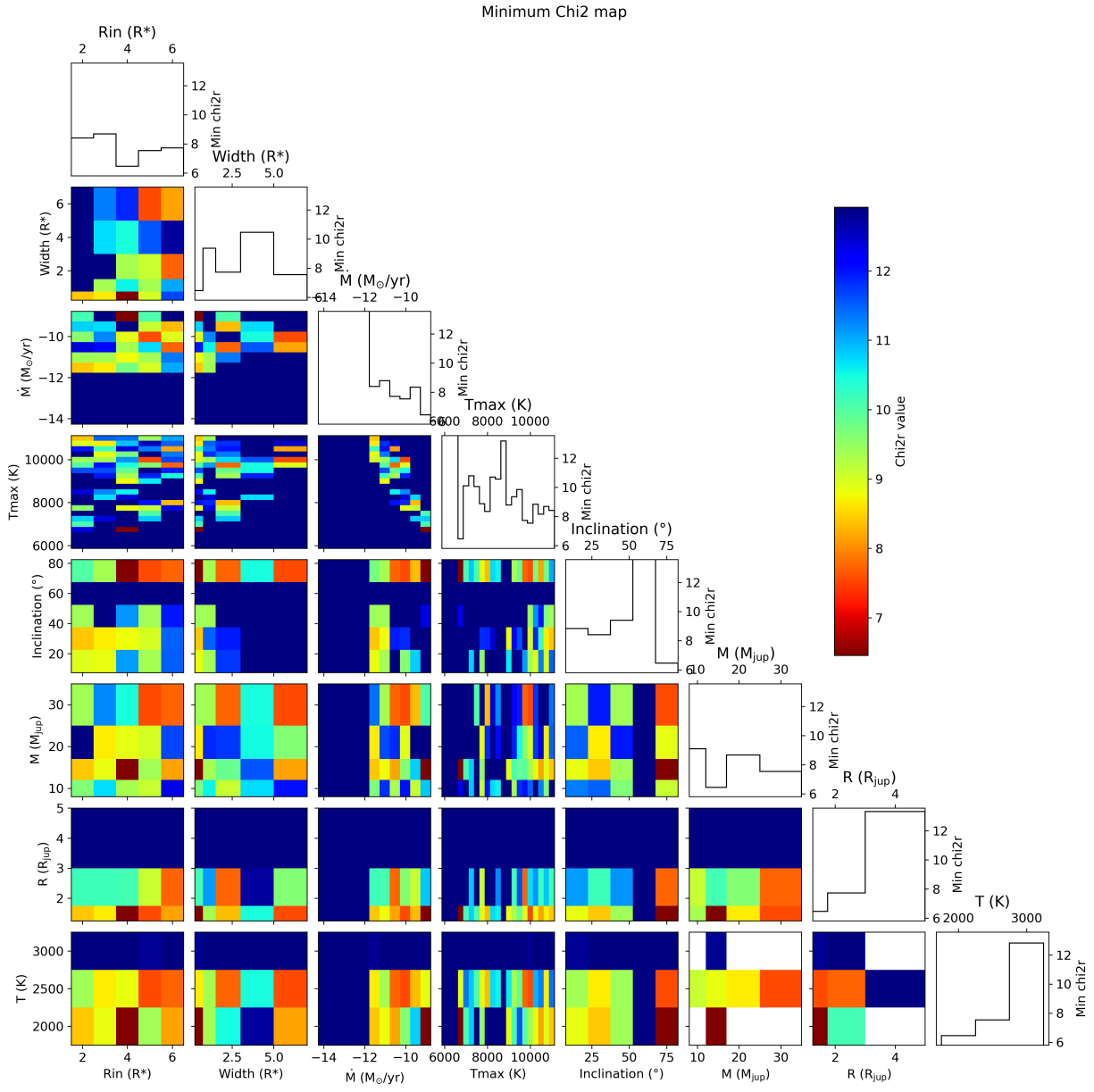


Figure A.11: GSC 06214-00210 b – 2010-07-09. Magnetospheric Accretion models for GSC 06214-00210 b, epoch 2010-07-09. χ^2_r slices represent the lowest value along the given axis.



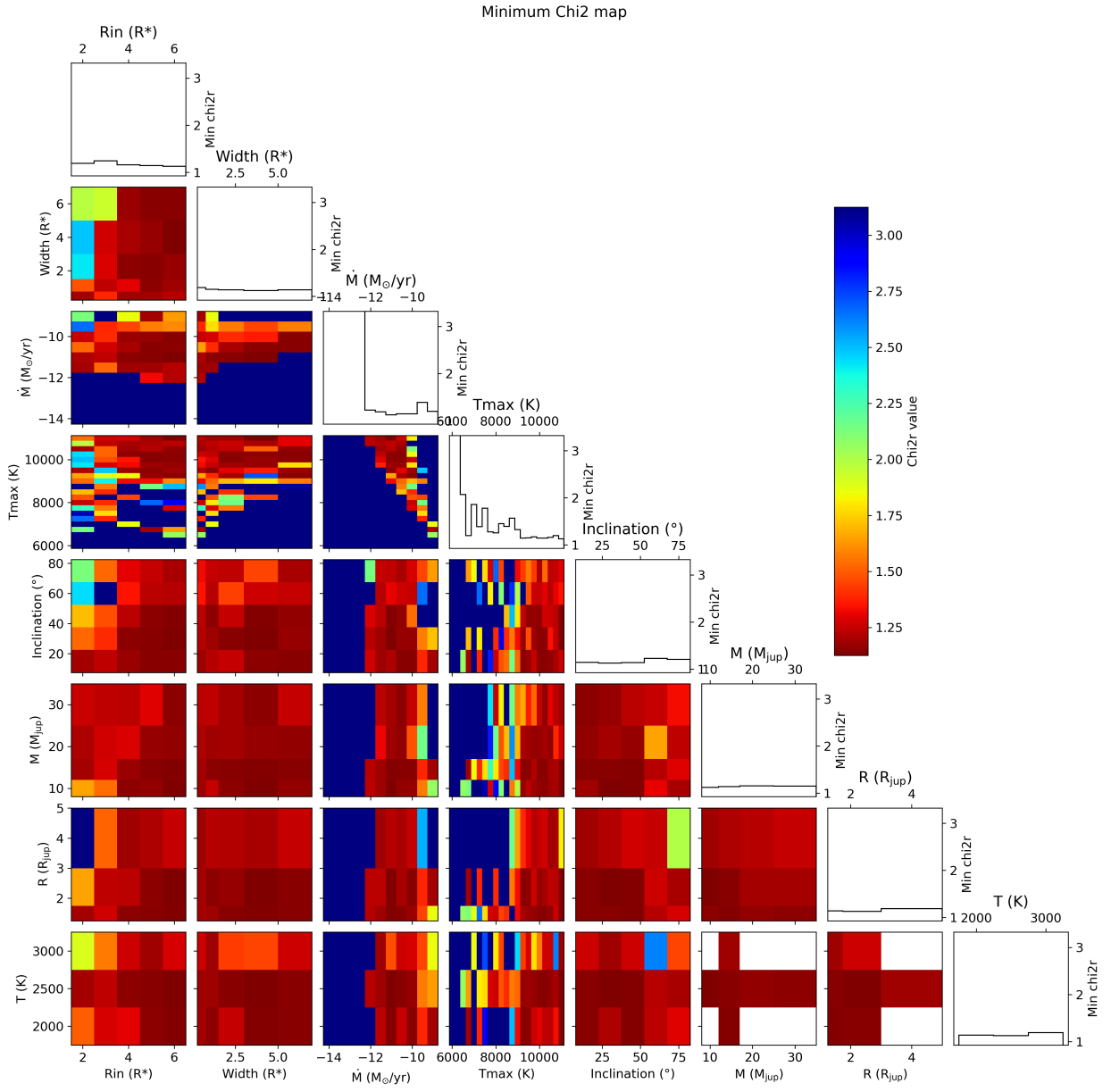


Figure A.12: GSC 06214-00210 b – 2017-04-25_set1. Magnetospheric Accretion models for GSC 06214-00210 b, epoch 2017-04-25_set1. χ^2_r slices represent the lowest value along the given axis.



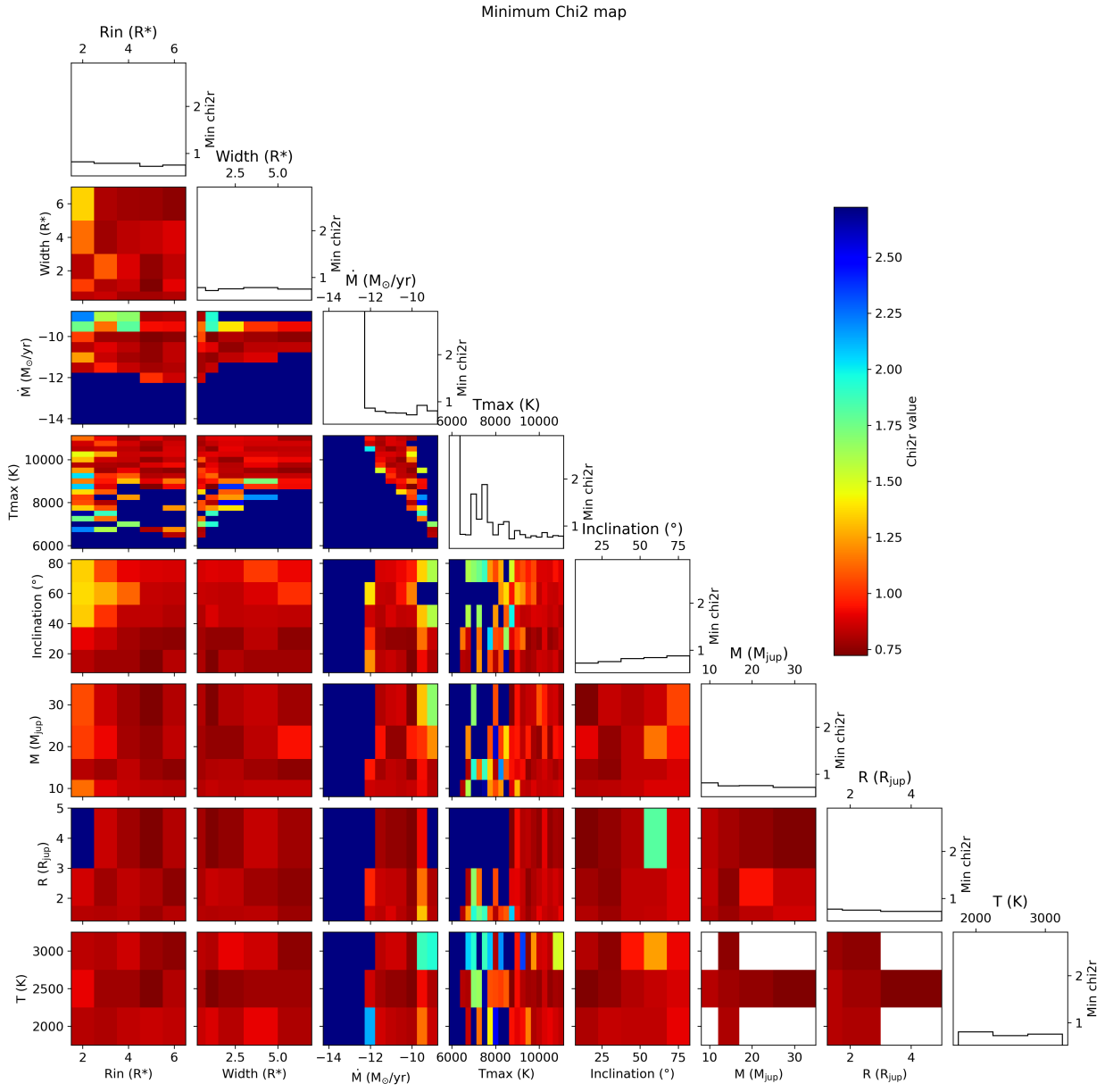


Figure A.13: GSC 06214-00210 b – 2017-04-25_set2. Magnetospheric Accretion models for GSC 06214-00210 b, epoch 2017-04-25_set2. χ^2_r slices represent the lowest value along the given axis.



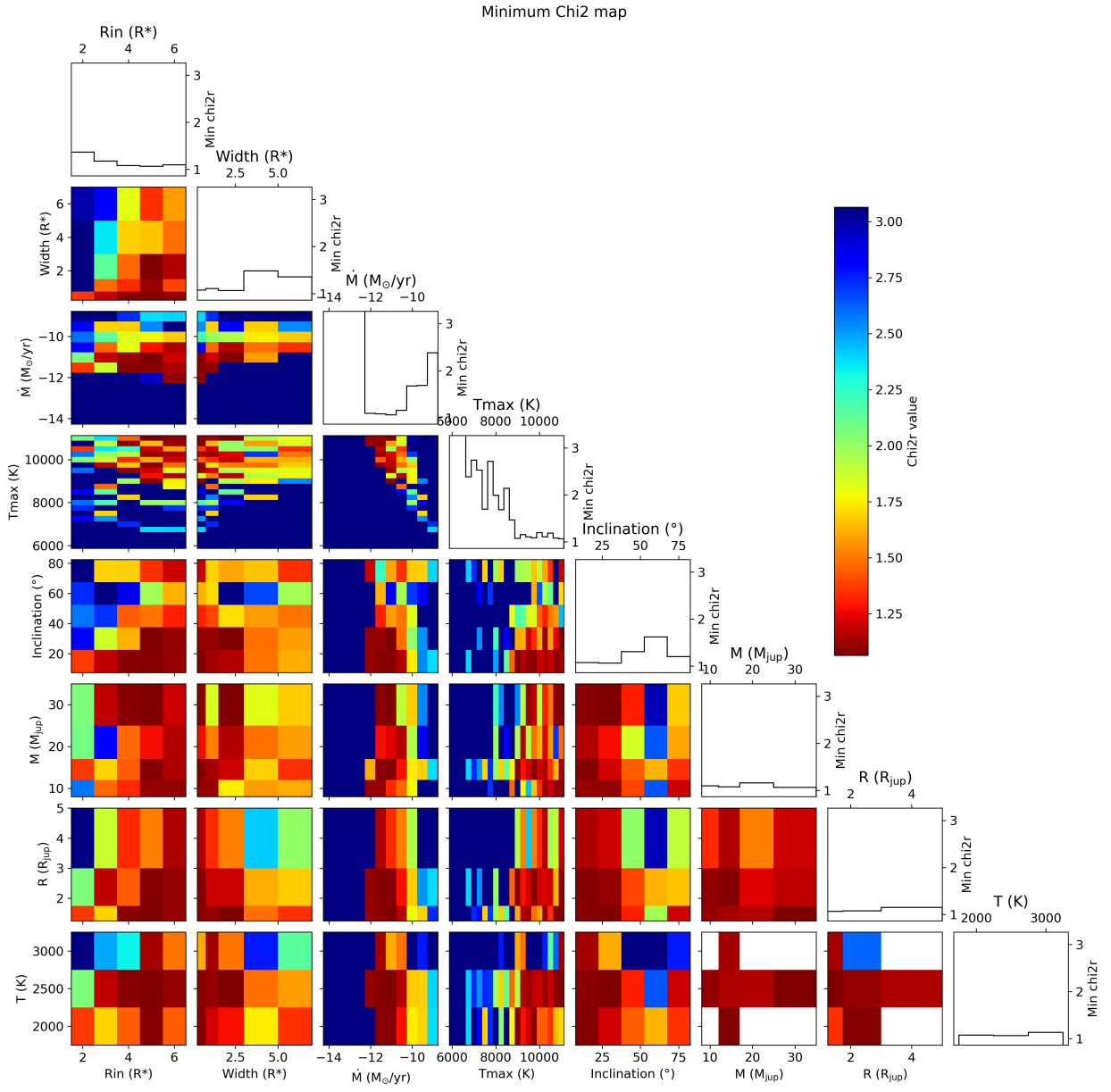


Figure A.14: GSC 06214-00210 b – 2017-05-04. Magnetospheric Accretion models for GSC 06214-00210 b, epoch 2017-05-04. χ^2_r slices represent the lowest value along the given axis.

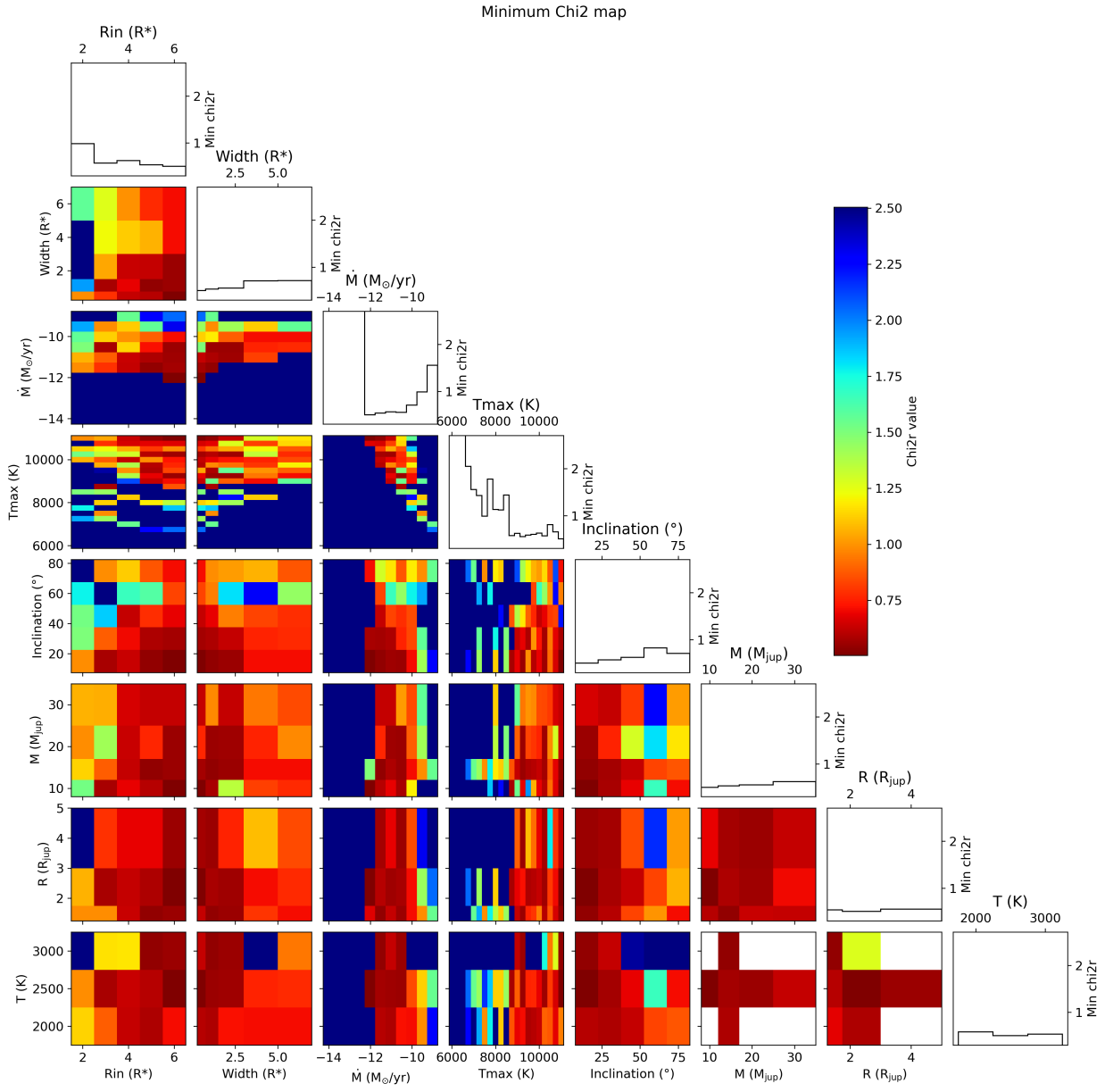


Figure A.15: GSC 06214-00210 b – 2017-06-01. Magnetospheric Accretion models for GSC 06214-00210 b, epoch 2017-06-01. χ^2_r slices represent the lowest value along the given axis.

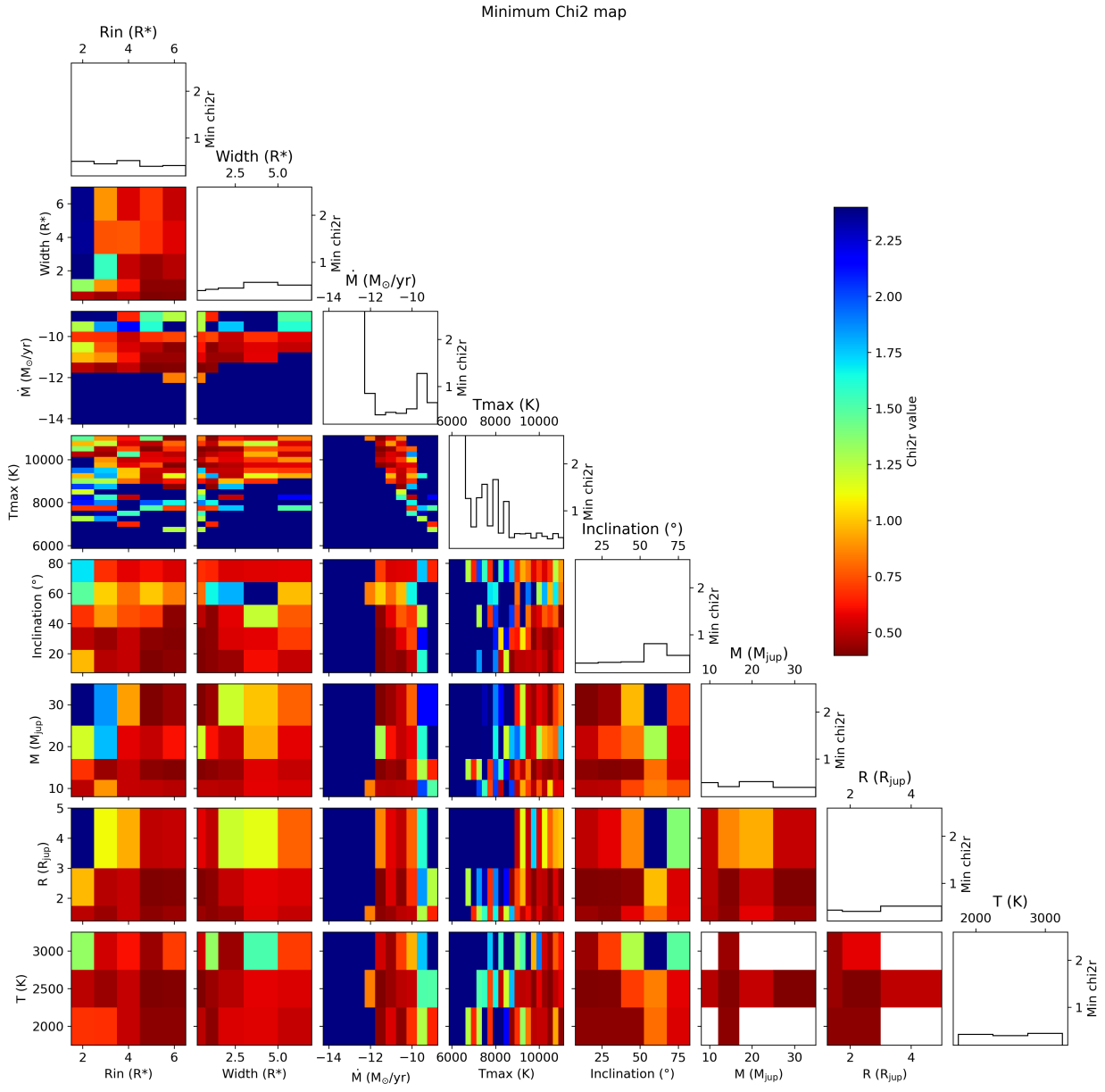


Figure A.16: GSC 06214-00210 b – 2017-08-19. Magnetospheric Accretion models for GSC 06214-00210 b, epoch 2017-08-19. χ^2_r slices represent the lowest value along the given axis.

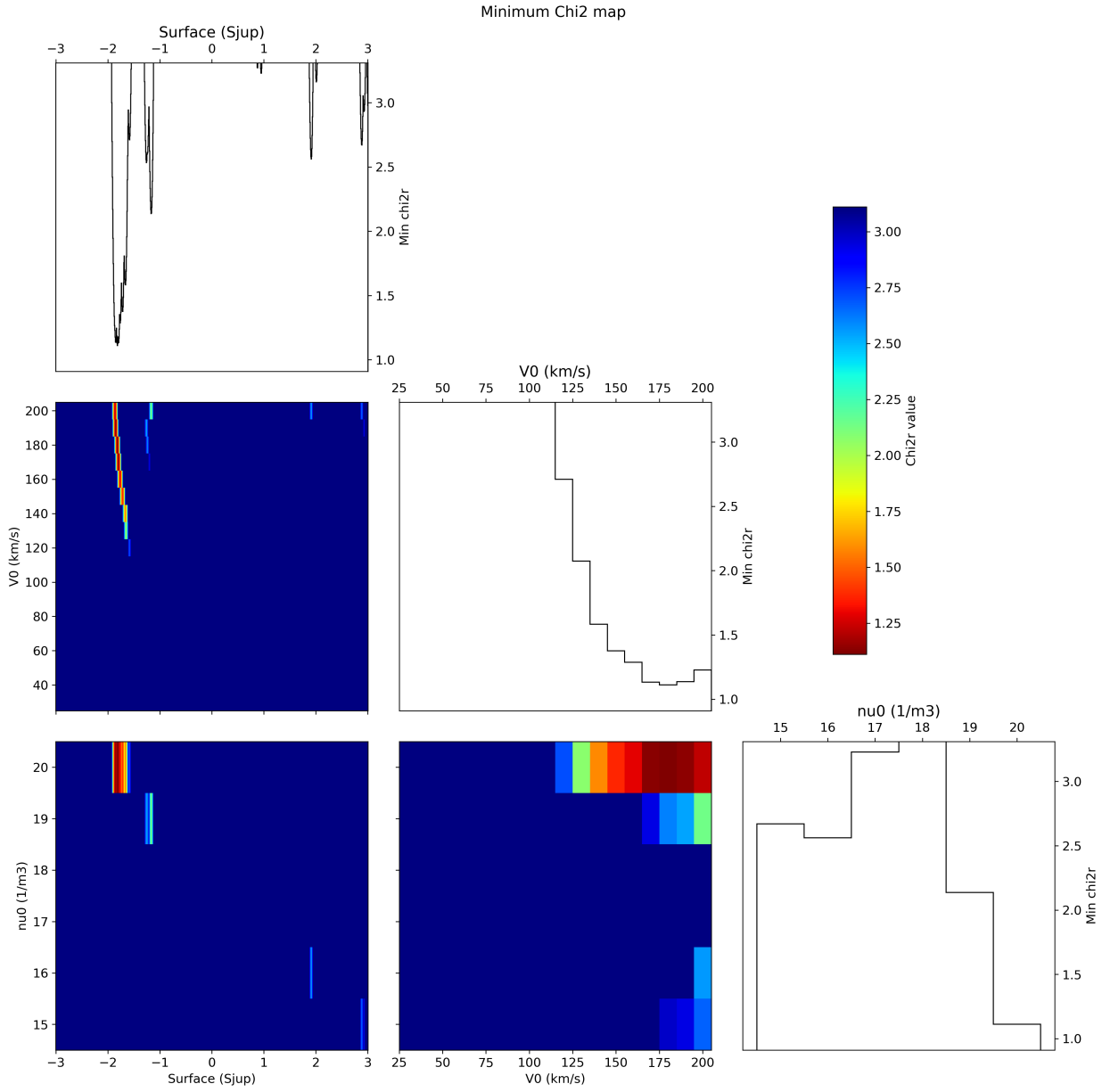


Figure A.17: GSC 06214-00210 b – 2010-07-09. Shock models for GSC 06214-00210 b, epoch 2010-07-09. χ^2_r slices represent the lowest value along the given axis.

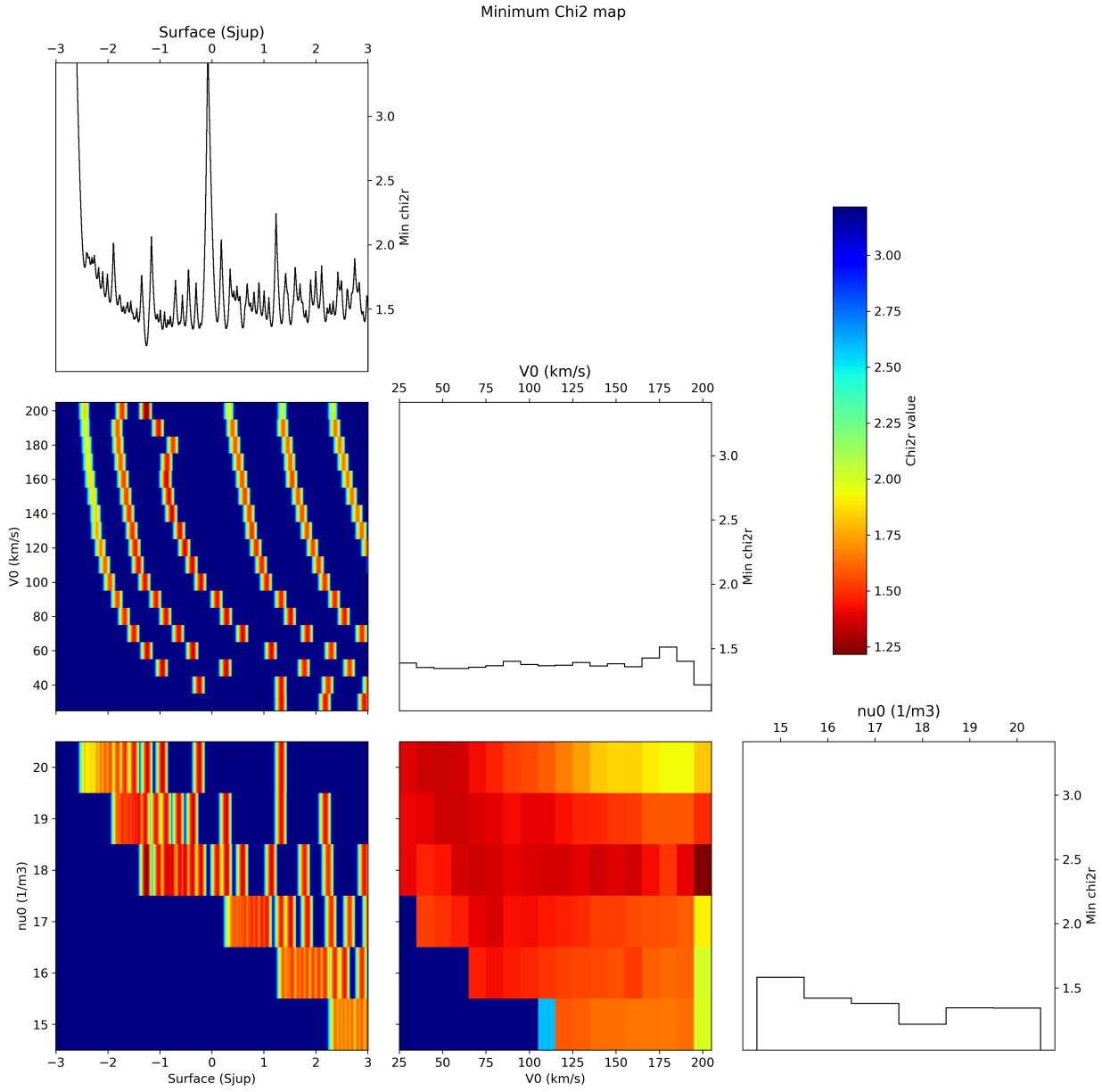


Figure A.18: GSC 06214-00210 b – 2017-04-25_set1. Shock models for GSC 06214-00210 b, epoch 2017-04-25_set1. χ^2_r slices represent the lowest value along the given axis.

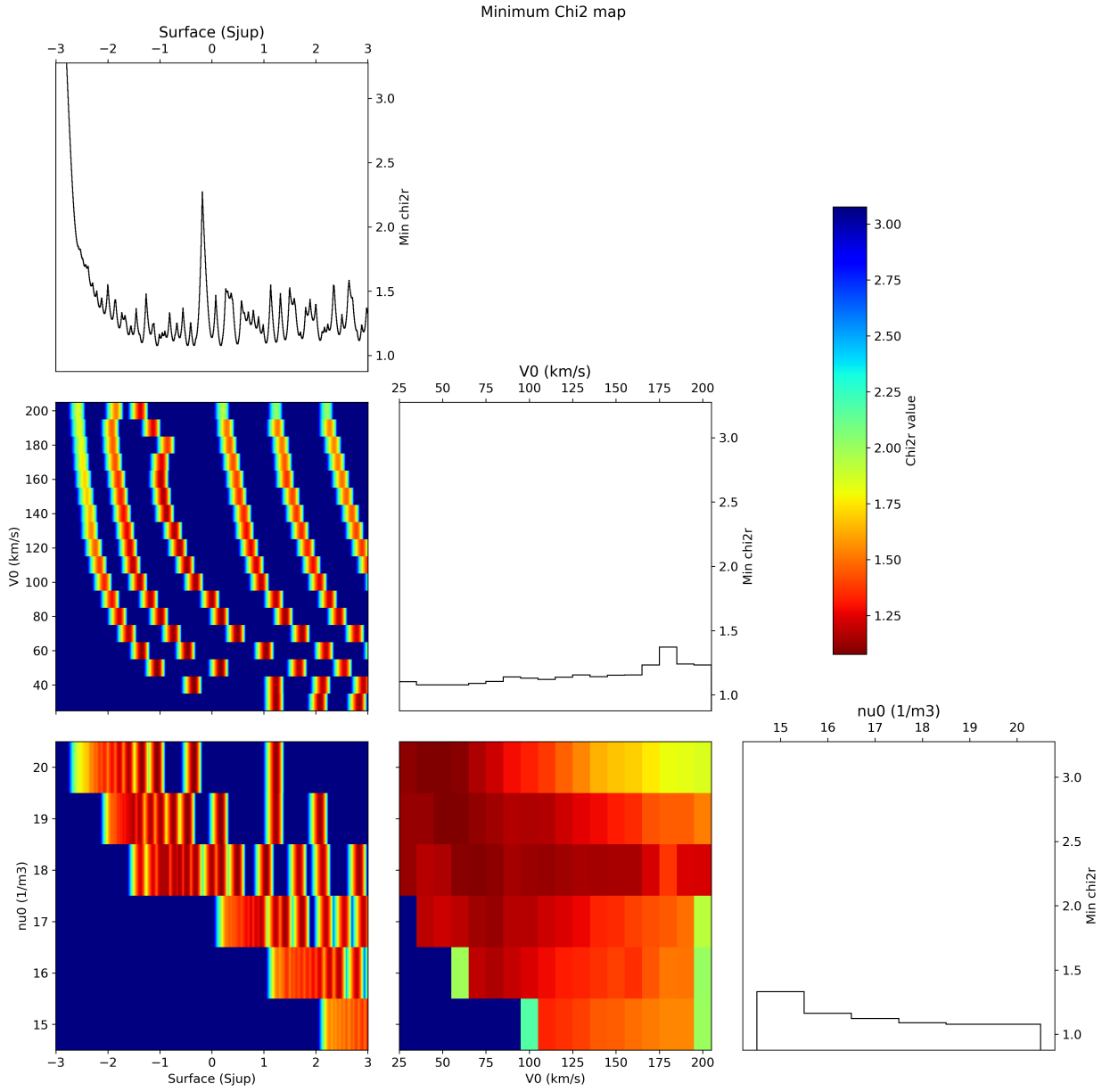


Figure A.19: GSC 06214-00210 b – 2017-04-25_set2. Shock models for GSC 06214-00210 b, epoch 2017-04-25_set2. χ^2_r slices represent the lowest value along the given axis.

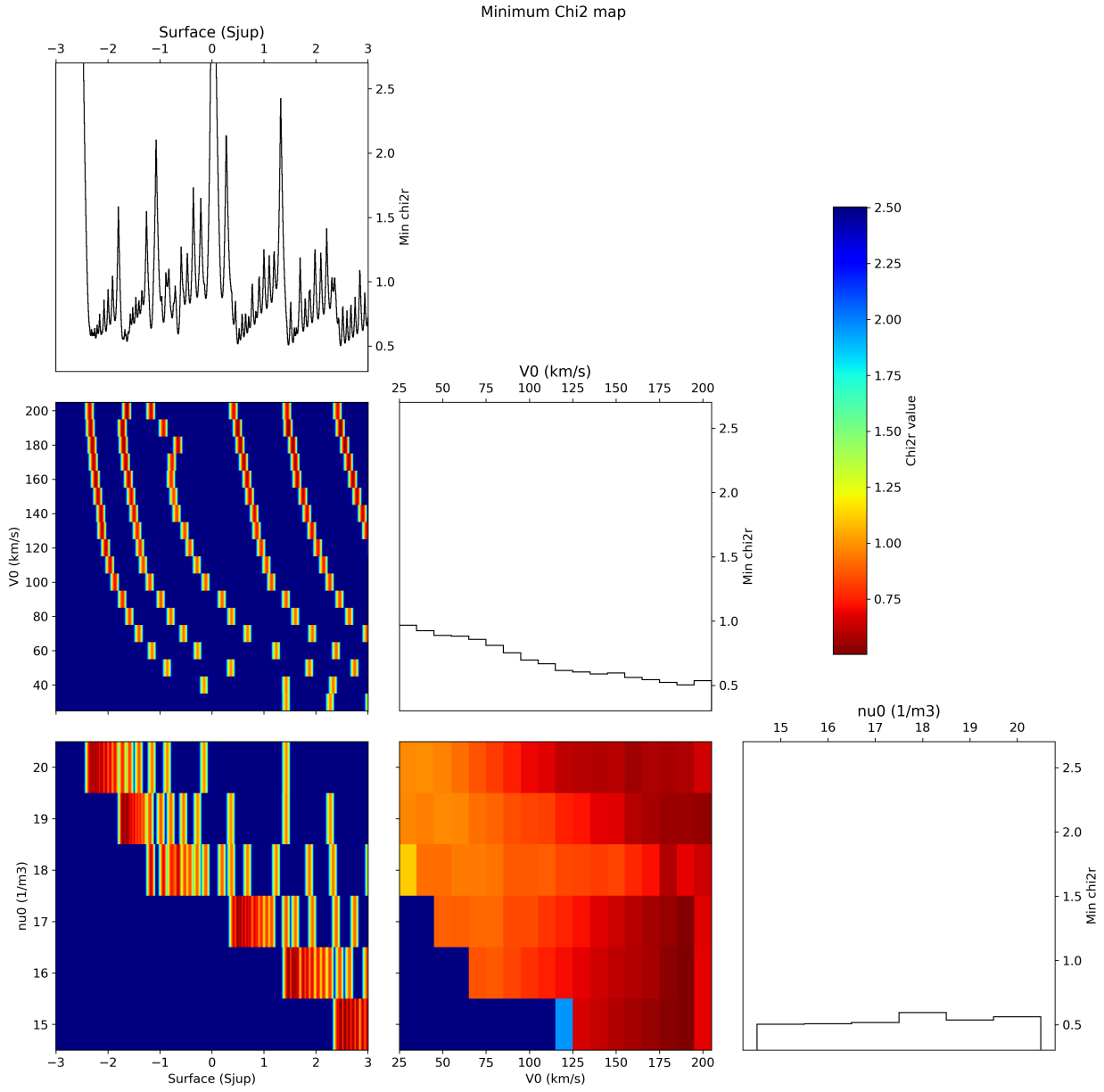


Figure A.20: GSC 06214-00210 b – 2017-05-04. Shock models for GSC 06214-00210 b, epoch 2017-05-04. χ^2_r slices represent the lowest value along the given axis.

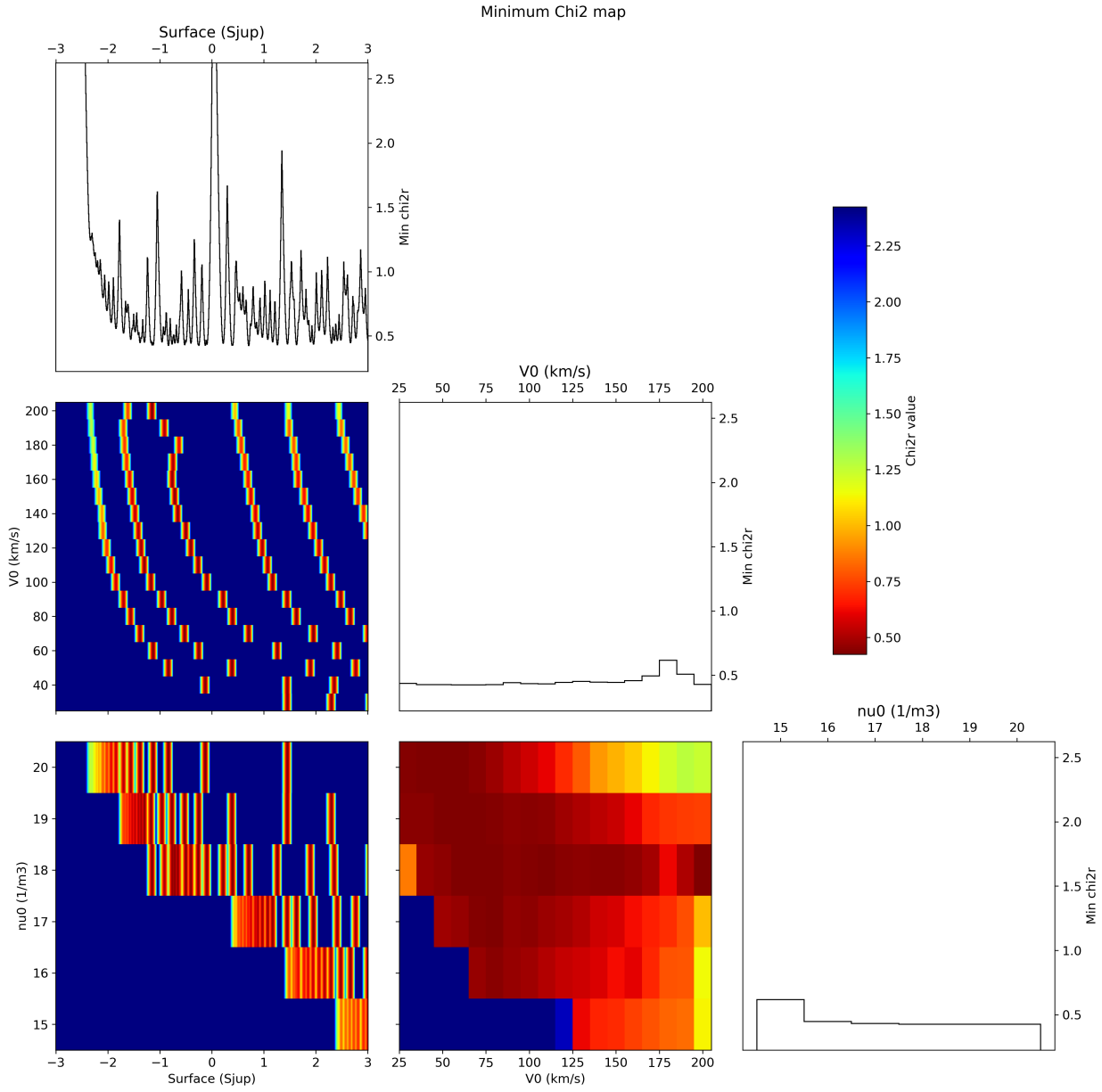


Figure A.21: GSC 06214-00210 b – 2017-06-01. Shock models for GSC 06214-00210 b, epoch 2017-06-01. χ^2_r slices represent the lowest value along the given axis.

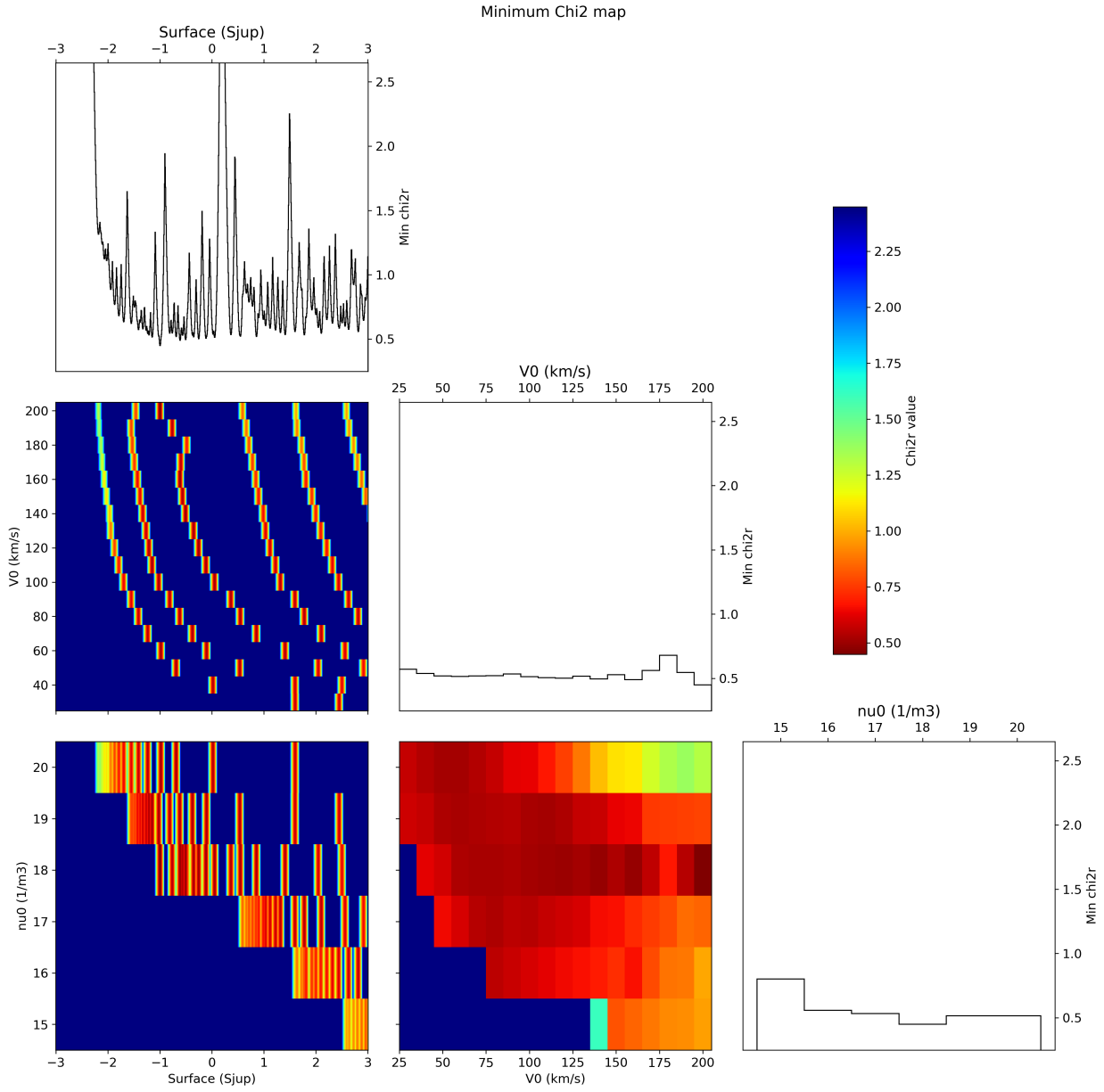


Figure A.22: GSC 06214-00210 b – 2017-08-19. Shock models for GSC 06214-00210 b, epoch 2017-08-19. χ^2_r slices represent the lowest value along the given axis.

Chapter B.

UVES appendix

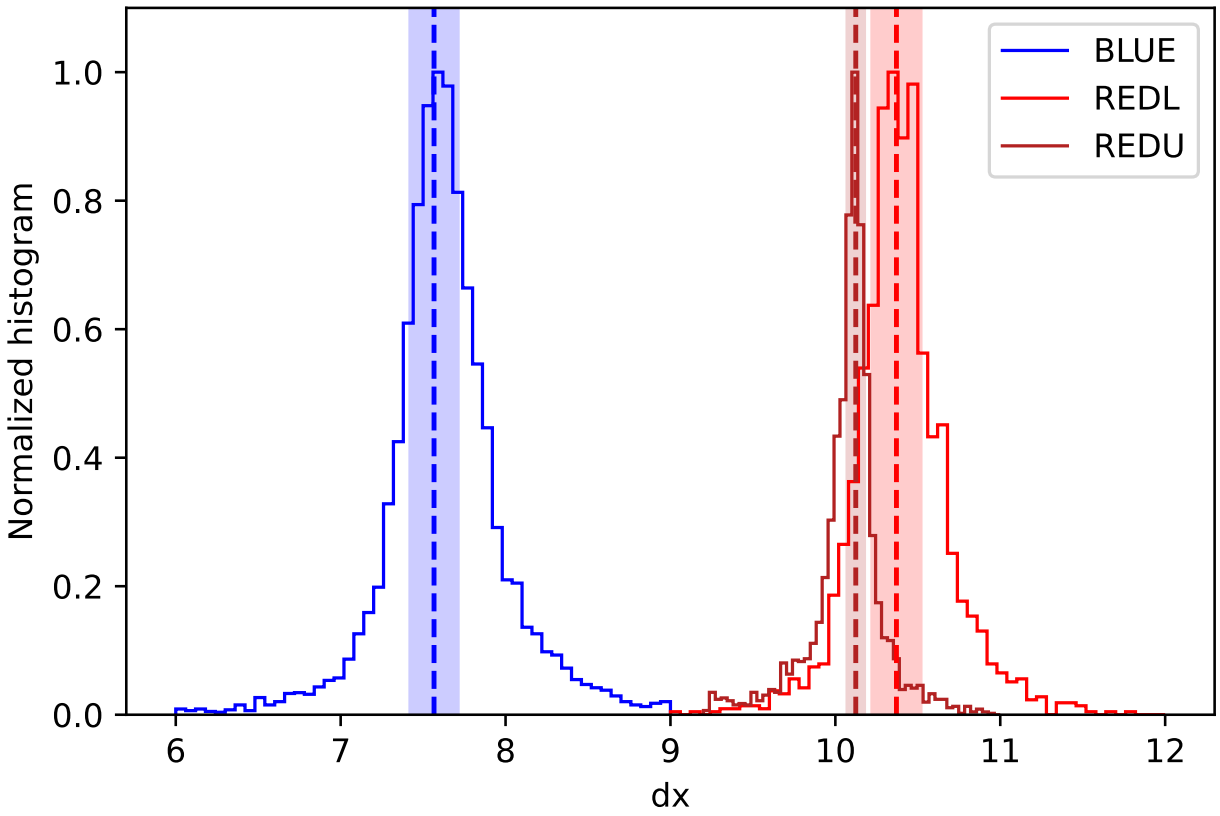


Figure B.1: Primary–Companion separation (in pixels) distribution depending on the detector. Dotted lines and corresponding shaded regions correspond to the chosen value for each detector.



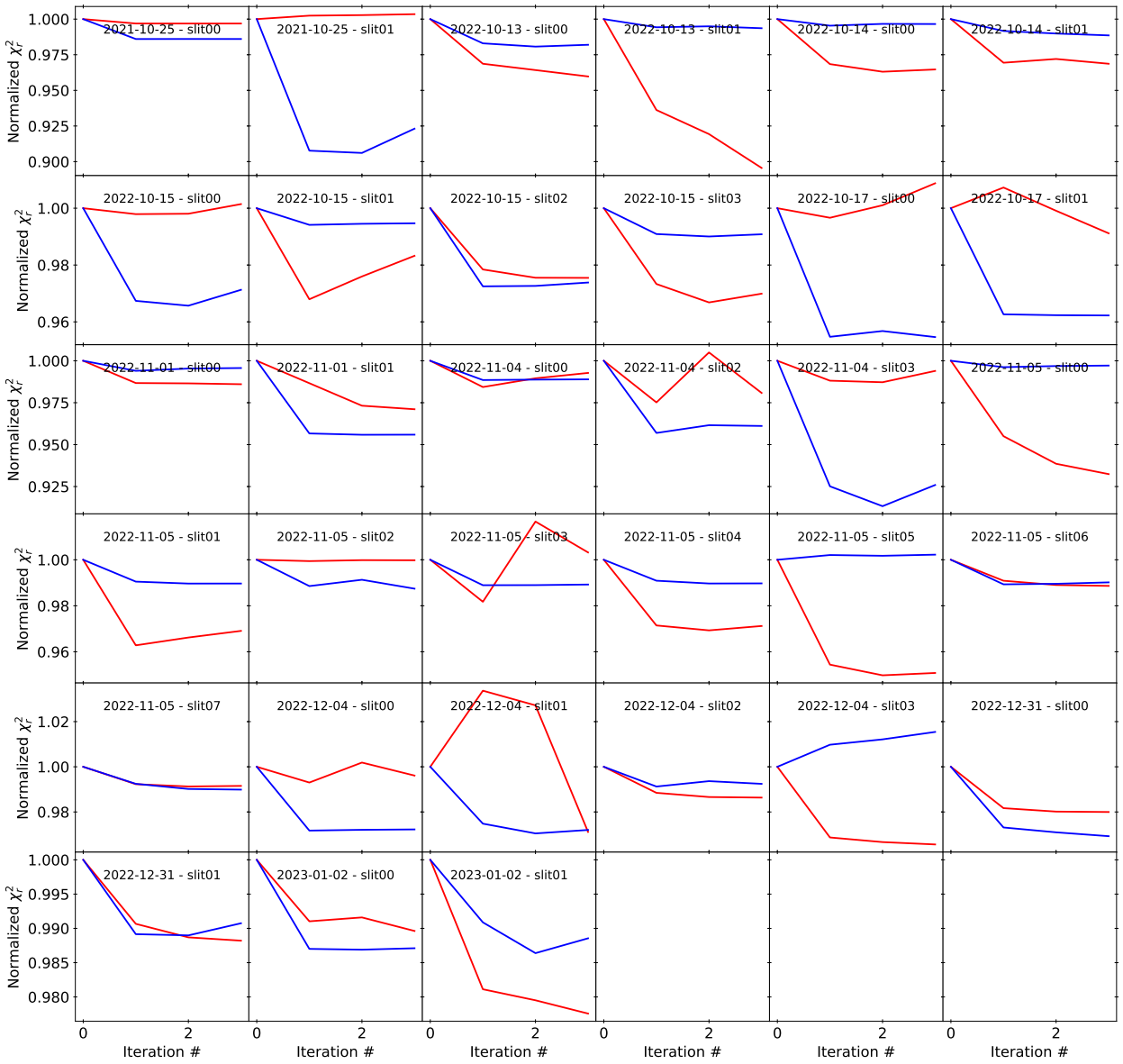


Figure B.2: Evolution of the χ^2_r along iteration for the extraction of each exposure. Blue lines represent the BLUE arm, Red lines represent the RED arm. For clarity, they are normalized to value after the first iteration (Iteration #0).



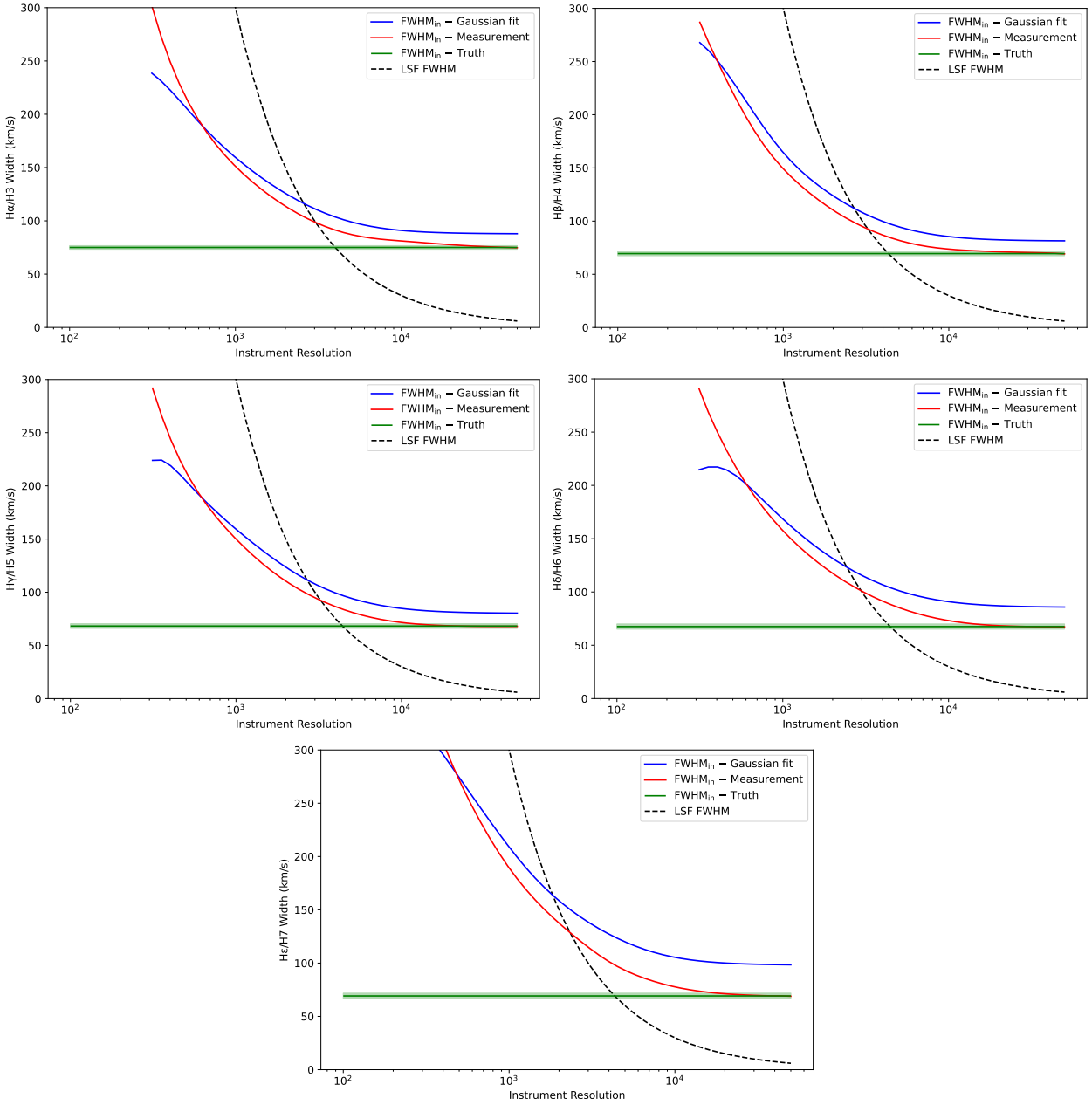


Figure B.3: Line width as a function of the observed resolution, for various Balmer lines. Green line is the true intrinsic FWHM, measure on the line at full resolution. Blue line is the intrinsic FWHM, inferred from Gaussian fitting. Red line is the intrinsic FWHM, inferred from direct measurement on the low-resolution line. Black dashed-line is the LSF FWHM at a given resolution. Intrinsic FWHMs are computed as $\mathrm{FWHM}^2_{\mathrm{in}} = \mathrm{FWHM}^2_{\mathrm{obs}} - \mathrm{FWHM}^2_{\mathrm{LSF}}$.



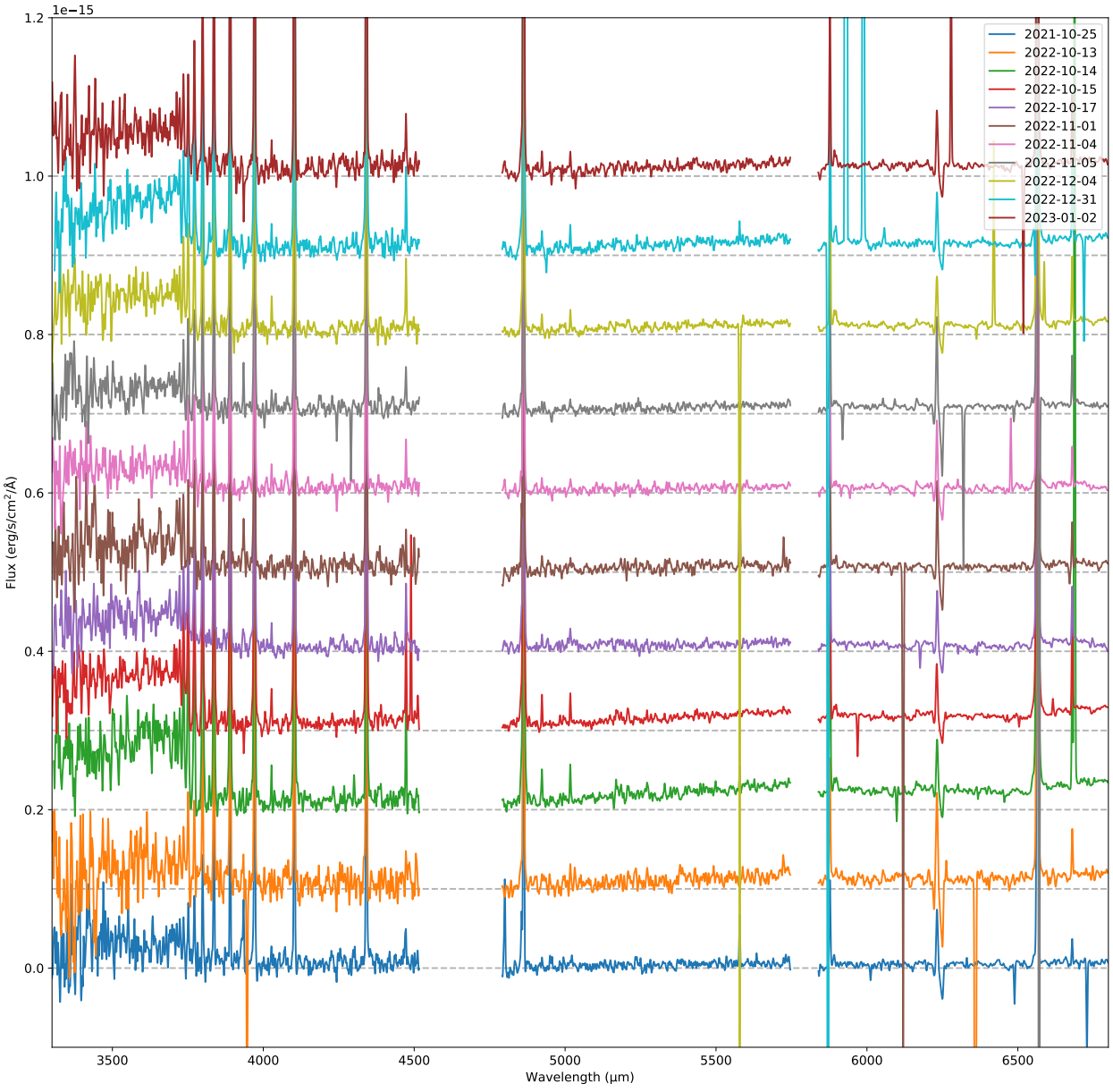


Figure B.4: Mean spectra of individual epochs of Delorme 1 (AB)b, smoothed with a gaussian of $\sigma = 50$ px.

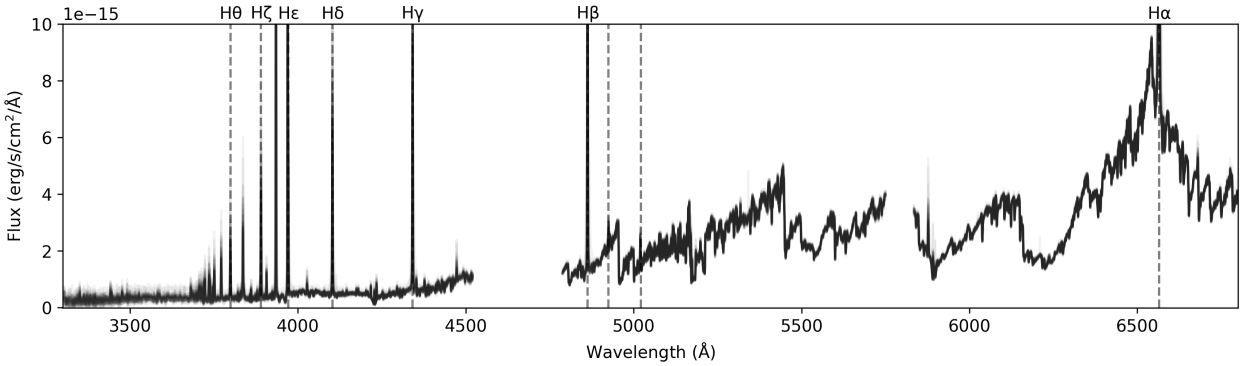


Figure B.5: Full spectrum of Delorme 1 (AB). The main Balmer lines are marked on the plot.

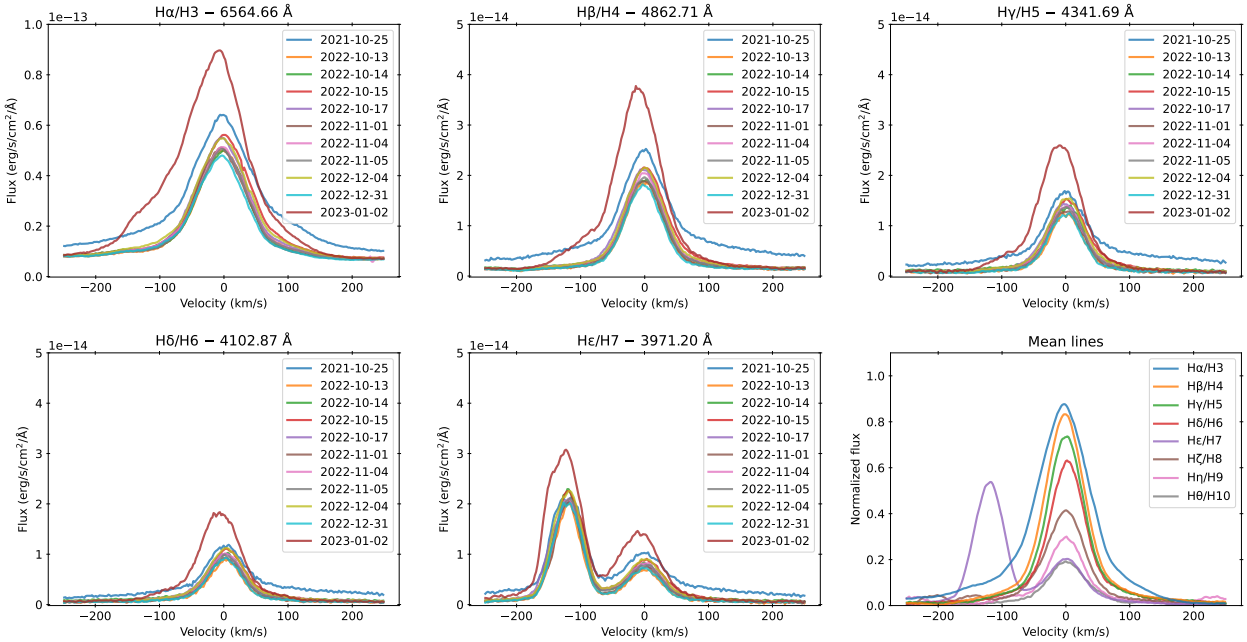


Figure B.6: All Balmer lines of Delorme 1 (AB).



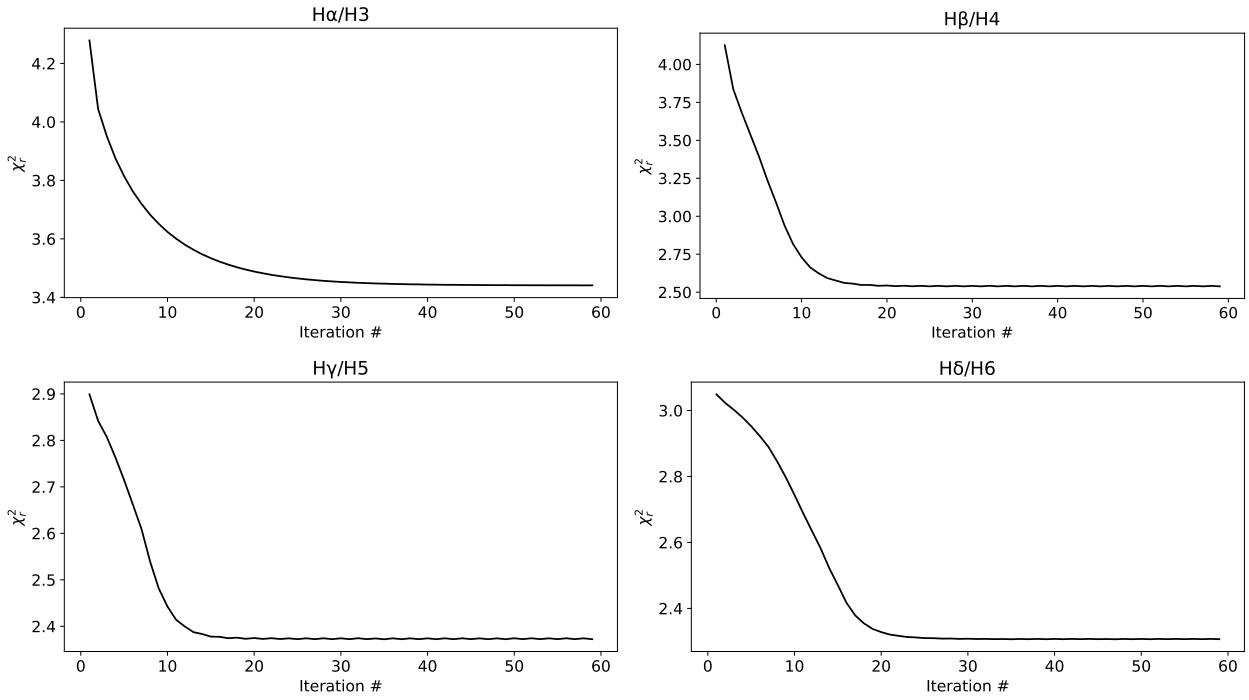


Figure B.7: χ^2_r along iterations for the decomposition of the H_α, H_β, H_γ and H_δ lines.



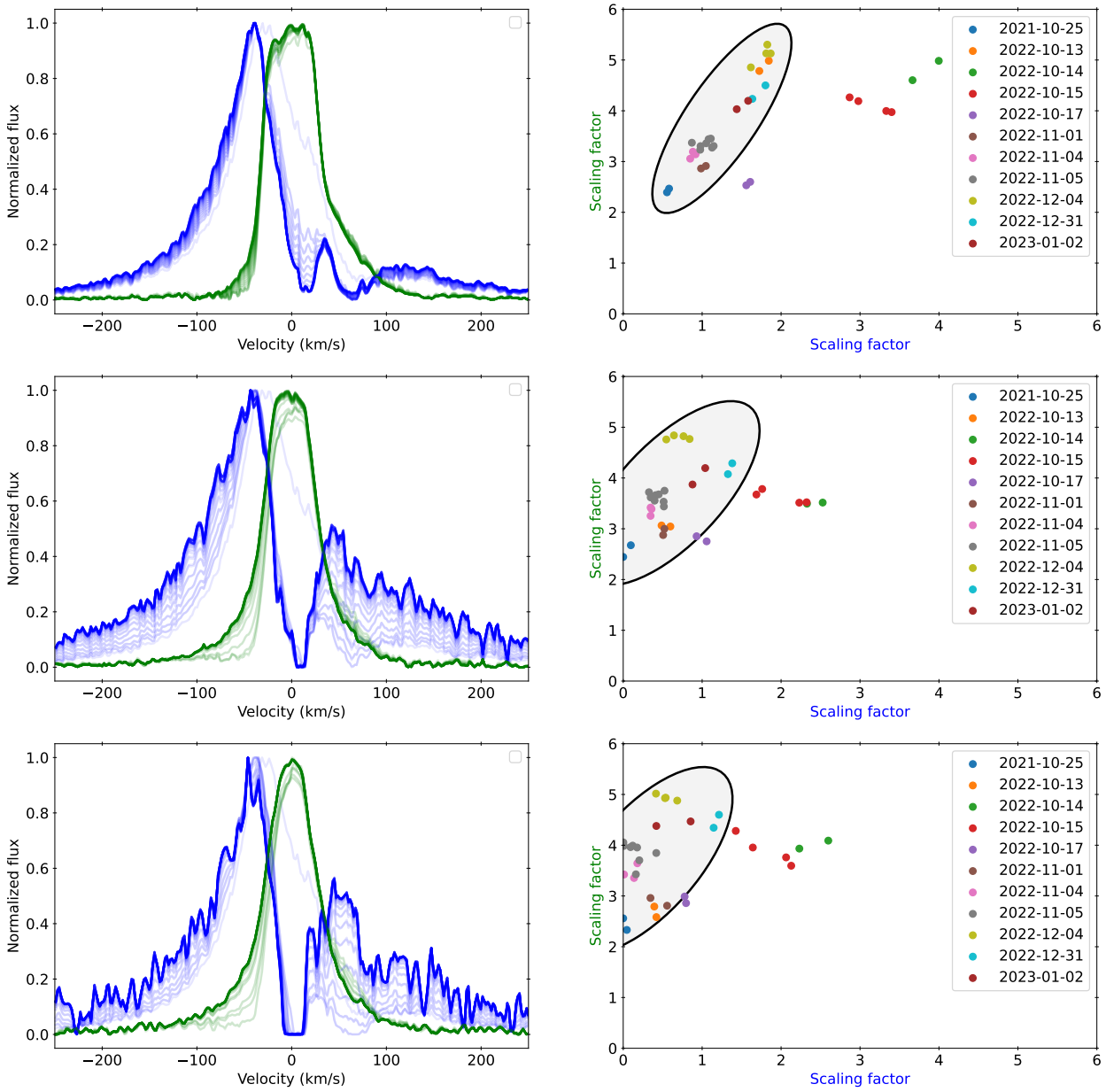


Figure B.8: Same as Fig. III.26, for H_β, H_γ and H_δ. Two-components decomposition for the H_α, H_β and H_γ lines respectively (rows), along iterations (transparent lines). The first column shows the two components normalized to 1. Second column are the scaling factors of each component depending on the epoch.

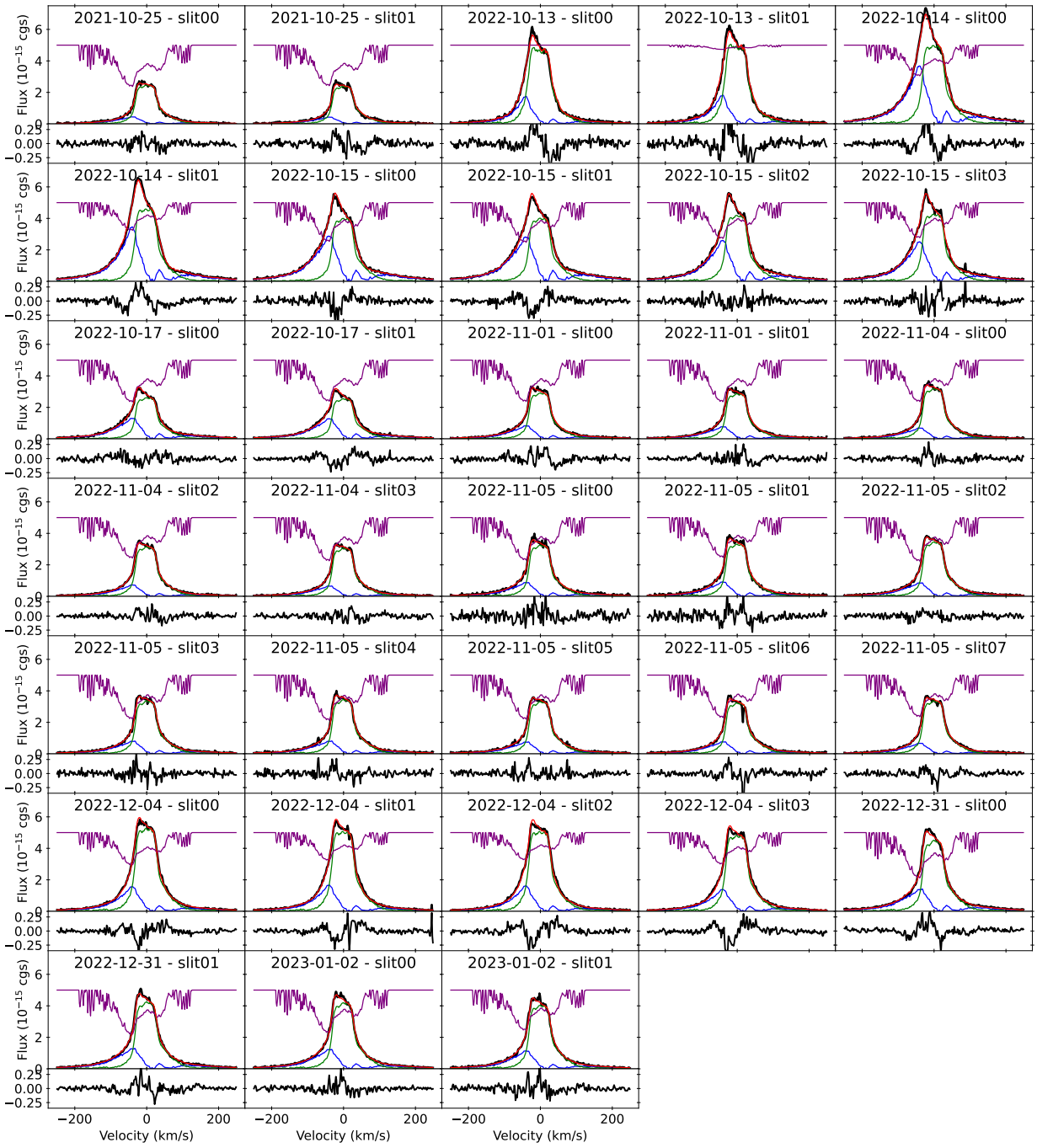


Figure B.9: Three-components fits of all epochs, at the last iteration. Each sub-panel is divided in the fit and the corresponding residuals.



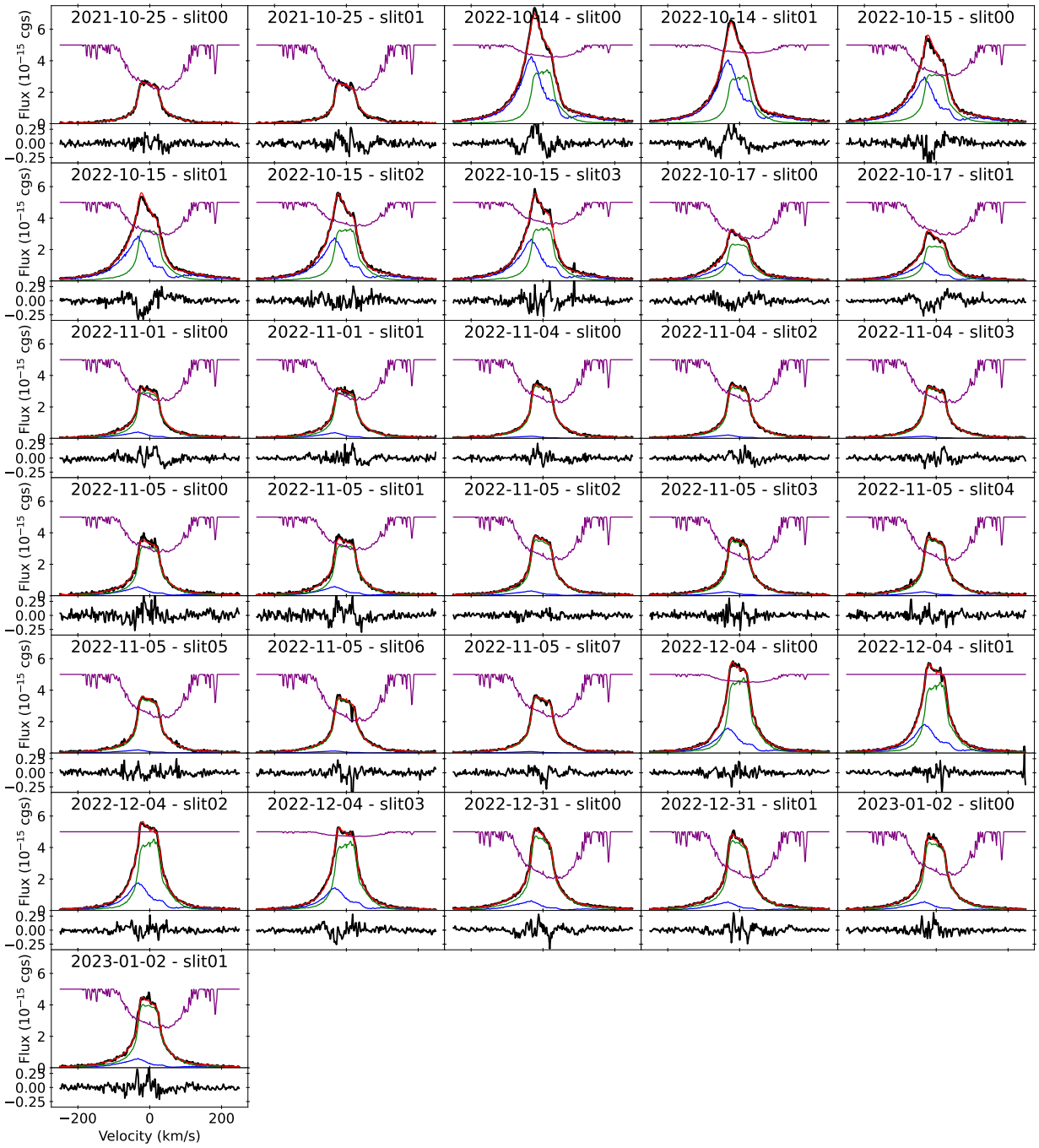


Figure B.10: Three-components fits of all epochs, at the last iteration, excluding the 2022-10-13 epoch. Each sub-panel is divided in the fit and the corresponding residuals.

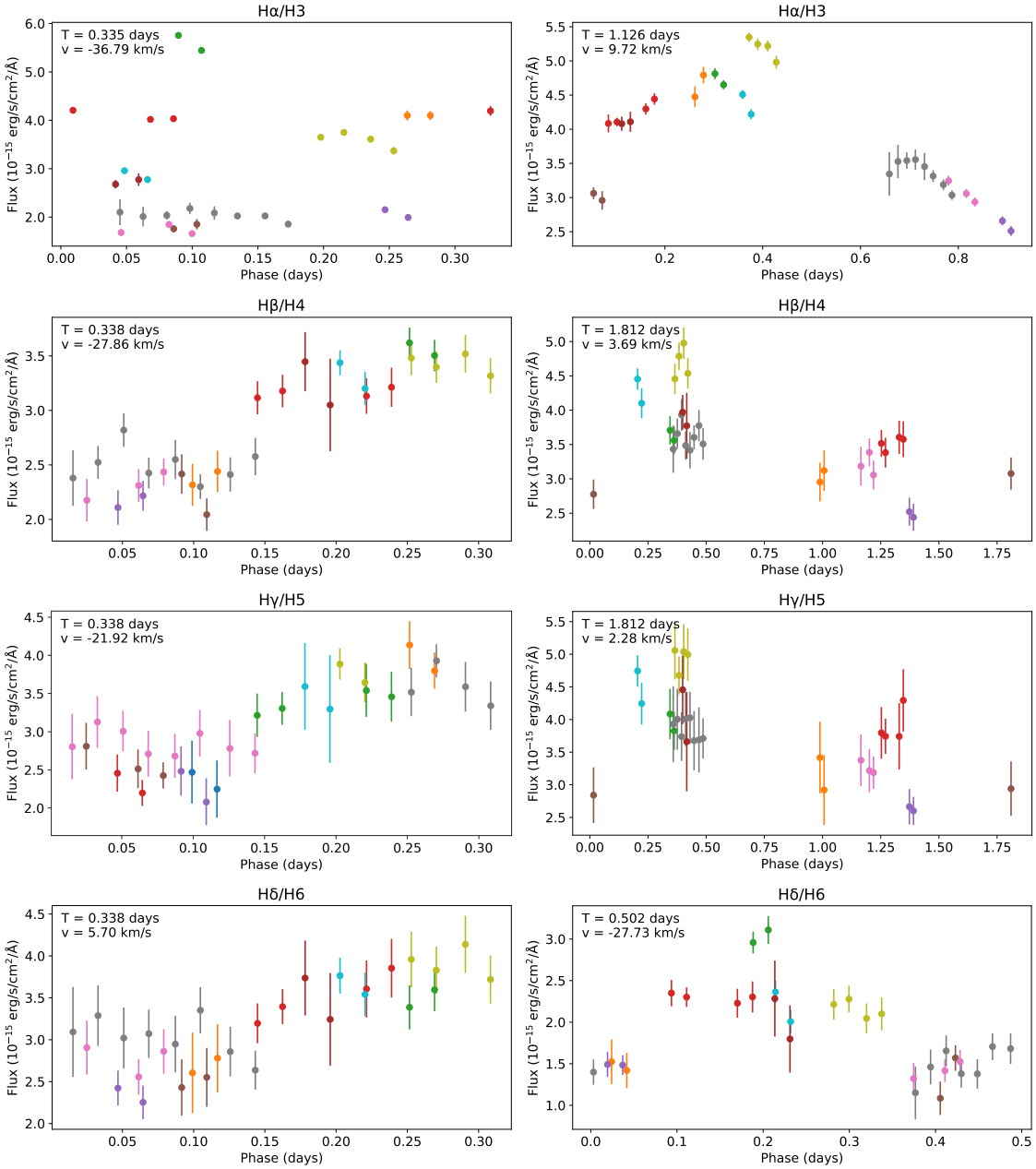


Figure B.11: 1D periodograms for the integrated flux of a a line (black), and the two-components decomposition of said line (blue/green). The left column is the Lomb-Scargle periodogram, the right column is the CLEAN periodogram. The CLEAN periodogram was normalized to 1 at the highest peak. For each periodogram, the location of its brightest peak is given in the top right corner of the plot.



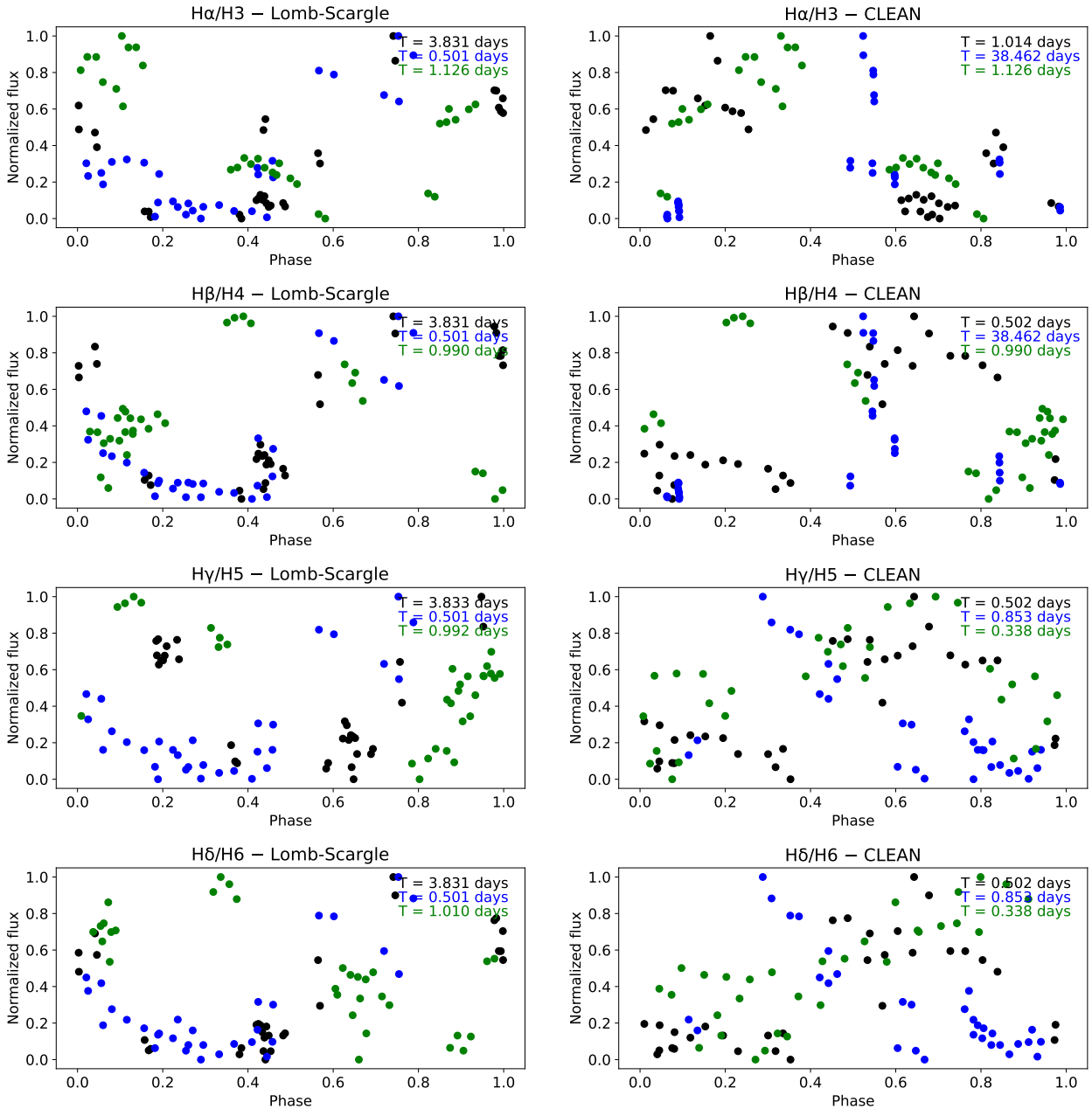


Figure B.12: Wrapped data for the best peak highlighted in Fig. III.39. Black points correspond to the integrated flux values, blue/green points correspond to the two-components decomposition of each line. The phase size is given in the top right corner of each plot, in days.



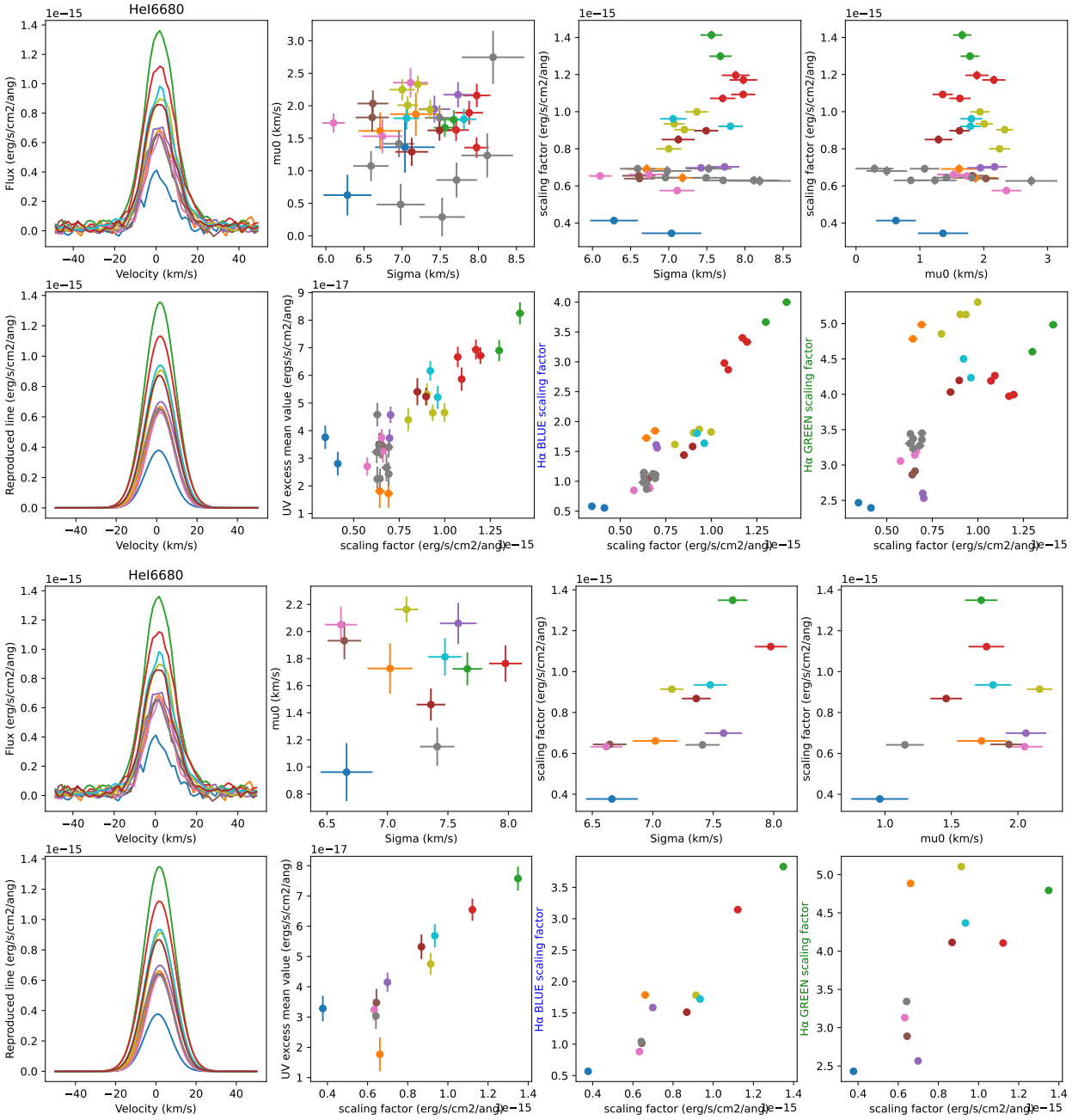


Figure B.13: HeI6680 line: Gaussian fitting results. First two rows: results for all exposures. Last two rows: results for mean line of each epoch. The color code is the same as the one Fig. III.14.

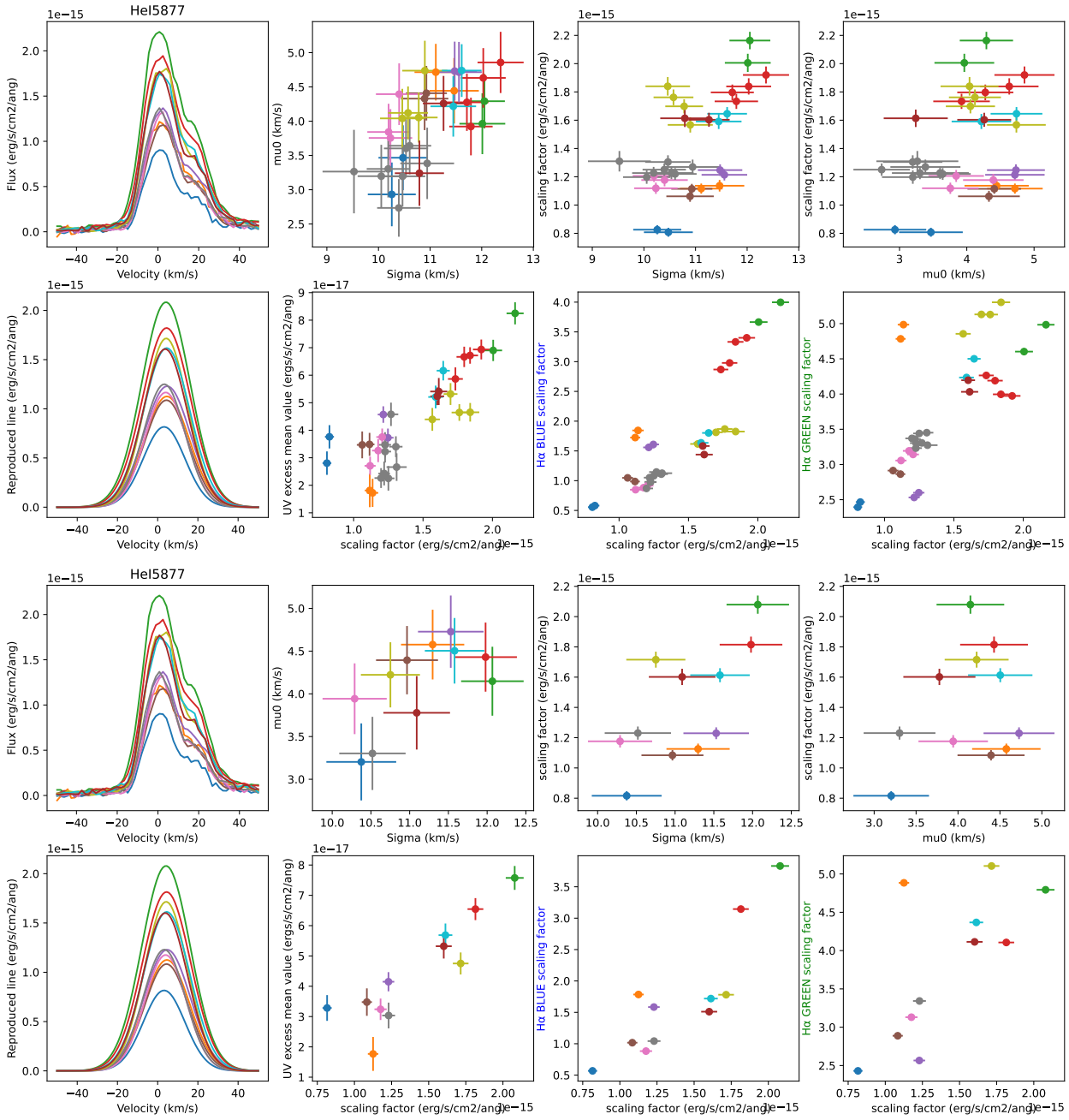


Figure B.14: HeI5877 line: Gaussian fitting results. First two rows: results for all exposures. Last two rows: results for mean line of each epoch. The color code is the same as the one Fig. III.14.



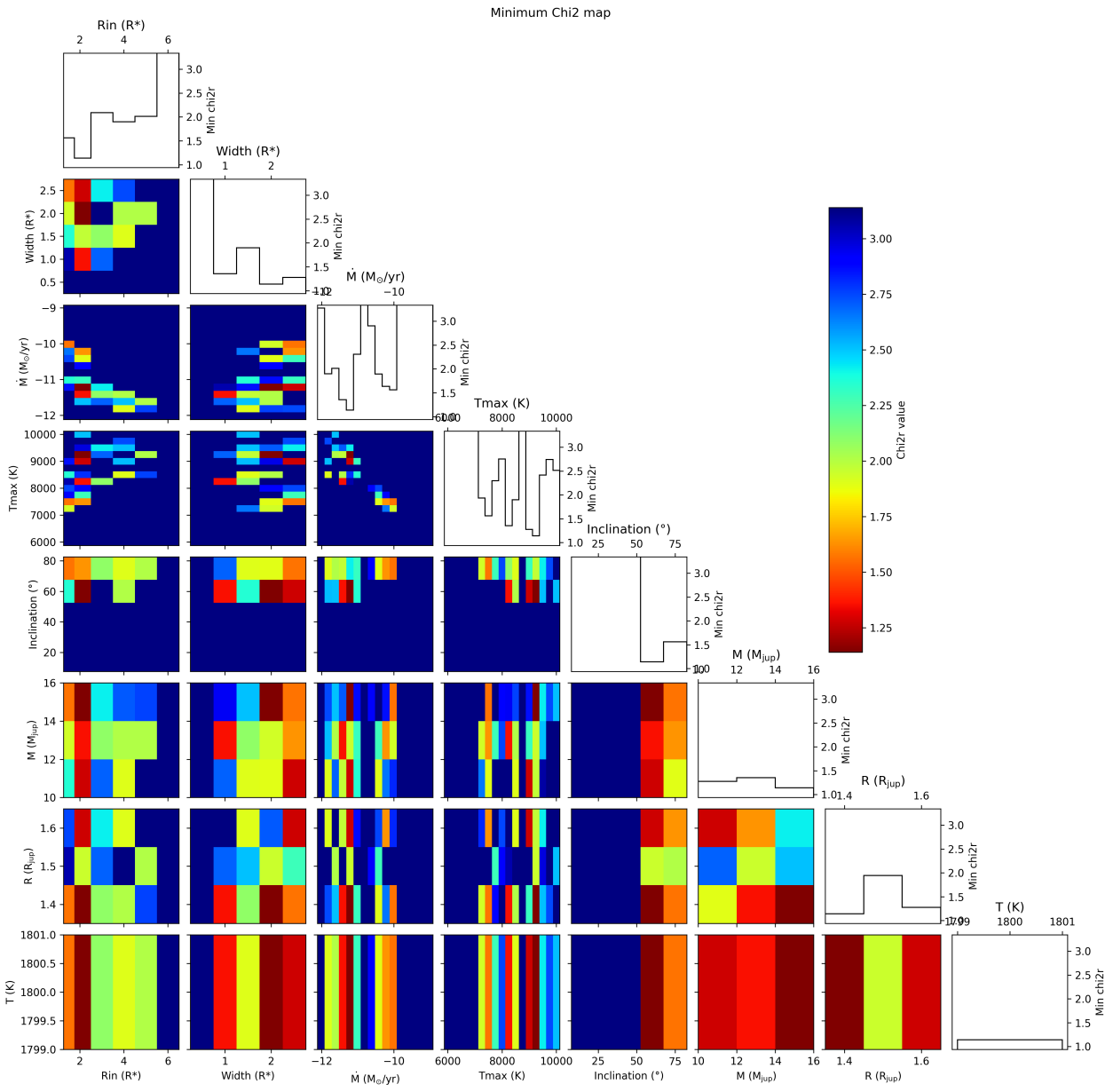


Figure B.15: Lines modeling results: H_{α}, blue component, **core**. Magnetospheric Accretion (Thanathibodee et al., 2019) modeling results for the core $(-50, +50$ km/s) of the blue component of H_{α}.

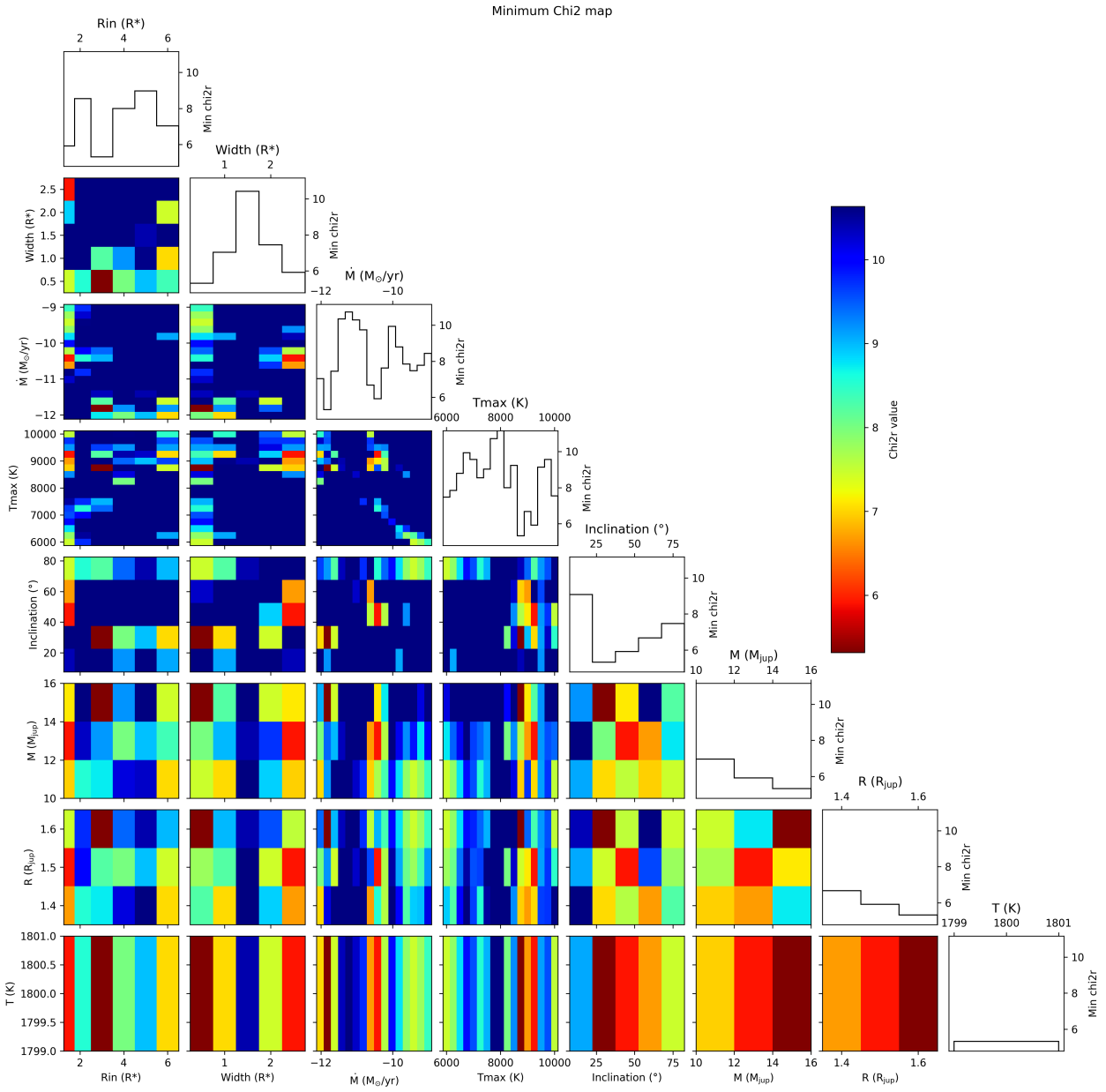


Figure B.16: Lines modeling results: H_{α}, green component, **core**. Magnetospheric Accretion (Thanathibodee et al., 2019) modeling results for the core $(-50, +50$ km/s) green component of H_{α}.

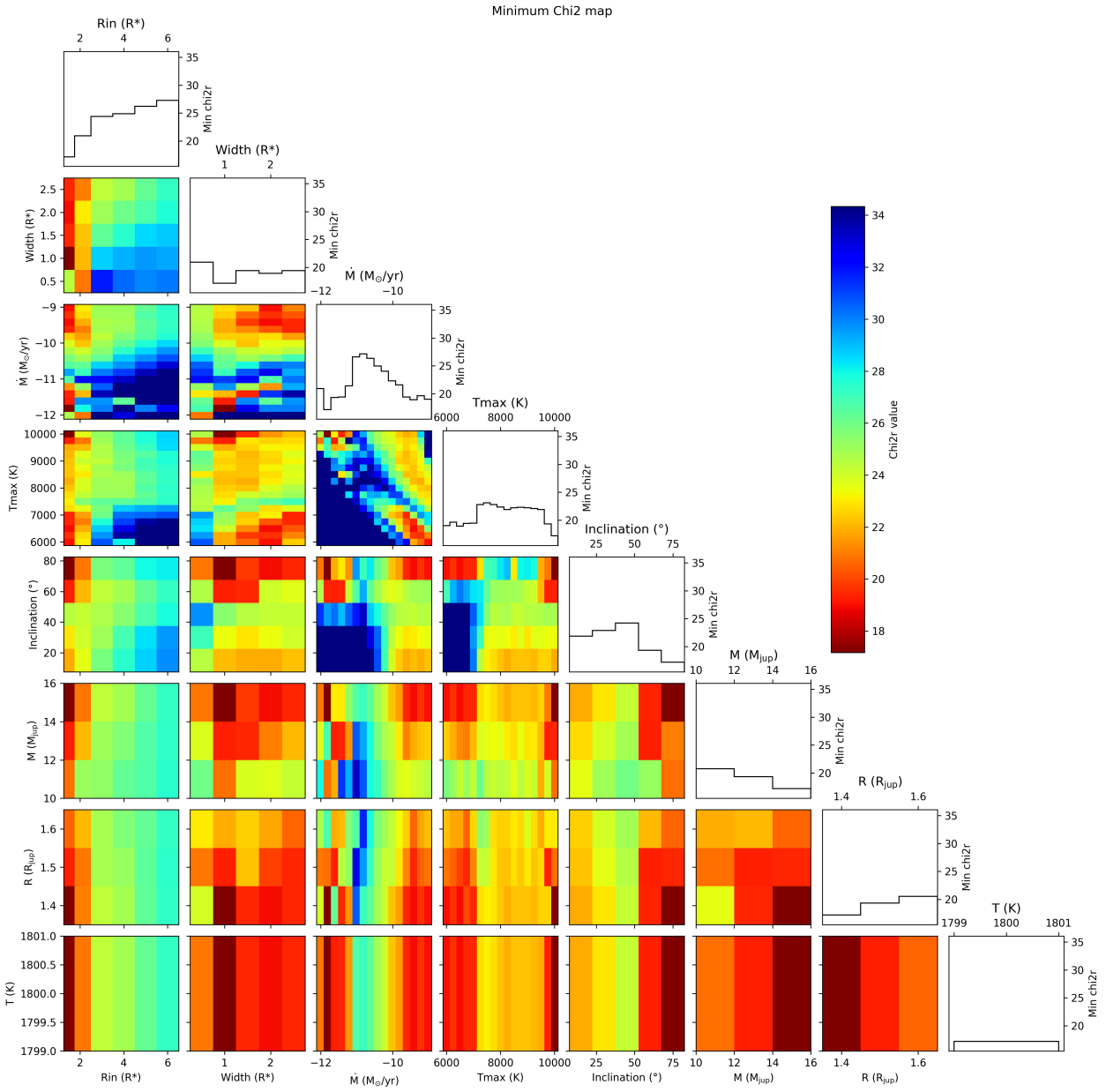


Figure B.17: Lines modeling results: H_{α}, blue component, **full range**. Magnetospheric Accretion (Thanathibodee et al., 2019) modeling results for the full range $(-250, +250$ km/s) of the blue component of H_{α}.

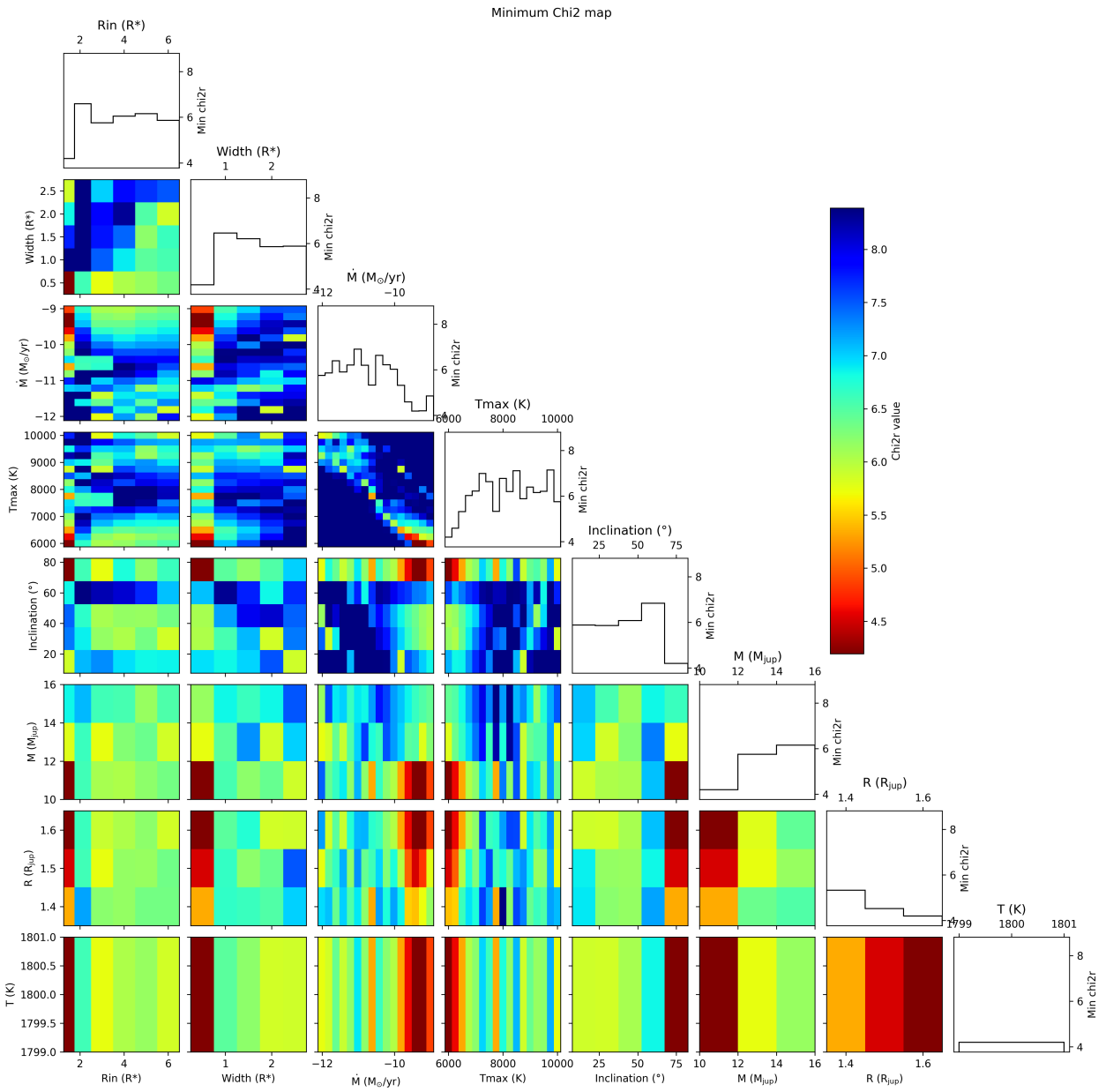


Figure B.18: Lines modeling results: H_{α}, green component, **full range**. Magnetospheric Accretion (Thanathibodee et al., 2019) modeling results for the full range $(-250, +250$ km/s) green component of H_{α}.

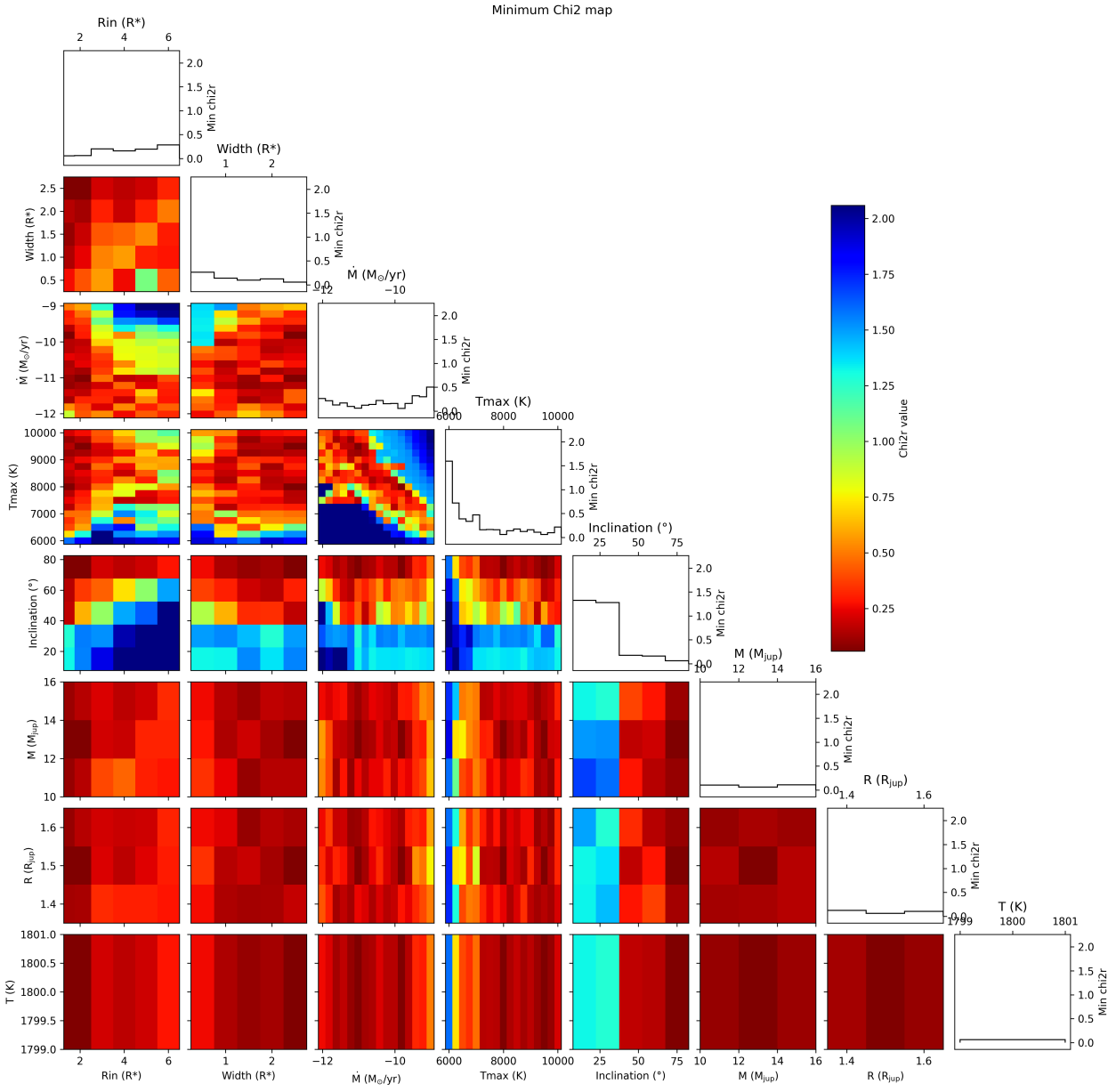


Figure B.19: Lines modeling results: H_β, blue component, **core**. Magnetospheric Accretion (Thanathibodee et al., 2019) modeling results for the core $(-50, +50$ km/s) of the blue component of H_β.

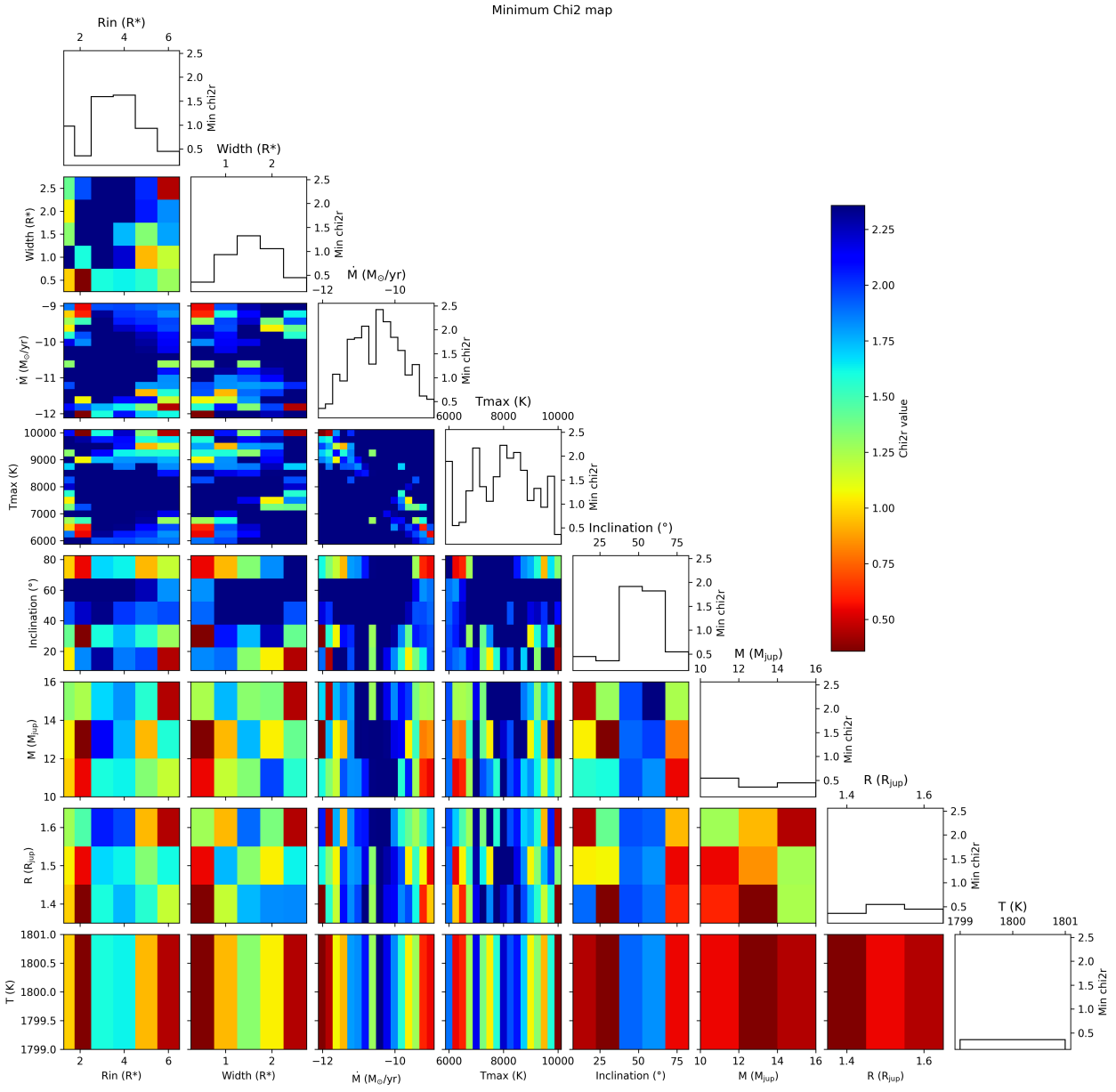


Figure B.20: Lines modeling results: H_β, green component, **core**. Magnetospheric Accretion (Thanathibodee et al., 2019) modeling results for the core $(-50, +50$ km/s) green component of H_β.



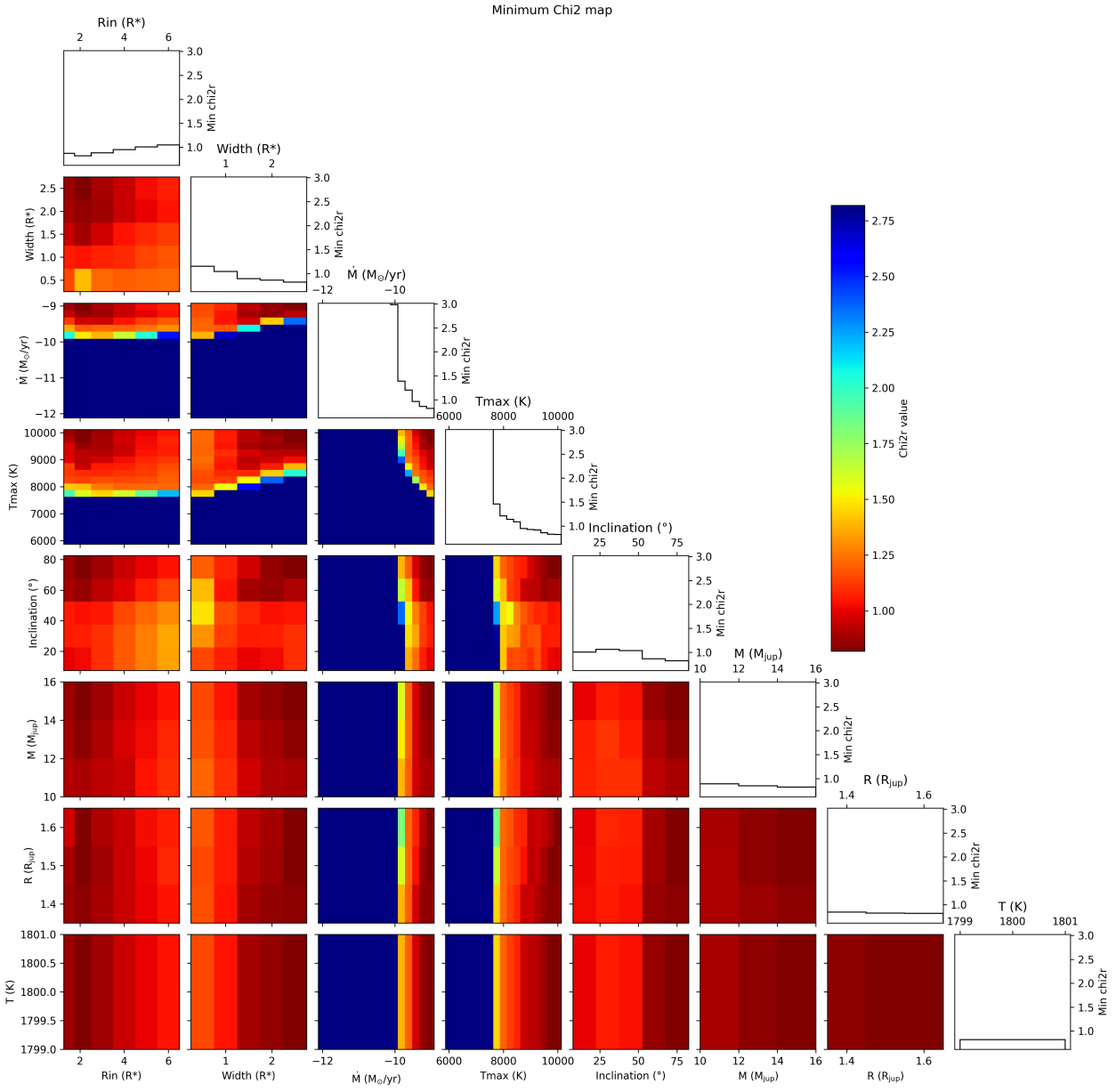


Figure B.21: Lines modeling results: H_β, blue component, **full range**. Magnetospheric Accretion (Thanathibodee et al., 2019) modeling results for the full range $(-250, +250$ km/s) of the blue component of H_β.

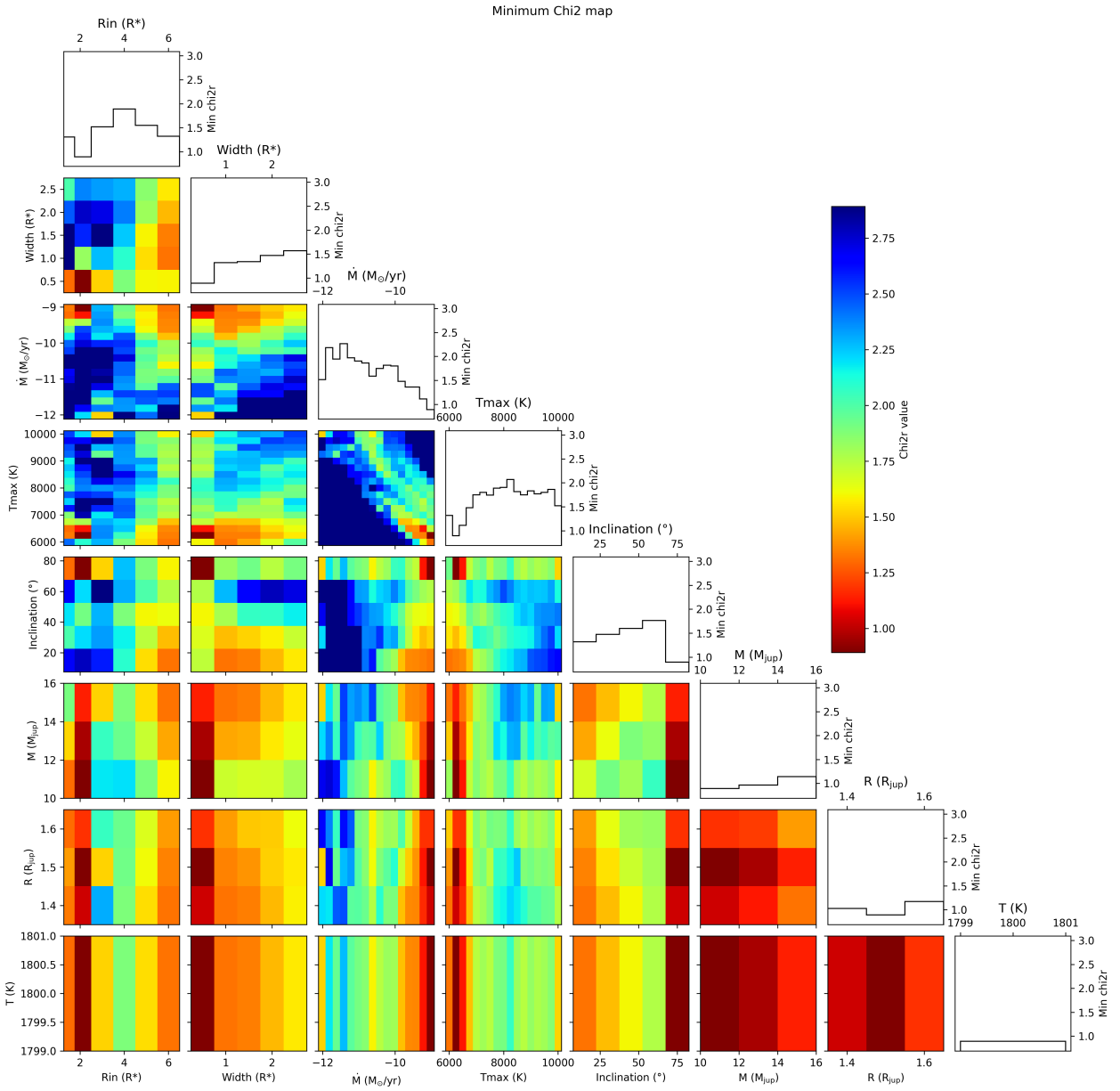


Figure B.22: Lines modeling results: H_β, green component, **full range**. Magnetospheric Accretion (Thanathibodee et al., 2019) modeling results for the full range $(-250, +250$ km/s) green component of H_β.

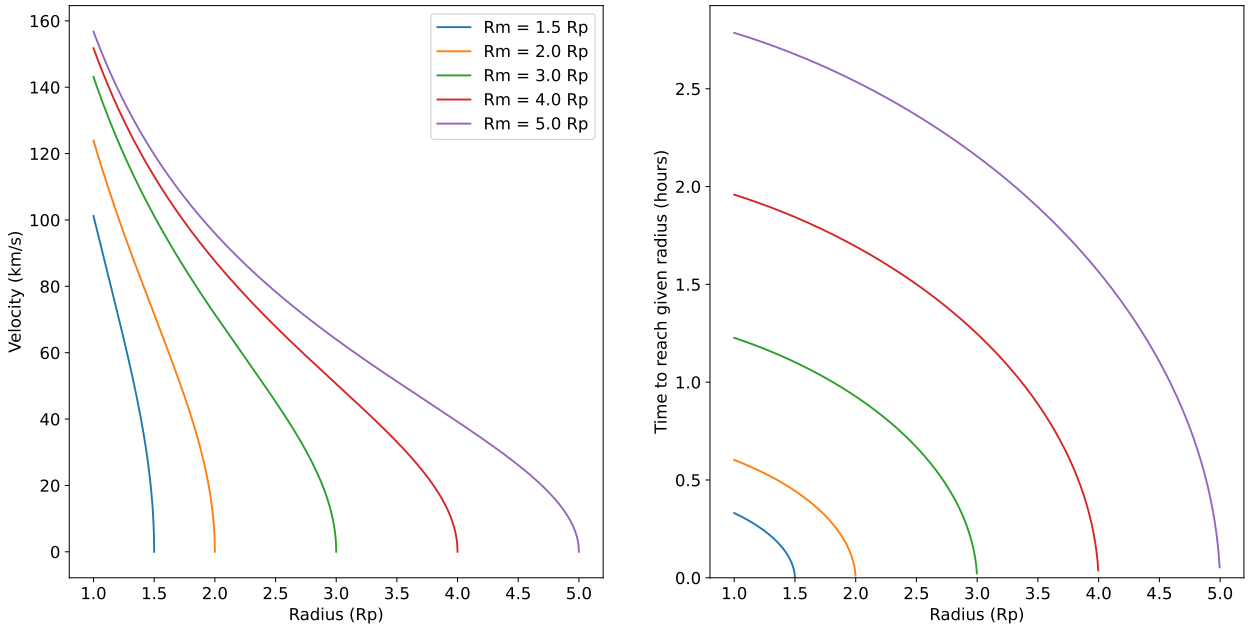


Figure B.23: Left: infall velocity at a given position. Right: Time elapsed to reach a given position, starting at a given truncation radius. The infall velocity is computed as given Equation 2. from Calvet and Hartmann (1992), assuming $M = 13$ M_{Jup} and $R = 1.5$ R_{Jup}.

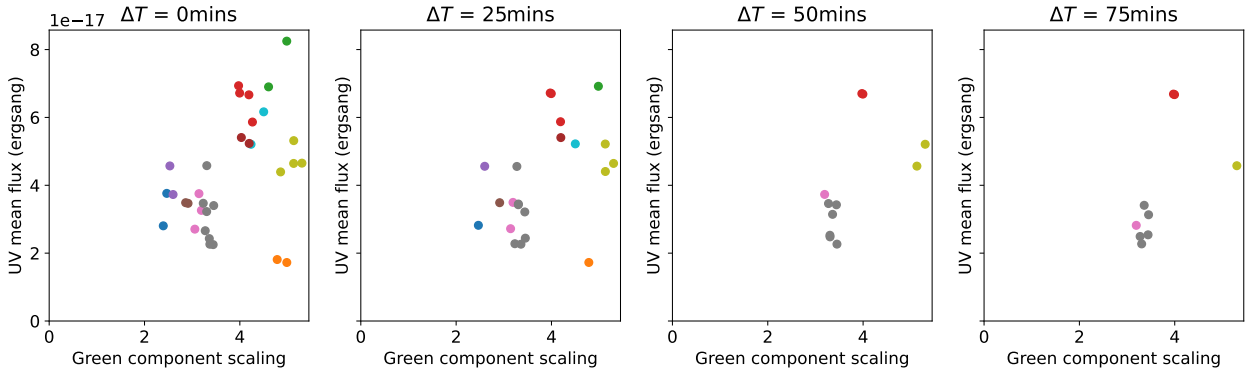


Figure B.24: Correlations between the green component scaling, and the UV excess value, assuming different time-delays, and UV excess emission occurring after the green component emission.

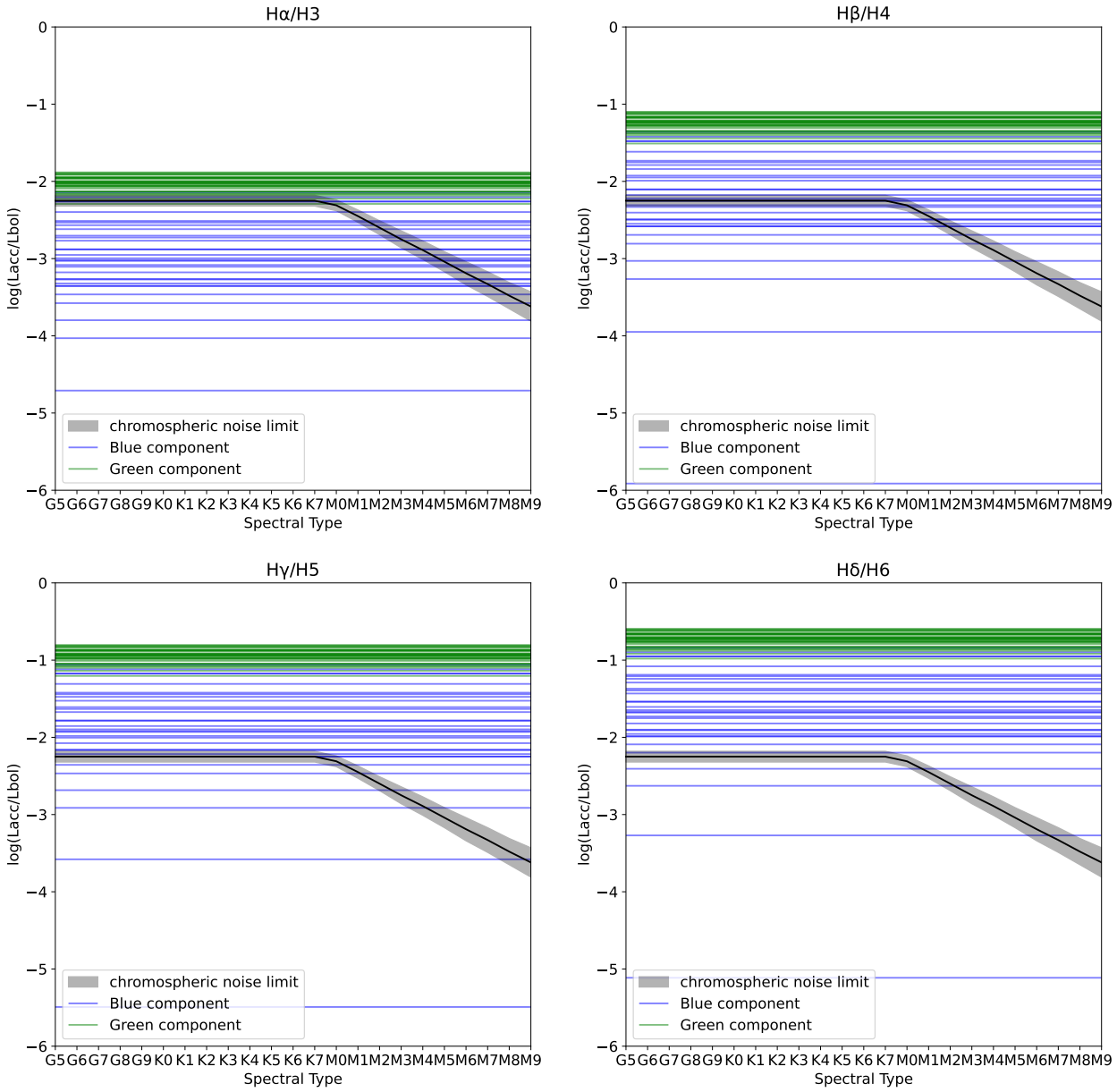


Figure B.25: Chromospheric noise limit (black, Table. 5 from Manara et al., 2017), for H_α, H_β, H_γ and H_δ. In green and blue, the green/blue components fluxes converted into accretion luminosity, using relations from Alcalá et al. (2017). The bolometric luminosity was obtained using ATMO2020 evolutionary tracks (Phillips et al., 2020; Tremblin et al., 2015, 2016), for a 13 M_{Jup} object at 43 Myr.



Astronomy & Astrophysics manuscript no. output
May 26, 2024
©ESO 2024

Exoplanet accretion monitoring spectroscopic survey (ENTROPY)

I. Evidence for magnetospheric accretion in the young isolated planetary-mass object 2MASS J11151597+1937266⋆

Gayathri Viswanath[1], Simon C. Ringqvist[1], Dorian Demars[2], Markus Janson[1], Mickaël Bonnefoy[2], Yuhiko Aoyama[3,4,5], Gabriel-Dominique Marleau[6,7,8,9], Catherine Dougados[2], Judit Szulágyi[10], and Thanawuth Thanathibodee[11,12]

[1] Institutionen för astronomi, Stockholms universitet, AlbaNova universitetscentrum, 106 91, Stockholm, Sweden
e-mail: gayathri.viswanath@astro.su.se
[2] Université Grenoble Alpes, CNRAS, IPAG, 38000 Grenoble, France
[3] Institute for Advanced Study, Tsinghua University, Beijing 100084, PR China
[4] Department of Astronomy, Tsinghua University, Beijing 100084, PR China
[5] Department of Earth and Planetary Science, The University of Tokyo, 7-3-1 Hongo, Bunkyo-ku, Tokyo 113-0033, Japan
[6] Fakultät für Physik, Universität Duisburg–Essen, Lotharstraße 1, 47057 Duisburg, Germany
[7] Institut für Astronomie und Astrophysik, Universität Tübingen, Auf der Morgenstelle 10, 72076 Tübingen, Germany
[8] Physikalisches Institut, Universität Bern, Gesellschaftsstr. 6, 3012 Bern, Switzerland
[9] Max-Planck-Institut für Astronomie, Königstuhl 17, 69117 Heidelberg, Germany
[10] ETH Zürich, Department of Physics, Wolfgang-Pauli-Str. 27, CH-8093, Zürich, Switzerland
[11] Department of Astronomy, University of Michigan, 323 West Hall, 1085 South University Avenue, Ann Arbor, MI 48109, USA
[12] Institute for Astrophysical Research and Department of Astronomy, Boston University, 725 Commonwealth Ave., Boston, MA 02215, USA

Received – ; accepted –

ABSTRACT

Context. Accretion among planetary mass companions is a poorly understood phenomenon, due to the lack of both observational and theoretical studies. Detection of emission lines from accreting gas giants facilitate detailed investigations into this process.
Aims. This work adds another young, sub-stellar object to the sample of few planetary-mass objects with observed emission lines: the isolated L2γ dwarf 2MASS J11151597+1937266 with a mass between 7 and 21 $M_{\rm Jup}$ and an age of 5–45 Myr, located at 45 ± 2 pc.
Methods. We obtained the first high-resolution ($R \sim 50,000$) spectrum of the target with VLT/UVES, an echelle spectrograph operating in the near-UV to visible wavelengths (3200–6800 Å).
Results. We report several resolved H I (H3–H6) and He I emission lines (λ5875.6 Å) in the spectrum. Based on the asymmetric line profiles of Hα and Hβ, 10% width of Hα (199 ± 1 km s^{-1}), tentative 6678 Å He I emission and indications of a disk from MIR excess, we confirm ongoing accretion at this object. We revise its physical parameters based on the more accurate *Gaia* parallax-based distance measurement and derive a mass accretion rate of $\dot{M}_{\rm acc} = 2^{+4}_{-1} \times 10^{-8}\ M_{\rm Jup}\ {\rm yr}^{-1}$ for 2MASS J11151597+1937266 based on H I line luminosities using planetary scaling relations for $L_{\rm line}$–$L_{\rm acc}$. Analysis of observed H I profiles using 1D planet-surface shock model implies a pre-shock gas velocity of $v_0 = 120^{+80}_{-30}$ km s^{-1} and a pre-shock density of $n_0 = 10^{14\ (-5)}$ cm^{-3}.
Conclusions. The line-emitting area predicted from planet-surface shock model is very small ($\sim$ 0.04%), and points to a shock at the base of a magnetospherically induced funnel. The Hα profile exhibits much stronger flux than predicted by the model that best fits the rest of the H I profiles, indicating that another mechanism than shock emission contributes to the Hα emission. Comparison of line fluxes and mass accretion rates from archival moderate-resolution SDSS spectra indicate variable accretion at 2MASS J11151597+1937266.

Key words. planets and satellites: individual: 2MASS J11151597+1937266 – brown dwarfs – accretion, accretion disks – Line: profiles – Techniques: spectroscopic

1. Introduction

The exact nature of accretion among sub-stellar companions has been the subject of several studies for the last two decades. In the stellar regime, the accretion process is well observed and understood, with the collapse of a molecular cloud resulting in a protostar and a circumstellar disk (Adams et al. 1987). The protostar then grows over the next few million years by accreting material from the inner regions of the disk (separated from the star due to the strong magnetic field), along its magnetic field lines, in a process called magnetospheric accretion (Koenigl 1991; Hartmann 1998). Whether the same formation process extends to the sub-stellar regime is still unclear. An alternative theory is that planets have insufficient magnetic field strengths to truncate their disks and instead accrete material via a boundary layer (Lynden-Bell & Pringle 1974; Owen & Menou 2016); recent studies have however indicated that newly formed giant planets and brown dwarfs can possess magnetic field strengths

⋆ Based on observations collected at the European Southern Observatory under ESO programme 0111.C-0166(A).

of up to a few kilogauss (Reiners & Christensen 2010; Batygin 2018; Kao et al. 2018). Consequently, there is ambiguity regarding whether hydrogen emission lines from accreting giant protoplanets originate from the gas in magnetospheric accretion funnels (Thanathibodee et al. 2019), similar to the stellar case (Calvet & Gullbring 1998; Muzerolle et al. 2001), or from shock-heated gas at the surface of the planet or from the circumplanetary disk (CPD), or from both (Szulágyi et al. 2014; Zhu 2015; Szulágyi & Mordasini 2017; Aoyama et al. 2018; Szulágyi & Ercolano 2020; Aoyama et al. 2021). It is also yet to be confirmed if the decreasing trend seen among stars and brown dwarfs between their accretion rate and mass (Rebull et al. 2000; Muzerolle et al. 2003; Natta et al. 2004; Mohanty et al. 2005; Muzerolle et al. 2005; Venuti et al. 2019) extends down to the planetary mass range. A major reason behind the lack of a conclusive explanation on formation of brown dwarfs and planetary mass companions (PMCs) has been the absence of observational evidence of accretion from such objects, mainly due to the technical limitations up to now.

With the recent era of sensitive, high-resolution instruments, there has been a rising number of observations of accreting planetary mass objects in the last few years. The PDS 70 system serves as a benchmark in this context, with Hα detection from both its protoplanets b and c (in $\sim$ 20 and $\sim$ 30 au orbits respectively) at several epochs via circumstellar disk imaging (Wagner et al. 2018; Haffert et al. 2019; Hashimoto et al. 2020; Zhou et al. 2021) and ALMA (ALMA Partnership et al. 2015) detection of the CPD around PDS 70c (Isella et al. 2019; Benisty et al. 2021). Hα emission has also been reported around the protoplanetary candidate LkCa 15b (Sallum et al. 2015); however imaging and spectroscopic follow-up at subsequent epochs (Whelan et al. 2015; Mendigutía et al. 2018; Currie et al. 2019) have attributed the detection to disk features and extended Hα emission around the star LkCa 15. Lately, accretion signatures have been detected spectroscopically in the form of H I emission lines from brown dwarf and planetary mass companions like Delorme 1 (AB)b (Eriksson et al. 2020; Betti et al. 2022; Ringqvist et al. 2023), TWA 27B (Luhman et al. 2023), GSC 06214-00210 b, GQ Lup b (Demars et al. 2023) and SR 12C (Santamaría-Miranda et al. 2018, 2019), which are all essentially isolated companions in wide orbits ($>$ 50 au), with the exception of TWA 27B. High resolution observations of emission lines from such accreting targets enable detailed investigations of line luminosities and profile asymmetries, which in turn give a wealth of information about the nature of accretion process itself. Such direct spectroscopic observations of low-mass objects in the cradle of formation help in the continuing effort to constrain formation mechanisms in the sub-stellar regime and understand the differences in accretion process (if any) not only among planets, brown dwarfs and stars but also between planetary mass objects in close orbits (like the PDS 70 system) and isolated/essentially isolated environments.

The target of this study, 2MASS J11151597+1937266 (hereafter 2M1115), joins the slow-growing sample accreting substellar objects that can be directly observed. It was identified by Theissen et al. (2017) as a young, low surface gravity object of spectral type L2 as part of the LaTE-MoVeRS survey. The object showed strong hydrogen (H I) and helium (He I) emission in its optical spectrum, as well as mid-infrared (MIR) excess in its spectral energy distribution (SED). A follow-up study by Theissen et al. (2018) points to the presence of H I and He I emission lines in the moderate-resolution (R$\sim$2000) optical spectrum from multiple SDSS (Sloan Digital Sky Survey; York et al. 2000) epochs, indicating that the object possesses either persistent enhanced magnetic activity or weak accretion or both. Based on the signs of possible ongoing accretion and the indications of a disk around the object from the excess MIR flux, the age was loosely constrained to 5–45 Myr. Using its low-resolution (R$\sim$120) near-infrared (NIR) spectrum from SpeX (Rayner et al. 2003), the spectral type of the object was constrained to L2γ and the mass to 7–21 $M_{\rm Jup}$ based on evolutionary models. Table 1 summarises the known properties of 2M1115. Theissen et al. (2018) also identified a potential co-moving, young ($\lesssim$100 Myr) M-type star 2MASS J11131089+2110086 (hereafter 2M1113) at an angular separation of 1.62° from the target with similar proper motion and radial velocities. Neither 2M1115 nor 2M1113 has been identified to be associated to any known nearby young moving groups (NYMGs), posing the possibility of being members of a yet undiscovered kinematic group or being ejected by a known NYMG. 2M1115 thus joins the growing population of young, isolated low mass stellar and sub-stellar objects, and is also relatively nearby (45.21 ± 2.20 pc). Therefore the object becomes an ideal target to study sub-stellar formation scenarios and pave the way to a deeper understanding of the nature of accretion in brown dwarfs and PMCs.

Here, we present the first high resolution observations of 2M1115 in the optical to near-UV wavelength range (described in Section 2). The data reduction is described in Section 3. In Section 4, we outline the results from the observations, with the detection of several emission lines that offer an in-depth look into the accretion at this young PMC. A detailed investigation of the line profiles is also presented in this section, along with a discussion on the possible association with 2M1113. Section 5 outlines the implication from these results.

2. Observations with VLT/UVES

2M1115 was observed as part of the "ExoplaNeT accRetion mOnitoring sPectroscopic surveY" (ENTROPY) survey with the Ultraviolet and Visual Echelle Spectrograph (UVES; Dekker et al. 2000) mounted at Unit Telescope 2 of the Very Large Telescope (VLT) at the Paranal Observatory, Chile, between 2023 June 10–11 (MJD 60105, 60106). A total of four frames at 740 s exposure each were obtained across the two nights, giving a total integration time of 0.82 hr. The seeing was measured to be $\sim$ 1.43″ on an average across both nights of observations, at an average air mass of $\sim$ 1.416. The observing log is given in Table A.1. The observations were carried out in Dichroic #1 mode with both the blue and red arms of the instrument, centered at 390 nm and 580 nm respectively, with overlapping wavelength ranges in the subsequent orders of each arm. Between the two arms, and using a slit width of 0.8″, these observations offer a high resolution[1] of $R_\lambda \sim 50,000$–$53,000$ over wavelengths from 3200–6800 Å.

3. Data reduction

Since the continuum of the target is very weak in the observed wavelength range, only its emission lines are readily visible in the raw data. As a result, the automatic ESO/UVES reduction and extraction pipeline failed to produce usable results. We therefore implemented a manual data reduction scheme, based on the raw data and existing calibration files. Basic reduction of the data was performed by subtracting the bias, correcting for flat-field and removing the inter-order background. Cosmic rays

[1] https://www.eso.org/observing/dfo/quality/UVES/reports/HEALTH/trend_report_ECH_RESOLUTION_DHC_HC.html

Parameter	Value	Reference
	Measured	
ICRS RA (α, ep=2016.0)	168.816234°	Gaia Collaboration (2022)
ICRS Dec. (δ, ep=2016.0)	+19.623939°	Gaia Collaboration (2022)
Parallax [mas]	22.12 ± 1.07	Gaia Collaboration (2022)
$\mu_{\alpha*} = \mu_\alpha \cos(\delta)$ [mas yr^{-1}]	−69.53 ± 1.32	Gaia Collaboration (2022)
μ_δ [mas yr^{-1}]	−25.21 ± 1.48	Gaia Collaboration (2022)
G [mag]	20.41 ± 0.02	Gaia Collaboration (2022)
J [mag]	15.59 ± 0.06	Cutri et al. (2003)
H [mag]	14.57 ± 0.06	Cutri et al. (2003)
K_S [mag]	13.80 ± 0.05	Cutri et al. (2003)
W1 (ALLWISE) [mag]	13.09 ± 0.02	Cutri et al. (2021)
W2 (ALLWISE) [mag]	12.55 ± 0.03	Cutri et al. (2021)
W3 (ALLWISE) [mag]	10.77 ± 0.12	Cutri et al. (2021)
W4 (ALLWISE) [mag]	> 8.68	Cutri et al. (2021)
	Derived	
Distance [pc]	45.21 ± 2.20	Gaia Collaboration (2022)
Spectral Type	L2γ ± 1	Theissen et al. (2018)
RV [km s^{-1}]	−14 ± 7	Theissen et al. (2018)
Age [Myr]	5–45	Theissen et al. (2018)
Mass [$M_{\rm Jup}$]	7–21	Theissen et al. (2018)
	6^{+8}_{-3}	This work
Radius [$R_{\rm Jup}$]	1.5 ± 0.1	This work
$T_{\rm eff}$ [K]	1816 ± 63	This work
$\log(L_{\rm bol}/L_\odot)$	−3.63 ± 0.05	This work

Table 1. Basic parameters for 2M1115, both from the literature and derived in this work. The mass estimate from Theissen et al. (2018) depends on their photometric distance estimate for the target, $d_{\rm phot}$ = 37 ± 6 pc (but see Section 5).

were accounted for by using a horizontal median filtering, as well as by masking out pixels higher than 10 times the photon noise at the location. Extraction of the object spectrum was performed using standard aperture photometry within an aperture size of 10 pixels in the spatial direction for the blue arm and 20 pixels for the red arm, centered on the object location in the slit. Sky background and telluric lines were removed by subtracting the flux within the respective aperture sizes of the blue and red arms, but with the apertures placed instead at both the ends of the slit. Wavelength calibration was performed using the arc lamp spectrum and a Th–Ar line list.

The 1D spectrum thus extracted was flux calibrated based on the instrument's response curve derived from the observations of a standard star taken with the same observing set-up as the target (see Section B for further details). Since the seeing was greater than 1″ for all four observations, the calibrated flux was compensated for the loss from seeing (∼ 30%) by determining a 1D point spread function (PSF) along the spatial direction in the data, constructing a corresponding 2D PSF by assuming circular symmetry, and calculating the fractional flux lost outside of the 0.8″ wide slit in the dispersion direction. A barycentric velocity correction was applied to the wavelength calibration for each frame using `astropy.skycoord` at Cerro Paranal at the respective time of observation. A stacked spectrum was then obtained by using the weighted average across all four observations, with the weights determined from the respective photon noise. The flux uncertainties were determined by the weighted standard deviation across the individual spectra. The stacked, calibrated UVES spectrum will be made available at the VizieR archives[2] hosted by the Strasbourg astronomical Data Center (CDS).

4. Results and Analysis

We report the first resolved H I and He I emission line detections from 2M1115 in the optical to near-UV wavelengths. We present confirmed detection of the H I emission lines Hα to H6, and He I line at 5875.62 Å (listed in Tables D.1 and G.1). Tentative detections of H7, He I at 6678.15 Å and possible metal lines Ca II H (3968.47 Å), Fe I (λ3834.22, 3967.42, 4259.99, 4839.54, 4970.50, 4986.22, 5329.99, 5684.43, 6083.66, 6636.96, and 6703.57 Å), Ti I (5720.43 Å) and Cr I (5991.07 Å) have also been noted but are not statistically significant with the signal-to-noise ratio (SNR) of the existing data; these are listed in Table G.1. The identification scheme for the confirmed and tentative lines are described in Appendix C.

4.1. Characteristics of neutral-hydrogen lines

We detected H I emission lines from H3–H6 with strong SNR ($> 5\sigma$) in the spectrum. H4 (Hβ) was detected in two consecutive orders 2 and 3 of the lower Red (RedL) arm, but had an SNR of only 4.3σ in order 3 as it was near the edge of the order where the spectrum was generally noisier. Hence, we only include the stronger detection in order 2 (9σ) in our main analysis. H5 (Hγ)

[2] https://cdsarc.cds.unistra.fr

was also detected in orders 34 and 35 of the Blue arm with similar SNR (4.6σ), resulting in a root mean square (rms) SNR of 6.5σ; hence the average of their respective line fluxes is used for the main analysis. Although H7 was detected in both orders 24 (1.7σ) and 25 (3.6σ) of the Blue arm, the rms SNR was still below 5σ and is thus classified as a tentative detection.

The line profiles were determined by performing Gaussian fits on the average-smoothed spectrum with a box size of 3 pixels, and are shown in Figure 1 and Figure 2 for the confirmed line detections, Hα–H6. The integrated line fluxes and luminosities of H I lines estimated thus are listed in Table 2 (refer Table D.1 for profile characteristics). We note that H6 is brighter than H5 in the spectrum[3] and is double peaked in all four individual spectra (see Figure 2, lower panel). The increase in the line flux corresponding to the two peaks could be caused by possible blending with Fe I lines at 4101.26 Å and 4101.65 Å. H5 in order 35 of the Blue arm has a clear flux increase at the bluer end of its line profile (see Figure 2, upper panel). We suspect the cause to be possible blending with a metal line; most likely with Fe I at 4340.49 Å. However the SNR is not high enough to make statistically reliable claims based on these features.

4.2. Mass accretion rate for 2M1115

The H I line luminosities can be used to estimate accretion luminosities for 2M1115 using scaling relations of the form

$$\log(L_{\rm acc}/L_\odot) = a \times \log(L_{\rm line}/L_\odot) + b, \quad (1)$$

where a and b represent the fit coefficients for the scaling relations of each transition. Given the existing estimate of mass range for the target ($M_{\rm p} \approx$ 7–21 $M_{\rm Jup}$), we used $L_{\rm line}$–$L_{\rm acc}$ relations from Aoyama et al. (2021) for the lines H3–H7, formulated for planetary mass objects ($M_{\rm p} \approx$ 2–20 $M_{\rm Jup}$) based on spectrally resolved, non-equilibrium models for hydrogen emission due to a shock on the planetary surface. The resulting accretion luminosities for the target are listed in Table 2.

We derived mass accretion rates for 2M1115 from the estimated accretion luminosities of the H I lines based on the established relation for stars

$$\dot{M}_{\rm acc} = \left(1 - \frac{R_{\rm p}}{R_{\rm in}}\right)^{-1} \frac{L_{\rm acc} R_{\rm p}}{G M_{\rm p}}, \quad (2)$$

where $M_{\rm p}$ represents the mass of the accreting object (taken here as 14 ± 7 $M_{\rm Jup}$), $R_{\rm p}$ its radius and $R_{\rm in}$ the inner radius of a truncated circumplanetary disk in a magnetospheric accretion scenario (Hartmann et al. 2016). On setting $R_{\rm in} = 5\ R_{\rm p}$ (Gullbring et al. 1998; Alcalá et al. 2017; Ringqvist et al. 2023), $\dot{M}_{\rm acc} \approx L_{\rm acc} R_{\rm p}/G M_{\rm p}$, which remains valid for a planet-surface shock scenario under the assumption that the entire kinetic energy from the shock is converted into radiation (Marleau et al. 2019).

The existing radius estimate for 2M1115 in the literature ($R_{\rm p} = 1.3 \pm 0.2\ R_{\rm Jup}$; Theissen et al. 2018) is based on an earlier photometric distance measurement of 37 ± 6 pc from before the *Gaia* DR3 observation of the target. With the more accurate *Gaia*-parallax-based distance measurement for the target (45.21 ± 2.20 pc), the radius estimate was in need of revision. For this purpose, we performed an SED fit to the existing photometry of 2M1115 using BT-Settl AGSS 20009 (Allard et al. 2012, 2013; Asplund et al. 2009), AMES-Dusty (Chabrier et al. 2000; Allard et al. 2001) and DRIFT-PHOENIX (Baron et al. 2003; Helling et al. 2008; Witte et al. 2011) model photospheres via the Virtual Observatory SED analyzer (VOSA[4]; Bayo et al. 2008) version 7.5 (see Section H for details). The corresponding parameters for the target from the best-fitting models are $T_{\rm eff} = 1816 \pm 63$ K, $\log(L_{\rm bol}/L_\odot) = -3.63 \pm 0.05$ and $R_{\rm p} = 1.5 \pm 0.1\ R_{\rm Jup}$.

Using this radius estimate and the mass for 2M1115, we derived a mass accretion rate from each detected H I line (H3–H7) using Equation 2 (listed in Table 2). The average mass accretion rate is $\log(\dot{M}_{\rm acc}/M_{\rm Jup}\,{\rm yr}^{-1}) = -7.75 \pm 0.48$ for the target. In Appendix I, we estimated H3–H7 line fluxes for 2M1115 from its existing, moderate-resolution SDSS DR9 (Ahn et al. 2012) and DR12 (Alam et al. 2015) spectra and, subsequently, derived mass accretion rates $\log(\dot{M}_{\rm acc}/M_{\rm Jup}\,{\rm yr}^{-1})$ of -8.00 ± 0.32 and -7.62 ± 0.32 for DR9 and DR12 respectively. The mass accretion rate estimate from the UVES data is, respectively, $\sim 0.5\sigma$ higher and $\sim 0.3\sigma$ lower (in dex) than those from SDSS DR9 and DR12. We discuss this difference further in Section 5.

We also estimated accretion rates using $L_{\rm line}$–$L_{\rm acc}$ scaling relations from Alcalá et al. (2017) that were derived empirically based on a sample of young, low-mass stars. Contrary to Aoyama et al. (2021), these relations assume that H I emission in case of stellar accretion is coming from gas in the accretion funnels that follow the magnetic field lines onto the stellar surface. The $L_{\rm acc}$ and $\dot{M}_{\rm acc}$ values estimated from the detected H I lines based on these stellar scaling relations are also listed in Table 2. The average mass accretion rate estimated thus for 2M1115 is $\log(\dot{M}_{\rm acc}/M_{\rm Jup}\,{\rm yr}^{-1}) = -8.61 \pm 0.64$. This is ∼1 dex lower than the estimate from Aoyama et al. (2021) scaling relations, similar to what was seen in Ringqvist et al. (2023) for Delorme 1 (AB)b.

As an independent check, we also derived a mass accretion rate for the target using the 10% width (W_{10}) of its Hα line. Natta et al. (2004) developed an empirical relation between $\dot{M}_{\rm acc}$ and Hα W_{10}, for accretors with $W_{10} \gtrsim 200$ km s^{-1} (Jayawardhana et al. 2003), using a sample of very low mass objects and T-Tauri stars, spanning a mass range of $0.04 \lesssim M_\star/M_\odot \lesssim 0.8$, given by

$$\log(\dot{M}_{\rm acc}) = -12.89(\pm0.3) + 9.7(\pm0.7) \times 10^{-3} W_{10}\,, \quad (3)$$

where W_{10} is in km s^{-1} and $\dot{M}_{\rm acc}$ is in $M_\odot\,{\rm yr}^{-1}$. Using the measured W_{10} of the overall Hα profile for the target (199.4 ± 1.2 km s^{-1}), we get an accretion rate of $\log(\dot{M}_{\rm acc}/M_{\rm Jup}\,{\rm yr}^{-1}) = -7.94 \pm 0.33$, which is consistent with the average $\dot{M}_{\rm acc}$ estimate from Aoyama et al. (2021) scaling relations within the uncertainties. It is important to note here that values of $\dot{M}_{\rm acc}$ and Hα 10% width of the sample used in Natta et al. (2004) are mostly not simultaneous measurements, and hence the resulting $\dot{M}_{\rm acc}$ from the relation should be interpreted with caution. Regardless, the value serves as a cross-check on the mass accretion rate for 2M1115, since it relates the observed Hα width directly to $\dot{M}_{\rm acc}$ instead of relying on a $L_{\rm line}$–$L_{\rm acc}$ scaling relation.

[3] Similar behaviour has also been observed in the ∼ 40 Myr PMC Delorme 1 (AB)b, where H6 was observed to be overluminous (see Ringqvist et al. 2023).

[4] http://svo2.cab.inta-csic.es/theory/vosa/

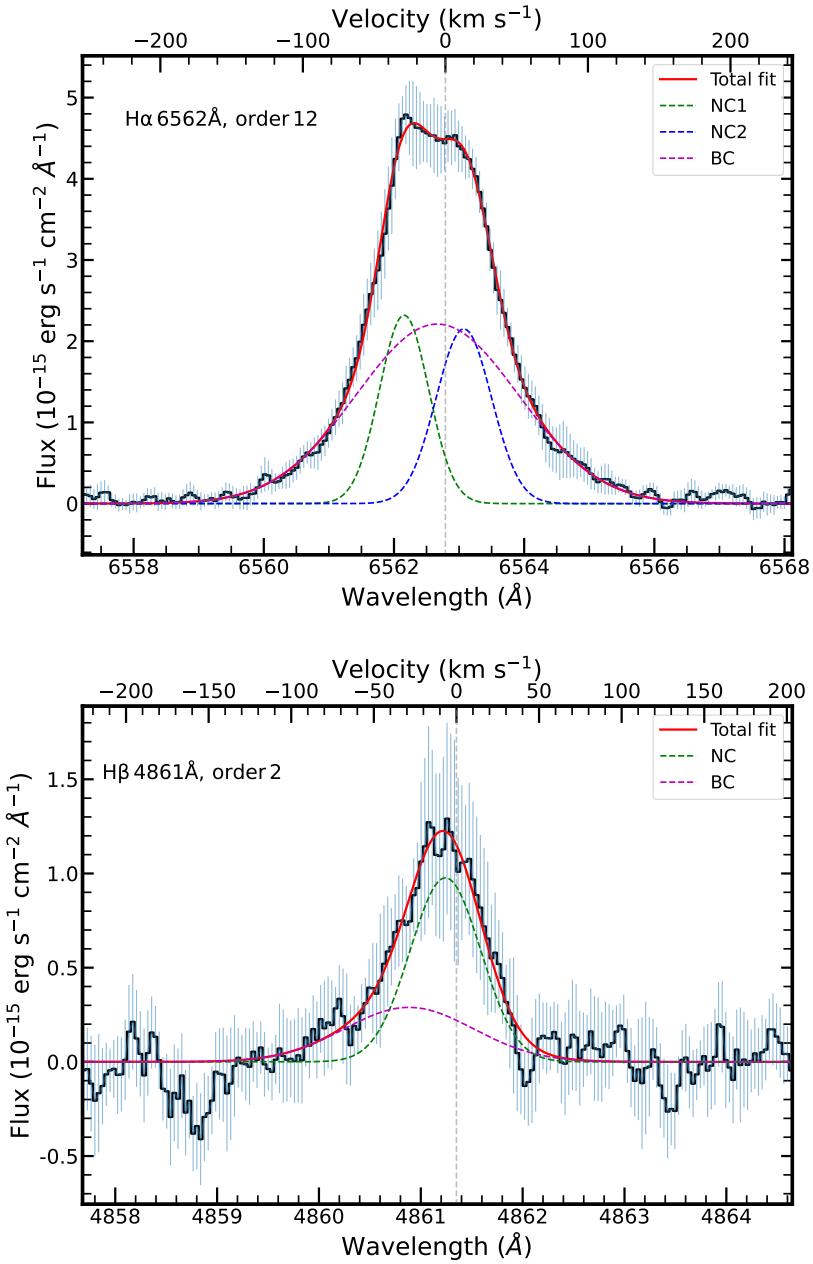


Fig. 1. Line profiles of Hα in the RedU arm (top panel), and Hβ in the RedL arm (bottom panel) of the UVES spectrum of 2M1115. NC, BC indicate narrow component and broad component, respectively, of the total Gaussian fit to the profile. The flux uncertainties are shown as vertical error bars and represent the weighted standard deviation among the four observations. Velocity is set with respect to the rest-frame wavelength (in air) of the respective lines.

4.3. Asymmetry in the line profiles

Among the detected H I lines, Hα and Hβ show clear asymmetries in their line profiles. Following Ringqvist et al. (2023), we fit multi-component Gaussian models to their line profiles, composed of a combination of narrow (NC) and broad (BC) components. The best model for each line was determined as the one that gave the least χ^2, calculated as

$$\chi^2 = \sum_i \left[\frac{N_i - fi}{\sigma_i} \right]^2 , \quad (4)$$

where σ_i is the error in the measurement N_i, and f_i is the corresponding model prediction. The resulting line profile fits for Hα and Hβ are given in Figure 1 and their characteristics are given in Table D.1. Such a multi-component profile fit is reasonable as explained in the planet-surface shock model of accretion

Line	order, arm	$F_{\rm line}/10^{-15}$ (erg s^{-1} cm^{-2})	$\log(L_{\rm line})$ ($L_\odot$)	$\log(L_{\rm acc})$ ($L_\odot$)		$\log(\dot{M}_{\rm acc})$ ($M_\odot$)	
				A21	Al17	A21	Al17
Hα (H3)	12, RedU	$11.39^{+4.65}_{-1.92}$	-6.14 ± 0.15	-4.22 ± 0.18	-5.20 ± 0.40	-7.54 ± 0.34	-8.52 ± 0.49
Hβ (H4)	2, RedL	$1.31^{+4.07}_{-0.64}$	-7.08 ± 0.45	-4.69 ± 0.41	-5.48 ± 0.61	-8.01 ± 0.50	-8.80 ± 0.67
Hγ (H5)	34-35, Blue	$0.52^{+2.71}_{-0.37}$	-7.48 ± 0.47	-4.76 ± 0.42	-5.61 ± 0.63	-8.08 ± 0.51	-8.93 ± 0.69
Hδ (H6)	28, Blue	$1.48^{+4.91}_{-0.72}$	-7.02 ± 0.45	-4.13 ± 0.41	-4.87 ± 0.59	-7.45 ± 0.50	-8.19 ± 0.66
Hϵ (H7)	25, Blue	$0.47^{+5.81}_{-0.34}$	-7.52 ± 0.48	-4.33 ± 0.43	-5.28 ± 0.62	-7.65 ± 0.52	-8.60 ± 0.68

Table 2. Integrated fluxes, luminosities and mass accretion rates for the H I lines detected in 2M1115 UVES spectrum. RedU, RedL refers to the upper and lower detectors of the Red arm of UVES respectively. $L_{\rm acc}$ values were estimated from $L_{\rm line}$ using both planetary scaling relations from Aoyama et al. (2021, A21) for H3–H7, as well as stellar scaling relations from Alcalá et al. (2017, Al17). The line flux for Hγ listed here is the average of the fluxes obtained in orders 34 and 35 of the Blue arm.

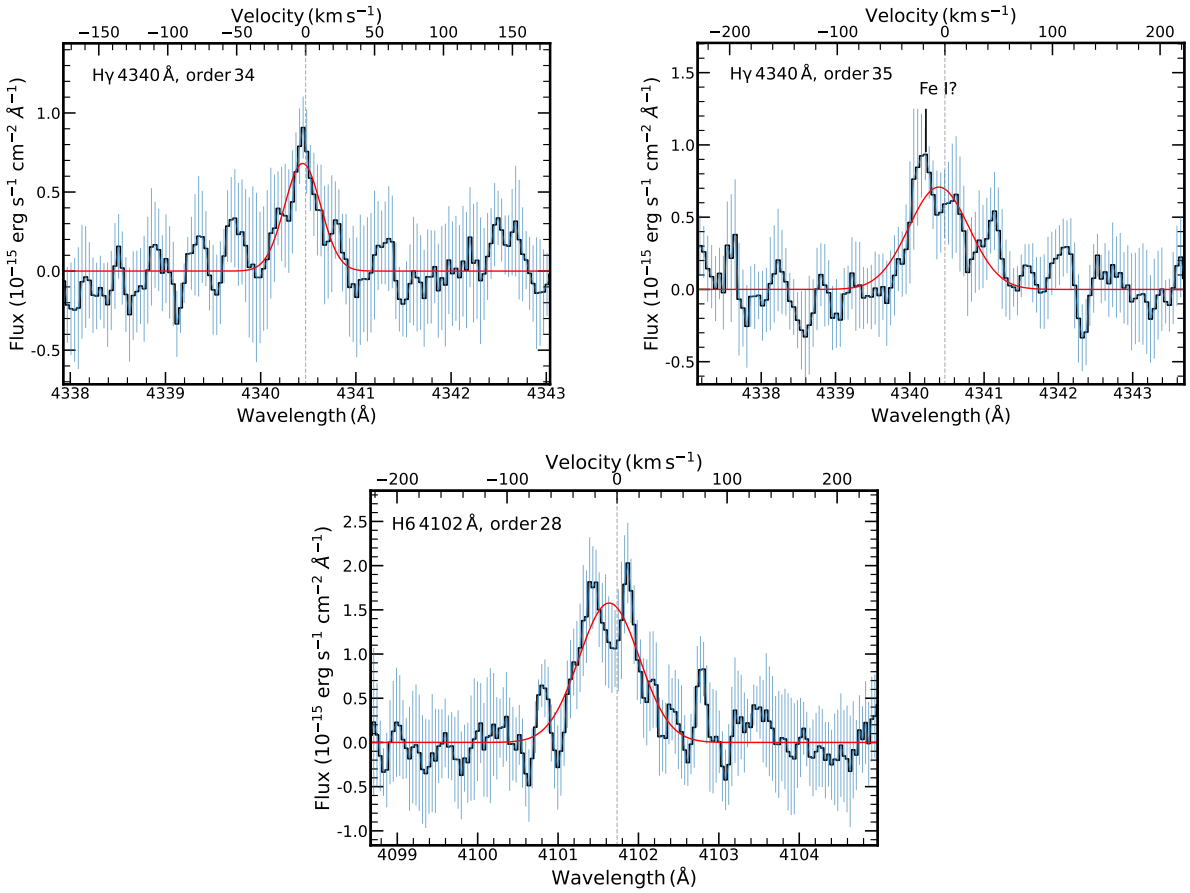


Fig. 2. Line profiles of (upper panel) Hγ in orders 34 and 35, and (lower panel) Hδ in order 28 detected in the UVES spectrum for 2M1115 in the Blue arm. The flux uncertainties are shown as vertical error bars and represent the weighted standard deviation among the four observations. Velocity is set with respect to the rest-frame wavelength (in air) of the respective lines.

in Aoyama et al. (2018, 2021), where the hotter ($\gtrsim 10^5$ K) gas in the immediate post-shock region is receding away from the observer into the planet and leads to a broad, redshifted profile. Comparatively, gas coming from deeper below the shock region originates at lower temperatures ($\approx 10^4$ K) and is thus narrower. In Section 5, we discuss the significance of these profile fits further.

We also fit the obtained H I line profiles with predictions from Aoyama et al. (2020, 2021) 1D planet-surface shock models as a function of pre-shock velocity v_0 and pre-shock number density n_0. We allowed the model grid to vary from v_0 = 50 – 200 km s^{-1} and n_0 = 10^9 – 10^{14} cm^{-3} during the fitting process. The observed Hα emission from the target is quite strong compared to the other H I lines. One reason could be the strong dependence of extinction on wavelength, as seen in PDS 70b and c (Hashimoto et al. 2020) . On setting the extinction to a high value of A_v = 3.5 mag, the model shows a good fit to both Hα and Hβ, but very weak predictions for H6 and

H7, making the overall model prediction unsatisfactory. A simple interpretation from this analysis could be that the main origin for Hα emission is not the shock-heated region. Aoyama et al. (in prep) has demonstrated similar, strong contamination for Hα with other than shock-heated gas (e.g., gas along accretion columns or chromospheric activity) using archival data for massive planets > 10 $M_{\rm Jup}$. In these cases the line profiles show better agreement with the model for Hβ and higher order lines, on excluding Hα from the analysis. Accordingly, we repeated our fitting process by including only the lines H4–H7 and fixing the extinction to $A_v = 0$ mag. The resulting fit reproduces the H4–H7 line profiles very well within their flux uncertainties, with model parameters of $v_0 = 120^{+80}_{-30}$ km s^{-1} and $n_0 = 10^{14\ (-5)}$ cm^{-3} (see Section E for details on the fitting process and the inference of uncertainties on these parameters). This is a strong indication for the possibility that shock emission is a minor component for Hα.

Considering the pre-shock gas velocity from the best-fit Aoyama et al. (2020, 2021) model as the free-fall velocity of the in-falling gas, we can derive a mass estimate $M_{\rm p}$ for the accreting PMC (Aoyama & Ikoma 2019) using

$$M_P = \frac{R_P v_0^2}{2G}. \quad (5)$$

With $R_{\rm p} = 1.5 \pm 0.1\ R_{\rm Jup}$ and $v_0 = 120^{+80}_{-30}$ km s^{-1}, we get a mass estimate of $M_{\rm p} = 6^{+8}_{-3}\ M_{\rm Jup}$ for 2M1115. The resulting mass range (3–14 $M_{\rm Jup}$) is lower than the mass range for the object in the literature (see Table 1). The best-fit pre-shock velocity and number density also help in estimating the fraction of the planetary surface from where the accretion flow emits the H I line radiation, the filling factor f_f (Aoyama & Ikoma 2019), as

$$\dot{M} = 4\pi R_P^2 f_f \mu' n_0 v_0. \quad (6)$$

Here, μ' is the mean weight per hydrogen nucleus. The resulting filling factor obtained from the best-fit n_0, v_0 values and the average mass accretion rate obtained from the observations is 0.04%.

4.4. Likelihood of being bound to 2M1113

As mentioned in Section 1, the M-type star 2MASS J1113+2110 has been suggested to be likely physically associated with 2M1115 based on their spatial proximity and similarity in age and space motion (Theissen et al. 2018), with a 1.8% probability of chance alignment between the two. In light of *Gaia* DR3 observations of these objects, we revisited their properties. Similar to Theissen et al. (2018), neither 2M1115 nor 2M1113 are seen belonging to any of the known stellar associations as implied from the membership probabilities calculated from the Bayesian Analysis for Nearby Young AssociatioNs Σ (BANYAN Σ; Gagné et al. 2018) tool based on their proper motion, parallax, distance and RV (both show 99.9% probability to be a field object). With the new *Gaia* distance measurements, the projected physical separation corresponding to the 1.62° angular separation between the two is 1.28 pc; approximately the same as the distance to Proxima Centauri from Sun (1.29 pc; Turbet et al. 2016). Although the proper motion of 2M1113 ($\mu_{\alpha^*} = -68.932 \pm 0.194$ mas yr^{-1}, $\mu_\delta = -21.985 \pm 0.190$ mas yr^{-1} Gaia Collaboration 2022) agrees within ≈ 1.6 mas yr^{-1} of that of 2M1115, their parallax differ by ≈ 4.4σ (parallax = 17.34 ± 0.25 mas for 2M1115; Theissen et al. 2018), which reduces the likelihood of the two objects being bound.

To investigate further the possibility that 2M1115 and 2M1113 are physically bound, we calculated the tidal radius of 2M1113 as $R_{\rm tid} = 1.35\ {\rm pc} \times (M_\star/M_\odot)^{1/3}$ (Jiang & Tremaine 2010; Mamajek et al. 2013). Based on the Theissen et al. (2018) mass range for the object (45–75 $M_{\rm Jup}$), we assumed a mass of 60 ± 15 $M_{\rm Jup}$ resulting in $R_{\rm tid} = 0.52 \pm 0.04$ pc. At the distance of 2M1113 (57.66 ± 0.84 pc) this corresponds to a tidal radius of 0.52 ± 0.04°. 2M1115 being at a projected angular separation of 1.62°, is significantly beyond the the tidal influence of 2M1113. Hence the hypothesis that the two are gravitationally bound can be ruled out. However, given the similar proper motion and radial velocities (RV= −10.1 ± 0.3 km s^{-1} for 2M1113; Theissen et al. 2018) there is a possibility for the two objects to share the same dynamical origin.

5. Discussion

From our observations using VLT/UVES at a high resolution $R \sim 50,000$ across the optical to near-UV wavelength range, we have detected the first resolved H I emission from the young, isolated, L2γ dwarf 2MASS J1115+1937, from Hα to H7. The Hα emission from the object is broad, with a full width at 10% peak flux of 199.4 ± 1.2 km s^{-1}. This puts 2M1115 right at the 200 km s^{-1} threshold for accretion in very low mass stars and brown dwarfs (Mohanty et al. 2005). Together with the asymmetries in the observed Hα, Hβ profiles and the tentative detection of the He I emission at 6678 Å (refer Table G.1), the object displays clear signs of accretion, corroborated by the indicative presence of a disk around the object as seen from the SED (see Figure H.1).

Mohanty et al. (2005) and Muzerolle et al. (2005) presented extensive catalogues of observed Hα profiles from low-mass stars and sub-stellar objects, along with their mass accretion rates measured from their Ca II (λ8662 Å) flux in the former, or using radiative transfer modelling based on magnetospheric accretion flows (Muzerolle et al. 2001) in the latter. Our profile fit for Hα emission from 2M1115 agrees well with those of the M7-type dwarf CFHT BD Tau 4 from Mohanty et al. (2005) and Cha Hα 1, KPNO 6 of spectral types M7.75, M8.5 respectively, from Muzerolle et al. (2005) (see Figure F.1). CFHT BD Tau 4, of mass ∼ 60 $M_{\rm Jup}$, is classified as a possible accretor based on its Hα 10% width, the presence of a disk and Ca II (λ8662 Å) emission, with a reported mass accretion rate $\dot{M}_{\rm acc} \approx 1.3 \times 10^{-8}\ M_{\rm Jup}\ {\rm yr}^{-1}$ estimated from the latter (Mohanty et al. 2005). The model-predicted profile fits in Muzerolle et al. (2005) to the accretors Cha Hα 1 (∼ 35 $M_{\rm Jup}$) and KPNO 6 (∼ 25 $M_{\rm Jup}$) indicate mass accretion rates of 5.25×10^{-9} and $4.17 \times 10^{-9}\ M_{\rm Jup}\ {\rm yr}^{-1}$ respectively. The average mass accretion rate obtained for 2M1115 using Aoyama et al. (2021) scaling relations ($1.8^{+3.6}_{-1.2} \times 10^{-8}\ M_{\rm Jup}\ {\rm yr}^{-1}$) agree within ∼ 1.1$\sigma$ with the estimated $\dot{M}_{\rm acc}$ for all the three objects, showing consistency with the matching line profiles. The $\dot{M}_{\rm acc}$ obtained based on the Hα W_{10} (Natta et al. 2004), $1.1^{+1.3}_{-0.6} \times 10^{-8}\ M_{\rm Jup}\ {\rm yr}^{-1}$, also agrees well with those of these three accretors. On the other hand, the average $\dot{M}_{\rm acc}$ obtained from the (Alcalá et al. 2017) scaling relations ($2.5^{+8.2}_{-1.9} \times 10^{-9}\ M_{\rm Jup}\ {\rm yr}^{-1}$) is an order of magnitude lower than that of CFHT BD Tau 4, but agrees with those of Cha Hα 1 and KPNO 6.

The associated accretion luminosity derived for 2M1115 from Aoyama et al. (2021) scaling relations is, on average, $\log(L_{\rm acc}/L_\odot) = -4.43 \pm 0.38$. The $T_{\rm eff}$-dependent chromospheric

noise limit from Manara et al. (2013) (see also Venuti et al. 2019) derived from a sample of non-accreting young stellar objects with $T_{\rm eff} \leq 4000$ K is given by

$$\log(L_{\rm acc,\,noise}/L_{\rm bol}) = 6.2(\pm0.5) \times \log(T_{\rm eff}) - 24.5(\pm1.9). \quad (7)$$

This limit describes the simulated luminosity from a non-accreting young star of a certain spectral type (or $T_{\rm eff}$) solely due to its chromospheric activity. The $T_{\rm eff}$ = 1816 ± 63 K we derived translates into a chromospheric noise limit of $\log(L_{\rm acc,\,noise}/L_{\rm bol}) = -4.29 \pm 2.50$ for 2M1115. Together with its estimated $L_{\rm bol}$ from SED fit, this corresponds to a luminosity limit of $\log(L_{\rm acc,\,noise}/L_{\odot}) = -7.92 \pm 2.50$. The estimated accretion luminosity from its H I emission is higher by more than three orders of magnitude (3.5 dex) compared to this noise limit. Thus, it seems unlikely that all the H I lines from 2M1115 are solely due to its chromospheric activity.

Among the detected H I lines, H6 and H7 show similar velocity shifts (within uncertainties) as the systemic RV of −14 ± 7 km s^{-1} (refer Table D.1), along with H5 in order 35 and Hβ in order 3. H5 in order 34 is slightly blue-shifted relative to the systemic velocity. The Hβ profile in order 2 has both broad and narrow components, which are blue-shifted (∼ −15 km s^{-1}) and red-shifted (+7 km s^{-1}) relative to the systemic RV. The Hα profile has two NC in addition to the BC. The BC is red-shifted relative to the system velocity, as predicted by the Aoyama et al. (2018, 2021) models (discussed in Section 4.3), along with a blue-shifted NC; however the red-shifted NC cannot be explained within the planetary accretion shock framework. The Hα emission is also significantly stronger than other detected H I lines, and does not agree with predicted flux from planet-surface shock model that fits the rest of the H I lines very well. This could, as discussed in Section 4.3, point to a partial or even dominating contribution from mechanisms other than shock-heating for Hα emission like heating along the accretion columns or chromospheric activity. The best-fit planet-surface shock model that fits all detected H I lines other than Hα predicts a filling factor of 0.04%, which hints at a magnetospheric accretion geometry for 2M1115 (Ringqvist et al. 2023). This provides a tentative indirect evidence for a magnetic field on such a low-mass and young isolated object.

Moderate-resolution SDSS spectra available for the target from DR9 (March 2007) and DR12 (April 2012) epochs, together with the UVES epoch (June 2023) data, facilitate an analysis of the accretion over time. From Tables 2 and H.1, it can be inferred that the Hα flux decreases by ∼ 7% between 2007 and 2012, and then increases by ∼ 70% between 2012 and 2023. On the other hand, line fluxes for Hβ–H7 increases by 200 − 300% between 2007 and 2012, and decreases by ∼ 100−200% between 2012 and 2023 for Hβ, H5 and H7. For H6, the flux further increases by ∼ 15% between 2012 and 2023. On average, the H I accretion luminosity in the DR12 epoch ($\log(L_{\rm acc}/L_{\odot}) = -4.30 \pm 0.14$) is higher by ∼ 150% from the DR9 epoch ($\log(L_{\rm acc}/L_{\odot}) = -4.68 \pm 0.14$) and by ∼ 35% from the UVES epoch ($\log(L_{\rm acc}/L_{\odot}) = -4.43 \pm 0.38$). The average mass accretion rates estimated from all the H I lines in all three epochs imply the same progression, varying as $\dot{M}_{\rm acc} \approx 1 \times 10^{-8}$, 2.4×10^{-8} and 1.8×10^{-8} $M_{\rm Jup}$ yr^{-1} between the DR9, DR12 and UVES epochs respectively. The trend seen from the hydrogen emission over the three epochs is suggestive of a variability in accretion in the target, and could benefit from a future detailed time-resolved monitoring of the emission lines to investigate this possibility.

A major source of uncertainty in the analysis presented in this work is the loosely constrained mass of the target. The previously reported mass for the target in the literature (7–21 $M_{\rm Jup}$; Theissen et al. 2018) was estimated from evolutionary models using the temperature estimate from SED fit to its *zJHK$_S$W1* photometry based on the photometric distance estimate of 37 pc, and the age range 5–45 Myr. The lower age limit was roughly based on the end of the accretion phase for brown dwarfs (Mohanty et al. 2005) and the upper age limit was taken as that of the oldest accreting object known to harbor primordial circumstellar material (Boucher et al. 2016). With the revised distance and resulting SED fit discussed in Section 4.2, we attempted to constrain the mass further. Using the updated absolute magnitudes in the J, H, K_S bands, from the DUSTY00 atmosphere isochronal models for very low mass stars and brown dwarfs (Chabrier et al. 2000) we infer a mass of ∼ 7.5 $M_{\rm Jup}$ at 5 Myr and ∼ 21 $M_{\rm Jup}$ at 50 Myr. Alternatively, we also interpolated the AMES-Cond (Allard et al. 2001) and BT-Settl (Allard et al. 2012, 2013) model isochronal grids for the temperature from our SED fit (1816 K) in the age range 5–50 Myr. This gives a slightly lower and stricter mass range of 9–15 $M_{\rm Jup}$. The surface gravity ($\log(g) = 3.83 \pm 0.24$) and radius from the best-fit atmospheric models to the SED (refer Appendix H) imply a slightly lower mass range of 6 ± 4 $M_{\rm Jup}$, while the best-fit Aoyama et al. (2018, 2021) model to the observed H I predicts a mass $M_{\rm p} = 6^{+8}_{-3}$ $M_{\rm Jup}$ (refer Section 4.2). The latter estimate is not quite independent from the former since it is calculated partly based on the radius estimate from the SED fit. Nevertheless, the implied mass range from our analysis is slightly lower than the existing mass range in the literature, but still remains fairly large. Depending on the lowest (2 $M_{\rm Jup}$) to highest (21 $M_{\rm Jup}$) value in the mass range listed for the target here, the estimated mass accretion rate ($\dot{M}_{\rm acc}/M_{\rm Jup}$ yr^{-1}) changes by a factor of approximately 1 dex.

Our observations of 2M1115 and the resulting findings demonstrate the great potential of VLT/UVES for studying young, accreting planets. Based on the conclusions from our analysis, we find that 2M1115 could greatly benefit from further study; better constraints on its age could be placed by obtaining photometry covering a longer wavelength range in its SED. A dynamic, model-independent estimate of its mass can be obtained by studying the disk kinematics using ALMA (ALMA Partnership et al. 2015). Imaging in the mid-infrared using instruments like JWST/MIRI (Wright et al. 2015) to study the spectral distribution of 2M1115 at the mid-infrared wavelengths could also help in constraining the properties of the disk. Further, spectroscopic observations of 2M1115 in the near-infrared to study accretion signatures such as Paschen and Brackett emission lines can serve as an independent check on the mass accretion rate, and give further insights into the accretion geometry. Monitoring emission lines from the target over various timescales with UVES or other upcoming high-resolution spectrographs like ANDES (formerly known as HIRES; Marconi et al. 2021) can help investigate accretion variability. Finally, continued monitoring of 2M1115's space motion could help solve the mystery of whether it belongs to yet undiscovered stellar associations or has been ejected from currently known ones.

Acknowledgements. M.J. gratefully acknowledges funding from the Knut and Alice Wallenberg Foundation and the Swedish Research Council. G.-D.M. acknowledges the support of the DFG priority program SPP 1992 "Exploring the Diversity of Extrasolar Planets" (MA 9185/1) and from the Swiss National Science Foundation under grant 200021_204847 "PlanetsInTime". Parts of this work have been carried out within the framework of the NCCR PlanetS supported by the Swiss National Science Foundation. This publication makes use of VOSA, developed under the Spanish Virtual Observatory (https://svo.

cab.inta-csic.es) project funded by MCIN/AEI/10.13039/501100011033/ through grant PID2020-112949GB-I00. VOSA has been partially updated by using funding from the European Union's Horizon 2020 Research and Innovation Programme, under Grant Agreement nº 776403 (EXOPLANETS-A). Funding for SDSS-III has been provided by the Alfred P. Sloan Foundation, the Participating Institutions, the National Science Foundation, and the U.S. Department of Energy Office of Science. The SDSS-III web site is http://www.sdss3.org. SDSS-III is managed by the Astrophysical Research Consortium for the Participating Institutions of the SDSS-III Collaboration including the University of Arizona, the Brazilian Participation Group, Brookhaven National Laboratory, Carnegie Mellon University, University of Florida, the French Participation Group, the German Participation Group, Harvard University, the Instituto de Astrofisica de Canarias, the Michigan State/Notre Dame/JINA Participation Group, Johns Hopkins University, Lawrence Berkeley National Laboratory, Max Planck Institute for Astrophysics, Max Planck Institute for Extraterrestrial Physics, New Mexico State University, New York University, Ohio State University, Pennsylvania State University, University of Portsmouth, Princeton University, the Spanish Participation Group, University of Tokyo, University of Utah, Vanderbilt University, University of Virginia, University of Washington, and Yale University.

References

Adams, F. C., Lada, C. J., & Shu, F. H. 1987, ApJ, 312, 788
Ahn, C. P., Alexandroff, R., Allende Prieto, C., et al. 2012, ApJS, 203, 21
Alam, S., Albareti, F. D., Allende Prieto, C., et al. 2015, ApJS, 219, 12
Alcalá, J. M., Manara, C. F., Natta, A., et al. 2017, A&A, 600, A20
Allard, F., Hauschildt, P. H., Alexander, D. R., Tamanai, A., & Schweitzer, A. 2001, ApJ, 556, 357
Allard, F., Homeier, D., & Freytag, B. 2012, Philosophical Transactions of the Royal Society of London Series A, 370, 2765
Allard, F., Homeier, D., & Freytag, B. 2013, Mem. Soc. Astron. Italiana, 84, 1053
ALMA Partnership, Brogan, C. L., Pérez, L. M., et al. 2015, ApJ, 808, L3
Aoyama, Y. & Ikoma, M. 2019, ApJ, 885, L29
Aoyama, Y., Ikoma, M., & Tanigawa, T. 2018, ApJ, 866, 84
Aoyama, Y., Marleau, G.-D., Ikoma, M., & Mordasini, C. 2021, ApJ, 917, L30
Aoyama, Y., Marleau, G.-D., Mordasini, C., & Ikoma, M. 2020, arXiv e-prints, arXiv:2011.06608
Asplund, M., Grevesse, N., Sauval, A. J., & Scott, P. 2009, ARA&A, 47, 481
Baron, E., Hauschildt, P. H., Allard, F., et al. 2003, in Modelling of Stellar Atmospheres, ed. N. Piskunov, W. W. Weiss, & D. F. Gray, Vol. 210, 19
Batygin, K. 2018, AJ, 155, 178
Bayo, A., Rodrigo, C., Barrado Y Navascués, D., et al. 2008, A&A, 492, 277
Benisty, M., Bae, J., Facchini, S., et al. 2021, ApJ, 916, L2
Betti, S. K., Follette, K. B., Ward-Duong, K., et al. 2022, ApJ, 935, L18
Boucher, A., Lafrenière, D., Gagné, J., et al. 2016, ApJ, 832, 50
Calvet, N. & Gullbring, E. 1998, ApJ, 509, 802
Chabrier, G., Baraffe, I., Allard, F., & Hauschildt, P. 2000, ApJ, 542, L119
Currie, T., Marois, C., Cieza, L., et al. 2019, ApJ, 877, L3
Cutri, R. M., Skrutskie, M. F., van Dyk, S., et al. 2003, VizieR Online Data Catalog: 2MASS All-Sky Catalog of Point Sources (Cutri+ 2003), VizieR On-line Data Catalog: II/246. Originally published in: 2003yCat.2246....0C
Cutri, R. M., Wright, E. L., Conrow, T., et al. 2021, VizieR Online Data Catalog: AllWISE Data Release (Cutri+ 2013), VizieR On-line Data Catalog: II/328. Originally published in: IPAC/Caltech (2013)
Dekker, H., D'Odorico, S., Kaufer, A., Delabre, B., & Kotzlowski, H. 2000, in Society of Photo-Optical Instrumentation Engineers (SPIE) Conference Series, Vol. 4008, Optical and IR Telescope Instrumentation and Detectors, ed. M. Iye & A. F. Moorwood, 534–545
Demars, D., Bonnefoy, M., Dougados, C., et al. 2023, A&A, 676, A123
Eriksson, S. C., Asensio Torres, R., Janson, M., et al. 2020, A&A, 638, L6
Gagné, J., Mamajek, E. E., Malo, L., et al. 2018, ApJ, 856, 23
Gaia Collaboration. 2022, VizieR Online Data Catalog: Gaia DR3 Part 1. Main source (Gaia Collaboration, 2022), VizieR On-line Data Catalog: I/355. Originally published in: Astron. Astrophys., in prep. (2022)
Gullbring, E., Hartmann, L., Briceño, C., & Calvet, N. 1998, ApJ, 492, 323
Haffert, S. Y., Bohn, A. J., de Boer, J., et al. 2019, Nature Astronomy, 3, 749
Hartmann, L. 1998, Accretion Processes in Star Formation (Cambridge University Press)
Hartmann, L., Herczeg, G., & Calvet, N. 2016, ARA&A, 54, 135
Hashimoto, J., Aoyama, Y., Konishi, M., et al. 2020, AJ, 159, 222
Helling, C., Woitke, P., & Thi, W. F. 2008, A&A, 485, 547
Isella, A., Benisty, M., Teague, R., et al. 2019, ApJ, 879, L25
Jayawardhana, R., Mohanty, S., & Basri, G. 2003, ApJ, 592, 282
Jiang, Y.-F. & Tremaine, S. 2010, MNRAS, 401, 977
Kao, M. M., Hallinan, G., Pineda, J. S., Stevenson, D., & Burgasser, A. 2018, ApJS, 237, 25
Kirkpatrick, J. D. 2005, ARA&A, 43, 195
Koenigl, A. 1991, ApJ, 370, L39
Kramida, A., Yu. Ralchenko, Reader, J., & and NIST ASD Team. 2023, NIST Atomic Spectra Database (ver. 5.11), [Online]. Available: https://physics.nist.gov/asd [2024, May 10]. National Institute of Standards and Technology, Gaithersburg, MD.
Luhman, K. L., Tremblin, P., Birkmann, S. M., et al. 2023, ApJ, 949, L36
Lynden-Bell, D. & Pringle, J. E. 1974, MNRAS, 168, 603
Mamajek, E. E., Bartlett, J. L., Seifahrt, A., et al. 2013, AJ, 146, 154
Manara, C. F., Testi, L., Rigliaco, E., et al. 2013, A&A, 551, A107
Marconi, A., Abreu, M., Adibekyan, V., et al. 2021, The Messenger, 182, 27
Marleau, G.-D., Mordasini, C., & Kuiper, R. 2019, ApJ, 881, 144
Mendigutía, I., Oudmaijer, R. D., Schneider, P. C., et al. 2018, A&A, 618, L9
Mohanty, S., Jayawardhana, R., & Basri, G. 2005, ApJ, 626, 498
Muzerolle, J., Calvet, N., & Hartmann, L. 2001, ApJ, 550, 944
Muzerolle, J., Hillenbrand, L., Calvet, N., Briceño, C., & Hartmann, L. 2003, ApJ, 592, 266
Muzerolle, J., Luhman, K. L., Briceño, C., Hartmann, L., & Calvet, N. 2005, ApJ, 625, 906
Natta, A., Testi, L., Muzerolle, J., et al. 2004, A&A, 424, 603
Owen, J. E. & Menou, K. 2016, ApJ, 819, L14
Rayner, J. T., Toomey, D. W., Onaka, P. M., et al. 2003, PASP, 115, 362
Rebull, L. M., Hillenbrand, L. A., Strom, S. E., et al. 2000, AJ, 119, 3026
Reiners, A. & Christensen, U. R. 2010, A&A, 522, A13
Ringqvist, S. C., Viswanath, G., Aoyama, Y., et al. 2023, A&A, 669, L12
Rubin, D., Aldering, G., Antilogus, P., et al. 2022, ApJS, 263, 1
Sallum, S., Follette, K. B., Eisner, J. A., et al. 2015, Nature, 527, 342
Santamaría-Miranda, A., Cáceres, C., Schreiber, M. R., et al. 2018, MNRAS, 475, 2994
Santamaría-Miranda, A., Cáceres, C., Schreiber, M. R., et al. 2019, MNRAS, 488, 5852
Sicilia-Aguilar, A., Fang, M., Roccatagliata, V., et al. 2015, A&A, 580, A82
Szulágyi, J. & Ercolano, B. 2020, ApJ, 902, 126
Szulágyi, J., Morbidelli, A., Crida, A., & Masset, F. 2014, ApJ, 782, 65
Szulágyi, J. & Mordasini, C. 2017, MNRAS, 465, L64
Thanathibodee, T., Calvet, N., Bae, J., Muzerolle, J., & Hernández, R. F. 2019, ApJ, 885, 94
Theissen, C. A., Burgasser, A. J., Bardalez Gagliuffi, D. C., et al. 2018, ApJ, 853, 75
Theissen, C. A., West, A. A., Shippee, G., Burgasser, A. J., & Schmidt, S. J. 2017, AJ, 153, 92
Turbet, M., Leconte, J., Selsis, F., et al. 2016, A&A, 596, A112
Venuti, L., Stelzer, B., Alcalá, J. M., et al. 2019, A&A, 632, A46
Wagner, K., Follete, K. B., Close, L. M., et al. 2018, ApJ, 863, L8
Whelan, E. T., Huélamo, N., Alcalá, J. M., et al. 2015, A&A, 579, A48
Witte, S., Helling, C., Barman, T., Heidrich, N., & Hauschildt, P. H. 2011, A&A, 529, A44
Wright, G. S., Wright, D., Goodson, G. B., et al. 2015, PASP, 127, 595
York, D. G., Adelman, J., Anderson, John E., J., et al. 2000, AJ, 120, 1579
Zhou, Y., Bowler, B. P., Wagner, K. R., et al. 2021, AJ, 161, 244
Zhu, Z. 2015, ApJ, 799, 16

Appendix A: Details of observations

Table A.1 gives the observing log for 2M1115 with VLT/UVES during 2023 June 10–11, as part of the ESO programme 0111.C-0166(A). The integration time was 740 s for each observation with the number of integrations, NDIT=1. The seeing measurements quoted here are estimated from the FWHM of the 2D spatial PSF of the Hα line from the data.

Date (MJD)	UT Time (hh:mm)	Seeing ($''$)	Air mass
60105.96795718	23:13	1.504	1.408
60105.97697917	23:26	1.350	1.424
60106.96561343	23:10	1.401	1.408
60106.97460648	23:23	1.451	1.425

Table A.1. Observing log for the VLT/UVES observations of 2M1115 on 2023 June 10, 11 during the ESO programme.

Appendix B: Flux calibration

The low resolution spectrum from SDSS DR12 (Alam et al. 2015) and DR9 (Ahn et al. 2012) does not reveal any significant continuum for 2M1115 in the relevant wavelength range for the UVES data. The stacked UVES spectrum when binned to ~ 5 Å resolution also does not show any continuum, except for a faint continuum that begins to appear near the higher wavelength end of the upper red arm (> 6000 Å). With no considerable continuum emission from the object, flux calibration based on a theoretical model fit to the object's SED would not be ideal since the photometric bands in the optical wavelength range will be mostly dominated by the flux from the emission lines.

An alternative method would be to calibrate the object's flux based on the observing instrument's response curve. For this purpose, we utilise the observations of the standard star LTT 6248 taken with UVES on 2023 June 11 with the same observing setup as 2M1115. A well-calibrated spectrum for this star exists in the literature (Rubin et al. 2022) in the required wavelength range. The UVES spectrum for LTT 6248 was extracted using the default ESO pipeline and was corrected for atmospheric transmission at an air mass of 1.7 corresponding to its observing conditions, using the sky transmission curve obtained from ESO's SKYCALC Sky Model Calculator[5]. The instrument response for UVES was derived by dividing the spectrophotometric calibrated spectrum of LTT 6248 from Rubin et al. (2022) with its uncalibrated UVES spectrum normalised for the corresponding integration time (500 s).

We then flux calibrated the 2M1115 UVES spectrum by first correcting it for atmospheric transmission at the average air mass of its observations (1.415), then normalising it for its integration time of 740 s and finally multiplying it by the instrument response curve derived above. The resulting calibrated spectrum for the target shows consistency between the integrated flux for H I emission lines with those from earlier SDSS epochs (refer Table I.1).

[5] https://www.eso.org/observing/etc/bin/gen/form?INS.MODE=swspectr+INS.NAME=SKYCALC

Appendix C: Identification of potential lines

Potential emission lines were selected from the stacked spectrum and classified as confirmed or tentative detection based on a detection confidence determined as described here. For each potential line identified in the spectrum, a region of 20 Å width is defined around the line, usually centered on the line except when the line is near the beginning/end of an order (in which case the region is shifted by 5 Å away from the noisier part). The local noise is calculated as the standard deviation within this region, avoiding ±2 Å around the center of the line. A single Gaussian is then fit to the line and the detection confidence is determined as the strength of the line, estimated as the peak of the resulting Gaussian fit. Identified emission lines are classified as confirmed detections if the corresponding detection confidence is higher than 5σ, with σ being the local noise. We note that a high threshold of 5σ is used since we do fit for a continuum in the spectrum (as discussed in Appendix B) and thus may be underestimating the corresponding noise. Alternatively, if the line is recurrent in two subsequent orders, and the rms of the two line strengths is higher than 5σ, it is also classified as a confirmed detection. Lines identified similarly with a confidence of 3–5σ are classified as tentative detections.

Appendix D: Characteristics of H I line profiles

Figure D.1 illustrate the Gaussian fits to the profile of the tentatively detected Hβ in order 3 of the RedL arm (4.3σ) and H7 in order 25 of the Blue arm (3.6σ). H7 shows a slight increase in flux at the blue side of the line, indicative of a possible blending with either Fe I at 3970.63 Å or Cr I at 3969.74 Å. H7 was also detected in order 24, but since the detection confidence is only 1.7σ, we do not include it in our analysis. We also detected a clear flux increase in orders 20 and 21 of the Blue arm corresponding to the H9 line at 3835.40 Å (see Figure D.2) but the detection strength for both were not formally significant (1.9σ and 1.7σ respectively) and has not been listed among detections in this work. The characteristics of the line profiles for all the H I emission lines detected in the spectrum are given in Table D.1. Hα and Hβ are best explained with a triple (t) and double (d) Gaussian fits respectively while the rest of the H I lines, being of lower SNR, are fitted with single (s) Gaussians.

Appendix E: Analysis with planet-surface shock model

We fit the observed H3–H7 line profiles of 2M1115 with the Aoyama et al. (2020, 2021) model grids assuming H I line emission from shock at the planet surface.

The quality of the fit was determined by reduced χ^2 ($\chi^2_{\rm red}$) with χ^2 defined as

$$\chi^2 = \sum_i \left(\frac{F_{\rm model,\,i} - F_{\rm obs,\,i}}{\sigma_i} \right)^2 . \quad \text{(E.1)}$$

Here, σ is the uncertainty in the observed flux $F_{\rm obs,\,i}$ for bin i and $F_{\rm model,\,i}$ is the corresponding flux prediction from the model. The value of $\chi^2_{\rm red}$ for the fit is then obtained by dividing χ^2 by the degree of freedom, which is the number of bins used in the fitting process. A $\chi^2_{\rm red} \approx 1$ (light blue) indicates good agreement between the model prediction and the observed profile, and $\chi^2_{\rm red} < 1$ (darker blue) indicates that the difference is less than the uncertainty in the flux.

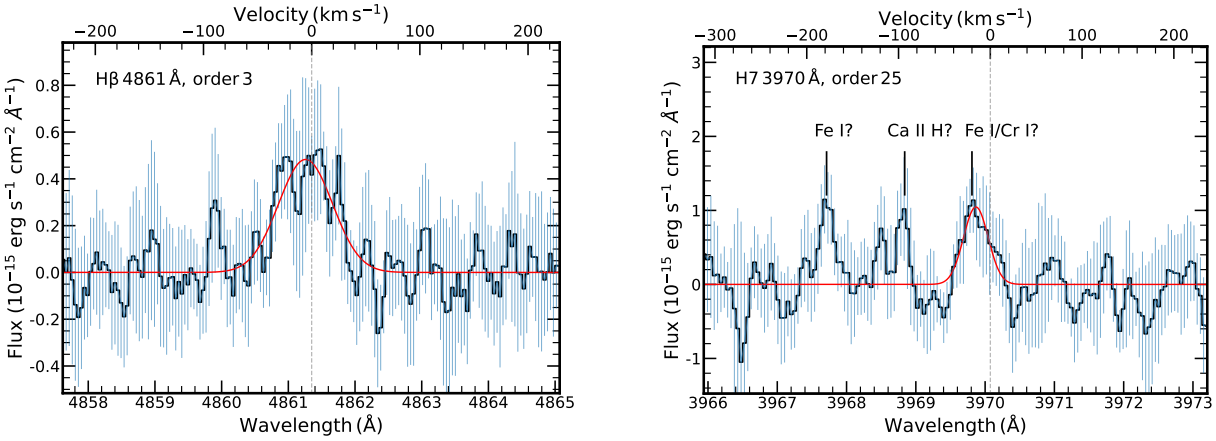


Fig. D.1. (Left) Hβ detected at 4.3σ in order 3 of the RedL arm, and (Right) H7 line detected at 3.6σ in order 25 of the Blue arm of UVES in the 2M1115 data. The red line indicates the Gaussian fit to the observed flux (blue line). The vertical lines indicate the uncertainty in the flux. The tentatively detected Ca II H (3968.47 Å) at 3.1σ and Fe I (3967.42 Å) at 3.2σ next to H7 are also indicated in the figure.

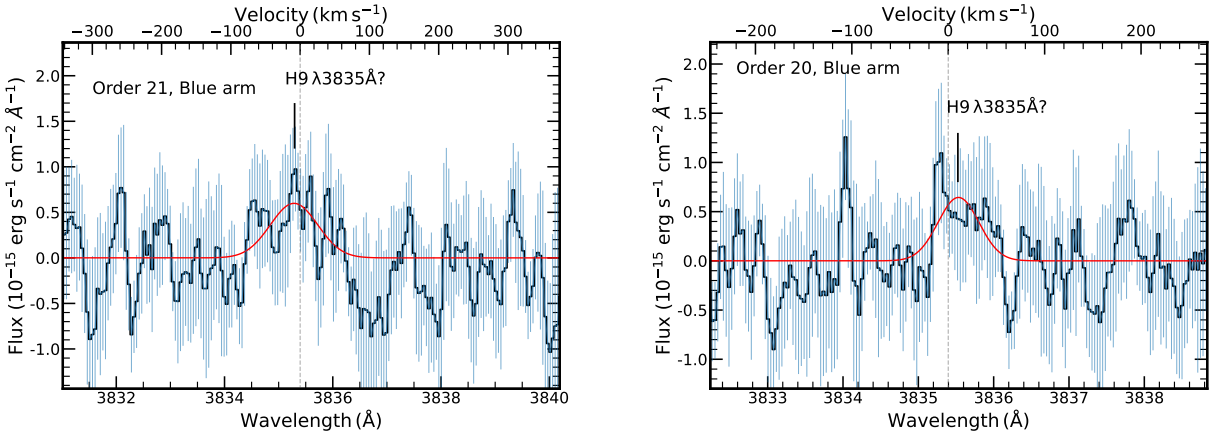


Fig. D.2. The flux increase detected at the location of H9 in (Left) order 21, and (Right) order 20 of the Blue arm of UVES in the 2M1115 data, at 1.7σ and 1.9σ respectively. Colors and symbols hold the same meaning as in the previous figure.

Hα is significantly brighter than the rest of the H I lines detected; trying to fit for Hα using a high extinction of 3.5 mag shows very poor agreement with H5, H6 and H7 profiles. Hence, Hα has been excluded from the following analysis. For fitting H5, we took the average of its line profiles from orders 34 and 35. For H5–H7, we also masked the bins corresponding to possible contamination from metal lines, as described in Section 4.1 and Appendix D. The resulting quality of the fit improved greatly, with good agreement over a wider parameter range (see Figure E.1) as compared to when these possible metal lines were included in the fitting process. This highlights the importance of the high spectral resolution such as with UVES, which helps identify overlapping metal lines in the line profile.

Among the models that show good agreement with $\chi^2_{\rm red} \leq 1$, adopting a pre-shock gas velocity of $v_0 = 120$ km s^{-1} and a pre-shock gas density of $n_0 = 10^{14}$ cm^{-3} reproduces all the line profiles (H4–H7) very well (see Figure E.2), while others reproduce some of the lines well but not others. The blue region in the figure indicate those values of v_0, n_0 for which fitting residuals are not statistically significant at the 1σ level. The pre-shock gas parameters over this region range from $v_0 = 90 - 200$ km s^{-1} and $n_0 = 10^9 - 10^{14}$ cm^{-3}. Accordingly, we define the uncertainties in the best-fit model parameters as $v_0 = 120^{+80}_{-30}$ km s^{-1} and $n_0 = 10^{14\ (-5)}$ cm^{-3}.

Appendix F: Comparison of H3 with standard line profiles in the literature

The comparison of the obtained Hα line profile for the target with the best-matching Hα profiles from Muzerolle et al. (2005) and Mohanty et al. (2005) is illustrated in Figure F.1. The line profile for all the objects have been normalised by their peak flux for the sake of comparison. The Hα profile for 2M1115 in this plot has been corrected for the line's observed radial velocity shift (-7.3 ± 1.4 km s^{-1}) as determined from a single Gaussian fit to its line profile.

Appendix G: Non-Hydrogen line detections

Apart from H I lines, we also detected He I emission (see Figure G.1) and several metal lines including Ca II H, Fe I, Cr I and Ti I. He I emission at 5876 Å was detected at high confidence (8.6σ) while He I emission at 6678 Å was detected tentatively (3.2σ). Ca II H was detected tentatively in order 25 of

Line	$\lambda_{\rm rest,\,air}$ (Å)	Det. conf. (σ)	Fit	$\lambda_{\rm observed}$ (Å)	RV (km s^{-1})	FWHM (Å)	W_{10} (Å)
Hα (H3)	6562.79	59.0	t, BC	6562.66 ± 0.02	−5.70 ± 1.68	2.93 ± 0.08	5.32 ± 0.09
			t, NC_1	6562.16 ± 0.05	−28.96 ± 2.82	0.89 ± 0.03	1.58 ± 0.03
			t, NC_2	6563.07 ± 0.03	12.95 ± 1.95	1.00 ± 0.03	1.79 ± 0.03
Hβ_2 ($H4_2$)	4861.35	9.0	d, BC	4860.88 ± 0.43	−28.79 ± 26.69	1.49 ± 0.35	2.71 ± 0.37
			d, NC	4861.24 ± 0.12	−6.69 ± 8.18	0.82 ± 0.10	1.48 ± 0.10
Hβ_3 ($H4_3$)	4861.35	4.3	s	4861.26 ± 0.03	−5.65 ± 3.63	0.95 ± 0.07	1.74 ± 0.03
Hγ_{34} ($H5_{34}$)	4340.47	4.6	s	4340.44 ± 0.02	−2.15 ± 1.37	0.45 ± 0.04	0.80 ± 0.01
Hγ_{35} ($H5_{35}$)	4340.47	4.6	s	4340.39 ± 0.04	−5.56 ± 2.52	0.95 ± 0.08	1.73 ± 0.03
Hδ (H6)	4101.73	7.0	s	4101.64 ± 0.02	−7.15 ± 1.61	0.88 ± 0.05	1.60 ± 0.02
Hϵ (H7)	3970.07	3.6	s	3969.87 ± 0.03	−15.73 ± 2.55	0.42 ± 0.08	0.75 ± 0.02

Table D.1. Characteristics of the line profiles for H I emission lines detected in the 2M1115 UVES spectrum. H7 is tentatively detected. 'Det. conf.' stands for detection confidence, which is expressed in units of σ, the standard deviation within ±20 Å around the line (refer Section C). (s), (d) and (t) denote single, double and triple Gaussian fits respectively, and BC and NC denote broad and narrow Gaussian components.

the Blue arm (see Figure D.1, right panel) at 3.1σ; the line also recurred in order 24 but at only 1.6σ with no formal significance to include in the detection list. Both the Ca II H detections were at an RV of ∼ 24 km s^{-1}, much redder compared to the systemic RV of −14 ± 7 km s^{-1}. Among the possible metal lines detected (all < 5σ), Fe I emission lines at λ3967.42, 4970.50, 4986.22, and 5684.43 Å were detected at similarly redder RV shifts (∼ 17 − 35 km s^{-1}), while Fe I emission lines at λ4259.99, 4839.54, and 6703.57 Å were detected at bluer RV shifts (−25 to −37 km s^{-1}) compared to the systemic velocity. We note that this is different from the expected behaviour of metal lines as seen from the stellar cases, which adhere more or less to the systemic velocity (Sicilia-Aguilar et al. 2015). Table G.1 lists the characteristics of the line profiles for all the non-hydrogen lines detected in the data.

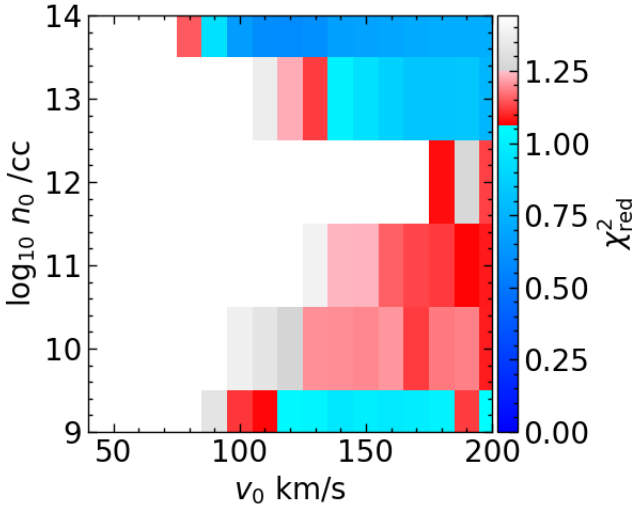


Fig. E.1. Results from fitting Aoyama et al. (2020, 2021) model-grid to the observed H4–H7 line profiles of 2M1115. The model-grid allows n_0 to range from $10^9 - 10^{14}$ cm^{-3} and v_0 to range from 50 − 200 km s^{-1}. The corresponding $\chi^2_{\rm red}$ is represented by the colorbar, with $\chi^2_{\rm red}$ = 1 indicating a good fit.

Appendix H: Fitting atmospheric models to 2M1115 SED

Using VOSA, we queried the existing SDSS (*u, g, r, i, z*), *Gaia* DR3 (G, $G_{\rm BP}$, $G_{\rm RP}$), 2MASS (*J, H,* K_S) and WISE (*W1, W2, W3, W4*) photometry of 2M1115. Since *W*4 magnitude is a lower limit, we exclude it from the analysis and fit the remaining 14 photometry points (refer Table H.1) with BT-Settl AGSS2009 (Allard et al. 2012, 2013), AMES-Dusty (Chabrier et al. 2000; Allard et al. 2001) and DRIFT-PHOENIX (Baron et al. 2003; Helling et al. 2008; Witte et al. 2011) atmospheric models constrained to near-solar metallicities (−0.5 to 0.5), log(g) range 3–4 (based on the spectral type L2γ; Kirkpatrick 2005; Theissen et al. 2018) and a temperature range of 1200–2500 *K* (based on existing $T_{\rm eff}$ estimate of 1724^{184}_{-38} *K*; Theissen et al. 2018). We assumed A_V = 0 since, although the extinction is currently unknown for the object, it is still well within the Local Bubble given its location and hence extinction is likely negligible. We do note, however, that the presence of an accretion disk around the target can lead to some intrinsic extinction within the system; this extinction is currently not constrained due to lack of sufficient data, and has not been accounted for in our analysis. Figure H.1 shows the best-fitting model from each of the three model grids that gives the minimum χ^2 with the observed photometry. From the Figure, we see a clear near-UV and optical flux excess compared to the model as well as MIR excess prominent towards the W3 band (indicative of a disk around the object), as previously noted in Theissen et al. (2018). The overall best-fit with least χ^2 that fits 13 out of the 14 data points (with IR excess from *W*3) corresponds to DRIFT-PHOENIX models at $T_{\rm eff}$ = 1800 ± 50 *K*, log(g) = 4 ± 0.25 and metallicity of 0.3±0.15. VOSA also predicts the object parameters corresponding the least χ^2 based on a polynomial fit to the χ^2 vs. parameter-value space for each of the model grids used. Additionally, for each model grid, statistical analysis of the top least χ^2 fits also gives average values of the best-fitting model parameters. To arrive at the optimal value of the target parameters, we took the set of parameters corresponding to the least χ^2 fits, those predicted from the above-mentioned polynomial fit (as long as the value corresponding to the minimum χ^2 falls within the constrained parameter range for the fit) as well as those derived from the average of the best-fits, for each of the three model grids. The rms of these sets of values give the following parameters for the target, which we adopt for our analysis; $T_{\rm eff}$ = 1816.29 ± 62.57 K,

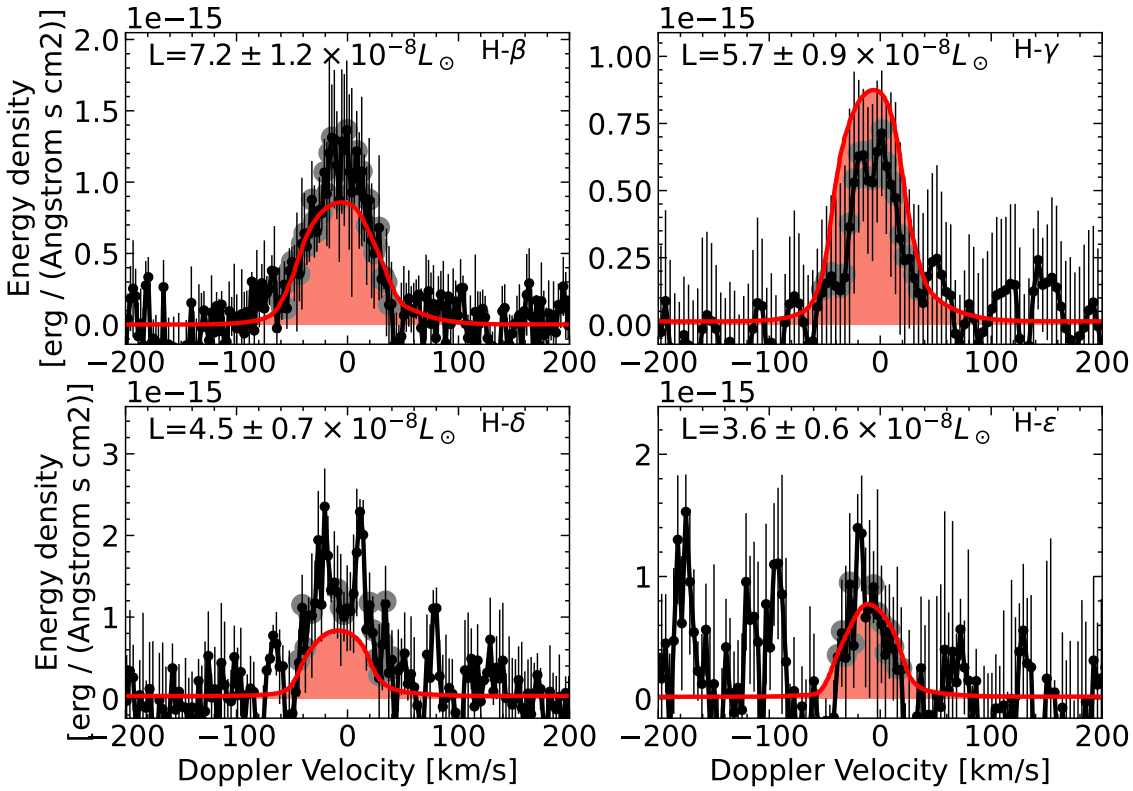


Fig. E.2. The SED with Aoyama et al. (2020, 2021) model corresponding to $\chi^2_{\rm red} \leq 1$ that fits all the line profiles (H4–H7) reasonably well. The y-axis represents the observed flux in units of erg s^{-1} cm^{-2} Å^{-1} and the x-axis represents the velocity shift with respect to the rest wavelength of the line, in km s^{-1}. The solid black curve represents the observed data, and the red curve represents the model prediction. The black vertical lines are the uncertainties in the observed flux, and the grey filled circles are the points along the observed profile the model was fitted to. The model-predicted luminosity from each line is also indicated in the figure.

$\log(g) = 3.83 \pm 0.24$, metallicity $= 0.24 \pm 0.13$ and the integrated flux $F_{\rm tot} = (3.68 \pm 0.28) \times 10^{-12}$ erg s^{-1} cm^{-2}. We derived a bolometric luminosity of $L_{\rm bol} = (2.34 \pm 0.29) \times 10^{-4}\, L_\odot$ based on the obtained $F_{\rm tot}$ and the *Gaia* distance for the target. This $L_{\rm bol}$ together with the obtained $T_{\rm eff}$ above gives a radius of $R_{\rm p} = 1.54 \pm 0.14\, R_{\rm Jup}$. As a cross-check on the VOSA results, we also fit the model grids to the SED of 2M1115 by including its SDSS DR12 spectrum (green curve in Figure H.1) instead of the SDSS photometry. The resulting χ^2 gives best-fitting models consistent with those from VOSA, adding robustness to the results derived above.

Appendix I: Mass accretion rates from SDSS epochs

We downloaded the existing, public, moderate-resolution optical spectrum for 2M1115 from the two SDSS epochs DR9 (Ahn et al. 2012) and DR12 (Alam et al. 2015) using the SDSS Science Archive Server (SAS). For the detected H I emission lines H3–H7 in the spectrum, we estimated a local continuum as the median flux within ±40 Å around the line, devoid of ±10 Å region centered on the line. After subtracting the continuum from the spectrum, we fit a single Gaussian profile to the line and estimated the line flux and line luminosities. The uncertainty in the line fluxes are estimated as the rms of the corresponding local continuum. We then used the planetary scaling relations from Aoyama et al. (2021) to estimate accretion luminosities and mass accretion rates for the object, assuming the same values for $M_{\rm p}$ and $R_{\rm p}$ as in Section 4.2. The resulting line parameters for the lines H3–H7 are given in Table I.1. The average accretion luminosity $\log(L_{\rm acc}/L_\odot)$ calculated from lines H3–H7 is -4.68 ± 0.14 for the DR9 epoch and -4.30 ± 0.14 for the DR12 epoch. The corresponding mass accretion rates $\log(\dot{M}_{\rm acc}/M_{\rm Jup}\ {\rm yr}^{-1})$ in the two epochs are -8.00 ± 0.32 and -7.62 ± 0.32 respectively. In the DR9 epoch, the mass accretion rate estimated from Hα seems to be slightly higher than those estimated from H4 and H5 but is consistent with those from H6 and H7 within uncertainties. In the DR 12 epoch, the individual mass accretion rates derived from all the H I lines are consistent with each other within the uncertainties, except for that from H7 which is slightly higher.

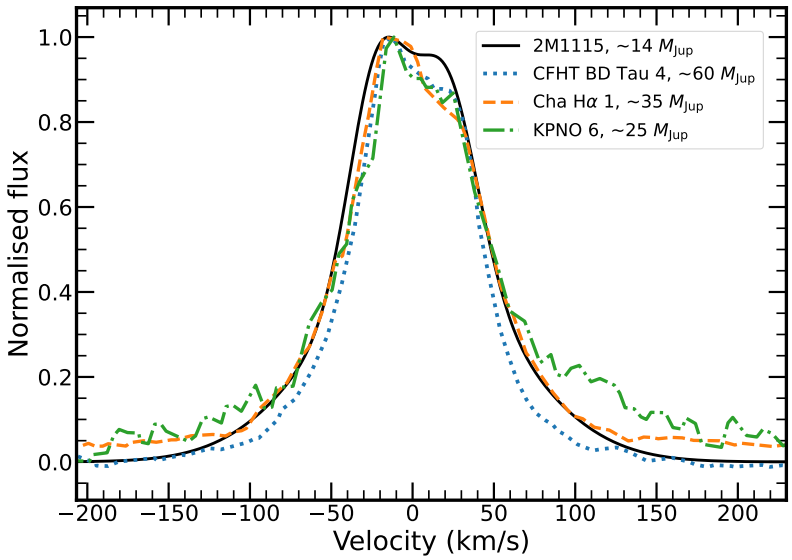


Fig. F.1. Profile fit to Hα emission from 2M1115 compared to normalised Hα profiles for CFHT BD Tau 4 from Mohanty et al. (2005) and Cha Hα 1, KPNO 6 from Muzerolle et al. (2005). The Hα profile for 2M1115 in this plot has been corrected for its observed velocity shift.

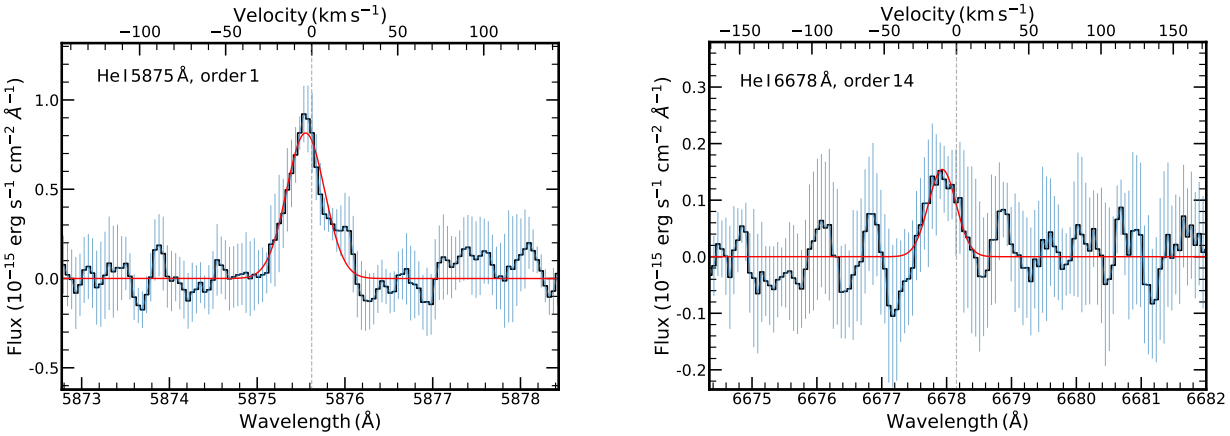


Fig. G.1. Line profiles of He I at (Left) 5876 Å and (Right) 6678 Å detected in the order 1 and 14 of the UVES RedU arm at 8.6σ and 3.2σ respectively in the 2M1115 data. Colors and symbols hold the same meaning as in previous figures.

Line	$\lambda_{\rm rest,\,air}$ (Å)	order, arm	Det. conf. (σ)	$\lambda_{\rm observed}$ (Å)	RV (km s^{-1})	FWHM (Å)	W_{10} (Å)
Confirmed Detections							
He I	5875.62	1, RedU	8.6	5875.55 ± 0.01	−3.53 ± 0.64	0.51 ± 0.03	0.92 ± 0.01
Tentative Detections							
Fe I	3834.22	20, Blue	3.4	3834.03 ± 0.01	−14.61 ± 0.98	0.10 ± 0.03	0.18 ± 0.01
Fe I	3967.42	25, Blue	3.2	3967.72 ± 0.03	22.47 ± 1.94	0.26 ± 0.06	0.45 ± 0.02
Ca II H_{25}	3968.47	25, Blue	3.1	3968.81 ± 0.02	25.57 ± 1.71	0.17 ± 0.05	0.30 ± 0.02
Fe I	4259.99	32, Blue	3.0	4259.47 ± 0.01	−36.90 ± 1.01	0.10 ± 0.03	0.16 ± 0.02
Fe I	4839.54	2, RedL	3.1	4839.13 ± 0.02	−25.48 ± 0.99	0.12 ± 0.04	0.21 ± 0.02
Fe I	4970.50	5, RedL	3.5	4970.78 ± 0.01	16.92 ± 0.81	0.12 ± 0.03	0.21 ± 0.02
Fe I	4986.22	6, RedL	4.8	4986.80 ± 0.01	34.67 ± 0.71	0.14 ± 0.03	0.25 ± 0.01
Fe I	5329.99	14, RedL	3.4	5329.71 ± 0.02	−15.55 ± 1.08	0.19 ± 0.04	0.32 ± 0.02
Fe I	5684.43	21, RedL	4.4	5684.81 ± 0.02	20.09 ± 0.90	0.22 ± 0.04	0.38 ± 0.02
Ti I	5720.43	21, RedL	3.0	5720.44 ± 0.02	0.10 ± 1.30	0.25 ± 0.06	0.45 ± 0.02
Cr I	5991.07	3, RedU	4.4	5991.05 ± 0.01	−1.11 ± 2.10	0.13 ± 0.03	0.22 ± 0.01
Fe I	6083.66	5, RedU	3.3	6083.42 ± 0.02	−11.72 ± 1.20	0.24 ± 0.06	0.43 ± 0.02
Fe I	6636.96	13, RedU	4.7	6636.51 ± 0.02	−20.37 ± 0.73	0.21 ± 0.04	0.37 ± 0.01
He I	6678.15	14, RedU	3.2	6677.93 ± 0.04	−9.84 ± 1.70	0.50 ± 0.09	0.91 ± 0.03
Fe I	6703.57	14, RedU	3.1	6702.99 ± 0.04	−25.69 ± 1.80	0.54 ± 0.09	0.97 ± 0.03

Table G.1. Characteristics of the line profiles for confirmed and tentative non-Hydrogen lines detected in the 2M1115 UVES spectrum. Line list is taken from the NIST Atomic Spectra Database (Kramida et al. 2023). Ca II H is detected in two consecutive orders 25 and 24 of the BLUE arm, with much lower SNR for order 24; so only the detection in order 25 is indicated here.

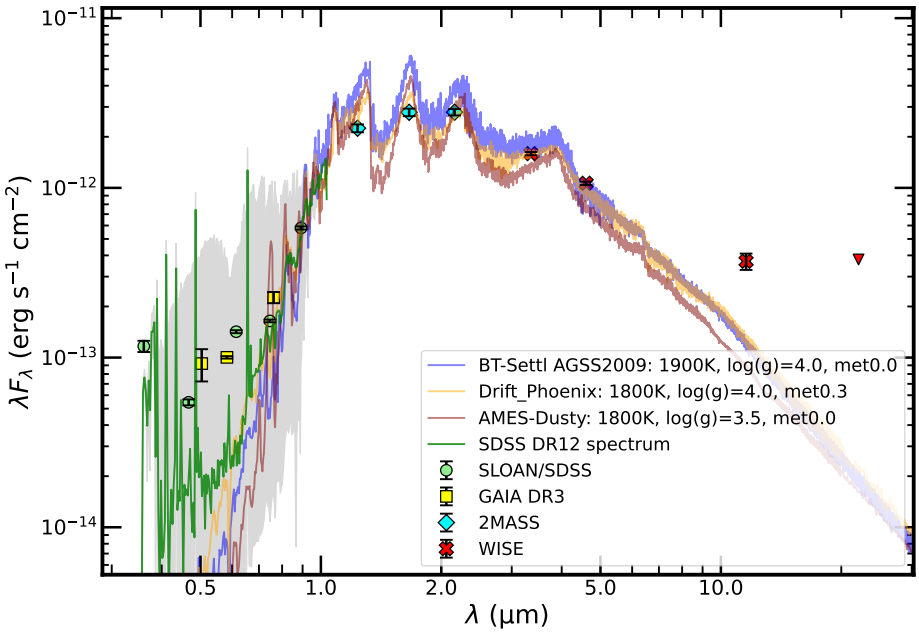


Fig. H.1. Least-χ^2 fits to the SED of 2M1115 with DRIFT-PHOENIX, BT-Settl-AGSS2009 and AMES-Dusty atmospheric models. The overall best fit with the minimum χ^2 corresponds to DRIFT-PHOENIX model at $T_{\rm eff}$ = 1800 ± 50 K, log(g)= 4.0 ± 0.25 and metallicity= 0.3 ± 0.15. The SDSS DR12 spectrum for 2M1115 is also shown, along with its flux uncertainty (grey shaded region). Note that the flux in the WISE $W4$ band is a 2σ upper limit, denoted by the red downward-pointing arrow, and is not included in the fitting process.

Source	Filter	Brightness (mag)
SDSS	u	$m_{\rm u} = 21.06 \pm 0.08$
	g	$m_{\rm g} = 21.56 \pm 0.04$
	r	$m_{\rm r} = 20.23 \pm 0.02$
	i	$m_{\rm i} = 19.86 \pm 0.02$
	z	$m_{\rm z} = 18.30 \pm 0.02$
Gaia	G	$M_G = 17.13 \pm 0.11$
2MASS	J	$M_J = 12.31 \pm 0.12$
	H	$M_H = 11.29 \pm 0.12$
	K_S	$M_{K_S} = 10.52 \pm 0.12$
ALLWISE	$W1$	$M_{W1} = 9.81 \pm 0.11$
	$W2$	$M_{W2} = 9.27 \pm 0.11$
	$W3$	$M_{W3} = 7.49 \pm 0.16$

Table H.1. Photometry for 2M1115 used for the SED fit. For the apparent 2MASS, *Gaia* and WISE magnitudes, refer Table 1. The u, g, r, i, z magnitudes are from SDSS DR12 (Alam et al. 2015) and the $W1$, $W2$, $W3$ magnitudes are from the ALLWISE catalogue (Cutri et al. 2021). The absolute magnitudes for the 2MASS, *Gaia* and WISE bands have been computed based on the parallax-based distance estimate of 45.21 ± 2.20 pc. M_J, M_H and M_{K_S} are $\sim 1.2\sigma$ brighter than the previously reported values in Theissen et al. (2018).

Line	Parameter	SDSS DR9	SDSS DR12
Hα	$F_{\rm line}/10^{-15}$ [erg s^{-1} cm^{-2}]	7.28 ± 0.03	6.78 ± 0.02
	$\log(L_{\rm line}/L_\odot)$	−6.33 ± 0.04	−6.36 ± 0.04
	$\log(L_{\rm acc}/L_\odot)$	−4.40 ± 0.12	−4.43 ± 0.12
	$\log(\dot{M}_{\rm acc}/M_{\rm Jup}\,{\rm yr}^{-1})$	−7.72 ± 0.31	−7.75 ± 0.31
Hβ	$F_{\rm line}/10^{-15}$ [erg s^{-1} cm^{-2}]	0.68 ± 0.03	2.22 ± 0.03
	$\log(L_{\rm line}/L_\odot)$	−7.36 ± 0.05	−6.85 ± 0.04
	$\log(L_{\rm acc}/L_\odot)$	−4.93 ± 0.13	−4.49 ± 0.12
	$\log(\dot{M}_{\rm acc}/M_{\rm Jup}\,{\rm yr}^{-1})$	−8.25 ± 0.32	−7.81 ± 0.31
Hγ	$F_{\rm line}/10^{-15}$ [erg s^{-1} cm^{-2}]	0.41 ± 0.03	1.64 ± 0.05
	$\log(L_{\rm line}/L_\odot)$	−7.58 ± 0.05	−6.98 ± 0.04
	$\log(L_{\rm acc}/L_\odot)$	−4.84 ± 0.15	−4.33 ± 0.14
	$\log(\dot{M}_{\rm acc}/M_{\rm Jup}\,{\rm yr}^{-1})$	−8.16 ± 0.32	−7.65 ± 0.32
H6	$F_{\rm line}/10^{-15}$ [erg s^{-1} cm^{-2}]	0.29 ± 0.04	1.29 ± 0.05
	$\log(L_{\rm line}/L_\odot)$	−7.73 ± 0.07	−7.08 ± 0.05
	$\log(L_{\rm acc}/L_\odot)$	−4.72 ± 0.16	−4.18 ± 0.16
	$\log(\dot{M}_{\rm acc}/M_{\rm Jup}\,{\rm yr}^{-1})$	−8.04 ± 0.33	−7.50 ± 0.33
H7	$F_{\rm line}/10^{-15}$ [erg s^{-1} cm^{-2}]	0.27 ± 0.04	1.02 ± 0.05
	$\log(L_{\rm line}/L_\odot)$	−7.76 ± 0.08	−7.19 ± 0.05
	$\log(L_{\rm acc}/L_\odot)$	−4.53 ± 0.16	−4.06 ± 0.16
	$\log(\dot{M}_{\rm acc}/M_{\rm Jup}\,{\rm yr}^{-1})$	−7.85 ± 0.33	−7.38 ± 0.33

Table I.1. Line fluxes, luminosities and mass accretion rates calculated based on Gaussian fits to the respective lines detected in SDSS DR9 and DR12. Accretion luminosities are calculated from line luminosities using Aoyama et al. (2021) scaling relations.

European Organisation for Astronomical Research in the Southern Hemisphere
Observing Programmes Office • Karl-Schwarzschild-Strasse 2 • D-85748 Garching bei München • email: opo@eso.org • Tel: +49 89 3200 6473

Cycle: P113
Type: Normal
Status: Valid
Printed: 15 Nov 2023

APPLICATION FOR OBSERVING TIME 113.26J1

IMPORTANT NOTICE

By submitting this proposal, the PI takes full responsibility for the content of the proposal, in particular with regard to the names of CoIs and the agreement to act according to the ESO policy and regulations, should observing time be granted.

Disentangling accretion flow geometry on a planetary-mass companion

ABSTRACT

Giant planets acquire part of their mass through gas accretion which is expected to be sustained by a mass reservoir: the circumstellar disk itself or a circum-planetary disk (CPD) where exomoons could form. Accretion lines (Hα, Paβ,...) have been detected on a handful of planetary-mass companions, and two main mechanisms have been proposed to explain the lines : Magnetospheric Accretion where lines are triggered in funnels, and Shock accretion where the lines are triggered in a shock at the planetary or CPD surface.
Betti+2022 showed that shock-accretion is likely occuring on Delorme 1 (AB)b, through line ratios comparisons. We wish to confirm that by resolving the line profile at R=43000, and place constraints on the flow geometry, by constraining the flow infall speed, while also looking at possible rotational modulation of the line if it were to be emitted through magnetospheric accretion.

SCIENTIFIC KEYWORDS

exoplanets, stars: brown dwarfs, planet-disk interactions

RUNS

Run	Period	Instrument	Tel. Setup	Constraints	Mode	Type	Propr. Time	Time Constr.	Req. Time
113.26J1.001 • Run 1	113	CRIRES	UT3	FLI: 100% • Turb.: 10% • pwv: 5.0mm • Sky: Clear	SM	Normal	12m	×	07h28m

AWARDED AND FUTURE TIME REQUESTS

Time already awarded to this project

- none -

Future time requests to complete this project

- none -

Special Remarks

The slit will be placed along the Binary-Companion axis.
The host binary will not saturate the detector, nor reach non-linear regime, according to the ETC.

DESCRIPTION OF THE PROPOSED PROGRAMME

A- Scientific Rationale

The planet accretion phase: Giant planets acquire part of their mass through gas accretion from the surrounding circumstellar disks, or their circumplanetary disk (CPD), in which exomoons could form. These accretion processes are thought to set the initial energy budget of the planet (entropy), its internal structure and composition, and its rotational velocity, all of which contribute to defining its evolutionary pathway.

Young solar type stars are known to power strong kG magnetic fields that truncate the circumstellar disk and shape accretion funnels where strong emission lines are emitted ([1], H_α, Pa_β, Br_γ, ...), a scenario known as magnetospheric accretion (illustrated in Panel C, emission zone #3). Such **accretion lines** have also been detected on a handful of planetary-mass companions (10–30 M_{Jup}), such as PDS70 b and c [2]. Unlike, optical emission lines (e.g., H_α), **Pa_β emission is not contaminated by the strong chromospheric activity [3]** on late type young objects and its properties are directly related to the accretion mechanism at play.

However, the mass and environment differences between these objects and classical T-Tauri stars (CTTS) cast doubts as to whether magnetospheric accretion is truly at play in the planetary mass regime. One pending question is whether planet interiors can fuel sufficiently strong magnetic fields (several 10 to 100 G) for the mechanism to operate. The most recent protoplanet accretion models do not consider magnetic fields and rather propose that emission lines arise from an accretion shock at the planetary (Panel C, #1) and/or CPD surface [4] (Panel C, #4). However, they make no assumption about the origin of the accretion flow, and it might in fact be magnetospherically induced (Panel C, #2).

Shock or Magnetospheric accretion? Strong H I and He I emission lines have been recently identified in VLT/MUSE medium resolution (R=2700) optical spectra of the planetary-mass (12–15 M_{Jup}) companion Delorme 1 (AB)b [5] which can unambiguously be attributed to active accretion. The companion forms a bound 84 au-wide system (1.8") with a tight (12 au) pair of 0.19 and 0.17 $M_\odot$ stars also displaying H I emission lines (e.g., H_α). Excess emission has been recently confirmed on the binary star AND on the companion with the JWST, indicating mass reservoirs around both the hosts and the companion (priv. com). It can not be excluded that material from the star's disk channels up to the companion CPD. Surprisingly, the system belongs to the 30–40 Myr old Tucana-Horologium moving group which proves that PMCs can still be found accreting at substantial levels at these late ages.

Betti et al. (2022) [6] recently detected Pa_β emission at Delorme 1 (AB)b and found that the line is consistent with a shock origin (Panel C, #1 #2, & #4). Moreover, they found parameters to be mostly consistent with a shock at the planetary surface but they **could not firmly discriminate between #1 or #2** because of the limited spectral resolution of their observations. However, because of the variable nature of accretion mechanism on PMC [7], the relative contribution of column emission (#3, if present) and shock emission (#1 & #2) might also be variable ([8], Fig. 2), making all three scenarios (#1, #2 & #3) plausible. Still, MagAcc is a good candidate for Delorme 1 (AB)b as it is known to develop at late stages on stars and one needs to provide more definite proofs with complementary diagnostics.

Placing constraints on the line emission: If the line is emitted within a shock at the planetary surface, one can discriminate between cases #1 and #2 by the infall velocity. Given the uncertainty on the mass estimate of the target, material originating from a few planetary radii away would have a low infall velocity (< 150 km/s), while material originating from further away would have a high infall velocity (150-170 km/s). The width of the shock profiles are dependent on the infall velocity (Panel B, left), and an accuracy of ~40 km/s would permit to place constraints on the low and high velocity cases, along with an accuracy on the launching radius of a few planetary radii. An accuracy of ~20 km/s would permit an accurate discrimination at the 150-170 km/s limit. If the line is emitted within a magnetospheric accretion funnel (#3), the line profile is expected to be modulated by the rotational modulation of the funnels: as funnels come and go out of sight, asymmetries within the line will appear (Panel B, right). Redshifted absorption below the continuum level is also possible and would be the telltale sign of magnetospheric accretion.

Delorme 1 (AB)b, thanks to its *moderate* separation from AB (1.8"), is an ideal target to test the origin of the Pa_β emission in planetary-mass companions. Current constraints [6] are only based on line ratios, and spectrally resolved profiles would provide stringent constraints on the mechanism at play. **Magnetospherically-induced accretion flows would be a clear sign that planetary-mass objects have ionized and convective interiors that can fuel strong magnetic fields.**

B- Immediate Objective

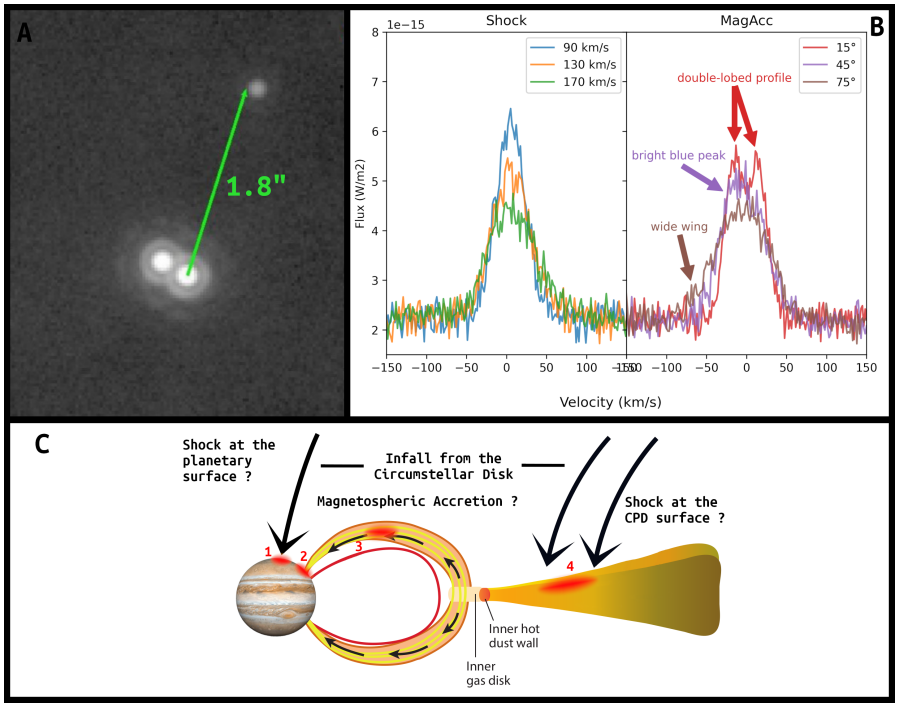
We propose to use CRIRES R=43000 to test the origin of Delorme 1 (AB)b accretion flow. We will study the Pa_β line profile of b and infer the infall velocity and shock density (#1 & #2) by model fitting [4],

or retrieve line asymmetries if it were to be magnetospherically induced ([9], #3). At CRIRES resolution, all shock and magnetospheric accretion lines profiles will be Nyquist-resolved (Panel B). We performed MCMC runs of simulated data at various S/N to determine which is required to distinguish two lines, depending on their shock velocity difference (Δv). We find that at a 5σ confidence level, the $\Delta v = 40$ km/s is achieved for S/N> 13. The $\Delta v = 20$ km/s is achieved at a 3σ confidence level for S/N> 15 depending on the infalling material density. The magnetospheric accretion profiles variations (Panel B, right) are easily distinguished with S/N> 11

Magnetospheric accretion vs shock: To distinguish between the two and provide additional information on each scenario, we wish to reach S/N>15, reached with 900x24s exposures in 10% atmospheric conditions, with an ABBA pattern. Panel B shows that we will also be able to study profiles variations that are expected in the magnetospheric accretion scenario, reaching S/N∼11 with 900x8s stacking, giving insights in the aforementioned rotational modulations of the line. The total of 3x900x8s exposures is 7h28m including overheads.

Data reduction and analysis: The data will be reduced using standard ESO pipeline recipes to obtain reconstructed 2D slit-spectrum data. The binary PSF will be modeled and subtracted to remove any residual contamination to the companion line profile. The spectra will be corrected from telluric features using MOLECFIT. Line profiles will be studied through profile modeling ([4] and [9]) and Bayesian analysis to retrieve each model parameters, in a similar fashion as [7].

Figures



A: VLT/NaCo image of the Delorme system from [11], with the binary in the center and the companion in the top right. **B:** Left: Pa$_\beta$ line profiles predicted by shock-accretion models [4], showing how the the infall speed affects the profile, mainly its width. Right: same with magnetospheric accretion models [9] at different viewing angles. Clear changes in the profiles are annotated on the figure. Both are at S/N=11, R=43000 and scaled to the observed Pa$_\beta$ line flux [6]. **C:** Adapted from Hartmann et al. (2016) [12]. Schematic of the various accretion mechanisms mentioned in the text. #1 & #2: lines emitted in a shock at the planetary surface, respectively originating from material infalling from the circumstellar disk or an accretion funnel. #3: lines emitted in the accretion funnel. #4: lines emitted in a shock at the CPD surface.

References

1. Hartmann, L., G. Herczeg, & N. Calvet (2016), A&A, 54, 135 – **2.** Haffert, S. Y., et al. (2019), NatAs, 3, 749 – **3.** Manara, C. F., et al. (2013), A&A, 551, A107 – **4.** Aoyama, Y., M. Ikoma, & T. Tanigawa (2018), ApJ, 866, 84 – **5.** Eriksson, S. C., et al. (2020), A&A, 638, L6 – **6.** Betti, S. K., et al. (2022), ApJL, 935, L18 – **7.** Demars, D., et al. (2023), A&A, 676, A123 – **8.** Aoyama, Y., et al. (2021), ApJL, 917, L30 – **9.** Thanathibodee, T., et al. (2019), ApJ, 885, 94 – **11.** Delorme, P., et al. (2013), A&A, 553, L5 – **12.** Hartmann, L., G. Herczeg, & N. Calvet (2016), ARA&A, 54, 135

TARGETS

Name	RA	Dec	Coord	Runs	Comment
SCR J0103-5515	01:03:35.655	-55:15:56.243	J2000	1	Host binary, NGS

B=16.99; V=15.4; G=13.947; R=14.96; I=12.09; J=10.162; H=9.58; K=9.237; g=16.18; r=14.84; i=12.91

Target Notes

- none -

REMARKS & JUSTIFICATIONS

Lunar Phase and Constraints Justification

Please justify here the requested lunar phase and other observing constraints.

N/A

Time Justification

Please describe here a detailed computation of the necessary time to execute the observations, including time-critical aspects if any. Parameters used in the ETC should be mentioned so the computation can be reproduced.

=== General justification
The Paschen Beta line of this target is bright enough to be accessible to CRIRES in a reasonable time.
Still, the noise budget will be largely dominated by the Read-On Noise, making, even with the maximum DIT time of 900s.
900x8s exposures (2h) provide access to a resolved line with a S/N of 11, and 900x8s (6) exposures provide access to a S/N of 15
These 900x8s exposures will be performed 3 times successively, giving access to time-modulation of the line, which is expected to be due to rotational modulation of the line.
The stacking of all 24 exposures will provide a S/N of 15 and permit the differentiate between shock models.
Because the line brightness is just at the limit of what is accessible to CRIRES, observations require really good atmospheric condition (10%)

=== OB lengths
Because of the RON limit, we want to maximize the DIT, for which CRIRES has a limit of 900s. We also want to maximize the number of NDIT per OB.
We will therefore make OBs consisting of an acquisition setup, and 3 science exposures, for a total of 8x(900x3s + 11mins) OBs (56mins per OB).

=== ETC parameters :
- Custom continuum spectrum
- Jmag = 15.47 (Vega)
- airamss: 1.5
- FLI: 1.0
- PWV: 2.5mm
- NGS: R mag= 14.96
- Turbulence: 10%
- Extraction Aperture: 15px
- Setting: J1228
- Slit width: 0.4"
- Polarimetry: free
- DITxNDIT: 900x8 and 900x24 (S/N = 11 and 15 respectively)

Telescope Justification

Please justify why the telescope requested is the best choice for this programme.

High resolution (R=43000) of the Paschen Beta line has never been done yet, and CRIRES provides access to this line, while others spectrograph usually only reach R~10000. High resolution will provide critical insights in the line emitting mechanism.

Observing Mode Selection

Please explain your choice of SM, VM, or dVM.

The observations should be performed successively within a night, which is best suited for Service Mode observations.

Calibration Request

If you need any special calibration not included in the instrument calibration plan, please specify it here.

N/A

Duplication with ESO Science Archive

If observations of the same target(s) using the same instrument(s) already exist in the ESO archive, please justify why this programme requests further observations.

N/A

GTO Target Duplication Justification

If an instrument GTO team aims at the same target(s), please justify why this programme requests further observations.

N/A

Background and Expertise

Short description of the background, expertise and roles of the various team members in the context of the science case discussed in the proposal. For small teams the applicants may wish to provide a sentence for the qualifications of each member, while for larger teams (e.g. in Large Programmes), only the leading roles need to be specified.

The team is composed experts of :
- Empirical comprehension of accretion processes on both stars and planets (C. Dougados, M. Bonnefoy, D. Demars, S. Ringqvist, M. Janson, G. Viswanath)
- Modelling of accretion processes (T. Thanathibodee, Y. Aoyama, G.-D. Marleau, B. Tessore)
- Substellar objects behaviors, properties and modelling (S. Petrus, P. Palma Bifani, B. Bowler, P. Tremblin)

The team has experience in working with slit-spectrographs, notably UVES.

REPORT ON PREVIOUS USAGE OF ESO FACILITIES

Run	PI	Instrument	Time	Mode	Comment
0101.C-0015(A)	Mickael Bonnefoy	SPHERE	18.0h	Service	No data taken by ESO
A focused search for planetary systems around Sco-Cen A-F stars harboring holey debris-disks					
0104.C-0598(A)	Mickael Bonnefoy	MUSE	4.0h	Service	Data analysed. No detection. Paper in preparation.
Reconnaissance of two young emblematic systems at optical wavelengths					
107.22UE.001	Mickael Bonnefoy	MUSE	1.3h	Service	No observation executed by ESO
Confirming active accretion on an exotic exoplanet (SCTYPE-C)					
109.22YA.001	Mickael Bonnefoy	MUSE	1.3h	Service	Carry-over in P111
Confirming active accretion on an exotic exoplanet					
110.257P.001	Mickael Bonnefoy	ERIS	2.7h	Service	Ongoing analysis
Investigating an extreme exo-system with IFU spectroscopy and referential-differential imaging					
111.24XD.001	Mickael Bonnefoy	ERIS	6.0h	Service	Ongoing analysis
Formation and status of the first imaged planetary mass companion. Exoplanet or brown-dwarf?					
111.24P3.001	Mickael Bonnefoy	UVES	1.6n	Visitor	Paper in preparation
Can exoplanet undergo magnetospheric accretion at early ages?					
108.21ZE.001	Markus Janson	UVES	1.0h	Service	Paper published
Accretion from the circumplanetary disk around a young directly imaged circumbinary planet					

RECENT PI/CoIs PUBLICATIONS MOST RELEVANT TO THE SUBJECT OF THIS PROPOSAL

1. Betti, S. K., Follette, K. B., Ward-Duong, K., et al. (2022) "Near-infrared Accretion Signatures from the Circumbinary Planetary-mass Companion Delorme 1 (AB)b," ApJL, 935, L18 - 2022ApJ...935L..18B

2. Ringqvist, S. C., Viswanath, G., Aoyama, Y., et al. (2023) "Resolved near-UV hydrogen emission lines at 40-Myr super-Jovian protoplanet Delorme 1 (AB)b. Indications of magnetospheric accretion," A&A, 669, L12 - 2023A&A...669L..12R

3. Eriksson, S. C., Asensio Torres, R., Janson, M., et al. (2020) "Strong Hα emission and signs of accretion in a circumbinary planetary mass companion from MUSE," A&A, 638, L6 - 2020A&A...638L...6E

4. Thanathibodee, T., Calvet, N., Bae, J., et al. (2019) "Magnetospheric Accretion as a Source of Hα Emission from Protoplanets around PDS 70," ApJ, 885, 94 - 2019ApJ...885...94T

5. Aoyama, Y., Marleau, G.-D., Mordasini, C., et al. (2020) "Spectral appearance of the planetary-surface accretion shock: Global spectra and hydrogen-line profiles and fluxes," arXiv, arXiv:2011.06608 - 2020arXiv201106608A

6. Aoyama, Y., Marleau, G.-D., Ikoma, M., et al. (2021) "Comparison of Planetary Hα-emission Models: A New Correlation with Accretion Luminosity," ApJL, 917, L30 - 2021ApJ...917L..30A

7. Marleau, G.-D., Aoyama, Y., Kuiper, R., et al. (2022) "Accreting protoplanets: Spectral signatures and magnitude of gas and dust extinction at H α," A&A, 657, A38 - 2022A&A...657A..38M

8. Demars, D., Bonnefoy, M., Dougados, C., et al. (2023) "Emission line variability of young 10-30 M_{Jup} companions. I. The case of GQ Lup b and GSC 06214-00210 b," A&A, 676, A123 - 2023A&A...676A.123D

9. Petrus, S., Bonnefoy, M., Chauvin, G., et al. (2020) "A new take on the low-mass brown dwarf companions on wide orbits in Upper-Scorpius," A&A, 633, A124 - 2020A&A...633A.124P

INVESTIGATORS

Dorian Demars, Institut de Planetologie et d'Astrophysique de Grenoble, France (PI)
Mickael Bonnefoy, Université Grenoble Alpes, France (Delegated PI)
C. Dougados, Université Grenoble Alpes, France
Sarah Betti, University of Massachusetts at Amherst, United States
Katherine Follette, Amherst College, United States
P. Delorme, Université Grenoble Alpes, France
Gabriel-Dominique Marleau, Universität Duisburg-Essen, Germany
Yuhiko Aoyama, Kavli Institute for Astronomy and Astrophysics - Peking University, China
Simon Petrus, Universidad de Valparaìso, Chile
Gael Chauvin, Observatoire de la Côte d'Azur, France
Paulina Palma Bifani, Observatoire de la Côte d'Azur, France
Markus Janson, Stockholm University, Sweden
Simon Ringqvist, Stockholm University, Sweden
Thanawuth Thanathibodee, Boston University, United States
Benjamin Tessore, Institut de Planetologie et d'Astrophysique de Grenoble, France
Gayathri Viswanath, Stockholm University, Sweden

OBSERVATIONS

In the table below, the repeat factor is applied to the complete observation on that target, including its overhead.

✔ The PI acknowledged that all the telescope times listed below include overheads.

Run 113.26J1.001 • Run 1 • P113 • CRIRES • SM — Tel. Time: 07h28m

FLI: 100% • Turb.: 10% (Seeing < 0.6 arcsec, t0 > 5.2 ms) • pwv: 5.0mm • Sky: Clear • Airmass: 1.4

Target • SCR J0103-5515 • 01:03:35.655 • -55:15:56.243 — Tel. Time: 07h28m

OB1 Tel. Time: 3360 s Repeat: 1 x Total Tel. Time: 3360s	**Spec-AO** Gas cell: FREE Entrance slit width: w_0.4 Telescope Overheads: 360 s	**Observation** Gas cell: FREE Reference wavelength: 1228.488 Integration Time: 0 s Instrument Overheads: 0 s Signal/Noise: 0.0	**Observation** Gas cell: FREE Reference wavelength: 1228.488 Integration Time: 0 s Instrument Overheads: 0 s Signal/Noise: 0.0
	Observation Gas cell: FREE Reference wavelength: 1228.488 Integration Time: 0 s Instrument Overheads: 0 s Signal/Noise: 0.0		

Reference Targets

Type	Name	RA	Dec	Coord	Comment
NGS	SCR J0103-5515	01:03:35.655	-55:15:56.243	J2000	Host binary, NGS
SVGS	SCR J0103-5515	01:03:35.655	-55:15:56.243	J2000	Host binary, NGS

OB2 Tel. Time: 3360 s Repeat: 1 x Total Tel. Time: 3360s	**Spec-AO** Gas cell: FREE Entrance slit width: w_0.4 Telescope Overheads: 360 s	**Observation** Gas cell: FREE Reference wavelength: 1228.488 Integration Time: 0 s Instrument Overheads: 0 s Signal/Noise: 0.0	**Observation** Gas cell: FREE Reference wavelength: 1228.488 Integration Time: 0 s Instrument Overheads: 0 s Signal/Noise: 0.0
	Observation Gas cell: FREE Reference wavelength: 1228.488 Integration Time: 0 s Instrument Overheads: 0 s Signal/Noise: 0.0		

Reference Targets

Type	Name	RA	Dec	Coord	Comment
NGS	SCR J0103-5515	01:03:35.655	-55:15:56.243	J2000	Host binary, NGS
SVGS	SCR J0103-5515	01:03:35.655	-55:15:56.243	J2000	Host binary, NGS

OB3
Tel. Time: 3360 s
Repeat: 1 x
Total Tel. Time: 3360s

Spec-AO
Gas cell: FREE
Entrance slit width: w_0.4
Telescope Overheads: 360 s

Observation
Gas cell: FREE
Reference wavelength: 1228.488
Integration Time: 0 s
Instrument Overheads: 0 s
Signal/Noise: 0.0

Observation
Gas cell: FREE
Reference wavelength: 1228.488
Integration Time: 0 s
Instrument Overheads: 0 s
Signal/Noise: 0.0

Observation
Gas cell: FREE
Reference wavelength: 1228.488
Integration Time: 0 s
Instrument Overheads: 0 s
Signal/Noise: 0.0

Reference Targets

Type	Name	RA	Dec	Coord	Comment
NGS	SCR J0103-5515	01:03:35.655	-55:15:56.243	J2000	Host binary, NGS
SVGS	SCR J0103-5515	01:03:35.655	-55:15:56.243	J2000	Host binary, NGS

OB4
Tel. Time: 3360 s
Repeat: 1 x
Total Tel. Time: 3360s

Spec-AO
Gas cell: FREE
Entrance slit width: w_0.4
Telescope Overheads: 360 s

Observation
Gas cell: FREE
Reference wavelength: 1228.488
Integration Time: 0 s
Instrument Overheads: 0 s
Signal/Noise: 0.0

Observation
Gas cell: FREE
Reference wavelength: 1228.488
Integration Time: 0 s
Instrument Overheads: 0 s
Signal/Noise: 0.0

Observation
Gas cell: FREE
Reference wavelength: 1228.488
Integration Time: 0 s
Instrument Overheads: 0 s
Signal/Noise: 0.0

Reference Targets

Type	Name	RA	Dec	Coord	Comment
NGS	SCR J0103-5515	01:03:35.655	-55:15:56.243	J2000	Host binary, NGS
SVGS	SCR J0103-5515	01:03:35.655	-55:15:56.243	J2000	Host binary, NGS

OB5
Tel. Time: 3360 s
Repeat: 1 x
Total Tel. Time: 3360s

Spec-AO
Gas cell: FREE
Entrance slit width: w_0.4
Telescope Overheads: 360 s

Observation
Gas cell: FREE
Reference wavelength: 1228.488
Integration Time: 0 s
Instrument Overheads: 0 s
Signal/Noise: 0.0

Observation
Gas cell: FREE
Reference wavelength: 1228.488
Integration Time: 0 s
Instrument Overheads: 0 s
Signal/Noise: 0.0

Observation
Gas cell: FREE
Reference wavelength: 1228.488
Integration Time: 0 s
Instrument Overheads: 0 s
Signal/Noise: 0.0

Reference Targets

Type	Name	RA	Dec	Coord	Comment
NGS	SCR J0103-5515	01:03:35.655	-55:15:56.243	J2000	Host binary, NGS
SVGS	SCR J0103-5515	01:03:35.655	-55:15:56.243	J2000	Host binary, NGS

OB6
Tel. Time: 3360 s
Repeat: 1 x

Spec-AO
Gas cell: FREE
Entrance slit width: w_0.4

Observation
Gas cell: FREE
Reference wavelength: 1228.488

Observation
Gas cell: FREE
Reference wavelength: 1228.488

Total Tel. Time: 3360s	Telescope Overheads: 360 s	Integration Time: 0 s Instrument Overheads: 0 s Signal/Noise: 0.0	Integration Time: 0 s Instrument Overheads: 0 s Signal/Noise: 0.0
	Observation Gas cell: FREE Reference wavelength: 1228.488 Integration Time: 0 s Instrument Overheads: 0 s Signal/Noise: 0.0		

Reference Targets

Type	Name	RA	Dec	Coord	Comment
NGS	SCR J0103-5515	01:03:35.655	-55:15:56.243	J2000	Host binary, NGS
SVGS	SCR J0103-5515	01:03:35.655	-55:15:56.243	J2000	Host binary, NGS

OB7 Tel. Time: 3360 s Repeat: 1 x Total Tel. Time: 3360s	**Spec-AO** Gas cell: FREE Entrance slit width: w_0.4 Telescope Overheads: 360 s	**Observation** Gas cell: FREE Reference wavelength: 1228.488 Integration Time: 0 s Instrument Overheads: 0 s Signal/Noise: 0.0	**Observation** Gas cell: FREE Reference wavelength: 1228.488 Integration Time: 0 s Instrument Overheads: 0 s Signal/Noise: 0.0
	Observation Gas cell: FREE Reference wavelength: 1228.488 Integration Time: 0 s Instrument Overheads: 0 s Signal/Noise: 0.0		

Reference Targets

Type	Name	RA	Dec	Coord	Comment
NGS	SCR J0103-5515	01:03:35.655	-55:15:56.243	J2000	Host binary, NGS
SVGS	SCR J0103-5515	01:03:35.655	-55:15:56.243	J2000	Host binary, NGS

OB8 Tel. Time: 3360 s Repeat: 1 x Total Tel. Time: 3360s	**Spec-AO** Gas cell: FREE Entrance slit width: w_0.4 Telescope Overheads: 360 s	**Observation** Gas cell: FREE Reference wavelength: 1228.488 Integration Time: 0 s Instrument Overheads: 0 s Signal/Noise: 0.0	**Observation** Gas cell: FREE Reference wavelength: 1228.488 Integration Time: 0 s Instrument Overheads: 0 s Signal/Noise: 0.0
	Observation Gas cell: FREE Reference wavelength: 1228.488 Integration Time: 0 s Instrument Overheads: 0 s Signal/Noise: 0.0		

Reference Targets

Type	Name	RA	Dec	Coord	Comment
NGS	SCR J0103-5515	01:03:35.655	-55:15:56.243	J2000	Host binary, NGS
SVGS	SCR J0103-5515	01:03:35.655	-55:15:56.243	J2000	Host binary, NGS

Bibliography

[1] R. Abuter, J. Schreiber, F. Eisenhauer, T. Ott, M. Horrobin, and S. Gillesen. SINFONI data reduction software. *New Astronomy Reviews*, 50:398–400, June 2006. ISSN 1387-6473. doi: 10.1016/j.newar.2006.02.008. URL https://ui.adsabs.harvard.edu/abs/2006NewAR..50..398A. ADS Bibcode: 2006NewAR..50..398A.

[2] Jéa I. Adams Redai, Katherine B. Follette, Jason Wang, Clare Leonard, William Balmer, Laird M. Close, Beck Dacus, Jared R. Males, Katie M. Morzinski, Joseph Palmo, Laurent Pueyo, Elijah Spiro, Helena Treiber, Kimberly Ward-Duong, and Alex Watson. The Giant Accreting Protoplanet Survey (GAPlanetS): Optimization Techniques for Robust Detections of Protoplanets. *The Astronomical Journal*, 165:57, February 2023. ISSN 0004-6256. doi: 10.3847/1538-3881/aca60d. URL https://ui.adsabs.harvard.edu/abs/2023AJ....165...57A. Publisher: IOP ADS Bibcode: 2023AJ....165...57A.

[3] J. M. Alcalá, A. Natta, C. F. Manara, L. Spezzi, B. Stelzer, A. Frasca, K. Biazzo, E. Covino, S. Randich, E. Rigliaco, L. Testi, F. Comerón, G. Cupani, and V. D'Elia. X-shooter spectroscopy of young stellar objects. IV. Accretion in low-mass stars and substellar objects in Lupus. *Astronomy and Astrophysics*, 561:A2, January 2014. ISSN 0004-6361. doi: 10.1051/0004-6361/201322254. URL https://ui.adsabs.harvard.edu/abs/2014A&A...561A...2A. ADS Bibcode: 2014A&A...561A...2A.

[4] J. M. Alcalá, C. F. Manara, A. Natta, A. Frasca, L. Testi, B. Nisini, B. Stelzer, J. P. Williams, S. Antoniucci, K. Biazzo, E. Covino, M. Esposito, F. Getman, and E. Rigliaco. X-shooter spectroscopy of young stellar objects in Lupus. Accretion properties of class II and transitional objects. *Astronomy and Astrophysics*, 600:A20, April 2017. ISSN 0004-6361. doi: 10.1051/0004-6361/201629929. URL https://ui.adsabs.harvard.edu/abs/2017A&A...600A..20A. ADS Bibcode: 2017A&A...600A..20A.

[5] J. M. Alcalá, F. Z. Majidi, S. Desidera, A. Frasca, C. F. Manara, E. Rigliaco, R. Gratton, M. Bonnefoy, E. Covino, G. Chauvin, R. Claudi, V. D'Orazi, M. Langlois, C. Lazzoni, D. Mesa, J. E. Schlieder, and A. Vigan. 2MASS J15491331-3539118: a new low-mass wide companion of the GQ Lup system. *Astronomy & Astrophysics*, 635:L1, March 2020. ISSN 0004-6361, 1432-0746. doi: 10.1051/0004-6361/201937309. URL https://www.aanda.org/10.1051/0004-6361/201937309.

[6] S. H. P. Alencar, J. Bouvier, F. M. Walter, C. Dougados, J. F. Donati, R. Kurosawa, M. Romanova, X. Bonfils, G. H. R. A. Lima, S. Massaro, M. Ibrahimov, and E. Poretti. Accretion dynamics in the classical T Tauri star V2129 Ophiuchi. *Astronomy and Astrophysics*, 541:A116, May 2012. ISSN 0004-6361. doi: 10.1051/0004-6361/201118395. URL https://ui.adsabs.harvard.edu/abs/2012A&A...541A.116A. ADS Bibcode: 2012A&A...541A.116A.

[7] S. Antoniucci, B. Nisini, T. Giannini, E. Rigliaco, J. M. Alcalá, A. Natta, and B. Stelzer. X-shooter spectroscopy of young stellar objects. VI. H I line decrements. *Astronomy and Astrophysics*, 599:A105, March 2017. ISSN 0004-6361. doi: 10.1051/0004-6361/201629683. URL https://ui.adsabs.harvard.edu/abs/2017A&A...599A.105A. ADS Bibcode: 2017A&A...599A.105A.

[8] Yuhiko Aoyama and Masahiro Ikoma. Constraining Planetary Gas Accretion Rate from H α Line Width and Intensity: Case of PDS 70 b and c. *The Astrophysical Journal*, 885(2):L29, November 2019. ISSN 2041-8213. doi: 10.3847/2041-8213/ab5062. URL https://iopscience.iop.org/article/10.3847/2041-8213/ab5062.

[9] Yuhiko Aoyama, Masahiro Ikoma, and Takayuki Tanigawa. Theoretical Model of Hydrogen Line Emission from Accreting Gas Giants. *The Astrophysical Journal*, 866:84, October 2018. ISSN 0004-637X. doi: 10.3847/1538-4357/aadc11. URL https://ui.adsabs.harvard.edu/abs/2018ApJ...866...84A. Publisher: IOP ADS Bibcode: 2018ApJ...866...84A.

[10] Yuhiko Aoyama, Gabriel-Dominique Marleau, Masahiro Ikoma, and Christoph Mordasini. Comparison of Planetary Hα-emission Models: A New Correlation with Accretion Luminosity. *The Astrophysical Journal Letters*, 917(2):L30, August 2021. ISSN 2041-8205, 2041-8213. doi: 10.3847/2041-8213/ac19bd. URL https://iopscience.iop.org/article/10.3847/2041-8213/ac19bd.

[11] I. Appenzeller and B. Wolf. S CrA: a bright southern YY Orionis star. *Astronomy and Astrophysics*, 54:713–722, February 1977. ISSN 0004-6361. URL https://ui.adsabs.harvard.edu/abs/1977A&A....54..713A. ADS Bibcode: 1977A&A....54..713A.

[12] Ben A. Ayliffe and Matthew R. Bate. Gas accretion on to planetary cores: three-dimensional self-gravitating radiation hydrodynamical calculations. *Monthly Notices of the Royal Astronomical Society*, 393:49–64, February 2009. ISSN 0035-8711. doi: 10.1111/j.1365-2966.2008.14184.x. URL https://ui.adsabs.harvard.edu/abs/2009MNRAS.393...49A. Publisher: OUP ADS Bibcode: 2009MNRAS.393...49A.

[13] J. Bally, R. L. Snell, and R. Predmore. Radio images of the bipolar HII region S 106. *The Astrophysical Journal*, 272: 154–162, September 1983. ISSN 0004-637X. doi: 10.1086/161272. URL https://ui.adsabs.harvard.edu/abs/1983ApJ...272..154B. ADS Bibcode: 1983ApJ...272..154B.

[14] Isabelle Baraffe, Derek Homeier, France Allard, and Gilles Chabrier. New evolutionary models for pre-main sequence and main sequence low-mass stars down to the hydrogen-burning limit. *Astronomy and Astrophysics*, 577:A42, May 2015. ISSN 0004-6361. doi: 10.1051/0004-6361/201425481. URL https://ui.adsabs.harvard.edu/abs/2015A&A...577A..42B. ADS Bibcode: 2015A&A...577A..42B.

[15] David Barrado y Navascués and Eduardo L. Martín. An Empirical Criterion to Classify T Tauri Stars and Substellar Analogs Using Low-Resolution Optical Spectroscopy. *The Astronomical Journal*, 126:2997–3006, December 2003. ISSN 0004-6256. doi: 10.1086/379673. URL https://ui.adsabs.harvard.edu/abs/2003AJ....126.2997B. Publisher: IOP ADS Bibcode: 2003AJ....126.2997B.

[16] C. Batalha, D. F. Lopes, and N. M. Batalha. Variability of Southern T Tauri Stars. I. The Continuum and the Hβ Inverse P Cygni Profile of GQ Lupi. *The Astrophysical Journal*, 548:377–393, February 2001. ISSN 0004-637X. doi: 10.1086/318653. URL https://ui.adsabs.harvard.edu/abs/2001ApJ...548..377B. Publisher: IOP ADS Bibcode: 2001ApJ...548..377B.

[17] Myriam Benisty, Jaehan Bae, Stefano Facchini, Miriam Keppler, Richard Teague, Andrea Isella, Nicolas T. Kurtovic, Laura M. Pérez, Anibal Sierra, Sean M. Andrews, John Carpenter, Ian Czekala, Carsten Dominik, Thomas Henning, Francois Menard, Paola Pinilla, and Alice Zurlo. A Circumplanetary Disk around PDS70c. *The Astrophysical Journal*, 916: L2, July 2021. ISSN 0004-637X. doi: 10.3847/2041-8213/ac0f83. URL https://ui.adsabs.harvard.edu/abs/2021ApJ...916L...2B. Publisher: IOP ADS Bibcode: 2021ApJ...916L...2B.

[18] Georgina Beristain, Suzan Edwards, and John Kwan. Helium Emission from Classical T Tauri Stars: Dual Origin in Magnetospheric Infall and Hot Wind. *The Astrophysical Journal*, 551:1037–1064, April 2001. ISSN 0004-637X. doi: 10.1086/320233. URL https://ui.adsabs.harvard.edu/abs/2001ApJ...551.1037B. ADS Bibcode: 2001ApJ...551.1037B.

[19] C. Bertout, J. Krautter, C. Moellenhoff, and B. Wolf. Spectroscopic and photometric observations of the highly variable young star DR Tauri. *Astronomy and Astrophysics*, 61:737–745, December 1977. ISSN 0004-6361. URL https://ui.adsabs.harvard.edu/abs/1977A&A....61..737B. ADS Bibcode: 1977A&A....61..737B.

[20] Claude Bertout, Gibor Basri, and Jerome Bouvier. Accretion Disks around T Tauri Stars. *The Astrophysical Journal*, 330: 350, July 1988. ISSN 0004-637X. doi: 10.1086/166476. URL https://ui.adsabs.harvard.edu/abs/1988ApJ...330..350B. ADS Bibcode: 1988ApJ...330..350B.

[21] S. K. Betti, K. B. Follette, K. Ward-Duong, Y. Aoyama, G. D. Marleau, J. Bary, C. Robinson, M. Janson, W. Balmer, G. Chauvin, and P. Palma-Bifani. Erratum: "Near-infrared Accretion Signatures from the Circumbinary Planetary-mass Companion Delorme 1 (AB)b" (2022, ApJL, 935, L18). *The Astrophysical Journal*, 941:L20, December 2022. ISSN 0004-637X. doi: 10.3847/2041-8213/aca331. URL https://ui.adsabs.harvard.edu/abs/2022ApJ...941L..20B. Publisher: IOP ADS Bibcode: 2022ApJ...941L..20B.

[22] S. K. Betti, K. B. Follette, K. Ward-Duong, Y. Aoyama, G. D. Marleau, J. Bary, C. Robinson, M. Janson, W. Balmer, G. Chauvin, and P. Palma-Bifani. Near-infrared Accretion Signatures from the Circumbinary Planetary-mass Companion Delorme 1 (AB)b. *The Astrophysical Journal*, 935:L18, August 2022. ISSN 0004-637X. doi: 10.3847/2041-8213/ac85ef. URL https://ui.adsabs.harvard.edu/abs/2022ApJ...935L..18B. Publisher: IOP ADS Bibcode: 2022ApJ...935L..18B.



[23] S. K. Betti, K. B. Follette, K. Ward-Duong, A. E. Peck, Y. Aoyama, J. Bary, B. Dacus, S. Edwards, G. D. Marleau, K. Mohamed, J. Palmo, C. Plunkett, C. Robinson, and H. Wang. The Comprehensive Archive of Substellar and Planetary Accretion Rates. *The Astronomical Journal*, 166:262, December 2023. ISSN 0004-6256. doi: 10.3847/1538-3881/ad06b8. URL https://ui.adsabs.harvard.edu/abs/2023AJ....166..262B. Publisher: IOP ADS Bibcode: 2023AJ....166..262B.

[24] K. Biazzo, A. Frasca, J. M. Alcalá, M. Zusi, E. Covino, S. Randich, M. Esposito, C. F. Manara, S. Antoniucci, B. Nisini, E. Rigliaco, and F. Getman. X-shooter spectroscopy of young stellar objects in Lupus. Lithium, iron, and barium elemental abundances. *Astronomy and Astrophysics*, 605:A66, September 2017. ISSN 0004-6361. doi: 10.1051/0004-6361/201730850. URL https://ui.adsabs.harvard.edu/abs/2017A&A...605A..66B. ADS Bibcode: 2017A&A...605A..66B.

[25] Lauren I. Biddle, Brendan P. Bowler, Yifan Zhou, Kyle Franson, and Zhoujian Zhang. Deep Paβ Imaging of the Candidate Accreting Protoplanet AB Aur b. *The Astronomical Journal*, 167:172, April 2024. ISSN 0004-6256. doi: 10.3847/1538-3881/ad2a52. URL https://ui.adsabs.harvard.edu/abs/2024AJ....167..172B. Publisher: IOP ADS Bibcode: 2024AJ....167..172B.

[26] P. Bodenheimer and J. B. Pollack. Calculations of the accretion and evolution of giant planets: The effects of solid cores. *Icarus*, 67:391–408, September 1986. ISSN 0019-1035. doi: 10.1016/0019-1035(86)90122-3. URL https://ui.adsabs.harvard.edu/abs/1986Icar...67..391B. ADS Bibcode: 1986Icar...67..391B.

[27] Aaron C. Boley, Tristen Hayfield, Lucio Mayer, and Richard H. Durisen. Clumps in the outer disk by disk instability: Why they are initially gas giants and the legacy of disruption. *Icarus*, 207:509–516, June 2010. ISSN 0019-1035. doi: 10.1016/j.icarus.2010.01.015. URL https://ui.adsabs.harvard.edu/abs/2010Icar..207..509B. ADS Bibcode: 2010Icar..207..509B.

[28] Aaron C. Boley, Ravit Helled, and Matthew J. Payne. The Heavy-element Composition of Disk Instability Planets Can Range from Sub- to Super-nebular. *The Astrophysical Journal*, 735:30, July 2011. ISSN 0004-637X. doi: 10.1088/0004-637X/735/1/30. URL https://ui.adsabs.harvard.edu/abs/2011ApJ...735...30B. Publisher: IOP ADS Bibcode: 2011ApJ...735...30B.

[29] M. Bonnefoy, G. Chauvin, A. M. Lagrange, P. Rojo, F. Allard, C. Pinte, C. Dumas, and D. Homeier. A library of near-infrared integral field spectra of young M-L dwarfs. *Astronomy and Astrophysics*, 562:A127, February 2014. ISSN 0004-6361. doi: 10.1051/0004-6361/201118270. URL https://ui.adsabs.harvard.edu/abs/2014A&A...562A.127B. ADS Bibcode: 2014A&A...562A.127B.

[30] A. P. Boss. Giant planet formation by gravitational instability. *Science*, 276:1836–1839, January 1997. ISSN 0036-8075. doi: 10.1126/science.276.5320.1836. URL https://ui.adsabs.harvard.edu/abs/1997Sci...276.1836B. ADS Bibcode: 1997Sci...276.1836B.

[31] Alan P. Boss. Bipolar Flows, Molecular Gas Disks, and the Collapse and Accretion of Rotating Interstellar Clouds. *The Astrophysical Journal*, 316:721, May 1987. ISSN 0004-637X. doi: 10.1086/165237. URL https://ui.adsabs.harvard.edu/abs/1987ApJ...316..721B. ADS Bibcode: 1987ApJ...316..721B.

[32] Anne Boucher, David Lafrenière, Jonathan Gagné, Lison Malo, Jacqueline K. Faherty, René Doyon, and Christine H. Chen. BANYAN. VIII. New Low-mass Stars and Brown Dwarfs with Candidate Circumstellar Disks. *The Astrophysical Journal*, 832:50, November 2016. ISSN 0004-637X. doi: 10.3847/0004-637X/832/1/50. URL https://ui.adsabs.harvard.edu/abs/2016ApJ...832...50B. Publisher: IOP ADS Bibcode: 2016ApJ...832...50B.

[33] J. Bouvier, S. Cabrit, M. Fernandez, E. L. Martin, and J. M. Matthews. COYOTES I : the photometric variability and rotational evolution of T Tauri stars. *Astronomy and Astrophysics*, 272:176–206, May 1993. ISSN 0004-6361. URL https://ui.adsabs.harvard.edu/abs/1993A&A...272..176B. ADS Bibcode: 1993A&A...272..176B.

[34] J. Bouvier, A. Chelli, S. Allain, L. Carrasco, R. Costero, I. Cruz-Gonzalez, C. Dougados, M. Fernández, E. L. Martín, F. Ménard, C. Mennessier, R. Mujica, E. Recillas, L. Salas, G. Schmidt, and R. Wichmann. Magnetospheric accretion onto the T Tauri star AA Tauri. I. Constraints from multisite spectrophotometric monitoring. *Astronomy and Astrophysics*, 349:619–635, September 1999. ISSN 0004-6361. URL https://ui.adsabs.harvard.edu/abs/1999A&A...349..619B. ADS Bibcode: 1999A&A...349..619B.



[35] J. Bouvier, K. N. Grankin, S. H. P. Alencar, C. Dougados, M. Fernández, G. Basri, C. Batalha, E. Guenther, M. A. Ibrahimov, T. Y. Magakian, S. Y. Melnikov, P. P. Petrov, M. V. Rud, and M. R. Zapatero Osorio. Eclipses by circumstellar material in the T Tauri star AA Tau. II. Evidence for non-stationary magnetospheric accretion. *Astronomy and Astrophysics*, 409:169–192, October 2003. ISSN 0004-6361. doi: 10.1051/0004-6361:20030938. URL https://ui.adsabs.harvard.edu/abs/2003A&A...409..169B. ADS Bibcode: 2003A&A...409..169B.

[36] J. Bouvier, S. P. Matt, S. Mohanty, A. Scholz, K. G. Stassun, and C. Zanni. *Angular Momentum Evolution of Young Low-Mass Stars and Brown Dwarfs: Observations and Theory*. eprint: arXiv:1309.7851, January 2014. doi: 10.2458/azu_uapress_9780816531240-ch019. URL https://ui.adsabs.harvard.edu/abs/2014prpl.conf..433B. Conference Name: Protostars and Planets VI Pages: 433-450 ADS Bibcode: 2014prpl.conf..433B.

[37] Brendan P. Bowler and Eric L. Nielsen. *Occurrence Rates from Direct Imaging Surveys*. January 2018. doi: 10.1007/978-3-319-55333-7_155. URL https://ui.adsabs.harvard.edu/abs/2018haex.bookE.155B. Pages: 155 Publication Title: Handbook of Exoplanets ADS Bibcode: 2018haex.bookE.155B.

[38] Brendan P. Bowler, Michael C. Liu, Adam L. Kraus, Andrew W. Mann, and Michael J. Ireland. A Disk around the Planetary-mass Companion GSC 06214-00210 b: Clues about the Formation of Gas Giants on Wide Orbits. *The Astrophysical Journal*, 743:148, December 2011. ISSN 0004-637X. doi: 10.1088/0004-637X/743/2/148. URL https://ui.adsabs.harvard.edu/abs/2011ApJ...743..148B. Publisher: IOP ADS Bibcode: 2011ApJ...743..148B.

[39] Brendan P. Bowler, Michael C. Liu, Adam L. Kraus, and Andrew W. Mann. SPECTROSCOPIC CONFIRMATION OF YOUNG PLANETARY-MASS COMPANIONS ON WIDE ORBITS. *The Astrophysical Journal*, 784(1):65, March 2014. ISSN 0004-637X, 1538-4357. doi: 10.1088/0004-637X/784/1/65. URL https://iopscience.iop.org/article/10.1088/0004-637X/784/1/65.

[40] Brendan P. Bowler, Sean M. Andrews, Adam L. Kraus, Michael J. Ireland, Gregory Herczeg, Luca Ricci, John Carpenter, and Michael E. Brown. AN ALMA CONSTRAINT ON THE GSC 6214-210 B CIRCUM-SUBSTELLAR ACCRETION DISK MASS. *The Astrophysical Journal*, 805(2):L17, May 2015. ISSN 2041-8213. doi: 10.1088/2041-8205/805/2/L17. URL https://iopscience.iop.org/article/10.1088/2041-8205/805/2/L17.

[41] Brendan P. Bowler, Quang H. Tran, Zhoujian Zhang, Marvin Morgan, Katelyn B. Ashok, Sarah Blunt, Marta L. Bryan, Analis E. Evans, Kyle Franson, Daniel Huber, Vighnesh Nagpal, Ya-Lin Wu, and Yifan Zhou. Rotation Periods, Inclinations, and Obliquities of Cool Stars Hosting Directly Imaged Substellar Companions: Spin-Orbit Misalignments Are Common. *The Astronomical Journal*, 165:164, April 2023. ISSN 0004-6256. doi: 10.3847/1538-3881/acbd34. URL https://ui.adsabs.harvard.edu/abs/2023AJ....165..164B. Publisher: IOP ADS Bibcode: 2023AJ....165..164B.

[42] Sean D. Brittain, Joan R. Najita, Ruobing Dong, and Zhaohuan Zhu. The Planetary Luminosity Problem: "Missing Planets" and the Observational Consequences of Episodic Accretion. *The Astrophysical Journal*, 895:48, May 2020. ISSN 0004-637X. doi: 10.3847/1538-4357/ab8388. URL https://ui.adsabs.harvard.edu/abs/2020ApJ...895...48B. Publisher: IOP ADS Bibcode: 2020ApJ...895...48B.

[43] C. Broeg, T. O. B. Schmidt, E. Guenther, A. Gaedke, A. Bedalov, R. Neuhäuser, and F. M. Walter. Rotational period of GQ Lupi. *Astronomy and Astrophysics*, 468:1039–1044, June 2007. ISSN 0004-6361. doi: 10.1051/0004-6361:20066793. URL https://ui.adsabs.harvard.edu/abs/2007A&A...468.1039B. ADS Bibcode: 2007A&A...468.1039B.

[44] Marta L. Bryan, Björn Benneke, Heather A. Knutson, Konstantin Batygin, and Brendan P. Bowler. Constraints on the spin evolution of young planetary-mass companions. *Nature Astronomy*, 2:138–144, December 2018. ISSN 2397-3366. doi: 10.1038/s41550-017-0325-8. URL https://ui.adsabs.harvard.edu/abs/2018NatAs...2..138B. ADS Bibcode: 2018NatAs...2..138B.

[45] Eric J. Bubar, Marc Schaeuble, Jeremy R. King, Eric E. Mamajek, and John R. Stauffer. Lithium in the Upper Centaurus Lupus and Lower Centaurus Crux Subgroups of Scorpius-Centaurus. *The Astronomical Journal*, 142:180, December 2011. ISSN 0004-6256. doi: 10.1088/0004-6256/142/6/180. URL https://ui.adsabs.harvard.edu/abs/2011AJ....142..180B. Publisher: IOP ADS Bibcode: 2011AJ....142..180B.

[46] Nuria Calvet and Erik Gullbring. The Structure and Emission of the Accretion Shock in T Tauri Stars. *The Astrophysical Journal*, 509:802–818, December 1998. ISSN 0004-637X. doi: 10.1086/306527. URL https://ui.adsabs.harvard.edu/abs/1998ApJ...509..802C. ADS Bibcode: 1998ApJ...509..802C.



[47] Nuria Calvet and Lee Hartmann. Balmer Line Profiles for Infalling T Tauri Envelopes. *The Astrophysical Journal*, 386:239, February 1992. ISSN 0004-637X. doi: 10.1086/171010. URL https://ui.adsabs.harvard.edu/abs/1992ApJ...386..239C. ADS Bibcode: 1992ApJ...386..239C.

[48] V. Christiaens, M. Samland, Th. Henning, B. Portilla-Revelo, G. Perotti, E. Matthews, O. Absil, L. Decin, I. Kamp, A. Boccaletti, B. Tabone, G. D. Marleau, E. F. van Dishoeck, M. Güdel, P. O. Lagage, D. Barrado, A. Caratti o Garatti, A. M. Glauser, G. Olofsson, T. P. Ray, S. Scheithauer, B. Vandenbussche, L. B. F. M. Waters, A. M. Arabhavi, S. L. Grant, H. Jang, J. Kanwar, J. Schreiber, K. Schwarz, M. Temmink, and G. Östlin. MINDS: JWST/NIRCam imaging of the protoplanetary disk PDS 70. A spiral accretion stream and a potential third protoplanet. *Astronomy and Astrophysics*, 685:L1, May 2024. ISSN 0004-6361. doi: 10.1051/0004-6361/202349089. URL https://ui.adsabs.harvard.edu/abs/2024A&A...685L...1C. ADS Bibcode: 2024A&A...685L...1C.

[49] L. M. Close, K. B. Follette, J. R. Males, A. Puglisi, M. Xompero, D. Apai, J. Najita, A. J. Weinberger, K. Morzinski, T. J. Rodigas, P. Hinz, V. Bailey, and R. Briguglio. Discovery of Hα Emission from the Close Companion inside the Gap of Transitional Disk HD 142527. *The Astrophysical Journal*, 781:L30, February 2014. ISSN 0004-637X. doi: 10.1088/2041-8205/781/2/L30. URL https://ui.adsabs.harvard.edu/abs/2014ApJ...781L..30C. Publisher: IOP ADS Bibcode: 2014ApJ...781L..30C.

[50] G. Costigan, Jorick S. Vink, A. Scholz, T. Ray, and L. Testi. Temperaments of young stars: rapid mass accretion rate changes in T Tauri and Herbig Ae stars. *Monthly Notices of the Royal Astronomical Society*, 440:3444–3461, June 2014. ISSN 0035-8711. doi: 10.1093/mnras/stu529. URL https://ui.adsabs.harvard.edu/abs/2014MNRAS.440.3444C. Publisher: OUP ADS Bibcode: 2014MNRAS.440.3444C.

[51] Gabriele Cugno, Polychronis Patapis, Andrea Banzatti, Michael Meyer, Felix A. Dannert, Tomas Stolker, Ryan J. MacDonald, and Klaus M. Pontoppidan. Mid-infrared Spectrum of the Disk around the Forming Companion GQ Lup B Revealed by JWST/MIRI. *The Astrophysical Journal*, 966:L21, May 2024. ISSN 0004-637X. doi: 10.3847/2041-8213/ad3cbc. URL https://ui.adsabs.harvard.edu/abs/2024ApJ...966L..21C. Publisher: IOP ADS Bibcode: 2024ApJ...966L..21C.

[52] Andrew Cumming, Ravit Helled, and Julia Venturini. The primordial entropy of Jupiter. *Monthly Notices of the Royal Astronomical Society*, 477:4817–4823, July 2018. ISSN 0035-8711. doi: 10.1093/mnras/sty1000. URL https://ui.adsabs.harvard.edu/abs/2018MNRAS.477.4817C. Publisher: OUP ADS Bibcode: 2018MNRAS.477.4817C.

[53] Hans Dekker, Sandro D'Odorico, Andreas Kaufer, Bernard Delabre, and Heinz Kotzlowski. Design, construction, and performance of UVES, the echelle spectrograph for the UT2 Kueyen Telescope at the ESO Paranal Observatory. 4008:534–545, August 2000. doi: 10.1117/12.395512. URL https://ui.adsabs.harvard.edu/abs/2000SPIE.4008..534D. Conference Name: Optical and IR Telescope Instrumentation and Detectors ADS Bibcode: 2000SPIE.4008..534D.

[54] P. Delorme, J. Gagné, J. H. Girard, A. M. Lagrange, G. Chauvin, M. E. Naud, D. Lafrenière, R. Doyon, A. Riedel, M. Bonnefoy, and L. Malo. Direct-imaging discovery of a 12-14 Jupiter-mass object orbiting a young binary system of very low-mass stars. *Astronomy and Astrophysics*, 553:L5, May 2013. ISSN 0004-6361. doi: 10.1051/0004-6361/201321169. URL https://ui.adsabs.harvard.edu/abs/2013A&A...553L...5D. ADS Bibcode: 2013A&A...553L...5D.

[55] D. Demars, M. Bonnefoy, C. Dougados, Y. Aoyama, T. Thanathibodee, G. D. Marleau, P. Tremblin, P. Delorme, P. Palma-Bifani, S. Petrus, B. P. Bowler, G. Chauvin, and A. M. Lagrange. Emission line variability of young 10-30 MJup companions. I. The case of GQ Lup b and GSC 06214-00210 b. *Astronomy and Astrophysics*, 676:A123, August 2023. ISSN 0004-6361. doi: 10.1051/0004-6361/202346221. URL https://ui.adsabs.harvard.edu/abs/2023A&A...676A.123D. ADS Bibcode: 2023A&A...676A.123D.

[56] Hongping Deng, Lucio Mayer, and Farzana Meru. Convergence of the Critical Cooling Rate for Protoplanetary Disk Fragmentation Achieved: The Key Role of Numerical Dissipation of Angular Momentum. *The Astrophysical Journal*, 847:43, September 2017. ISSN 0004-637X. doi: 10.3847/1538-4357/aa872b. URL https://ui.adsabs.harvard.edu/abs/2017ApJ...847...43D. Publisher: IOP ADS Bibcode: 2017ApJ...847...43D.

[57] J. F. Donati, M. M. Jardine, S. G. Gregory, P. Petit, J. Bouvier, C. Dougados, F. Ménard, A. Collier Cameron, T. J. Harries, S. V. Jeffers, and F. Paletou. Magnetic fields and accretion flows on the classical T Tauri star V2129 Oph. *Monthly Notices of the Royal Astronomical Society*, 380:1297–1312, October 2007. ISSN 0035-8711. doi: 10.1111/j.1365-2966.2007.12194.x. URL https://ui.adsabs.harvard.edu/abs/2007MNRAS.380.1297D. ADS Bibcode: 2007MNRAS.380.1297D.



[58] J. F. Donati, J. Bouvier, F. M. Walter, S. G. Gregory, M. B. Skelly, G. A. J. Hussain, E. Flaccomio, C. Argiroffi, K. N. Grankin, M. M. Jardine, F. Ménard, C. Dougados, and M. M. Romanova. Non-stationary dynamo and magnetospheric accretion processes of the classical T Tauri star V2129 Oph. *Monthly Notices of the Royal Astronomical Society*, 412: 2454–2468, April 2011. ISSN 0035-8711. doi: 10.1111/j.1365-2966.2010.18069.x. URL https://ui.adsabs.harvard.edu/abs/2011MNRAS.412.2454D. Publisher: OUP ADS Bibcode: 2011MNRAS.412.2454D.

[59] J. Drążkowska, B. Bitsch, M. Lambrechts, G. D. Mulders, D. Harsono, A. Vazan, B. Liu, C. W. Ormel, K. Kretke, and A. Morbidelli. Planet Formation Theory in the Era of ALMA and Kepler: from Pebbles to Exoplanets. 534:717, July 2023. doi: 10.48550/arXiv.2203.09759. URL https://ui.adsabs.harvard.edu/abs/2023ASPC..534..717D. Conference Name: Protostars and Planets VII Place: eprint: arXiv:2203.09759 ADS Bibcode: 2023ASPC..534..717D.

[60] Simon C. Eriksson, Rubén Asensio Torres, Markus Janson, Yuhiko Aoyama, Gabriel-Dominique Marleau, Mickael Bonnefoy, and Simon Petrus. Strong H α emission and signs of accretion in a circumbinary planetary mass companion from MUSE. *Astronomy & Astrophysics*, 638:L6, June 2020. ISSN 0004-6361, 1432-0746. doi: 10.1051/0004-6361/202038131. URL https://www.aanda.org/10.1051/0004-6361/202038131.

[61] Claire F. Esau, Tim J. Harries, and Jerome Bouvier. Line and continuum radiative transfer modelling of AA Tau. *Monthly Notices of the Royal Astronomical Society*, 443:1022–1043, September 2014. ISSN 0035-8711. doi: 10.1093/mnras/stu1211. URL https://ui.adsabs.harvard.edu/abs/2014MNRAS.443.1022E. ADS Bibcode: 2014MNRAS.443.1022E.

[62] C. C. Espaillat, C. E. Robinson, M. M. Romanova, T. Thanathibodee, J. Wendeborn, N. Calvet, M. Reynolds, and J. Muzerolle. Measuring the density structure of an accretion hot spot. *Nature*, 597:41–44, September 2021. ISSN 0028-0836. doi: 10.1038/s41586-021-03751-5. URL https://ui.adsabs.harvard.edu/abs/2021Natur.597...41E. ADS Bibcode: 2021Natur.597...41E.

[63] W. J. Fischer, L. A. Hillenbrand, G. J. Herczeg, D. Johnstone, A. Kospal, and M. M. Dunham. Accretion Variability as a Guide to Stellar Mass Assembly. 534:355, July 2023. doi: 10.48550/arXiv.2203.11257. URL https://ui.adsabs.harvard.edu/abs/2023ASPC..534..355F. Conference Name: Protostars and Planets VII Place: eprint: arXiv:2203.11257 ADS Bibcode: 2023ASPC..534..355F.

[64] Katherine B. Follette, Laird M. Close, Jared R. Males, Kimberly Ward-Duong, William O. Balmer, Jéa Adams Redai, Julio Morales, Catherine Sarosi, Beck Dacus, Robert J. De Rosa, Fernando Garcia Toro, Clare Leonard, Bruce Macintosh, Katie M. Morzinski, Wyatt Mullen, Joseph Palmo, Raymond Nzaba Saitoti, Elijah Spiro, Helena Treiber, Kevin Wagner, Jason Wang, David Wang, Alex Watson, and Alycia J. Weinberger. The Giant Accreting Protoplanet Survey (GAPlanetS)-Results from a 6 yr Campaign to Image Accreting Protoplanets. *The Astronomical Journal*, 165:225, June 2023. ISSN 0004-6256. doi: 10.3847/1538-3881/acc183. URL https://ui.adsabs.harvard.edu/abs/2023AJ....165..225F. Publisher: IOP ADS Bibcode: 2023AJ....165..225F.

[65] A. Frasca, K. Biazzo, J. M. Alcalá, C. F. Manara, B. Stelzer, E. Covino, and S. Antoniucci. X-shooter spectroscopy of young stellar objects in Lupus. Atmospheric parameters, membership, and activity diagnostics. *Astronomy and Astrophysics*, 602:A33, June 2017. ISSN 0004-6361. doi: 10.1051/0004-6361/201630108. URL https://ui.adsabs.harvard.edu/abs/2017A&A...602A..33F. ADS Bibcode: 2017A&A...602A..33F.

[66] W. Freudling, M. Romaniello, D. M. Bramich, P. Ballester, V. Forchi, C. E. García-Dabló, S. Moehler, and M. J. Neeser. Automated data reduction workflows for astronomy. The ESO Reflex environment. *Astronomy and Astrophysics*, 559: A96, November 2013. ISSN 0004-6361. doi: 10.1051/0004-6361/201322494. URL https://ui.adsabs.harvard.edu/abs/2013A&A...559A..96F. ADS Bibcode: 2013A&A...559A..96F.

[67] B. Fuhrmeister, S. Czesla, J. H. M. M. Schmitt, S. V. Jeffers, J. A. Caballero, M. Zechmeister, A. Reiners, I. Ribas, P. J. Amado, A. Quirrenbach, V. J. S. Béjar, D. Galadí-Enríquez, E. W. Guenther, M. Kürster, D. Montes, and W. Seifert. The CARMENES search for exoplanets around M dwarfs. Wing asymmetries of Hα, Na I D, and He I lines. *Astronomy and Astrophysics*, 615:A14, July 2018. ISSN 0004-6361. doi: 10.1051/0004-6361/201732204. URL https://ui.adsabs.harvard.edu/abs/2018A&A...615A..14F. ADS Bibcode: 2018A&A...615A..14F.

[68] Jonathan Gagné, Eric E. Mamajek, Lison Malo, Adric Riedel, David Rodriguez, David Lafrenière, Jacqueline K. Faherty, Olivier Roy-Loubier, Laurent Pueyo, Annie C. Robin, and René Doyon. BANYAN. XI. The BANYAN Σ Multivariate Bayesian Algorithm to Identify Members of Young Associations with 150 pc. *The Astrophysical Journal*, 856:23, March 2018. ISSN 0004-637X. doi: 10.3847/1538-4357/aaae09. URL https://ui.adsabs.harvard.edu/abs/2018ApJ...856...23G. Publisher: IOP ADS Bibcode: 2018ApJ...856...23G.



[69] Gaia Collaboration, T. Prusti, J. H. J. de Bruijne, A. G. A. Brown, A. Vallenari, C. Babusiaux, C. A. L. Bailer-Jones, U. Bastian, M. Biermann, D. W. Evans, L. Eyer, F. Jansen, C. Jordi, S. A. Klioner, U. Lammers, L. Lindegren, X. Luri, F. Mignard, D. J. Milligan, C. Panem, V. Poinsignon, D. Pourbaix, S. Randich, G. Sarri, P. Sartoretti, H. I. Siddiqui, C. Soubiran, V. Valette, F. van Leeuwen, N. A. Walton, C. Aerts, F. Arenou, M. Cropper, R. Drimmel, E. Høg, D. Katz, M. G. Lattanzi, W. O'Mullane, E. K. Grebel, A. D. Holland, C. Huc, X. Passot, L. Bramante, C. Cacciari, J. Castañeda, L. Chaoul, N. Cheek, F. De Angeli, C. Fabricius, R. Guerra, J. Hernández, A. Jean-Antoine-Piccolo, E. Masana, R. Messineo, N. Mowlavi, K. Nienartowicz, D. Ordóñez-Blanco, P. Panuzzo, J. Portell, P. J. Richards, M. Riello, G. M. Seabroke, P. Tanga, F. Thévenin, J. Torra, S. G. Els, G. Gracia-Abril, G. Comoretto, M. Garcia-Reinaldos, T. Lock, E. Mercier, M. Altmann, R. Andrae, T. L. Astraatmadja, I. Bellas-Velidis, K. Benson, J. Berthier, R. Blomme, G. Busso, B. Carry, A. Cellino, G. Clementini, S. Cowell, O. Creevey, J. Cuypers, M. Davidson, J. De Ridder, A. de Torres, L. Delchambre, A. Dell'Oro, C. Ducourant, Y. Frémat, M. García-Torres, E. Gosset, J. L. Halbwachs, N. C. Hambly, D. L. Harrison, M. Hauser, D. Hestroffer, S. T. Hodgkin, H. E. Huckle, A. Hutton, G. Jasniewicz, S. Jordan, M. Kontizas, A. J. Korn, A. C. Lanzafame, M. Manteiga, A. Moitinho, K. Muinonen, J. Osinde, E. Pancino, T. Pauwels, J. M. Petit, A. Recio-Blanco, A. C. Robin, L. M. Sarro, C. Siopis, M. Smith, K. W. Smith, A. Sozzetti, W. Thuillot, W. van Reeven, Y. Viala, U. Abbas, A. Abreu Aramburu, S. Accart, J. J. Aguado, P. M. Allan, W. Allasia, G. Altavilla, M. A. Álvarez, J. Alves, R. I. Anderson, A. H. Andrei, E. Anglada Varela, E. Antiche, T. Antoja, S. Antón, B. Arcay, A. Atzei, L. Ayache, N. Bach, S. G. Baker, L. Balaguer-Núñez, C. Barache, C. Barata, A. Barbier, F. Barblan, M. Baroni, D. Barrado y Navascués, M. Barros, M. A. Barstow, U. Becciani, M. Bellazzini, G. Bellei, A. Bello García, V. Belokurov, P. Bendjoya, A. Berihuete, L. Bianchi, O. Bienaymé, F. Billebaud, N. Blagorodnova, S. Blanco-Cuaresma, T. Boch, A. Bombrun, R. Borrachero, S. Bouquillon, G. Bourda, H. Bouy, A. Bragaglia, M. A. Breddels, N. Brouillet, T. Brüsemeister, B. Bucciarelli, F. Budnik, P. Burgess, R. Burgon, A. Burlacu, D. Busonero, R. Buzzi, E. Caffau, J. Cambras, H. Campbell, R. Cancelliere, T. Cantat-Gaudin, T. Carlucci, J. M. Carrasco, M. Castellani, P. Charlot, J. Charnas, P. Charvet, F. Chassat, A. Chiavassa, M. Clotet, G. Cocozza, R. S. Collins, P. Collins, G. Costigan, F. Crifo, N. J. G. Cross, M. Crosta, C. Crowley, C. Dafonte, Y. Damerdji, A. Dapergolas, P. David, M. David, P. De Cat, F. de Felice, P. de Laverny, F. De Luise, R. De March, D. de Martino, R. de Souza, J. Debosscher, E. del Pozo, M. Delbo, A. Delgado, H. E. Delgado, F. di Marco, P. Di Matteo, S. Diakite, E. Distefano, C. Dolding, S. Dos Anjos, P. Drazinos, J. Durán, Y. Dzigan, E. Ecale, B. Edvardsson, H. Enke, M. Erdmann, D. Escolar, M. Espina, N. W. Evans, G. Eynard Bontemps, C. Fabre, M. Fabrizio, S. Faigler, A. J. Falcão, M. Farràs Casas, F. Faye, L. Federici, G. Fedorets, J. Fernández-Hernández, P. Fernique, A. Fienga, F. Figueras, F. Filippi, K. Findeisen, A. Fonti, M. Fouesneau, E. Fraile, M. Fraser, J. Fuchs, R. Furnell, M. Gai, S. Galleti, L. Galluccio, D. Garabato, F. García-Sedano, P. Garé, A. Garofalo, N. Garralda, P. Gavras, J. Gerssen, R. Geyer, G. Gilmore, S. Girona, G. Giuffrida, M. Gomes, A. González-Marcos, J. González-Núñez, J. J. González-Vidal, M. Granvik, A. Guerrier, P. Guillout, J. Guiraud, A. Gúrpide, R. Gutiérrez-Sánchez, L. P. Guy, R. Haigron, D. Hatzidimitriou, M. Haywood, U. Heiter, A. Helmi, D. Hobbs, W. Hofmann, B. Holl, G. Holland, J. A. S. Hunt, A. Hypki, V. Icardi, M. Irwin, G. Jevardat de Fombelle, P. Jofré, P. G. Jonker, A. Jorissen, F. Julbe, A. Karampelas, A. Kochoska, R. Kohley, K. Kolenberg, E. Kontizas, S. E. Koposov, G. Kordopatis, P. Koubsky, A. Kowalczyk, A. Krone-Martins, M. Kudryashova, I. Kull, R. K. Bachchan, F. Lacoste-Seris, A. F. Lanza, J. B. Lavigne, C. Le Poncin-Lafitte, Y. Lebreton, T. Lebzelter, S. Leccia, N. Leclerc, I. Lecoeur-Taibi, V. Lemaitre, H. Lenhardt, F. Leroux, S. Liao, E. Licata, H. E. P. Lindstrøm, T. A. Lister, E. Livanou, A. Lobel, W. Löffler, M. López, A. Lopez-Lozano, D. Lorenz, T. Loureiro, I. MacDonald, T. Magalhães Fernandes, S. Managau, R. G. Mann, G. Mantelet, O. Marchal, J. M. Marchant, M. Marconi, J. Marie, S. Marinoni, P. M. Marrese, G. Marschalkó, D. J. Marshall, J. M. Martín-Fleitas, M. Martino, N. Mary, G. Matijevič, T. Mazeh, P. J. McMillan, S. Messina, A. Mestre, D. Michalik, N. R. Millar, B. M. H. Miranda, D. Molina, R. Molinaro, M. Molinaro, L. Molnár, M. Moniez, P. Montegriffo, D. Monteiro, R. Mor, A. Mora, R. Morbidelli, T. Morel, S. Morgenthaler, T. Morley, D. Morris, A. F. Mulone, T. Muraveva, I. Musella, J. Narbonne, G. Nelemans, L. Nicastro, L. Noval, C. Ordénovic, J. Ordieres-Meré, P. Osborne, C. Pagani, I. Pagano, F. Pailler, H. Palacin, L. Palaversa, P. Parsons, T. Paulsen, M. Pecoraro, R. Pedrosa, H. Pentikäinen, J. Pereira, B. Pichon, A. M. Piersimoni, F. X. Pineau, E. Plachy, G. Plum, E. Poujoulet, A. Prša, L. Pulone, S. Ragaini, S. Rago, N. Rambaux, M. Ramos-Lerate, P. Ranalli, G. Rauw, A. Read, S. Regibo, F. Renk, C. Reylé, R. A. Ribeiro, L. Rimoldini, V. Ripepi, A. Riva, G. Rixon, M. Roelens, M. Romero-Gómez, N. Rowell, F. Royer, A. Rudolph, L. Ruiz-Dern, G. Sadowski, T. Sagristà Sellés, J. Sahlmann, J. Salgado, E. Salguero, M. Sarasso, H. Savietto, A. Schnorhk, M. Schultheis, E. Sciacca, M. Segol, J. C. Segovia, D. Segransan, E. Serpell, I. C. Shih, R. Smareglia, R. L. Smart, C. Smith, E. Solano, F. Solitro, R. Sordo, S. Soria Nieto, J. Souchay, A. Spagna, F. Spoto, U. Stampa, I. A. Steele, H. Steidelmüller, C. A. Stephenson, H. Stoev, F. F. Suess, M. Süveges, J. Surdej, L. Szabados, E. Szegedi-Elek, D. Tapiador, F. Taris, G. Tauran, M. B. Taylor, R. Teixeira, D. Terrett, B. Tingley, S. C. Trager, C. Turon, A. Ulla, E. Utrilla, G. Valentini, A. van Elteren, E. Van Hemelryck, M. van Leeuwen, M. Varadi, A. Vecchiato, J. Veljanoski, T. Via, D. Vicente, S. Vogt, H. Voss, V. Votruba, S. Voutsinas, G. Walmsley, M. Weiler, K. Weingrill, D. Werner, T. Wevers, G. Whitehead, Ł. Wyrzykowski, A. Yoldas, M. Žerjal, S. Zucker, C. Zurbach, T. Zwitter, A. Alecu, M. Allen, C. Allende Prieto, A. Amorim, G. Anglada-Escudé, V. Arsenijevic, S. Azaz, P. Balm, M. Beck, H. H. Bernstein, L. Bigot, A. Bijaoui, C. Blasco, M. Bonfigli, G. Bono, S. Boudreault, A. Bressan, S. Brown, P. M. Brunet, P. Bunclark,

R. Buonanno, A. G. Butkevich, C. Carret, C. Carrion, L. Chemin, F. Chéreau, L. Corcione, E. Darmigny, K. S. de Boer, P. de Teodoro, P. T. de Zeeuw, C. Delle Luche, C. D. Domingues, P. Dubath, F. Fodor, B. Frézouls, A. Fries, D. Fustes, D. Fyfe, E. Gallardo, J. Gallegos, D. Gardiol, M. Gebran, A. Gomboc, A. Gómez, E. Grux, A. Gueguen, A. Heyrovsky, J. Hoar, G. Iannicola, Y. Isasi Parache, A. M. Janotto, E. Joliet, A. Jonckheere, R. Keil, D. W. Kim, P. Klagyivik, J. Klar, J. Knude, O. Kochukhov, I. Kolka, J. Kos, A. Kutka, V. Lainey, D. LeBouquin, C. Liu, D. Loreggia, V. V. Makarov, M. G. Marseille, C. Martayan, O. Martinez-Rubi, B. Massart, F. Meynadier, S. Mignot, U. Munari, A. T. Nguyen, T. Nordlander, P. Ocvirk, K. S. O'Flaherty, A. Olias Sanz, P. Ortiz, J. Osorio, D. Oszkiewicz, A. Ouzounis, M. Palmer, P. Park, E. Pasquato, C. Peltzer, J. Peralta, F. Péturaud, T. Pieniluoma, E. Pigozzi, J. Poels, G. Prat, T. Prod'homme, F. Raison, J. M. Rebordao, D. Risquez, B. Rocca-Volmerange, S. Rosen, M. I. Ruiz-Fuertes, F. Russo, S. Sembay, I. Serraller Vizcaino, A. Short, A. Siebert, H. Silva, D. Sinachopoulos, E. Slezak, M. Soffel, D. Sosnowska, V. Straižys, M. ter Linden, D. Terrell, S. Theil, C. Tiede, L. Troisi, P. Tsalmantza, D. Tur, M. Vaccari, F. Vachier, P. Valles, W. Van Hamme, L. Veltz, J. Virtanen, J. M. Wallut, R. Wichmann, M. I. Wilkinson, H. Ziaeepour, and S. Zschocke. The Gaia mission. *Astronomy and Astrophysics*, 595:A1, November 2016. ISSN 0004-6361. doi: 10.1051/0004-6361/201629272. URL https://ui.adsabs.harvard.edu/abs/2016A&A...595A...1G. ADS Bibcode: 2016A&A...595A...1G.

[70] Gaia Collaboration, A. G. A. Brown, A. Vallenari, T. Prusti, J. H. J. de Bruijne, C. Babusiaux, C. A. L. Bailer-Jones, M. Biermann, D. W. Evans, L. Eyer, F. Jansen, C. Jordi, S. A. Klioner, U. Lammers, L. Lindegren, X. Luri, F. Mignard, C. Panem, D. Pourbaix, S. Randich, P. Sartoretti, H. I. Siddiqui, C. Soubiran, F. van Leeuwen, N. A. Walton, F. Arenou, U. Bastian, M. Cropper, R. Drimmel, D. Katz, M. G. Lattanzi, J. Bakker, C. Cacciari, J. Castañeda, L. Chaoul, N. Cheek, F. De Angeli, C. Fabricius, R. Guerra, B. Holl, E. Masana, R. Messineo, N. Mowlavi, K. Nienartowicz, P. Panuzzo, J. Portell, M. Riello, G. M. Seabroke, P. Tanga, F. Thévenin, G. Gracia-Abril, G. Comoretto, M. Garcia-Reinaldos, D. Teyssier, M. Altmann, R. Andrae, M. Audard, I. Bellas-Velidis, K. Benson, J. Berthier, R. Blomme, P. Burgess, G. Busso, B. Carry, A. Cellino, G. Clementini, M. Clotet, O. Creevey, M. Davidson, J. De Ridder, L. Delchambre, A. Dell'Oro, C. Ducourant, J. Fernández-Hernández, M. Fouesneau, Y. Frémat, L. Galluccio, M. García-Torres, J. González-Núñez, J. J. González-Vidal, E. Gosset, L. P. Guy, J. L. Halbwachs, N. C. Hambly, D. L. Harrison, J. Hernández, D. Hestroffer, S. T. Hodgkin, A. Hutton, G. Jasniewicz, A. Jean-Antoine-Piccolo, S. Jordan, A. J. Korn, A. Krone-Martins, A. C. Lanzafame, T. Lebzelter, W. Löffler, M. Manteiga, P. M. Marrese, J. M. Martín-Fleitas, A. Moitinho, A. Mora, K. Muinonen, J. Osinde, E. Pancino, T. Pauwels, J. M. Petit, A. Recio-Blanco, P. J. Richards, L. Rimoldini, A. C. Robin, L. M. Sarro, C. Siopis, M. Smith, A. Sozzetti, M. Süveges, J. Torra, W. van Reeven, U. Abbas, A. Abreu Aramburu, S. Accart, C. Aerts, G. Altavilla, M. A. Álvarez, R. Alvarez, J. Alves, R. I. Anderson, A. H. Andrei, E. Anglada Varela, E. Antiche, T. Antoja, B. Arcay, T. L. Astraatmadja, N. Bach, S. G. Baker, L. Balaguer-Núñez, P. Balm, C. Barache, C. Barata, D. Barbato, F. Barblan, P. S. Barklem, D. Barrado, M. Barros, M. A. Barstow, S. Bartholomé Muñoz, J. L. Bassilana, U. Becciani, M. Bellazzini, A. Berihuete, S. Bertone, L. Bianchi, O. Bienaymé, S. Blanco-Cuaresma, T. Boch, C. Boeche, A. Bombrun, R. Borrachero, D. Bossini, S. Bouquillon, G. Bourda, A. Bragaglia, L. Bramante, M. A. Breddels, A. Bressan, N. Brouillet, T. Brüsemeister, E. Brugaletta, B. Bucciarelli, A. Burlacu, D. Busonero, A. G. Butkevich, R. Buzzi, E. Caffau, R. Cancelliere, G. Cannizzaro, T. Cantat-Gaudin, R. Carballo, T. Carlucci, J. M. Carrasco, L. Casamiquela, M. Castellani, A. Castro-Ginard, P. Charlot, L. Chemin, A. Chiavassa, G. Cocozza, G. Costigan, S. Cowell, F. Crifo, M. Crosta, C. Crowley, J. Cuypers, C. Dafonte, Y. Damerdji, A. Dapergolas, P. David, M. David, P. de Laverny, F. De Luise, R. De March, D. de Martino, R. de Souza, A. de Torres, J. Debosscher, E. del Pozo, M. Delbo, A. Delgado, H. E. Delgado, P. Di Matteo, S. Diakite, C. Diener, E. Distefano, C. Dolding, P. Drazinos, J. Durán, B. Edvardsson, H. Enke, K. Eriksson, P. Esquej, G. Eynard Bontemps, C. Fabre, M. Fabrizio, S. Faigler, A. J. Falcão, M. Farràs Casas, L. Federici, G. Fedorets, P. Fernique, F. Figueras, F. Filippi, K. Findeisen, A. Fonti, E. Fraile, M. Fraser, B. Frézouls, M. Gai, S. Galleti, D. Garabato, F. García-Sedano, A. Garofalo, N. Garralda, A. Gavel, P. Gavras, J. Gerssen, R. Geyer, P. Giacobbe, G. Gilmore, S. Girona, G. Giuffrida, F. Glass, M. Gomes, M. Granvik, A. Gueguen, A. Guerrier, J. Guiraud, R. Gutiérrez-Sánchez, R. Haigron, D. Hatzidimitriou, M. Hauser, M. Haywood, U. Heiter, A. Helmi, J. Heu, T. Hilger, D. Hobbs, W. Hofmann, G. Holland, H. E. Huckle, A. Hypki, V. Icardi, K. Janßen, G. Jevardat de Fombelle, P. G. Jonker, Á. L. Juhász, F. Julbe, A. Karampelas, A. Kewley, J. Klar, A. Kochoska, R. Kohley, K. Kolenberg, M. Kontizas, E. Kontizas, S. E. Koposov, G. Kordopatis, Z. Kostrzewa-Rutkowska, P. Koubsky, S. Lambert, A. F. Lanza, Y. Lasne, J. B. Lavigne, Y. Le Fustec, C. Le Poncin-Lafitte, Y. Lebreton, S. Leccia, N. Leclerc, I. Lecoeur-Taibi, H. Lenhardt, F. Leroux, S. Liao, E. Licata, H. E. P. Lindstrøm, T. A. Lister, E. Livanou, A. Lobel, M. López, S. Managau, R. G. Mann, G. Mantelet, O. Marchal, J. M. Marchant, M. Marconi, S. Marinoni, G. Marschalkó, D. J. Marshall, M. Martino, G. Marton, N. Mary, D. Massari, G. Matijevič, T. Mazeh, P. J. McMillan, S. Messina, D. Michalik, N. R. Millar, D. Molina, R. Molinaro, L. Molnár, P. Montegriffo, R. Mor, R. Morbidelli, T. Morel, D. Morris, A. F. Mulone, T. Muraveva, I. Musella, G. Nelemans, L. Nicastro, L. Noval, W. O'Mullane, C. Ordénovic, D. Ordóñez-Blanco, P. Osborne, C. Pagani, I. Pagano, F. Pailler, H. Palacin, L. Palaversa, A. Panahi, M. Pawlak, A. M. Piersimoni, F. X. Pineau, E. Plachy, G. Plum, E. Poggio, E. Poujoulet, A. Prša, L. Pulone, E. Racero, S. Ragaini, N. Rambaux, M. Ramos-Lerate, S. Regibo, C. Reylé, F. Riclet, V. Ripepi, A. Riva, A. Rivard, G. Rixon, T. Roegiers, M. Roelens, M. Romero-Gómez, N. Rowell, F. Royer, L. Ruiz-Dern, G. Sadowski, T. Sagristà Sellés, J. Sahlmann, J. Salgado, E. Salguero, N. Sanna, T. Santana-Ros, M. Sarasso,



H. Savietto, M. Schultheis, E. Sciacca, M. Segol, J. C. Segovia, D. Ségransan, I. C. Shih, L. Siltala, A. F. Silva, R. L. Smart, K. W. Smith, E. Solano, F. Solitro, R. Sordo, S. Soria Nieto, J. Souchay, A. Spagna, F. Spoto, U. Stampa, I. A. Steele, H. Steidelmüller, C. A. Stephenson, H. Stoev, F. F. Suess, J. Surdej, L. Szabados, E. Szegedi-Elek, D. Tapiador, F. Taris, G. Tauran, M. B. Taylor, R. Teixeira, D. Terrett, P. Teyssandier, W. Thuillot, A. Titarenko, F. Torra Clotet, C. Turon, A. Ulla, E. Utrilla, S. Uzzi, M. Vaillant, G. Valentini, V. Valette, A. van Elteren, E. Van Hemelryck, M. van Leeuwen, M. Vaschetto, A. Vecchiato, J. Veljanoski, Y. Viala, D. Vicente, S. Vogt, C. von Essen, H. Voss, V. Votruba, S. Voutsinas, G. Walmsley, M. Weiler, O. Wertz, T. Wevers, Ł. Wyrzykowski, A. Yoldas, M. Žerjal, H. Ziaeepour, J. Zorec, S. Zschocke, S. Zucker, C. Zurbach, and T. Zwitter. Gaia Data Release 2. Summary of the contents and survey properties. *Astronomy and Astrophysics*, 616:A1, August 2018. ISSN 0004-6361. doi: 10.1051/0004-6361/201833051. URL https://ui.adsabs.harvard.edu/abs/2018A&A...616A...1G. ADS Bibcode: 2018A&A...616A...1G.

[71] Gaia Collaboration, A. Vallenari, A. G. A. Brown, T. Prusti, J. H. J. de Bruijne, F. Arenou, C. Babusiaux, M. Biermann, O. L. Creevey, C. Ducourant, D. W. Evans, L. Eyer, R. Guerra, A. Hutton, C. Jordi, S. A. Klioner, U. L. Lammers, L. Lindegren, X. Luri, F. Mignard, C. Panem, D. Pourbaix, S. Randich, P. Sartoretti, C. Soubiran, P. Tanga, N. A. Walton, C. A. L. Bailer-Jones, U. Bastian, R. Drimmel, F. Jansen, D. Katz, M. G. Lattanzi, F. van Leeuwen, J. Bakker, C. Cacciari, J. Castañeda, F. De Angeli, C. Fabricius, M. Fouesneau, Y. Frémat, L. Galluccio, A. Guerrier, U. Heiter, E. Masana, R. Messineo, N. Mowlavi, C. Nicolas, K. Nienartowicz, F. Pailler, P. Panuzzo, F. Riclet, W. Roux, G. M. Seabroke, R. Sordo, F. Thévenin, G. Gracia-Abril, J. Portell, D. Teyssier, M. Altmann, R. Andrae, M. Audard, I. Bellas-Velidis, K. Benson, J. Berthier, R. Blomme, P. W. Burgess, D. Busonero, G. Busso, H. Cánovas, B. Carry, A. Cellino, N. Cheek, G. Clementini, Y. Damerdji, M. Davidson, P. de Teodoro, M. Nuñez Campos, L. Delchambre, A. Dell'Oro, P. Esquej, J. Fernández-Hernández, E. Fraile, D. Garabato, P. García-Lario, E. Gosset, R. Haigron, J. L. Halbwachs, N. C. Hambly, D. L. Harrison, J. Hernández, D. Hestroffer, S. T. Hodgkin, B. Holl, K. Janßen, G. Jevardat de Fombelle, S. Jordan, A. Krone-Martins, A. C. Lanzafame, W. Löffler, O. Marchal, P. M. Marrese, A. Moitinho, K. Muinonen, P. Osborne, E. Pancino, T. Pauwels, A. Recio-Blanco, C. Reylé, M. Riello, L. Rimoldini, T. Roegiers, J. Rybizki, L. M. Sarro, C. Siopis, M. Smith, A. Sozzetti, E. Utrilla, M. van Leeuwen, U. Abbas, P. Ábrahám, A. Abreu Aramburu, C. Aerts, J. J. Aguado, M. Ajaj, F. Aldea-Montero, G. Altavilla, M. A. Álvarez, J. Alves, F. Anders, R. I. Anderson, E. Anglada Varela, T. Antoja, D. Baines, S. G. Baker, L. Balaguer-Núñez, E. Balbinot, Z. Balog, C. Barache, D. Barbato, M. Barros, M. A. Barstow, S. Bartolomé, J. L. Bassilana, N. Bauchet, U. Becciani, M. Bellazzini, A. Berihuete, M. Bernet, S. Bertone, L. Bianchi, A. Binnenfeld, S. Blanco-Cuaresma, A. Blazere, T. Boch, A. Bombrun, D. Bossini, S. Bouquillon, A. Bragaglia, L. Bramante, E. Breedt, A. Bressan, N. Brouillet, E. Brugaletta, B. Bucciarelli, A. Burlacu, A. G. Butkevich, R. Buzzi, E. Caffau, R. Cancelliere, T. Cantat-Gaudin, R. Carballo, T. Carlucci, M. I. Carnerero, J. M. Carrasco, L. Casamiquela, M. Castellani, A. Castro-Ginard, L. Chaoul, P. Charlot, L. Chemin, V. Chiaramida, A. Chiavassa, N. Chornay, G. Comoretto, G. Contursi, W. J. Cooper, T. Cornez, S. Cowell, F. Crifo, M. Cropper, M. Crosta, C. Crowley, C. Dafonte, A. Dapergolas, M. David, P. David, P. de Laverny, F. De Luise, R. De March, J. De Ridder, R. de Souza, A. de Torres, E. F. del Peloso, E. del Pozo, M. Delbo, A. Delgado, J. B. Delisle, C. Demouchy, T. E. Dharmawardena, P. Di Matteo, S. Diakite, C. Diener, E. Distefano, C. Dolding, B. Edvardsson, H. Enke, C. Fabre, M. Fabrizio, S. Faigler, G. Fedorets, P. Fernique, A. Fienga, F. Figueras, Y. Fournier, C. Fouron, F. Fragkoudi, M. Gai, A. Garcia-Gutierrez, M. Garcia-Reinaldos, M. García-Torres, A. Garofalo, A. Gavel, P. Gavras, E. Gerlach, R. Geyer, P. Giacobbe, G. Gilmore, S. Girona, G. Giuffrida, R. Gomel, A. Gomez, J. González-Núñez, I. González-Santamaría, J. J. González-Vidal, M. Granvik, P. Guillout, J. Guiraud, R. Gutiérrez-Sánchez, L. P. Guy, D. Hatzidimitriou, M. Hauser, M. Haywood, A. Helmer, A. Helmi, M. H. Sarmiento, S. L. Hidalgo, T. Hilger, N. Hładczuk, D. Hobbs, G. Holland, H. E. Huckle, K. Jardine, G. Jasniewicz, A. Jean-Antoine Piccolo, Ó. Jiménez-Arranz, A. Jorissen, J. Juaristi Campillo, F. Julbe, L. Karbevska, P. Kervella, S. Khanna, M. Kontizas, G. Kordopatis, A. J. Korn, Á. Kóspál, Z. Kostrzewa-Rutkowska, K. Kruszyńska, M. Kun, P. Laizeau, S. Lambert, A. F. Lanza, Y. Lasne, J. F. Le Campion, Y. Lebreton, T. Lebzelter, S. Leccia, N. Leclerc, I. Lecoeur-Taibi, S. Liao, E. L. Licata, H. E. P. Lindstrøm, T. A. Lister, E. Livanou, A. Lobel, A. Lorca, C. Loup, P. Madrero Pardo, A. Magdaleno Romeo, S. Managau, R. G. Mann, M. Manteiga, J. M. Marchant, M. Marconi, J. Marcos, M. M. S. Marcos Santos, D. Marín Pina, S. Marinoni, F. Marocco, D. J. Marshall, L. Martin Polo, J. M. Martín-Fleitas, G. Marton, N. Mary, A. Masip, D. Massari, A. Mastrobuono-Battisti, T. Mazeh, P. J. McMillan, S. Messina, D. Michalik, N. R. Millar, A. Mints, D. Molina, R. Molinaro, L. Molnár, G. Monari, M. Monguió, P. Montegriffo, A. Montero, R. Mor, A. Mora, R. Morbidelli, T. Morel, D. Morris, T. Muraveva, C. P. Murphy, I. Musella, Z. Nagy, L. Noval, F. Ocaña, A. Ogden, C. Ordenovic, J. O. Osinde, C. Pagani, I. Pagano, L. Palaversa, P. A. Palicio, L. Pallas-Quintela, A. Panahi, S. Payne-Wardenaar, X. Peñalosa Esteller, A. Penttilä, B. Pichon, A. M. Piersimoni, F. X. Pineau, E. Plachy, G. Plum, E. Poggio, A. Prša, L. Pulone, E. Racero, S. Ragaini, M. Rainer, C. M. Raiteri, N. Rambaux, P. Ramos, M. Ramos-Lerate, P. Re Fiorentin, S. Regibo, P. J. Richards, C. Rios Diaz, V. Ripepi, A. Riva, H. W. Rix, G. Rixon, N. Robichon, A. C. Robin, C. Robin, M. Roelens, H. R. O. Rogues, L. Rohrbasser, M. Romero-Gómez, N. Rowell, F. Royer, D. Ruz Mieres, K. A. Rybicki, G. Sadowski, A. Sáez Núñez, A. Sagristà Sellés, J. Sahlmann, E. Salguero, N. Samaras, V. Sanchez Gimenez, N. Sanna, R. Santoveña, M. Sarasso, M. Schultheis, E. Sciacca, M. Segol, J. C. Segovia, D. Ségransan, D. Semeux, S. Shahaf, H. I. Siddiqui, A. Siebert, L. Siltala, A. Silvelo, E. Slezak, I. Slezak,



R. L. Smart, O. N. Snaith, E. Solano, F. Solitro, D. Souami, J. Souchay, A. Spagna, L. Spina, F. Spoto, I. A. Steele, H. Steidelmüller, C. A. Stephenson, M. Süveges, J. Surdej, L. Szabados, E. Szegedi-Elek, F. Taris, M. B. Taylor, R. Teixeira, L. Tolomei, N. Tonello, F. Torra, J. Torra, G. Torralba Elipe, M. Trabucchi, A. T. Tsounis, C. Turon, A. Ulla, N. Unger, M. V. Vaillant, E. van Dillen, W. van Reeven, O. Vanel, A. Vecchiato, Y. Viala, D. Vicente, S. Voutsinas, M. Weiler, T. Wevers, Ł. Wyrzykowski, A. Yoldas, P. Yvard, H. Zhao, J. Zorec, S. Zucker, and T. Zwitter. Gaia Data Release 3. Summary of the content and survey properties. *Astronomy and Astrophysics*, 674:A1, June 2023. ISSN 0004-6361. doi: 10.1051/0004-6361/202243940. URL https://ui.adsabs.harvard.edu/abs/2023A&A...674A...1G. ADS Bibcode: 2023A&A...674A...1G.

[72] R. D. Gehrz, G. L. Grasdalen, M. Castelaz, C. Gullixson, D. Mozurkewich, and J. A. Hackwell. Anatomy of a region of star formation : infrared images of S 106 (AFGL 2584). *The Astrophysical Journal*, 254:550–561, March 1982. ISSN 0004-637X. doi: 10.1086/159765. URL https://ui.adsabs.harvard.edu/abs/1982ApJ...254..550G. ADS Bibcode: 1982ApJ...254..550G.

[73] Gravity Collaboration, A. Soulain, K. Perraut, J. Bouvier, G. Pantolmos, A. Caratti O Garatti, P. Caselli, P. Garcia, R. Garcia Lopez, N. Aimar, A. Amorin, M. Benisty, J. P. Berger, G. Bourdarot, W. Brandner, Y. Clénet, T. de Zeeuw, R. Davies, A. Drescher, A. Eckart, F. Eisenhauer, N. M. Förster Schreiber, E. Gendron, R. Genzuel, S. Gillessen, G. Heißel, Th. Henning, S. Hippler, M. Horrobin, L. Jocou, P. Kervella, L. Labadie, S. Lacour, V. Lapeyrere, J. B. Le Bouquin, P. Léna, D. Lutz, F. Mang, T. Ott, T. Paumard, G. Perrin, J. Sanchez, S. Scheithauer, J. Shangguan, T. Shimizu, O. Straub, C. Straubmeier, E. Sturm, L. J. Tacconi, F. Vincent, E. van Dishoeck, F. Widmann, E. Wieprecht, E. Wiezorrek, and S. Yazici. The GRAVITY young stellar object survey. X. Probing the inner disk and magnetospheric accretion region of CI Tau. *Astronomy and Astrophysics*, 674:A203, June 2023. ISSN 0004-6361. doi: 10.1051/0004-6361/202346446. URL https://ui.adsabs.harvard.edu/abs/2023A&A...674A.203G. ADS Bibcode: 2023A&A...674A.203G.

[74] O. Gressel, R. P. Nelson, N. J. Turner, and U. Ziegler. Global Hydromagnetic Simulations of a Planet Embedded in a Dead Zone: Gap Opening, Gas Accretion, and Formation of a Protoplanetary Jet. *The Astrophysical Journal*, 779: 59, December 2013. ISSN 0004-637X. doi: 10.1088/0004-637X/779/1/59. URL https://ui.adsabs.harvard.edu/abs/2013ApJ...779...59G. Publisher: IOP ADS Bibcode: 2013ApJ...779...59G.

[75] E. Gullbring. Polar accretion and light variability on T Tauri stars. *Astronomy and Astrophysics*, 287:131–144, July 1994. ISSN 0004-6361. URL https://ui.adsabs.harvard.edu/abs/1994A&A...287..131G. ADS Bibcode: 1994A&A...287..131G.

[76] Erik Gullbring, Lee Hartmann, Cesar Briceño, and Nuria Calvet. Disk Accretion Rates for T Tauri Stars. *The Astrophysical Journal*, 492:323–341, January 1998. ISSN 0004-637X. doi: 10.1086/305032. URL https://ui.adsabs.harvard.edu/abs/1998ApJ...492..323G. ADS Bibcode: 1998ApJ...492..323G.

[77] H. M. Günther, J. H. M. M. Schmitt, J. Robrade, and C. Liefke. X-ray emission from classical T Tauri stars: accretion shocks and coronae? *Astronomy and Astrophysics*, 466:1111–1121, May 2007. ISSN 0004-6361. doi: 10.1051/0004-6361:20065669. URL https://ui.adsabs.harvard.edu/abs/2007A&A...466.1111G. ADS Bibcode: 2007A&A...466.1111G.

[78] S. Y. Haffert, A. J. Bohn, J. de Boer, I. A. G. Snellen, J. Brinchmann, J. H. Girard, C. U. Keller, and R. Bacon. Two accreting protoplanets around the young star PDS 70. *Nature Astronomy*, 3(8):749–754, August 2019. ISSN 2397-3366. doi: 10.1038/s41550-019-0780-5. URL http://www.nature.com/articles/s41550-019-0780-5.

[79] Lee Hartmann, Robert Hewett, and Nuria Calvet. Magnetospheric Accretion Models for T Tauri Stars. I. Balmer Line Profiles without Rotation. *The Astrophysical Journal*, 426:669, May 1994. ISSN 0004-637X. doi: 10.1086/174104. URL https://ui.adsabs.harvard.edu/abs/1994ApJ...426..669H. ADS Bibcode: 1994ApJ...426..669H.

[80] Lee Hartmann, Gregory Herczeg, and Nuria Calvet. Accretion onto Pre-Main-Sequence Stars. *Annual Review of Astronomy and Astrophysics*, 54:135–180, September 2016. ISSN 0066-4146. doi: 10.1146/annurev-astro-081915-023347. URL https://ui.adsabs.harvard.edu/abs/2016ARA&A..54..135H. ADS Bibcode: 2016ARA&A..54..135H.

[81] G. H. Herbig. Observations of RY Tauri. *The Astrophysical Journal*, 133:337, January 1961. ISSN 0004-637X. doi: 10.1086/147033. URL https://ui.adsabs.harvard.edu/abs/1961ApJ...133..337H. ADS Bibcode: 1961ApJ...133..337H.

[82] G. H. Herbig. The Properties and Problems of T Tauri Stars and Related Objects. *Advances in Astronomy and Astrophysics*, 1:47–103, January 1962. doi: 10.1016/B978-1-4831-9919-1.50006-6. URL https://ui.adsabs.harvard.edu/abs/1962AdA&A...1...47H. ADS Bibcode: 1962AdA&A...1...47H.



[83] G. H. Herbig. Introductory Remarks. *Memoires of the Societe Royale des Sciences de Liege*, 19:13, January 1970. URL https://ui.adsabs.harvard.edu/abs/1970MSRSL..19...13H. ADS Bibcode: 1970MSRSL..19...13H.

[84] Gregory J. Herczeg and Lynne A. Hillenbrand. UV Excess Measures of Accretion onto Young Very Low Mass Stars and Brown Dwarfs. *The Astrophysical Journal*, 681:594–625, July 2008. ISSN 0004-637X. doi: 10.1086/586728. URL https://ui.adsabs.harvard.edu/abs/2008ApJ...681..594H. Publisher: IOP ADS Bibcode: 2008ApJ...681..594H.

[85] N. Huélamo, G. Chauvin, I. Mendigutía, E. Whelan, J. M. Alcalá, G. Cugno, H. M. Schmid, I. de Gregorio-Monsalvo, A. Zurlo, D. Barrado, M. Benisty, S. P. Quanz, H. Bouy, B. Montesinos, Y. Beletsky, and J. Szulagyi. Searching for Hα-emitting sources in the gaps of five transitional disks. SPHERE/ZIMPOL high-contrast imaging. *Astronomy and Astrophysics*, 668:A138, December 2022. ISSN 0004-6361. doi: 10.1051/0004-6361/202243918. URL https://ui.adsabs.harvard.edu/abs/2022A&A...668A.138H. ADS Bibcode: 2022A&A...668A.138H.

[86] R. I. Hynes. An optimal extraction of spatially blended spectra. *Astronomy and Astrophysics*, 382:752–757, February 2002. ISSN 0004-6361. doi: 10.1051/0004-6361:20011657. URL https://ui.adsabs.harvard.edu/abs/2002A&A...382..752H. ADS Bibcode: 2002A&A...382..752H.

[87] J. A. Högbom. Aperture Synthesis with a Non-Regular Distribution of Interferometer Baselines. *Astronomy and Astrophysics Supplement Series*, 15:417, June 1974. ISSN 0365-01380004-6361. URL https://ui.adsabs.harvard.edu/abs/1974A&AS...15..417H. ADS Bibcode: 1974A&AS...15..417H.

[88] Laura Ingleby, Nuria Calvet, Gregory Herczeg, Alex Blaty, Frederick Walter, David Ardila, Richard Alexander, Suzan Edwards, Catherine Espaillat, Scott G. Gregory, Lynne Hillenbrand, and Alexander Brown. Accretion Rates for T Tauri Stars Using Nearly Simultaneous Ultraviolet and Optical Spectra. *The Astrophysical Journal*, 767:112, April 2013. ISSN 0004-637X. doi: 10.1088/0004-637X/767/2/112. URL https://ui.adsabs.harvard.edu/abs/2013ApJ...767..112I. ADS Bibcode: 2013ApJ...767..112I.

[89] M J Ireland, A Kraus, F Martinache, N Law, and L A Hillenbrand. TWO WIDE PLANETARY-MASS COMPANIONS TO SOLAR-TYPE STARS IN UPPER SCORPIUS. *The Astrophysical Journal*, page 11, 2011.

[90] Anders Johansen and Michiel Lambrechts. Forming Planets via Pebble Accretion. *Annual Review of Earth and Planetary Sciences*, 45:359–387, August 2017. ISSN 0084-6597. doi: 10.1146/annurev-earth-063016-020226. URL https://ui.adsabs.harvard.edu/abs/2017AREPS..45..359J. ADS Bibcode: 2017AREPS..45..359J.

[91] A. Jones, S. Noll, W. Kausch, C. Szyszka, and S. Kimeswenger. An advanced scattered moonlight model for Cerro Paranal. *Astronomy and Astrophysics*, 560:A91, December 2013. ISSN 0004-6361. doi: 10.1051/0004-6361/201322433. URL https://ui.adsabs.harvard.edu/abs/2013A&A...560A..91J. ADS Bibcode: 2013A&A...560A..91J.

[92] Alfred H. Joy. A Survey of the Spectra and Radial Velocities of the Less Regular M-Type Variable Stars. *The Astrophysical Journal*, 96:344, November 1942. ISSN 0004-637X. doi: 10.1086/144469. URL https://ui.adsabs.harvard.edu/abs/1942ApJ....96..344J. ADS Bibcode: 1942ApJ....96..344J.

[93] Alfred H. Joy. T Tauri Variable Stars. *The Astrophysical Journal*, 102:168, September 1945. ISSN 0004-637X. doi: 10.1086/144749. URL https://ui.adsabs.harvard.edu/abs/1945ApJ...102..168J. ADS Bibcode: 1945ApJ...102..168J.

[94] Alfred H. Joy. Bright-Line Stars among the Taurus Dark Clouds. *The Astrophysical Journal*, 110:424, November 1949. ISSN 0004-637X. doi: 10.1086/145217. URL https://ui.adsabs.harvard.edu/abs/1949ApJ...110..424J. ADS Bibcode: 1949ApJ...110..424J.

[95] M. Keppler, M. Benisty, A. Müller, Th. Henning, R. van Boekel, F. Cantalloube, C. Ginski, R. G. van Holstein, A. L. Maire, A. Pohl, M. Samland, H. Avenhaus, J. L. Baudino, A. Boccaletti, J. de Boer, M. Bonnefoy, G. Chauvin, S. Desidera, M. Langlois, C. Lazzoni, G. D. Marleau, C. Mordasini, N. Pawellek, T. Stolker, A. Vigan, A. Zurlo, T. Birnstiel, W. Brandner, M. Feldt, M. Flock, J. Girard, R. Gratton, J. Hagelberg, A. Isella, M. Janson, A. Juhasz, J. Kemmer, Q. Kral, A. M. Lagrange, R. Launhardt, A. Matter, F. Ménard, J. Milli, P. Mollière, J. Olofsson, L. Pérez, P. Pinilla, C. Pinte, S. P. Quanz, T. Schmidt, S. Udry, Z. Wahhaj, J. P. Williams, E. Buenzli, M. Cudel, C. Dominik, R. Galicher, M. Kasper, J. Lannier, D. Mesa, D. Mouillet, S. Peretti, C. Perrot, G. Salter, E. Sissa, F. Wildi, L. Abe, J. Antichi, J. C. Augereau, A. Baruffolo, P. Baudoz, A. Bazzon, J. L. Beuzit, P. Blanchard, S. S. Brems, T. Buey, V. De Caprio, M. Carbillet, M. Carle, E. Cascone, A. Cheetham, R. Claudi, A. Costille, A. Delboulbé, K. Dohlen, D. Fantinel, P. Feautrier, T. Fusco, E. Giro, L. Gluck, C. Gry, N. Hubin, E. Hugot, M. Jaquet, D. Le Mignant, M. Llored, F. Madec, Y. Magnard, P. Martinez, D. Maurel, M. Meyer, O. Möller-Nilsson, T. Moulin, L. Mugnier, A. Origné, A. Pavlov, D. Perret, C. Petit, J. Pragt,



P. Puget, P. Rabou, J. Ramos, F. Rigal, S. Rochat, R. Roelfsema, G. Rousset, A. Roux, B. Salasnich, J. F. Sauvage, A. Sevin, C. Soenke, E. Stadler, M. Suarez, M. Turatto, and L. Weber. Discovery of a planetary-mass companion within the gap of the transition disk around PDS 70. *Astronomy and Astrophysics*, 617:A44, September 2018. ISSN 0004-6361. doi: 10.1051/0004-6361/201832957. URL https://ui.adsabs.harvard.edu/abs/2018A&A...617A..44K. ADS Bibcode: 2018A&A...617A..44K.

[96] W. Kley. Mass flow and accretion through gaps in accretion discs. *Monthly Notices of the Royal Astronomical Society*, 303:696–710, March 1999. ISSN 0035-8711. doi: 10.1046/j.1365-8711.1999.02198.x. URL https://ui.adsabs.harvard.edu/abs/1999MNRAS.303..696K. Publisher: OUP ADS Bibcode: 1999MNRAS.303..696K.

[97] Arieh Koenigl. Disk Accretion onto Magnetic T Tauri Stars. *The Astrophysical Journal*, 370:L39, March 1991. ISSN 0004-637X. doi: 10.1086/185972. URL https://ui.adsabs.harvard.edu/abs/1991ApJ...370L..39K. ADS Bibcode: 1991ApJ...370L..39K.

[98] Eiichiro Kokubo and Shigeru Ida. On Runaway Growth of Planetesimals. *Icarus*, 123:180–191, September 1996. ISSN 0019-1035. doi: 10.1006/icar.1996.0148. URL https://ui.adsabs.harvard.edu/abs/1996Icar..123..180K. ADS Bibcode: 1996Icar..123..180K.

[99] A. E. Kramida. A critical compilation of experimental data on spectral lines and energy levels of hydrogen, deuterium, and tritium. *Atomic Data and Nuclear Data Tables*, 96:586–644, November 2010. ISSN 0092-640X. doi: 10.1016/j.adt.2010.05.001. URL https://ui.adsabs.harvard.edu/abs/2010ADNDT..96..586K. ADS Bibcode: 2010ADNDT..96..586K.

[100] Kaitlin M. Kratter and Ruth A. Murray-Clay. Fragment Production and Survival in Irradiated Disks: A Comprehensive Cooling Criterion. *The Astrophysical Journal*, 740:1, October 2011. ISSN 0004-637X. doi: 10.1088/0004-637X/740/1/1. URL https://ui.adsabs.harvard.edu/abs/2011ApJ...740....1K. Publisher: IOP ADS Bibcode: 2011ApJ...740....1K.

[101] Adam L. Kraus, Michael J. Ireland, Frantz Martinache, and James P. Lloyd. Mapping the Shores of the Brown Dwarf Desert. I. Upper Scorpius. *The Astrophysical Journal*, 679:762–782, May 2008. ISSN 0004-637X. doi: 10.1086/587435. URL https://ui.adsabs.harvard.edu/abs/2008ApJ...679..762K. Publisher: IOP ADS Bibcode: 2008ApJ...679..762K.

[102] Stefan Kraus, Daniel Mortimer, Sorabh Chhabra, Yi Lu, Isabelle Codron, Tyler Gardner, Narsireddy Anugu, John D. Monnier, Jean-Baptiste Le Bouquin, Michael Ireland, Frantz Martinache, Denis Defrère, and Marc-Antoine Martinod. High spectral-resolution interferometry down to one micron with Asgard/BIFROST at VLTI: science drivers and project overview. 12183:121831S, August 2022. doi: 10.1117/12.2627973. URL https://ui.adsabs.harvard.edu/abs/2022SPIE12183E..1SK. Conference Name: Optical and Infrared Interferometry and Imaging VIII Place: eprint: arXiv:2208.04959 ADS Bibcode: 2022SPIE12183E..1SK.

[103] P. Kuan. Photometric variations of T Tauri stars. *The Astrophysical Journal*, 210:129–136, November 1976. ISSN 0004-637X. doi: 10.1086/154810. URL https://ui.adsabs.harvard.edu/abs/1976ApJ...210..129K. ADS Bibcode: 1976ApJ...210..129K.

[104] L. V. Kuhi. Mass Loss from T Tauri Stars. *The Astrophysical Journal*, 140:1409, November 1964. ISSN 0004-637X. doi: 10.1086/148047. URL https://ui.adsabs.harvard.edu/abs/1964ApJ...140.1409K. ADS Bibcode: 1964ApJ...140.1409K.

[105] L. V. Kuhi. Ultraviolet Continuous Emission in T Tauri Stars. *Publications of the Astronomical Society of the Pacific*, 78:430, October 1966. ISSN 0004-6280. doi: 10.1086/128380. URL https://ui.adsabs.harvard.edu/abs/1966PASP...78..430K. ADS Bibcode: 1966PASP...78..430K.

[106] L. V. Kuhi. Spectral energy distributions of T Tauri stars. *Astronomy and Astrophysics Supplement Series*, 15:47–89, January 1974. ISSN 0365-0138. URL https://ui.adsabs.harvard.edu/abs/1974A&AS...15...47K. ADS Bibcode: 1974A&AS...15...47K.

[107] Gerard P. Kuiper. On the Origin of the Solar System. *Proceedings of the National Academy of Science*, 37:1–14, January 1951. ISSN 0027-8424. doi: 10.1073/pnas.37.1.1. URL https://ui.adsabs.harvard.edu/abs/1951PNAS...37....1K. ADS Bibcode: 1951PNAS...37....1K.

[108] M. Kuzuhara, M. Tamura, M. Ishii, T. Kudo, S. Nishiyama, and R. Kandori. The Widest-separation Substellar Companion Candidate to a Binary T Tauri Star. *The Astronomical Journal*, 141:119, April 2011. ISSN 0004-6256. doi: 10.1088/0004-6256/141/4/119. URL https://ui.adsabs.harvard.edu/abs/2011AJ....141..119K. Publisher: IOP ADS Bibcode: 2011AJ....141..119K.



[109] John Kwan and William Fischer. Origins of the H, He I and Ca II line emission in classical T Tauri stars. *Monthly Notices of the Royal Astronomical Society*, 411:2383–2425, March 2011. ISSN 0035-8711. doi: 10.1111/j.1365-2966.2010.17863.x. URL https://ui.adsabs.harvard.edu/abs/2011MNRAS.411.2383K. ADS Bibcode: 2011MNRAS.411.2383K.

[110] John Kwan, Suzan Edwards, and William Fischer. Modeling T Tauri Winds from He I λ10830 Profiles. *The Astrophysical Journal*, 657:897–915, March 2007. ISSN 0004-637X. doi: 10.1086/511057. URL https://ui.adsabs.harvard.edu/abs/2007ApJ...657..897K. ADS Bibcode: 2007ApJ...657..897K.

[111] François-René Lachapelle, David Lafrenière, Jonathan Gagné, Ray Jayawardhana, Markus Janson, Christiane Helling, and Soeren Witte. Characterization of Low-mass, Wide-separation Substellar Companions to Stars in Upper Scorpius: Near-infrared Photometry and Spectroscopy. *The Astrophysical Journal*, 802:61, March 2015. ISSN 0004-637X. doi: 10.1088/0004-637X/802/1/61. URL https://ui.adsabs.harvard.edu/abs/2015ApJ...802...61L. Publisher: IOP ADS Bibcode: 2015ApJ...802...61L.

[112] M. Lambrechts and A. Johansen. Rapid growth of gas-giant cores by pebble accretion. *Astronomy and Astrophysics*, 544: A32, August 2012. ISSN 0004-6361. doi: 10.1051/0004-6361/201219127. URL https://ui.adsabs.harvard.edu/abs/2012A&A...544A..32L. ADS Bibcode: 2012A&A...544A..32L.

[113] S. A. Lamzin. On the structure of the accretion shock wave in the case of young stars. *Astronomy and Astrophysics*, 295:L20–L22, March 1995. ISSN 0004-6361. URL https://ui.adsabs.harvard.edu/abs/1995A&A...295L..20L. ADS Bibcode: 1995A&A...295L..20L.

[114] Jean-François Lavigne, René Doyon, David Lafrenière, Christian Marois, and Travis Barman. Near-Infrared Observations of GQ Lup b Using the Gemini Integral Field Spectrograph NIFS. *The Astrophysical Journal*, 704:1098–1106, October 2009. ISSN 0004-637X. doi: 10.1088/0004-637X/704/2/1098. URL https://ui.adsabs.harvard.edu/abs/2009ApJ...704.1098L. Publisher: IOP ADS Bibcode: 2009ApJ...704.1098L.

[115] C. Lazzoni, R. Gratton, J. M. Alcalá, S. Desidera, A. Frasca, C. F. Manara, D. Mesa, E. Rigliaco, A. Vigan, and A. Zurlo. Disk of 2MASS 15491331-3539118 = GQ Lup C as seen by HST and WISE. *Astronomy and Astrophysics*, 635:L11, March 2020. ISSN 0004-6361. doi: 10.1051/0004-6361/202037622. URL https://ui.adsabs.harvard.edu/abs/2020A&A...635L..11L. ADS Bibcode: 2020A&A...635L..11L.

[116] D. N. C. Lin. *The nebular origin of the solar system.* January 1986. URL https://ui.adsabs.harvard.edu/abs/1986sosy.book...28L. Pages: 28-77 Publication Title: The Solar System ADS Bibcode: 1986sosy.book...28L.

[117] D. N. C. Lin and J. Papaloizou. *On the dynamical origin of the solar system.* January 1985. URL https://ui.adsabs.harvard.edu/abs/1985prpl.conf..981L. Conference Name: Protostars and Planets II Pages: 981-1072 ADS Bibcode: 1985prpl.conf..981L.

[118] Jack J. Lissauer and Glen R. Stewart. *Growth of Planets from Planetesimals.* January 1993. URL https://ui.adsabs.harvard.edu/abs/1993prpl.conf.1061L. Conference Name: Protostars and Planets III Pages: 1061 ADS Bibcode: 1993prpl.conf.1061L.

[119] Beibei Liu and Jianghui Ji. A tale of planet formation: from dust to planets. *Research in Astronomy and Astrophysics*, 20:164, October 2020. ISSN 1674-4527. doi: 10.1088/1674-4527/20/10/164. URL https://ui.adsabs.harvard.edu/abs/2020RAA....20..164L. Publisher: IOP ADS Bibcode: 2020RAA....20..164L.

[120] N. R. Lomb. Least-Squares Frequency Analysis of Unequally Spaced Data. *Astrophysics and Space Science*, 39:447–462, February 1976. ISSN 0004-640X. doi: 10.1007/BF00648343. URL https://ui.adsabs.harvard.edu/abs/1976Ap&SS..39..447L. Publisher: Springer ADS Bibcode: 1976Ap&SS..39..447L.

[121] Christophe Lovis, Nicolas Blind, Bruno Chazelas, Jonas G. Kühn, Ludovic Genolet, Ian Hughes, Michaël. Sordet, Robin Schnell, Martin Turbet, Thierry Fusco, Jean-François Sauvage, Maddalena Bugatti, Nicolas Billot, Janis Hagelberg, Eddy Hocini, and Olivier Guyon. RISTRETTO: high-resolution spectroscopy at the diffraction limit of the VLT. 12184:121841Q, August 2022. doi: 10.1117/12.2627923. URL https://ui.adsabs.harvard.edu/abs/2022SPIE12184E..1QL. Conference Name: Ground-based and Airborne Instrumentation for Astronomy IX Place: eprint: arXiv:2208.14838 ADS Bibcode: 2022SPIE12184E..1QL.

[122] S. H. Lubow and G. D'Angelo. Gas Flow across Gaps in Protoplanetary Disks. *The Astrophysical Journal*, 641:526–533, April 2006. ISSN 0004-637X. doi: 10.1086/500356. URL https://ui.adsabs.harvard.edu/abs/2006ApJ...641..526L. Publisher: IOP ADS Bibcode: 2006ApJ...641..526L.



[123] K. L. Luhman. A Census of the Circumstellar Disk Populations in the Sco-Cen Complex. *The Astronomical Journal*, 163: 25, January 2022. ISSN 0004-6256. doi: 10.3847/1538-3881/ac35e3. URL https://ui.adsabs.harvard.edu/abs/2022AJ....163...25L. Publisher: IOP ADS Bibcode: 2022AJ....163...25L.

[124] D. Lynden-Bell and J. E. Pringle. The evolution of viscous discs and the origin of the nebular variables. *Monthly Notices of the Royal Astronomical Society*, 168:603–637, September 1974. ISSN 0035-8711. doi: 10.1093/mnras/168.3.603. URL https://ui.adsabs.harvard.edu/abs/1974MNRAS.168..603L. ADS Bibcode: 1974MNRAS.168..603L.

[125] Meredith A. MacGregor, David J. Wilner, Ian Czekala, Sean M. Andrews, Y. Sophia Dai, Gregory J. Herczeg, Kaitlin M. Kratter, Adam L. Kraus, Luca Ricci, and Leonardo Testi. ALMA MEASUREMENTS OF CIRCUMSTELLAR MATERIAL IN THE GQ LUP SYSTEM. *The Astrophysical Journal*, 835(1):17, January 2017. ISSN 1538-4357. doi: 10.3847/1538-4357/835/1/17. URL https://iopscience.iop.org/article/10.3847/1538-4357/835/1/17.

[126] C. F. Manara, L. Testi, E. Rigliaco, J. M. Alcalá, A. Natta, B. Stelzer, K. Biazzo, E. Covino, S. Covino, G. Cupani, V. D'Elia, and S. Randich. X-shooter spectroscopy of young stellar objects. II. Impact of chromospheric emission on accretion rate estimates. *Astronomy and Astrophysics*, 551:A107, March 2013. ISSN 0004-6361. doi: 10.1051/0004-6361/201220921. URL https://ui.adsabs.harvard.edu/abs/2013A&A...551A.107M. ADS Bibcode: 2013A&A...551A.107M.

[127] C. F. Manara, A. Frasca, J. M. Alcalá, A. Natta, B. Stelzer, and L. Testi. An extensive VLT/X-shooter library of photospheric templates of pre-main sequence stars. *Astronomy and Astrophysics*, 605:A86, September 2017. ISSN 0004-6361. doi: 10.1051/0004-6361/201730807. URL https://ui.adsabs.harvard.edu/abs/2017A&A...605A..86M. ADS Bibcode: 2017A&A...605A..86M.

[128] Elena Manjavacas, Pascal Tremblin, Stephan Birkmann, Jeff Valenti, Catarina Alves de Oliveira, Tracy L. Beck, G. Giardino, N. Lützgendorf, B. J. Rauscher, and M. Sirianni. Medium-resolution 0.97–5.3 μm Spectra of Very Young Benchmark Brown Dwarfs with NIRSpec on Board the James Webb Space Telescope. *The Astronomical Journal*, 167:168, April 2024. ISSN 0004-6256. doi: 10.3847/1538-3881/ad2938. URL https://ui.adsabs.harvard.edu/abs/2024AJ....167..168M. Publisher: IOP ADS Bibcode: 2024AJ....167..168M.

[129] G. D. Marleau, Y. Aoyama, R. Kuiper, K. Follette, N. J. Turner, G. Cugno, C. F. Manara, S. Y. Haffert, D. Kitzmann, S. C. Ringqvist, K. R. Wagner, R. van Boekel, S. Sallum, M. Janson, T. O. B. Schmidt, L. Venuti, Ch. Lovis, and C. Mordasini. Accreting protoplanets: Spectral signatures and magnitude of gas and dust extinction at H α. *Astronomy and Astrophysics*, 657:A38, January 2022. ISSN 0004-6361. doi: 10.1051/0004-6361/202037494. URL https://ui.adsabs.harvard.edu/abs/2022A&A...657A..38M. ADS Bibcode: 2022A&A...657A..38M.

[130] Gabriel-Dominique Marleau and Yuhiko Aoyama. Planetary Line-to-accretion Luminosity Scaling Relations: Extrapolating to Higher-order Hydrogen Lines. *Research Notes of the American Astronomical Society*, 6:262, December 2022. ISSN 2515-5172. doi: 10.3847/2515-5172/acaa34. URL https://ui.adsabs.harvard.edu/abs/2022RNAAS...6..262M. Publisher: IOP ADS Bibcode: 2022RNAAS...6..262M.

[131] Gabriel-Dominique Marleau, Hubert Klahr, Rolf Kuiper, and Christoph Mordasini. The Planetary Accretion Shock. I. Framework for Radiation-hydrodynamical Simulations and First Results. *The Astrophysical Journal*, 836:221, February 2017. ISSN 0004-637X. doi: 10.3847/1538-4357/836/2/221. URL https://ui.adsabs.harvard.edu/abs/2017ApJ...836..221M. Publisher: IOP ADS Bibcode: 2017ApJ...836..221M.

[132] Gabriel-Dominique Marleau, Yuhiko Aoyama, Jun Hashimoto, and Yifan Zhou. Revisiting the Helium and Hydrogen Accretion Indicators at TWA 27B: Weak Mass Flow at Near-freefall Velocity. *The Astrophysical Journal*, 964:70, March 2024. ISSN 0004-637X. doi: 10.3847/1538-4357/ad1ee9. URL https://ui.adsabs.harvard.edu/abs/2024ApJ...964...70M. Publisher: IOP ADS Bibcode: 2024ApJ...964...70M.

[133] Mark S. Marley, Jonathan J. Fortney, Olenka Hubickyj, Peter Bodenheimer, and Jack J. Lissauer. On the Luminosity of Young Jupiters. *The Astrophysical Journal*, 655:541–549, January 2007. ISSN 0004-637X. doi: 10.1086/509759. URL https://ui.adsabs.harvard.edu/abs/2007ApJ...655..541M. Publisher: IOP ADS Bibcode: 2007ApJ...655..541M.

[134] Christian Marois, Bruce Macintosh, and Travis Barman. GQ Lup B Visible and Near-Infrared Photometric Analysis. *The Astrophysical Journal*, 654:L151–L154, January 2007. ISSN 0004-637X. doi: 10.1086/511071. URL https://ui.adsabs.harvard.edu/abs/2007ApJ...654L.151M. Publisher: IOP ADS Bibcode: 2007ApJ...654L.151M.

[135] Steven C. Martin. The Thermal Structure of Magnetic Accretion Funnels in Young Stellar Objects. *The Astrophysical Journal*, 470:537, October 1996. ISSN 0004-637X. doi: 10.1086/177886. URL https://ui.adsabs.harvard.edu/abs/1996ApJ...470..537M. ADS Bibcode: 1996ApJ...470..537M.



[136] Lucio Mayer, Thomas Quinn, James Wadsley, and Joachim Stadel. Formation of Giant Planets by Fragmentation of Protoplanetary Disks. *Science*, 298:1756–1759, November 2002. ISSN 0036-8075. doi: 10.1126/science.1077635. URL https://ui.adsabs.harvard.edu/abs/2002Sci...298.1756M. ADS Bibcode: 2002Sci...298.1756M.

[137] Richard M. McDermid, Giovanni Cresci, Francois Rigaut, Jean-Claude Bouret, Gayandhi De Silva, Marco Gullieuszik, Laura Magrini, J. Trevor Mendel, Simone Antoniucci, Giuseppe Bono, Devika Kamath, Stephanie Monty, Holger Baumgardt, Luca Cortese, Deanne Fisher, Filippo Mannucci, Alessandra Migliorini, Sarah Sweet, Eros Vanzella, Stefano Zibetti, and with additional contributions from the authors of the MAVIS White Papers. Phase A Science Case for MAVIS – The Multi-conjugate Adaptive-optics Visible Imager-Spectrograph for the VLT Adaptive Optics Facility, September 2020. URL https://ui.adsabs.harvard.edu/abs/2020arXiv200909242M. Publication Title: arXiv e-prints ADS Bibcode: 2020arXiv200909242M.

[138] Michael W. McElwain, Stanimir A. Metchev, James E. Larkin, Matthew Barczys, Christof Iserlohe, Alfred Krabbe, Andreas Quirrenbach, Jason Weiss, and Shelley A. Wright. First High-Contrast Science with an Integral Field Spectrograph: The Substellar Companion to GQ Lupi. *The Astrophysical Journal*, 656:505–514, February 2007. ISSN 0004-637X. doi: 10.1086/510063. URL https://ui.adsabs.harvard.edu/abs/2007ApJ...656..505M. Publisher: IOP ADS Bibcode: 2007ApJ...656..505M.

[139] Eugenio E. Mendoza V. Infrared Photometry of T Tauri Stars and Related Objects. *The Astrophysical Journal*, 143:1010, March 1966. ISSN 0004-637X. doi: 10.1086/148584. URL https://ui.adsabs.harvard.edu/abs/1966ApJ...143.1010M. ADS Bibcode: 1966ApJ...143.1010M.

[140] Eugenio E. Mendoza V. Infrared Excesses in T Tauri Stars and Related Objects. *The Astrophysical Journal*, 151:977, March 1968. ISSN 0004-637X. doi: 10.1086/149497. URL https://ui.adsabs.harvard.edu/abs/1968ApJ...151..977M. ADS Bibcode: 1968ApJ...151..977M.

[141] Anthony Mercer and Dimitris Stamatellos. The effect of radiative feedback on disc fragmentation. *Monthly Notices of the Royal Astronomical Society*, 465:2–18, February 2017. ISSN 0035-8711. doi: 10.1093/mnras/stw2714. URL https://ui.adsabs.harvard.edu/abs/2017MNRAS.465....2M. Publisher: OUP ADS Bibcode: 2017MNRAS.465....2M.

[142] Farzana Meru and Matthew R. Bate. Exploring the conditions required to form giant planets via gravitational instability in massive protoplanetary discs. *Monthly Notices of the Royal Astronomical Society*, 406:2279–2288, August 2010. ISSN 0035-8711. doi: 10.1111/j.1365-2966.2010.16867.x. URL https://ui.adsabs.harvard.edu/abs/2010MNRAS.406.2279M. Publisher: OUP ADS Bibcode: 2010MNRAS.406.2279M.

[143] N. Meunier and A. M. Lagrange. Activity time series of old stars from late F to early K. II. Radial velocity jitter and exoplanet detectability. *Astronomy and Astrophysics*, 628:A125, August 2019. ISSN 0004-6361. doi: 10.1051/0004-6361/201935347. URL https://ui.adsabs.harvard.edu/abs/2019A&A...628A.125M. ADS Bibcode: 2019A&A...628A.125M.

[144] N. Meunier and A. M. Lagrange. Radial-velocity variations due to meridional flows in the Sun and solar-type stars: impact on exoplanet detectability. *Astronomy and Astrophysics*, 638:A54, June 2020. ISSN 0004-6361. doi: 10.1051/0004-6361/201937354. URL https://ui.adsabs.harvard.edu/abs/2020A&A...638A..54M. ADS Bibcode: 2020A&A...638A..54M.

[145] N. Meunier, A. M. Lagrange, T. Boulet, and S. Borgniet. Activity time series of old stars from late F to early K. I. Simulating radial velocity, astrometry, photometry, and chromospheric emission. *Astronomy and Astrophysics*, 627:A56, July 2019. ISSN 0004-6361. doi: 10.1051/0004-6361/201834796. URL https://ui.adsabs.harvard.edu/abs/2019A&A...627A..56M. ADS Bibcode: 2019A&A...627A..56M.

[146] N. Meunier, A. M. Lagrange, and S. Borgniet. Activity time series of old stars from late F to early K. V. Effect on exoplanet detectability with high-precision astrometry. *Astronomy and Astrophysics*, 644:A77, December 2020. ISSN 0004-6361. doi: 10.1051/0004-6361/202038710. URL https://ui.adsabs.harvard.edu/abs/2020A&A...644A..77M. ADS Bibcode: 2020A&A...644A..77M.

[147] N. Meunier, R. Pous, S. Sulis, D. Mary, and A. M. Lagrange. Activity time series of old stars from late F to early K. VI. Exoplanet mass characterisation and detectability in radial velocity. *Astronomy and Astrophysics*, 676:A82, August 2023. ISSN 0004-6361. doi: 10.1051/0004-6361/202346218. URL https://ui.adsabs.harvard.edu/abs/2023A&A...676A..82M. ADS Bibcode: 2023A&A...676A..82M.

[148] S. Miki. The Gaseous Flow around a Protoplanet in the Primordial Solar Nebula. *Progress of Theoretical Physics*, 67: 1053–1067, April 1982. ISSN 0033-06840033-068X. doi: 10.1143/PTP.67.1053. URL https://ui.adsabs.harvard.edu/abs/1982PThPh..67.1053M. ADS Bibcode: 1982PThPh..67.1053M.



[149] H. Mizuno. Formation of the Giant Planets. *Progress of Theoretical Physics*, 64:544–557, August 1980. ISSN 0033-06840033-068X. doi: 10.1143/PTP.64.544. URL https://ui.adsabs.harvard.edu/abs/1980PThPh..64..544M. ADS Bibcode: 1980PThPh..64..544M.

[150] S. Mohanty, G. Basri, and R. Jayawardhana. Accretion in brown dwarfs down to nearly planetary masses. *Astronomische Nachrichten*, 326:891–894, December 2005. ISSN 0004-6337. doi: 10.1002/asna.200510450. URL https://ui.adsabs.harvard.edu/abs/2005AN....326..891M. ADS Bibcode: 2005AN....326..891M.

[151] Subhanjoy Mohanty, Ray Jayawardhana, and Gibor Basri. The T Tauri Phase Down to Nearly Planetary Masses: Echelle Spectra of 82 Very Low Mass Stars and Brown Dwarfs. *The Astrophysical Journal*, 626:498–522, June 2005. ISSN 0004-637X. doi: 10.1086/429794. URL https://ui.adsabs.harvard.edu/abs/2005ApJ...626..498M. ADS Bibcode: 2005ApJ...626..498M.

[152] P. Muheki, E. W. Guenther, T. Mutabazi, and E. Jurua. High-resolution spectroscopy of flares and CMEs on AD Leonis. *Astronomy and Astrophysics*, 637:A13, May 2020. ISSN 0004-6361. doi: 10.1051/0004-6361/201936904. URL https://ui.adsabs.harvard.edu/abs/2020A&A...637A..13M. ADS Bibcode: 2020A&A...637A..13M.

[153] Simon J. Murphy, Meridith Joyce, Timothy R. Bedding, Timothy R. White, and Mihkel Kama. A precise asteroseismic age and metallicity for HD 139614: a pre-main-sequence star with a protoplanetary disc in Upper Centaurus-Lupus. *Monthly Notices of the Royal Astronomical Society*, 502:1633–1646, April 2021. ISSN 0035-8711. doi: 10.1093/mnras/stab144. URL https://ui.adsabs.harvard.edu/abs/2021MNRAS.502.1633M. Publisher: OUP ADS Bibcode: 2021MNRAS.502.1633M.

[154] James Muzerolle, Nuria Calvet, and Lee Hartmann. Magnetospheric Accretion Models for the Hydrogen Emission Lines of T Tauri Stars. *The Astrophysical Journal*, 492:743–753, January 1998. ISSN 0004-637X. doi: 10.1086/305069. URL https://ui.adsabs.harvard.edu/abs/1998ApJ...492..743M. ADS Bibcode: 1998ApJ...492..743M.

[155] James Muzerolle, Nuria Calvet, and Lee Hartmann. Emission-Line Diagnostics of T Tauri Magnetospheric Accretion. II. Improved Model Tests and Insights into Accretion Physics. *The Astrophysical Journal*, 550:944–961, April 2001. ISSN 0004-637X. doi: 10.1086/319779. URL https://ui.adsabs.harvard.edu/abs/2001ApJ...550..944M. ADS Bibcode: 2001ApJ...550..944M.

[156] James Muzerolle, Lynne Hillenbrand, Nuria Calvet, César Briceño, and Lee Hartmann. Accretion in Young Stellar/Substellar Objects. *The Astrophysical Journal*, 592:266–281, July 2003. ISSN 0004-637X. doi: 10.1086/375704. URL https://ui.adsabs.harvard.edu/abs/2003ApJ...592..266M. ADS Bibcode: 2003ApJ...592..266M.

[157] James Muzerolle, Kevin L. Luhman, César Briceño, Lee Hartmann, and Nuria Calvet. Measuring Accretion in Young Substellar Objects: Approaching the Planetary Mass Regime. *The Astrophysical Journal*, 625:906–912, June 2005. ISSN 0004-637X. doi: 10.1086/429483. URL https://ui.adsabs.harvard.edu/abs/2005ApJ...625..906M. Publisher: IOP ADS Bibcode: 2005ApJ...625..906M.

[158] A. Müller, M. Keppler, Th. Henning, M. Samland, G. Chauvin, H. Beust, A. L. Maire, K. Molaverdikhani, R. van Boekel, M. Benisty, A. Boccaletti, M. Bonnefoy, F. Cantalloube, B. Charnay, J. L. Baudino, M. Gennaro, Z. C. Long, A. Cheetham, S. Desidera, M. Feldt, T. Fusco, J. Girard, R. Gratton, J. Hagelberg, M. Janson, A. M. Lagrange, M. Langlois, C. Lazzoni, R. Ligi, F. Ménard, D. Mesa, M. Meyer, P. Mollière, C. Mordasini, T. Moulin, A. Pavlov, N. Pawellek, S. P. Quanz, J. Ramos, D. Rouan, E. Sissa, E. Stadler, A. Vigan, Z. Wahhaj, L. Weber, and A. Zurlo. Orbital and atmospheric characterization of the planet within the gap of the PDS 70 transition disk. *Astronomy and Astrophysics*, 617:L2, September 2018. ISSN 0004-6361. doi: 10.1051/0004-6361/201833584. URL https://ui.adsabs.harvard.edu/abs/2018A&A...617L..2M. ADS Bibcode: 2018A&A...617L...2M.

[159] A. Natta, L. Testi, J. M. Alcalá, E. Rigliaco, E. Covino, B. Stelzer, and V. D'Elia. X-shooter spectroscopy of young stellar objects. V. Slow winds in T Tauri stars. *Astronomy and Astrophysics*, 569:A5, September 2014. ISSN 0004-6361. doi: 10.1051/0004-6361/201424136. URL https://ui.adsabs.harvard.edu/abs/2014A&A...569A...5N. ADS Bibcode: 2014A&A...569A...5N.

[160] R. Neuhäuser, E. W. Guenther, G. Wuchterl, M. Mugrauer, A. Bedalov, and P. H. Hauschildt. Evidence for a co-moving sub-stellar companion of GQ Lup. *Astronomy & Astrophysics*, 435(1):L13–L16, May 2005. ISSN 0004-6361, 1432-0746. doi: 10.1051/0004-6361:200500104. URL http://www.aanda.org/10.1051/0004-6361:200500104.



[161] S. Noll, W. Kausch, M. Barden, A. M. Jones, C. Szyszka, S. Kimeswenger, and J. Vinther. An atmospheric radiation model for Cerro Paranal. I. The optical spectral range. *Astronomy and Astrophysics*, 543:A92, July 2012. ISSN 0004-6361. doi: 10.1051/0004-6361/201219040. URL https://ui.adsabs.harvard.edu/abs/2012A&A...543A..92N. ADS Bibcode: 2012A&A...543A..92N.

[162] H. Nowacki, E. Alecian, K. Perraut, B. Zaire, C. P. Folsom, K. Pouilly, J. Bouvier, R. Manick, G. Pantolmos, A. P. Sousa, C. Dougados, G. A. J. Hussain, S. H. P. Alencar, and J. B. Le Bouquin. Star-disk interactions in the strongly accreting T Tauri star S CrA N. *Astronomy and Astrophysics*, 678:A86, October 2023. ISSN 0004-6361. doi: 10.1051/0004-6361/202347145. URL https://ui.adsabs.harvard.edu/abs/2023A&A...678A..86N. ADS Bibcode: 2023A&A...678A..86N.

[163] C. W. Ormel and H. H. Klahr. The effect of gas drag on the growth of protoplanets. Analytical expressions for the accretion of small bodies in laminar disks. *Astronomy and Astrophysics*, 520:A43, September 2010. ISSN 0004-6361. doi: 10.1051/0004-6361/201014903. URL https://ui.adsabs.harvard.edu/abs/2010A&A...520A..43O. ADS Bibcode: 2010A&A...520A..43O.

[164] Chris W. Ormel. The Emerging Paradigm of Pebble Accretion. 445:197, January 2017. doi: 10.1007/978-3-319-60609-5_7. URL https://ui.adsabs.harvard.edu/abs/2017ASSL..445..197O. Conference Name: Formation, Evolution, and Dynamics of Young Solar Systems ADS Bibcode: 2017ASSL..445..197O.

[165] Paolo Padoan and Åke Nordlund. The "Mysterious" Origin of Brown Dwarfs. *The Astrophysical Journal*, 617:559–564, December 2004. ISSN 0004-637X. doi: 10.1086/345413. URL https://ui.adsabs.harvard.edu/abs/2004ApJ...617..559P. Publisher: IOP ADS Bibcode: 2004ApJ...617..559P.

[166] Logan A. Pearce, Adam L. Kraus, Trent J. Dupuy, Michael J. Ireland, Aaron C. Rizzuto, Brendan P. Bowler, Eloise K. Birchall, and Alexander L. Wallace. Orbital Motion of the Wide Planetary-mass Companion GSC 6214-210 b: No Evidence for Dynamical Scattering. *The Astronomical Journal*, 157:71, February 2019. ISSN 0004-6256. doi: 10.3847/1538-3881/aafacb. URL https://ui.adsabs.harvard.edu/abs/2019AJ....157...71P. Publisher: IOP ADS Bibcode: 2019AJ....157...71P.

[167] P. P. Petrov, G. F. Gahm, G. J. Herczeg, H. C. Stempels, and F. M. Walter. Doppler probe of accretion onto a T Tauri star. *Astronomy and Astrophysics*, 568:L10, August 2014. ISSN 0004-6361. doi: 10.1051/0004-6361/201424374. URL https://ui.adsabs.harvard.edu/abs/2014A&A...568L..10P. ADS Bibcode: 2014A&A...568L..10P.

[168] S. Petrus, M. Bonnefoy, G. Chauvin, C. Babusiaux, P. Delorme, A. M. Lagrange, N. Florent, A. Bayo, M. Janson, B. Biller, E. Manjavacas, G. D. Marleau, and T. Kopytova. A new take on the low-mass brown dwarf companions on wide orbits in Upper-Scorpius. *Astronomy and Astrophysics*, 633:A124, January 2020. ISSN 0004-6361. doi: 10.1051/0004-6361/201935732. URL https://ui.adsabs.harvard.edu/abs/2020A&A...633A.124P. ADS Bibcode: 2020A&A...633A.124P.

[169] S. Petrus, M. Bonnefoy, G. Chauvin, B. Charnay, G. D. Marleau, R. Gratton, A. M. Lagrange, J. Rameau, C. Mordasini, M. Nowak, P. Delorme, A. Boccaletti, A. Carlotti, M. Houllé, A. Vigan, F. Allard, S. Desidera, V. D'Orazi, H. J. Hoeijmakers, A. Wyttenbach, and B. Lavie. Medium-resolution spectrum of the exoplanet HIP 65426 b. *Astronomy and Astrophysics*, 648:A59, April 2021. ISSN 0004-6361. doi: 10.1051/0004-6361/202038914. URL https://ui.adsabs.harvard.edu/abs/2021A&A...648A..59P. ADS Bibcode: 2021A&A...648A..59P.

[170] S. Petrus, G. Chauvin, M. Bonnefoy, P. Tremblin, B. Charnay, P. Delorme, G. D. Marleau, A. Bayo, E. Manjavacas, A. M. Lagrange, P. Mollière, P. Palma-Bifani, B. Biller, J. S. Jenkins, J. M. Goyal, and K. Hoch. X-SHYNE: X-shooter spectra of young exoplanet analogs. I. A medium-resolution 0.65-2.5 μm one-shot spectrum of VHS 1256–1257 b. *Astronomy and Astrophysics*, 670:L9, February 2023. ISSN 0004-6361. doi: 10.1051/0004-6361/202244494. URL https://ui.adsabs.harvard.edu/abs/2023A&A...670L...9P. ADS Bibcode: 2023A&A...670L...9P.

[171] M. W. Phillips, P. Tremblin, I. Baraffe, G. Chabrier, N. F. Allard, F. Spiegelman, J. M. Goyal, B. Drummond, and E. Hébrard. A new set of atmosphere and evolution models for cool T-Y brown dwarfs and giant exoplanets. *Astronomy and Astrophysics*, 637:A38, May 2020. ISSN 0004-6361. doi: 10.1051/0004-6361/201937381. URL https://ui.adsabs.harvard.edu/abs/2020A&A...637A..38P. ADS Bibcode: 2020A&A...637A..38P.

[172] James B. Pollack, Olenka Hubickyj, Peter Bodenheimer, Jack J. Lissauer, Morris Podolak, and Yuval Greenzweig. Formation of the Giant Planets by Concurrent Accretion of Solids and Gas. *Icarus*, 124:62–85, November 1996. ISSN 0019-1035. doi: 10.1006/icar.1996.0190. URL https://ui.adsabs.harvard.edu/abs/1996Icar..124...62P. ADS Bibcode: 1996Icar..124...62P.



[173] Thomas Preibisch, Hans Zinnecker, Eike Guenther, Michael Sterzik, Sabine Frink, and Siegfried Roser. T Tauri Stars in the Scorpius-Centaurus OB Association. 154:1780, January 1998. URL https://ui.adsabs.harvard.edu/abs/1998ASPC..154.1780P. Conference Name: Cool Stars, Stellar Systems, and the Sun ADS Bibcode: 1998ASPC..154.1780P.

[174] A. Reiners and U. R. Christensen. A magnetic field evolution scenario for brown dwarfs and giant planets. *Astronomy and Astrophysics*, 522:A13, November 2010. ISSN 0004-6361. doi: 10.1051/0004-6361/201014251. URL https://ui.adsabs.harvard.edu/abs/2010A&A...522A..13R. ADS Bibcode: 2010A&A...522A..13R.

[175] Emily L. Rice, T. Barman, Ian S. Mclean, L. Prato, and J. Davy Kirkpatrick. Physical Properties of Young Brown Dwarfs and Very Low Mass Stars Inferred from High-resolution Model Spectra. *The Astrophysical Journal Supplement Series*, 186:63–84, January 2010. ISSN 0067-0049. doi: 10.1088/0067-0049/186/1/63. URL https://ui.adsabs.harvard.edu/abs/2010ApJS..186...63R. Publisher: IOP ADS Bibcode: 2010ApJS..186...63R.

[176] Adric R. Riedel, Charlie T. Finch, Todd J. Henry, John P. Subasavage, Wei-Chun Jao, Lison Malo, David R. Rodriguez, Russel J. White, Douglas R. Gies, Sergio B. Dieterich, Jennifer G. Winters, Cassy L. Davison, Edmund P. Nelan, Sarah C. Blunt, Kelle L. Cruz, Emily L. Rice, and Philip A. Ianna. The Solar Neighborhood. XXXIII. Parallax Results from the CTIOPI 0.9 m Program: Trigonometric Parallaxes of Nearby Low-mass Active and Young Systems. *The Astronomical Journal*, 147:85, April 2014. ISSN 0004-6256. doi: 10.1088/0004-6256/147/4/85. URL https://ui.adsabs.harvard.edu/abs/2014AJ....147...85R. Publisher: IOP ADS Bibcode: 2014AJ....147...85R.

[177] E. Rigliaco, A. Natta, L. Testi, S. Randich, J. M. Alcalà, E. Covino, and B. Stelzer. X-shooter spectroscopy of young stellar objects. I. Mass accretion rates of low-mass T Tauri stars in σ Orionis. *Astronomy and Astrophysics*, 548:A56, December 2012. ISSN 0004-6361. doi: 10.1051/0004-6361/201219832. URL https://ui.adsabs.harvard.edu/abs/2012A&A...548A..56R. ADS Bibcode: 2012A&A...548A..56R.

[178] Simon C. Ringqvist, Gayathri Viswanath, Yuhiko Aoyama, Markus Janson, Gabriel-Dominique Marleau, and Alexis Brandeker. Resolved near-UV hydrogen emission lines at 40-Myr super-Jovian protoplanet Delorme 1 (AB)b. Indications of magnetospheric accretion. *Astronomy and Astrophysics*, 669:L12, January 2023. ISSN 0004-6361. doi: 10.1051/0004-6361/202245424. URL https://ui.adsabs.harvard.edu/abs/2023A&A...669L..12R. ADS Bibcode: 2023A&A...669L..12R.

[179] D. H. Roberts, J. Lehar, and J. W. Dreher. Time series analysis with CLEAN. I. Derivation of a spectrum. *The Astronomical Journal*, 93:968–989, April 1987. ISSN 0004-6256. doi: 10.1086/114383. URL https://ui.adsabs.harvard.edu/abs/1987AJ.....93..968R. Publisher: IOP ADS Bibcode: 1987AJ.....93..968R.

[180] C. Rodrigo and E. Solano. *The SVO Filter Profile Service*. July 2020. URL https://ui.adsabs.harvard.edu/abs/2020sea..confE.182R. Conference Name: XIV.0 Scientific Meeting (virtual) of the Spanish Astronomical Society Pages: 182 ADS Bibcode: 2020sea..confE.182R.

[181] Carlos Rodrigo, Enrique Solano, and Amelia Bayo. SVO Filter Profile Service Version 1.0. Technical report, October 2012. URL https://ui.adsabs.harvard.edu/abs/2012ivoa.rept.1015R. Publication Title: IVOA Working Draft 15 October 2012 ADS Bibcode: 2012ivoa.rept.1015R.

[182] Carlos Rodrigo, Patricia Cruz, John F. Aguilar, Alba Aller, Enrique Solano, Maria Cruz Gálvez-Ortiz, Francisco Jiménez-Esteban, Pedro Mas-Buitrago, Amelia Bayo, Miriam Cortés-Contreras, Raquel Murillo-Ojeda, Silvia Bonoli, Javier Cenarro, Renato Dupke, Carlos López-Sanjuan, Antonio Marín-Franch, Claudia Mendes de Oliveira, Mariano Moles, Keith Taylor, Jesús Varela, and Héctor Vázquez Ramió. Photometric segregation of dwarf and giant FGK stars using the SVO Filter Profile Service and photometric tools. *Astronomy and Astrophysics*, 689:A93, September 2024. ISSN 0004-6361. doi: 10.1051/0004-6361/202449998. URL https://ui.adsabs.harvard.edu/abs/2024A&A...689A..93R. Publisher: EDP ADS Bibcode: 2024A&A...689A..93R.

[183] M. M. Romanova, G. V. Ustyugova, A. V. Koldoba, J. V. Wick, and R. V. E. Lovelace. Three-dimensional Simulations of Disk Accretion to an Inclined Dipole. I. Magnetospheric Flows at Different θ. *The Astrophysical Journal*, 595:1009–1031, October 2003. ISSN 0004-637X. doi: 10.1086/377514. URL https://ui.adsabs.harvard.edu/abs/2003ApJ...595.1009R. ADS Bibcode: 2003ApJ...595.1009R.

[184] M. M. Romanova, G. V. Ustyugova, A. V. Koldoba, and R. V. E. Lovelace. Three-dimensional Simulations of Disk Accretion to an Inclined Dipole. II. Hot Spots and Variability. *The Astrophysical Journal*, 610:920–932, August 2004. ISSN 0004-637X. doi: 10.1086/421867. URL https://ui.adsabs.harvard.edu/abs/2004ApJ...610..920R. ADS Bibcode: 2004ApJ...610..920R.



[185] Marina M. Romanova, Akshay K. Kulkarni, and Richard V. E. Lovelace. Unstable Disk Accretion onto Magnetized Stars: First Global Three-dimensional Magnetohydrodynamic Simulations. *The Astrophysical Journal*, 673:L171, February 2008. ISSN 0004-637X. doi: 10.1086/527298. URL https://ui.adsabs.harvard.edu/abs/2008ApJ...673L.171R. ADS Bibcode: 2008ApJ...673L.171R.

[186] David Rubin, G. Aldering, P. Antilogus, C. Aragon, S. Bailey, C. Baltay, S. Bongard, K. Boone, C. Buton, Y. Copin, S. Dixon, D. Fouchez, E. Gangler, R. Gupta, B. Hayden, W. Hillebrandt, A. G. Kim, M. Kowalski, D. Küsters, P.-F. Léget, F. Mondon, J. Nordin, R. Pain, E. Pecontal, R. Pereira, S. Perlmutter, K. A. Ponder, D. Rabinowitz, M. Rigault, K. Runge, C. Saunders, G. Smadja, N. Suzuki, C. Tao, S. Taubenberger, R. C. Thomas, M. Vincenzi, and (The Nearby Supernova Factory). Uniform Recalibration of Common Spectrophotometry Standard Stars onto the CALSPEC System Using the SuperNova Integral Field Spectrograph. *The Astrophysical Journal Supplement Series*, 263(1):1, November 2022. ISSN 0067-0049, 1538-4365. doi: 10.3847/1538-4365/ac7b7f. URL https://iopscience.iop.org/article/10.3847/1538-4365/ac7b7f.

[187] A. E. Rydgren, S. E. Strom, and K. M. Strom. The nature of the objects of Joy: a study of the T Tauri phenomenon. *The Astrophysical Journal Supplement Series*, 30:307–336, March 1976. ISSN 0067-0049. doi: 10.1086/190364. URL https://ui.adsabs.harvard.edu/abs/1976ApJS...30..307R. ADS Bibcode: 1976ApJS...30..307R.

[188] V. S. Safronov. On the gravitational instability in flattened systems with axial symmetry and non-uniform rotation. *Annales d'Astrophysique*, 23:979, February 1960. ISSN 0365-0499. URL https://ui.adsabs.harvard.edu/abs/1960AnAp..23..979S. ADS Bibcode: 1960AnAp...23..979S.

[189] V. S. Safronov. Sizes of the largest bodies falling onto the planets during their formation. *Soviet Astronomy*, 9:987–991, June 1966. ISSN 0038-5301. URL https://ui.adsabs.harvard.edu/abs/1966SvA.....9..987S. ADS Bibcode: 1966SvA.....9..987S.

[190] V. S. Safronov. *Evolution of the protoplanetary cloud and formation of the earth and planets.* January 1972. URL https://ui.adsabs.harvard.edu/abs/1972epcf.book.....S. Publication Title: Evolution of the protoplanetary cloud and formation of the earth and planets ADS Bibcode: 1972epcf.book.....S.

[191] V. S. Safronov and E. V. Zvjagina. Relative Sizes of the Largest Bodies during the Accumulation of Planets. *Icarus*, 10:109–115, January 1969. ISSN 0019-1035. doi: 10.1016/0019-1035(69)90013-X. URL https://ui.adsabs.harvard.edu/abs/1969Icar...10..109S. ADS Bibcode: 1969Icar...10..109S.

[192] S. Sallum, K. B. Follette, J. A. Eisner, L. M. Close, P. Hinz, K. Kratter, J. Males, A. Skemer, B. Macintosh, P. Tuthill, V. Bailey, D. Defrère, K. Morzinski, T. Rodigas, E. Spalding, A. Vaz, and A. J. Weinberger. Accreting protoplanets in the LkCa 15 transition disk. *Nature*, 527:342–344, November 2015. ISSN 0028-0836. doi: 10.1038/nature15761. URL https://ui.adsabs.harvard.edu/abs/2015Natur.527..342S. ADS Bibcode: 2015Natur.527..342S.

[193] Alejandro Santamaría-Miranda, Claudio Cáceres, Matthias R. Schreiber, Adam Hardy, Amelia Bayo, Steven G. Parsons, Mariusz Gromadzki, and Aurora Belén Aguayo Villegas. Accretion signatures in the X-shooter spectrum of the substellar companion to SR12. *Monthly Notices of the Royal Astronomical Society*, 475:2994–3003, April 2018. ISSN 0035-8711. doi: 10.1093/mnras/stx3325. URL https://ui.adsabs.harvard.edu/abs/2018MNRAS.475.2994S. Publisher: OUP ADS Bibcode: 2018MNRAS.475.2994S.

[194] Alejandro Santamaría-Miranda, Claudio Cáceres, Matthias R. Schreiber, Adam Hardy, Amelia Bayo, Steven G. Parsons, Mariusz Gromadzki, and Aurora Belén Aguayo Villegas. Erratum: Accretion signatures in the X-shooter spectrum of the substellar companion to SR12. *Monthly Notices of the Royal Astronomical Society*, 488:5852–5853, October 2019. ISSN 0035-8711. doi: 10.1093/mnras/stz2173. URL https://ui.adsabs.harvard.edu/abs/2019MNRAS.488.5852S. Publisher: OUP ADS Bibcode: 2019MNRAS.488.5852S.

[195] J. D. Scargle. Studies in astronomical time series analysis. II. Statistical aspects of spectral analysis of unevenly spaced data. *The Astrophysical Journal*, 263:835–853, December 1982. ISSN 0004-637X. doi: 10.1086/160554. URL https://ui.adsabs.harvard.edu/abs/1982ApJ...263..835S. Publisher: IOP ADS Bibcode: 1982ApJ...263..835S.

[196] Kevin C. Schlaufman. Evidence of an Upper Bound on the Masses of Planets and Its Implications for Giant Planet Formation. *The Astrophysical Journal*, 853:37, January 2018. ISSN 0004-637X. doi: 10.3847/1538-4357/aa961c. URL https://ui.adsabs.harvard.edu/abs/2018ApJ...853...37S. Publisher: IOP ADS Bibcode: 2018ApJ...853...37S.



[197] Henriette Schwarz, Christian Ginski, Remco J. de Kok, Ignas A. G. Snellen, Matteo Brogi, and Jayne L. Birkby. The slow spin of the young substellar companion GQ Lupi b and its orbital configuration. *Astronomy & Astrophysics*, 593: A74, September 2016. ISSN 0004-6361, 1432-0746. doi: 10.1051/0004-6361/201628908. URL http://www.aanda.org/10.1051/0004-6361/201628908.

[198] A. Seifahrt, R. Neuhäuser, and P. H. Hauschildt. Near-infrared integral-field spectroscopy of the companion to GQ Lupi. *Astronomy and Astrophysics*, 463:309–313, February 2007. ISSN 0004-6361. doi: 10.1051/0004-6361:20066463. URL https://ui.adsabs.harvard.edu/abs/2007A&A...463..309S. ADS Bibcode: 2007A&A...463..309S.

[199] John Skilling. Nested Sampling. 735:395–405, November 2004. doi: 10.1063/1.1835238. URL https://ui.adsabs.harvard.edu/abs/2004AIPC..735..395S. Conference Name: Bayesian Inference and Maximum Entropy Methods in Science and Engineering: 24th International Workshop on Bayesian Inference and Maximum Entropy Methods in Science and Engineering Publisher: AIP ADS Bibcode: 2004AIPC..735..395S.

[200] B. A. Smith and R. J. Terrile. A Circumstellar Disk around β Pictoris. *Science*, 226:1421–1424, December 1984. ISSN 0036-8075. doi: 10.1126/science.226.4681.1421. URL https://ui.adsabs.harvard.edu/abs/1984Sci...226.1421S. ADS Bibcode: 1984Sci...226.1421S.

[201] A. P. Sousa, J. Bouvier, S. H. P. Alencar, J. F. Donati, E. Alecian, J. Roquette, K. Perraut, C. Dougados, A. Carmona, S. Covino, D. Fugazza, E. Molinari, C. Moutou, A. Santerne, K. Grankin, É. Artigau, X. Delfosse, G. Hebrard, and SPIRou Consortium. Star-disk interaction in the T Tauri star V2129 Ophiuchi: An evolving accretion-ejection structure. *Astronomy and Astrophysics*, 649:A68, May 2021. ISSN 0004-6361. doi: 10.1051/0004-6361/202140346. URL https://ui.adsabs.harvard.edu/abs/2021A&A...649A..68S. ADS Bibcode: 2021A&A...649A..68S.

[202] Dimitris Stamatellos. The Migration of Gas Giant Planets in Gravitationally Unstable Disks. *The Astrophysical Journal*, 810:L11, September 2015. ISSN 0004-637X. doi: 10.1088/2041-8205/810/1/L11. URL https://ui.adsabs.harvard.edu/abs/2015ApJ...810L..11S. Publisher: IOP ADS Bibcode: 2015ApJ...810L..11S.

[203] Dimitris Stamatellos and Gregory J. Herczeg. The properties of discs around planets and brown dwarfs as evidence for disc fragmentation. *Monthly Notices of the Royal Astronomical Society*, 449:3432–3440, June 2015. ISSN 0035-8711. doi: 10.1093/mnras/stv526. URL https://ui.adsabs.harvard.edu/abs/2015MNRAS.449.3432S. Publisher: OUP ADS Bibcode: 2015MNRAS.449.3432S.

[204] B. Stelzer, A. Frasca, J. M. Alcalá, C. F. Manara, K. Biazzo, E. Covino, E. Rigliaco, L. Testi, S. Covino, and V. D'Elia. X-shooter spectroscopy of young stellar objects. III. Photospheric and chromospheric properties of Class III objects. *Astronomy and Astrophysics*, 558:A141, October 2013. ISSN 0004-6361. doi: 10.1051/0004-6361/201321979. URL https://ui.adsabs.harvard.edu/abs/2013A&A...558A.141S. ADS Bibcode: 2013A&A...558A.141S.

[205] Tomas Stolker, Sebastiaan Y. Haffert, Aurora Y. Kesseli, Rob G. van Holstein, Yuhiko Aoyama, Jarle Brinchmann, Gabriele Cugno, Julien H. Girard, Gabriel-Dominique Marleau, Gabriele Cugno, Michael R. Meyer, Julien Milli, Sascha P. Quanz, Ignas A. G. Snellen, and Kamen O. Todorov. Characterizing the protolunar disk of the accreting companion GQ Lupi B. *arXiv:2110.04307 [astro-ph]*, October 2021. doi: 10.3847/1538-3881/ac2c7f. URL http://arxiv.org/abs/2110.04307. arXiv: 2110.04307.

[206] L. Suárez-Andrés, G. Israelian, J. I. González Hernández, V. Zh. Adibekyan, E. Delgado Mena, N. C. Santos, and S. G. Sousa. C/O vs. Mg/Si ratios in solar type stars: The HARPS sample. *Astronomy and Astrophysics*, 614:A84, June 2018. ISSN 0004-6361. doi: 10.1051/0004-6361/201730743. URL https://ui.adsabs.harvard.edu/abs/2018A&A...614A..84S. ADS Bibcode: 2018A&A...614A..84S.

[207] C. Swastik, Ravinder K. Banyal, Mayank Narang, P. Manoj, T. Sivarani, Bacham E. Reddy, and S. P. Rajaguru. Host Star Metallicity of Directly Imaged Wide-orbit Planets: Implications for Planet Formation. *The Astronomical Journal*, 161: 114, March 2021. ISSN 0004-6256. doi: 10.3847/1538-3881/abd802. URL https://ui.adsabs.harvard.edu/abs/2021AJ....161..114S. Publisher: IOP ADS Bibcode: 2021AJ....161..114S.

[208] J. Szulágyi. Effects of the Planetary Temperature on the Circumplanetary Disk and on the Gap. *The Astrophysical Journal*, 842:103, June 2017. ISSN 0004-637X. doi: 10.3847/1538-4357/aa7515. URL https://ui.adsabs.harvard.edu/abs/2017ApJ...842..103S. Publisher: IOP ADS Bibcode: 2017ApJ...842..103S.

[209] J. Szulágyi, A. Morbidelli, A. Crida, and F. Masset. ACCRETION OF JUPITER-MASS PLANETS IN THE LIMIT OF VANISHING VISCOSITY. *The Astrophysical Journal*, 782(2):65, January 2014. ISSN 0004-637X, 1538-4357. doi: 10.1088/0004-637X/782/2/65. URL https://iopscience.iop.org/article/10.1088/0004-637X/782/2/65.



[210] J. Szulágyi, G. van der Plas, M. R. Meyer, A. Pohl, S. P. Quanz, L. Mayer, S. Daemgen, and V. Tamburello. Observability of forming planets and their circumplanetary discs - I. Parameter study for ALMA. *Monthly Notices of the Royal Astronomical Society*, 473:3573–3583, January 2018. ISSN 0035-8711. doi: 10.1093/mnras/stx2602. URL https://ui.adsabs.harvard.edu/abs/2018MNRAS.473.3573S. Publisher: OUP ADS Bibcode: 2018MNRAS.473.3573S.

[211] Judit Szulágyi and Barbara Ercolano. Hydrogen Recombination Line Luminosities and Variability from Forming Planets. *The Astrophysical Journal*, 902(2):126, October 2020. ISSN 1538-4357. doi: 10.3847/1538-4357/abb5a2. URL https://iopscience.iop.org/article/10.3847/1538-4357/abb5a2.

[212] Shinsuke Takasao, Yuhiko Aoyama, and Masahiro Ikoma. Hydrodynamic Model of Hα Emission from Accretion Shocks of Proto-Giant Planet and Circumplanetary Disk. *arXiv:2106.16113 [astro-ph]*, November 2021. doi: 10.3847/1538-4357/ac0f7e. URL http://arxiv.org/abs/2106.16113. arXiv: 2106.16113.

[213] Takayuki Tanigawa, Keiji Ohtsuki, and Masahiro N. Machida. Distribution of Accreting Gas and Angular Momentum onto Circumplanetary Disks. *The Astrophysical Journal*, 747:47, March 2012. ISSN 0004-637X. doi: 10.1088/0004-637X/747/1/47. URL https://ui.adsabs.harvard.edu/abs/2012ApJ...747...47T. Publisher: IOP ADS Bibcode: 2012ApJ...747...47T.

[214] G. Tautvaišienė, Š. Mikolaitis, A. Drazdauskas, E. Stonkutė, R. Minkevičiūtė, E. Pakštienė, H. Kjeldsen, K. Brogaard, Y. Chorniy, C. von Essen, F. Grundahl, M. Ambrosch, V. Bagdonas, A. Sharma, and C. Viscasillas Vázquez. Chemical Composition of Bright Stars in the Northern Hemisphere: Star-Planet Connection. *The Astrophysical Journal Supplement Series*, 259:45, April 2022. ISSN 0067-0049. doi: 10.3847/1538-4365/ac50b5. URL https://ui.adsabs.harvard.edu/abs/2022ApJS..259...45T. Publisher: IOP ADS Bibcode: 2022ApJS..259...45T.

[215] S. Terebey, F. H. Shu, and P. Cassen. The collapse of the cores of slowly rotating isothermal clouds. *The Astrophysical Journal*, 286:529–551, November 1984. ISSN 0004-637X. doi: 10.1086/162628. URL https://ui.adsabs.harvard.edu/abs/1984ApJ...286..529T. ADS Bibcode: 1984ApJ...286..529T.

[216] B. Tessore, A. Soulain, G. Pantolmos, J. Bouvier, C. Pinte, and K. Perraut. Spectroscopic and interferometric signatures of magnetospheric accretion in young stars. *Astronomy and Astrophysics*, 671:A129, March 2023. ISSN 0004-6361. doi: 10.1051/0004-6361/202245039. URL https://ui.adsabs.harvard.edu/abs/2023A&A...671A.129T. ADS Bibcode: 2023A&A...671A.129T.

[217] Thanawuth Thanathibodee, Nuria Calvet, Jaehan Bae, James Muzerolle, and Ramiro Franco Hernández. Magnetospheric Accretion as a Source of Hα Emission from Protoplanets around PDS 70. *The Astrophysical Journal*, 885:94, November 2019. ISSN 0004-637X. doi: 10.3847/1538-4357/ab44c1. URL https://ui.adsabs.harvard.edu/abs/2019ApJ...885...94T. Publisher: IOP ADS Bibcode: 2019ApJ...885...94T.

[218] Thanawuth Thanathibodee, Brandon Molina, Nuria Calvet, Javier Serna, Jaehan Bae, Mark Reynolds, Jesús Hernández, James Muzerolle, and Ramiro Franco Hernández. Variable Accretion onto Protoplanet Host Star PDS 70. *The Astrophysical Journal*, 892:81, April 2020. ISSN 0004-637X. doi: 10.3847/1538-4357/ab77c1. URL https://ui.adsabs.harvard.edu/abs/2020ApJ...892...81T. ADS Bibcode: 2020ApJ...892...81T.

[219] Christopher A. Theissen, Andrew A. West, Guillaume Shippee, Adam J. Burgasser, and Sarah J. Schmidt. The Late-Type Extension to MoVeRS (LaTE-MoVeRS): Proper Motion Verified Low-mass Stars and Brown Dwarfs from SDSS, 2MASS, and WISE. *The Astronomical Journal*, 153:92, March 2017. ISSN 0004-6256. doi: 10.3847/1538-3881/153/3/92. URL https://ui.adsabs.harvard.edu/abs/2017AJ....153...92T. Publisher: IOP ADS Bibcode: 2017AJ....153...92T.

[220] Christopher A. Theissen, Adam J. Burgasser, Daniella C. Bardalez Gagliuffi, Kevin K. Hardegree-Ullman, Jonathan Gagné, Sarah J. Schmidt, and Andrew A. West. 2MASS J11151597+1937266: A Young, Dusty, Isolated, Planetary-mass Object with a Potential Wide Stellar Companion. *The Astrophysical Journal*, 853:75, January 2018. ISSN 0004-637X. doi: 10.3847/1538-4357/aaa0cf. URL https://ui.adsabs.harvard.edu/abs/2018ApJ...853...75T. Publisher: IOP ADS Bibcode: 2018ApJ...853...75T.

[221] Ingo Thies, Jan Pflamm-Altenburg, Pavel Kroupa, and Michael Marks. Characterizing the Brown Dwarf Formation Channels from the Initial Mass Function and Binary-star Dynamics. *The Astrophysical Journal*, 800:72, February 2015. ISSN 0004-637X. doi: 10.1088/0004-637X/800/1/72. URL https://ui.adsabs.harvard.edu/abs/2015ApJ...800...72T. Publisher: IOP ADS Bibcode: 2015ApJ...800...72T.



[222] A. Toomre. On the gravitational stability of a disk of stars. *The Astrophysical Journal*, 139:1217–1238, May 1964. ISSN 0004-637X. doi: 10.1086/147861. URL https://ui.adsabs.harvard.edu/abs/1964ApJ...139.1217T. Publisher: IOP ADS Bibcode: 1964ApJ...139.1217T.

[223] P. Tremblin, D. S. Amundsen, P. Mourier, I. Baraffe, G. Chabrier, B. Drummond, D. Homeier, and O. Venot. Fingering Convection and Cloudless Models for Cool Brown Dwarf Atmospheres. *The Astrophysical Journal*, 804:L17, May 2015. ISSN 0004-637X. doi: 10.1088/2041-8205/804/1/L17. URL https://ui.adsabs.harvard.edu/abs/2015ApJ...804L..17T. Publisher: IOP ADS Bibcode: 2015ApJ...804L..17T.

[224] P. Tremblin, D. S. Amundsen, G. Chabrier, I. Baraffe, B. Drummond, S. Hinkley, P. Mourier, and O. Venot. Cloudless Atmospheres for L/T Dwarfs and Extrasolar Giant Planets. *The Astrophysical Journal*, 817:L19, February 2016. ISSN 0004-637X. doi: 10.3847/2041-8205/817/2/L19. URL https://ui.adsabs.harvard.edu/abs/2016ApJ...817L..19T. Publisher: IOP ADS Bibcode: 2016ApJ...817L..19T.

[225] Taichi Uyama, Takayuki Tanigawa, Jun Hashimoto, Motohide Tamura, Yuhiko Aoyama, Timothy D. Brandt, and Masato Ishizuka. Constraining Accretion Signatures of Exoplanets in the TW Hya Transitional Disk. *The Astronomical Journal*, 154:90, September 2017. ISSN 0004-6256. doi: 10.3847/1538-3881/aa816a. URL https://ui.adsabs.harvard.edu/abs/2017AJ....154...90U. Publisher: IOP ADS Bibcode: 2017AJ....154...90U.

[226] Jeff A. Valenti, Gibor Basri, and Christopher M. Johns. T Tauri Stars in Blue. *The Astronomical Journal*, 106:2024, November 1993. ISSN 0004-6256. doi: 10.1086/116783. URL https://ui.adsabs.harvard.edu/abs/1993AJ....106.2024V. ADS Bibcode: 1993AJ....106.2024V.

[227] R. G. van Holstein, T. Stolker, R. Jensen-Clem, C. Ginski, J. Milli, J. de Boer, J. H. Girard, Z. Wahhaj, A. J. Bohn, M. A. Millar-Blanchaer, M. Benisty, M. Bonnefoy, G. Chauvin, C. Dominik, S. Hinkley, C. U. Keller, M. Keppler, M. Langlois, S. Marino, F. Ménard, C. Perrot, T. O. B. Schmidt, A. Vigan, A. Zurlo, and F. Snik. A survey of the linear polarization of directly imaged exoplanets and brown dwarf companions with SPHERE-IRDIS. First polarimetric detections revealing disks around DH Tau B and GSC 6214-210 B. *Astronomy and Astrophysics*, 647:A21, March 2021. ISSN 0004-6361. doi: 10.1051/0004-6361/202039290. URL https://ui.adsabs.harvard.edu/abs/2021A&A...647A..21V. ADS Bibcode: 2021A&A...647A..21V.

[228] Carlos M. Varsavsky. Radial Velocities and Theree-Color Light-Curves of Some RR Lyrae Variables. *The Astrophysical Journal*, 131:623, May 1960. ISSN 0004-637X. doi: 10.1086/146875. URL https://ui.adsabs.harvard.edu/abs/1960ApJ...131..623V. ADS Bibcode: 1960ApJ...131..623V.

[229] L. Venuti, B. Stelzer, J. M. Alcalá, C. F. Manara, A. Frasca, R. Jayawardhana, S. Antoniucci, C. Argiroffi, A. Natta, B. Nisini, S. Randich, and A. Scholz. X-shooter spectroscopy of young stars with disks. The TW Hydrae association as a probe of the final stages of disk accretion. *Astronomy and Astrophysics*, 632:A46, December 2019. ISSN 0004-6361. doi: 10.1051/0004-6361/201935745. URL https://ui.adsabs.harvard.edu/abs/2019A&A...632A..46V. ADS Bibcode: 2019A&A...632A..46V.

[230] Rico G. Visser and Chris W. Ormel. On the growth of pebble-accreting planetesimals. *Astronomy and Astrophysics*, 586: A66, February 2016. ISSN 0004-6361. doi: 10.1051/0004-6361/201527361. URL https://ui.adsabs.harvard.edu/abs/2016A&A...586A..66V. ADS Bibcode: 2016A&A...586A..66V.

[231] E. I. Vorobyov and Shantanu Basu. Mass Accretion Rates in Self-Regulated Disks of T Tauri Stars. *The Astrophysical Journal*, 676:L139, April 2008. ISSN 0004-637X. doi: 10.1086/587514. URL https://ui.adsabs.harvard.edu/abs/2008ApJ...676L.139V. ADS Bibcode: 2008ApJ...676L.139V.

[232] Kevin Wagner, Katherine B. Follete, Laird M. Close, Dániel Apai, Aidan Gibbs, Miriam Keppler, André Müller, Thomas Henning, Markus Kasper, Ya-Lin Wu, Joseph Long, Jared Males, Katie Morzinski, and Melissa McClure. Magellan Adaptive Optics Imaging of PDS 70: Measuring the Mass Accretion Rate of a Young Giant Planet within a Gapped Disk. *The Astrophysical Journal*, 863:L8, August 2018. ISSN 0004-637X. doi: 10.3847/2041-8213/aad695. URL https://ui.adsabs.harvard.edu/abs/2018ApJ...863L...8W. Publisher: IOP ADS Bibcode: 2018ApJ...863L...8W.

[233] J. J. Wang, A. Vigan, S. Lacour, M. Nowak, T. Stolker, R. J. De Rosa, S. Ginzburg, P. Gao, R. Abuter, A. Amorim, R. Asensio-Torres, M. Bauböck, M. Benisty, J. P. Berger, H. Beust, J. L. Beuzit, S. Blunt, A. Boccaletti, A. Bohn, M. Bonnefoy, H. Bonnet, W. Brandner, F. Cantalloube, P. Caselli, B. Charnay, G. Chauvin, E. Choquet, V. Christiaens, Y. Clénet, V. Coudé Du Foresto, A. Cridland, P. T. de Zeeuw, R. Dembet, J. Dexter, A. Drescher, G. Duvert, A. Eckart, F. Eisenhauer, S. Facchini, F. Gao, P. Garcia, R. Garcia Lopez, T. Gardner, E. Gendron, R. Genzel,



S. Gillessen, J. Girard, X. Haubois, G. Heißel, T. Henning, S. Hinkley, S. Hippler, M. Horrobin, M. Houllé, Z. Hubert, A. Jiménez-Rosales, L. Jocou, J. Kammerer, M. Keppler, P. Kervella, M. Meyer, L. Kreidberg, A. M. Lagrange, V. Lapeyrère, J. B. Le Bouquin, P. Léna, D. Lutz, A. L. Maire, F. Ménard, A. Mérand, P. Mollière, J. D. Monnier, D. Mouillet, A. Müller, E. Nasedkin, T. Ott, G. P. P. L. Otten, C. Paladini, T. Paumard, K. Perraut, G. Perrin, O. Pfuhl, L. Pueyo, J. Rameau, L. Rodet, G. Rodríguez-Coira, G. Rousset, S. Scheithauer, J. Shangguan, T. Shimizu, J. Stadler, O. Straub, C. Straubmeier, E. Sturm, L. J. Tacconi, E. F. van Dishoeck, F. Vincent, S. D. von Fellenberg, K. Ward-Duong, F. Widmann, E. Wieprecht, E. Wiezorrek, J. Woillez, and Gravity Collaboration. Constraining the Nature of the PDS 70 Protoplanets with VLTI/GRAVITY. *The Astronomical Journal*, 161:148, March 2021. ISSN 0004-6256. doi: 10.3847/1538-3881/abdb2d. URL https://ui.adsabs.harvard.edu/abs/2021AJ....161..148W. Publisher: IOP ADS Bibcode: 2021AJ....161..148W.

[234] S. J. Weidenschilling. Aerodynamics of solid bodies in the solar nebula. *Monthly Notices of the Royal Astronomical Society*, 180:57–70, July 1977. ISSN 0035-8711. doi: 10.1093/mnras/180.2.57. URL https://ui.adsabs.harvard.edu/abs/1977MNRAS.180...57W. Publisher: OUP ADS Bibcode: 1977MNRAS.180...57W.

[235] E. B. Weston and L. A. Aller. Short Period Changes in the Spectrum of T Tauri. 6:251–255, January 1955. URL https://ui.adsabs.harvard.edu/abs/1955LIACo...6..251W. Conference Name: Liege International Astrophysical Colloquia ADS Bibcode: 1955LIACo...6..251W.

[236] G. W. Wetherill and G. R. Stewart. Accumulation of a swarm of small planetesimals. *Icarus*, 77:330–357, February 1989. ISSN 0019-1035. doi: 10.1016/0019-1035(89)90093-6. URL https://ui.adsabs.harvard.edu/abs/1989Icar...77..330W. ADS Bibcode: 1989Icar...77..330W.

[237] Russel J. White and Gibor Basri. Very Low Mass Stars and Brown Dwarfs in Taurus-Auriga. *The Astrophysical Journal*, 582:1109–1122, January 2003. ISSN 0004-637X. doi: 10.1086/344673. URL https://ui.adsabs.harvard.edu/abs/2003ApJ...582.1109W. ADS Bibcode: 2003ApJ...582.1109W.

[238] A. P. Whitworth and D. Stamatellos. The minimum mass for star formation, and the origin of binary brown dwarfs. *Astronomy and Astrophysics*, 458:817–829, November 2006. ISSN 0004-6361. doi: 10.1051/0004-6361:20065806. URL https://ui.adsabs.harvard.edu/abs/2006A&A...458..817W. ADS Bibcode: 2006A&A...458..817W.

[239] Ya-Lin Wu and Patrick D. Sheehan. An ALMA Dynamical Mass Estimate of the Proposed Planetary-mass Companion FW Tau C. *The Astrophysical Journal*, 846:L26, September 2017. ISSN 0004-637X. doi: 10.3847/2041-8213/aa8771. URL https://ui.adsabs.harvard.edu/abs/2017ApJ...846L..26W. Publisher: IOP ADS Bibcode: 2017ApJ...846L..26W.

[240] Ya-Lin Wu, Laird M. Close, Josh A. Eisner, and Patrick D. Sheehan. An Explanation of the Very Low Radio Flux of Young Planet-mass Companions. *The Astronomical Journal*, 154:234, December 2017. ISSN 0004-6256. doi: 10.3847/1538-3881/aa93db. URL https://ui.adsabs.harvard.edu/abs/2017AJ....154..234W. Publisher: IOP ADS Bibcode: 2017AJ....154..234W.

[241] Ya-Lin Wu, Brendan P. Bowler, Patrick D. Sheehan, Laird M. Close, Joshua A. Eisner, William M. J. Best, Kimberly Ward-Duong, Zhaohuan Zhu, and Adam L. Kraus. ALMA Discovery of a Disk around the Planetary-mass Companion SR 12 c. *The Astrophysical Journal*, 930:L3, May 2022. ISSN 0004-637X. doi: 10.3847/2041-8213/ac6420. URL https://ui.adsabs.harvard.edu/abs/2022ApJ...930L...3W. Publisher: IOP ADS Bibcode: 2022ApJ...930L...3W.

[242] Jerry W. Xuan, Chih-Chun Hsu, Luke Finnerty, Jason J. Wang, Jean-Baptiste Ruffio, Yapeng Zhang, Heather A. Knutson, Dimitri Mawet, Eric E. Mamajek, Julie Inglis, Nicole L. Wallack, Marta L. Bryan, Geoffrey A. Blake, Paul Mollière, Neda Hejazi, Ashley Baker, Randall Bartos, Benjamin Calvin, Sylvain Cetre, Jacques-Robert Delorme, Greg Doppmann, Daniel Echeverri, Michael P. Fitzgerald, Nemanja Jovanovic, Joshua Liberman, Ronald A. López, Evan Morris, Jacklyn Pezzato, Ben Sappey, Tobias Schofield, Andrew Skemer, James K. Wallace, Ji Wang, Shubh Agrawal, and Katelyn Horstman. Are these planets or brown dwarfs? Broadly solar compositions from high-resolution atmospheric retrievals of ~10-30 $M_\textrm{Jup}$ companions, May 2024. URL https://ui.adsabs.harvard.edu/abs/2024arXiv240513128X. Publication Title: arXiv e-prints ADS Bibcode: 2024arXiv240513128X.

[243] Donald G. York, J. Adelman, John E. Anderson, Jr., Scott F. Anderson, James Annis, Neta A. Bahcall, J. A. Bakken, Robert Barkhouser, Steven Bastian, Eileen Berman, William N. Boroski, Steve Bracker, Charlie Briegel, John W. Briggs, J. Brinkmann, Robert Brunner, Scott Burles, Larry Carey, Michael A. Carr, Francisco J. Castander, Bing Chen, Patrick L. Colestock, A. J. Connolly, J. H. Crocker, István Csabai, Paul C. Czarapata, John Eric Davis, Mamoru Doi, Tom Dombeck, Daniel Eisenstein, Nancy Ellman, Brian R. Elms, Michael L. Evans, Xiaohui Fan, Glenn R. Federwitz, Larry Fiscelli, Scott

Friedman, Joshua A. Frieman, Masataka Fukugita, Bruce Gillespie, James E. Gunn, Vijay K. Gurbani, Ernst de Haas, Merle Haldeman, Frederick H. Harris, J. Hayes, Timothy M. Heckman, G. S. Hennessy, Robert B. Hindsley, Scott Holm, Donald J. Holmgren, Chi-hao Huang, Charles Hull, Don Husby, Shin-Ichi Ichikawa, Takashi Ichikawa, Željko Ivezić, Stephen Kent, Rita S. J. Kim, E. Kinney, Mark Klaene, A. N. Kleinman, S. Kleinman, G. R. Knapp, John Korienek, Richard G. Kron, Peter Z. Kunszt, D. Q. Lamb, B. Lee, R. French Leger, Siriluk Limmongkol, Carl Lindenmeyer, Daniel C. Long, Craig Loomis, Jon Loveday, Rich Lucinio, Robert H. Lupton, Bryan MacKinnon, Edward J. Mannery, P. M. Mantsch, Bruce Margon, Peregrine McGehee, Timothy A. McKay, Avery Meiksin, Aronne Merelli, David G. Monet, Jeffrey A. Munn, Vijay K. Narayanan, Thomas Nash, Eric Neilsen, Rich Neswold, Heidi Jo Newberg, R. C. Nichol, Tom Nicinski, Mario Nonino, Norio Okada, Sadanori Okamura, Jeremiah P. Ostriker, Russell Owen, A. George Pauls, John Peoples, R. L. Peterson, Donald Petravick, Jeffrey R. Pier, Adrian Pope, Ruth Pordes, Angela Prosapio, Ron Rechenmacher, Thomas R. Quinn, Gordon T. Richards, Michael W. Richmond, Claudio H. Rivetta, Constance M. Rockosi, Kurt Ruthmansdorfer, Dale Sandford, David J. Schlegel, Donald P. Schneider, Maki Sekiguchi, Gary Sergey, Kazuhiro Shimasaku, Walter A. Siegmund, Stephen Smee, J. Allyn Smith, S. Snedden, R. Stone, Chris Stoughton, Michael A. Strauss, Christopher Stubbs, Mark SubbaRao, Alexander S. Szalay, Istvan Szapudi, Gyula P. Szokoly, Anirudda R. Thakar, Christy Tremonti, Douglas L. Tucker, Alan Uomoto, Dan Vanden Berk, Michael S. Vogeley, Patrick Waddell, Shu-i. Wang, Masaru Watanabe, David H. Weinberg, Brian Yanny, Naoki Yasuda, and SDSS Collaboration. The Sloan Digital Sky Survey: Technical Summary. *The Astronomical Journal*, 120:1579–1587, September 2000. ISSN 0004-6256. doi: 10.1086/301513. URL https://ui.adsabs.harvard.edu/abs/2000AJ....120.1579Y. Publisher: IOP ADS Bibcode: 2000AJ....120.1579Y.

[244] Yifan Zhou, Gregory J. Herczeg, Adam L. Kraus, Stanimir Metchev, and Kelle L. Cruz. Accretion onto Planetary Mass Companions of Low-mass Young Stars. *The Astrophysical Journal*, 783:L17, March 2014. ISSN 0004-637X. doi: 10.1088/2041-8205/783/1/L17. URL https://ui.adsabs.harvard.edu/abs/2014ApJ...783L..17Z. Publisher: IOP ADS Bibcode: 2014ApJ...783L..17Z.

[245] Yifan Zhou, Brendan P. Bowler, Kevin R. Wagner, Glenn Schneider, Dániel Apai, Adam L. Kraus, Laird M. Close, Gregory J. Herczeg, and Min Fang. Hubble Space Telescope UV and Hα Measurements of the Accretion Excess Emission from the Young Giant Planet PDS 70 b. *The Astronomical Journal*, 161:244, May 2021. ISSN 0004-6256. doi: 10.3847/1538-3881/abeb7a. URL https://ui.adsabs.harvard.edu/abs/2021AJ....161..244Z. Publisher: IOP ADS Bibcode: 2021AJ....161..244Z.

[246] Zhaohuan Zhu. Accreting Circumplanetary Disks: Observational Signatures. *The Astrophysical Journal*, 799:16, January 2015. ISSN 0004-637X. doi: 10.1088/0004-637X/799/1/16. URL https://ui.adsabs.harvard.edu/abs/2015ApJ...799...16Z. Publisher: IOP ADS Bibcode: 2015ApJ...799...16Z.

[247] G. Zsidi, C. F. Manara, Á. Kóspál, G. A. J. Hussain, P. Ábrahám, E. Alecian, A. Bódi, A. Pál, and P. Sarkis. Accretion variability from minute to decade timescales in the classical T Tauri star CR Cha. *Astronomy & Astrophysics*, 660:A108, April 2022. ISSN 0004-6361, 1432-0746. doi: 10.1051/0004-6361/202142203. URL https://www.aanda.org/10.1051/0004-6361/202142203.

[248] A. Zurlo, G. Cugno, M. Montesinos, S. Perez, H. Canovas, S. Casassus, V. Christiaens, L. Cieza, and N. Huelamo. The widest Hα survey of accreting protoplanets around nearby transition disks. *Astronomy and Astrophysics*, 633:A119, January 2020. ISSN 0004-6361. doi: 10.1051/0004-6361/201936891. URL https://ui.adsabs.harvard.edu/abs/2020A&A...633A.119Z. ADS Bibcode: 2020A&A...633A.119Z.



I believe we've reached the end of our journey. All that remains is to collapse the innumerable possibilities before us. Are you ready to learn what comes next?

SOLANUM